Evaluating and tuning atomic-scale interactions at interfaces of electrocatalytic and electronic materials through first principles calculations

By

Ellen A. Murray

A dissertation submitted in partial fulfillment of

the requirements for the degree of

Doctor of Philosophy

(Chemical Engineering)

at the

UNIVERSITY OF WISCONSIN-MADISON

2020

Date of final oral examination: 12/15/2020

The dissertation is approved by the following members of the Final Oral Committee:

Manos Mavrikakis, Professor, Chemical & Biological Engineering
Reid C. Van Lehn, Assistant Professor, Chemical & Biological Engineering
Matthew A. Gebbie, Assistant Professor, Chemical & Biological Engineering
Michael S. Arnold, Professor, Materials Science & Engineering

Abstract

Almost every major challenge we face, from developing renewable energy technologies to designing faster and more efficient microelectronics, relies on our ability to design and manufacture new materials that address these challenges. Given the overwhelming amount of design considerations involved in creating these materials, theoretical atomistic modeling can provide key insights into the properties of materials that can be difficult or impossible to ascertain experimentally. Furthermore, the highly parallel nature of theoretical models allows us to rapidly screen for promising materials in a manner that is less time consuming and expensive than in a laboratory. By interfacing atomic-scale models with experiments, we can provide a holistic view of materials properties and effectively design new materials.

In this thesis, we utilize density functional theory (DFT) to examine the catalytic properties of electronic materials on an atomic scale and develop models that allow us to relate nanoscale properties to macroscopic observables used in experiments. In particular, we utilize *ab initio* molecular dynamics (AIMD) to evaluate the catalytic properties the water/electrode interface for Au(100), Au(111), and Pt(111) catalysts towards the oxygen reduction reaction (ORR) in alkaline media. Our holistic approach demonstrates that the catalyst structure/composition, hydrogen bonding from water, and coverage effects from spectator species on the catalyst surface come together to determine the overall activity of these interfaces. Additionally, we present a high-throughput screening study for identifying improved metal-alloy catalysts with improved formic acid oxidation activity. Finally, we utilize DFT calculations to evaluate graphene nanoribbon

growth on Ge(001) with a focus on characterizing the interactions between graphene and the Ge surface.

This work provides several examples of how atomic-scale theoretical modeling can be applied to gain key insights into catalytic materials. We use a holistic approach to modeling a wide range of interactions in both electrocatalysts and electronic material systems to determine catalyst properties. In the end, we show that this approach helps us identify atomic interactions that are necessary to describe the properties of materials.

Acknowledgements

I could not have completed the contents of this thesis without the help and guidance of many individuals in my graduate studies. First and foremost, I would like to thank my advisor, Prof. Manos Mavrikakis, for his support and guidance throughout the course of my graduate work. His creativity, passion for his research, and his work ethic have made a monumental impact on my work, and his encouragement to be bold and think deeply about scientific problems has made me a better researcher.

In addition to my advisor, I would also like to thank many other faculty members at UW-Madison for their guidance both during my studies and outside of research. I would like to thank Prof. James Dumesic, Prof. George Huber, Prof. Michael Arnold, Prof. Reid Van Lehn, and Prof. Matthew Gebbie, for serving on my preliminary exam, fourth year exam, and thesis defense committees. I want to thank Prof. Victor Zavala, Prof. Michael Graham, Prof. Brian Pfleger, Prof. Jennifer Reed, Prof. Chris Brace, and Prof. Laura Albert for their support and mentorship outside of the classroom and research.

During my graduate studies, I have had the opportunity to work with exceptional collaborators at UW-Madison and at other institutions. I want to thank Prof. Michael Arnold, Dr. Robert Jacobberger, and Dr. Austin Way for our fruitful collaborations on examining graphene nanoribbon growth. Much of the work in this thesis focused on alkaline electrocatalysis came from the feedback and support from members of the Center for Alkaline Based Energy Solutions, particularly Prof. Héctor Abruña, Prof. Tomás Arias, Prof. Jin Suntivich, Dr. Paul Mutolo, Prof.

Francis DiSalvo, Prof. Jiye Fang, Prof. Robert DiStasio (Cornell University), Prof. Thomas Mallouk (University of Pennsylvania), Dr. Piotr Zelenay (Los Alamos National Lab), and Prof. Sharon Hammes-Schiffer (Yale University), and the researchers in their groups. I would also like to thank Prof. Vojislav Stamenkovic and Dr. Nenad Markovic for inspiring our studies on the oxygen reduction reaction in alkaline systems. I would also like to thank Prof. Younan Xia and his group for collaborative work performed during my time at UW-Madison.

I am fortunate to have worked with many distinguished undergraduate students, graduate students, and post-doctoral fellows within UW-Madison. I would like to especially acknowledge all of the fellow members of the Surface Science and Catalysis group that I have worked with over the years. I cannot imagine working with a more thoughtful, supportive, and intelligent group of people. The work in these thesis would not be possible without the direct contributions and guidance of Dr. Ahmed Elnabawy, Dr. Sean Tacey, Dr. Roberto Schimmenti, Dr. Benjamin Chen, Prof. Florian Göltl, and Prof. Srinivas Rangarajan. I would also like to thank Prof. Tibor Szilvási, Dr. Thomas Kropp, Dr. Lang Xu, Dr. Duygu Gerceker, Dr. Saurabh Bhandari, Jake Gold, Michael Rebarchik, Trent Wolter, Lisa Je, and Alex von Reuden for their support, insightful scientific discussions, and all of the ridiculous office banter.

I am grateful for all of the support I have received from staff within the Department of Chemical and Biological Engineering, including Russ Poyner, Kate Fanis, Susanne Ely, Kathy Heinzen, Oscar Garcia-Romero, Theresa R. Neisius, Beth Brandl, Michelle Kirch, Mary Heimbecker, Christi Levenson.

I would also like to acknowledge financial support from the U.S. Department of Energy – Office of Basic Energy Sciences (DOE-BES) as well as the Wisconsin Alumni Research

Foundation. This work would also not be possible without computational resources from the National Energy Research Scientific Computing Center (NERSC), Department of Defense High Performance Computing Modernization Program (DOD HPCMP), and the Center for High Throughput Computing (CHTC) at UW-Madison.

Outside of UW-Madison, I am incredibly to have the support of friends like Holly Garrod, Devon Tippit, and Bernard Beecher.

Finally, I would like to thank my family for their support throughout graduate school. In particular, I would like to thank my sisters, Katie and Shannon, my brother, James, my father, Terry, his wife, Val, and my husband, Jordan, for their love, patience, and support.

Table of Contents

List of Tables

List of Figures

Chapter 1: Introduction

1.1 Density Functional Theory for Materials Evaluation and Design

By evaluating and designing new materials, we can address a substantial portion of the challenges that we face as a society, including the need for renewable energy solutions and the demand for faster, more efficient computers. Simply evaluating and screening for improved materials in a laboratory makes the material discovery process incredibly challenging given the overwhelming amount of design considerations involved. Therefore, atomic-scale modeling provides unique opportunities to evaluate the energies and structures of new materials that are inaccessible using experimental measurements. In the field of catalysis, these tools offer a means to evaluate the detailed thermochemistry and kinetics of reactions facilitated by catalytic materials. Furthermore, these insights into the properties of materials can be distilled into key descriptors, which can then be utilized to rapidly screen for improved catalysts and materials.

In the context of heterogenous catalysis, atomistic modeling in the form of density functional theory (DFT) allows us to evaluate the binding strength of reaction intermediates and the activation barriers for all elementary steps in the reaction. By examining the detailed kinetic pathways for a reaction on a range of catalyst surfaces, we can employ linear scaling relationships and Brønsted-Evans-Polanyi (BEP) relationships to reduce dimensionality of our problem.[1–11] Scaling relationships relate the adsorption energies of species that bind to a surface through similar atoms (e.g., oxygen reduction reaction (ORR) intermediates such as OOH*, OH*, and O*), while BEP relationships correlate the activation energy of reactions to the reaction thermochemistry.

After utilizing linear scaling relations and BEP relations, we typically identify a limited number of variables that control the behavior of a catalyst surface. Oftentimes, we identify a number of adsorbate binding energies that dictate the overall activity of a catalyst. According to the Sabatier principle, the ideal catalyst for a reaction should bind adsorbed species with an intermediate strength. In other words, catalysts that bind adsorbates weaker than optimal will have difficulty activating reactants, and catalysts that bind adsorbates stronger than optimal will be quickly poisoned and covered by adsorbates. By using DFT calculations, we can then rapidly screen for catalysts that have optimal binding energies (or whatever descriptor we are interested in) for a given reaction.

This framework afforded to researchers through atomic-scale modeling has provided detailed mechanistic insights for a wide range of reactions, including the oxygen reduction/oxygen evolution reactions,[12–17] the hydrogen oxidation/hydrogen evolution reactions,[18–20] the water-gas shift reaction,[21–23] ammonia synthesis,[24,25] methanol synthesis,[26–28] synthesis-gas conversion,[29–31] and many other reactions. These studies provide insights into catalytic materials that cannot be achieved experimentally, and therefore can be used in conjunction with experiments to fully evaluate catalyst performance. Furthermore, these insights have also provided a foundation on which to rapidly screen for improved catalysts using atomistic models that can identify new catalysts in a manner that is faster and cheaper than what can be achieved in a laboratory alone.

Here, we present an outline of the work that is discussed in this thesis. This work focus on utilizing first-principles DFT calculations to evaluate the electrocatalytic activity of solid/aqueous interfaces, screen for improved electrocatalysts, and evaluate epitaxial graphene growth on germanium.

1.2 Catalytic Materials for Fuel Cells

To address rising global temperatures, we need to dramatically reduce greenhouse gas emissions that lead to global warming. Over the last 150 years, the largest source of greenhouse gas emissions from human activities in the United States comes from burning fossil fuels for electricity, heat, and transportation.[32] Therefore, we need to design renewable energy alternatives for each of these sectors. One especially promising technology that utilizes renewable fuels is fuel cells, which could dramatically reduce our carbon footprint in the transportation, backup power, and portable power sectors. A fuel cell is an electrochemical device that oxidizes hydrogen (or a fuel containing hydrogen) at the anode and reduces oxygen at the cathode to generate a current, and they are the most efficient devices for extracting energy from fuels. For comparison, a gasoline engine in a typical car has an energy efficiency of less than 20% under normal driving conditions, while fuel cells can generate electricity at efficiencies of up to 60%.[33] Using hydrogen as a fuel source, fuel cells produce only water as a biproduct. If we utilize carbon-containing fuels, such as methanol or formic acid, fuel cells will generate stoichiometric amounts of CO_2. However, if we source these fuels from biomass or other renewable means, we can capture the CO_2 the fuel cells emit to create a closed-cycle process where we recapture any CO_2 we generate.

Two major obstacles stand in the way of commercializing fuel cells. The most significant is the cost of producing fuel cells, which often utilize expensive materials, particularly for the catalysts. The easiest way to bring down the cost of fuel cells is to utilize fuel cell architectures where we can readily use cheaper and more abundant materials. Alkaline fuel cells can utilize a much broader range of materials compared to acidic fuel cells, including many cheaper alternative catalytic materials.[34] However, the best performing alkaline fuel cells often utilize Pt, which makes these fuel cells prohibitively expensive and negates the advantage of using the alkaline fuel cell

architecture. While researchers have made some advances in developing more active and cheaper catalysts, including Mn-Co spinel catalysts for the anode of alkaline fuel cells that outperform Pt by many metrics,[35] we still have ample opportunities to optimize the performance of catalysts used in alkaline fuel cells.

Ideally, we could apply well-established reactivity descriptors to screen for improved catalysts for the oxygen reduction reaction (ORR) and the hydrogen oxidation reaction (HOR), which take place at the cathode and anode of alkaline fuel cells, respectively. We expect that the ideal catalyst has an intermediate binding strength of oxygenates and hydrogen, for the ORR and the HOR, respectively. However, Au(100), which weakly binds oxygenates, is one of the most active ORR catalysts in alkaline media, and the HOR is two orders of magnitude slower in alkaline versus acidic environments. These findings show that other factors, besides the intrinsic binding strength of an adsorbate to a catalyst, can influence the activity of electrocatalysts. For both the ORR and HOR, water has been shown to play a major role in determining the activity of electrode/solvent interfaces.[36,37] In this thesis, we evaluate the role of water in alkaline electrochemistry using *ab initio* molecular dynamics simulations, focusing on the ORR in alkaline media. In Chapter 3, we evaluate the role of water in catalyzing the ORR on Au(100). We show that the interactions between water, potential-dependent surface reconstructions, and adsorbed reaction intermediates at the water/Au(100) interface can lead to an unexpectedly active ORR catalyst. In Chapter 4, we extend our analysis into the ORR in alkaline media by evaluating the impact of water on the reactivity of Au(111) and Pt(111) surfaces. In Chapters 5 and 6, we further analyze the potential-dependent water structures that form on Au(100) and Pt(111), respectively, and examine how adsorbed OH* impacts the structure of water on both surfaces.

In addition to the cost of the components used in fuel cells, the other major challenge that stands in the way of commercializing fuel cell technologies is the difficulty of adapting to a hydrogen economy. Practically speaking, hydrogen gas is difficult to store, and we do not have an infrastructure that supports generating, moving, and storing hydrogen. Therefore, a great deal of research has investigated other liquid fuel alternatives that contain hydrogen, such as methanol,[38–44] ethanol[45–49], dimethyl ether,[50–52] and formic acid[53–61]. In Chapter 7, we employ DFT calculations to rapidly screen transition metal alloyed catalysts for improved activity towards formic acid electrooxidation.

1.3 Optimizing Materials for Microelectronics

Over the past few decades, integrated circuits have become cheaper and more powerful, giving rise to more advanced computing capabilities (including the high-performance computing clusters that we used for the calculations in this thesis). With each new generation of microchips, microelectronic manufacturers have managed to increase the density of silicon-based transistors used within the microchips by making the transistors smaller and more sophisticated. However, as silicon-based technologies have begun to reach their fundamental physical limits as these transistors become smaller, silicon will need to be replaced by alternative materials with high charge carrier mobility and the potential for further miniaturization. One such material that is currently under consideration is graphene, a 2D carbon material which exhibits excellent charge and thermal conduction.[62–65] Extended graphene sheets are semi-metallic and contain no band gap, so they cannot be used in semiconducting logic. However, by reducing the width of a graphene sheet to form graphene nanoribbons (GNRs) we can induce a band gap within graphene,[66] allowing GNRs to be utilized in semiconductor logic, photonics, and sensing applications.[67–69] GNRs with

armchair edges have been predicted to have the largest band gaps,[70,71] and a technologically-relevant band gap can be induced in GNRs when they have smooth, armchair edges and are restricted to 10 nm or less in width.[72,73]

A promising bottom-up approach for producing narrow GNRs with armchair edges was discovered by Jacobberger et al., who found that chemical vapor deposition (CVD) of methane and hydrogen on Ge(001) causes GNRs to grow on the Ge surface.[72] This technique produces high-aspect ratio GNRs with smooth armchair edges and widths below 5nm.[74] The GNRs synthesized using this method also have superior charge transport properties compared to others in the literature, with an on/off conductance ratio of up to 2×10^4 and an on-state conductance of 5 μS.[75] However, this methodology had several problems that hindered the growth of well-ordered arrays of GNRs that would be necessary in microelectronic applications. The main concerns were that the GNRs (i) grow in random locations on the Ge(001) surface, (ii) are polydisperse due to varying nucleation times during the growth process, and (iii) grow in both Ge$\langle 110 \rangle$ directions, meaning that the obtained GNRs are rotated 90° from each other.[72,76] In Chapter 8 and 9 of this thesis, we show a collaborative effort between experiments and theory aimed at evaluating how GNRs grow on Ge(001) and optimizing the growth process to address the above problems. In Chapter 8, we discuss growing GNRs on vicinal Ge surfaces, which introduce step edges into the Ge(001) surface that anchor GNRs to the surface and cause them to grow in a uniform direction. In Chapter 9, we utilize graphene seeds to control the position and orientation of GNRs on the Ge(001) and discuss the diffusion of graphene precursor species to growing GNRs. In Chapter 10, we provide a theoretical study aimed and evaluating the graphene/Ge(001) interface to determine the fundamental interactions that control the orientation of graphene seeds on Ge(001) and the

structure of GNR edges based on interactions with the Ge substrate.

Chapter 2: Research Design and Methods

2.1 Introduction

In this chapter, we provide a brief overview of the computational methods used in the studies presented in this work. The descriptions provided here introduce density functional theory (DFT), the role of DFT in catalysis, and how we adapt DFT models for electrocatalytic materials.

2.2 Density Functional Theory

2.2.1 The Schrödinger Equation

Research on the nanoscale often requires a firm knowledge of both the structure and energy of ensembles of atoms or molecules. At this length scale, matter obeys the laws of quantum mechanics. Therefore, we can apply first principles to determine this information by solving the time-independent Schrödinger equation:

$$\hat{H}\psi = E\psi \tag{2.1}$$

where $\hat{H}$ is the Hamiltonian operator and ψ is the set of wavefunctions describing the eigenstates of a system. For each wavefunction, ψ_n, there is an associated eigenvalue, E_n, that describes the energy of that wavefunction. The form of the Hamiltonian operator is system-dependent, and there are several famous examples, like a particle in a box or a harmonic oscillator, where the Hamiltonian is simple enough for us to solve the Schrödinger equation exactly.

However, most atomistic systems are comprised of multiple nuclei and electrons, which makes the Hamiltonians for such systems far too complex to evaluate analytically. Consequently,

we utilize several approximations to simplify atomistic systems. Because nuclei are far heavier than electrons (with the mass of an electron being 1800 times smaller than that of a proton or neutron), we assume that electrons respond to changes in their environment much more rapidly than nuclei. As a result, we can apply the Born-Oppenheimer approximation, which allows us to split our atomistic systems into a nuclei component and an electron component. This allows us to fix the positions of nuclei in our atoms and then solve the equations that govern electron motion to extract the lowest energy configuration of electrons, i.e., the ground state. By varying the positions of the nuclei in each atom, we can calculate the electronic ground-state energy as a function of the position of an atom. This function is known as the adiabatic potential energy surface of an atomic system. After applying the Born-Oppenheimer approximation, the Hamiltonian of an atomistic system comprised of N electrons and multiple nuclei interacting with one another is:

$$\widehat{H} = -\frac{\hbar^2}{2m}\sum_{i=1}^{N}\nabla_i^2 + \sum_{i=1}^{N}V(\boldsymbol{r_i}) + \sum_{i=1}^{N}\sum_{j<i}U(\boldsymbol{r_i}, \boldsymbol{r_j}) \tag{2.2}$$

where $\hbar$ is the reduced Planck constant, m is the mass of an electron, r_i corresponds to the spatial coordinates of the electron i, $V(\boldsymbol{r_i})$ is the interaction between the nuclei and the electron i, and $U(\boldsymbol{r_i}, \boldsymbol{r_j})$ is the interaction between electrons i and j. The three terms in this expression correspond to, in order, the kinetic energy of each electron, the interaction energy between each electron and a collection of nuclei, and the interaction energy between different electrons. The challenge in solving this form of the Hamiltonian largely arises from the electron-electron interaction term, which quickly becomes far too complex to solve even for small numbers of electrons. Over the years, several methods have been developed to obtain approximate solutions to this problem, including Hartree-Frock, Coupled Cluster, and Møller-Plesset perturbation theories. However,

DFT has emerged as one of the most widely adopted methods of evaluating the Schrödinger equation due to its computational efficiency ($\sim O(N^3)$).

2.2.2 Simplifying the Problem with Electron Density

The field of DFT originated with two mathematical theorems proposed by W. Kohn and P. Hohenberg and a set of equations derived by W. Kohn and L. J. Sham. Rather than attempting to evaluate the Schrödinger equation by solving for the electronic ground-state wavefunction, which contains $3N$ variables, they proposed that one could instead evaluate the ground-state electron density, which only contains 3 dimensions. This concept serves as the first theorem proposed by Hohenberg and Kohn:

> *Theorem 1: The ground-state energy from the Schrödinger equation is a unique functional of the electron density, $\rho(\boldsymbol{r})$.*

While the first Hohenberg-Kohn theorem rigorously proves that a one-to-one mapping exists between the ground-state wavefunction and the ground-state electron energy of a system that can be used to solve the Schrödinger equation, this theorem does not tell us what form the functional takes. The second Hohenberg-Kohn theorem defines the most important property that this functional must have:

> *Theorem 2: The electron density that minimizes the energy of the overall functional is the true electron density corresponding to the full solution of the Schrödinger equation.*

In other words, if we knew the identity and form of the true functional, we would be able to vary the electron density until we minimized the electronic energy. This would provide us with

both the true minimum ground-state energy and ground-state electron density that corresponds to the solution from the Schrödinger equation. Kohn and Sham demonstrated that the electron density, $\rho(\boldsymbol{r})$, can be determined from the individual wavefunctions from each electron, $\psi_i(\boldsymbol{r_i})$:

$$\rho(\boldsymbol{r}) = 2\sum_{i=1}^{N} \psi_i^*(\boldsymbol{r_i})\psi_i(\boldsymbol{r_i}) \tag{2.3}$$

where $\psi_i^*(\boldsymbol{r_i})$ denotes the complex conjugate of wavefunction $\psi_i(\boldsymbol{r_i})$. Critically, Kohn and Sham also demonstrated $\rho(\boldsymbol{r})$ could be calculated by solving a set of Schrödinger-like equations involving only a single electron. These equations, known as the Kohn-Sham equations, have the form:

$$\left[-\frac{\hbar}{2m}\nabla^2 + V(\boldsymbol{r}) + V_H(\boldsymbol{r}) + V_{XC}(\boldsymbol{r})\right]\psi_i(\boldsymbol{r}) = E_i\psi_i(\boldsymbol{r}) \tag{2.4}$$

where $-\frac{\hbar}{2m}\nabla^2$ corresponds to the kinetic energy, $V(\boldsymbol{r})$ corresponds to the electron-nuclei interaction, $V_H(\boldsymbol{r})$ corresponds to the Hartree potential (representing the Coulombic repulsions between an electron and the total electron density), and $V_{XC}(\boldsymbol{r})$ corresponds to the exchange-correlation potential (a catch-all term that describes all quantum mechanical effects that are not included in the other terms). While there are also kinetic energy and electron-nuclei interaction terms in the Schrödinger equation, the other two terms differ between the two equations. The Hartree potential, $V_H(\boldsymbol{r})$, can be defined as:

$$V_H(\boldsymbol{r}) = e^2\int \frac{\rho(\boldsymbol{r'})}{|\boldsymbol{r}-\boldsymbol{r'}|}d^3\boldsymbol{r'} \tag{2.5}$$

where *e* is the elementary charge of an electron. The Hartree potential includes an unphysical self-

interaction term because it describes the interaction between an electron and the electron density for which that electron is a part of. A correction for this self-interaction error, and several other effects, are lumped together in the exchange correlation energy, $E_{XC}(\boldsymbol{r})$. The exchange correlation potential, $V_{XC}(\boldsymbol{r})$, is defined as:

$$V_{XC}(\boldsymbol{r}) = \frac{\delta E_{XC}(\boldsymbol{r})}{\delta \rho(\boldsymbol{r})} \tag{2.6}$$

As of today, we only know the detailed functional form of $E_{XC}(\boldsymbol{r})$ for a uniform electron gas, and $V_{XC}(\boldsymbol{r})$ has only been analytically derived for this case. For most applications in surface science today, we typically utilize the generalized gradient approximation (GGA)[77] to evaluate $V_{XC}(\boldsymbol{r})$. In this thesis, we utilize the Perdew-Wang 1991 (PW91) functional,[78] the Perdew-Burke-Ernzerhof (PBE) functional,[79] and revised Perdew-Burke-Ernzerhof functional with Pade Approximation (RPBE).[80] Additionally, we compare the efficacy of various exchange correlations and van der Waals corrections in describing molecular adsorption on Ni(111) in Appendices A and B.

To solve the Kohn-Sham equations to calculate $\rho(\boldsymbol{r})$, we need to define the Hartree potential, and to define the Hartree potential, we need to know $\rho(\boldsymbol{r})$. Therefore, we must employ an integrative approach to evaluate the Kohn-Sham equations that utilize the following algorithm:

1. *Select an initial guess for the electron density.*
2. *Solve the Kohn-Sham equations using the initial guess for the electron density to find the single-particle wave functions.*
3. *Calculate the electron density defined by the Kohn-sham single particle wave functions as determined in step 2.*

4. *Compare the new calculated electron density to the initial electron density. Based on the outcome of this comparison, update the electron density and repeat steps 1-4 until a self-consistent solution is reached.*

In this work, we utilize the Vienna *Ab Initio* Simulation Package (VASP)[81,82] to evaluate the Kohn-Sham equations to approximate the solutions to the Schrödinger equation for catalytic systems of interest.

2.3 The Role of DFT in Heterogeneous Catalysis

2.3.1 Modeling the Catalyst Structure

In this thesis, we utilize DFT to determine the atomistic structures and energies relevant to describing the properties of catalytic materials. We focus our discussion on heterogenous catalysts in the solid phase that catalyze reactions where the reactants are in the gas or liquid phase. These solid catalysts are comprised of a bulk material where the surface of the material is exposed to reactants, and different facets of the material can be exposed at the surface (an example of an fcc metal with the (111) and (100) facets exposed is shown in Fig. 2.1). Because these the surface atoms for each facet have different coordination environments, we expect that the structure of atoms at the surface will make a difference in the catalytic activity. Therefore, heterogenous catalysis research often focuses on characterizing properties of the facets that we expect to be most abundant in catalyst particles or facets that might have beneficial properties for a given reaction. To this end, we characterize solid catalytic surfaces using “slab” models where we represent the surface using infinite, periodic unit cells with one exposed facet. Starting with this catalyst model, we then study the thermodynamics of reaction intermediates and kinetics of elementary steps that occur on these catalyst surface models.

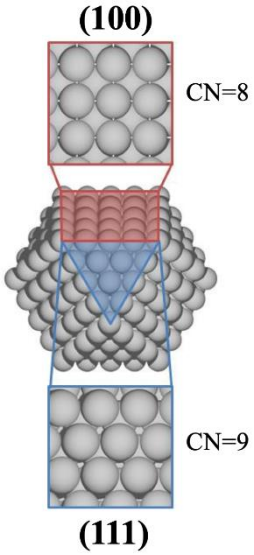

Figure 2.1: Schematic showing the close-packed (111) and open (100) facets of a metal nanoparticle. CN refers to coordination number of surface atoms.

2.3.2 Reaction Thermochemistry: Binding Energies and Reaction Energies

The first step in heterogeneously catalyzed reactions involves the reactant(s) adsorbing to the surface of the catalyst. Once adsorbed, the reactant can undergo a range of bond-breaking/bond-forming steps that lead to the final product(s). Thus, the interaction strengths and binding structures of reaction intermediates adsorbed to a catalyst surface play a critical role in determining the reaction rate and the selectivity of a catalyst. We define the binding energy, BE_X, as the interaction strength between an adsorbate, X, and a catalyst surface as:

$$BE_X = E_{slab+X^*} - E_{slab} - E_{X(gas)} \tag{2.7}$$

where * denotes that a reaction intermediate is adsorbed on a catalyst surface, E_{slab+X^*} is the total energy of a system comprised of a catalyst surface and adsorbed X, E_{slab+X^*} is the total energy of a catalyst surface slab, and $E_{X(gas)}$ is the total energy of X in the gas phase. Negative values indicate a favorable interactions between an adsorbate and a catalyst surface, and the more negative

the binding energy is, the stronger the adsorbate binds to the surface. When using DFT calculations to describe catalytic surfaces, we typically study multiple potential adsorption configurations (i.e., we consider multiple binding sites and structures) to determine the most energetically favorable configurations. Overall reactions are comprised of multiple elementary reaction steps that describe each bond-breaking or bond-forming step in a reaction network. We can utilize the binding energies of adsorbates involved in an elementary step to calculate the corresponding change in internal energy, ΔE_{rxn}, for that step:

$$\Delta E_{rxn} = \sum_{i \in products} BE_{i^*} + E_{i(gas)} - \sum_{j \in reactants} BE_{j^*} + E_{j(gas)} \quad (2.8)$$

Oftentimes, we are interested in calculating the heat of reaction, ΔH_{rxn}, rather than just ΔE_{rxn}. The two quantities are related by ΔH_{rxn}= ΔE_{rxn} + PV. Typically, the PV (where P is pressure and V is volume) term is negligible compared to the internal energy term, and we approximate ΔH_{rxn} as ΔE_{rxn}. A negative value of ΔH_{rxn} corresponds to an exothermic reaction while a positive value corresponds to an endothermic reaction.

2.3.3 Vibrational Frequencies and Calculating Entropy

DFT-derived vibrational frequencies provide critical information that helps connect DFT calculations with experiments. In particular, calculated vibrational frequencies can be directly compared to frequencies obtained from experimental spectroscopic techniques. Furthermore, the vibrational entropy, S_{vib}, makes up a portion of the total entropy of a system, which is critical for calculating the Gibbs free energy of a species. To calculate vibrational frequencies, we assume that gas-phase and adsorbed species act as quantum harmonic oscillators. We can calculate the harmonic frequencies by diagonalizing the mass-weighted Hessian matrix, which provide us the

frequencies and normal modes. We can derive the second derivatives of the energies using a finite-difference approximation. By displacing the position of the atoms by a small step size from their minimum energy configuration, we can determine the energy of these perturbed structures.

These vibrational modes can be utilized to calculate the zero-point energy (ZPE) of a system, calculated as:

$$ZPE = \frac{h}{2}\sum_{i=1}^{n} \nu_i \tag{2.9}$$

where h is the Planck constant, n is the number of vibrational modes, and ν_i is the i^{th} frequency.

Using statistical mechanics, we can then determine the entropy of both gas-phase species and adsorbates bound to a catalyst surface. For gas-phase species, the entropy, S^{gas}, is comprised of the following terms:

$$S^{gas} = S_{trans}^{3D} + S_{rot} + S_{vib} \tag{2.10}$$

where S_{trans}^{3D} is the three-dimensional translational entropy, S_{rot} is the rotational entropy, and S_{vib} is the vibrational entropy based on calculated vibrational frequencies. We calculate S_{trans}^{3D} as:

$$S_{trans}^{3D} = R\left\{ln\left[\left(\frac{2\pi m k_B T}{h^2}\right)^{1.5}\frac{k_B T}{P}\right] + 2.5\right\} \tag{2.11}$$

where m is the molecular mass of the species, $k_B$is the Boltzmann constant, T is the absolute temperature, and R is the gas constant. We calculate S_{rot} for either a linear molecule, S_{rot}^{lin}, as:

$$S_{rot}^{lin} = R\left[\ln\left(\frac{8\pi^2 I k_B T}{\sigma h^2}\right) + 1\right] \tag{2.12}$$

or a non-linear molecule, $S_{rot}^{non-lin}$, as:

$$S_{rot}^{non-lin} = R\left[\ln\left(\frac{k_B T}{h}\right) - \ln(\sigma) - 0.5\ln\left(\frac{I}{\pi}\right) + 1.5\right] \tag{2.13}$$

where I is the moment of inertia and σ is the symmetry factor for the species. Finally, we calculate S_{vib} as:

$$S_{vib} = R\sum_{i=1}^{n}\left[ln\left(1 - e^{-\frac{h\nu_i}{k_B T}}\right)\right] + R\sum_{i=1}^{n}\frac{h\nu_i}{k_B T}\left(\frac{e^{-\frac{h\nu_i}{k_B T}}}{1 - e^{-\frac{h\nu_i}{k_B T}}}\right) \tag{2.14}$$

Unlike gas-phase species, the translational and rotational vibrational modes of adsorbed species are replaced by frustrated modes that are separated before diagonalizing the Hessian matrix but are treated as vibrational modes in entropy calculations.[83] After calculating the entropy of a species, the Gibbs free energy of a reaction step can be calculated as $\Delta G_{rxn} = \Delta H_{rxn} - T\Delta S_{rxn}$.

2.3.4 Reaction Kinetics: Transition-State Theory and Activation Energy Barriers

During each elementary step in a reaction, the species involved in that step undergo a transformation from the initial state to the final state via a transition state. When we consider the potential energy surface for a reaction, the initial and final states are found in local minima on the surface. The transition state represents a saddle point on the potential energy surface that corresponds the highest energy along the reaction coordinate. Most importantly, the transition state energy of an elementary step gives us critical information about the kinetics of the step. From transition state theory, we can determine the rate constant for an elementary step, k, which is

expressed as:

$$k = \frac{k_B T}{h} \exp\left(-\frac{\Delta G^{\ddagger}}{k_B T}\right) \tag{2.15}$$

where $\Delta G^{\ddagger}$is the free energy difference between the transition state and the initial state.

In this thesis, we utilize the climbing-image nudged elastic band method (CI-NEB)[84] to determine the transition states for elementary steps in reactions. For this method, we first define the initial and final states involved in an elementary step before interpolating a series of discrete intermediate images along the reaction coordinate that connect the two states. We use seven images for CI-NEB calculations in this work. Each image in a CI-NEB calculation is connected to adjacent images through "elastic bands" with defined spring constants. The DFT energies and structures of the intermediate images are then simultaneously optimized, and the forces that act parallel and perpendicular to the bands are evaluated. Once all the forces fall below a predetermined cutoff, we can then select the image corresponding to the highest energy state along the reaction coordinate as the transition state for the elementary step. We can confirm that this image is indeed the transition state by calculating the vibrational frequencies of the transition state; the transition state will have a single imaginary frequency along the reaction coordinate. Using the energy of this transition state, we can then determine the activation energy barrier, E_a, for a step, which is the difference in energy between the initial state and final state. $\Delta G^{\ddagger}$ can then be calculated by calculating the entropy of the transition state.

2.4 Adapting DFT Models for Electrocatalysis

A significant portion of this thesis focuses on electrochemical reactions and evaluating the

nature of electrocatalytic active sites. In this work, we use theoretical methods to evaluate electrochemical systems where the applied potentials are referenced to the reversible hydrogen electrode (RHE). The RHE measures the absolute potential drop across the surface (relative to the standard hydrogen electrode (SHE), defined at pH = 0, T = 298.15 K, P_{H2} = 1 atm) and applies a correction term for deviations in pH:

$$U_{RHE} = U_{SHE} - k_B T ln(10) pH/e \tag{2.16}$$

where U_{RHE} is the applied potential relative to the RHE and U_{SHE} is the applied potential relative to the SHE.

To evaluate electrochemical reactions using DFT, we account for how the chemical potential of a proton/electron pair changes as we change the applied potential using the computational hydrogen electrode (CHE).[17] The CHE assumes that at 0 V vs SHE, hydrogen in the gas-phase is in equilibrium with protons and electrons:

$$\frac{1}{2} H_2 \leftrightarrow H^+ + e^-$$

Therefore, the chemical potential of a proton/electron pair ($\mu_{H^+} + \mu_{e^-}$) at standard conditions is then defined as:

$$\mu_{H^+} + \mu_{e^-} = \frac{1}{2} G_{H_2} - eU_{SHE} - k_B T ln(10) pH = \frac{1}{2} G_{H_2} - eU_{RHE} \tag{2.17}$$

where G_{H_2} is the Gibbs free energy of H_2 in the gas phase. Moving to more positive applied potentials causes the chemical potential of a proton/electron pair to have more negative values, thus causing oxidation reactions to become more exergonic. By instead moving to more negative

applied potentials, the chemical potential of a proton/electron pair moves to more positive values, thus causing reduction reactions to become more exergonic.

Oftentimes, we assume that the primary driving force for charge transfer reactions is the change in the chemical potential of a proton/electron pair and that changing the applied potential does not impact the binding energies or adsorption structures on the surface. This assumption is often reasonable when screening for improved catalysts, because evaluating how the applied potential impacts adsorbates on the surface can be a costly endeavor. However, there are cases where we need to evaluate how adsorbate energies vary as we alter the applied potential. In this thesis, we evaluate the role of applied potential using the double-reference method (DRM).[85,86] In this approach, we include either an implicit or explicit solvent layer to evaluate both solvation effects and effects from the potential drop across the solvated layer. Because VASP utilizes a conventional canonical ensemble to model electrons in a DFT calculation, the number of electrons is always constant in a given calculation. Therefore, we change the applied potential in our calculations by selecting the number of electrons within the metal layer of our catalyst surface. To maintain a neutral supercell, we then compensate the charge with a uniform background countercharge in our simulation. We can then evaluate adsorption structures at a range of applied potentials. Using the DRM, one can then calculate the workfunction of the solid/liquid interface, which can then be referenced to the workfunction of the SHE:

$$U_{SHE} = -(\emptyset_{interface} + \emptyset_{H_2/H^+}) \tag{2.18}$$

where $\emptyset_{interface}$ is the calculated workfunction across the interface in eV and $\emptyset_{H_2/H^+}$ is the workfunction of the H_2/H^+ couple in eV at standard conditions. The calculated value of $\emptyset_{H_2/H^+}$

ranges from 4.4-4.8 eV,[87] and we take the average value of 4.6 eV for our work. Because changing the number of electrons in our simulation changes the energy in the DRF, we also correct our calculated energies:

$$E_{corr} = E + \int_0^q \overline{\langle V_{tot} \rangle}\, dQ + \; q\phi_{interface} \tag{2.19}$$

where E_{corr} is the corrected energy, E is the potential energy, q is the charge added/removed from the unit cell, and $\overline{\langle V_{tot} \rangle}$ is the average electrostatic potential across the unit cell. We model the role of an applied potential in unit cells where we do not add or remove electrons (therefore modeling the point of zero charge (PZC)), in unit cells where we add electrons, and unit cells where we remove electrons. We can then use the energies from each potential to calculate the quadratic relationship between energy and applied potential:

$$E(U) = \; -\frac{1}{2} C\big(\langle U_{SHE} \rangle - \; \langle U_{pzc} \rangle\big)^2 + \langle E_{pzc} \rangle \tag{2.20}$$

where C is the capacitance of the system, U_{pzc} is the potential of zero charge vs SHE and E_{pzc} is the energy at the pzc.

The largest implication from modeling the applied potential across a surface is that we can consider both the role of the absolute applied potential (which is essentially the applied potential relative to the SHE) and the pH separately.

Chapter 3: Interfacial Water Structures on Gold Electrodes Lead to Increased Oxygen Reduction Rates in Alkaline Media

3.1 Introduction

The future of advanced energy-storage solutions relies on our ability to comprehend the fundamental interactions that occur at electrified solid/liquid interfaces. Water, in particular, is ubiquitous throughout many of these electrochemical interfaces, and altering the structure or composition of the solid phase and/or modifying the applied potential across the interface impacts molecular orientations and the hydrogen bonding network within the water layer. Although interfacial water structures at electrode interfaces are notoriously difficult to probe, researchers have devoted significant efforts both experimentally and computationally to elucidate water structures at electrified surfaces.[37,88–94] These potential-dependent water structures play a key role in the overall structure of the electric double layer (EDL), which includes solvated ions neighboring the surface in the outer Helmholtz plane (OHP) and specifically adsorbed species on the electrode surface in the inner Helmholtz plane (IHP).[95] Taken together, the electrode surface composition and solvated structures within the double layer can both play a role in influencing reactions occurring within the IHP.[37,96,97] However, trends in catalytic activity are often explained with simple activity descriptors that neglect the complexity of the EDL, such as the binding energy of reaction intermediates to a surface under vacuum.

Nonetheless, binding energy descriptors based on the Sabatier principle have successfully rationalized activity trends for many reactions, including the oxygen reduction reaction (ORR).[16,17,35,98–103] Accordingly, the optimal catalyst for the ORR should have an intermediate binding energy of ORR intermediates (O*, OH*, or OOH*). Catalysts that bind oxygenates too

strongly (e.g., Ir, Pd[16,17,104]) readily adsorb and dissociate O_2 but cannot effectively remove oxygenates from the surface. Alternatively, surfaces that bind oxygenates too weakly cannot activate O_2. One such metal that binds oxygenates weakly is Au,[105] which produces low ORR currents in acidic media because Au catalysts only partially reduce oxygen due to weak oxygenate binding. Astoundingly, Au(100) has long been recognized as one of the most active catalysts for the ORR in alkaline media. This perplexing finding on Au(100) is further confounded by a potential-dependent pathway preference that is unlike any other catalyst. ORR polarization curves (Fig. 3.1) on single crystals in 0.1 M KOH indicate that the onset potential for the $4e^-$ pathway ($O_2 + 2H_2O + 4e^- \rightarrow 4OH^-$) on Au(100) is ~0.9-1.0 V/RHE, but the generated current markedly decreases at ~0.6-0.7 V/RHE when the $2e^-$ pathway ($O_2 + 2H_2O + 2e^- \rightarrow H_2O_2 + 2OH^-$) becomes active.[36] Complicating matters further, Au(100) undergoes a well-known reconstruction from a (1×1) to hexagonal (hex) surface during anodic sweeps. However, this reconstruction occurs over a broader potential range than the transition in reduction kinetics, indicating that the transition alone cannot account for the change in ORR activity.[106]

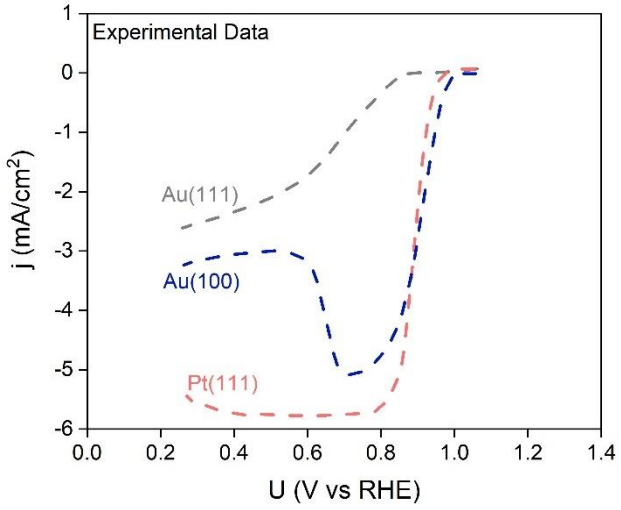

Figure 3.1: Polarization curves for the ORR in 0.1 M KOH on Au(111) (grey), Au(100) (blue), and Pt(111) (pink). Data adapted with permission from ref. 36.

This puzzling behavior suggests that other factors, such as the pH- and potential-dependent structure of the EDL, can also play a role in ORR activity. Indeed, Staszak-Jirkovský et al. have shown that the ORR is structure-sensitive on Au catalysts only in the presence of water, with Au(100) being far more active than Au(111).[36] This finding suggests that structure-function relationships for the ORR on Au surfaces could be governed by structure-sensitive water configurations. In this case, the authors proposed that surface-structure-dependent "activated complexes" between water and spectator OH* place water in a configurationally favorable geometry to transfer protons to adsorbed oxygenates.[36,107] Theoretical studies have suggested that stabilizing OOH* through hydrogen bonding with spectator OH*[108] or an increased electric field from the alkaline environment[109] are the keys to increasing ORR kinetics on Au(100) in alkaline conditions. However, the role of water on the molecular level that leads to this surprising result is still unknown.

In this study, we use a combination of static density functional theory (DFT) calculations and *ab initio* molecular dynamics (AIMD) simulations to determine the role of interfacial water on ORR activity on Au(100). We investigate three different catalyst active site models that account for the potential-induced (1×1)-hex surface reconstruction on Au(100) and show that in the absence of water, none of these reconstructions alone promote high ORR activity. By explicitly including interfacial water within AIMD simulations, we demonstrate that structure-sensitive water configurations form at the electrochemical interface between hexagonally reconstructed Au and water. These water structures stabilize ORR intermediates on Au(100), producing an unexpectedly active catalyst.

3.2 Results

3.2.1 Static, Unsolvated DFT Calculations

We start our analysis by evaluating the native activity of Au(100) surface reconstructions present under the potential range relevant for the ORR by utilizing static, unsolvated DFT calculations. During the anodic sweep for the ORR, the Au(100) surface (Au(100)-(1×1)) reconstructs, first forming an Au(100) surface with additional rows of Au atoms (Au(100)-AR) and then forming a hexagonal structure on the top layer of the surface (Au(100)-hex).[110,111] The transition between these reconstructions is highly sensitive to pH and adsorbates on the surface,[110,112] and the surface reconstructs over a broad potential range[106] as the surface shifts from being positively to negatively charged.[113] The optimized geometries of the Au(100)-(1×1), Au(100)-AR, and Au(100)-hex surface models for this study are shown in Fig. 3.2a.

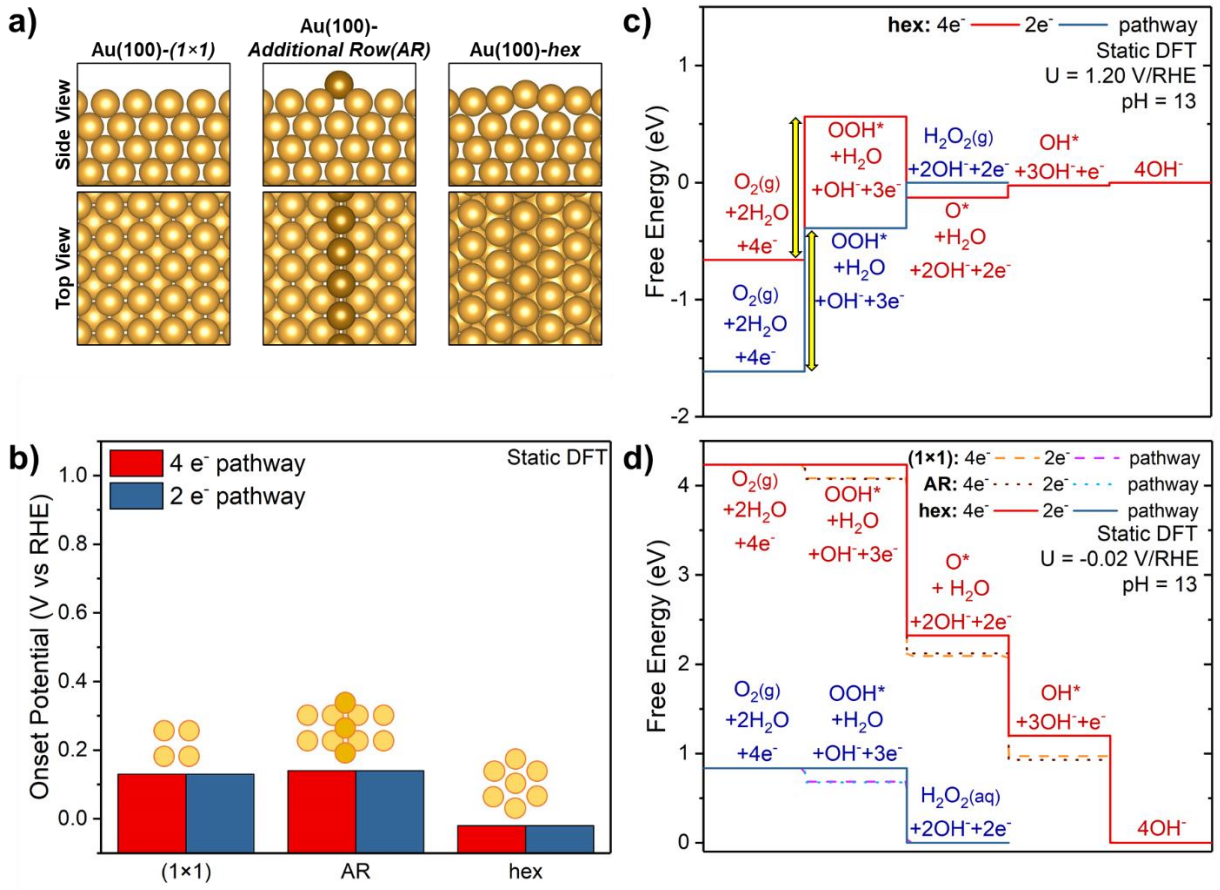

Figure 3.2: (a) Three Au(100) surface reconstructions considered in this study. **(b)** Onset potentials for the ORR on Au(100) surface reconstructions as determined from static DFT calculations. **(c)** Free energy diagram for the ORR on Au(100)-hex at 1.20 V/RHE and pH = 13 as determined from static, unsolvated DFT calculations. The yellow arrows indicate the origin of the overpotential for the ORR (O_2 activation) on Au(100)-hex. **(d)** Free energy diagram for the ORR on all Au(100) surface reconstructions at 0.42 V/RHE (the onset potential for the Au(100)-hex surface and pH=13 as determined from static, unsolvated DFT calculations). Au atoms are shown in gold and Au additional row atoms (AR) are shown in brown.

We calculate the energies of ORR reaction intermediates in their most stable binding sites on each surface (structures shown in Fig. C.1-3) and utilize the computational hydrogen electrode (CHE) formalism to evaluate the influence of the applied potential on the chemical potential of a hydroxide-electron pair.[17] We then calculate the onset potential for reach reaction pathway, defined as the minimum overpotential that must be applied for all proton-electron transfer steps to take place spontaneously ($\Delta G \leq 0$). The full reaction mechanism we consider in this analysis is

shown in Section 3.4. The onset potentials for both ORR pathways as determined from static, unsolvated DFT calculations (Fig. 3.2b) are 0.13 V/RHE for Au(100)-(1×1), 0.14 V/RHE for Au(100)-AR, and -0.02 V/RHE for Au(100)-hex. By examining the free energy diagrams for the ORR, we find at the start of the potential sweep at 1.20 V, (Fig. 3.2c for Au(100)-hex, Fig. C.4a and C.4b for Au(100)-(1×1) and Au(100)-AR, respectively) there is a large thermochemical barrier for activating O_2 to form OOH* on all three surfaces, making O_2 activation the potential-determining step for both the $4e^-$ and $2e^-$ pathways.

These results align with the conventional wisdom that Au does not bind oxygenates strongly enough to activate O_2, making Au a far more inactive catalyst than what it is shown experimentally in alkaline media. Furthermore, the top layer of Au(100)-hex has a 20% higher atom density compared to the other surfaces, imparting a compressive strain that destabilizes OOH* and leads to a particularly low onset potential of -0.02 V/RHE. Fig. 3.2d shows the free energy diagram for the ORR on each surface at -0.02 V/RHE (corresponding figures for Au(100)-(1×1) and Au(100)-AR are shown in Fig. C.4c and C.4d, respectively). At this potential, both the $4e^-$ and $2e^-$ pathways activate as O_2 spontaneously forms OOH*. Because this potential-determining step is shared between the $4e^-$ and $2e^-$ pathways on all three surfaces, the onset potential for the two pathways is the same, which contradicts experiments that demonstrate that the onset potential for the $4e^-$ pathway is ~0.3 V higher than for the $2e^-$ pathway (Fig. 3.1). Therefore, structure-sensitivity of the ORR on unsolvated surface reconstructions alone cannot explain the remarkable ORR activity on Au(100).

3.2.2 AIMD Simulations of Solvated Electrodes

Next, we investigate how interfacial water impacts ORR activity on Au(100). Because

experiments have shown that water behaves as a co-catalyst for the ORR in alkaline media,[36] we performed AIMD simulations that capture the structures and energetics of ORR intermediates in the presence of water. A representative unit cell containing 102 water molecules used for these solvated systems is shown in Fig. 3.3a. To determine the role of applied potential on the structures and energetics of interfacial Au(100) and water, we performed simulations at five potentials (which vary by system): one at the potential of zero charge (pzc), two below the pzc, and two above the pzc. The calculated pzc values for each system are reported in Tables C.1-3.

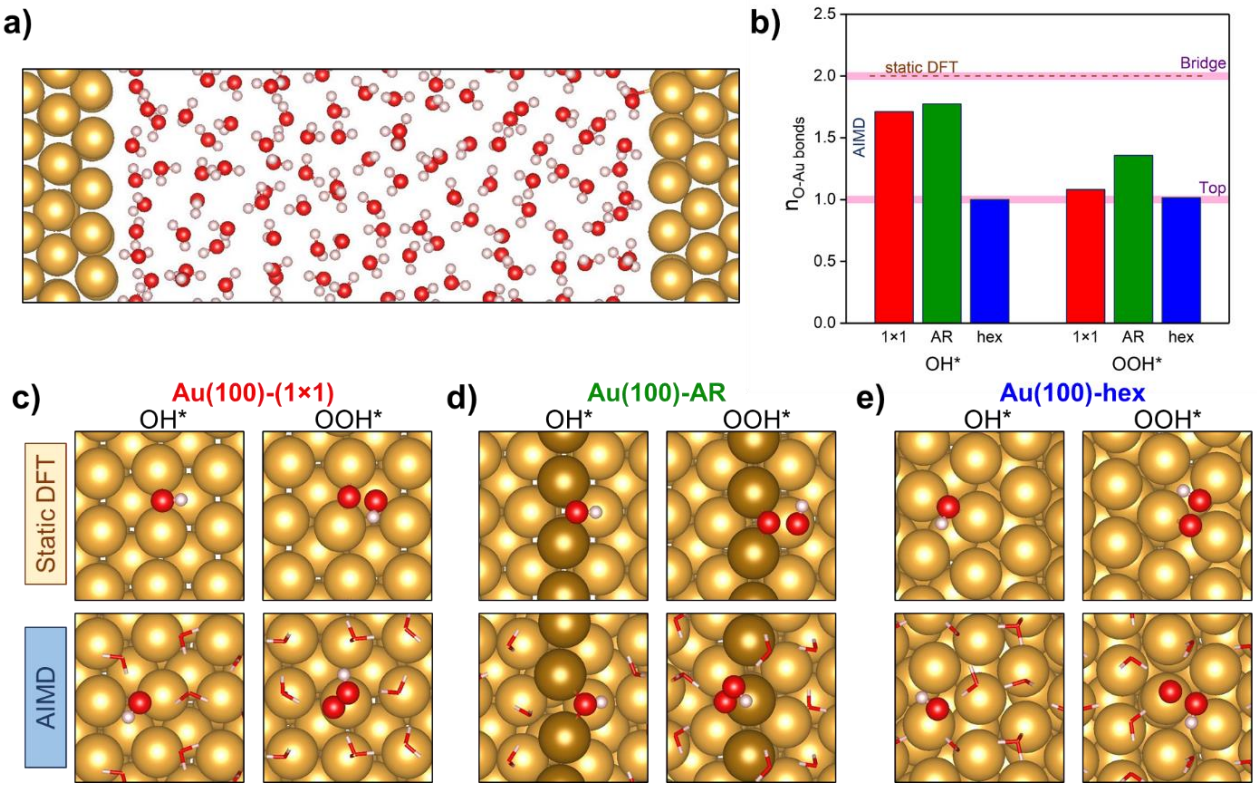

Figure 3.3: Structures of interfacial water and adsorbed ORR intermediates. **(a)** Representative unit cell for Au(100)-(1×1) double-sided surface with interfacial water at the pzc. **(b)** The average number of bonds formed between adsorbates and Au atoms ($n_{O\text{-}Au\ bonds}$) in static DFT calculations (brown dashed line) and AIMD simulations (colored vertical bars). The horizontal pink bars indicate the expected binding based on the number of bonds formed. Representative structures for adsorbates in static DFT and AIMD simulations on **(c)** Au(100)-(1×1), **(d)** Au(100)-AR, and **(e)** Au(100)-hex. Au atoms are shown in gold, Au additional row atoms (AR) are shown in brown, O atoms are shown in red, and H atoms are shown in white. Interfacial water in **(c-e)** are shown as stick models for clarity.

We note several critical differences between the adsorbate structures predicted by unsolvated static DFT and solvated AIMD simulations. First, we found that O* is highly unstable on Au(100) in the presence of water. In our AIMD simulations, O* quickly reacts with water to form OH* before the calculations reach equilibrium. The only conditions where O* was relatively stable were potentials at or above the pzc (~0 V/SHE) on Au(100)-hex. By integrating the first peak of the radial distribution function between O and Au (Fig. C.8), we calculate that O* forms 2.93 bonds with Au on average ($n_{O\text{-}Au\ bonds}$) at the pzc on Au(100)-hex; this shows that Au(100)-hex likely stabilizes O* because the orbitals from O form a tetrahedral geometry that can easily bind to the 3-fold hollow sites on this surface. Therefore, we expect that the coverage of O* should be negligible under reaction conditions and that directly reducing OOH* to OH^- and O* in the $4e^-$ pathway is unlikely. This finding indicates that the overall reaction mechanism for this process is directly affected by interfacial water and that calculations that exclude water cannot capture the energetics of O*. Second, we found that static DFT and AIMD calculations predict different OH* and OOH* binding sites. Static DFT calculations predict that OH* and OOH* bind to bridge sites, while top sites are unstable. Instead, AIMD simulations show that these species move between bridge and top sites. To quantify this behavior, we calculated $n_{O\text{-}Au\ bonds}$ (Fig. 3.3b) for the most energetically favorable static DFT and AIMD simulations at the pzc. Representative binding structures for OH* and OOH* on all three surfaces from static DFT calculations and AIMD calculations at the pzc are shown in Fig. 3.3c-e. Additional figures are shown in Fig. C.5-7. For Au(100)-(1×1) and Au(100)-AR, OH* moves between a bridge ($n_{O\text{-}Au\ bonds} = 2$) and top site ($n_{O\text{-}Au\ bonds} = 1$), and OOH* prefers top sites. On Au(100)-hex, both OH* and OOH* strongly prefer top sites. These results indicate that binding site preferences are not only sensitive to the Au(100) surface structure, but also to interfacial water structures that are excluded in typical DFT

calculations.

Next, we calculated the potential-dependent energies of the solvated intermediates from AIMD simulations, which capture the effect of potential-dependent water structures and surface charge in the energetics of our model. First, we analyzed the binding energy of OH* and OOH* as calculated from the static DFT and AIMD simulations (Fig. 3.4a and Fig. 3.4b, respectively). We find that water within the EDL not only greatly stabilizes both OH* and OOH* by ~0.4-0.8 eV relative to the static DFT calculations under vacuum (at potentials relevant for the ORR), but these water structures also alter each adsorbate's relative binding strength to each of the three surface reconstructions. While OH* is the most stable on Au(100)-AR under vacuum, water leads to OH* being the most stable on Au(100)-(1×1) instead. At potentials relevant for the ORR, we would expect that OOH* would be the least stable on Au(100)-hex. However, water causes OOH* be the most stable on Au(100)-hex, a critical feature for promoting the $2e^-$ pathway.

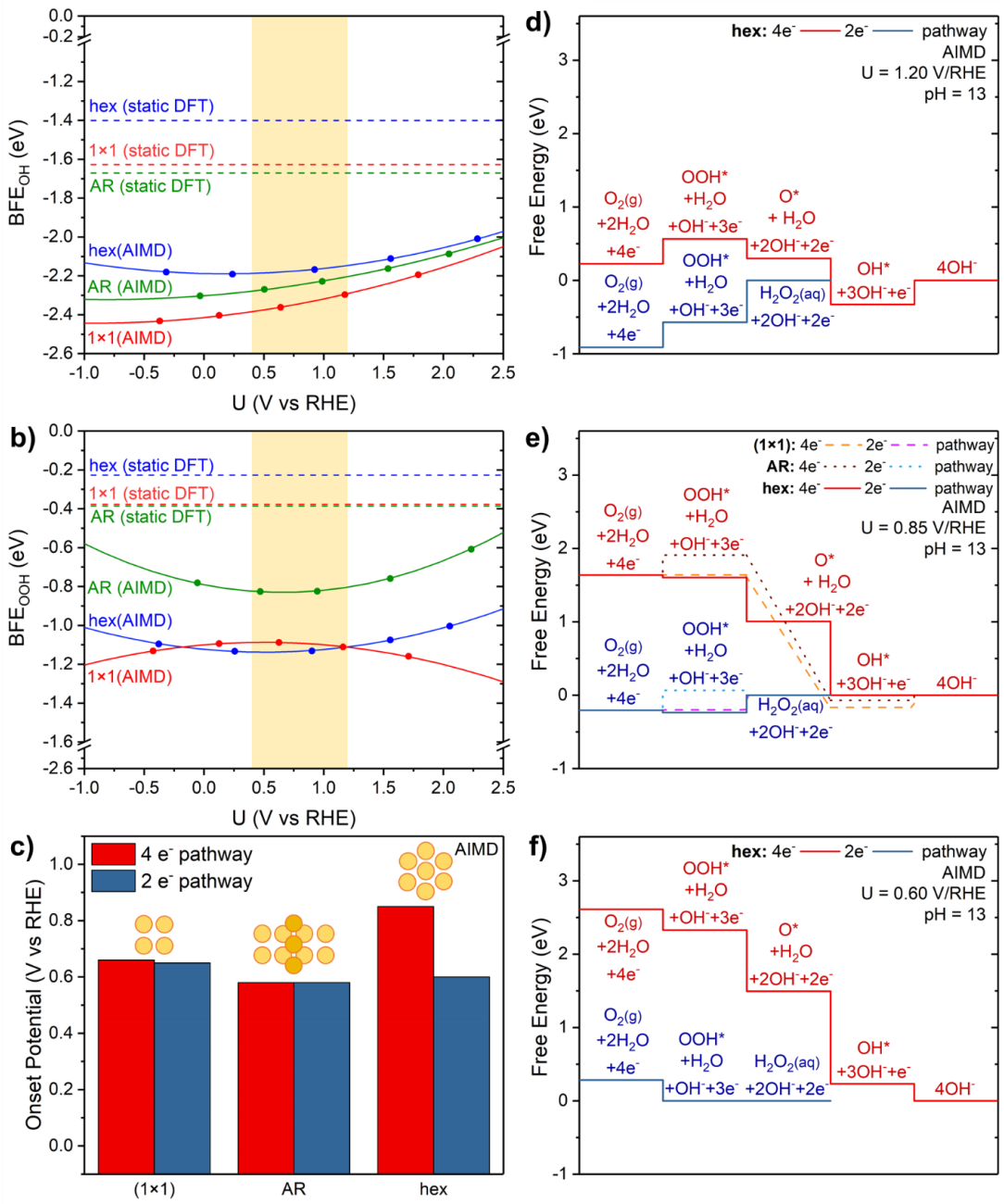

Figure 3.4: Binding free energies of key reaction intermediates and free energy diagrams for ORR from AIMD. Binding free energy of **(a)** OH (BFE_{OH}) relative to OH in the gas phase and **(b)** OOH (BFE_{OOH}) as a function of applied potential as calculated from static DFT and solvated AIMD simulations at pH = 13. Yellow region corresponds to potential region typically considered for ORR. **(c)** Onset potentials for the ORR on Au(100) surface reconstructions as determined from solvated AIMD simulations at pH = 13. **(d)** Free energy diagram for the ORR on the Au(100)-hex surface at 1.20 V/RHE and pH = 13 as determined from solvated AIMD simulations. **(e)** Free energy diagram for the ORR on all Au(100) surface reconstructions at 0.85 V/RHE (the onset potential for the 4e$^-$ pathway on Au(100)-hex at pH=13 as determined from solvated AIMD simulations. **(f)** Free energy diagram for the ORR on the Au(100)-hex surface at a potential of 0.60 V/RHE (the onset potential for the 2e$^-$ pathway) and pH = 13 as determined from solvated AIMD simulations.

Using energetic data from our solvated AIMD model, we then calculated the onset potentials for the $2e^-$ and $4e^-$ pathways on each of the Au(100) surface reconstructions (Fig. 3.4c). Experiments indicate that the $4e^-$ pathway and $2e^-$ pathway should have onset potentials of ~0.9-1.0 V/RHE and ~0.6-0.7 V/RHE, respectively (Fig. 3.1). On Au(100)-(1×1) and Au(100)-AR, the onset potentials for the $4e^-$ and $2e^-$ pathways are essentially identical. In the case of Au(100)-(1×1), the free energy diagrams for the ORR (Fig. C.9a-c) reveal that the potential-determining step for the $4e^-$ pathway is removing OH* from the surface, which is energetically favorable starting at 0.66 V/RHE. However, the onset potential for the $2e^-$ pathway is 0.65 V/RHE, the potential at which reducing OOH* to form H_2O_2 becomes thermoneutral. For Au(100)-AR, the free energy diagrams for the ORR (Fig. C.9d-e) show that the potential-determining step for both the $4e^-$ and $2e^-$ pathway is activating O_2; thus, at 0.58 V/RHE, both pathways become thermodynamically active. Because the onset potentials for the $4e^-$ and $2e^-$ pathways coincide with each other (when they should be ~0.3 V/RHE apart) and do not match experiments, we find no evidence that Au(100)-(1×1) and Au(100)-AR contribute to the impressive ORR activity on Au(100) in alkaline conditions.

Remarkably, the onset potentials for both ORR pathways on Au(100)-hex agree well with experiments (Fig. 3.1).[36] Starting at the beginning of the potential sweep (1.20 V, Fig. 3.4d), the ORR is not active on Au(100)-hex. At 0.85 V/RHE (Fig. 3.4e), the $4e^-$ pathway becomes thermodynamically active when removing OH* from the surface becomes thermoneutral. This calculated onset potential is in excellent agreement with the experimentally determined onset potential of ~0.9-1.0 V/RHE. Furthermore, at 0.85 V/RHE, the $4e^-$ pathway is not active on Au(100)-(1×1) because OH* is over-stabilized by 0.17 eV, and the $4e^-$ pathway is not active on

Au(100)-AR because OOH* is destabilized by 0.27 eV, preventing O_2 activation. As we decrease the potential, OOH* is further stabilized on Au(100)-hex until 0.51 V/RHE (Fig. 3.4b). Although the chemical potential of a hydroxide/electron pair continues to increase, stabilizing OOH* suppresses the $2e^-$ pathway until 0.60 V/RHE (Fig. 3.4f). At 0.60 V/RHE, reducing OOH* to form H_2O_2 becomes thermoneutral. Again, this finding is in excellent agreement with experiments, where the transition from the $4e^-$ pathway to the $2e^-$ pathway occurs at ~0.6-0.7 V/RHE.

Given that static, unsolvated DFT calculations predicted that Au(100)-hex should be the least active of the Au(100) surface reconstructions, our AIMD results are surprising. We would normally predict that compressive strain in the top layer of Au(100)-hex atoms should destabilize adsorbates on the surface.[114] However, because Au(100)-hex stabilizes OOH* more than the other Au(100) surface reconstructions in the potential region that is relevant for the ORR, this reconstruction both enhances O_2 activation (promoting the $4e^-$ pathway at lower overpotentials) and suppresses OOH* reduction to H_2O_2 in the $2e^-$ pathway. Since the Au(100)-hex surface cannot promote high ORR activity without water, we further examined how water stabilizes adsorbed oxygenates through hydrogen bonding. First, we assessed the native hydrogen bonding environments formed by interfacial water and the Au(100) surface reconstructions without adsorbates. Fig. 3.5a-c show the average number of hydrogen bonds formed per water molecule as a function of distance from the surface for each surface reconstruction. We also denote the average distance from the surface for key adsorbates for comparison. For each reconstruction, water near the surface has a peak in the number of hydrogen bonds that are formed. Au(100)-(1×1) and Au(100)-AR, which have near-identical structures besides the additional row of atoms, both form 2.3 hydrogen bonds per water molecule near the surface. However, Au(100)-hex promotes

2.8 hydrogen bonds per water molecule near the surface, and OH* and OOH* are found in positions where water forms the highest density of hydrogen bonds on Au(100)-hex.

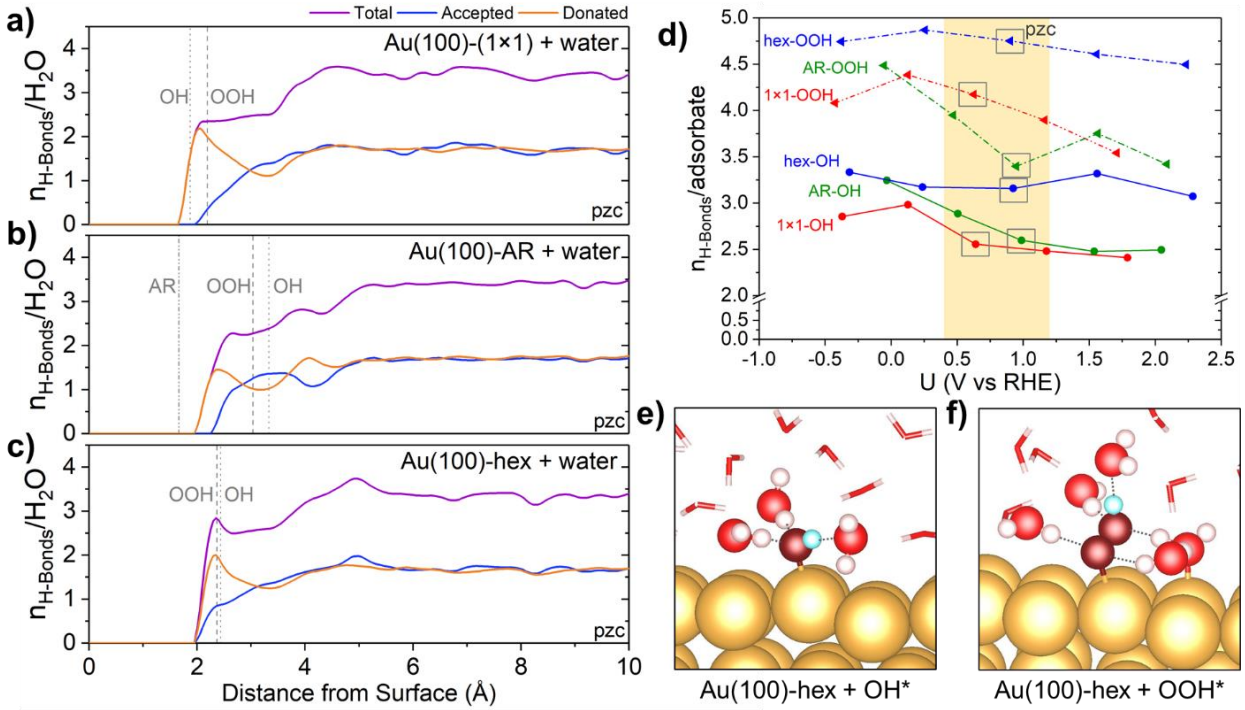

Figure 3.5: Hydrogen bonding environments with and without adsorbates on Au(100) surfaces from AIMD. Average number of hydrogen bonds formed per water molecule ($n_{H\text{-}bonds}/H_2O$) along the surface normal direction (zero corresponds to Au atoms on the top layer of the slab, excluding the AR atoms) for solvated **(a)** Au(100)-(1×1), **(b)** Au(100)-AR, and **(c)** Au(100)-hex surfaces without adsorbates at the pzc. The total $n_{H\text{-}bonds}/H_2O$ is shown purple, the accepted $n_{H\text{-}bonds}/H_2O$ is shown in blue, and the donated $n_{H\text{-}bonds}/H_2O$ is shown in orange. Grey dashed lines and dotted lines indicate the average position of the bottom-most oxygen in OH* and OOH*, respectively, in the most energetically favorable AIMD simulations for reference. A grey dash-dotted line indicates the location of the AR atoms in **(b)**. **(d)** Average number of hydrogen bonds formed between OH* or OOH* and water ($n_{H\text{-}bonds}$/adsorbate) at all potentials studied. Yellow region corresponds to potential region typically considered for ORR. Lines in the figure are to guide the eye. **(e)** Snapshot of OH* and **(f)** OOH*on Au(100)-hex with representative hydrogen bonds (black dashed lines). Au atoms are shown in gold, oxygen atoms are shown in red, and hydrogen atoms are shown in white. Water not hydrogen bonded to adsorbate in **(e)** & **(f)** are shown as stick models for clarity.

Next, we focused our analysis on hydrogen bonding between adsorbates and water by calculating the total number of hydrogen bonds formed on average as a function of applied potential. Detailed plots showing the total number of hydrogen bonds donated to water and accepted by adsorbates are shown in Fig. C.10 for O*, Fig. C.11 for OH*, and Fig. C.12 for OOH*. The total number of hydrogen bonds formed between adsorbates and water ($n_{H\text{-}bonds}$) as a function

of potential for OH* and OOH* are shown in Fig. 3.5d. We found that Au(100)-hex by far promotes the greatest number of hydrogen bonds between adsorbates on the surface and water, even around the pzc for each system (which roughly correspond to potentials where the $4e^-$ pathway is active on Au(100)). At the pzc, OH* forms 3.16 hydrogen bonds and OOH* forms 4.75 hydrogen bonds with water on the Au(100)-hex surface on average, leading to adsorbate-water clusters as shown in the representative images in Fig. 3.5e for OH* and Fig. 3.5f for OOH*.

To further validate the role of hydrogen bonding on this chemistry, we performed static DFT calculations using an implicit water model. Implicit solvent models have gained popularity in heterogenous catalysis research recently[115–118] since they capture the effects of electrostatics, cavitation, and dispersion on the solid/liquid interface. However, such models cannot capture the effects of hydrogen bonding and water orientation. We found that including an implicit solvent did not change the preferred binding sites for adsorbates relative to our unsolvated, static DFT calculations. Free energy diagrams for the ORR on all Au(100) surface reconstructions with implicit water (Fig. C.13) showed that the potential-determining step for both the $4e^-$ and $2e^-$ pathways is activating O_2 on all surfaces. Therefore, the onset potential for both pathways is 0.37 V/RHE on Au(100)-(1×1), 0.21 V/RHE on Au(100)-AR, and 0.11 V/RHE on Au(100)-hex. Like DFT calculations without a solvent, DFT calculations with an implicit solvent are unable to reproduce the experimental onset potentials for the ORR pathways, further highlighting the importance of hydrogen bonding in the ORR on Au(100) in alkaline media.

Considering our results, we propose that the potential-induced Au(100)-hex reconstruction leads to high ORR activity on Au(100) in alkaline environments. Au(100)-hex promotes a hydrogen bonding network that stabilizes other ORR intermediates, particularly OOH*. We

ascribe this behavior to the combined effect of interfacial water and the Au(100)-hex surface symmetry. Although beyond the scope of this investigation, we believe that future work can expand on the role of surface coverage and solvated ions within the EDL and their impact on electrocatalytic reactions.

3.3 Conclusions

In this work, we investigated the role of potential-dependent surface reconstructions and interfacial water on ORR activity on Au(100) in alkaline environments. We show that in the absence of water, Au(100) should not be an active ORR catalyst. By including the effects of interfacial water, we find that Au(100)-hex forms a high density of hydrogen bonds directly at the interface. These interactions stabilize OOH*, making the $4e^-$ pathway more favorable at lower overpotentials and suppressing the $2e^-$ pathway until higher overpotentials. Our study demonstrates that catalytic reactivity descriptors that only consider the solid phase can miss critical details in how the EDL contributes to overall activity. Furthermore, this study lays the groundwork for determining reactivity descriptors that accurately incorporate both the structure of a solid catalytic surface and a liquid solvent.

3.4 Methods

We performed DFT calculations using the Vienna *Ab Initio* Simulation Package (VASP)[81,82] and utilized the revised Perdew-Burke-Ernzerhof functional with Pade Approximation (RPBE)[80] form of the generalized-gradient approximation[78] with D3 van der Waals dispersion corrections.[119] Projector augmented wave (PAW) pseudo-potentials were used to describe electron-ion interactions, and valence electron wavefunctions were expanded using a plane-wave basis set with a 400 eV cutoff energy.[120,121] The surface Brillouin zones of the p(2×5) Au(100) surfaces were sampled via a 4×2×1 Monkhorst-Pack k-point mesh.[122]

For unsolvated calculations, we modeled the Au(100) surface with a six-layer slab with the bottom two layers fixed at the bulk Au lattice constant of 4.173 Å (4.08 Å experimentally[123]). Images of each of the unit cells are shown in Fig. C.14. Repeated images of the surface slab were separated by >13 Å of vacuum in the z-direction. We modeled adsorption on the top layer of the slab and utilized dipole corrections to adjust the electrostatic potential in the vacuum layer accordingly.[124]

For solvated calculations, we modeled the Au(100) surface with a five-layer double-sided slab with the middle layer fixed at the bulk lattice constant. Slabs were separated by ~36.9 Å of water in the z direction. For explicit solvents in AIMD calculations, this water layer contained 102 (Au(100)-(1×1) and Au(100)-hex) or 100 water molecules (Au(100)-AR) for a water density of 1 g/mL (Fig. C.15). For implicit solvents, we utilized a linearized Poisson-Boltzmann model as implemented in VASPsol.[125] We set the relative permittivity of the solvent to 78.4 and the Debye length to 9.61 Å. We modeled symmetric adsorption for all solvated systems and removed 1 water molecule/adsorbate for explicit water simulations.

For this study, we assume that the ORR proceeds through the associative mechanism and that the $4e^-$ pathway (overall: $O_2 + 2H_2O + 4e^- \rightarrow 4OH^-$) can be described by the following steps:

$$O_2 + 2H_2O + 4e^- \rightarrow OOH^* + H_2O + OH^- + 3e^- \quad (1)$$

$$OOH^* + H_2O + OH^- + 3e^- \rightarrow O^* + H_2O + 2OH^- + 2e^- \quad (2)$$

$$O^* + H_2O + 2OH^- + 2e^- \rightarrow OH^* + 3OH^- + e^- \quad (3)$$

$$OH^* + 3OH^- + e^- \rightarrow 4OH^- \quad (4)$$

Alternatively, O_2 can be partially reduced to form hydrogen peroxide in the less desirable $2e^-$ pathway (overall: $O_2 + 2H_2O + 2e^- \rightarrow H_2O_2 + 2OH^-$) described by the following steps:

$$O_2 + 2H_2O + 4e^- \rightarrow OOH^* + H_2O + OH^- + 3e^- \quad (1)$$

$$OOH^* + H_2O + OH^- + 3e^- \rightarrow H_2O_2 + 2OH^- + 2e^- \quad (5)$$

To account for the chemical potential of a hydroxide/electron pair in our calculations, we employed the computational hydrogen electrode (CHE).[17] Briefly, the CHE assumes that at 0 V vs standard hydrogen electrode (SHE) (pH = 0, T=298.15 K, P_{H2} = 1 atm), hydrogen in the gas-phase is in equilibrium with protons and electrons:

$$\frac{1}{2}H_2 \leftrightarrow H^+ + e^-$$

Under these conditions, the chemical potential of a proton/electron pair ($\mu_{H^+} + \mu_{e^-}$) is:

$$\mu_{H^+} + \mu_{e^-} = \frac{1}{2}G_{H_2} - eU_{SHE} - k_B T ln(10) pH \quad (3.1)$$

where G_{H_2} is the Gibbs free energy of H_2 in the gas phase, e is the charge of an electron, U_{SHE} is the applied potential relative to the SHE, k_B is Boltzmann's constant, and T is the temperature (298.15 K). We then assume that at a given pH, water is in equilibrium with a proton and hydroxide pair:

$$H_2O \leftrightarrow (H^+ + e^-) + (OH^- - e^-)$$

Therefore, the relationship between the chemical potential of a hydroxide/electron pair ($\mu_{OH^-} - \mu_{e^-}$) is then:

$$\mu_{OH^-} - \mu_{e^-} = G_{H_2O} - \frac{1}{2}G_{H_2} - eU_{SHE} - k_B T ln(10) pH \tag{3.2}$$

To capture the effect of potential-dependent interactions between the solvent and surface, we utilized the double-reference method (DRM).[85,86] Briefly, the DRM models the EDL at various applied potentials by varying the number of electrons within the metal layer. This charge is compensated using a uniform background countercharge to maintain a neutral supercell. The DRM provides a framework to calculate the workfunction of the solid/liquid interface, which can then be referenced to the workfunction of the SHE:

$$U_{SHE} = -(\emptyset_{interface} + \emptyset_{H_2/H^+}) \tag{3.3}$$

where $\emptyset_{interface}$ is the calculated workfunction across the interface in eV and $\emptyset_{H_2/H^+}$ is the workfunction of the H_2/H^+ couple in eV at standard conditions. The calculated value of $\emptyset_{H_2/H^+}$ ranges from 4.4-4.8 eV,[87] and we take the average value of 4.6 eV. In this work, we report ORR energetics and onset potentials relative to the RHE at pH =13 for comparison with experiments, where $U_{RHE} = U_{SHE} + k_B T ln(10) pH/e$. Since changing the number of electrons in our simulation changes the energy in the DRF, we also correct our AIMD calculated energies:

$$E_{corr} = E + \int_0^q \overline{\langle V_{tot} \rangle}\, dQ + q\phi_{interface} \tag{3.4}$$

where E_{corr} is the corrected energy, E is the potential energy, q is the charge added/removed from the unit cell, and $\overline{\langle V_{tot} \rangle}$ is the average electrostatic potential across the unit cell. We modeled

potentials at a range of -2e to +2e with a step size of 1e, and we calculated the average applied potential using data points collected every 0.1 ps. We used this data to then fit the time-averaged energy and applied potentials for each simulation to a quadratic expression:

$$E(U) = -\frac{1}{2}C\left(\langle U\rangle - \langle U_{pzc}\rangle\right)^2 + \langle E_{pzc}\rangle \tag{3.5}$$

where U_{pzc} is the potential of zero charge, E_{pzc} is the energy at the pzc, and C is the capacitance of the system. Parabolic fits for the free energy of each system are shown in Fig. C.16-18 and in Tables C.1-3 for AIMD calculations and Tables C.4-6 for implicit solvent calculations.

Additional computational details can be found in Section C.1 of the Appendix.

Chapter 4: Determining the Role of Water in the Electric Double Layer on the Oxygen Reduction Reaction on Au(111) and Pt(111) in Alkaline Media

4.1 Introduction

While a great deal of research has focused on developing renewable energy resources, many of these technologies will not be economically or technologically viable without developing new electrocatalysts or tailoring the solid-liquid interface at electrocatalytic surfaces. Despite their monumental importance in determining electrocatalytic activity and selectivity, little is known about the complex interactions between solvents contained within the electric double layer (EDL) and solid electrode surfaces at electrocatalytic interfaces. However, these interactions can determine the overall activity and selectivity of electrochemical reactions that take place at the interface of the two phases.[37,95,97,107,126]

As we showed in Chapter 3, one such system where the interactions between an electrode surface and a solvent dictate the reactivity of that interface is the oxygen reduction reaction (ORR) on Au(100) in alkaline media.[36] According to conventional catalysis wisdom, the ideal catalyst should obey the Sabatier principle (i.e. bind adsorbates with an intermediate strength). By this convention, catalysts that bind oxygenates too strongly (e.g. Ir or Pd[16,17,104]) can readily activate O_2 but are easily poisoned by oxygenates, and catalysts that bind oxygenates too weakly (e.g. Au[105]) struggle to activate O_2 and tend to only partially reduce O_2. In accordance with the Sabatier principle, the best monometallic catalyst with an intermediate oxygenate binding strength is Pt.[17] However, Au(100), which should be a poor ORR catalyst by this convention, is the best monometallic catalyst for the ORR in alkaline media at low overpotentials.[36,106,107,110,127,128] ORR

polarization curves (Fig. 4.1) on single crystals in 0.1 M KOH indicate that the onset potential for the $4e^-$ pathway ($O_2 + 2H_2O + 4e^- \rightarrow 4OH^-$) on Au(100) is ~0.9-1.0 V versus the reversible hydrogen electrode (RHE), but the generated current markedly decreases at ~0.6-0.7 V/RHE when the $2e^-$ pathway ($O_2 + 2H_2O + 2e^- \rightarrow H_2O_2 + 2OH^-$) becomes active.[36] However, the initial onset potential for the ORR on Pt(111) (~0.9 V/RHE) is slightly more negative than on Au(100), making Au(100) a superior catalyst at low overpotentials. Furthermore, Au(111) has a far lower onset potential (~0.8 V/RHE), indicating that this reaction is surface-structure sensitive. These results perplexed researchers for decades until Staszak-Jirkovský et al. showed that the ORR on Au(100) only displays remarkable activity in the presence of small amounts of water, highlighting how the interactions at the solid-liquid surface can greatly impact reactivity.[36]

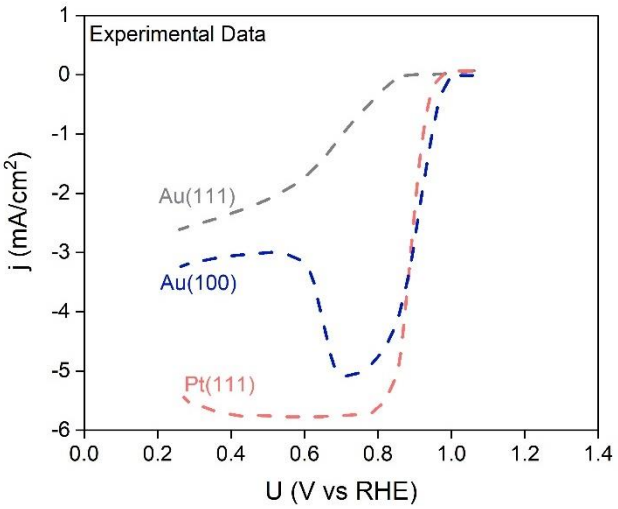

Figure 4.1: Polarization curves for the ORR in 0.1 M KOH on Au(111) (grey), Au(100) (blue), and Pt(111) (pink). Data adapted with permission from ref. 36.

In Chapter 3, our group further examined the interplay between surface structure, surface composition, and solvent effects using *ab initio* molecular dynamics (AIMD) simulations to show that Au(100) is only active in the presence of water. In particular, our results indicated that the potential-dependent hexagonal reconstruction of Au(100) (Au(100)-hex) served as the active site for the ORR and that this surface reconstruction facilitates the formation of a greater number of

hydrogen bonds between ORR intermediates and water. However, our findings still raised additional questions: How does water impact the energy and structure of ORR intermediates on other catalytic surfaces? If the Au(100)-hex surface reconstruction serves as the active site for the ORR on Au(100), why does the hexagonal Au(111) surface also not serve as an effective catalyst? What role, if any, does water play on what should be the optimal monometallic catalyst, Pt(111)?

To answer these questions, we use a combination of unsolvated, static density functional theory (DFT) calculations and solvated AIMD simulations to evaluate the activity of Au(111) and Pt(111) surfaces towards the ORR. For Au(111), we find that the activity of the native Au(111) surface is far lower than that of the native Au(100) surface when we exclude water. When we evaluate the impact of water on the Au(111) surface, we again find that the overpotentials required to drive the ORR on Au(111) are far higher than on Au(100), in agreement with experiments. By examining the native activity of the Pt(111) surface without water, we find that Pt(111) over-binds oxygenates which leads to high ORR overpotentials. When we consider the role of water on ORR activity on Pt(111), we still cannot explain the experimental results. However, by including experimentally relevant coverages of OH* ranging from 2/9 ML to 4/9 ML co-adsorbed OH*, we find a synergetic effect where a combination of spectator OH* and water destabilize oxygenates to produce an effective ORR catalyst and reproduce the experimental onset potentials. For both Au(111) and Pt(111), we find that by including relevant interactions from water and OH*, we can replicate the experimentally determined onset potentials for the ORR on both surfaces and explain the trends in activity for the Au(100), Au(111), and Pt(111) surfaces.

4.2 Methods

4.2.1 First Principles Calculations

We perform static DFT calculations and AIMD simulations using the Vienna *Ab Initio*

Simulation Package (VASP).[81,82] Our calculations utilize the revised Perdew-Burke-Ernzerhof functional with Pade Approximation (RPBE)[80] form of the generalized gradient approximation (GGA) with D3 van der Waals dispersion corrections.[119] We describe electron-ion calculations using projector augmented wave (PAW) pseudo-potentials,[120,121] and valence electron wavefunctions are expanded using a plane-wave basis set with a cutoff energy of 400 eV. The surface Brillion zone of the 3×3 slab models used were sampled using a 4×4×1 gamma centered k-point mesh.

For static, unsolvated DFT calculations, we utilize a 3×3 unit cell with a four-layer slab. The bottom two layers are fixed at the bulk lattice constant of 4.173 Å (4.08 Å experimentally[123]) for Au and 3.950 Å (3.924 Å experimentally[123]) for Pt. Repeated images of each slab are separated by at least 20 Å of vacuum. We model adsorption on one side of the slab and apply dipole corrections in the z-direction.[124] Each structure is relaxed until the forces acting upon each atom are $\leq$ 0.01 eV/Å. We calculate the vibrational frequencies of species using a numerical differentiation of forces using a second-order finite difference approach as determined from diagonalizing the mass-weighted Hessian matrix. All metal atoms in the surface are fixed for vibrational frequency calculations. We calculate the free energy of a species as:

$$G = E_{DFT} + ZPE - TS \tag{4.1}$$

where E_{DFT} is the total energy of a system from DFT, ZPE is the zero-point energy, T is the temperature (298 K), and S is the vibrational entropy.

For AIMD simulations, we model the Au(111) and Pt(111) surfaces with a double-sided slab with seven layers. The middle three layers of the slab are fixed at the calculated bulk lattice

constant for each metal. Au and Pt slabs are separated by 30 and 32 Å of water, respectively, in the z-direction. This water layer contains a total of 68 water molecules for Au and 64 water molecules for Pt in the absence of adsorbates, leading to a total water density of 1 g/mL. For models with adsorbates, we model symmetric adsorption on both sides of the unit cell and remove one water molecule per adsorbate added to maintain a consistent water density.

We perform molecular dynamics simulations using the standard Verlet algorithm to propagate ionic trajectories with a 1 fs time step. To accelerate convergence, we used the mass of deuterium for hydrogen. All simulations were performed in the NVT ensemble at 298 K, and we used a Nosé-Hoover thermostat to control the ionic temperature.[129,130] To extensively sample the configuration space within these simulations, we initialize a series of trajectories starting from a variety of adsorbate coverages and water structure configurations. Each trajectory typically runs for at least a 2 ps equilibrium period and a production period of 10 ps. For systems containing multiple adsorbate binding structures, we use up to 150 ps of data consisting of several trajectories. We calculate the average free energy of a system by calculating the average free energy of the combined trajectories for a given system as:

$$G(T) = \langle E \rangle + 1/\beta(\langle exp(\beta \Delta E) \rangle) \quad (4.2)$$

where β is $1/k_BT$ (k_B is Boltzmann's constant), E is the potential energy, and ΔE is the difference between the average potential energy and the energy in each step.

4.2.2 Modeling the Oxygen Reduction Reaction

For this study, we assume that the ORR proceeds through either the $4e^-$ pathway (overall: $O_2 + 2H_2O + 4e^- \rightarrow 4OH^-$) or the $2e^-$ pathway (overall: $O_2 + 2H_2O + 2e^- \rightarrow H_2O_2 + 2OH^-$).

***ORR on Au(111)*:** Because Au(111) is known to weakly bind oxygenates, we assume that the ORR proceeds through only an associative mechanism where the $4e^-$ pathway can be described with the following steps:

$$O_2 + 2H_2O + 4e^- \rightarrow OOH^* + H_2O + OH^- + 3e^- \quad (1)$$

$$OOH^* + H_2O + OH^- + 3e^- \rightarrow O^* + H_2O + 2OH^- + 2e^- \quad (2)$$

$$O^* + H_2O + 2OH^- + 2e^- \rightarrow OH^* + 3OH^- + e^- \quad (3)$$

$$OH^* + 3OH^- + e^- \rightarrow 4OH^- \quad (4)$$

Alternatively, O_2 can be only partially reduced to form hydrogen peroxide in the $2e^-$ pathway, which is described by:

$$O_2 + 2H_2O + 4e^- \rightarrow OOH^* + H_2O + OH^- + 3e^- \quad (1)$$

$$OOH^* + H_2O + OH^- + 3e^- \rightarrow H_2O_2 + 2OH^- + 2e^- \quad (5)$$

***ORR on Pt(111)*:** On Pt(111), we assume that Pt binds oxygenates strongly enough to proceed primarily though the $4e^-$ pathway, and we consider both an associative and dissociative mechanism. For the associative mechanism, we assume that the ORR proceeds through the following pathway:

$$O_2 + 2H_2O + 4e^- \rightarrow OOH^* + H_2O + OH^- + 3e^- \quad (1)$$

$$OOH^* + H_2O + OH^- + 3e^- \rightarrow O^* \mid OH^* + H_2O + OH^- + 3e^- \quad (6)$$

$$O^* \mid OH^* + H_2O + OH^- + 3e^- \rightarrow OH^* \mid OH^* + 2OH^- + 2e^- \quad (7)$$

$$OH^* \mid OH^* + 2OH^- + 2e^- \rightarrow 4OH^- \quad (8)$$

Unlike the $4e^-$ pathway for the associative mechanism on Au(111), we assume that OOH* dissociates to form O* + OH* rather than O* + OH^- due to how strongly Pt(111) binds oxygenates. We adjust the rest of the reaction mechanism accordingly to allow for this convention. For the dissociative pathway, we assume that the ORR proceeds through the following pathway:

$$O_2 + 2H_2O + 4e^- \rightarrow O^* \mid O^* + 2H_2O + 4e^- \quad (9)$$

$$O^* \mid O^* + 2H_2O + 4e^- \rightarrow O^* \mid OH^* + H_2O + OH^- + 3e^- \quad (10)$$

$$O^* \mid OH^* + H_2O + OH^- + 3e^- \rightarrow OH^* \mid OH^* + 2OH^- + 2e^- \quad (7)$$

$$OH^* \mid OH^* + 2OH^- + 2e^- \rightarrow 4OH^- \quad (8)$$

In our static, unsolvated DFT calculations, we use gas-phase O_2, H_2O, and H_2O_2 for our reference states. The energy of each species is calculated in a 14×15×16 Å box. In our solvated AIMD analysis, we reference gas-phase O_2 and solvated H_2O and H_2O_2 energies. To calculate the solvated energy of H_2O and H_2O_2, we run AIMD simulations in a 14.23×14.23×14.23Å box containing 96 water molecules and 97 water molecules plus H_2O_2, respectively.

4.2.3 Evaluating the Electrochemical Environment

To account for the chemical potential of a hydroxide/electron pair in our calculations, we employ the computational hydrogen electrode (CHE).[17] Briefly, the CHE assumes that at 0 V versus the standard hydrogen electrode (SHE) (pH = 0, T=298 K, P_{H2} = 1 atm), hydrogen in the gas phase is in equilibrium with protons and electrons:

$$½\ H_2 \leftrightarrow H^+ + e^-$$

Under these conditions, the chemical potential of a proton/electron pair ($\mu_{H^+} + \mu_{e^-}$) is:

$$\mu_{H^+} + \mu_{e^-} = \frac{1}{2}G_{H_2} - eU_{SHE} - k_B T ln(10) pH \tag{4.3}$$

where G_{H_2} is the Gibbs free energy of H_2 in the gas phase, *e* is the charge of an electron, and U_{SHE} is the applied potential relative to the SHE. We then assume that at a given pH, water is in equilibrium with a proton and hydroxide pair:

$$H_2O \leftrightarrow (H^+ + e^-) + (OH^- - e^-)$$

Therefore, the relationship between the chemical potential of a hydroxide/electron pair ($\mu_{OH^-} - \mu_{e^-}$) is:

$$\mu_{OH^-} - \mu_{e^-} = G_{H_2O} - \frac{1}{2}G_{H_2} - eU_{SHE} - k_B T ln(10) pH \tag{4.4}$$

To model the electrochemical environment at the interface between the metal surface and water in our solvated AIMD simulations, we utilize the double reference method (DRM).[85,86] The DRM allows us to evaluate the applied potential across the EDL by adjusting the number of electrons within the metal slab. A uniform background charge is then used to counterbalance the excess charge in the slab to maintain a neutral supercell. This method provides a framework to calculate the workfunction across the solid-liquid interface, which we reference to the workfunction of the SHE to determine the applied potential, *U*:

$$U = -(\emptyset_{interface} + \emptyset_{H_2/H^+}) \tag{4.5}$$

where $\emptyset_{interface}$ is the calculated workfunction across the interface in eV and $\emptyset_{H_2/H^+}$ is the work function of the H_2/H^+ couple in eV at standard conditions. The calculated value of $\emptyset_{H_2/H^+}$ ranges from 4.4-4.8 eV,[87] and we use an average value of 4.6 eV for this study. Because changing the number of electrons in our simulation changes the potential energy, we correct our calculated AIMD energies:

$$E_{corrected} = E + \int_0^q \overline{\langle V_{tot} \rangle}\, dQ + q\phi_{interface} \tag{4.6}$$

where E is the potential energy, q is the charge added or removed from the unit cell, and $\overline{\langle V_{tot} \rangle}$ is the averaged electrostatic potential across the unit cell. Since the applied potential fluctuates as adsorbates and the solvent restructure during the simulation, we used an average applied potential calculated using data points collected every 0.1 ps. For each molecular dynamics simulation, we perform calculations at a range of -2e to +2e with a step size of 1e. We omit data points where we could find no stable structures for a given adsorbate. We use this data to then fit the time-averaged energy and applied potentials for each simulation to a quadratic expression that relates the energy stored in a capacitor to the applied potential and capacitance:

$$E(U) = -\frac{1}{2} C\left(\langle U \rangle - \langle U_{pzc} \rangle\right)^2 + \langle E_{pzc} \rangle \tag{4.7}$$

where U_{pzc} is the potential of zero charge (pzc), E_{pzc} is the energy at the pzc, and C is the capacitance formed in the system. The quadratic fits for Au(111) systems are shown in Fig. D.1 (numerical values in Table D.1), and the quadratic fits for Pt(111) systems are shown in Fig. D.2 (numerical values in Table D.2).

4.3 Results and Discussion

4.3.1 Evaluating the Role of Water in the ORR on Au(111)

Our previous work studying the ORR on Au(100) in alkaline media demonstrated that a combination of a hexagonal surface reconstruction (Au(100)-hex) and water leads to impressive ORR activity at low overpotentials and diminished current at high overpotentials. Given that both the Au(100)-hex and Au(111) surfaces share similar hexagonal reconstructions, at least in the top Au layer, we might predict that both surfaces share similar activity. However, prior experimental results have shown that Au(111) does not display the same high ORR activity as Au(100) in alkaline aqueous environments.[36] To further assess the differences between Au(100)-hex and Au(111), we apply a combination of static DFT calculations and solvated AIMD calculations to evaluate the catalytic properties of Au(111) with and without water.

We start our analysis by considering the native ORR activity of the Au(111) surface under a vacuum. To do this, we calculate the energies of 1/9 ML of ORR reaction intermediates (OOH*, O*, and OH*) on the most stable binding sites on the Au(111) surface. We then employ the computational hydrogen electrode (CHE) formalism to determine how adjusting the applied potential impacts the chemical potential of a hydroxide-electron pair.[17] This allows us to determine the minimum overpotential that must be applied for all proton-electron transfer steps in a pathway to occur spontaneously ($\Delta G \leq 0$), which we assign as the onset potential for the pathway. At the beginning of the potential sweep at 1.20 V/RHE (Fig. 4.2a), we find several non-spontaneous steps in both the $4e^-$ and $2e^-$ pathways, and we do not expect to generate a current. Reducing O_2 to form OOH* is particularly unfavorable in both pathways, which aligns with the expectation that noble metals such as Au should have difficulty activating O_2. In fact, Au(111) binds OOH* so weakly that the binding energy of OOH* relative to OOH(g) is positive under a vacuum. To make this

step thermoneutral, we must lower the applied potential to -0.57 V/RHE (Fig. 4.2b), making -0.57 V/RHE the calculated onset potential for the ORR on Au(111) for both the $4e^-$ and $2e^-$ pathways.

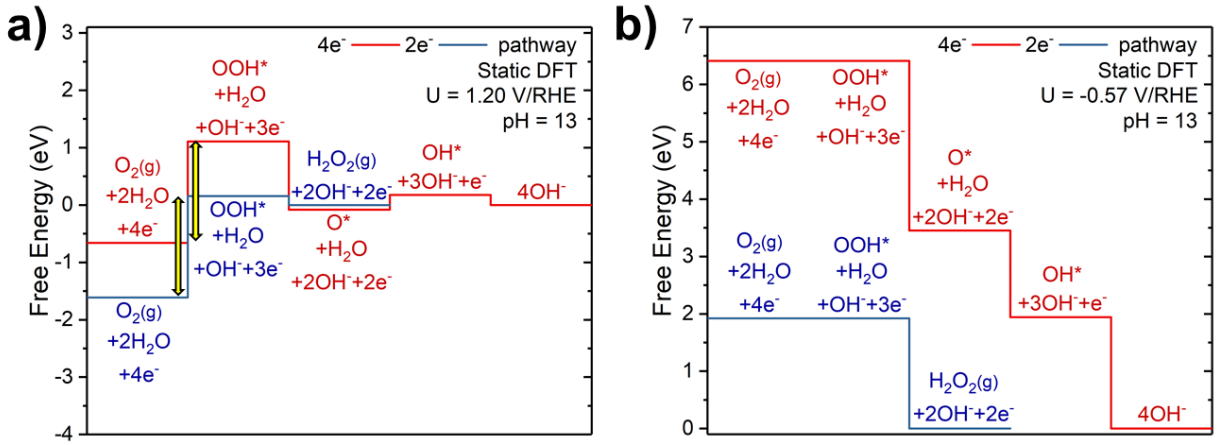

Figure 4.2: Free energy diagrams for the ORR on Au(111) at pH = 13 as determined from static, unsolvated DFT calculations at **(a)** 1.20 V/RHE and **(b)** -0.57 V/RHE (the onset potential for the ORR). The yellow arrows indicate the origin of the overpotential for the ORR (O_2 activation).

As we have shown previously, we expect that the ORR largely proceeds through the $2e^-$ pathway on Au surfaces if all the steps in the $2e^-$ pathway occur spontaneously. Therefore, our static DFT results suggest that we should not generate a significant current from the ORR on Au(111) compared to catalysts that suppress the $2e^-$ pathway due to stronger oxygenate binding, which is in line with experimental results. However, we expect that the onset potential of the ORR on Au(111) should be ~0.8 V/RHE on Au(111) according to experiments. Because our calculated onset potential is over 1.2 V/RHE too negative, this indicates that our model does not capture the interactions necessary to explain the overall ORR activity on Au(111).

Since water can play a dramatic and sometimes unexpected role in ORR behavior, as is the case for Au(100), we then investigate the role of interfacial water on catalyzing the ORR on Au(111). We perform AIMD simulations to capture the structures and energies of water and adsorbates on electrified Au(111) surfaces. A representative unit cell for these calculations

containing 68 water molecules within a 30 Å water layer is displayed in Fig. 4.3a. To account for the role of the applied potential on this system, we perform simulations at five potentials (which vary slightly by system): one at the potential of zero charge (pzc), two below the pzc, and two above the pzc.

We find that unsolvated static DFT calculations and solvated AIMD simulations predict different binding structures and binding energies of adsorbates. As is the case with Au(100), we find that water causes adsorbates to prefer more undercoordinated sites in the presence of water on Au(111). Representative adsorbate binding structures both with and without water for all ORR intermediates on Au(111) are shown in Fig. 4.3b (side views of adsorbates shown in Fig. D.3). In unsolvated DFT calculations, OOH* binds to a top site with the O-O bond laying almost flat on the surface, OH* binds to a bridge site, and O* binds to an fcc hollow site. To evaluate the average binding site of each adsorbate in the presence of water, we calculate the radial distribution function (rdf) between the closest oxygen atom of an adsorbate to the surface and Au from the AIMD trajectories (Fig. D.4). Integrating the first peak of this rdf gives us the average number of O-Au bonds formed between an adsorbate and the surface. We find that OOH* forms 1.05 bonds with Au (binds to top sites) at 0.63 V/RHE and that O* forms 2.36 bonds with Au (binds to hollow sites) at 0.32 V/RHE, indicating that the site preference for these two species does not change in the presence of water. However, we see that OH* forms 1.01 bonds with Au (binds to top sites) in the presence of water at 0.91 V/RHE, showing that the binding preference of OH* changes from a bridge site to a top site when we include solvation effects. We also note that water stabilizes all ORR intermediates on Au(111), thus increasing the binding energy of these adsorbates to the surface over a wide potential range (Fig. 4.3c). This result aligns with our expectation that

hydrogen bonds should form between adsorbates and water that dramatically stabilize all intermediates.

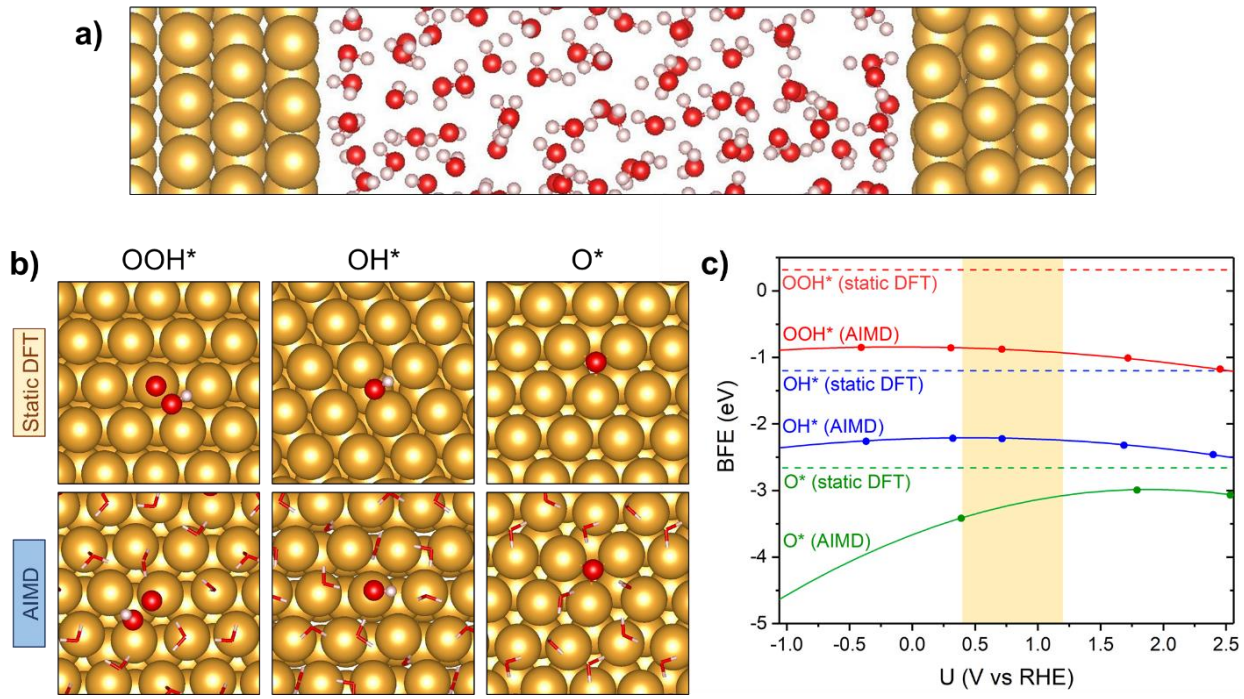

Figure 4.3: (a) Representative unit cell for Au(111) double-sided surface with interfacial water at the pzc. **(b)** Representative structures for adsorbates as seen from atop in static, unsolvated DFT and solvated AIMD simulations on Au(111). Au atoms are shown in gold, O atoms are shown in red, and H atoms are shown in white. Interfacial water molecules are shown as stick models for clarity. **(c)** Binding free energy (BFE) of OOH, OH, and O relative to the gas phase energy of each respective species as a function of applied potential as calculated from static DFT and solvated AIMD simulations at pH = 13.

We then utilize the potential-dependent energies of ORR intermediates on a solvated Au(111) surface in conjunction with the CHE formalism to recalculate the onset potential for the ORR on a solvated Au(111) electrode. At the start of the potential sweep at 1.20 V/RHE (Fig. 4.4a), we find that several steps in both the $4e^-$ and $2e^-$ pathways are non-spontaneous. By moving to more negative potentials, we reach an onset potential of 0.62 V/RHE for both the $4e^-$ and $2e^-$ pathways (Fig. 4.4b). At 0.62 V/RHE, the potential-determining step is reducing O_2 to form OOH*, which is the same potential-determining step that we find in our static DFT calculations. Therefore, we would again expect that we would not generate a significant current from the ORR

on Au(111) compared to catalysts that suppress the 2e$^-$ pathway, in agreement with experiments. Additionally, the calculated onset potential of 0.62 V/RHE from solvated AIMD calculations is in close agreement with the experimental onset potential of ~0.8 V/RHE. To further verify our findings, we compare the relative values of the onset potential for the ORR between Au(100) and Au(111) in alkaline environments. The experimental onset potential for the ORR on Au(111) is about ~0.1-0.2 V/RHE more negative than on Au(100) (Fig. 4.1). Given that our calculated onset potential for the ORR on Au(100) is 0.85 V/RHE using the fully solvated AIMD electrode model (which is also ~0.2 V/RHE more negative than seen experimentally), our models accurately predict the relative difference in onset potentials between solvated surfaces despite predicting absolute onset potentials that are slightly more negative than experimental values.

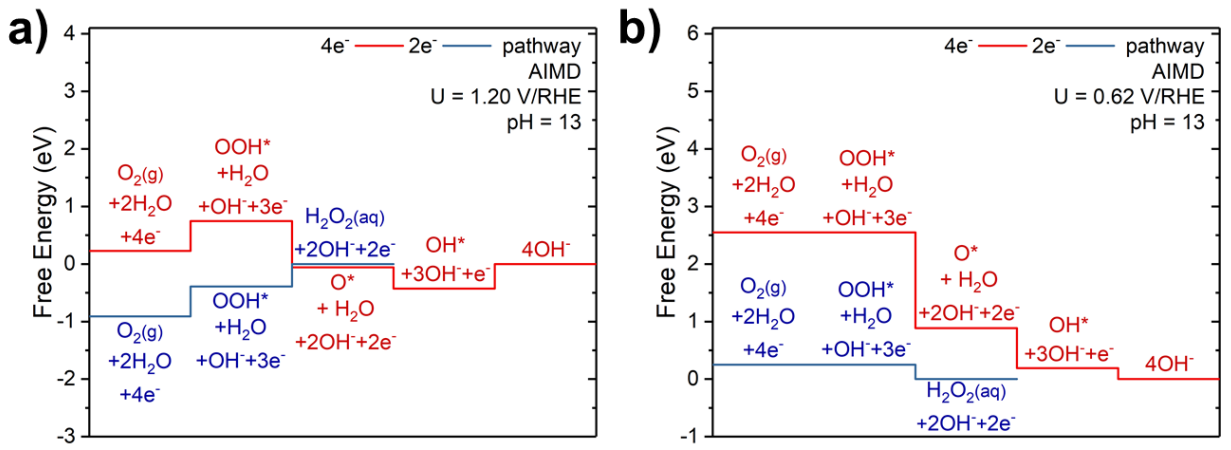

Figure 4.4: Free energy diagrams for the ORR on Au(111) at pH = 13 as determined from solvated AIMD simulations at **(a)** 1.20 V/RHE and **(b)** 0.62 V/RHE (the onset potential for the ORR).

Even though Au(111) and Au(100)-hex surfaces share a similar surface structure, we find that these surfaces do not share the same ability to stabilize ORR intermediates. For Au surfaces to be effective ORR catalysts, they must bind OOH* strongly enough to activate the 4e$^-$ pathway and to prevent OOH* from desorbing as H_2O_2 in the 2e$^-$ pathway, which is precisely how Au(100)-hex catalyzes the ORR at low overpotentials. Without water, neither Au(111) nor Au(100)-hex

effectively catalyzes the ORR due to weak binding of OOH*; however, OOH* has a binding energy of -0.23 eV on Au(100)-hex under vacuum, while we predict that OOH* does not bind to the Au(111) surface. This indicates that electronic differences between Au atoms in the two surfaces could lead to differences in adsorption strength. To further characterize the electronic structure of Au(111) and Au(100)-hex, we calculate the average d-band center for Au atoms in the top layer of each surface. We found that the d-band center for Au(100)-hex is -3.14 eV while the d-band center for Au(111) is -3.03 eV. This positive shift in the d-band center as we move from Au(100)-hex to Au(111) agrees with our finding that Au(100)-hex surface binds adsorbates more strongly.

By adding water, we stabilize all ORR intermediates (most importantly, OOH*) on both Au(111) and Au(100)-hex. As we have shown previously, the Au(100)-hex surface promotes increased hydrogen bond formation in water near the surface compared to other Au(100) surface reconstructions, thus leading to adsorbates being more stabilized on the Au(100)-hex surface. We therefore compare the water structures between the Au(100)-hex and Au(111) surfaces to determine the role that hydrogen bonding from water plays in stabilizing these intermediates. Fig. D.5a shows the average number of hydrogen bonds formed per water molecule as a function of distance from the surface for Au(111) without adsorbates. We also denote the average distance from the surface for key adsorbates for comparison. On transition metal surfaces, water near the surface has a peak in the number of hydrogen bonds formed. Au(111) promotes 2.8 hydrogen bonds per water molecule at this peak, while Au(111)-hex promotes 2.9 hydrogen bonds per water molecule. Additionally, we consider the total number of hydrogen bonds formed between key ORR intermediates and water as a function of applied potential on Au(111) and compare these values to

the values on Au(100)-hex, as shown in Fig. D.5b. We find that OH* forms more hydrogen bonds with water on Au(111) than Au(100), but we do not find a clear trend for OOH*. Nevertheless, we form adsorbate-water clusters on the Au(111) surface that are similar to those on Au(100)-hex, as shown in Fig. D.5c. Overall, we find that the water structures are comparable between Au(111) and Au(100)-hex. However, the additional stabilization effects from water cannot overcome the incredibly weak binding of OOH* to the Au(111) surface due to the electronic structure of surface Au atoms, thus rendering Au(111) as a far less active ORR catalyst than Au(100)-hex.

4.3.2 Evaluating the Role of Water in the ORR on Pt(111)

Next, we evaluate the ORR activity of Pt(111) in alkaline media. According to conventional scaling relationships and the Sabatier principle, Pt(111) should be the most active monometallic catalyst for the ORR. However, Au(100) is the most active monometallic ORR catalyst in alkaline media above ~0.9 V/RHE. Because first-principles calculations provided atomic-level details on what makes Au(100) an active ORR catalyst, our goal is to provide a similar analysis to identify the driving forces of the ORR on Pt(111) for comparison. We start our analysis by calculating the energy of 1/9 ML of ORR intermediates on Pt(111) in their most stable binding sites using static DFT calculations to evaluate the native activity of the Pt(111) surface in the absence of solvent. We again utilize the CHE formalism to calculate the onset potential for the ORR on Pt(111). At the beginning of the potential sweep at 1.20 V/RHE (Fig. 4.5a), the only spontaneous step is reducing O_2 in the dissociative pathway, while all other steps are endergonic. The onset of the ORR on Pt(111) occurs at 0.20 V/RHE (Fig. 4.5b) when reducing O* to OH* becomes thermoneutral; furthermore, the dissociative pathway is more energetically favorable than the associative pathway. Because the experimentally determined onset potential for the ORR in alkaline media is ~0.90 V/RHE (Fig. 4.1), this calculated onset potential of 0.20 V/RHE is far too

negative compared to experiments.

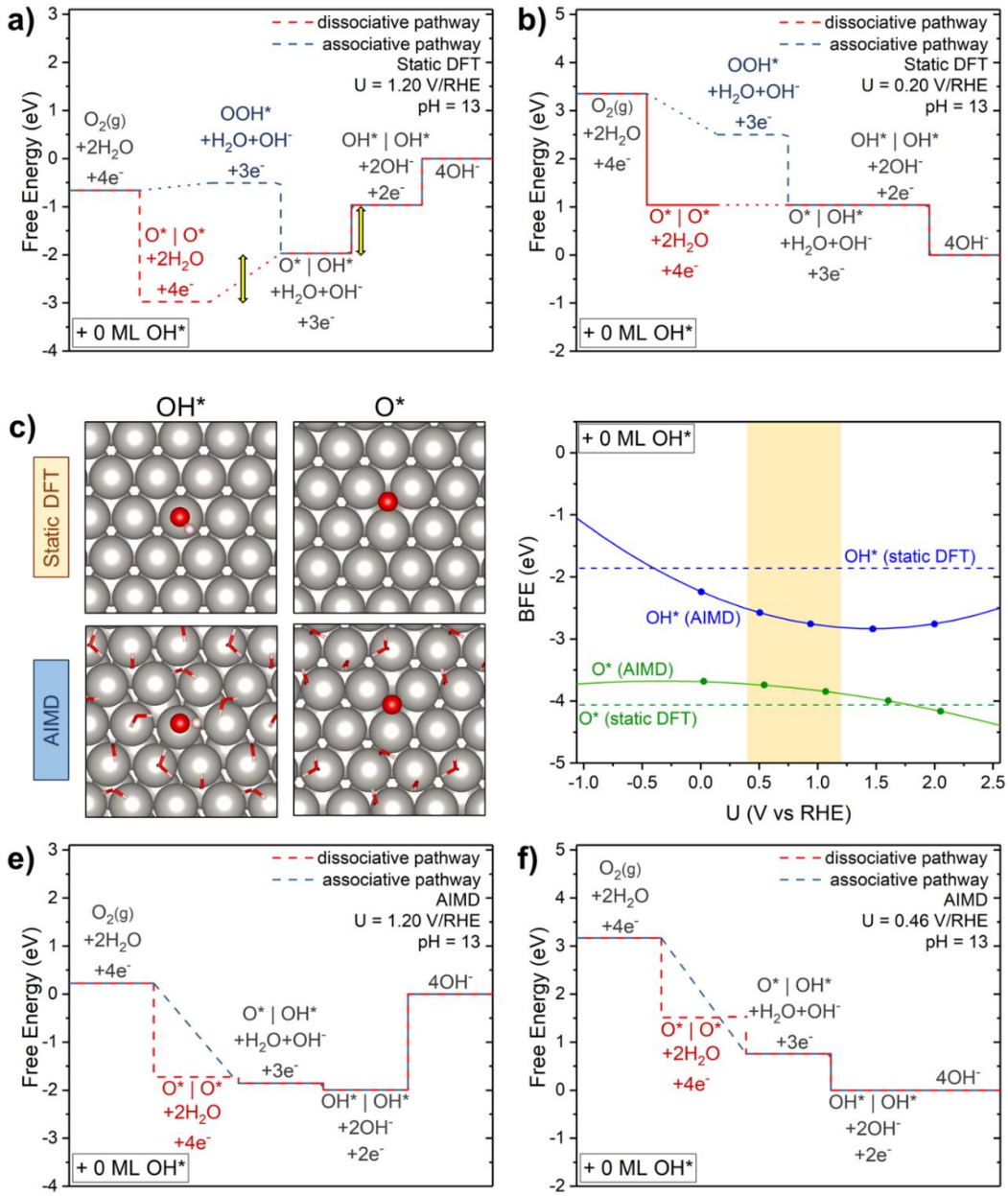

Figure 4.5: Free energy diagrams for the ORR on Pt(111) at pH = 13 and 0 ML co-adsorbed OH* as determined from static, unsolvated DFT calculations at **(a)** 1.20 V/RHE and **(b)** 0.20 V/RHE (the onset potential for the ORR). The yellow arrows indicate the origin of the overpotential for the ORR (O* reduction). **(c)** Representative structures for adsorbates in static, unsolvated DFT and solvated AIMD simulations on Pt(111). Pt atoms are shown in grey, O atoms are shown in red, and H atoms are shown in white. Interfacial water molecules are shown as stick models for clarity. **(d)** Binding free energy (BFE) of OH and O relative to the gas phase energy of each respective species as a function of applied potential as calculated from static DFT and solvated AIMD simulations at pH = 13 and 0 ML co-adsorbed OH*. Free energy diagrams for the ORR on Pt(111) at pH = 13 and 0 ML co-adsorbed OH* as determined from solvated AIMD simulations at **(e)** 1.20 V/RHE and **(f)** 0.46 V/RHE (the onset potential for the ORR).

Again, these results suggest that we need to consider a fully solvated electrode model to evaluate the onset potential of the ORR on Pt(111). We therefore performed AIMD simulations to capture the structures and energies of water and adsorbates on an electrified Pt(111) surface. Like we did for Au(111), we account for the role of the applied potential on this system by performing simulations at five potentials (which vary slightly by system): one at the potential of zero charge (pzc), two below the pzc, and two above the pzc.

Similar to Au(100) and Au(111), adding water changes the structures and energies of adsorbed intermediates on Pt(111). Most notably, OOH* is not stable in any of our solvated simulations and dissociates to O* and OH* in the first few steps of our AIMD simulations. Therefore, we consider a concerted mechanism in the associative pathway where O_2 is directly reduced to O* and OH*. However, unlike Au(100) and Au(111), adding water does not change the preferred binding sites of reaction intermediates. Representative images of adsorbates shown in Fig. 4.5c show that OH* prefers to bind to a top site and O* prefers to bind to an fcc hollow site regardless of the presence of water. Unlike Au surfaces, we find that including water does not always stabilize reaction intermediates. By considering the binding energy of adsorbates under vacuum and with water (Fig. 4.5d), we find that OH* is stabilized on the solvated electrode surface in the potential region relevant for the ORR while O* is destabilized on the solvated electrode surface. These results demonstrate that solvation effects may not always stabilize oxygenates, especially on charged surfaces.

Next, we use the potential-dependent energies of ORR intermediates on a solvated Pt(111) surface in conjunction with the CHE formalism to recalculate the onset potential for the ORR on Pt(111). At the beginning of the potential sweep at 1.20 V/RHE (Fig. 4.5e), O* is more destabilized

on the solvated electrode surface than under vacuum, thus preventing O* reduction to OH* from being the potential-determining step as was seen in our unsolvated, static DFT calculations. We find that the onset potential for the ORR on a solvated Pt(111) electrode is 0.46 V/RHE (Fig. 4.5f). Because OH* is highly stabilized on this solvated surface, the potential-determining step for the ORR is instead reducing OH* to OH^-. Under these conditions, both the dissociative and associative pathways are energetically favorable. Since the onset potential for the ORR on Pt(111) is ~0.9 V/RHE, the calculated onset potential of 0.46 V/RHE is still far too negative compared to experiments. These results indicate that this solvated electrode model does not fully capture all the interactions that dictate ORR activity on Pt(111).

Pt surfaces are known to strongly bind oxygenates, which we clearly see in our calculations. This indicates that the Pt(111) surface is likely covered with oxygenates that interact with adsorbates involved in the ORR. Staszak-Jirkovský et al. used cyclic voltammetry (CV) to estimate the coverage of oxygenates on Pt(111) near the onset of the ORR in alkaline media.[36] They estimated that ~0.5 ML of OH* populates the surface at these conditions. Therefore, we considered how 2/9-4/9 ML of co-adsorbed OH* impacts the energies of 1/9 ML O* and 1/9 ML OH* on the surface. We repeated both our static, unsolvated DFT calculations and our AIMD solvated electrode simulations with varying coverages of co-adsorbed OH*. We then utilized these energies to calculate the differential free binding energy of O* and OH* at each coverage of co-adsorbed OH*. Representative images of the most stable surface configurations of O* and OH* with and without water are shown in Fig. 4.6.

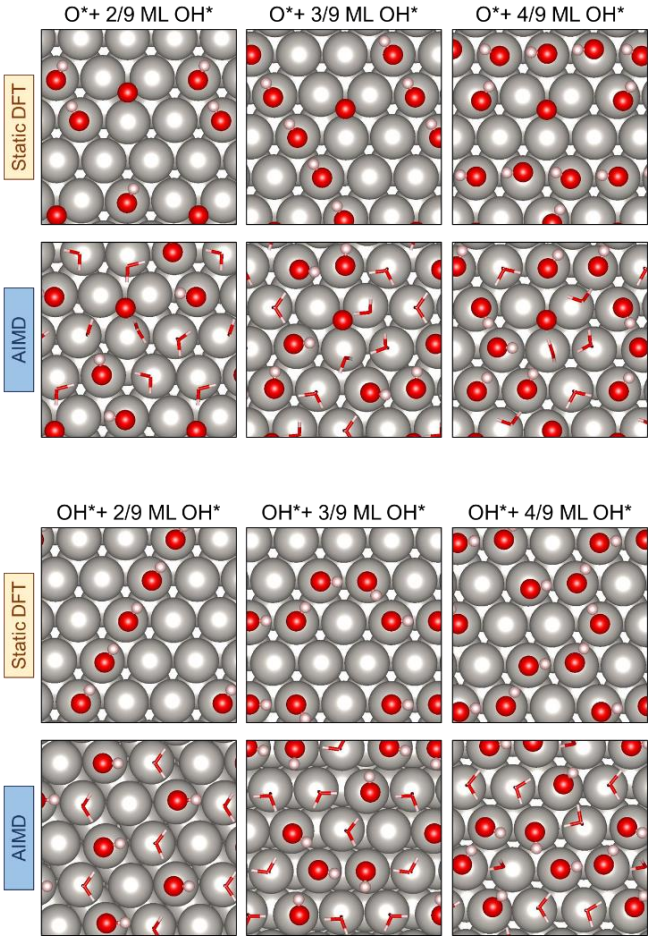

Figure 4.6: Representative structures for adsorbates in static, unsolvated DFT calculations and solvated AIMD simulations on Pt(111) with co-adsorbed OH*. Pt atoms are shown in grey, O atoms are shown in red, and H atoms are shown in white. Interfacial water molecules are shown as stick models for clarity.

The onset potentials for the ORR in the presence of varying OH* coverages are shown in Fig. 4.7a for both the static DFT model and fully solvated AIMD electrode model. Overall, the onset potentials as predicted by static DFT are far too negative compared to experimental values. By looking closer at the potential energy surfaces for OH*-covered surfaces as modeled with static DFT calculations (Fig. D.6), we find that the potential-determining step for the ORR in the presence of 2/9-4/9 ML OH* is always reducing OH* to OH^-. In other words, co-adsorbed OH* tends to stabilize other OH* species on the surface due to hydrogen bonding interactions, making the most difficult step removing OH* from the surface. Additionally, because O* is still highly

stable on the Pt(111) surface in these static, unsolvated DFT calculations, the dissociative pathway is always preferred over the associative pathway. Unlike the static DFT calculations without water, our fully solvated electrode models from AIMD simulations are in much better agreement with experiments (Fig. 4.1) at all co-adsorbed OH* coverages.

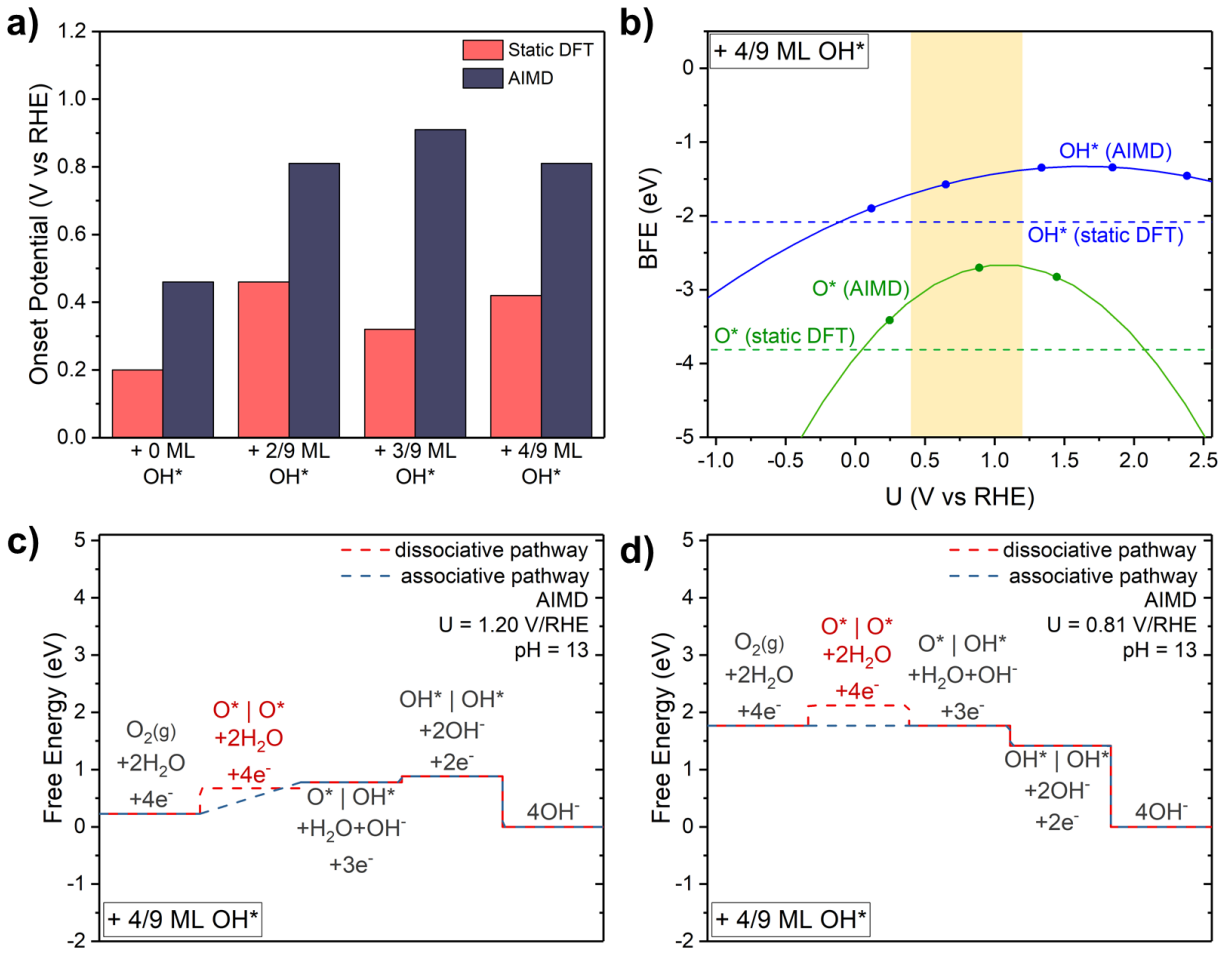

Figure 4.7: (a) Onset potentials for the ORR on Pt(111) at a range of co-adsorbed OH* coverages from static, unsolvated DFT calculations (pink bars) and solvated AIMD simulations (purple bars). **(b)** Binding free energy (BFE) of OH and O relative to the gas phase energy of each respective species as a function of applied potential as calculated from static DFT and solvated AIMD simulations at pH = 13 and 4/9 ML co-adsorbed OH*. Free energy diagrams for the ORR on Pt(111) at pH = 13 and 4/9 ML co-adsorbed OH* as determined from solvated AIMD simulations at **(c)** 1.20 V/RHE and **(d)** 0.81 V/RHE (the onset potential for the ORR).

By examining the binding free energy of O* and OH* on OH*-covered surfaces, we can see why the onset potentials are more positive on a fully solvated electrode surface compared to a

static model under vacuum. The binding free energy of O* and OH* with 4/9 ML co-adsorbed OH* using both models is shown in Fig. 4.7b. The corresponding binding free energy figures for O* and OH* with 2/9 ML and 3/9 ML co-adsorbed OH* are shown in Fig. D.7a and Fig. D.7b, respectively. For all three co-adsorbate coverages, O* and OH* are almost always more destabilized in the fully solvated electrode model than in the static DFT model under a vacuum in the potential region relevant for the ORR. The only exception is OH* in the presence of 2/9 ML co-adsorbed OH*. This suggests that the high density of adsorbed oxygenates on the surface and water causes some destabilization effects which help facilitate the reduction and removal of oxygenates from the surface.

By looking at the free energy diagram for the ORR at the start of the potential sweep (1.20 V/RHE) for the ORR with 4/9 ML spectator OH* species (Fig. 4.7c, corresponding figures for 2/9 ML and 3/9 ML spectator OH* shown in Fig. D.7c and Fig. D.7e, respectively), we can see that both O* and OH* are far more destabilized compared to clean Pt(111) surfaces (with and without water) and Pt(111) surfaces with co-adsorbed OH* but no water. In fact, O* is so destabilized on all solvated electrode surfaces by co-adsorbed OH* and water that the dissociative pathway is less favored than the associative pathway for all OH* coverages we have considered. At the onset potential of the ORR on Pt(111) with 2/9 ML co-adsorbed OH* (0.81 V/RHE, Fig. D.7e), the potential-determining step is reducing OH* to OH^- in the associative pathway. At higher coverages of OH*, the potential energy diagrams for the ORR (Fig. D.7f for 3/9 ML co-adsorbed OH* at 0.91 V/RHE and Fig. 4.7d for 4/9 ML co-adsorbed OH* at 0.81 V/RHE) show that the potential-determining step is activating O_2 to form O* + OH* in the associative pathway as the surface becomes more crowded with oxygenates. Nonetheless, the calculated onset potentials for the ORR

on Pt(111) with 2/9-4/9 ML co-adsorbed OH* are all in good agreement with experimental results (Fig. 4.1). The question becomes: which coverage of co-adsorbed OH* most accurately describes a realistic Pt(111) electrode at the onset potential?

While the calculated onset potential for the ORR on Pt(111) with 3/9 ML co-adsorbed OH* seems to be in best agreement with experiments, we note that the calculated onset potentials for the ORR from our solvated AIMD electrode models tend to be slightly too negative compared with experimental results for both Au(100) and for Au(111) by ~0.1-0.2 V/RHE. Furthermore, this OH* coverage is lower than what was estimated to be on the Pt(111) surface at the onset of the ORR in CV experiments. Therefore, we can compare the relative onset potentials between each surface we have studied. For example, the experimental onset potential for the ORR on Au(100) is ~0.9-1.0 V/RHE, and we calculate the onset potential as 0.85 V/RHE using a solvated AIMD electrode model. Experimentally, we would expect that the onset potential for the ORR on Pt(111) should be ~0.05 V/RHE more negative on Pt(111). Consequently, the 4/9 ML co-adsorbed OH* model best captures the relative difference in onset potentials for the ORR on Au(100) and Pt(111) while also being close to the experimentally estimated coverage of OH* of ~0.5 ML. Furthermore, experimental results suggest that activating O_2 in the associative pathway is the rate-determining step for the ORR in alkaline media on Pt(111),[131,132] which is in agreement with the potential-determining step for the ORR at this coverage of co-adsorbed OH*.

4.3.3 Water Plays a Key Role in Determining ORR Activity

In our work in Chapter 3, we showed that a combination of the Au(100)-hex reconstruction and interfacial water lead to high ORR activity on Au(100) in alkaline media. The combination of the binding strength of reaction intermediates on the native Au(100)-hex surface and structure of

interfacial water templated by Au(100)-hex leads to increased hydrogen bond formation with adsorbates. Taken together, these effects cause Au(100) to be the most active monometallic catalyst for the ORR in alkaline media at low overpotentials. In this work, we consider the role that water plays on Au(111) and Pt(111), and we show that the relative calculated onset potentials for the ORR on Au(100), Au(111), and Pt(111) in alkaline media can be fully explained using a solvated AIMD electrode model. We demonstrated that although Au(111) shares a hexagonal surface structure with Au(100)-hex, the binding strength of OOH* to Au(111) is far weaker than on Au(100) due to differences in the electronic structure of Au between the two surfaces. Even though water does indeed stabilize ORR intermediates through hydrogen bonding, these interactions are not enough to stabilize OOH* on Au(111) to the point that Au(111) is an effective catalyst. On Pt(111), we showed that a combination of interfacial water, adsorbed OH*, and the Pt(111) surface all lead to a highly active ORR catalyst. However, the role of water on Pt(111) is quite different than on Au surfaces. Because Pt(111) binds oxygenates strongly, including water and co-adsorbed OH* species helps destabilize ORR reaction intermediates to remove them from the surface.

These results emphasize that water plays a critical role in interacting with ORR intermediates to determine catalyst reactivity. Nonetheless, we show that the role of water is not the same on all surfaces: while water stabilizes adsorbed oxygenates on Au(100) and Au(111), water destabilizes adsorbed oxygenates on Pt(111). Therefore, we speculate that water does not serve a universal role in electrocatalysis and that water does not apply a constant stabilization/destabilization effect on adsorbates on all surfaces. Based on these results, we believe that the combination of a catalyst structure, composition, and water produce different interactions

with reaction intermediates on the catalyst surface. Furthermore, if the catalyst composition or structure tends to bind adsorbates strongly, then we also need to evaluate the role of co-adsorbates in determining the complex interactions at the solid/liquid interface. Although beyond the scope of this investigation, we believe that future work can expand on the role of water, surface coverage, and solvated ions within the EDL and their impact on electrocatalytic reactions. Furthermore, these results can be utilized in tandem with kinetic modeling, such as microkinetic modeling, to create in-depth analyses of the kinetics of solvated electrode surfaces.

4.4 Conclusions

In this work, we investigated the role of potential-dependent interfacial water structures on ORR activity on Au(111) and Pt(111) in alkaline environments using AIMD simulations of solvated electrode surfaces. For Au(111), we find that the activity of the native, unsolvated Au(111) surface is far lower than that of the native, unsolvated Au(100)-hex surface. By considering the role of water, we again find that the overpotentials required to drive the ORR on Au(111) are far higher than on Au(100), in agreement with experiments. By examining the native activity of unsolvated Pt(111), we find that Pt(111) over-binds oxygenates which leads to high ORR overpotentials. When we considered the role of water on ORR activity on Pt(111), we still could not explain the experimental results. However, by including experimentally relevant coverages of co-adsorbed OH* ranging from 2/9 ML to 4/9 ML, we find a that a combination of spectator OH* and water destabilize oxygenates to produce an effective ORR catalyst and captures the experimental onset potentials at the experimentally-determined OH* coverage. For both Au(111) and Pt(111), we find that by including relevant interactions from water and OH*, we can replicate the experimentally-determined onset potentials for the ORR on both surfaces and can explain the trends in activity between the Au(100), Au(111), and Pt(111) surfaces.

Chapter 5: Evaluating Interfacial Water Structures on Clean and Hydroxyl-covered Electrified Au(100) Surface Reconstructions with *Ab Initio* Molecular Dynamics Simulations'

5.1 Introduction

The structure and orientation of water has broad consequences in controlling many phenomena in nature. For example, as we show in Chapters 3 and 4, the complexities of how water in the electric double layer (EDL) interacts with electrodes at solid-liquid interfaces can play a role in modulating reactions occurring at the interface.[36,37] The overall structure of water at a solid surface is governed by the structure and composition of the solid phase and by the applied potential across the interface. Therefore, the hydrogen bonding interactions between water and adsorbed reaction intermediates will also be affected by both the catalyst surface and the applied potential. The shear complexity of measuring and evaluating the atomic structures at the water-solid interface and how they respond to changing potentials has limited detailed atomic-level insights into the structure of water at electrode surfaces. While researchers have made significant efforts both experimentally and computationally in elucidating these structures,[37,88–94] there are still many gaps in our knowledge.

Much of our understanding of water structures at electrified interfaces comes from studies on noble metal surfaces. For example, Toney et al. used X-ray scattering to determine the water density distribution profile in the first water layer on Ag.[133] Velasco-Velez et al. utilized a combination of X-ray absorption spectroscopy and *ab initio* molecular dynamics calculations to show that a significant portion of water on Au surfaces forms dangling bonds and that the number

of dangling bonds increases with more negative bias.[90] The structure of water on the Au(111) surface has been characterized by Li et al., who used a combination of shell-isolated nanoparticle-enhanced Raman spectroscopy (SHINERS) and AIMD calculations to show that interfacial water sequentially shifts from a 'parallel' orientation at the point of zero charge (pzc) to a 'one-H-down' orientation and then to a 'two-H-down' orientation at as the potential becomes more negative.[88] Despite these advances, little is known about the structure of water on electrified Au(100) surfaces, which arguably is one of the most consequential interfacial systems in electrochemistry.

According to theoretical predictions, Au surfaces should be poor catalysts for the oxygen reduction reaction (ORR).[17] However, experiments show that the Au(100) surface is the most active monometallic catalyst for the ORR in alkaline conditions, a result that has puzzled scientists for decades.[106,127,134] Mysteriously, this high activity can only be found at lower overpotentials, and the overall activity significantly decreases at higher overpotentials. The onset potential for the more desirable $4e^-$ pathway ($O_2 + 2H_2O + 4e^- \rightarrow 4OH^-$) on Au(100) is ~0.9 V vs the reversible hydrogen electrode (RHE) (i.e. 0.13 V vs the standard hydrogen electrode (SHE)), but the generated current markedly decreases at ~0.6 V vs RHE (-0.17 V vs RHE) when the $2e^-$ pathway ($O_2 + 2H_2O + 2e^- \rightarrow H_2O_2 + 2OH^-$) becomes preferred. A key break in the mystery came when Staszak-Jirkovský et al. showed that the ORR is structure-sensitive on Au catalysts only in the presence of water, indicating that the reaction is mediated by a combination of the Au(100) surface and water at the solid/electrolyte interface.[36] The authors proposed that structure-sensitive "activated complexes" between water and adsorbed hydroxyl (OH*) on the surface lead to high ORR activity from ~0.9 V/RHE to ~0.6 V/RHE because the shift from the $4e^-$ pathway to the $2e^-$ pathway at ~0.6 V coincides with OH* desorbing from the surface. However, little is known about

how water interacts with the Au(100) surface, let alone Au(100) covered with OH*.

In addition to the coverage of OH* species on the surface changing as the potential decreases, the Au(100) surface also undergoes a well-known reconstruction from a (1×1) to hexagonal (hex) surface during anodic sweeps that we described in Chapter 3.[110,111] Theoretical calculations have shown that the (1×1) reconstruction is more energetically favorable when the Au(100) surface is positively charged, while the hex surface becomes more stable when the surface is negatively charged.[113] During this reconstruction, the Au(100) surface (Au(100)-(1×1)) first forms a Au(100) surface with additional rows of Au atoms (Au(100)-AR) before forming a hexagonal structure only in the top layer of the surface (Au(100)-hex).[110] Because this reconstruction occurs over a broader potential range than the change in ORR kinetics, this transition alone cannot account for the change in ORR activity.[106] However, this means that any discussion of water structures on Au(100) must include a thorough analysis of water structures on each of these Au(100) surface reconstructions.

In this work, we utilize AIMD simulations to evaluate the structure of water on Au(100) surface reconstructions as a function of applied potential. We consider how the arrangement of surface atoms within each of these surface reconstructions impacts the overall distribution and orientation of water within the EDL. Furthermore, we study the impact of experimentally relevant[36] coverages of hydroxyl on impacting interfacial water structures, namely 1/10 monolayer (ML) and 1/5 ML of OH*. Our findings show that although OH* can make small modifications to water structures at the interface compared to on clean surfaces, Au(100) surface reconstructions play the predominant role in determining the overall structure of water at the Au(100) surface.

5.2 Methods

We perform density functional theory (DFT) calculations using the Vienna *Ab Initio* Simulation Package (VASP).[81,82] These calculations use the revised Perdew-Burke-Ernzerhof functional with the Pade Approximation (RPBE)[80] form of the generalized-gradient approximation (GGA)[78] with D3 van der Waals dispersion corrections.[119] Projector augmented wave (PAW) pseudo-potentials are used to describe electron-ion interactions,[120,121] and the valence electron wavefunctions are expanded using a plane-wave basis set with a 400 eV cutoff energy. The surface Brillouin zones of the p(2×5) Au(100) surfaces were sampled via a 4×2×1 Monkhorst-Pack k-point mesh.[122] The Au(100)-(1×1) surface is modeled as a pristine Au(100) surface. For the Au(100)-AR surface model, we add 1/5 ML of Au atoms to form a continuous, periodic row of Au atoms atop a (100) faceted surface. The Au(100)-hex surface is an 'isomer' of the Au(100)-AR surface where the additional row atoms are pushed into the surface, leading to the top Au surface layer having a hexagonal structure on top of a (100) lattice.

In our calculations, we model the Au(100) surface with a five-layer double-sided slab with the middle layer fixed at the bulk lattice constant of 4.173 Å (found to be 4.08 Å experimentally[123]). Each slab is separated by ~36.9 Å of space in the z direction containing 102 (Au(100)-(1×1) and Au(100)-hex) or 100 water molecules (Au(100)-AR) for a water density of 1 g/mL. For models with adsorbates, we modeled symmetric adsorption on equivalent sites on both sides of the unit cells and removed one water per adsorbate added to maintain a consistent water density.

We perform molecular dynamics simulations using the standard Verlet algorithm to propagate ionic trajectories with a 1 fs time step. To accelerate convergence, we use the mass of deuterium for hydrogen. All simulations were performed in the NVT ensemble at 298 K, and we used a Nosé-Hoover thermostat to control the ionic temperature.[129,130] To extensively sample the

configuration space within these simulations, we initialize a series of trajectories starting from a variety of adsorbate-coverage and water-structure configurations. Each trajectory is typically run for at least a 2 ps equilibrium period and a production period of 10 ps. For systems containing multiple configurations for the adsorbate arrangements, we use up to 130 ps of data consisting of many trajectories that sample all of these configurations in our calculations.

To model the electrochemical environment at the interface between Au and water, we utilize the double reference method (DRM).[85,86] The DRM allows us to evaluate the applied potential across the EDL at a range of potentials by adjusting the number of electrons within the Au slab. A uniform background charge is then used to counterbalance the excess charge in the slab and maintain a neutral supercell. This method allows us to calculate the workfunction across the solid-liquid interface, which we reference to the workfunction of the SHE to determine the applied potential, *U*:

$$U = -(\emptyset_{interface} + \emptyset_{H_2/H^+}) \quad (2)$$

where $\emptyset_{interface}$ is the calculated workfunction across the interface in eV and $\emptyset_{H_2/H^+}$ is the work function of the H_2/H^+ couple in eV at standard conditions. The calculated value of $\emptyset_{H_2/H^+}$ ranges from 4.4-4.8 eV,[87] and we take the average value of 4.6 eV for our calculations. Because the applied potential fluctuates as adsorbates and the solvent restructure during the simulation, we used an average applied potential calculated using data points collected every 0.1 ps. Unless stated otherwise, all potentials in this work are reported relative to the SHE. For each system, we perform calculations where we add/remove $2e^-$, $1e^-$, or 0 e^- from the surface to capture two potentials below the pzc, the pzc, and two potentials above the pzc. We calculate the pzc to be -0.13 V for Au(100)-

(1×1), 0.15 V for Au(100)-AR, and 0.08 V for Au(100)-hex without adsorbed hydroxyl.

5.3 Results and Discussion

5.3.1 Water Distribution on Au(100) Surface Reconstructions

The structure of interfacial water is often characterized by the density of water relative to a surface and the orientation of water near the surface. First, we consider the density of oxygen in water molecules, ρ_O, along the surface normal for the Au(100)-(1×1) (Fig. 5.1a), Au(100)-AR (Fig. 5.1b), and Au(100)-hex (Fig. 5.1c) surface reconstructions in the absence of adsorbed OH* over a range of applied potentials. On all surfaces, we find there is a peak ~3.0-3.5 Å from the surface where there is a sub-layer of water with the highest density at all potentials. Representative images of water on each surface, including water in this sub-layer (within 4 Å of the surface) as seen from above, are shown in Fig. 5.1d. Overall, the water density of this sub-layer is highest on Au-hex, followed closely by Au(100)-(1×1). Unsurprisingly, the additional row atoms on Au(100)-AR, which are located 1.7 Å from the Au(100) surface, reduce the overall density of water within this sublayer. Additionally, we find that increasing the applied potential to more positive values (i.e. shifting the charge of the surface from more negative to more positive) shifts the water density profiles so that water is closer to all of the surfaces.

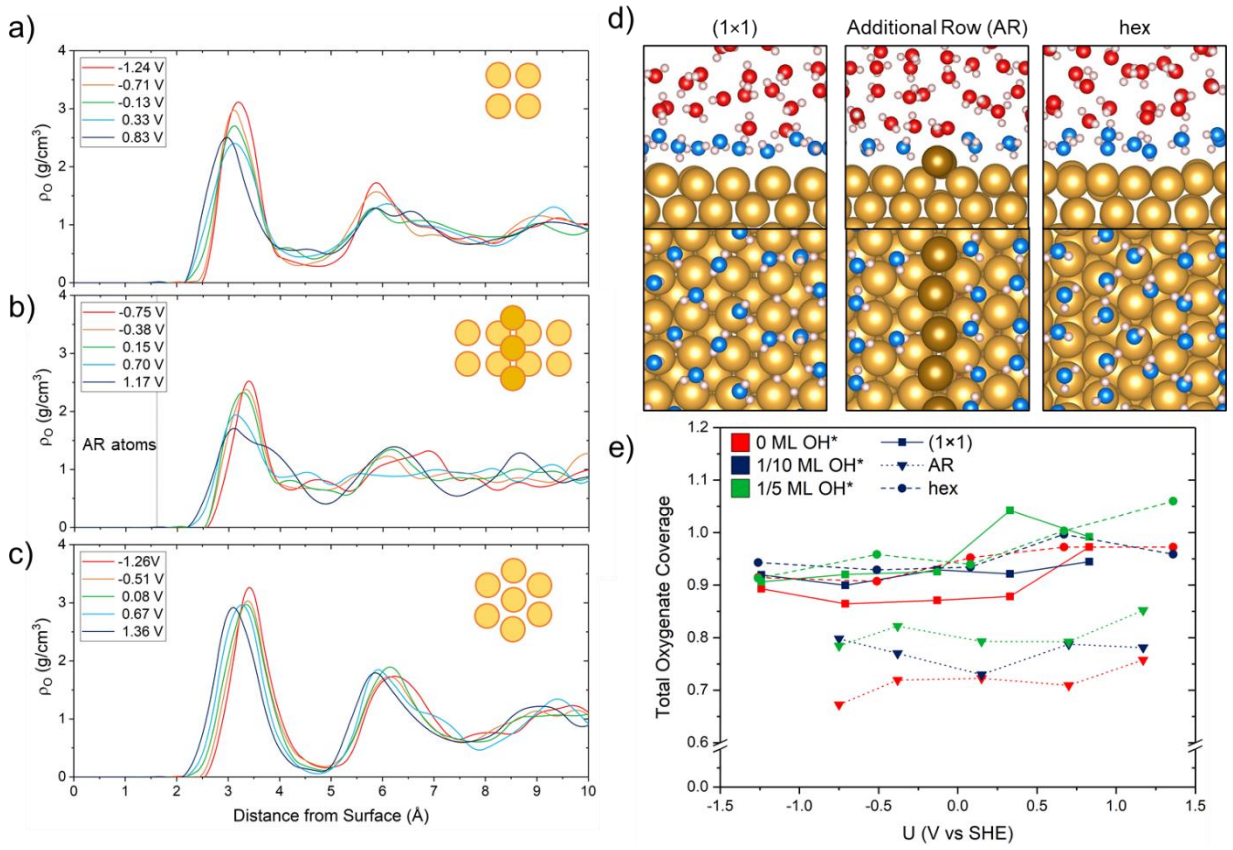

Figure 5.1: Density of oxygen atoms (ρ_O) in water as a function of distance from the surface for **(a)** Au(100)-(1×1), **(b)** Au(100)-AR, and **(c)** Au(100)-hex surfaces without OH*. The zero coordinate corresponds to the average position of Au atoms on the top surface layer of each model (excluding AR atoms on Au(100)-AR). Position of AR atoms is denoted with a line. **(d)** Representative images of water on Au(100) at the point of zero charge (pzc) for each system (red: O, blue: O (within 4 Å of the surface) white: H, gold: Au, dark gold: additional row (AR) Au). Top views of Au(100) surfaces are 4 Å from the surface and include water in the high-density sub layer closest to the surface. **(e)** Total oxygenate coverage (OH* and water) on the Au(100) surface reconstructions within 4 Å of the surface as a function of applied potential. All potentials are reported relative to the SHE.

Next, we consider how adsorbed OH* on the surface impacts the relative distribution of water along the surface normal of each of the Au(100) surface reconstructions. Cyclic voltammetry (CV) measurements estimate that the coverage of hydroxyl is ~0.25 ML between 0.65-1.15 V vs RHE (-0.12-0.38 V vs SHE).[36] Therefore, we consider how 1/10 ML and 1/5 ML of OH* impact the structure of water on each surface reconstruction. Representative images of the OH-covered Au(100) surfaces are shown in Fig. E.1. In this work, we define the coverage as the number of

species per surface Au atom on the Au(100)-(1×1) surface. Fig. E.2 shows the density of oxygen in water molecules (i.e., excluding oxygen in OH*) for all OH* coverages on each of the Au(100) surface reconstructions. As the coverage of OH* increases, the density of water in the sub-layer closest to the surface decreases, and the rest of the oxygen density profile farther from each surface remains largely unchanged for all reconstructions. Thus, adsorbed hydroxyl only alters the density of water within ~4 Å of each surface. Therefore, we consider the total coverage of all oxygenates (OH* and water) within this sub-layer close to the surface, which is shown in Fig. 5.1e. Although the density of water decreases as the coverage of OH* increases, the total coverage of oxygenates only slightly increases by ~0.0-0.1 ML as the coverage of OH* increases from 0 ML to 1/5 ML, regardless of potential. This indicates that as we add OH* to the surface, we generally remove water molecules to maintain a roughly constant oxygenate coverage on Au(100) surfaces.

5.3.2 Water Orientation on Au(100) Surface Reconstructions

In addition to considering the distribution of water on electrified Au(100) surface reconstructions both with and without adsorbed OH*, we also examined the orientation of water on the Au(100) surface reconstructions. We start by calculating the dipole orientation of water ($\rho_O \cos\varphi$, where ρ_O is the density of oxygen in water and φ is the angle between the water bisector and the surface normal) along the surface normal of the Au(100)-(1×1) (Fig. 5.2a), Au(100)-AR (Fig. 5.2b), and Au(100)-hex (Fig. 5.2c) surface reconstructions in the absence of adsorbed OH* at a range of applied potentials. Analyzing $\rho_O \cos\varphi$ tells us the average orientation of water as a function of distance from the surface and gives us information on the general orientation of water as we change the surface structure and applied potential. We expect $\rho_O \cos\varphi$ to be zero if the water density is zero, the water bisector is oriented perpendicular to the surface normal, or if there is no average net dipole orientation. Positive values of $\rho_O \cos\varphi$ indicate that the water bisector is oriented

in the same direction as the surface normal, while negative values of $\rho_O \cos\varphi$ indicate the opposite. On all three reconstructions, we find that there is a strong orientational preference for water in the closest sub-layer within ~4 Å of the Au surface. Nonetheless, water farther from the surface tends to assume a weak orientational preference that depends on the applied potential. At more negative applied potentials, water tends to orient itself so that the water bisector points in the opposite direction of the surface normal. As the potential becomes more positive, the water bisector turns until it is aligned with the surface normal. Despite these similarities, we do find that there are differences in the preferred orientation of water between the Au(100) surface reconstructions. On Au(100)-(1×1) and Au(100)-hex, water in the sub-layer closest to the surface has one preferred orientation except at the pzc (0.13 V for Au(100)-(1×1) and 0.08 V for Au(100)-hex). Below the pzc, the water bisector points towards the surface, and above the pzc, the water bisector points away from the surface. At the pzc, water has two different preferred orientations within this sub-layer: one where $\rho_O \cos\varphi$ is positive closest to the surface, and one where $\rho_O \cos\varphi$ is negative farther from the surface. These results align with previously reported findings from Le et al., who found that similar "bilayer" structures form on Pt(111), Au(111), Pd(111), and Ag(111) at the pzc[135] (we note that while we refer to this structure as a bilayer, this structure is entirely separate from a honeycomb bilayer structure that is a popular model for water adsorption on (111) facets). On Au(100)-AR, water also forms a "bilayer" structure within the closest sub-layer, but we find that this structure forms at a more positive potential relative to the pzc (at 0.70 V) rather than at the pzc. Below 0.70 V, the water bisector points towards the surface, and above 0.70 V, the water bisector points away from the surface.

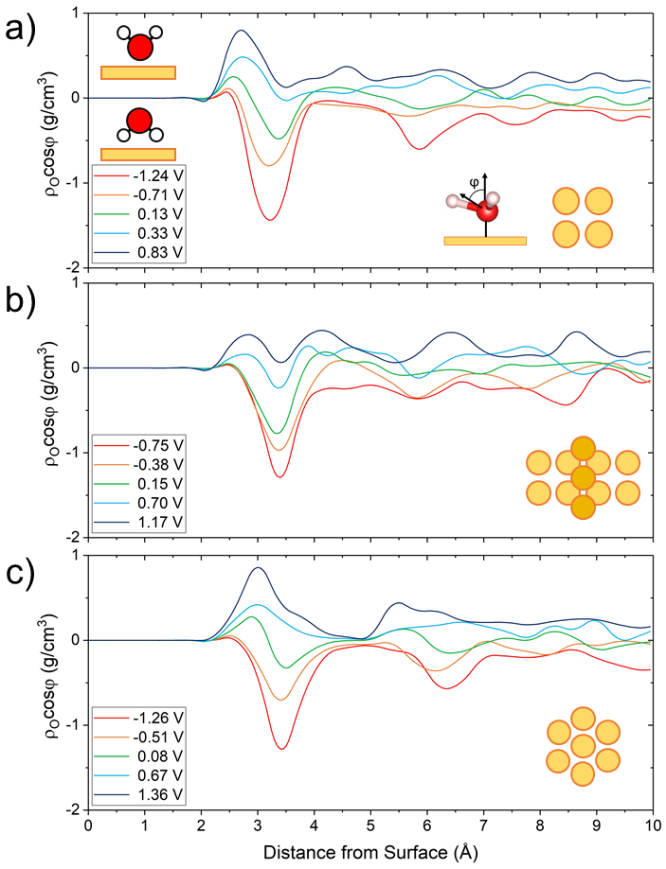

Figure 5.2: Water-dipole orientation distribution along the surface normal for **(a)** Au(100)-(1×1), **(b)** Au(100)-AR, and **(c)** Au(100)-hex surfaces at a range of potentials. The water-dipole orientation, φ, corresponds to the angle between the water bisector and the surface normal as shown in the inset of **(a)**. The zero coordinate corresponds to average position of Au atoms on the top surface layer of each model (excluding AR atoms on Au(100)-AR). All potentials are referenced with respect to the SHE.

Because water in the closest sub-layer to the surface has a strong orientational preference, we further characterize the structures and orientations of water in this layer. We calculate the distribution of the angle between the water bisector and the surface normal, φ, for the water within 4 Å of the surface on the Au(100)-(1×1) (Fig. 5.3a), Au(100)-AR (Fig. 5.3b), and Au(100)-hex (Fig. 5.3c) surface reconstructions in the absence of adsorbed hydroxyl. We also calculate the distribution of the angles between the O-H bonds of water and the surface normal, θ, for water on the Au(100)-(1×1) (Fig. 5.3d), Au(100)-AR (Fig. 5.3e), and Au(100)-hex (Fig. 5.3f) surface

reconstructions at the same conditions.

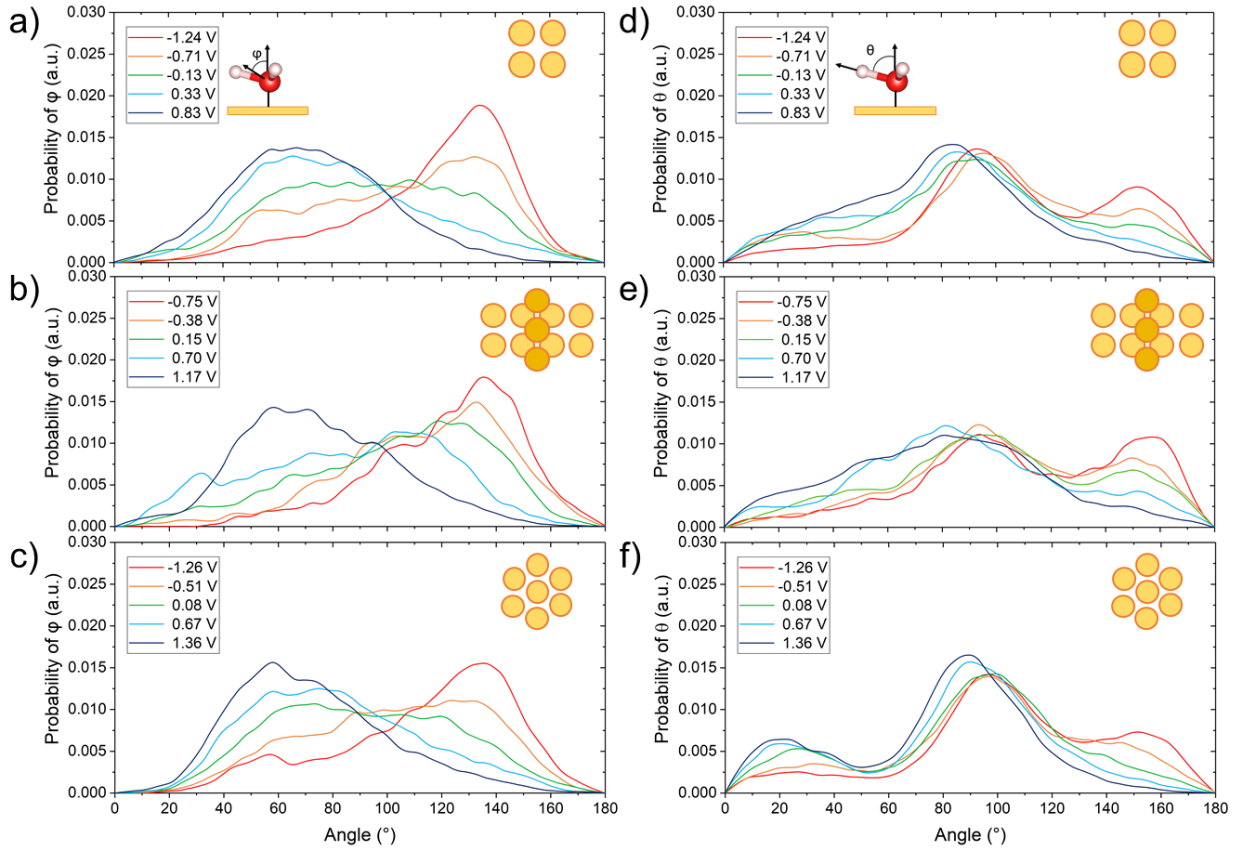

Figure 5.3: Orientation of water on clean Au(100) surface reconstructions. Distribution of the angle between the water bisector and the surface normal, φ, within 4 Å of the **(a)** Au(100)-(1×1), **(b)** Au(100)-AR, and **(c)** Au(100)-hex surfaces at a range of potentials. Distribution of the angle between the O-H bonds of water and the surface normal, θ, within 4 Å of the **(d)** Au(100)-(1×1), **(e)** Au(100)-AR, and **(f)** Au(100)-hex surfaces at a range of potentials. Inset of **(a)** illustrates φ, while the inset of **(d)** illustrates θ. All potentials are referenced with respect to the SHE.

On Au(100)-(1×1) at -1.24 V, there is a sharp peak in the φ distribution at ~140º and peaks in the θ distribution at ~100º and ~150º, which corresponds to a water structure with one O-H bond pointed parallel to the surface and the other O-H bond pointed directly down the surface (known as 'one-H-down' water). As the potential becomes more positive, the orientation of water shifts. At 0.83 V, there is a peak in the φ distribution at ~70º and a peak in the θ distribution at ~80º,

which corresponds to a structure where the molecular plane of water shifts so that water lies roughly parallel on the Au(100)-(1×1) (known as ‘parallel’ water) with the O-H bonds tilted slightly away from the surface. We find that water undergoes a similar transition on Au(100)-AR, where at more negative applied potentials water forms a ‘one-H-down’ structure that shifts to a ‘parallel’ orientation as the potential becomes more positive; however, the potentials at which this shift occurs are more positive than on Au(100)-(1×1). On Au(100)-hex at -1.26 V on Au, there again is a sharp peak in the φ distribution at ~140º and peaks in the θ distribution at ~100º and ~150º, which corresponds to ‘one-H-down’ water like what is seen on the other two Au(100) surfaces. However, as the potential becomes more positive, the orientation of water on Au(100)-hex shifts to a different configuration from the other two structures. At 1.36 V, there is a peak in the φ distribution at ~60º and peaks in the θ distribution at ~20º and ~90º, corresponding to a water orientation where one O-H bond points parallel to the surface and the other O-H bond points up away from the surface (known as ‘one-H-up’ water). Scheme 5.1 summarizes the general trends in how the orientation of interfacial water near the surface changes as we change the applied potential on Au(100) surface reconstructions based on results shown in Fig. 5.2 and 5.3.

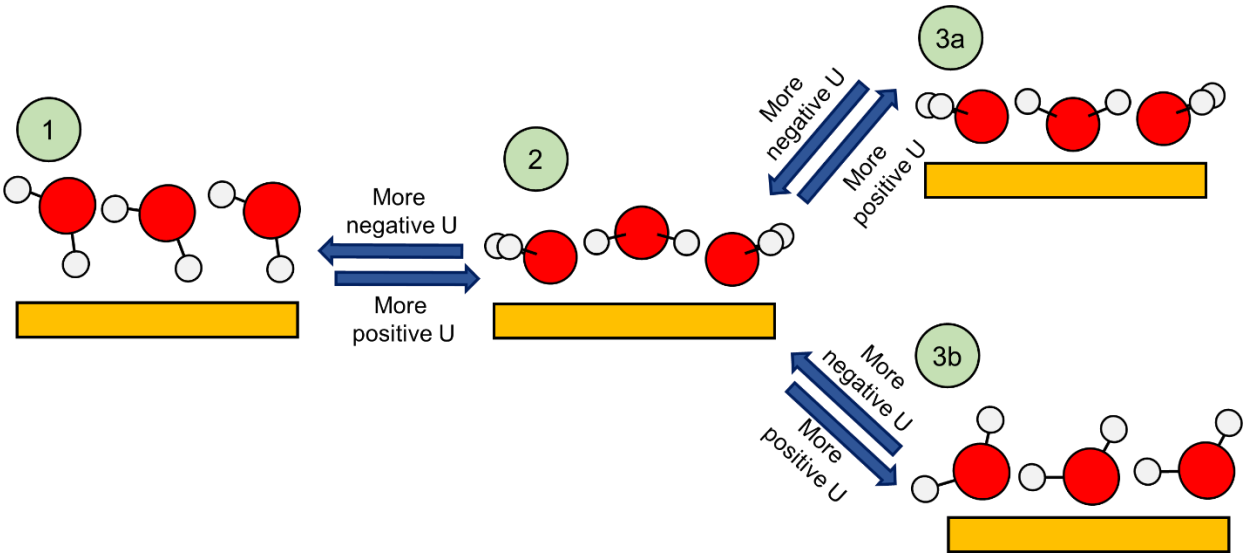

Scheme 5.1: Generalized trends in water structures formed on clean Au(100) electrodes. At more negative potentials (state 1), water adopts a 'one-H-down' orientation. At intermediate potentials (near the pzc for Au(100)-(1×1) and Au(100)-hex or ~0.5 V more positive than the pzc for Au(100)-AR), water adopts two orientations depending on the proximity of water from the surface (state 2). At more positive potentials, water adopts a 'parallel' orientation on Au(100)-(1×1) and Au(100)-AR (state 3a) or a 'one-H-up' orientation on Au(100)-hex (state 3b). O atoms are shown in red, H atoms are shown in white, and the Au surface is shown in gold.

Next, we consider how either 1/10 ML or 1/5 ML OH* impacts the orientation of water within 4 Å of the Au(100) surface reconstructions. We show the distribution of φ for water within 4 Å of the surface in the presence of 1/5 ML OH* on the Au(100)-(1×1) (Fig. 5.4a), Au(100)-AR (Fig. 5.4b), and Au(100)-hex (Fig. 5.4c) surface reconstructions. We also calculate the distribution of θ for water on the Au(100)-(1×1) (Fig. 5.4d), Au(100)-AR (Fig. 5.4e), and Au(100)-hex (Fig. 5.4f) surface reconstructions at the same conditions. The corresponding figures for the orientation of water in the presence of 1/10 ML of OH* are shown in Fig. E.3. We find that adsorbed hydroxyl alters the orientation of water in two ways: 1) As the coverage of OH* increases, water no longer forms a 'one-H-down' configuration at the most negative potentials that we studied on every reconstruction. Instead, water tends to adopt a planar orientation (we do note, however, that at potentials below ~-0.15 V, OH* should not be stable on any Au(100) surface[36]). 2) As the potential

becomes more positive, we find that increasing OH* coverage causes water on Au(100)-(1×1) to shift from a planar orientation to a ‘one-H-up’ orientation. However, we only see this configuration with 1/5 ML OH* at the highest potential studied, 1.12 V. Besides these small differences, we find that increasing the OH* coverage on the Au(100) surface reconstructions does not substantially alter the orientation of water near the surface. This is particularly true in the potential range relevant for the ORR (from ~-0.2 to 0.2 V vs SHE), where the orientation of water does not considerably change due to the presence of OH* on all surfaces. Therefore, we do not find strong evidence to suggest that OH* significantly alters interfacial water structures so as to enhance charge transfer from water to ORR intermediates.

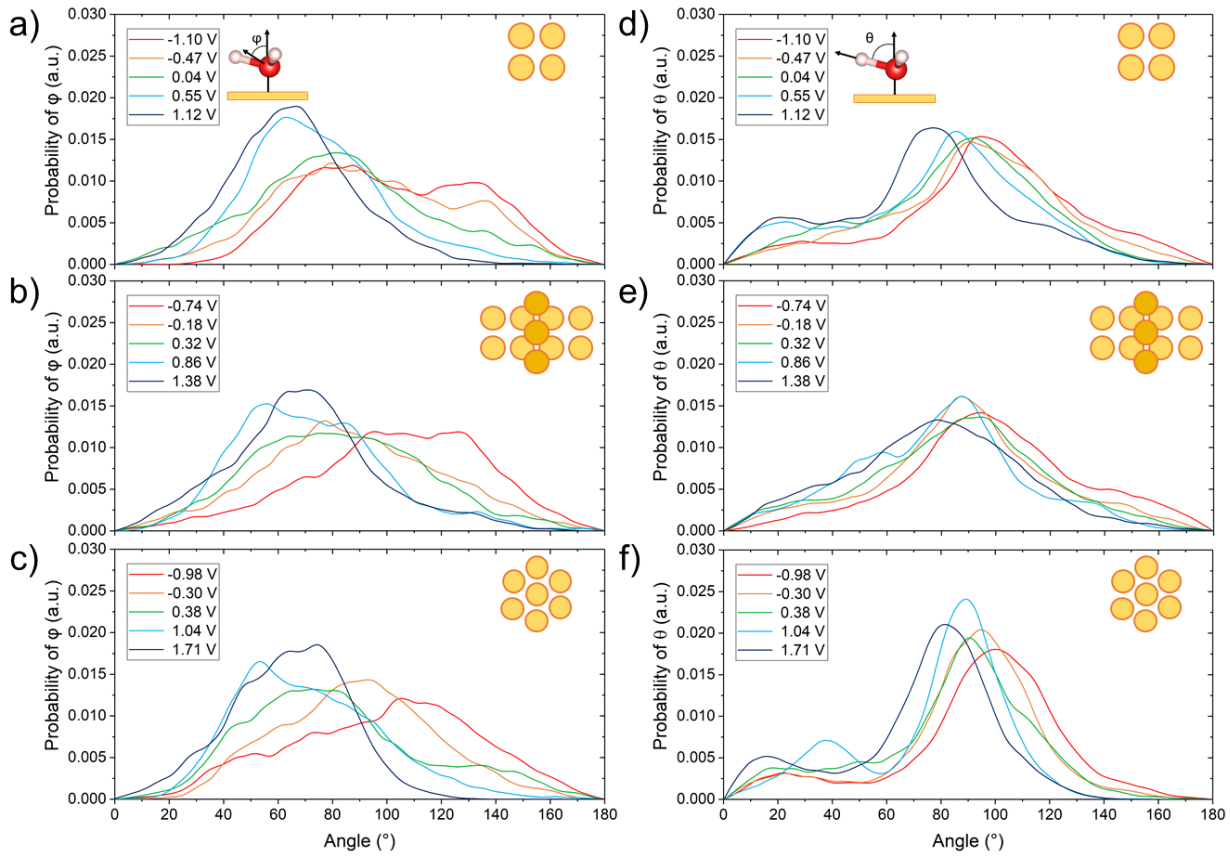

Figure 5.4: Orientation of water on Au(100) surface reconstructions with 1/5 ML OH*. Distribution of the angle between the water bisector and the surface normal, φ, within 4 Å of the **(a)** Au(100)-(1×1), **(b)** Au(100)-AR, and **(c)** Au(100)-hex surfaces at a range of potentials. Distribution of the angle between the O-H bonds of water and the surface normal, θ, within 4 Å of the **(d)** Au(100)-(1×1), **(e)** Au(100)-AR, and **(f)** Au(100)-hex surfaces at a range of potentials. Inset of **(a)** illustrates φ, while the inset of **(d)** illustrates θ. All potentials are referenced with respect to the SHE.

5.3.3 Hydrogen Bonding Properties of Water on Au(100) Surface Reconstructions

As the orientation of water near Au(100) shifts as the applied potential changes, the hydrogen bonding properties of water will also change in turn. For example, at more negative potentials, water in a 'one-H-down' orientation can only donate up to one hydrogen bond to other species, reducing the overall number of hydrogen bonds formed within interfacial water. As the potential becomes more positive and water starts to adopt a 'planar' orientation or 'one-H-up' orientation, water gains the ability to donate up to two hydrogen bonds. To analyze the hydrogen

bonding properties of interfacial water, we first calculate the average number of hydrogen bonds ($n_{H\text{-}bonds}/H_2O$) accepted and donated by water within 4 Å of the surface (Table 5.1) on clean Au(100) surface reconstructions. In this analysis, we defined a hydrogen bond with a cutoff of 3.5 Å for the O-O distance and a H-O-O angle less than 30°.[136] For reference, we expect bulk water accept two $n_{H\text{-}bonds}/H_2O$ and donate two $n_{H\text{-}bonds}/H_2O$.[135]

Table 5.1: Average number of hydrogen bonds accepted and donated by water on each Au(100) surface reconstruction within 4 Å of the surface as a function of applied potential.

Surface	Applied Potential (V)	$n_{H\text{-}bonds}/H_2O$ (Accepted)	$n_{H\text{-}bonds}/H_2O$ (Donated)
(1x1)	-1.24	1.41	1.08
	-0.71	1.32	1.15
	-0.13	1.29	1.29
	0.33	1.25	1.44
	0.83	1.24	1.60
AR	-0.75	1.29	0.90
	-0.38	1.31	1.03
	0.15	1.27	1.16
	0.70	1.28	1.36
	1.17	1.23	1.54
hex	-1.26	1.41	1.10
	-0.51	1.37	1.20
	0.08	1.33	1.35
	0.67	1.28	1.43
	1.36	1.24	1.52

Overall, we find that the number of hydrogen bonds accepted by water is far less sensitive to changes in applied potential than the number of hydrogen bonds donated by water. In other words, interfacial water can usually accept hydrogen bonds from other interfacial water molecules and from water molecules farther from the surface at a wide range of potentials. However, the dangling bonds that water forms in the ‘one-H-down’ orientation at more negative potentials

inhibits the ability of interfacial water to donate hydrogen bonds. As the applied potential becomes more positive, the number of hydrogen bonds accepted by interfacial water slightly decreases, most likely due to the hydrogen in O-H bonds of water pointing away from the surface and any interfacial water on the surface. Overall, the number of hydrogen bonds accepted by interfacial water is similar on all three Au(100) reconstructions. In agreement with Velasco-Velez et al., we find that water donates more hydrogen bonds towards more positive potentials,[90] resulting in less dangling bonds and more bulk-like water at more positive potentials. Based on this analysis, we also find that water on Au(100)-(1×1) and Au(100)-hex generally donate similar numbers of hydrogen bonds as a function of applied potential, while water on Au(100)-AR donates less hydrogen bonds at the same potentials compared to the other two surfaces. These results align with the expectation that the additional row of Au atoms on Au(100)-AR act as a boundary that interrupts hydrogen bonding.

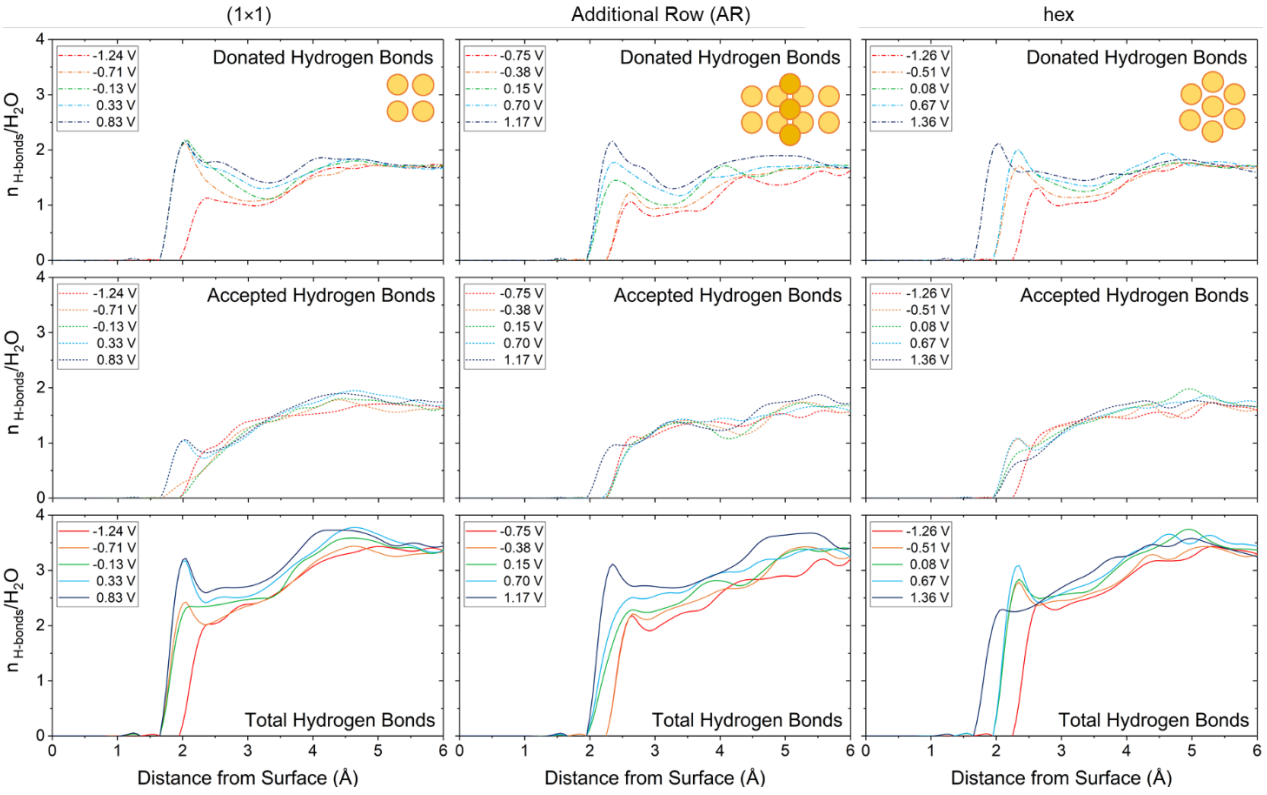

Figure 5.5: Hydrogen bond density ($n_{H\text{-}bonds}/H_2O$) along the surface normal direction on clean Au(100) surface reconstructions at a range of potentials. The zero coordinate corresponds to average position of Au atoms on the top surface layer of each model (excluding AR atoms on Au(100)-AR)). All potentials are referenced with respect to the SHE.

To further analyze the hydrogen bonding properties of water on each Au(100) surface reconstruction, we calculated the number of donated, accepted, and the total number of hydrogen bonds formed on each surface as a function of distance from the surface (we provide corresponding figures for water in the presence of 1/5 and 1/10 ML OH* in Fig. E.4 and E.5, respectively, which show similar trends to clean surfaces). Here, we find far more differences between the three surfaces than what was previously shown by looking at the population average for water within 4 Å of the surface. On Au(100)-(1×1), there is a sharp peak in the number of hydrogen bonds donated by water at a distance of 2 Å from the surface at potentials at and more positive than -0.17 V. Between 2-4 Å from the surface, water donates more hydrogen bonds as the potential becomes

more positive. At potentials at and above 0.33 V, there is a peak in the density of accepted hydrogen bonds on Au(100)-(1×1) at a distance of 2 Å from the surface. Overall, the total number of hydrogen bonds peaks on Au(100)-(1×1) at a distance of 2 Å from the surface, and this peak increases as the potential becomes more positive. On Au(100)-AR, the peak in number of hydrogen bonds donated by water shifts to distances closer to the surface and becomes larger as the potential becomes more positive. Because there are not substantial differences in the accepted hydrogen bonds from water as the potential changes, this means that a similar trend is seen for the total number of hydrogen bonds on Au(100)-AR. On Au(100)-hex, the peak in donated hydrogen bonds also shifts closer to the surface and becomes larger as the potential becomes more positive. However, when combined with accepted hydrogen bonds, water on the Au(100)-hex surface forms a peak in the total number of hydrogen bonds at potentials near the potential of zero charge, 0.08 V. As the potential becomes more positive or more negative, this peak diminishes. Therefore, the total hydrogen bond density closest to the surface becomes greater as the potential becomes more positive on Au(100)-(1×1) and Au(100)-AR or as the potential becomes more positive or negative than the potential of zero charge on Au(100)-hex.

5.4 Conclusions

In this work, we utilized AIMD simulations to elucidated interfacial water structures that form on potential-dependent Au(100) surface reconstructions with and without the presence of adsorbed hydroxyl. First, we considered the density of water near the Au(100) surfaces. We found that water forms a dense layer within 4 Å of the surface, regardless of the identity of the surface reconstruction. By including 1/10 or 1/5 ML of OH* , we found that the density of water within 4 Å of the surface decreases due to lateral interactions between water and OH*, but the total coverage of oxygenates (OH* + water) stays relatively constant at the same potential. Next, we evaluated

the orientation of water near the Au(100) surface. At the most negative potentials, water forms a ‘one-H-down’ structure. As the potential becomes more positive, water then adopts two distinct orientations depending the proximity of the molecules to the surface, forming a bilayer structure. We find this bilayer structure near the pzc on Au(100)-(1×1) and Au(100)-hex and ~0.5 V more positive than the pzc for Au(100)-AR. At even more positive potentials, water adopts a ‘parallel’ orientation on Au(100)-(1×1) and Au(100)-AR or a ‘one-H-up’ orientation on Au(100)-hex (state 3b). Adding 1/10 or 1/5 ML of OH* on the Au(100) surfaces did not substantially alter the orientation of water near the surface. This finding suggests that while OH* is present during peak ORR activity on Au(100), adsorbed OH* does not alter the structure of water in a manner that would lead to increased charge transfer kinetics relative to a clean Au(100) surface. However, this finding does not rule out the possibility that OH* could play other roles in influencing ORR kinetics on Au(100).

Finally, we analyzed the hydrogen bonding properties of water on each Au(100) surface reconstruction. On Au(100)-(1×1) and Au(100)-AR, water directly above the surface forms more hydrogen bonds at more negative potentials, while on Au(100)-hex, water directly above the surface forms the maximum number of hydrogen bonds near the pzc. This work provides new insights into the structure of interfacial water on Au(100) electrodes and serves as the basis for including relevant water structures in simplified models of Au(100) electrodes.

Chapter 6: Evaluating Interfacial Water Structures on Electrified Hydroxyl-covered Pt(111) through *Ab Initio* Molecular Dynamics Simulations

6.1 Introduction

The interactions between solids and liquids are ubiquitous throughout nature, and knowing the detailed atomic structures of solid/liquid interfaces can help us evaluate the properties of these interfaces. More specifically, these interactions can play a substantial role in altering chemical reactions that occur at electrified interfaces within the electric double layer (EDL). Most solvents used in electrochemical applications typically contain a significant amount of water, which forms potential-dependent structures at solid/liquid interfaces. Therefore, a significant amount of experimental and theoretical research has been devoted to elucidating water structures at the interfaces with well-defined electrified surfaces.[37,88–94] A large portion of this work has focused on evaluating water structures on Pt surfaces, as Pt catalysts are broadly used in many electrochemical applications and often serve as a benchmark when evaluating new catalysts. By evaluating how water interacts with Pt surfaces as well as common adsorbates and reaction intermediates on the surface, we can better determine and tailor the properties of the water/Pt interface.

By knowing all of the structural information about the location of water relative to a surface and how water orients itself at the solid interface at relevant conditions, we can make many predictions about how water might impact a multitude of processes, such as corrosion or electrochemical reactions, that occur on the surface. However, we cannot easily gain atomic-level structural details of an infinitesimally small portion (relative to the bulk) of dynamic, fluid water

molecules at an interface using experiments alone. Therefore, most of our knowledge of water structures from experiments comes from cryogenic ultra-high vacuum (UHV) experiments where we can remove any signals from water in the bulk and slow down the movement of atoms on the surface to obtain clear structural information. The earliest UHV experiments that probed the structure of water on flat metal surfaces utilized low energy electron diffraction (LEED)[137,138] patterns and later used scanning tunneling microscopy (STM)[139–141] images to evaluate the structure of a layer of water on Ru(0001). Initially, these studies concluded that water formed a $\sqrt{3} \times \sqrt{3}$ honeycomb "bilayer" structure covering 2/3 of the metal surface atoms; the term "bilayer" refers to the fact that water seemed to form a corrugated structure where molecules adsorbed at two different distances relative to the surface. Additionally, density functional theory (DFT) calculations appeared to corroborate this perspective that water formed a $\sqrt{3} \times \sqrt{3}$ honeycomb bilayer structure on the close-packed facet of metal surfaces.[142–146] The honeycomb bilayer model proved to be simple and intuitive— to this day, the honeycomb bilayer model is widely utilized to describe interfacial water on metallic surfaces despite the fact that most water/solid surfaces of interest do not exist at UHV conditions.

Even worse, very little experimental evidence exists that water forms a honeycomb bilayer, even under UHV conditions. A later LEED I-V study from Held and Menzel found that all oxygen atoms within the water "bilayer" were actually co-planar with the surface on Ru(0001) in UHV and cryogenic conditions, which should not be possible if water forms a buckled bilayer structure.[147] Feibelman realized that these new LEED results contradicted previous experiments and utilized DFT calculations to demonstrate that the water "bilayer" seen in earlier UHV experiments was actually a mixture of H_2O and OH* from H_2O that had dissociated, thus creating

a $\sqrt{3} \times \sqrt{3}$ honeycomb structure.[148] The honeycomb bilayer never existed on Ru(0001). Even metals that do not readily dissociate water do not form honeycomb water bilayers, but they form a diverse array of other 2D structures.[144] In the case of Pt(111), x-ray photoelectron spectroscopy (XPS) measurements have shown that Pt is too noble to dissociate water and is therefore unlikely to form a mixture of OH* and water that would lead to a honeycomb H_2O + OH* structure under UHV conditions.[149] High-resolution STM and DFT calculations have revealed that water forms a periodic structure consisting of pentagons, hexagons, and heptagons that form a $\sqrt{37} \times \sqrt{39}$ periodic arrangement on Pt(111) in UHV experiments.[150,151]

While electron spectroscopies carried out under UHV conditions have provided some insights into the structure of water on metal surfaces, they lack the ability to probe the combined interactions between the surface, interfacial water, and bulk water. Furthermore, these experiments cannot evaluate the dynamic and disordered nature of liquid water. Although some electron spectroscopies are able to assess interfacial structures in electrochemical environments, including infrared reflection absorption spectroscopy (IRAS),[152–154] surface-sensitive infrared-visible sum frequency generation spectroscopy (SFG),[155–158] surface-enhanced infrared absorption spectroscopy in the attenuated total reflection mode (ATR-SEIRAS),[159,160] surface X-ray scattering (SXS),[161,162] or in situ STM,[163,164] these techniques still struggle with assessing the structure of water on the surface due to water's high mobility and complex hydrogen bonding network. Using shell-isolated nanoparticle-enhanced Raman spectroscopy (SHINERS), Li et al. have shown that the O-H stretching mode in interfacial water is correlated with the number of hydrogen bonds donated by water.[88] However, detailed evaluations of the structures of water at the solid/liquid interface using experimental techniques have eluded researchers. Additionally,

very little is known about the combined structures formed between water and adsorbates present on Pt(111) electrodes at experimental conditions. Therefore, computational methods provide a unique perspective on evaluating interfacial water structures on Pt(111) electrodes. In particular, *ab initio* molecular dynamics (AIMD) simulations can provide atomic-level insights into interfacial water structures on electrode surfaces. Previous work in this area has focused on analyzing water structures at the potential of zero charge[135,165] or evaluating the role of H_3O^+ or OH^- in the liquid phase on altering water structures at the interface.[166]

In this study, we use *ab initio* molecular dynamics (AIMD) to probe interfacial water structures on electrified Pt(111) with and without adsorbed hydroxyl, which can be present depending on the applied potential and pH of the system. For clean Pt(111), we find that water forms an interfacial bilayer structure on the Pt(111) surface (distinct from a honeycomb bilayer structure). At more negative potentials, water in both layers of the bilayer form 'one-H-down' structures. As the potential becomes more positive, water in the bottom layer forms a 'parallel' structure while water in the top layer forms a 'one-H-up' structure. However, there are no conditions where a honeycomb water bilayer forms on the Pt(111) surface. Additionally, we study OH* coverages ranging from 0-6/9 ML. By including OH* on the Pt(111) surface, we find that honeycomb water + OH* bilayers form at intermediate OH* coverages, especially 3/9 ML OH*. Additionally, water tends to orient in a 'parallel' structure in the presence of OH*. However, we show that a honeycomb bilayer model for water predicts different hydrogen bonding structures and OH* binding energies than a fully solvated model of water within the EDL at the solid/liquid interface of a Pt(111) electrode surface. These findings show that water structures are drastically altered by changing the applied potential or coverage of OH*, which can lead to differences in

interactions between adsorbates on a catalyst surface and water at a range of conditions. These differences can alter the stability of adsorbates on a catalyst surface, which have implications in catalysis research where these interactions are critical for optimizing the performance of electrocatalysts.

6.2 Methods

We performed DFT simulations using the Vienna *Ab Initio* Simulation Package (VASP).[81,82] Our calculations utilized the revised Perdew-Burke-Ernzerhof functional with Pade Approximation (RPBE)[80] form of the generalized gradient approximation (GGA) with D3 van der Waals dispersion corrections.[119] We described electron-ion calculations using projector augmented wave (PAW) pseudo-potentials, and valence electron wavefunctions were expanded using a plane-wave basis set with a cutoff energy of 400 eV.[120,121] The surface Brillion zone of the 3×3 unit cell was sampled using a 4×4×1 gamma-centered k-point mesh.

To model a honeycomb bilayer water model on Pt(111), we utilized a 3×3 unit cell with a four-layer slab. The bottom two layers were fixed at the bulk lattice constant of 3.950 Å, which is in good agreement with the experimental value of 3.924 Å.[123] Repeated images of each slab were separated by at least 20 Å of a vacuum layer. We modeled adsorption on one side of the slab and applied dipole corrections in the z direction.[124] Each structure was relaxed until the forces acting upon each atom were $\leq$ 0.01 eV/Å. We calculated the vibrational frequencies of species using a numerical differentiation of forces using a second-order finite difference approach as determined from diagonalizing the mass-weighted Hessian matrix. All metal atoms in the surface were fixed for vibrational frequency calculations. We calculated the free energy of a species as:

$$G = E_{DFT} + ZPE - TS \quad (6.1)$$

where E_{DFT} is the total energy of a system from DFT, ZPE is the zero-point energy, T is the temperature (298 K), and S is the vibrational entropy.

To study the structures of a fully solvated Pt(111) electrode surface, we utilized a double-sided 3×3 slab model with seven layers. The middle three layers of the slab were fixed at the calculated Pt bulk lattice constant. Slabs were separated by 31.6 Å of water in the z direction. This water layer contained a total of 64 water molecules in the absence of OH*, leading to a total water density of 1 g/mL. For models with OH*, we modeled symmetric adsorption on both sides of the unit cells and removed one water molecule per adsorbate added to maintain a consistent water density for coverages ranging from 1/9-6/9 ML OH*. We determined the chemical potential of bulk water, μ_{H_2O}, by simulating 96 water molecules in a 14.23×14.23×14.23 Å box.

We performed molecular dynamics simulations using the standard Verlet algorithm to propagate ionic trajectories with a 1 fs time step. To accelerate convergence, we used the mass of deuterium for hydrogen. All simulations were performed in the NVT ensemble at 298 K, and we used an a Nosé-Hoover thermostat to control the ionic temperature.[129,130] To extensively sample the configuration space within these simulations, we initialized a series of trajectories starting from a variety of adsorbate coverages and water structure configurations. For calculations with OH*, trajectories include every permutation of possible adsorbate configurations possible within the 3×3 unit cell. Each trajectory was typically run for at least a 2 ps equilibrium period and a production period of 10 ps. For systems containing multiple adsorbate binding structures or configurations, we used up to 55 ps of molecular data consisting of several trajectories. We calculated the average free energy of a system by calculating the average free energy of the combined trajectories for a

given system as:

$$G(T) = \langle E \rangle + 1/\beta(\langle exp(\beta \Delta E) \rangle) \quad (6.2)$$

where β is $1/k_BT$ (k_B is Boltzmann's constant), E is the potential energy, and ΔE is the difference between the average potential energy and the energy in each step.

To model the electrochemical environment at the interface between Pt(111) and water, we utilized the double reference method (DRM).[85,86] The DRM provides a framework to evaluate the applied potential across the EDL at a range of potentials by adjusting the number of electrons within the Pt slab. A uniform background charge is then used to counterbalance the excess charge in the slab to maintain a neutral supercell. This method provides a framework to calculate the workfunction across the solid-liquid interface, which we reference to the workfunction of the SHE to determine the applied potential, U:

$$U = -(\emptyset_{interface} + \emptyset_{H_2/H^+}) \quad (6.3)$$

where $\emptyset_{interface}$ is the calculated workfunction across the interface in eV and $\emptyset_{H_2/H^+}$ is the work function of the H_2/H^+ couple in eV at standard conditions. The calculated value of $\emptyset_{H_2/H^+}$ ranges from 4.4-4.8 eV,[87] so we take the average value of 4.6 eV for this study. Unless stated otherwise, all values of U reported in this study are relative to the SHE. Since changing the number of electrons in our simulation changes the energy in the double reference formalism, we also correct our AIMD calculated energies:

$$E_{corrected} = E + \int_0^q \overline{\langle V_{tot} \rangle}\, dQ + q\phi_{interface} \tag{6.4}$$

where E is the potential energy, q is the charge added or removed from the unit cell, and $\overline{\langle V_{tot} \rangle}$ is the averaged electrostatic potential across the unit cell. Because the applied potential fluctuates as adsorbates and the solvent restructure during the simulation, we used an average applied potential calculated using data points collected every 0.1 ps. For each MD simulation, we performed calculations at a range of -2e to +2e with a step size of 1e. This gave us structural information at a range of applied potentials for each system. We used this data to then fit the time-averaged energy and applied potentials for each simulation to a quadratic expression that relates the energy stored in a capacitor to the applied potential and capacitance:

$$E(U) = -\frac{1}{2} C\left(\langle U \rangle - \langle U_{pzc} \rangle\right)^2 + \langle E_{pzc} \rangle \tag{6.5}$$

where U_{pzc} is the potential of zero charge (pzc), E_{pzc} is the energy at the pzc, and C is the capacitance formed in the system.

To determine the most stable OH* adsorbate coverages at a range of relevant applied potentials and pH values, we constructed a Pourbaix diagram based on the AIMD-determined energetics. To do this, we used a similar method as outlined by Hansen et al. for generating Pourbaix diagrams from static DFT calculations.[167] We start by assuming that OH* on the surface is in equilibrium with protons and liquid water at 298 K:

$$H_2O(l) + * \leftrightarrow OH* + H^+(aq) + e^-$$

where * denotes a free site. To evaluate the effect of applied potential and pH on the most stable

phase, we then use the computational hydrogen electrode formalism[17] to describe the chemical potential of a proton-electron pair, $\mu_{H^+} + \mu_{e^-}$:

$$\mu_{H^+} + \mu_{e^-} = \frac{1}{2} G_{H_2} - eU - k_B T ln(10) pH \tag{6.6}$$

where G_{H_2} is the Gibbs free energy of H_2 in the gas phase, e is the charge of an electron, U is the applied potential relative to the SHE, and T is the temperature (298 K). Therefore, we can determine the most stable coverage of a phase at a given U and pH by determining the coverage that minimizes ΔG of reaction (5):

$$\Delta G = G_{slab+xOH*+yH_2O} - (x+y)\mu_{H_2O} + x(\mu_{H^+} + \mu_{e^-}) \tag{6.7}$$

where x refers to the number of OH* on a surface, and y refers to the number of water molecules in a calculation or simulation.

6.3 Results and Discussion

6.3.1 Water Structures on Clean Pt(111)

We begin our analysis by analyzing the geometry of water on a clean Pt(111) surface in the absence of adsorbed hydroxyl. Because the honeycomb water bilayer structure still serves as a popular motif utilized to model solvated metal surfaces, we start by briefly noting the key differences between the honeycomb water bilayer model and the water structures predicted by a fully solvated electrode surface model. The lowest energy structure of a honeycomb bilayer model and a representative image from the solvated electrode model at 1.51 V are shown in Fig. 6.1. Afterwards, we then focus on characterizing water structures found on fully solvated Pt(111) electrode surfaces.

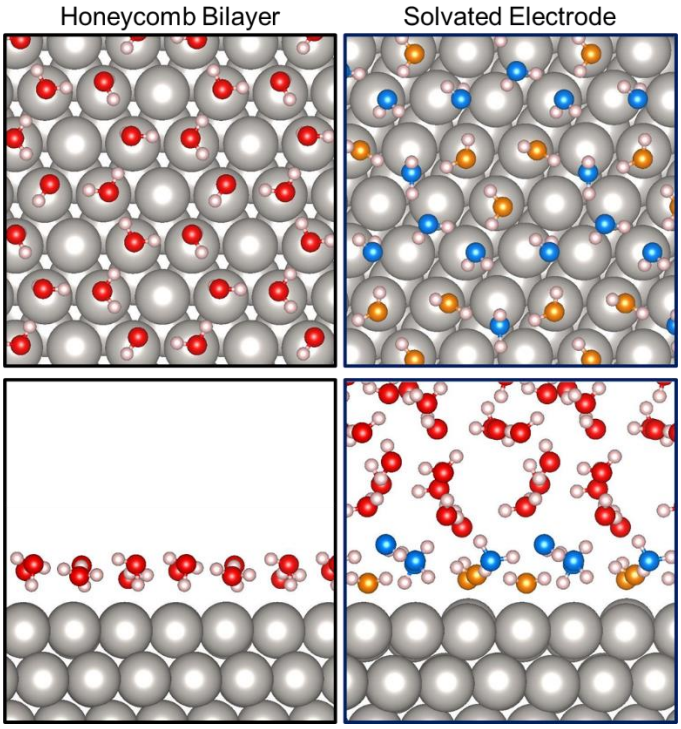

Figure 6.1: Water structures on Pt(111) modeled using a honeycomb bilayer model with static DFT versus a fully solvated electrode model (at 1.51 V vs SHE) modeled with AIMD. The top images show the solvated surfaces as seen from above, while the bottom images provide a cross-sectional view. Pt atoms are shown in gray, O atoms are shown in red, and H atoms are shown in white. For the solvated electrode model, O atoms within the bottom of the interfacial bilayer (within 3.0 Å of the surface) are shown in orange and O atoms within the top of the interfacial bilayer (within 3.0 and 4.5 Å of the surface) are shown in blue.

We start by analyzing the geometry of water on Pt(111) in the absence of adsorbed hydroxyl. Two of the most fundamental properties for describing the geometry of interfacial water at a metal surface are the location of the molecules and how the molecules orient themselves relative to the surface. This first piece of information is encoded in the water oxygen density profile relative to the surface normal. The water oxygen density profiles for interfacial water adsorbed to Pt(111) at a range of applied potentials are shown in Fig. 6.2a. At all potentials, there is higher density of interfacial water (compared to the bulk density of 1 g/cm^3) between ~2-4 Å of the Pt(111) surface. Depending on the applied potential, interfacial water forms two separate sub-layers: the bottom layer (within ~3 Å from the surface, shown in orange in Fig. 6.1) and the top layer (between ~3 and ~4.5 Å from the surface, shown in blue in Fig. 6.1). Although these two

layers are also form a “bilayer”, we emphasize that these bilayer structures are distinct from the honeycomb bilayer that was postulated in early UHV experiments. We distinguish between the two in this work by calling the hexagonal water structure under vacuum a “honeycomb bilayer” and the fully solvated electrode model with two peaks in the water oxygen density profile an “interfacial bilayer”. We also note that oxygen in water within a honeycomb bilayer has a calculated maximum distance of 3.1 Å from the Pt(111) surface, meaning that water in a honeycomb bilayer falls in approximately the same distance range from the surface as water within the bottom layer of the interfacial bilayer. In our fully solvated Pt(111) electrode model, starting from a potential of -0.75 V, water is almost exclusively found in the top layer of the interfacial bilayer. As the applied potential increases to more positive values, the density of water in the top layer of the interfacial bilayer decreases, and the density of water within the bottom layer of the interfacial bilayer close to the surface increases. At a potential of 1.51 V, the density of water in each portion of the interfacial bilayer is roughly equivalent.

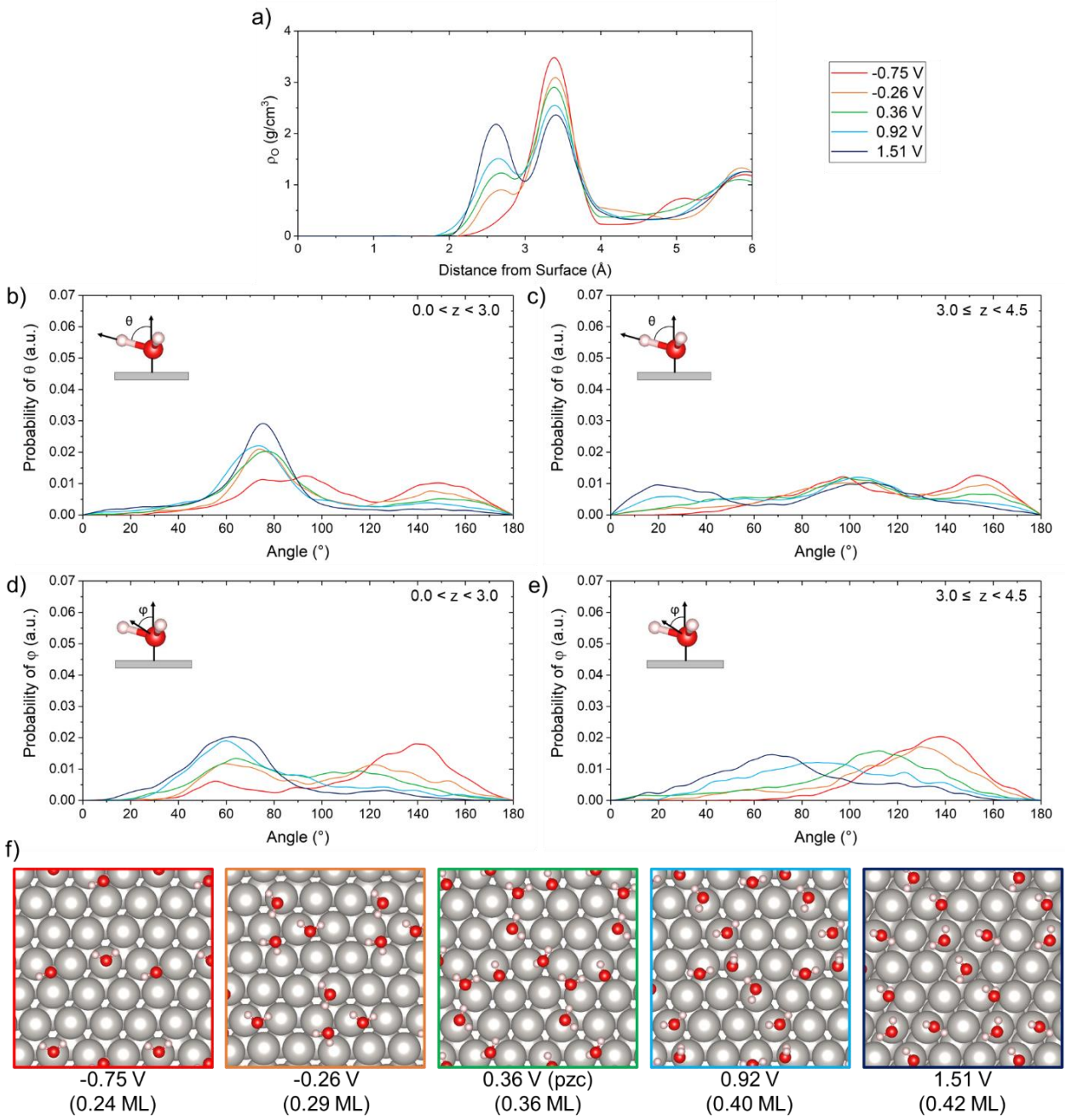

Figure 6.2: Water structures on clean electrified Pt(111) surfaces. **(a)** Density of oxygen in water (ρ_O) along the surface normal direction, where zero distance corresponds to the center of the top layer of Pt. Probability distribution of angle θ between the O-H bonds of water and the surface normal for interfacial water **(b)** within 3.0 Å of the surface and **(c)** within 3.0 and 4.5 Å of the surface. Probability distribution of angle φ between the water bisector and the surface normal of interfacial water **(d)** within 3.0 Å of the surface and **(e)** within 3.0 and 4.5 Å of the surface. **(f)** Representative images of interfacial water within 3.1 Å of the surface from AIMD simulations. Coverages refer to the average total coverage of water within 3.1 Å of the Pt(111) surface. Pt atoms are shown in gray, O atoms are shown in red, and H atoms are shown in white. All potentials are referenced with respect to the SHE.

In addition to examining the relative location of water with respect to the Pt(111) surface, we also analyze the overall orientation of water within the interfacial bilayer of the fully solvated electrode model. We consider the orientation of water within the bottom and top layers of the interfacial bilayer. The orientation of water is fully defined by 1) the angle between the O-H bonds in water and the surface normal (θ) for water within the bottom layer (Fig. 6.2b) and top layer (Fig. 6.2c) of the interfacial bilayer and 2) the angle between the water bisector (φ) and the surface normal for water within the bottom layer (Fig. 6.2d) and top layer (Fig. 6.2e) of the interfacial bilayer.

First, we consider water structures within the bottom layer of the bilayer. At -0.75 V, the distribution of θ peaks at ~90º and ~160º, while the distribution of φ peaks around ~140º. These features correspond to a water molecule with one O-H bond pointed almost directly downwards towards the surface and one O-H bond oriented parallel to the surface, otherwise known as 'one-H-down' water. Given that the Pt surface is negatively charged at this potential, we would expect that water would align itself so that hydrogen can point towards the surface. As the potential increases to more positive potentials, peaks form around $\varphi \approx 60º$ and $\theta \approx 75º$. In this orientation, the water molecules lie almost flat on the Pt(111) surface, and both O-H bonds within the molecule are pointed slightly upward at the same angle with respect to the surface. Therefore, we classify these water molecules as having a 'parallel' orientation. Again, these results align with the expectation that water will prefer to orient itself so that oxygen can face the surface while hydrogen faces away from the surface as the Pt surface becomes more positively charged at higher potentials. Furthermore, the probability of finding water in this position increases as the applied potential becomes more positive from -0.26 V to 1.51 V.

Next, we consider water structures within the top layer of the bilayer. At -0.75 V, the probability distributions for θ and φ in the top layer are similar to those at the same potential in the bottom layer. At a potential of -0.75 V, water in both layers of the bilayer orient in a 'one-H-down' position. As we move to more positive potentials, the applied potential has less of an effect on the orientation of water within the top layer compared to water within the bottom layer of the interfacial bilayer. Nevertheless, the water bisector orients itself from pointing towards the surface to pointing away from the surface due to the changing charge of the surface as the potential becomes more positive. Only at a highly positive potential of 1.51 V does water adopt a more consistently oriented structure. At this potential, θ peaks at ~20º and ~110º, while φ peaks around ~70º. These features correspond to a water molecule with one O-H bond pointed almost directly up away from the surface and one O-H bond pointed roughly parallel to the surface, which we can classify as 'one-H-up' water.

Oftentimes, DFT studies assume that water forms a 2/3 ML honeycomb water bilayer structure based on the original misinterpretation of water structures in UHV experiments. As stated previously, water in this configuration has a calculated maximum distance of 3.1 Å from the Pt(111) surface. Therefore, we examine representative images of water structures within 3.1 Å of the surface in our solvated electrode model (i.e., in the bottom layer of the interfacial bilayer structure) in Fig. 6.2f to directly compare these structures to the honeycomb bilayer model. As confirmed from our water oxygen density profiles in Fig. 6.2a, we find that moving to more positive applied potentials increases the density of water and the total coverage of water on the bottom layer of the interfacial bilayer. Within the potential range we studied for this work, we do not find any states where a honeycomb-bilayer-type structure forms on the surface, even at

potentials of 1.51 V. By increasing the applied potential beyond this point, we would expect Pt to dissolve in acidic conditions.[167] Furthermore, the average water coverage at 1.51 V is 0.42 ML, which is far below the 2/3 ML of water we would expect for a honeycomb bilayer structure. These findings confirm that in the absence of adsorbates, the honeycomb bilayer model is a poor representation of fully solvated Pt(111) electrode interfaces.

Because the density and orientation of interfacial water change on Pt(111) as the applied potential changes, we expect that the number of hydrogen bonds formed by water will also change as the applied potential changes. The local hydrogen bonding environment could play a substantial role in charge-transfer kinetics. For example, Ledezma-Yanez et al. have suggested that pH-dependent water reorganization can explain why the hydrogen oxidation reaction (HOR) and hydrogen evolution reaction (HER) are two orders of magnitude slower in alkaline versus acidic solutions despite the binding energy of hydrogen (a key descriptor for these reactions) not changing between the two conditions.[37] This finding is bolstered by the fact that the HOR and HER are far slower in alkaline versus acidic media on all platinum group metals, suggesting the structure of the solvent plays a role in the in the overall kinetics.[168] They proposed that water can form more favorable configurations for transferring protons (i.e. forming hydrogen bonds in the desired direction for charge transfer) near the potential of zero charge and that water can more easily reorient to transfer protons due to the reduced electric field. Typically, these experiments are performed relative to the reversible hydrogen electrode (RHE), which is related to the SHE by the following:

$$U_{RHE} = U_{SHE} + k_B T ln(10) pH/e \tag{6.8}$$

Because the onset of the HER at ~0 V vs RHE regardless of pH, this means that the applied

potential relative to the SHE (which is essentially a measure of the potential drop across an electrochemical interface) must change as the pH changes. Therefore, the local potential drop near the surface at the onset potential of the HER (i.e., on the SHE scale) is closer to the potential of zero charge in acidic conditions versus alkaline conditions. Because the hydrogen bonding properties change as the potential drop across the interface changes, these findings suggest that interfacial water environments that form a higher density of hydrogen bonds may also facilitate charge transfer kinetics.

We examine the number of hydrogen bonds ($n_{H\text{-}bonds}/H_2O$) accepted by water, donated by water, and accepted + donated (total) by water as a function of distance from the surface for each of the applied potentials considered in this study in Fig. 6.3 (we define a hydrogen bond with a 3.5 Å cutoff for the O-O distance and an H-O-O angle less than 30° [136]). For comparison, the onset potential of the HER is 0 V vs SHE at pH = 1 and -0.8 V vs SHE at pH=13. For accepted $n_{H\text{-}bonds}/H_2O$, there is no clear trend in $n_{H\text{-}bonds}/H_2O$ values as a function of potential below ~3.0 Å from the surface. Between ~3.0-4.0 Å, the accepted $n_{H\text{-}bonds}/H_2O$ increases as the applied potential becomes more positive. For donated $n_{H\text{-}bonds}/H_2O$, there are much clearer trends. Near the surface, there is a peak in donated $n_{H\text{-}bonds}/H_2O$; At -0.36 V and below, this peak occurs ~2.4 Å from the surface. At more positive potentials, this peak shifts closer to the Pt(111) surface, centered at ~2.0 Å. The shift in this peak can be rationalized by the transition of water within the bottom of the interfacial bilayer from a ‘one-H-down’ to ‘parallel’ water structure as the potential increases. In ‘one-H-down’ water, hydrogen bonds are formed with hydrogen in water that is farther from the Pt(111) surface (i.e. with the O-H bond running parallel to the surface rather than the O-H bond pointed towards the surface), while in ‘parallel’ water both O-H bonds are closer to the surface.

From ~2.5-4.0 Å, the donated $n_{H\text{-}bonds}/H_2O$ behaves similarly to accepted $n_{H\text{-}bonds}/H_2O$, where the donated $n_{H\text{-}bonds}/H_2O$ increases as the applied potential becomes more positive. Overall, the total $n_{H\text{-}bonds}/H_2O$ generally increases below ~4.0 Å from the surface as the potential becomes more positive. In the context of the HOR/HER, this would indicate that more hydrogen bonds form within interfacial water near the interface in more acidic conditions (more positive potentials) versus alkaline conditions (more negative potentials). Given that hydrogen bonding is a precursor for proton transfer reactions,[169] we suggest that the local hydrogen bonding near the interface could also play a role in influencing the different HOR/HER activities as a function of pH. However, more detailed analyses of water structures on other metals and analyses of how hydronium and hydroxide molecules impact these hydrogen bonding networks are necessary to fully evaluate the role of local hydrogen bonding environments on HOR/HER kinetics.

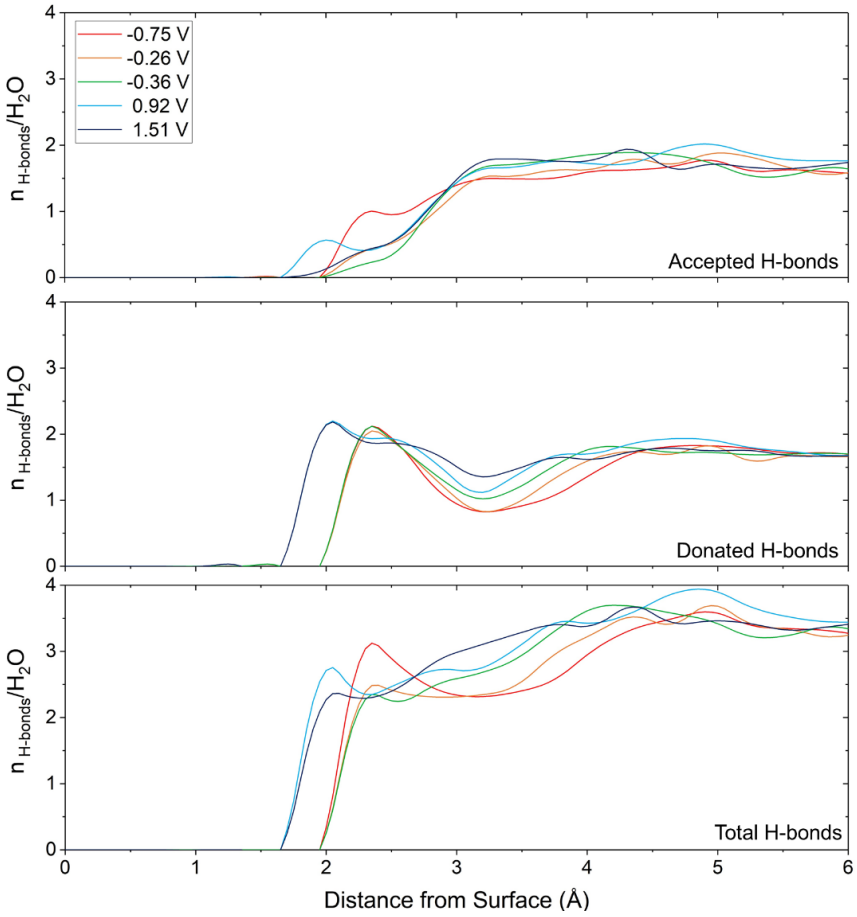

Figure 6.3: Hydrogen bond density ($n_{H\text{-}bonds}/H_2O$) along the surface normal direction, where zero distance corresponds to the center of the top layer of Pt. All potentials are referenced with respect to the SHE.

6.3.2 Water Structures on Hydroxyl-Covered Pt(111)

Depending on the applied potential and pH, the Pt(111) surface will not only be covered in water but will also be covered in oxygenates. Here, we focus on the role that adsorbed hydroxyl, OH*, plays in altering the structure of water within the EDL on Pt(111). Additionally, OH* is a key reaction intermediate in many electrocatalytic reactions, particularly the oxygen reduction reaction (ORR). We repeat our structural analysis of water to evaluate how OH* alters the local water structure around the solvated Pt(111) electrode interface.

We studied a range of hydroxyl coverages from 1/9 ML to 6/9 ML (considering all possible combinations of hydroxyl coverage configurations), which allowed us to calculate the potential-

dependent energy and structures of hydroxyl at each coverage. To determine at what conditions each of these structures would be the most stable, we constructed a Pourbaix diagram based on our calculated AIMD energetics, which is shown in Fig. 6.4. Although there is not experimental evidence to corroborate the entirety of the Pourbaix diagram, we can validate this diagram by comparing the most stable phases with cyclic voltammetry (CV) data from Stamenkovic et al.[170] Their measurements at pH=1 indicate Pt(111) should not adsorb oxygenates below 0.6 V vs RHE. From ~0.6 to ~0.8 V vs RHE, the coverage of oxygenates increases from 0 ML to 0.4 ML before plateauing at 0.4 ML at more positive potentials. Our calculated Pourbaix diagram indicates that at pH=1, oxygenates should start to adsorb at ~0.2 V/RHE in an anodic sweep and reach a coverage of 3/9 ML at ~1.0 V/RHE before plateauing at 3/9 ML at more positive potentials. This indicates that 2/9 ML OH* structures are over-stabilized on Pt(111) in our AIMD models, even though we do capture similar coverages of OH* as seen experimentally. Nonetheless, within our Pourbaix diagram, we find that 2/9 ML, 3/9 ML, and 6/9 ML of OH* are stable depending on the applied potential and pH.

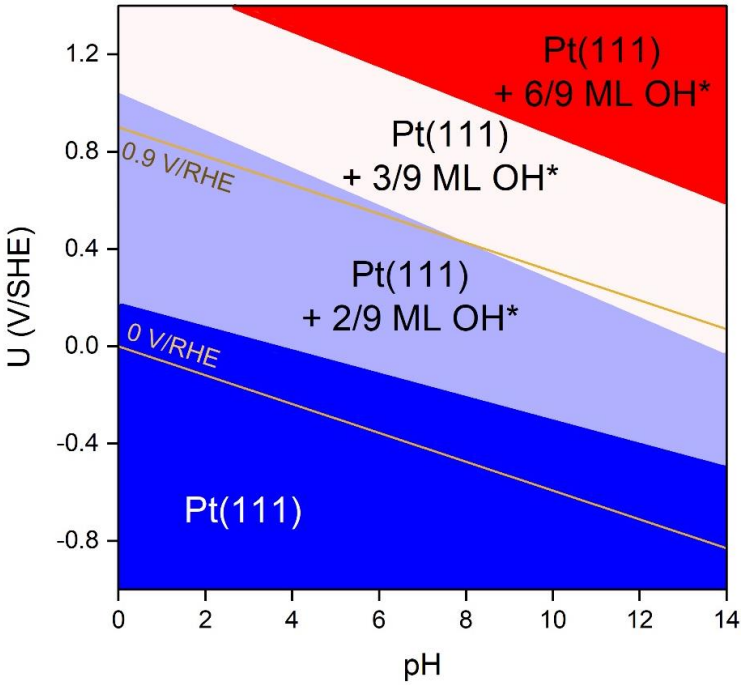

Figure 6.4: Pourbaix diagram showing most stable coverages of OH* on the Pt(111) surface. Yellow lines indicate 0 V/RHE, the approximate onset potential for the HER on Pt(111), and 0.9 V, the approximate onset potential for the ORR on Pt(111) for reference.

Next, we can examine how interfacial water structures are impacted by adsorbed hydroxyl on Pt(111). Here in the main text, we focus on the most stable structures as seen in our Pourbaix diagram. We start by examining how the density of water at the interface changes as we change both the applied potential and the hydroxyl coverage on the surface, which we show in Fig. 6.5 (OH* coverages not present in Pourbaix diagram are shown in Fig. F.1). Similar to the clean Pt(111) surface, we again find that there is a higher density of interfacial water between ~2-4 Å that forms an interfacial bilayer consisting of the bottom layer (less than 3.0 Å from the surface) and the top layer (between 3.0 and 4.5 Å from the surface). We also find that increasing the hydroxyl coverage increases the ratio of water in the bottom layer to water in the top layer of the interfacial bilayer within a given potential range. This effect becomes so pronounced that at 6/9 ML of OH*, there is almost no water in the top layer of the bilayer at potentials more positive than -0.72 V.

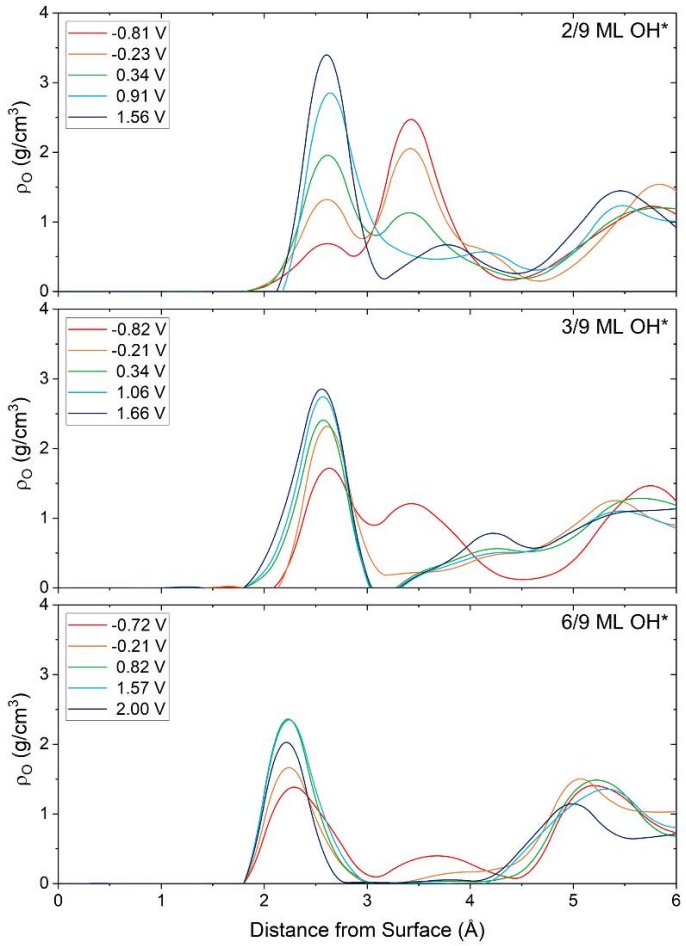

Figure 6.5: Density of oxygen in water (ρ_O) along the surface normal direction on hydroxyl-covered, electrified Pt(111) surfaces, where zero distance corresponds to the center of the top layer of Pt. All potentials are referenced with respect to the SHE.

Next, we consider the orientation of water within this interfacial water bilayer when OH* is present. Again, we analyze the orientation of water within the bottom and top layers of the interfacial bilayer. We describe the orientation of the water by calculating 1) the angle between the O-H bonds in water and the surface normal (θ) for water within the bottom layer and top layer of the bilayer (Fig. 6.6, OH* coverages not present in Pourbaix diagram are shown in Fig. F.2) and 2) the angle between the water bisector (φ) and the surface normal for water within the bottom layer and top layer of the bilayer (Fig. 6.7, OH* coverages not present in Pourbaix diagram are shown in Fig. F.3).

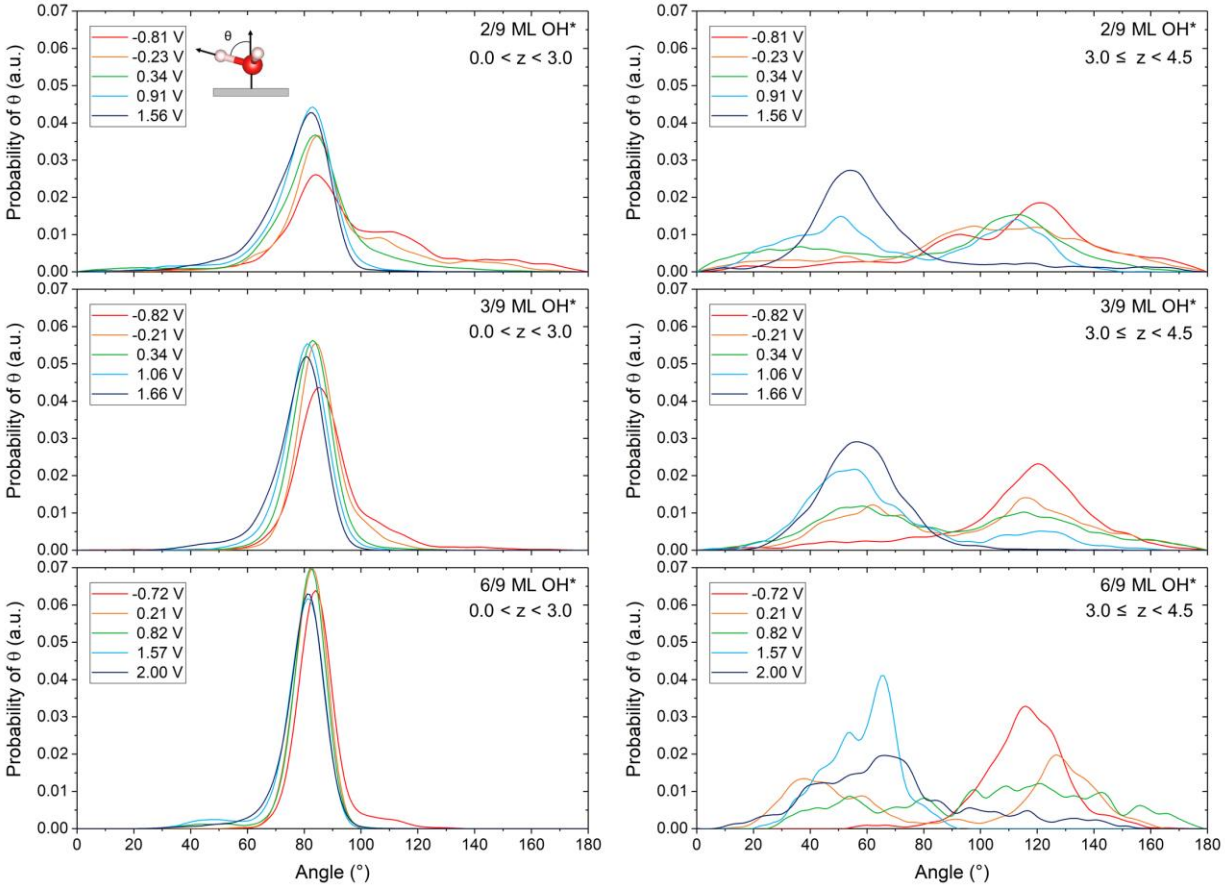

Figure 6.6: Probability distribution of angle θ between the O-H bonds of water and the surface normal for interfacial water for the most stable OH* coverages within 3.0 Å of the surface and within 3.0 and 4.5 Å of the surface. All potentials are referenced with respect to the SHE.

We first analyze water within the bottom layer of the interfacial bilayer. For all OH* coverages, we find that there is a sharp peak in θ at ~80º, indicating that water within this layer is oriented 'parallel' to the surface. At 2/9 ML OH*, increasing the applied potential to more positive values increases the probability of finding θ at ~80º. As the coverage of OH* increases, changing the applied potential has little effect on the probability of finding θ in a given state as the O-H bond angle is entirely fixed by the coverage of OH*. When we examine φ, we find that water in the bottom of the bilayer orients itself so that there is a peak in φ from 65-70º depending on the coverage and applied potential, again showing that water within this layer adopts a 'parallel'

orientation. At 2/9 ML OH*, the peak in φ grows as the peak shifts from 75º at -0.81 V to 65º at 1.56 V. In other words, water orients 'parallel' on the surface, and as the charge of the surface increases as the applied potential increases, hydrogen in water tilts farther away from the surface. As the OH* coverage increases, changing the applied potential has little effect on the probability of finding φ in a given state, similar to the case with θ. Overall, we find that water within the bottom layer of the interfacial bilayer forms a parallel orientation on the Pt(111) surface in the presence of OH*.

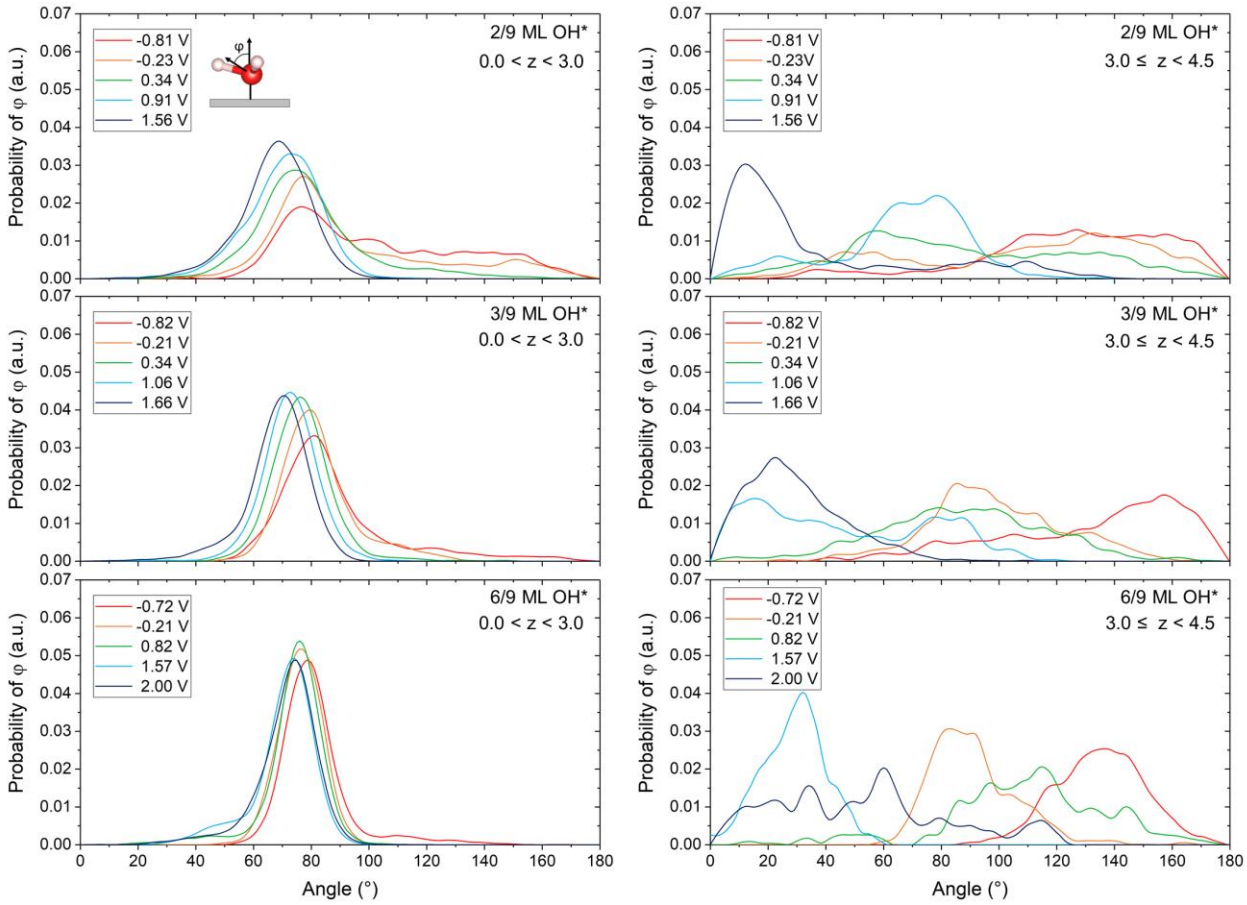

Figure 6.7: Probability distribution of angle φ between the water bisector and the surface normal of interfacial water for the most stable OH* coverages within 3.0 Å of the surface and within 3.0 and 4.5 Å of the surface. All potentials are referenced with respect to the SHE.

Next, we consider the orientation of water within the top layer of the interfacial water bilayer in the presence of OH*. At all OH* coverages, we find similar trends for the probability of

finding θ in a given orientation. At more negative potentials, water orients itself so that both O-H bonds point slightly towards the surface. As more positive potentials, both O-H bonds in water tilt away from the surface. When we examine φ at 2/9 ML OH*, there is not a strong correlation between the applied potential and the orientation of φ until 0.91V. At 0.91 V, there is a broad peak centered around the probability of finding φ at ~70 º, indicating that the water bisector is oriented slightly away from the surface. At 2/9 ML OH* and 0.91 V, water roughly adapts a 'parallel' orientation. As the potential increases to 1.56 V, the water bisector orients so that it points away from the surface, and water orients in a 'two-H-up' orientation. At higher OH* coverages, the little water in the top layer of the interfacial bilayer generally shifts so that the water bisector shifts from tilting towards the surface at low potentials to tilting away from the surface at higher potentials. Nevertheless, the amount of 'noise' in the probability of finding θ or φ increases as the coverage increases because the density of water within the top layer of the interfacial bilayer becomes almost zero as the OH* coverage increases.

Finally, we show representative images of interfacial water structures within the bottom layer of the bilayer (within 3.1 Å of the Pt(111) surface) and the associated average coverage of oxygenates (OH* + H_2O*) in Fig. 6.8. OH* coverages not present in Pourbaix diagram are shown in Fig. F.4. For these surfaces, we do find conditions where the oxygenate coverage is close to the 2/3 ML required for a honeycomb structure. Through inspecting these structures, we find that honeycomb overlayer structures form at some conditions on the Pt(111) surface, which is in accordance with the results from OH*/H_2O* co-adsorbed structures seen in UHV experiments. In particular, we find these types of honeycomb structures at some potentials for 2/9 ML OH* and a large range of potentials for 3/9 ML OH*. When the surface has 6/9 ML of OH*, the surface is

almost entirely covered in oxygenates at all potentials, suggesting that the Pt(111) surface oxidizes at these conditions rather than forming a OH*/H_2O* co-adsorbed structure.

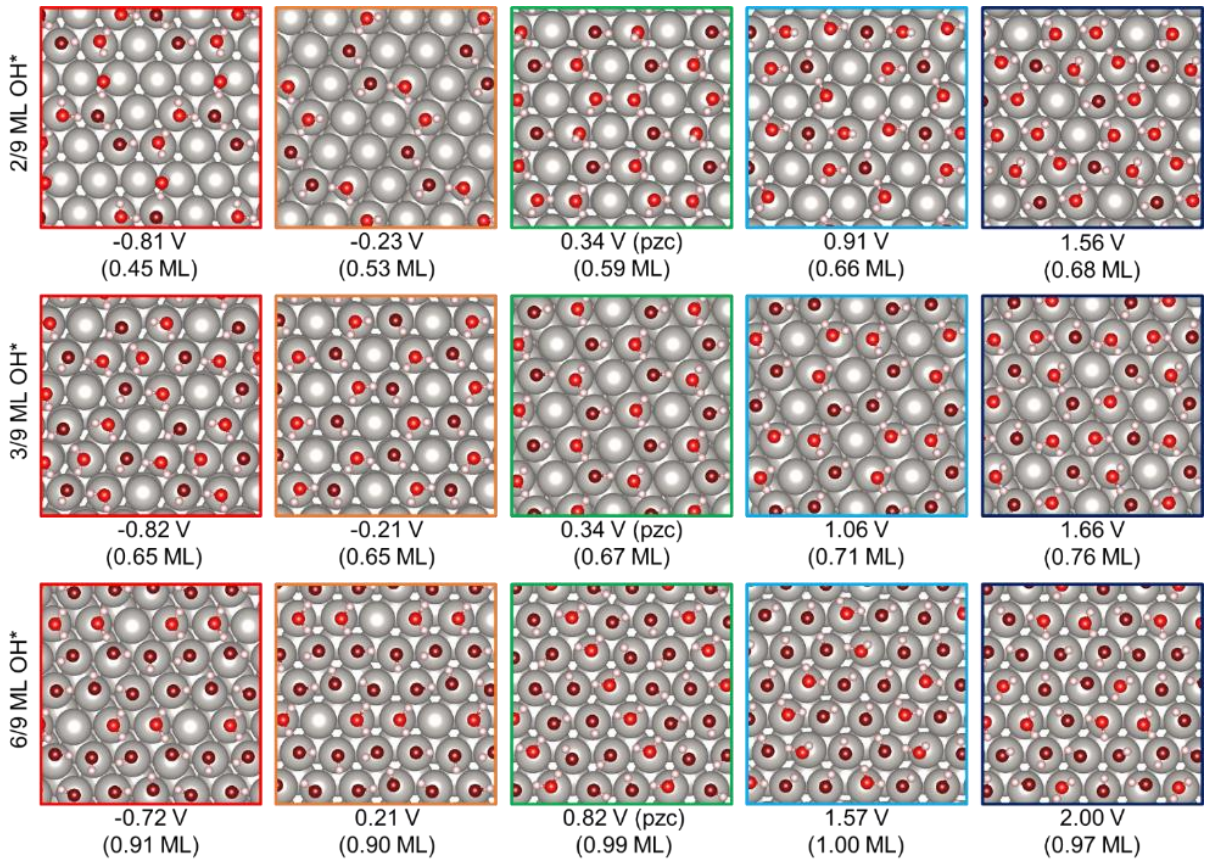

Figure 6.8: Representative images of interfacial water within 3.1 Å of the Pt(111) surface from AIMD simulations. Coverages refer to the average total coverage of oxygenates (OH* + H2O). Pt atoms are shown in gray, O atoms from water are shown in red, O atoms from OH* are shown in dark red, and H atoms are shown in white. All potentials are referenced with respect to the SHE.

6.3.3 Trends in Water Structures on Pt(111) Electrodes

We summarize the water structures seen on Pt(111) at a range of applied potentials and OH* coverages in Scheme 6.1. Overall, water on Pt(111) forms an interfacial bilayer structure on the surface with an increased density of water relative to the bulk. At more negative potentials, water in both layers of the bilayer form 'one-H-down' structures, and the density of water is concentrated in the top layer of the interfacial bilayer. As the potential becomes more positive, water in the bottom layer forms a 'parallel' structure while water in the top layer forms a 'one-H-up structure'. The ratio of water in the top layer to the bottom layer approaches one. Adding OH* to the Pt(111) surface shifts the balance of water in the interfacial water bilayer from the top layer to the bottom layer. Additionally, water tends to be oriented in a 'parallel' structure in the presence of OH*.

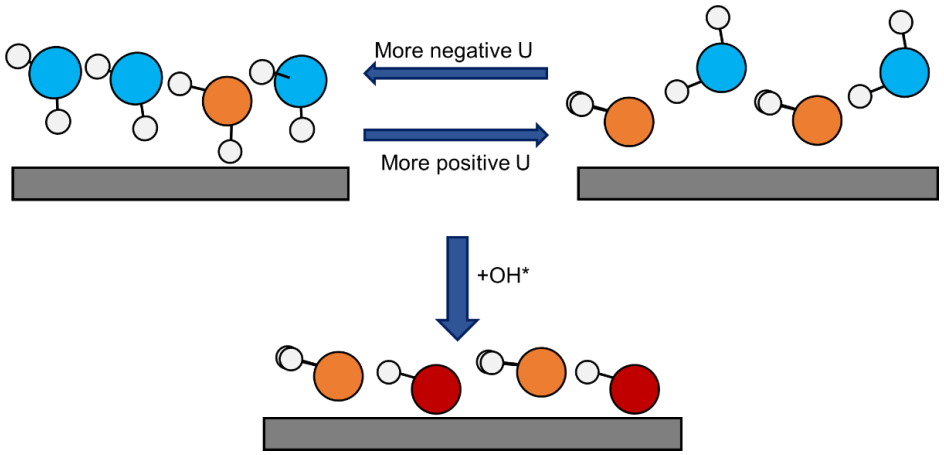

Scheme 6.1: Generalized trends in water structures formed on Pt(111) electrodes. O atoms within the bottom of the interfacial bilayer (within 3.0 Å of the surface) are shown in orange, O atoms within the top of the interfacial bilayer (within 3.0 and 4.5 Å of the surface) are shown in blue, O atoms in OH* are shown in dark red, H atoms are shown in white, and the Pt surface is shown in gray.

6.3.4 Comparing OH Structures Between a Honeycomb Bilayer and Full Interfacial Water Layer*

Considering that honeycomb structures form on the Pt(111) at some potentials and OH* coverages, one might expect that interfacial water structures could be approximated by a honeycomb bilayer structure where water molecules are replaced with adsorbates on Pt(111).

Furthermore, this approach is often used to approximate interfacial water structures in DFT calculations. Therefore, we compare how OH* interacts with water in a simplified honeycomb bilayer and a fully solvated electrode model. The minimum energy structures for 1/9-6/9 ML of OH* adsorbed on Pt(111) with a honeycomb water bilayer are shown in Fig. F.5.

We start by comparing the number of hydrogen bonds formed between OH* and water molecules or other OH* molecules. The total number of hydrogen bonds (donated and accepted) by OH* at each coverage studied is shown in Fig. 6.9. At all coverages of OH* above 1/9 ML, we find that OH* forms more hydrogen bonds in the full interfacial water model than the simplified honeycomb bilayer model. Because OH* forms more hydrogen bonds, we then evaluate whether these hydrogen bonds lead to more stabilized OH* species on the Pt(111) surface.

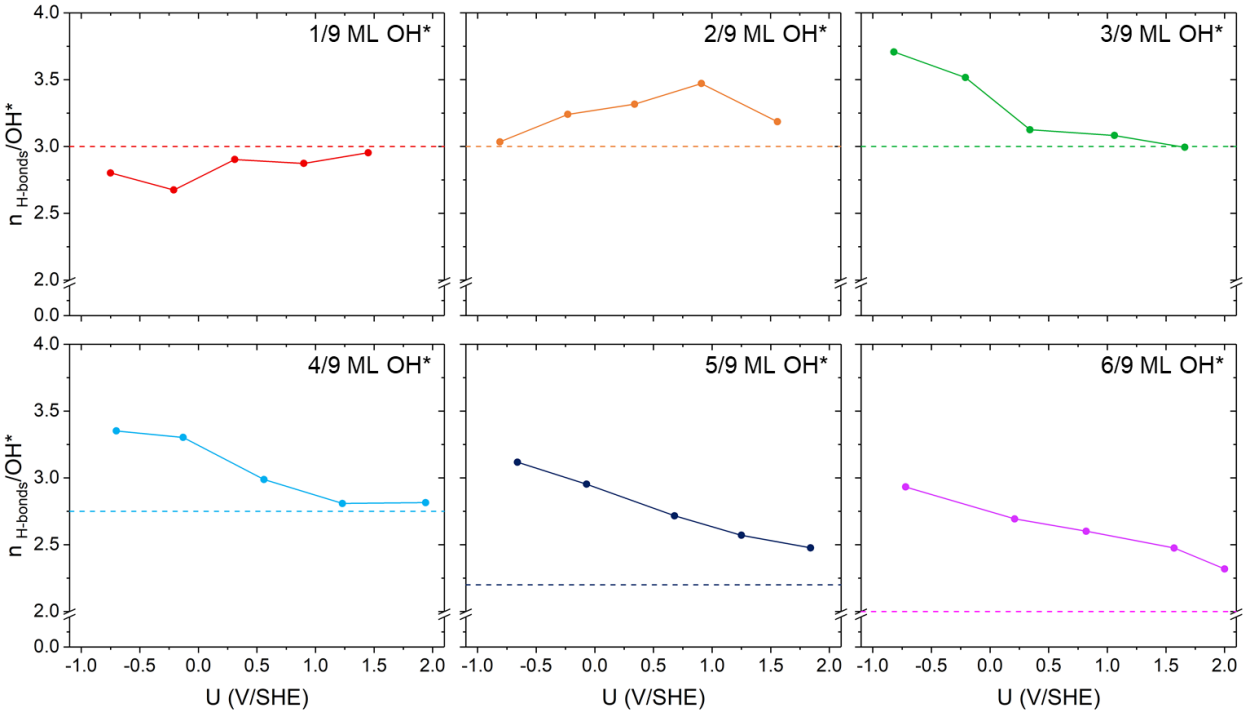

Figure 6.9: Number of hydrogen bonds formed between OH* and water or other OH* species within a simplified honeycomb water bilayer structure (dashed lines) and a full electrified interfacial water structure (points connected by solid lines to guide the eye) as a function of applied potential.

We calculate the differential free binding energy of hydroxyl with both a honeycomb

bilayer and a full interfacial water layer. We calculate the differential binding energy, $\Delta G_{OH,diff}$, of OH* in each system as:

$$\Delta G_{OH,diff} = G_{slab+xOH*+yH_2O} - G_{slab+(x-1)OH*+(y+1)H_2O} + \mu_{H_2O(l)} - G_{OH(g)} \qquad (6.9)$$

where G is the free energy, x refers to the number of OH* on a surface, and y refers to the number of water molecules in the system. For a fair comparison between the two water models, we use the free energy of OH in the gas phase as our reference state. The differential binding energy as a function of applied potential for both water models is shown in Fig. 6.10.

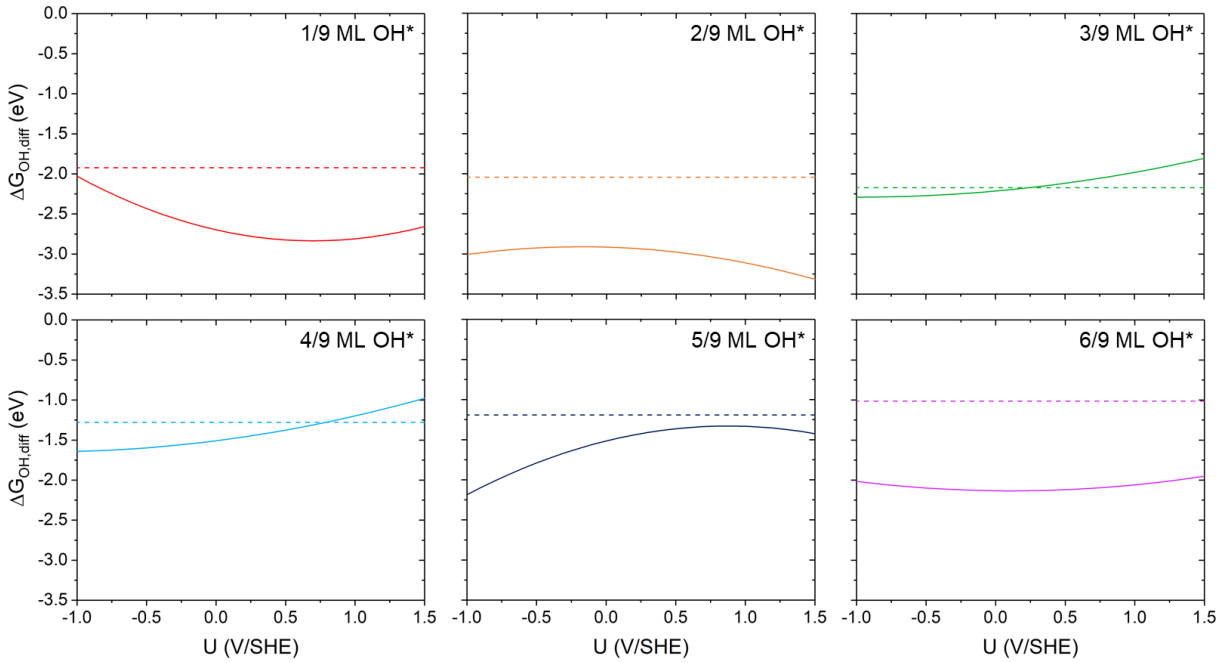

Figure 6.10: Differential free binding energy of hydroxyl ($\Delta G_{OH,diff}$) within a simplified honeycomb water bilayer structure (dashed lines) and a full electrified interfacial water structure (points connected by solid lines to guide the eye) as a function of applied potential.

The first thing to note is that $\Delta G_{OH,diff}$ is always constant for the honeycomb bilayer model, while $\Delta G_{OH,diff}$ changes as a function of potential for the full interfacial bilayer model. This is due to the fact that for the honeycomb bilayer model, we cannot calculate how the energy of the system changes as we change the applied potential across the water/electrode interface; however, for the

full solvated electrode model, $G_{slab+xOH^*+yH_2O}$ and $G_{slab+(x-1)OH^*+(y+1)H_2O}$ are a function of the applied potential and incorporate how the charge of the Pt(111) surface and the orientation and density of water molecules impact the binding energy of OH*. For 1/9 ML OH*, we find that even though OH* forms less hydrogen bonds in the fully solvated electrode model, OH* binds stronger on the surface in the fully solvated electrode model than in a honeycomb bilayer. In fact, OH* always binds stronger to the surface in a fully solvated electrode model than in a honeycomb bilayer model for all OH* coverages except 3/9 and 4/9 ML OH*. For these coverages, OH* can bind weaker in the fully solvated electrode model at more positive potentials.

These results indicate that while hydrogen bonds are critical for stabilizing OH* species, other factors, like the charge of the surface, the applied potential, and repulsive interactions within high densities of oxygenates can also impact the stability of OH* on a Pt(111) surface. Furthermore, we only expect to see honeycomb-bilayer-like structures consistently with 3/9 ML OH* in the fully solvated electrode model, so the honeycomb bilayer model cannot accurately depict the water structures that form at other coverages. However, a fully solvated electrode model that utilizes AIMD can take all of these factors into account to provide a holistic view of OH* bonding strength within the EDL. These results indicate that the binding properties of adsorbates on electrode surfaces are highly influenced by interactions with water molecules and charged electrode surfaces. More detailed models of adsorbates at electrocatalytic active sites that include surface charge, applied potential, and solvent interactions can help us better understand and tailor these interactions so that we can design improved electrocatalysts.

6.4 Conclusions

In this work, we examine interfacial water structures on Pt(111) and evaluate how the

applied potential and OH* surface coverage impacts interfacial water structures. Because these structures are nearly impossible to probe experimentally, we utilized AIMD models to elucidate these water structures. On clean Pt(111) surfaces, the density and orientation of water at the solid/liquid interface strongly depend on applied potential. However, there were no conditions where a honeycomb water bilayer, a popular method for evaluating solvent effects in theoretical models, forms at the Pt(111) surface. By including OH* on the Pt(111) surface, we find that honeycomb water bilayers form at some OH* coverages (around 3/9 ML OH*) and applied potentials on the surface. We then show that a simple water honeycomb bilayer model predicts different hydrogen bonding networks and OH* binding energies than a full model of water within the electric double layer at the solid/liquid interface. These findings show that water structures are drastically altered by changes in the applied potential and coverage of OH*. In turn, these structural changes can lead to differences in interactions between adsorbates on a catalyst surface and water under a range of conditions. These differences can alter the stability of adsorbates on a catalyst surface, which have implications in catalysis research where these interactions are critical for optimizing the performance of electrocatalysts.

Chapter 7: First-Principles Trends of Formic Acid Electro-oxidation on Transition Metals Alloyed with Platinum and Palladium

7.1 Introduction

Although fossil fuels played a critical role in increasing living standards across the globe, rising greenhouse gas emissions continue to introduce widespread consequences to society and the environment. We must therefore find new ways to generate energy that utilize sustainable fuel sources to shift the focus of our energy economy away from fossil fuels. Low-temperature polymer electrolyte membrane (PEM) fuel cells are a promising alternative-energy solution in the transportation and mobile power sectors.[171] Unlike combustion engines, fuel cells are not limited by Carnot efficiencies[172] and can utilize a wide array of fuels that are carbon-neutral or are produced using renewable energy sources.[38,39,50,52,173–176]

Hydrogen is a popular potential fuel for use in PEM fuel cells because oxidizing hydrogen results in water as the sole product. However, there is limited technology available to efficiently and safely transport and store hydrogen, and there would need to be a massive change in infrastructure to support a hydrogen fuel economy. Such limitations do not exist for liquid fuels, making them a more attractive alternative to hydrogen. Because many liquid fuels are carbon based, they ideally should be produced from renewable sources like carbon dioxide[177] or biomass.[178] Formic acid (FA) has emerged as a viable potential liquid fuel source due to its facile oxidation kinetics at room temperature,[179–184] low crossover through Nafion membranes,[185] and easy sourcing through biomass conversion through levulinic acid.[186] Additionally, FA has a higher equilibrium cell voltage (1.40 V) compared other potential fuels such as hydrogen (1.23 V),

dimethyl ether (1.20 V), and methanol (1.21 V).[187] For these reasons, direct formic acid fuel cells (DFAFCs) have emerged as a promising technology for generating clean energy for transportable power.

Platinum and palladium are the most widely studied catalysts for formic acid oxidation (FAO) due to their relatively high activity.[187] However, these metals are easily poisoned by CO, require prohibitively large overpotentials to oxidize FA, and are unstable in acidic conditions found in DFAFCs. One way to address these shortcomings by alloying Pt and Pd with other metals. Indeed, DiSalvo and coworkers developed PtBi and PtPb catalysts that have superior activity towards FA electro-oxidation compared to Pt, PtRu, and Pd catalysts.[55,56] Additionally, PtAu[53,54] and PtIr[188] catalysts have been shown to have superior activity towards methanol and FA electro-oxidation. Because Pd in particular has the highest electrocatalytic activity of any of the transition metals for oxidizing formic acid, there have been several successful efforts to improve the activity of Pd by alloying it with Au,[57] Cu,[58] Ni,[58–60] Co,[60] Ru,[61] Fe,[60] Ti,[60] V.[60]

Due to the large combination of potential alloys, experimental efforts in synthesizing new catalysts for FAO remains a challenge. Therefore, *ab initio* screening methods are an invaluable tool for identifying potentially more active catalysts that can then be further explored experimentally and theoretically to further assess their activity, selectivity, and stability. In this work, we use periodic density functional theory (DFT) calculations to examine the reactivity of alloyed catalysts that consist of transition metal solutes (Au, Ag, Cu, Ir, Pd, Pt, Ir, Rh, Ru, and Re) alloyed with Pt or Pd solvents. Based on our previous work studying trends in FA oxidation on transition metal surfaces, we believe that these transition metal solutes provide a wide array of properties that could be of benefit in FA electro-oxidation when alloyed with Pt or Pd.[174,181] In this

work, we calculate the free energies of key surface intermediates involved in FA electro-oxidation on the (111) facet of Pt- and Pd-based bimetallic alloys to study key reactivity trends and identify promising candidates for new catalysts for FA electro-oxidation.

7.2 Methods

7.2.1 *DFT Calculations*

We performed periodic DFT calculations as implemented in the Vienna *Ab Initio* Simulation Package (VASP)[81,82] to calculate the free energies of critical adsorbed intermediates in FA electro-oxidation. Core states were represented by projector augmented wave (PAW) pseudopotentials,[120,121] and valence states were expanded in a plane wave basis set with a cutoff energy of 400 eV. We utilized the PW-91 form of the generalized gradient approximation (GGA).[78] Our analysis focuses on the most relevant FAO reaction intermediates on each surface, namely formate (HCOO*), carboxyl (COOH*), carbon monoxide (CO*), and hydroxyl (OH*) (* denotes an adsorbed species). These surfaces include the close-packed facets of Pd, Pt, Ir, Rh, Ru, and Re as well as the close-packed facets of P_3M alloys (P = Pt or Pd, M = Au, Ag, Cu, Ir, Pd, Pt, Rh, Ru, or Re, where $P \neq M$). Lattice constants for these systems are given in Table G.1. In this work, our analysis focuses on Pt, Pd, and P_3M alloys, while values for other surfaces are given for comparison in Appendix G. The bulk of the alloys were modeled as a $L1_2$ crystal structure (Cu_3Au prototype), where each solute metal atom has twelve nearest-neighbor solvent atoms. Lattice constants for bulk alloys were calculated using a cubic unit cell with one overall lattice constant. We modeled each surface using a four-layer slab model where the bottom two layers of the slab were fixed at their bulk lattice constant (see Table G.1) and the top two layers and adsorbates were fully relaxed. All surfaces were modeled with a (2 × 2) unit cell, resulting in a coverage of ¼ monolayer (ML) for all adsorbates. Although our previous work on FAO utilized (3 × 3) unit

cells,[174,181] we utilized this smaller unit cell to accommodate the structure of an ordered P_3M alloyed surface. Periodic images in the *z* direction were separated by ~14 Å of vacuum, and we modeled the adsorption of reaction intermediates on one side of the surface and applied corresponding dipole corrections to the electrostatic potential.[124,189] To sample the surface Brillouin zone, we used an (8 × 8 × 1) k-point mesh.[122]

7.2.2 Surface Segregation in Alloys

Studying ordered alloys with a bulk termination gives us key trends in how different transition metal solutes can adjust the reactivity of Pt or Pd. However, alloyed surfaces can reconstruct and lead to atoms segregating on the surface of catalysts with and without adsorbates. To capture the potential effects of surface segregation, we fixed the bottom two layers of our slabs and examined the energetics of every permutation of the top surface atoms with and without adsorbates. For the top two layers, we repeated our calculations for every unique arrangement of the eight atoms in the top two layers of each unit cell, resulting in seven different structures, as shown in Fig. 7.1. Each structure is denoted as $P_3M\text{-}x_y$, where x is the number of solute atoms in the topmost layer (x = 0, 1, or 2) and y differentiates structures with the same x value. Alloyed surfaces that contain the same structure in the top two layers as in the bulk are denoted as $P_3M\text{-}1_1$. The most-stable binding structures for clean surfaces and surfaces with each adsorbate (at ¼ ML coverage) can be found in Section G.3 of Appendix G.

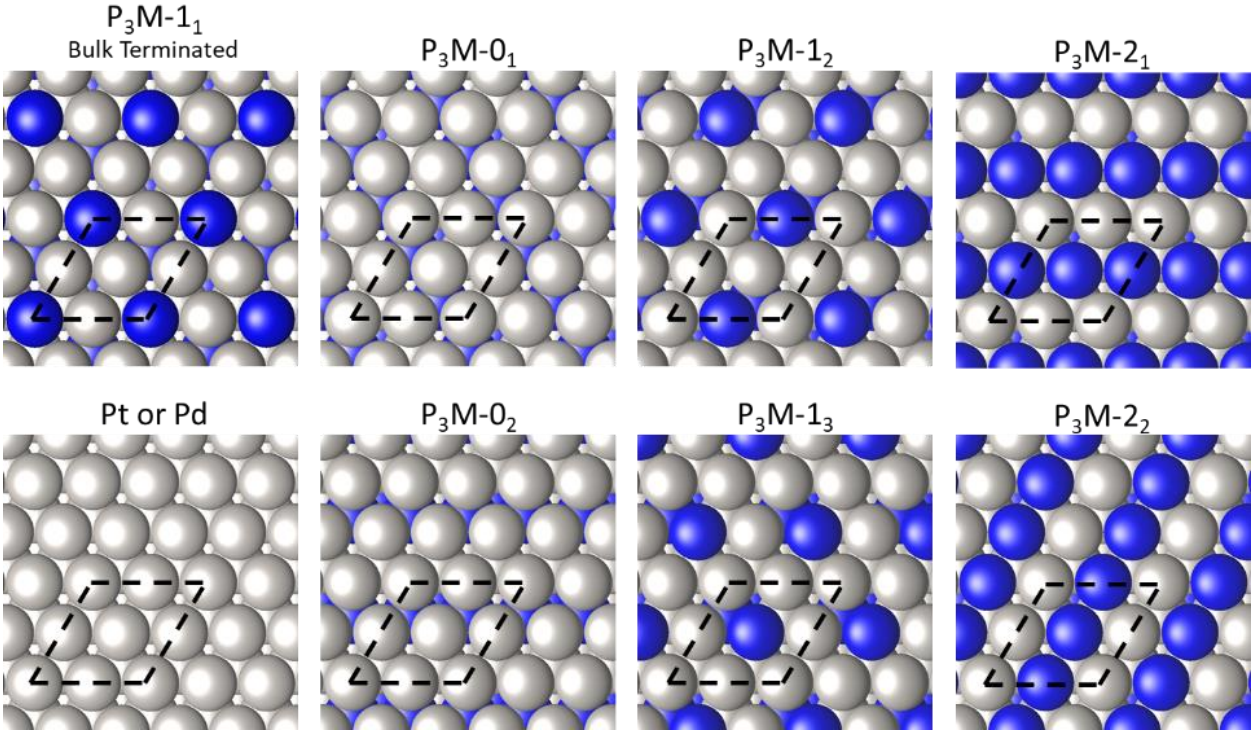

Figure 7.1: Top-down views of studied surfaces. Each structure is denoted as $P_3M\text{-}x_y$, where x is the number of solute atoms in the topmost layer per unit cell (x = 0, 1, or 2) and y differentiates between structures with the same x value. Note that while the top atom structures may appear similar, the hollow site structures vary between different models. Pt or Pd atoms are shown in grey, and solute atoms (Au, Ag, Cu, Ir, Pd, Pt, Ir, Rh, Ru, and Re) are shown in blue. Dashed black lines delineate the unit cell.

7.2.3 Modeling FA Electro-oxidation

In accordance with previous work,[174] we study FA electro-oxidation in the context of the following elementary steps:

$$HCOOH(g) + * \rightarrow HCOO* + H^+ + e^- \quad (1)$$

$$HCOO* \rightarrow CO_2(g) + * + H^+ + e^- \quad (2)$$

$$HCOOH(g) + * \rightarrow COOH* + H^+ + e^- \quad (3)$$

$$COOH* \rightarrow CO_2(g) + * + H^+ + e^- \quad (4)$$

$$COOH^* + * \rightarrow CO^* + OH^* \quad (5)$$

$$CO^* + OH^* \rightarrow CO_2(g) + 2^* + H^+ + e^- \quad (6)$$

$$COOH^* + H^+ + e^- \rightarrow CO^* + H_2O(g) \quad (7)$$

$$H_2O(g) + * \rightarrow OH^* + H^+ + e^- \quad (8)$$

These steps form the basis of the three pathways considered in our analysis. The first pathway is the direct oxidation of FA via formate, which consists of steps (1) and (2). Second, we consider the direct oxidation of FA via carboxyl, which consists of steps (3) and (4). Finally, we consider the indirect oxidation of FA via carboxyl, which consists of steps (3) and (5)-(8). Like our previous research,[174,181,190] our work excludes the indirect oxidation of FA via formate, where CO* is produced from formate due; this reaction is energetically unfavorable, especially when compared to how easily CO* can form through carboxyl.[181,191]

To model the effect of an electric potential in our calculations, we utilized the *post facto* computational hydrogen electrode (CHE) formalism as developed by Nørskov and coworkers.[17] According to the CHE formalism, hydrogen gas is in equilibrium with protons and electrons at standard conditions of 298 K, 1 bar H_2, and all pH values, at a defined potential of 0.00 V with reference to the reversible hydrogen electrode (RHE), according to the following reaction:

$$H_2(g) \leftrightarrow 2(H^+ + e^-), \Delta G = 0 \text{ at } 0.00\ U_{RHE}$$

All potentials hereafter are relative to the RHE. The applied bias (U) is accounted for by shifting the free energy of a proton-electron pair by -|e|U, where |e| is the absolute charge of an electron. To examine how changing the potential changes our reaction energetics, we calculate

Gibbs free energy (G) of each reaction intermediate:

$$G = E_{total} + ZPE - TS \tag{7.1}$$

where E_{total} is the total energy of the system (slab + adsorbate) calculated from DFT, ZPE is the calculated zero-point energy, S is the calculated entropy, and T is the standard temperature of 298 K. For consistency with previously published work on methanol[38–40] and formic acid electro-oxidation,[174] all calculated values of G are relative to those of gas-phase CO_2, H_2, and H_2O.

After calculating the energetic information for each step in our reaction network, we then calculate the activity, A, of each reaction step:

$$A = k_B T min_i \left(log \frac{k_i}{k_0} \right), \text{ where } k_i = \nu_i e^{-E_{a,i}/k_B T} \tag{7.2}$$

where k_B is Boltzmann's constant, T is the absolute temperature (298K in this work), k_i is the forward rate constant of reaction i, v_i is the prefactor for reaction i, and $E_{a,i}$ is the activation barrier for reaction i, and k_0 normalizes the activity of non-activated electron/proton transfer steps to zero. In this work, we assume that activation barriers for each step are correlated with the corresponding reaction thermochemistry through Brønsted-Evans-Polanyi relationships.[1,192] In other words, the more endothermic a reaction is, the higher its corresponding activation barrier. In particular, the CHE formalism establishes that the kinetic barriers of proton-electron transfer steps are approximated by their potential-dependent free energy change (ΔG), meaning that the activation barrier for a faradaic step equals ΔG if ΔG is positive and equals zero if ΔG is zero or negative. In the above reaction mechanism step (5) is the only non-faradaic step. However, we do not explicitly calculate the barrier for step (5) and instead take ΔG as a first approximation for the reaction barrier, in accordance with what we have done in previous work.[174,190] Based on these assumptions,

we simplify our expression for activity to $A = \min_i(-\Delta G_i)$.

To analyze each of the three pathways involved in our reaction network, we calculate the onset potential as the minimum applied potential needed to ensure that all proton-electron transfer steps in the pathway take place spontaneously (i.e., $\Delta G \leq 0$). We therefore define the potential-determining step as the most endergonic (or least exergonic if all steps are exergonic) step in each path.

7.3 Results and Discussion

In the following section, we first examine FA electro-oxidation on Pt and Pd to highlight the benefits and pitfalls of each catalyst. After examining Pt and Pd, we then focus our discussion on trends in the reactivity of alloyed catalysts.

7.3.1 Formic Acid Electro-oxidation on Pt and Pd

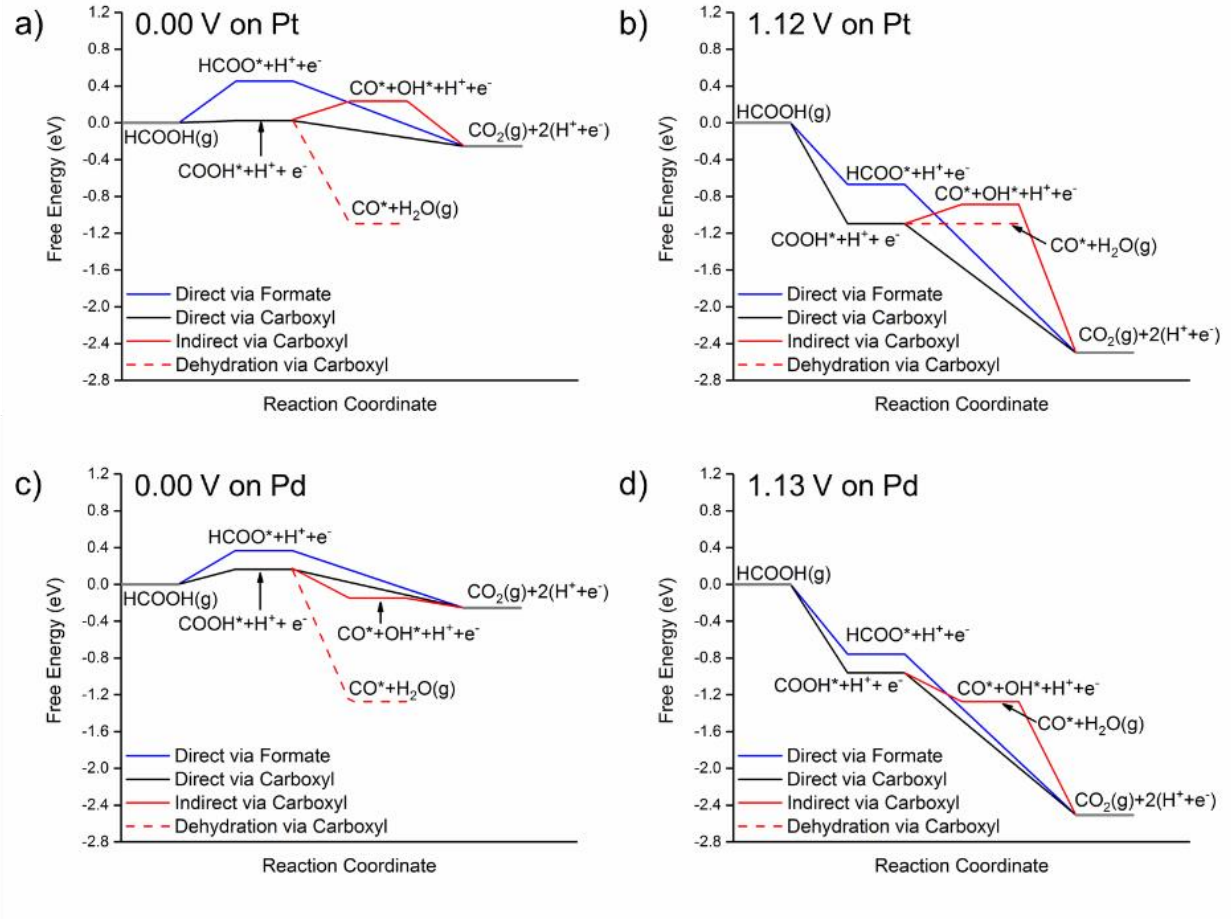

Figure 7.2: Free energy diagrams for formic acid electro-oxidation on Pt(111) at **(a)** 0.00 V and **(b)** 1.12 V (onset potential of indirect mechanism) and on Pd(111) at **(c)** 0.00 V and **(d)** 1.13 V (onset potential of indirect mechanism).

Free energy diagrams for FAO on Pt(111) and Pd(111) are shown in Fig. 7.2. Starting with Pt, the initial deprotonation of FA to form HCOO* or COOH* is endergonic at 0.00 V (Fig. 7.2a). Therefore, the direct oxidation of FA via HCOO* begins at an onset potential of 0.45 V, and the direct oxidation of FA via COOH* begins at an onset potential of 0.02 V. Because the formation of both intermediates requires the removal of one proton, HCOO* will always be 0.43 eV less stable than COOH* at all potentials according to the CHE formalism, and COOH* formation will always be preferred. Once COOH* is formed, it can undergo a further deprotonation step to form

either CO_2 directly or CO* and H_2O(g). At 0.00 V, CO* formation is energetically preferred, thus poisoning the catalyst surface. CO* can be removed by increasing the potential to 1.12 V to initiate the indirect oxidation of FA (Fig. 7.2b), at which point the free energy of COOH* + H^+ + e- is equivalent to that of CO* + H_2O. After COOH* forms at this potential, it can then deprotonate to form CO_2.

Next, we focus on FA-oxidation on Pd. Like Pt, the initial deprotonation of FA to form HCOO* or COOH* is also endergonic at 0.00 V on Pd (Fig. 7.2c). The direct oxidation of FA via HCOO* has an onset potential of 0.37 V, while the direct oxidation of FA via COOH* has an onset potential of 0.16 V. Like Pt, COOH* is still energetically more stable than HCOO*, but only by 0.20 eV. When COOH* forms, it can either deprotonate to form CO_2 or undergo a more energetically favorable dehydration reaction to form surface-poisoning CO*. By increasing the potential to 1.13 V (Fig. 7.2d), H_2O can be activated to form OH* and a proton-electron pair, and OH* can then react to form CO_2(g) and a second proton-electron pair.

Finally, we briefly discuss the effect of coverage on the energetics of FAO. In our prior work examining FAO on monometallic catalysts,[174] we studied all reactants at a 1/9 ML coverage as opposed to the 1/4 ML coverage considered here. We note that the binding energy of adsorbates changes by $\leq$ 0.1 eV between the two coverages, well within expected errors for DFT,[193] but that these differences could result in some kinetic variation. For both Pt and Pd, we found that increasing the coverage from 1/9 ML to 1/4 ML destabilizes formate, resulting in the onset potential for the direct oxidation via formate increasing by 0.09 V for Pt and 0.11 V for Pd. Conversely, increasing the coverage from 1/9 ML to 1/4 stabilizes carboxyl for both metals, resulting in the onset potential for the direct oxidation via carboxyl pathway decreasing by 0.03 V

for Pt and 0.08 V for Pd. We also consider how changing the coverage impacts the onset potentials for the indirect pathway via carboxyl. Both the CO* + OH* state and the CO* + H_2O are destabilized at 1/4 ML relative to the same states at 1/9 ML on both metals. Overall, this makes removing CO* + OH* by forming COOH* or by generating CO_2 and a proton-electron pair more facile at 1/4 ML versus 1/9 ML coverage. Therefore, the onset potential for the indirect pathway via carboxyl is 0.1 V lower on Pt at 1/9 ML compared to 1/4 ML. If the potential determining step is activating water to form OH* and a proton-electron pair, then the relative difference between the CO* + OH* state and the CO* + H_2O state will determine whether the onset potential for the indirect pathway via carboxyl increases or decreases. In the case of Pd, this step is more difficult at 1/4 ML versus 1/9 ML; therefore, the onset potential for the indirect pathway via carboxyl is 0.08 V higher at 1/4 ML versus 1/9 ML. In general, we expect that the onset potential will increase for the direct oxidation via formate pathway, decrease for the direct oxidation via carboxyl pathway, and could increase or decrease for the indirect oxidation via carboxyl for 1/4 ML compared to 1/9 ML of adsorbates.

Although Pt and Pd are the most active monometallic catalysts for FA electro-oxidation, they both have drawbacks. Because COOH* is more stable than HCOO*, both catalysts will tend to form CO*, poisoning the catalyst surface. Therefore, large overpotentials are needed to remove CO*. By alloying Pt and Pd with other transition metals, we aim to design new catalysts with fundamentally enhanced properties compared to Pt and Pd. The ideal catalyst should: 1) promote the formation of HCOO* relative to COOH* to avoid poisoning the catalyst surface with CO* formed from COOH*, and 2) destabilize CO* and/or stabilize OH* so that CO* can be removed at lower onset potentials. In the following subsection, we analyze the properties of catalysts containing a 3:1 ratio of Pt or Pd alloyed with a second metal to screen for catalysts that are more

active for FAO. The free energy of adsorbates on each alloyed surface are reported in Table G.2 for Pt alloys and Table G.3 for Pd alloys. We use this energetic data to calculate the onset potential of the direct oxidation pathway via formate, the direct oxidation pathway via carboxyl, and the indirect oxidation pathway via carboxyl, which we report in Table G.4 for Pt alloys and Table G.5 for Pd alloys. Additionally, we report the reaction free energy for each step in the FA electro-oxidation pathway in Table G.6 for Pt alloys and Table G.7 for Pd alloys.

7.3.2 Bulk-terminated Alloys

In this next section, we focus our analysis on alloyed surfaces. The relative energies of each alloy surface structure are reported in Table G.8 for Pt alloys and Table G.9 for Pd alloys. We first examine the FAO mechanism on each of the surfaces terminated with their bulk structure.

Direct oxidation via formate: As a first step, we examine how the bulk structure of a P_3M alloy with a solute metal M (M = Au, Ag, Cu, Ir, Pd, Pt, Rh, Ru, or Re) in a solvent metal P (P = Pt or Pd, where P ≠ M) affects a catalyst's reactivity towards FA electro-oxidization. In this case, we examine the reaction free energies for all P3M-1_1 systems (see Fig. 7.1 for structure), in which the top two layers of the alloy slab model have the same structure as the bulk alloy in the bottom two layers.

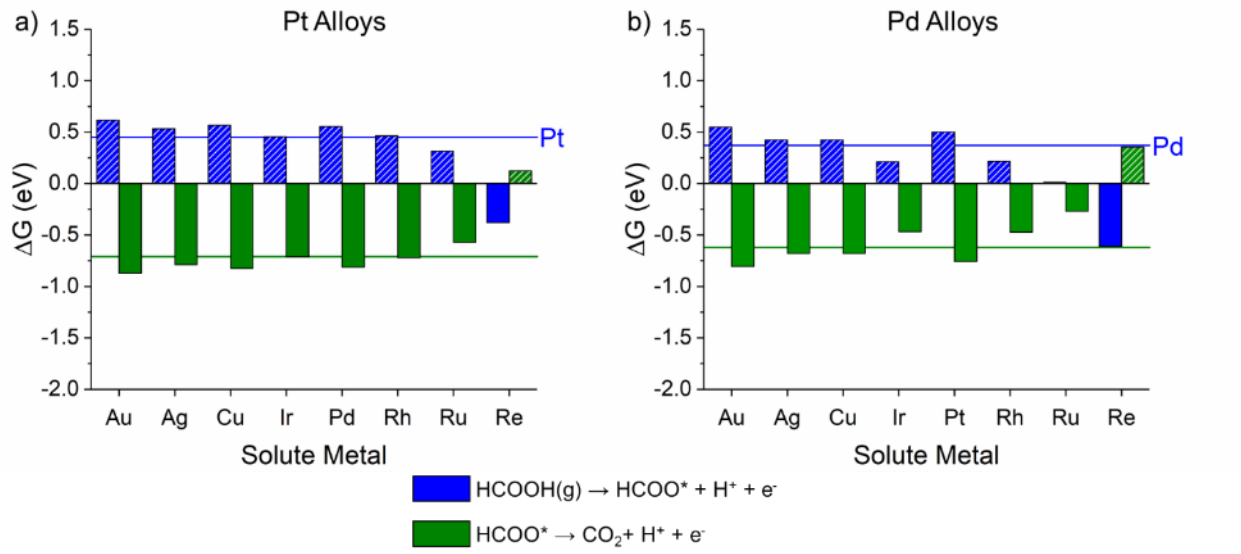

Figure 7.3: ΔG for direct oxidation of formate pathway on **(a)** Pt alloys and **(b)** Pd alloys. The potential-determining step is indicated with a dashed bar. The blue and green lines indicate ΔG of a reaction step for pure **(a)** Pt or **(b)** Pd, and the color of the line label indicates the potential-determining step for each respective metal. (Blue bars: HCOOH(g) → HCOO* + H^+ + e^- Green bars: HCOO* → CO_2(g) + H^+ + e^-)

In the direct oxidation via formate pathway, FA first oxidizes to form HCOO* and a proton-electron pair before oxidizing again to form CO_2 and a second proton-electron pair. Fig. 7.3 shows the reaction free energy associated with each step in this pathway for each alloy. From this data, we extract trends in how a solute metal affects the reactivity of Pt or Pd-based alloys towards FA electro-oxidation. For both Pt_3M and Pd_3M alloys, Pt or Pd and the coinage metals Au, Ag, and Cu increase the free energy needed to deprotonate HCOOH and form HCOO* on the surface, making HCOO* formation more difficult when alloyed with Pt or Pd. Alternatively, alloys containing Ru oxidize FA to form HCOO* more easily than Pt and Pd while still maintaining HCOO* formation as the potential-determining step for this pathway. Re is the only solute that causes HCOO* formation from HCOOH to be exergonic for both Pt_3M and Pd_3M alloys. In this case, the potential-determining step for Pt or Pd alloyed with Re in this reaction path is not forming HCOO*, but rather removing HCOO* to produce CO_2 and a proton-electron pair. For the other transition-metal solutes, there is not a clear trend as to how each metal affects reactivity. Alloying

Pt with Ir or Rh has little effect on the reaction free energies in this compared to pure Pt. However, alloying Pd with Ir or Rh results in a surface where FA is oxidized to HCOO* far easier than on pure Pd.

Direct oxidation via carboxyl: Next, we discuss how the direct oxidation via carboxyl pathway is affected by alloying Pt or Pd with other transition metals. In this pathway, FA is first oxidized to form COOH* and a proton-electron pair before oxidizing again to form CO_2 and a second proton-electron pair. Fig. 7.4 shows the free energy of reaction for each step in this reaction pathway.

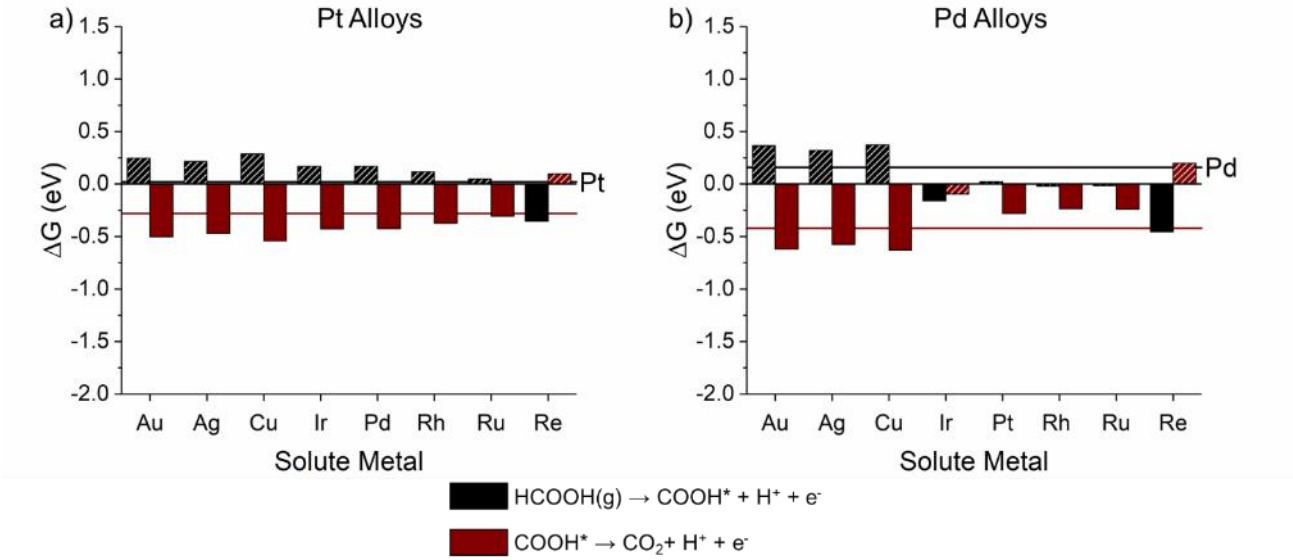

Figure 7.4: ΔG for direct oxidation of carboxyl pathway on **(a)** Pt alloys and **(b)** Pd alloys. The potential-determining step is indicated with a dashed bar. The black and ruby lines indicate ΔG of a reaction step for pure **(a)** Pt or **(b)** Pd, and the color of the line label indicates the potential-determining step for each respective metal. (Black bars: $HCOOH(g) \rightarrow COOH^* + H^+ + e^-$, Red bars: $COOH^* \rightarrow CO_2(g) + H^+ + e^-$)

Coinage metals have a similar effect on the initial formation of COOH* as they did on the initial formation of HCOO*, whereby they increase the free energy of reaction required to generate both species from FA compared to pure Pt and Pd. We also find that forming COOH* from FA is highly exothermic on Pt and Pd alloyed with Re, similar to the effect that Re has on HCOO* formation from FA. There are no clear trends, however, for alloying Pt or Pd with the remaining

transition-metal solutes. Alloying Pt with Ir, Pd, Rh, and Ru makes oxidizing FA to form COOH* less favorable than pure Pt. For Pd_3M alloys, Ir, Pt, Rh, and Ru all significantly lower the free energy of formation for oxidizing FA to COOH* compared to pure Pd. With the exception of Pd_3Pt, the free energy of reaction for forming COOH* from FA is actually negative on the remaining non-coinage metal solutes.

Indirect oxidation via carboxyl: Finally, we address the activity of bimetallic Pt and Pd catalysts towards FA electro-oxidation through the indirect oxidation via carboxyl pathway. When COOH* forms, it can dehydrate to form CO* instead of being directly oxidized to form CO_2(g). To remove CO* from the surface, it can either undergo a reverse hydration reaction to form COOH* (which can be oxidized form CO_2(g) through the direct oxidation via carboxyl pathway) or water must first be activated to generate OH* which can then react with CO* to produce CO_2(g) and a proton-electron pair. In this way, the indirect oxidation via carboxyl pathway is composed of two sub-pathways, the COOH* formation pathway and the water activation pathway. Therefore, we can establish the potential-determining step for the indirect oxidation via carboxyl pathway by comparing the free energy of reaction for forming COOH* from CO* to the most endergonic reaction step between activating water to form OH* and reacting OH* with CO* to form CO_2(g). The least endergonic step between the COOH* formation pathway and the water activation pathway will then be the potential determining step in the indirect oxidation via carboxyl pathway. The free energy of reaction for each of these three steps on bulk terminated alloys is shown in Fig. 7.5.

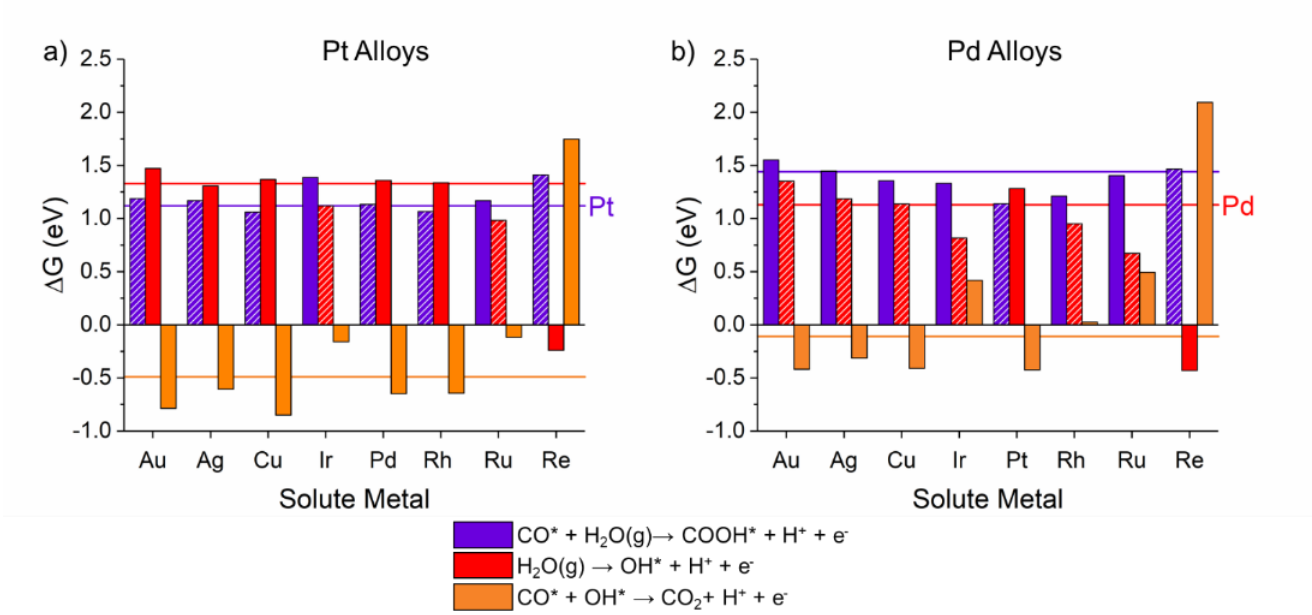

Figure 7.5: ΔG for indirect oxidation of carboxyl pathway on **(a)** Pt alloys and **(b)** Pd alloys. The potential-determining step is indicated with a dashed bar. The purple, red, and orange lines indicate ΔG of a reaction step for pure **(a)** Pt or **(b)** Pd, and the color of the line label indicates the potential-determining step for each respective metal. (Purple bars: $CO^* + H_2O(g) \rightarrow COOH^* + H^+ + e^-$, Red bars: $CO^* + H_2O(g) \rightarrow CO^* + OH^* + H^+ + e^-$, Orange bars: $CO^* + OH^* \rightarrow CO_2(g) + H^+ + e^-$)

We begin our analysis by focusing on solute metals alloyed with Pt. As mentioned previously, the potential-determining step for the indirect oxidation of FA via carboxyl on pure Pt is hydrating CO* to produce COOH*. Aside from Ir and Ru, all solute metals produce Pt-based catalysts that retain the same potential-determining step. The potential determining step on Pt_3Ir and Pt_3Ru is activating water instead of hydrating CO*. Pt catalysts alloyed with Au, Ag, and Re have larger reaction free energies, and thus larger onset potentials, for hydrating CO* to form COOH* compared to pure Pt . On the other hand, alloying Pt with Cu, Rh, or Ru results in catalysts with slightly lower onset potentials for this step as compared to pure Pt. The overall reaction free energy for activating water on Pt_3Ir is the same as hydrating CO* on pure Pt, so the onset potentials should be the same for these two surfaces. However, the reaction free energy for activating water on Pt_3Ru lower than hydrating CO* on pure Pt, making the indirect oxidation via carboxyl pathway more favorable on Pt_3Ru than pure Pt.

For most Pd_3M alloys, the potential-determining step is activating water to produce OH*, similar to that of pure Pd. The only exceptions to this trend are Pd_3Pt and Pd_3Re, where hydrating CO* to produce COOH* is the potential-determining step. Pd catalysts alloyed with Au, Ag, and Re have larger reaction free energies, and thus larger onset potentials, for activating water compared to pure Pd, resulting in a larger onset potential for this pathway. Alloying Pd with Ir, Rh, and Ru solutes results in lower reaction free energies, and therefore lower onset potentials, for water activation than for pure Pd. Pd_3Pt and Pd_3Re catalysts prefer hydrating CO* to produce COOH*. However, the reaction free energy for this step is the same (in the case of Pd_3Pt) or larger (in the case of Pd_3Re) than activating water on pure Pd.

Overall reactivity: After analyzing the direct oxidation via formate, the direct oxidation via carboxyl pathways, and the indirect oxidation via carboxyl pathways in depth individually, we then combined the critical information about each pathway. Using the free energy of reaction for each step in each pathway, we calculated the onset potential based on the potential-determining step for each pathway, as shown in Fig. 7.6. This allows us to examine the interplay between the three pathways and further analyze the balance of these pathways that would lead to improved catalysts for formic acid electro-oxidation. Ideally, catalysts for FA electro-oxidation should have lower onset potentials for the direct oxidation via formate pathway and have higher onset potentials for forming COOH* to avoid CO* formation. Additionally, the ideal catalysts should also have lower onset potentials for the indirect oxidation via carboxyl pathway to facilitate removing CO*. Out of all of the bulk-terminated alloyed surfaces we have studied, only Pt_3Ru offers all three of these benefits. Additionally, Pd_3Ir, Pd_3Rh, Pd_3Ru, and Pt_3Rh meet two out of the three selection criteria. Unsurprisingly, many of these alloys have experimentally been identified as active

catalysts for FA, methanol, or ethanol oxidation.[55,194–197]

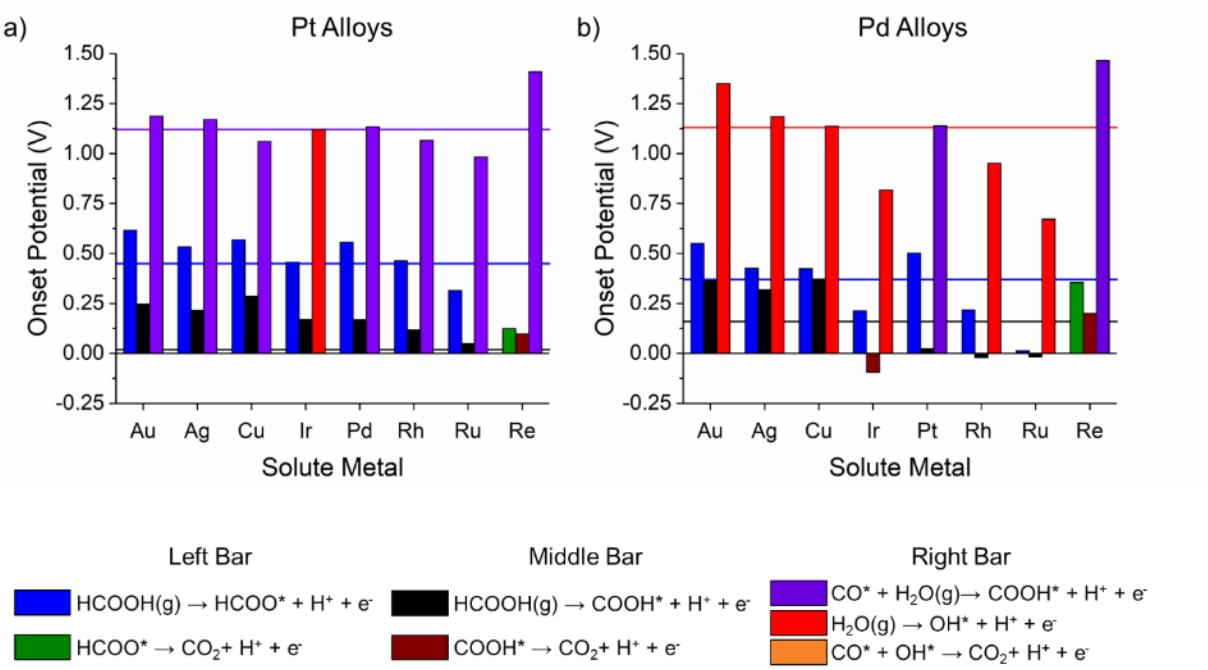

Figure 7.6: Onset potentials for FA electro-oxidation pathways on **(a)** Pt alloys and **(b)** Pd alloys. The color of each bar indicates the potential-determining step for each pathway. The bars for each alloy from left to right indicate the onset potential for the direct oxidation via formate pathway (Blue bars: HCOOH(g) → HCOO* + H^+, Green bars: HCOO* → CO_2* + H^+), the direct oxidation via carboxyl pathway (Black bars: HCOOH(g) → COOH* + H^+, Red bars: COOH* → CO_2* + H^+), and the indirect oxidation via carboxyl pathway (Purple bars: CO* + H_2O(g) → COOH* + H^+, Red bars: CO* + H_2O(g) → CO* + OH* + H^+, Orange bars: CO* + OH* → CO_2(g) + H^+).

7.3.3 Role of Surface Reconstruction

Studying ordered alloys with a bulk termination gives us key trends in how different transition metal solutes can adjust the reactivity of Pt or Pd. However, alloyed surfaces can reconstruct, leading to atoms segregating on the surface of catalysts with and without adsorbates. To capture the effects of surface segregation, we examined every possible configuration of atoms in the top two layers of the alloys to calculate the energy of each system with and without adsorbates. In these next sections, we focus on the lowest energy surfaces for both clean surfaces and surfaces that have experienced metal segregation due to 1/4 ML CO*.

Surface segregation on clean surfaces: We begin our discussion of analyzing FA electro-oxidation on reconstructed surfaces by first focusing on the most stable clean surfaces for each alloy. The most stable surfaces under vacuum for each alloy are listed in Table 7.1.

Table 7.1: The most stable reconstructions for clean Pt and Pd alloys. The structures for each stable reconstruction are shown in Fig. 7.1, and the relative energies of each surface are shown in Table G.8 for Pt alloys and Table G.9 for Pd alloys.

Pt Alloys	**Most Stable Surface Structure**	**Pd Alloys**	**Most Stable Surface Structure**
Pt_3Au	2_1	Pd_3Au	2_2
Pt_3Ag	2_1	Pd_3Ag	2_1
Pt_3Cu	0_1	Pd_3Cu	0_1
Pt_3Ir	0_1	Pd_3Ir	0_1
Pt_3Pd	0_1	Pd_3Pt	0_1
Pt_3Rh	0_1	Pd_3Rh	0_1
Pt_3Ru	0_1	Pd_3Ru	0_1
Pt_3Re	0_2	Pd_3Re	0_2

Alloys containing Au or Ag adopt structures where half of the top layer of the surface contains the solute metal and the second layer is composed of entirely Pt or Pd. All other metal solutes prefer to segregate into the surface so that the top layer of the surface is composed of Pt or Pd and half of the atoms in the second layer are solute atoms. These results are in agreement with previous work on surface segregation in alloyed systems.[198] Additionally, several experimental studies of bimetallic catalysts showed that Pt_3M and Pd_3M systems often prefer to form Pt or Pd skins atop a bulk alloy structure for many of the metals shown in this study.[58,60,199] After identifying these surfaces as the most stable structures, we then repeated our analysis from above and identified the potential determining step as well as the onset potential for each pathway based on

the reaction free energies for each step. The onset potential for each surface and the potential determining step are shown in Fig. 7.7 for both Pt and Pd alloys.

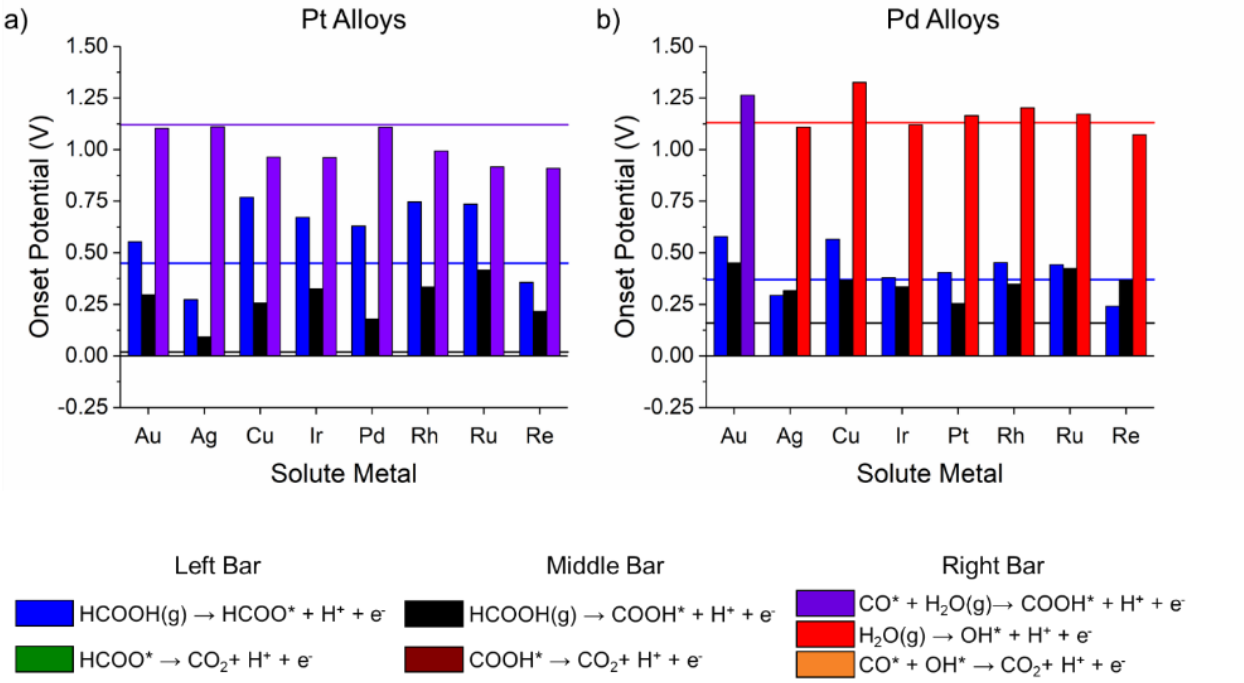

Figure 7.7: Onset potentials for FA electro-oxidation pathways on **(a)** Pt alloys and **(b)** Pd alloys with the structures most stable under vacuum. The color of each bar indicates the potential-determining step for each pathway. The bars for each alloy from left to right indicate the onset potential for the direct oxidation via formate pathway (Blue bars: HCOOH(g) → HCOO* + H^+, Green bars: HCOO* → CO_2* + H^+), the direct oxidation via carboxyl pathway (Black bars: HCOOH(g) → COOH* + H^+, Red bars: COOH* → CO_2* + H^+), and the indirect oxidation via carboxyl pathway (Purple bars: CO* + H_2O(g) → COOH* + H^+, Red bars: CO* + H_2O(g) → CO* + OH* + H^+, Orange bars: CO* + OH* → CO_2(g) + H^+).

We first begin our discussion by focusing on Pt alloys. We find that the potential determining steps for all alloys are the same as they are on pure Pt. However, the onset potential for each pathway shifts for alloys compared to pure Pt. We find that all solute metals except Ag and Re increase the onset potential of the direct oxidation via formate, and all solute metals increase the onset potential of the direct oxidation via carboxyl. Thus, alloying Pt with Au or Re results in catalysts that more readily form HCOO* and less readily form COOH* compared to Pt, which are both desirable characteristics in FAO catalysts. We also find an inherent link between the onset potential of the direct oxidation via carboxyl and the indirect oxidation via carboxyl

pathways. As the onset potential for forming COOH* from FA increases, the onset potential to remove CO* by hydrating it to produce COOH* decreases. This trend results in several promising Pt-based bimetallic catalysts that have lower onset potentials for the indirect oxidation via carboxyl, namely Pt_3M catalysts with Cu, Ir, Rh, Ru, and Re as solutes.

For Pd alloys, we find some similar trends as for Pt alloys. Almost all alloys share the same potential-determining step for each pathway with Pd. The only exception for this trend is Pd_3Au, where the potential determining step in the indirect oxidation via carboxyl pathway is oxidizing CO* with water to form COOH* rather than activating water to form OH*. All Pd alloys have an increased onset potential for direct oxidation via formate compared to pure Pd except for alloys containing Ag and Re. Furthermore, all Pd alloyed systems have an increased onset potential for the direct oxidation via carboxyl pathway compared to the pure Pd. We also find a link connecting the onset potential for the direct oxidation via formate and the indirect oxidation via carboxyl. As discussed later in more detail, the binding free energy of HCOO* scales with the binding free energy of OH*, as both species bind to the surface through oxygen. Thus, surfaces that stabilize HCOO*, thereby reducing the energy required to form HCOO* from FA, should also reduce the energy required to activate water and form OH* on the surface to facilitate the removal of CO*. Based on this analysis, Pd_3Ag catalysts and Pd_3Re catalysts should both have lower onset potentials for the direct oxidation via formate and the indirect oxidation via carboxyl compared to pure Pd, which are desirable traits for improved FAO catalysts. Furthermore, the onset potential for the direct oxidation via formate is lower than the direct oxidation via carboxyl for Pd_3Re.

Based on the above analysis, we would expect that the most stable surfaces under vacuum of Pt_3Ag, Pt_3Re, Pd_3Ag and Pd_3Re should both promote HCOO* formation and suppress COOH*

formation, enhancing catalytic activity. Additionally, Pt_3Cu, Pt_3Ir, Pt_3Rh, Pt_3Ru, Pt_3Re, Pt_3Ru, Pt_3Re, Pd_3Ag, and Pd_3Re alloys should have a greater ability to remove CO* than their Pt or Pd counterparts.

CO covered surfaces: During catalyst operation, the presence of adsorbates can lead to metals segregating from the bulk to the surface of the alloy, resulting in different metal compositions in the topmost layers. To understand the role that adsorbate-induced surface segregation can play in our bimetallic catalysts, we calculated the reaction energetics for FA electro-oxidation on surfaces that the most energetically stable when CO* is present, because we expect high coverages of CO* on our Pt and Pt-based alloys. The most stable surfaces in the presence of CO* are listed in Table 7.2. Work by van Spronsen et al.[200] has shown that dosing PdAg alloys with CO* causes the alloyed surface to reconstruct and stay in the same state even when CO* pressures are substantially lowered at room temperature. In our analysis, we assume that CO-induced surface segregation will lead to a relatively stable surface structure that will not substantially change even if active sites are briefly free or occupied by other intermediates. We do note that the nature of the active sites could deviate from what we have shown here based on the coverage of intermediates at various electrochemical conditions. However, we can still gather trends in how FAO catalysts will behave after the surface has restructured due to CO* adsorption.

Table 7.2: The most stable reconstructions for Pt and Pd alloys with ¼ ML CO* coverage. We note the CO* binding site on each surface, as well as the metals that CO* are bound to. The structures for each stable reconstruction are shown in Fig. 7.1, and the relative energies of each surface are shown in Table G.8 for Pt alloys and Table G.9 for Pd alloys. Figures for the adsorption structures of CO* on each surface are shown in Section G.3 of Appendix G.

Pt Alloys	**Most Stable Surface Structure**	**CO* Binding Site**	**Pd Alloys**	**Most Stable Surface Structure**	**CO* Binding Site**
Pt_3Au	2_1	Bridge (Pt,Pt)	Pd_3Au	2_1	Bridge (Pd,Pd)
Pt_3Ag	2_1	Bridge (Pt,Pt)	Pd_3Ag	1_2	FCC (Pd, Pd, Pd)
Pt_3Cu	0_1	HCP (Pt,Pt,Pt)	Pd_3Cu	1_2	FCC (Pd, Pd, Pd)
Pt_3Ir	1_3	Top (Ir)	Pd_3Ir	1_3	Top (Ir)
Pt_3Pd	2_2	Bridge (Pt,Pt)	Pd_3Pt	1_2	FCC (Pd, Pd, Pt)
Pt_3Rh	0_1	Bridge (Pt,Pt)	Pd_3Rh	0_2	FCC (Pd,Pd,Pd)
Pt_3Ru	0_2	Bridge (Pt,Pt)	Pd_3Ru	0_2	FCC (Pd,Pd,Pd)
Pt_3Re	0_2	FCC (Pt,Pt,Pt)	Pd_3Re	0_2	FCC (Pd,Pd,Pd)

When CO* is present, we find that there are several different surface reconstructions with various distributions of solute atoms in the top two surface layers that are energetically favorable depending on the alloy. In general, CO* prefers to bind to only Pd or Pt on almost all of the reconstructed surfaces. The exception to this trend is alloys containing Ir, where CO* binds to the top site of the Ir atom on the top surface layer. After identifying the most stable surfaces in the presence of ¼ ML CO*, we then calculated the potential determining step and onset potential for each pathway on these most-stable surfaces based on the reaction free energies at a total coverage of ¼ ML for all adsorbates, which are shown in Fig. 7.8 for both Pt and Pd alloys.

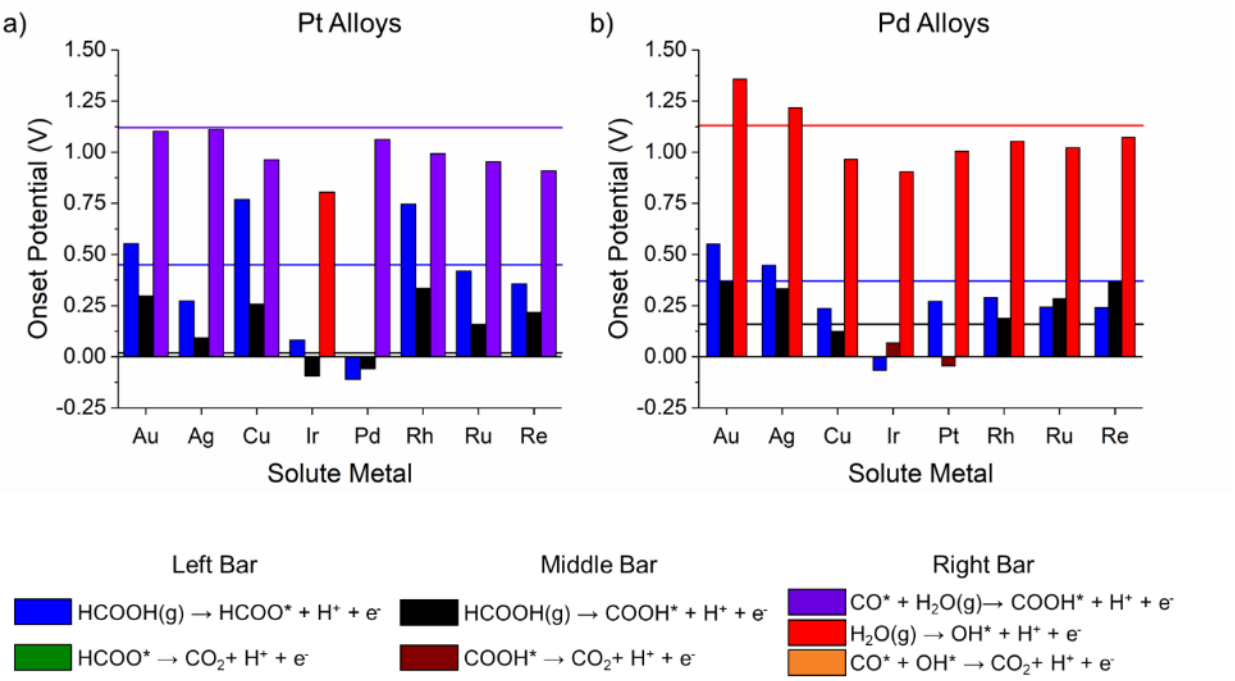

Figure 7.8: Onset potentials for FA electro-oxidation pathways on **(a)** Pt alloys and **(b)** Pd alloys most stable in the presence of ¼ ML CO*. The color of each bar indicates the potential-determining step for each pathway. The bars for each alloy from left to right indicate the onset potential for the direct oxidation via formate pathway (Blue bars: HCOOH(g) → HCOO* + H^+, Green bars: HCOO* → CO_2* + H^+) , the direct oxidation via carboxyl pathway (Black bars: HCOOH(g) → COOH* + H^+, Red bars: COOH* → CO_2(g) + H^+), and the indirect oxidation via carboxyl pathway (Purple bars: CO* + H_2O(g) → COOH* + H^+, Red bars: CO* + H_2O(g) → CO* + OH* + H^+, Orange bars: CO* + OH* → CO_2(g) + H^+).

For Pt alloys, the potential-determining step for the direct oxidation via formate and the direct oxidation via carboxyl steps are identical to pure Pt. Additionally, all Pt alloys besides Pt_3Ir have the same potential-determining step for the indirect oxidation via carboxyl pathway as pure Pt. In the case of Pt_3Ir, the potential determining step for this pathway is activating water to form OH* rather than oxidizing CO* with water to form COOH*. All surfaces except those containing Au, Cu, and Rh as a solute metal have lower onset potentials for the direct oxidation via formate pathway, meaning that the these surfaces promote the oxidation of HCOOH(g) to HCOO* more than pure Pt. Additionally, all surfaces, except those containing Ir and Pd, have higher onset potentials for forming COOH* than pure Pt, which is ideal for reducing the amount of CO* formed on the catalyst surface. Furthermore, the onset potential for the indirect oxidation via carboxyl is

the same or lower for all Pt_3M catalysts with respect to pure Pt, suggesting that CO* removal should also be easier on these surfaces than on pure Pt. In particular, Pt_3Ru and Pt_3Re catalysts have lower onset potentials for forming HCOO* than on Pt, higher onset potentials for forming COOH* than on Pt (thus reducing CO* formation), and lower onset potentials than Pt for removing CO* via the indirect oxidation via carboxyl pathway. These three features make these catalysts particularly attractive for FA electro-oxidation.

For almost all Pd alloy surfaces altered by CO*-induced surface segregation, the potential determining step for each pathway is the same as it is for pure Pd. The exceptions to this trend are for Pd_3Ir and Pd_3Pt, where the potential determining step for the direct oxidation via carboxyl pathway is oxidizing COOH* rather than oxidizing HCOOH(g). Besides Au and Ag, all solute metals lower the onset potential for the direct oxidation via formate pathway relative to pure Pd. Additionally, all solute metals increase the onset potentials for the direct oxidation via carboxyl pathway relative to pure Pd, with Cu, Ir, and Pt as the exceptions. In particular, Pd_3Rh, Pd_3Ru, and Pd_3Re all offer lower onset potentials for the direct oxidation via formate compared to Pd and higher onset potentials for oxidizing HCOOH(g) to COOH* compared to Pd, meaning that the reaction flux through the direct oxidation via formate pathway should be increased compared to pure Pd. This observation is especially true for Pd_3Ru and Pd_3Re, which have lower onset potentials for the direct oxidation via formate pathway than oxidizing HCOOH(g) to COOH*. Additionally, these two alloys are among several that have lower onset potentials for the indirect oxidation via carboxyl, meaning that CO* is easier to remove from these surfaces than from pure Pd surfaces. These promising attributes indicate that if CO* leads to adsorbate-induced surface segregation to the surfaces we have studied for Pd_3Rh, Pd_3Ru, and Pd_3Re, these surfaces should still be more active towards FA electro-oxidation compared to pure Pd, especially Pd_3Ru and

Pd_3Re.

7.3.4 Reaction Phase Diagrams

In this section, we combine the insights from our analyses to create phase diagrams that describe the reactivity of the studied catalysts as a function of key reactivity descriptors. Doing so allows us to rationally identify characteristics that ideal catalysts for FA electro-oxidation should have. In this case, we selected the binding free energy of CO* (G_{CO*}) and OH* (G_{OH*}) as our reactivity descriptors. By comparing the binding free energy of all adsorbates for Pt, Pd, and all of the studied alloyed surfaces, we find that the free binding energy of COOH* (G_{COOH*}) linearly scales with G_{CO*} and that the binding free energy of HCOO* (G_{HCOO*}) linearly scales with G_{OH*} (see Fig. G.1). This result is not surprising, as we expect that the binding free energy of species that bind through the same atom (e.g., carbon and oxygen in this case) should be connected through linear scaling relationships. We cannot, however, select only G_{CO*} or G_{OH*} as a descriptor, as the binding free energies of the two species do not follow as strong linear correlation with one another (see Fig. G.1). Furthermore, other studies on the electro-oxidation of oxygen-containing organic molecules such as methanol,[38,39] dimethyl ether,[50–52] and ethanol/ethylene glycol[201] have noted that both G_{CO*} and G_{OH*} are needed as descriptors for this type of chemistry. Calculated reaction phase diagrams as a function of G_{CO}* and G_{OH*} at 0.0 V and 0.6 V are shown in Fig. 7.9, where the colored contours indicate the free energy of reaction associated with the rate determining step, while different sectors of the plot denote the corresponding rate determining step.

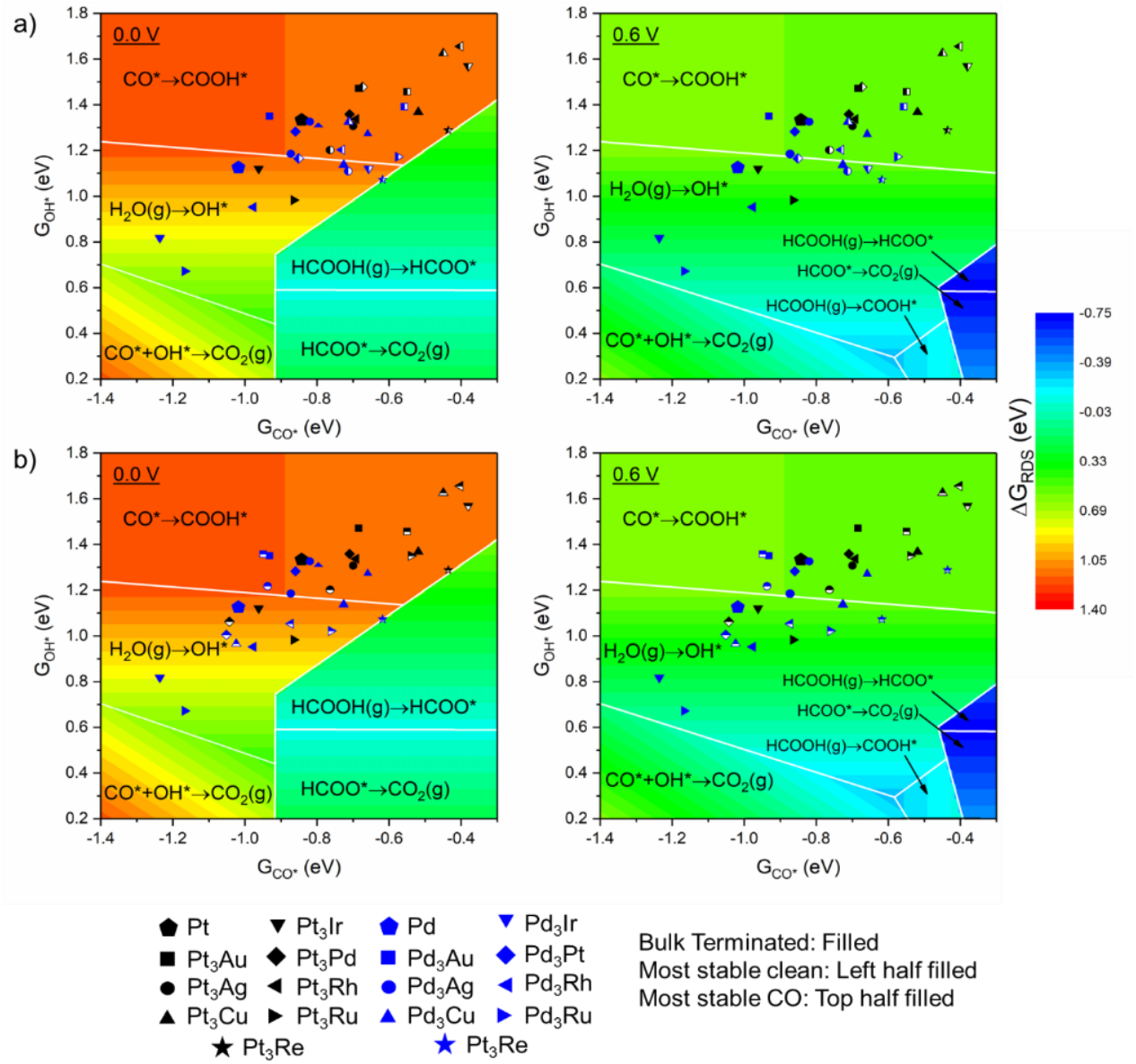

Figure 7.9: Calculated reaction phase diagrams for FAO on all alloyed surfaces at 0.0 V and 0.6 V on alloyed surfaces. For clarity, we have only included points for the reactivity on the bulk terminated surfaces (filled symbols) and **(a)** most stable clean surfaces (left half-filled symbols) and **(b)** most stable CO*-covered surfaces (top half filled symbols). Black points correspond to Pt and Pt alloys, and blue points correspond to Pd and Pd alloys. The color scale represents the free energy of the most endergonic step in the FAO pathway, and color levels are separated by 0.06 eV, corresponding to the energy difference that leads to an order-of-magnitude difference in reaction rate at 298 K. Regions corresponding to the most endergonic step are marked on the phase diagrams.

We first discuss the phase diagram for FAO at 0.0 V. Two pathways dictate the reactivity of the studied catalysts at this potential, namely the direct oxidation via formate and the indirect oxidation via carboxyl pathways. When OH* is bound weakly to the surface, i.e., in regions at the

top of the phase diagram, HCOO* also binds weakly, causing the reaction flux to proceed through the indirect oxidation via carboxyl pathway and produce CO* on the catalyst surface. In this case, activating water is difficult because OH* is not sufficiently stable, meaning that reactivity is limited by the ability of the catalyst to hydrate CO* to form COOH* which then reacts to form CO_2(g). As OH* is stabilized, i.e., shifts downward on the phase diagram, two distinct regions emerge that correspond to weak and strong CO* binding. In the case of strong CO* binding, as the stability of OH* increases, activating water to form OH* which then reacts with CO* to form COOH* becomes the rate-determining step. By further increasing the stability of OH* we enter another region in the phase diagram where activating water is no longer as difficult and removing OH* and CO* to form CO_2(g) becomes the rate-determining step. On the other hand, when CO* is weakly bound and OH* has an intermediate binding strength, COOH* formation becomes difficult relative to HCOO* formation. At this point, activating FA to form HCOO* becomes the rate-determining step. If we further stabilize OH*, we also stabilize HCOO* such that its removal becomes the new potential-determining step. The peak in our catalytic activity (the light blue region at the bottom right of the volcano plot) comes when HCOO* is bound strongly enough that FA can be activated but weak enough so that it can then be easily removed to form CO_2.

At 0.0 V, most of the studied catalysts have similar activities, and most catalysts have a potential-determining step that lies within the indirect oxidation of via carboxyl pathway. However, we find that bulk terminated Pt_3Ru, Pd_3Ir, Pd_3Rh, and Pd_3Ru show significantly higher activity than most of the other catalysts. Additionally, we do find that the most stable clean reconstructions for the Pt_3Re and Pd_3Re surfaces are on the border between having CO* reacting to form COOH* and HCOOH(g) forming HCOO* as the potential-determining step (the most stable clean surfaces for both alloys are also the most stable surfaces in the presence of HCOO*,

COOH*, and CO*). The right side of this border is part of a region of activity where the potential-determining step is not dictated by removing CO* but rather by activating FA to form HCOO* in the direct oxidation via formate pathway. Catalysts operating in this region should have higher activity and not form CO* as easily as catalysts on the left side of the border. Therefore, around 0.0 V, Pt_3Re and Pd_3Re should be highly active for FA electro-oxidation.

Next, we discuss the phase diagram for FAO at a potential of 0.6 V. As we increase the potential, all faradaic reactions become more exergonic, and we find regions on the calculated phase diagram with higher activities than at any point on the corresponding 0.0 V phase diagram. Additionally, a second, local peak in activity occurs, and the regions on the phase diagram in the bottom right corner where OH* binding is stabilized and CO* binding is destabilized are altered. As we increased the applied bias, regions corresponding the direct oxidation via formate pathway shrink as COOH* is further stabilized, which also leads to an additional region on our phase diagram where OH* is stabilized and CO* is destabilized in which activating FA to form COOH* becomes the rate-determining step.

According to the CHE formalism, as we increase the applied potential, the binding free energy of adsorbates on the catalyst surface should not change (the free energy of the reaction, and therefore the rate-determining step, shift due to the changing chemical potential of a proton-electron pair as an electric potential is applied to the system). Therefore, Pt_3Re-0_2 and Pd_3Re-0_2 surfaces, which we identified as being close to the region in which the potential-determining step is activating FA to form HCOO* at 0.0 V, are no longer close to that region at 0.6 V. However, bulk terminated Pd_3Ru remains more active than all of the catalysts shown on the phase diagram. To design catalysts that approach the maximum activity for this reaction at higher potentials, we

need to identify catalysts that further stabilize OH* and destabilize CO* compared to current transition metal alloys. On these surfaces, there exists a weak correlation between the binding free energy of CO* and the binding free energy of OH* (Fig. G.1). This makes it difficult to find new transition-metal catalysts with improved activity towards FA electro-oxidation but also leaves room for some potential design opportunities. For example, rationally combining overlayer structures with alloy structures or moving to new classes of materials could lead to more active catalysts for FA electro-oxidation.

7.4 Conclusions

Alloying Pt and Pd with other transition metals can improve the activity and selectivity of FA electro-oxidation catalysts. Here, we presented a density functional theory study of FA electro-oxidation on the (111) facet of bimetallic P_3M catalysts (P = Pt or Pd, M = Au, Ag, Cu, Pd, Pt, Ir, Rh, Ru, or Re, where $P \neq M$) to better understand the activity of these catalysts. For each catalyst, we calculated free energy diagrams to investigate formic acid oxidation through CO, OH, carboxyl (COOH), and formate (HCOO) on the surface. We used this information to calculate the onset potential for three key reaction mechanisms: direct oxidation of FA via HCOO, direct oxidation of FA via COOH, and the indirect oxidation of FA via COOH that forms CO for each surface. By comparing the onset potential of the three pathways on Pt or Pd alloyed catalysts, we identified several promising candidates for improved activity towards FA electro-oxidation. In particular, alloying Pt or Pd with Ir, Ru, or Re may result in far more active catalysts. These most promising catalysts have lower onset potentials for the direct oxidation via formate and indirect oxidation via carboxyl pathways and have higher onset potentials for forming carboxyl.

Chapter 8: Alignment of Semiconducting Graphene Ribbons on Vicinal Ge(001)*

8.1 Introduction

Graphene nanoribbons are promising candidates for semiconductor electronics because, unlike continuous graphene sheets, they can have bandgaps suitable for substantial conductance modulation at room temperature. The bandgap depends on ribbon width and edge structure, and the largest bandgaps are expected in ribbons < 10 nm wide with smooth armchair edges (*i.e.*, C–C bonds parallel to the ribbon long-axis).[70] Semiconducting nanoribbons also have potential to achieve high charge carrier mobility[66] and velocity,[68] current density,[202] and elelctrical[68] and thermal[203] conductivity, and their atomic thickness enables excellent electrostatic control.[204] To improve feasibility of nanoribbon integration into semiconductor electronics and maximize device performance, ribbons must be highly aligned in one direction. For example, in field-effect transistors (FETs), unaligned ribbons can result in charge screening and lengthen the charge conduction pathway, decreasing on-state conductance and on/off conductance ratio.[205,206]

One of the most successful approaches to fabricate aligned nanoribbons while also achieving high precision over ribbon width and edge structure is polymerization and

---

*Adapted from **"Alignment of semiconducting graphene nanoribbons on vicinal Ge(001)"**, R. M. Jacobberger, E. A. Murray, M. Fortin-Deschênes, F. Göltl, W. A. Behn, Z. J. Krebs, P. L. Levesque, D. E. Savage, C. Smoot, M. G. Lagally, P. Desjardins, R. Martel, V. Brar, O. Moutanabbir, M. Mavrikakis, M. S. Arnold, *Nanoscale* **11**, 4864 (2019).

Graphene growth experiments and graphene characterization *via* SEM, TEM, SAED, AFM, and charge transport measurements performed by R. M. Jacobberger, C. Smoot, and M. S. Arnold. Graphene characterization *via* LEEM and LEED performed by M. Fortin-Deschênes, P. L. Levesque, P. Desjardins, R. Martel, and O. Moutanabbir. Graphene characterization *via* STM performed by W. A. Behn, Z. J. Krebs, and V. Brar. R. M. Jacobberger served as the primary author for this work.

cyclodehydrogenation of molecular precursors on stepped Au(788) surfaces.[207–211] This technique yields densely-packed, aligned ribbons with sub-2 nm widths and atomically-smooth armchair edges, in which the average distance between the long-axis of neighboring ribbons is 1–2 nm [212] and ribbons are aligned within ~9°.[210] However, these ribbons are typically only 20–30 nm in length,[207,208,211,212] making them difficult to electrically contact and integrate into scalable technologies. The ribbons also have relatively large bandgaps due to their especially narrow widths, leading to Schottky barriers at the ribbon/electrode interface and, consequently, formation of high-impedance electrical contacts.[213–215] Furthermore, the high ribbon density can lead to electrostatic screening and, thus, reduced conductance modulation in FETs.[205,206]

Replicating the precise control over ribbon alignment, width, and edge structure afforded by polymerization/cyclodehydrogenation while also achieving sub-10 nm ribbons that are wider (to obtain smaller bandgaps) and longer (to facilitate widespread integration) has been difficult. Aligned ribbons can be fabricated using subtractive lithography of continuous graphene.[216,217] However, the ribbons have rough, defective edges that degrade the exceptional transport properties expected in pristine ribbons, and ribbons with sub-10 nm widths cannot be fabricated to induce technologically relevant bandgaps >> k_BT at room temperature.

Nanoribbon alignment has also been achieved via growth on SiC nanofacets[218] and Ni nanobars,[219] substrate-controlled, metal-assisted etching of continuous graphene,[220] and unzipping carbon nanotubes.[221] Semiconducting ribbons, however, have not been reported via growth on SiC nanofacets and Ni nanobars. Metal-assisted etching and growth on nanobars suffer from poor yield, inability to controllably produce ribbons with sub-10 nm widths, and formation of ribbons with relatively rough edges. Fabricating aligned ribbons with controlled edges via nanotube unzipping relies on the requisite ability to align nanotubes from solution, which is a major challenge by

itself.[222,223]

Alternately, we recently reported a scalable, bottom-up technique to directly synthesize narrow, polydisperse nanoribbons with predominately smooth armchair edges via chemical vapor deposition (CVD).[72] In this process, CVD of CH_4 on Ge(001) at ~910 °C in a flow of H_2 and Ar results in anisotropic growth of ribbons, provided the growth rate is relatively slow (nanometers per hour). In this regime, ribbons with sub-10 nm width can still have lengths of hundreds of nanometers. The ribbons grow with self-defining armchair edges, and width can be continuously tuned to nearly zero by controlling growth rate and time. For example, scanning tunneling microscopy (STM) has shown the ribbon edges consist of smooth armchair segments, with edge roughness of < 5 Å over lengths of tens of nanometers, and has confirmed synthesis of ribbons as narrow as 2 nm.[72,224] In FETs, these ribbons have simultaneously exhibited on/off conductance ratio of 2×10^4 and on-state conductance of 5 μS, among the highest charge transport metrics reported for ribbons.[75] Width polydispersity leads to variability in FET on/off conductance ratio, although initiating nanoribbon synthesis from seeds provides a promising path to overcome this polydispersity.[225] Furthermore, such ribbon synthesis has only been demonstrated on Ge(001) surfaces.

Nanoribbons that spontaneously nucleate and grow on Ge(001) also adapt two predominate orientations roughly aligned along the perpendicular Ge⟨110⟩ directions with equal probability, limiting ribbon alignment and packing density.[72] However, unidirectional alignment can be realized by initiating growth from nanoscale graphene seeds with rationally-controlled lattice orientation.[225] The lattice orientation of the ribbon matches that of the seeds from which they grow, the ribbons always have armchair edges, and growth anisotropy is maximized when the armchair direction is along Ge⟨110⟩. Thus, by controlling the seed armchair direction to be along Ge[110]

or Ge[$\bar{1}$10], the long-axis of each of the resulting armchair ribbons also aligns unidirectionally along Ge[110] or Ge[$\bar{1}$10], respectively.

These data suggest that if graphene nuclei that naturally form can be globally aligned, it may be possible to orient ribbons unidirectionally without seeding. Such alignment is possible via epitaxial growth on Ge(110) and is a result of strong binding between graphene and Ge step edges.[226,227] However, anisotropic growth cannot be driven on Ge(110) to yield ribbons.[72] If steps on Ge(001) can be engineered in one direction, for example by introducing a miscut, it may be possible to realize epitaxial alignment and, consequently, aligned ribbons without seeds, which is desirable for improved manufacturability and furthering the fundamental understanding of anisotropic ribbon synthesis.

Here, we find by conducting growth on vicinal Ge surfaces, ~90% of the crystals can evolve as armchair nanoribbons oriented perpendicular to the miscut. When the growth rate is slow, graphene crystals evolve as nanoribbons. However, as growth rate increases, graphene islands transition from being rectangular to trapezoidal to semicircular. Density functional theory (DFT) calculations indicate this asymmetric evolution may be due to different chemical binding or termination at the downhill and uphill ribbon edges. We also demonstrate the growth conditions can be tailored to directly synthesize aligned semiconducting nanoribbons with sub-10 nm widths, and these ribbons can exhibit promising charge transport properties such as high on/off conductance ratio and on-state conductance.

8.2 Results and Discussion

8.2.1 Effect of Miscut on Nanoribbon Growth

First, we explore graphene synthesis on Ge(001) surfaces with 0°, 6°, and 9° miscut towards Ge[110] (*i.e.*, Ge(001)-0°, -6°, and -9°, respectively) to determine the effect of miscut on

ribbon growth and crystallinity and the effect of growth rate on crystal shape evolution and anisotropy. Relatively wide ribbons (~10–100 nm in width) are synthesized to ease in characterization of crystal dimensions and shapes using scanning electron microscopy (SEM). Later, we synthesize narrower ribbons with sub-10 nm widths, simply by decreasing the growth rate or time, enabling characterization of charge transport properties of semiconducting nanoribbons in FETs.

Fig. 8.1d-f shows SEM images of isolated graphene islands grown on each surface. To determine the effect of miscut on synthesis, crystal alignment, width, length, and aspect ratio are characterized with SEM (Fig. 8.1g-j and Fig. H.1). On Ge(001)-0°, graphene crystals evolve as high-aspect ratio nanoribbons with their long-axis rotated +2.8° or –2.8° from Ge⟨110⟩,[72] resulting in four ribbon orientations roughly aligned along perpendicular Ge[110] and Ge[$\bar{1}$10] directions with equal probability. Ribbons oriented near Ge[110] and Ge[$\bar{1}$10] have similar widths, lengths, and aspect ratios (Fig. 8.1h-j), which is expected because these directions are equivalent on Ge(001)-0°.

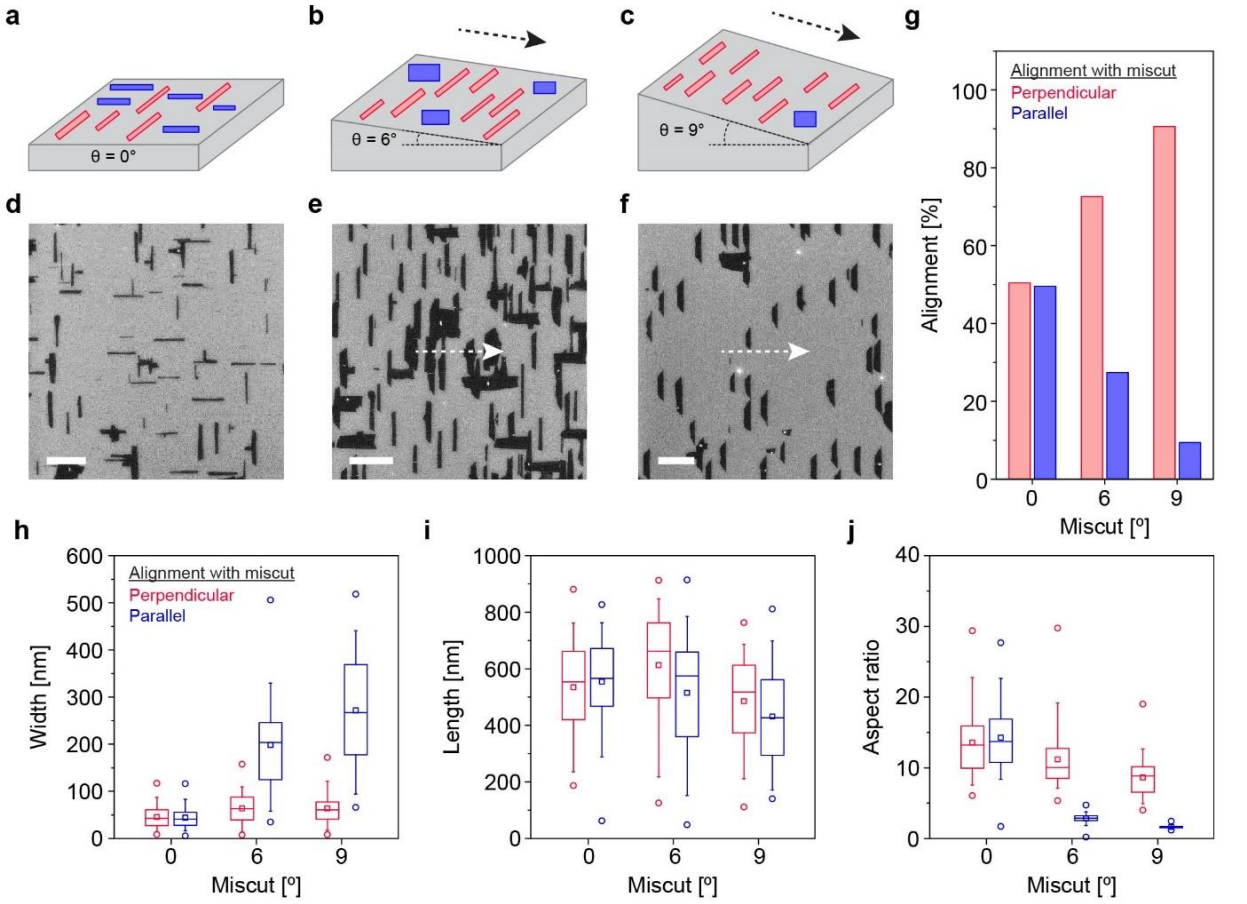

Figure 8.1: Effect of Ge miscut on nanoribbon growth. **(a-f)** Schematic diagrams **(a-c)** and SEM images **(d-f)** of graphene crystals grown on Ge(001) with 0° **(a,d)**, 6° **(b,e)**, and 9° **(c,f)** miscut toward Ge[110]. Red and blue crystals in a-c are perpendicular and parallel, respectively, to the miscut. Dashed arrows in **(b,c,e,f)** point downhill. Scale bars in d-f are 1 μm. **(g-j)** Alignment **(g)**, width **(h)**, length **(i)**, and aspect ratio **(j)** versus miscut angle for ribbons oriented perpendicular (red, left) and parallel (blue, right) to the miscut on Ge(001)-6° and Ge(001)-9° and oriented along [110] and [$\bar{1}$10] on Ge(001)-0°. Horizontal lines in the boxes in h-j define 25th, 50th, and 75th percentiles, whiskers indicate 5th and 95th percentiles, circles define the range, and squares give the mean.

In contrast, as the miscut angle increases, the long axis of the crystals becomes preferentially oriented perpendicular to the miscut, resulting in unidirectional alignment of a majority of the crystals. For example, 73% and 91% of the crystals on Ge(001)-6° and Ge(001)-9°, respectively, are perpendicular to the miscut (Fig. 8.1g). Moreover, the more prevalent crystals aligned perpendicular to the miscut are narrower and have higher aspect ratios (*i.e.* they can be ribbons, with longer lengths per width) than the less common crystals parallel to the miscut (Fig.

8.1h-j), which evolve as more isotropic quadrilaterals. These trends are depicted schematically in Fig. 8.1a-c. Crystals perpendicular to the miscut can also be much wider than the average Ge terrace width of ~1 nm, and thus are not confined to a single terrace but instead can grow across Ge steps. The probability of graphene growth uphill and downhill, however, is not equivalent, as demonstrated below. Furthermore, the ribbon length does not saturate and is similar on each surface, indicating either that the length is not limited by kinks in Ge steps or that kinks rearrange to form straight Ge steps during growth.

X-ray diffraction (XRD) shows the miscut in these Ge(001)-6° and Ge(001)-9° wafers deviates azimuthally from Ge[110] by 4 ± 1° and 0.5 ± 1°, respectively. Thus, we cannot conclude whether the higher alignment on Ge(001)-9° is due to larger miscut angle or smaller miscut deviation azimuthally from Ge[110]. Nonetheless, ~90% of nanoribbons can be aligned unidirectionally on miscut surfaces. It is possible alignment can be further increased, for example by growing on surfaces with a larger miscut angle or less azimuthal deviation in the miscut from Ge[110]. Ribbon alignment also depends on anneal time and H_2:CH_4 flux ratio used during synthesis (Fig. H.2). In the following studies, we primarily focus on characterization of the more common anisotropic nanoribbons perpendicular to the miscut, rather than the crystals parallel to the miscut with lower aspect ratios.

8.2.2 Dependence of Ribbon Anisotropy and Crystal Shape Evolution on Growth Rate

For specific growth conditions, nanoribbons grown perpendicular to the miscut on Ge(001)-6° and Ge(001)-9° are wider and less anisotropic than those directed along ⟨110⟩ on Ge(001)-0° (Fig. 8.1h-j). However, it has been found that the anisotropy on Ge(001)-0° can be increased by reducing the growth rate, either by increasing H_2 flux or decreasing CH_4 flux.[72] The H_2 and CH_4 fluxes are also important factors for controlling the shape evolution[228–230] and

crystallinity[231–233] of graphene grown on metal surfaces.

Therefore, we next study the effect of H_2:CH_4 flux ratio, and thus growth rate, on graphene island morphology and crystal shape evolution. Graphene is synthesized using progressively larger growth rates by reducing the H_2:CH_4 ratio from 50 to 22 to 16, and crystal shapes are characterized with SEM (Fig. 8.2a-i). Raman spectroscopy (Fig. H.3) shows that graphene crystals have relatively low defect density when H_2:CH_4 is at least 22, as the D band is immeasurably small with a D:G peak amplitude ratio < 0.1. When H_2:CH_4 is 16, defect density is increased compared to graphene grown using higher H_2:CH_4, as indicated by the measurable presence of the D band and D:G peak amplitude ratio ~0.25.

Fig. H.4 and H.5 show for each vicinal surface, the crystal shape anisotropy decreases with increasing growth rate. Furthermore, for a given rate, anisotropy is largest on Ge(001)-0° and smallest on Ge(001)-9°. For example, on Ge(001)-0°, aspect ratio decreases from 35.5 ± 9.8 to 9.7 ± 4.0 as growth rate increases from 18.1 ± 4.6 to 270 ± 130 nm h^{-1}, respectively, whereas on Ge(001)-9°, aspect ratio decreases from 12.6 ± 4.0 to 3.32 ± 0.39 as growth rate increases from 30.1 ± 6.9 to 480 ± 200 nm h^{-1}, respectively.

Growth rate also affects shape evolution of graphene crystals. When growth rate is slow (*i.e.*, large H_2:CH_4), crystals evolve as high-aspect ratio nanoribbons in which both edges along the long-axis are approximately the same length (Fig. 8.2a,d,g). As growth rate increases (*i.e.*, H_2:CH_4 decreases) on Ge(001)-0°, both edges continue to be nearly the same length, although some edges become less straight and roughen (Fig. 8.2b,c). In contrast, on Ge(001)-6° and Ge(001)-9°, the downhill crystal edge becomes longer than the uphill edge, forming trapezoids (Fig. 8.2e,h). As growth rate increases further, the uphill edge becomes rough and rounded, forming hemisphere-like shapes (Fig. 8.2f,i). Interestingly, the downhill edge stays relatively

smooth and straight for hundreds of nanometers, indicating the uphill and downhill edges are inequivalent growth fronts, as studied further below.

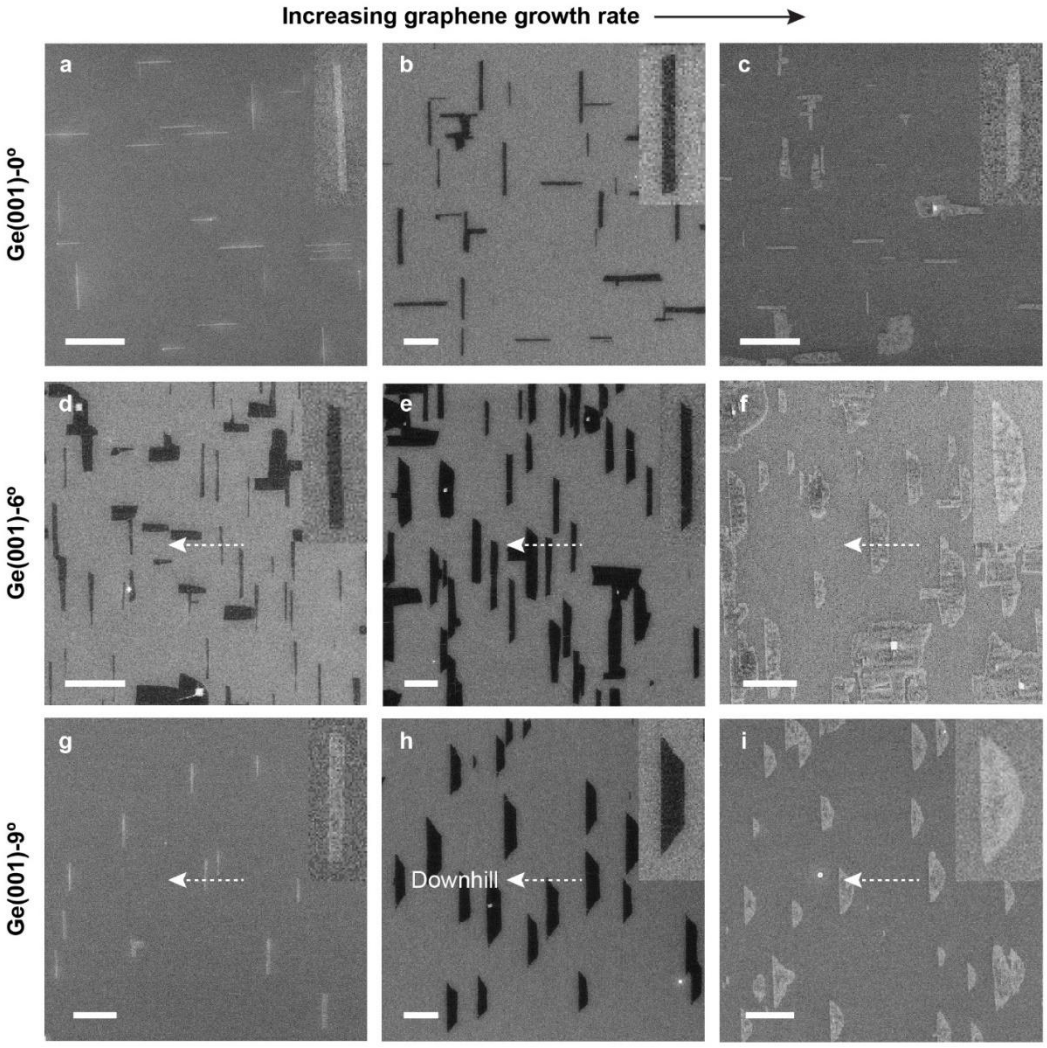

Figure 8.2: Effect of growth rate on crystal shape evolution and anisotropy. (a-i) SEM images of graphene crystals grown on Ge(001)-0° **(a-c)**, Ge(001)-6° **(d-f)**, and Ge(001)-9° **(g-i)** with increasing growth rate. Dashed arrows point downhill, as determined by XRD. Scale bars are 500 nm. Insets are magnified images of a representative crystal. Contrast reversal is attributed to amorphous carbon deposition upon sample exposure to the electron beam and oxidation of the Ge surface (Fig. H.7 and H.8).

Notably, this crystal shape transition is primarily a result of increasing growth rate, and either has no dependence or much weaker dependence on crystal size. For example, crystals as narrow as ~15 nm can grow as trapezoids at a growth rate of ~240 nm h^{-1} (Fig. 8.2e,h), but crystals

as wide as ~50 nm can evolve as rectangles at a slower growth rate of ~30 nm h^{-1} (Fig. 8.2d,g). Similarly, crystals as narrow as ~15 nm can grow as semicircles at a growth rate of ~470 nm h^{-1} (Fig. 8.2f,i), but crystals as wide as ~200 nm can evolve as trapezoids at a slower growth rate of ~240 nm h^{-1} (Fig. 8.2e,h).

8.2.3 Electron Microscopy and Diffraction Studies

Low-energy electron microscopy (LEEM) and diffraction (LEED) are used to characterize the graphene crystallographic orientation with respect to the Ge(001)-9° surface. Fig. 8.3a shows a LEED pattern from isolated crystals on Ge(001)-9° (Fig. H.9), in which gray dashed lines enclose a circular sector of the pattern with central angle of 60°. Splitting of the (00) LEED spot is observed, characteristic of vicinal surfaces.[234] This splitting is also observed for graphene {01} spots. In Fig. 8.3a, the three (00) spots are highlighted in white, and the set of graphene diffraction spots corresponding to the central (00) spot follow the dashed arc.

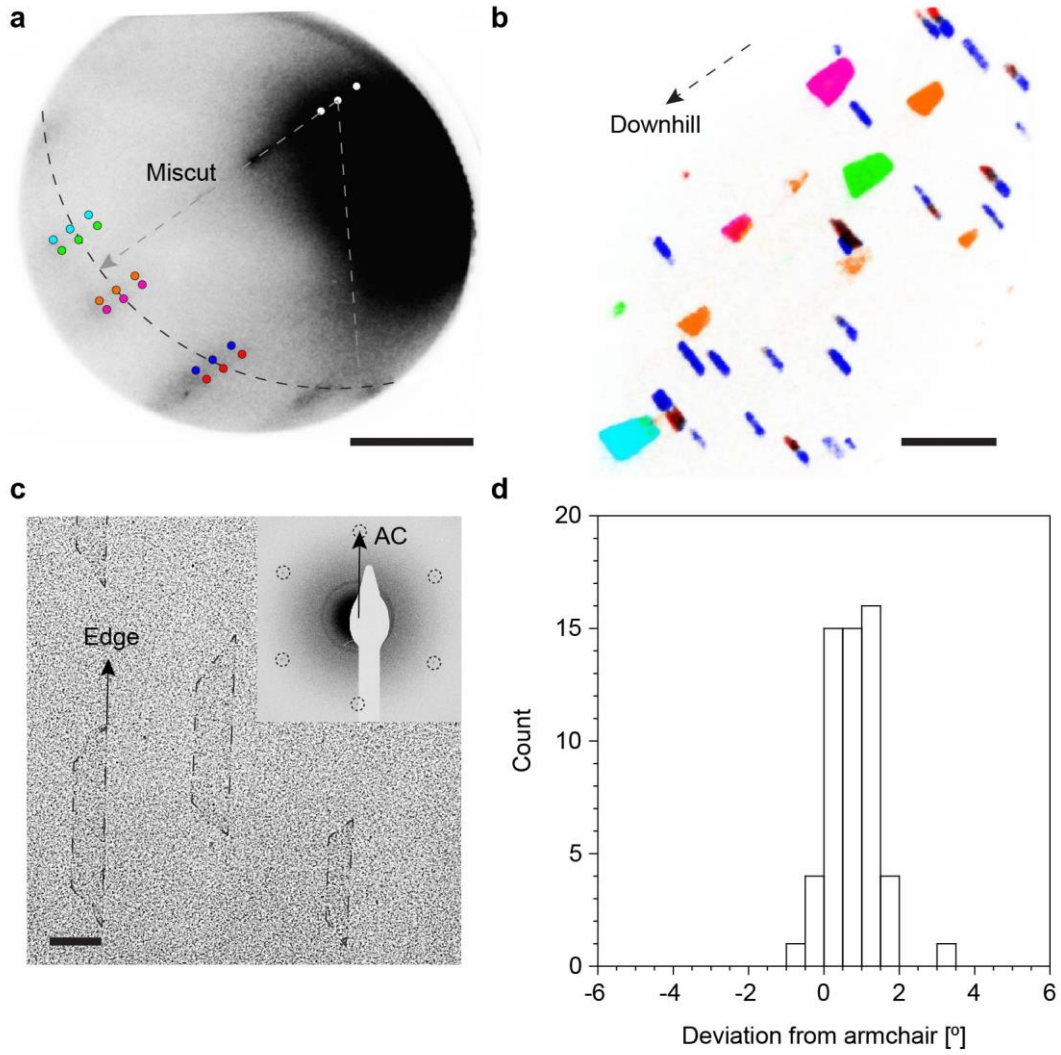

Figure 8.3: LEEM and TEM characterization of graphene grown on Ge(001)-9°. **(a)** LEED pattern in which the {01} graphene diffraction spots are highlighted in cyan, green, orange, magenta, blue, and red. {00} diffraction spots are highlighted in white. **(b)** Superposition of dark-field images in which the color of each crystal corresponds to the {01} spot with the same color in a. Dashed arrow points downhill, as determined from the trapezoidal island orientation. Scale bar is 2 μm. **(c)** TEM image of graphene crystals with their edges highlighted by dashed lines. Inset is an SAED pattern from the labelled crystal. The armchair (AC) direction and ribbon long-axis are aligned. Scale bar is 200 nm. **(d)** Histogram of edge deviation from the armchair direction for 56 ribbons, as determined from TEM and SAED.

There are six main graphene orientations on Ge(001)-9°, as highlighted in cyan, green, orange, magenta, blue, and red in Fig. 8.3a in which the armchair graphene direction is rotated from the miscut direction by -8.5, -7.0, 5.8, 8.2, 28.5, and 31.2°, respectively. Dark-field LEEM is conducted to correlate each set of diffraction patterns with the island morphology and alignment.

Fig. 8.3b shows a composite image of graphene crystals with each of the six diffraction patterns. These data show the diffraction spots in red and blue correspond to high-aspect ratio ribbons oriented perpendicular to the miscut, indicating the ribbon edges are roughly aligned along the armchair direction. Some islands are single-crystals, whereas others are bi-crystals in which approximately half the ribbon has an orientation rotated ~2.7° from that in the other half. Single- and bi-crystals were also observed on Ge(001)-0°.[72] Existence of bi-crystals indicates ribbons nucleate in their center and then grow in opposite directions along their length. Interestingly, crystals with low-aspect ratios (*i.e.*, cyan, green, orange, and magenta data in Fig. 8.3a,b) have rotated lattices with respect to that of ribbons, indicating anisotropic ribbon growth is only driven when there is a specific relative orientation between graphene and the underlying Ge surface, similar to growth on Ge(001)-0°.[72,225]

Transmission electron microscopy (TEM) and selected-area electron diffraction (SAED) are used to more precisely characterize crystallographic alignment of ribbon edges grown on Ge(001)-9°. Fig. 8.3c provides an SAED pattern from the labelled crystal, showing the smooth crystal edge is aligned closely to the armchair direction. Analysis of 56 crystals indicates the edges are aligned, on average, within 0.85° of the armchair direction (Fig. 8.3d), similar to the deviation of 1.6° for ribbons grown on Ge(001)-0°.[225]

8.2.4 Growth of Nanoribbons with Sub-10 nm Widths

Most ribbons in Fig. 8.1, 8.2, and 8.3 are relatively wide (~10–100 nm in width). However, narrower nanoribbons can also be synthesized by decreasing growth rate or time. For example, Fig. 8.4a,b shows aligned ribbons with average width of 12.2 ± 3.6 nm can be grown using short growth time of 2.5 h at ~30 nm h^{-1}. Even narrower nanoribbons with width of 3–4 nm (below the SEM resolution of ~10 nm) are grown by further decreasing growth time to 40 min and rate to ~10 nm h^{-1}, as shown in Fig. 8.4c,d. The ribbon edges are relatively smooth, as width varies < 5 Å over > 90% of the ribbon length in 4d. Charge transport of ribbons with sub-10 nm widths is characterized, below.

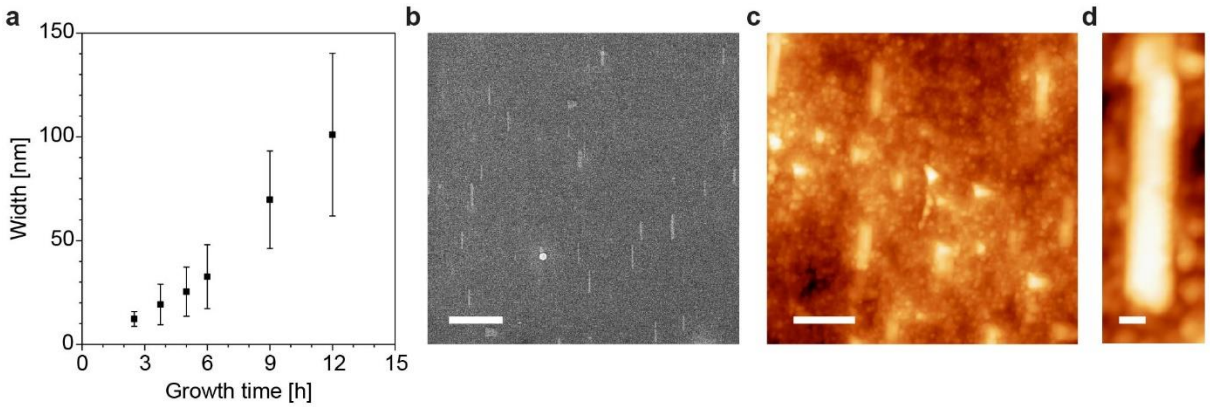

Figure 8.4: Growth of narrow nanoribbons on Ge(001)-9°. **(a)** Plot of ribbon width *versus* growth time. **(b)** SEM image of ribbons with average width of 12.2 ± 3.6 nm. (c-d) STM images of nanoribbons with average width of 3–4 nm [I = 20 pA, V = -2 V **(c)**; I = 200 pA, V = -2 V **(d)**]. Scale bars in b-d are 400, 20, and 2 nm, respectively.

8.2.5 Density Functional Theory (DFT) Calculations

The trapezoidal (Fig. 8.2e,h) and hemispherical (Fig. 8.2f,i) islands formed at high growth rates on Ge(001)-6° and Ge(001)-9° are similar to crystal shapes observed for graphene growth on Ru(0001)[235] and WSe_2 growth on c-plane sapphire.[236] In the latter cases, the crystal shape is caused by pinning of the uphill edge to a substrate step edge, resulting in a smooth, planar interface that does not grow or grows relatively slowly. In contrast, the downhill edge does not interact as strongly with the substrate, causing it to grow faster in a carpet-like fashion, resulting in a rougher

semicircular growth front.

To determine if a similar mechanism is responsible for the crystal shape evolution observed in Fig. 8.2, we study the stability and edge passivation of ribbons on Ge(001)-9° using periodic DFT (see Section H.1 of Appendix H for details). We model armchair nanoribbons ~1.5 nm wide on the lowest-energy Ge(001)-9° surface containing dimerized Ge atoms. The surface is bare because the equilibrium H coverage on Ge is low (~$1/16^{th}$ monolayer) at typical temperatures and H_2 partial pressures (P_{H_2}) used for growth (Fig. H.10). Simulations are performed in which the Ge lattice constant is (1) the calculated relaxed bulk value of 5.67 Å, similar to the experimental value of 5.66 Å, and (2) expanded to 6.04 Å to match the periodicity of the armchair direction and eliminate strain along the ribbon length. It is likely that the Ge lattice constant during graphene growth is between the relaxed and strained values. Nonetheless, at both extremes, the trends observed in our calculations are qualitatively similar.

First, we calculate the minimum-energy structure for ribbons perpendicular to the miscut in which (1) both edges are terminated with H, (2) neither edge is terminated with H, (3) the downhill (uphill) edge is (is not) terminated with H (Fig. 8.5a,b), and (4) the uphill (downhill) edge is (is not) terminated with H (Fig. 8.5c,d). When the edges are not terminated with H, the atomic orbitals of C at the ribbon edge and of Ge on the surface rehybridize to form relatively strong covalent bonds, which correspond to regions of large charge transfer as shown in the charge density difference maps in Fig. 8.5a-d. We accordingly refer to ribbon edges as “pinned” or “unpinned” if they are covalently bonded to Ge or H, respectively.

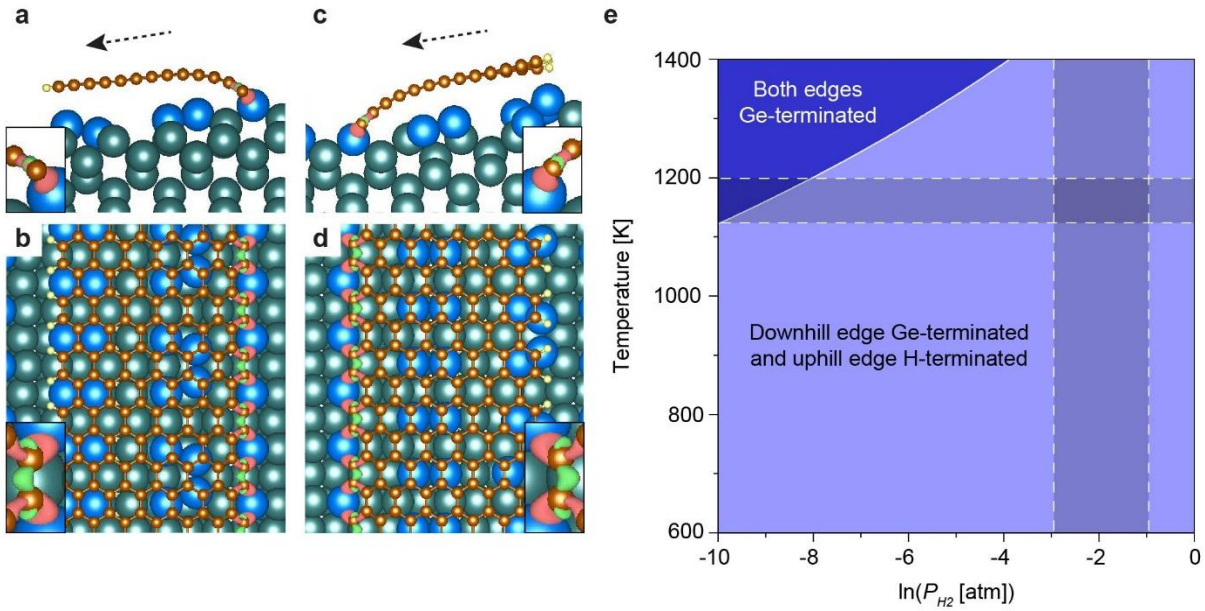

Figure 8.5: DFT calculations of graphene nanoribbons on Ge(001)-9°. **(a-d)** Side **(a,c)** and top view **(b,d)** of the minimum-energy structure in which the uphill (downhill) edge is not (is) terminated by H **(a,b)** and vice versa **(c,d)**. Charge density isosurfaces (insets) show regions of increased (red) and decreased (green) electron density upon ribbon adsorption onto Ge(001)-9°. Green, blue, orange, and white atoms are Ge (saturated, bulk), Ge (unsaturated, surface), C, and H, respectively, and dashed arrows point downhill. (e) Thermodynamic phase diagram plotted against temperature and P_{H_2}. CH_4 partial pressure (P_{CH_4}) is 0.0067 atm. Shaded regions indicate a range of temperatures and P_{H_2} at which ribbons have been synthesized. Results in a-e are calculated on strained Ge. Results for relaxed Ge are in Fig. H.11 and H.12.

To determine the thermodynamically stable edge termination, we construct a phase diagram for ribbons on Ge(001)-9° exposed to CH_4 and H_2 using the minimum-energy structure for each termination (Fig. 8.5e). Under typical growth conditions, ribbons with their downhill (uphill) edge pinned (unpinned) are predicted to be the most stable phase by 0.16 and 0.18 eV per edge C atom on relaxed and strained Ge surfaces, respectively (Fig. H.11 and H.12). The increased stability of the downhill edge is due to energy contributions from the minimum-energy structure of the ribbon, minimum-energy structure of the Ge slab, van der Waals forces, and covalent forces, as summarized in Table 8.1. More specifically, this increased stability is primarily derived from interactions between the ribbon and the Ge surface, as ~78% and 72% of the total energy difference on relaxed and strained Ge, respectively, are due to van der Waals and covalent forces.

Table 8.1: Contribution to the total relative stability of nanoribbons with their downhill edge pinned compared to ribbons with their uphill edge pinned. A negative entry means the downhill edge pinned is more stable.

Contribution	Relative energy per edge C atom (downhill pinned – uphill pinned) [eV]	
	Relaxed Ge lattice	Strained Ge lattice
Graphene nanoribbon	-0.01	-0.04
Ge slab	-0.03	-0.01
van der Waals interactions	-0.09	-0.05
Covalent interactions	-0.05	-0.07
Total	-0.18	-0.16

While these calculations provide valuable insight, the phase diagrams only consider ribbons with each edge fully pinned or fully unpinned. Consequently, additional stable ribbon phases with partial Ge- and H-passivated edges may also exist. Nonetheless, these data indicate a larger percentage of C atoms at the downhill edge are pinned than at the uphill edge, and thus the edge termination and binding strength at the downhill and uphill edges are not equivalent. Moreover, we observe in experiments that Ge below graphene is nanofaceted (Fig. H.13), which is not accounted for in these simulations due to prohibitively large unit cells that are required.[237,238]

8.2.6 Discussion of Anisotropic Growth Mechanism and Formation of Smooth Armchair Edges

It has been shown theoretically[239] and experimentally[240] that on Cu and Ni, graphene growth at slow rates (*i.e.*, low supersaturation) proceeds via a kink-flow mechanism in which growth species add to a smooth crystal edge row-by-row. Growth proceeds via the slow, unfavorable formation of a kink (*i.e.*, the addition of one or more new atoms to an edge), followed by the fast sequential attachment of species to the kink site to propagate the kink along the crystal edge and complete the new atomic row.[239,240] The resulting crystals are terminated with zigzag edges because the zigzag edge is the slowest growing facet on Cu and Ni. If the growth rate is increased (*i.e.*, high supersaturation), attachment is less selective and defects incorporate into the growth front more frequently, resulting in more isotropic growth of crystals with rougher edges.[239]

On Ge(001)-0°, we have shown armchair facets grow slowest, and growth velocity depends on the angle between the armchair edges and Ge⟨110⟩.[225] We hypothesize that the kink formation rate (and subsequent formation of atomic rows) depends on the graphene edge orientation with respect to the surface. This dependence can be caused by differences in edge termination and interaction strength of the edge with Ge, which can affect kink formation via factors such as the attachment energy barrier and mechanism, and diffusion of species along the edge, as reported for graphene growth on Cu(111).[241] We hypothesize the kink formation rate at the short crystal edges is faster than at the long edges. On Ge(001)-0°, we expect this rate at each long edge is the same because the long edges are equivalent. On Ge(001)-6° and Ge(001)-9°, however, we expect the kink formation rate at the long downhill edge is slower than at the long uphill edge because of its increased stability, stronger interaction with Ge, and larger fraction of edge C atoms that are covalently bonded to Ge, as indicated by the DFT calculations above.

We propose when the growth rate is slow, kink formation occurs primarily at the short crystal edges, giving rise to anisotropic growth of ribbons with high-aspect ratios (Fig. 8.2a,d,g). In particular, on Ge(001)-6° and Ge(001)-9°, the downhill and uphill edges evolve relatively symmetrically as smooth armchair facets because the kink formation rate is relatively slow at both long edges.

In contrast, we propose when the growth rate is fast, the kink formation rate at the uphill edge on Ge(001)-6° and Ge(001)-9° also becomes significant. Consequently, the uphill edge grows faster than the downhill edge and species attach to the uphill edge less selectively (*i.e.*, atomic rows nucleate before the previous row is completed). This rapid, less discriminate growth results in roughening and formation of a more isotropic semicircular growth front, and a decrease in aspect ratio (Fig. 8.2f,i). Meanwhile, the kink formation rate at the downhill edge also increases but is

relatively slow compared to that at the uphill and short edges, resulting in a smooth, straight growth front that evolves row-by-row. With increasing growth rate on Ge(001)-0°, we expect the kink formation rate at the equivalent long edges also increases relative to that at the short edges, resulting in a decrease in aspect ratio (Fig. 8.2c). However, species still likely add to the long edges more selectively via row-by-row kink flow, as the growth front is fairly straight and does not roughen to the extent of becoming semicircular.

This balance between slow, row-by-row kink-flow growth and fast, less selective, more isotropic growth may explain our observation of increased growth anisotropy and smoother ribbon edges on all Ge(001)-like surfaces in a regime of low supersaturation (*i.e.*, low CH_4 flux or high H_2 flux). Therefore, these results highlight the importance of conducting synthesis in a regime in which growth is particularly slow and may indicate that a strong interaction between the graphene edge and the Ge surface is critical for achieving anisotropic ribbon growth and smooth armchair edges.

8.2.7 Charge Transport Properties of Narrow Graphene Nanoribbons

Finally, we conduct room-temperature charge transport measurements of individual narrow ribbons grown on Ge(001)-9° via CVD. Charge transport measurements are conducted using an FET architecture, in which individual nanoribbons are contacted by Cr/Pd/Au source and drain electrodes with channel lengths (L_{ch}) of 30–50 nm, and Si and SiO_2 (15 nm) serve as the gate electrode and gate dielectric, respectively (Fig. 8.6a). Nanoribbons are synthesized using high H_2:CH_4 of 50:1 (slow rate of ~30 nm h^{-1}) and short growth time of 2 h (similar to Fig. 8.4b) to obtain a polydisperse mixture of ribbons with, on average, narrow widths of ~10 nm (standard deviation is roughly 40% of the average width) and aspect ratios > 6.5. Width polydispersity can lead to variability in FET on/off conductance ratio. Nonetheless, the goal of the charge transport

measurements is to demonstrate that the ribbons can have high on-state conductance and, in some cases (*i.e.*, when ribbons are particularly narrow), can also exhibit high on/off conductance ratio.

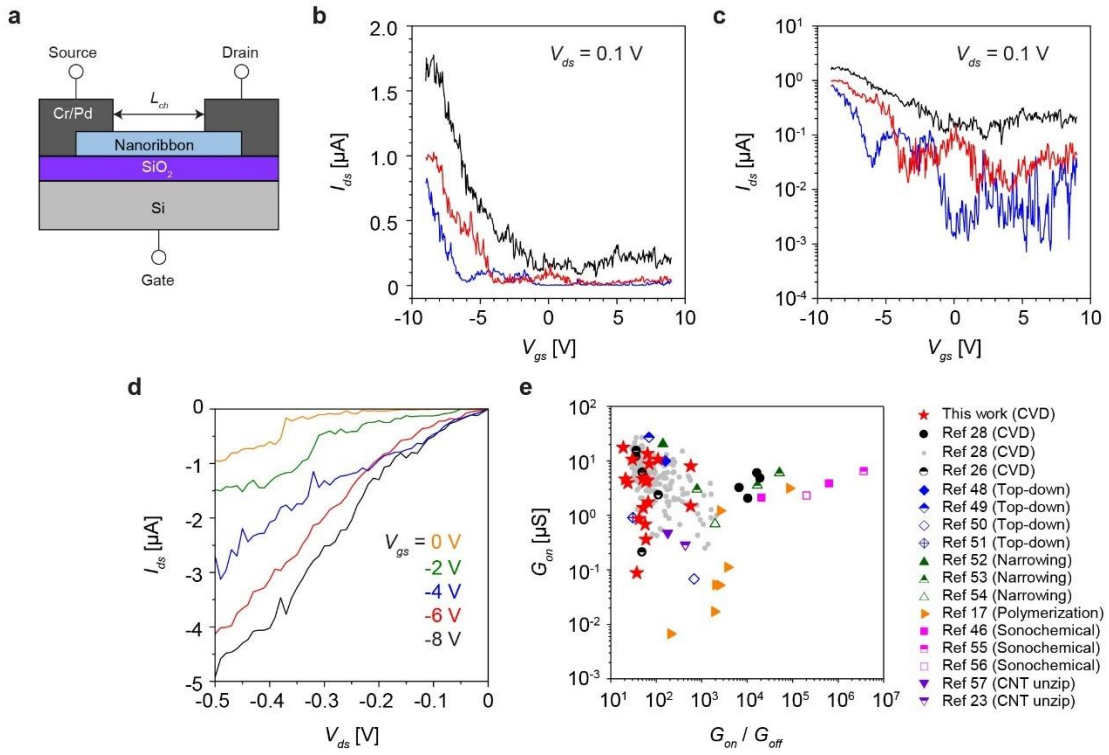

Figure 8.6: Charge transport of nanoribbons grown on Ge(001)-9°. (a) FET architecture used for room-temperature transport measurements. **(b-c)** Plot of I_{ds} *versus* V_{gs} on a linear **(b)** and log **(c)** scale for three nanoribbons at V_{ds} of 0.1 V. Forward sweeps, in which bias is varied from negative to positive voltage, are shown. Reverse sweeps and source-gate current (I_{gs}) *versus* V_{gs} are plotted in Fig. H.14. Hysteresis is exhibited in I_{ds} *versus* V_{gs} curves, as expected for ribbons on SiO_2 measured in air. **(d)** Plot of I_{ds} *versus* V_{ds} for the ribbon in b,c (blue curve) at V_{gs} of 0 to -8 V. **(e)** Plot of G_{on} *versus* G_{on}/G_{off} for ribbons grown on Ge(001)-9° via CVD and for ribbons grown via other techniques in the literature.

Fig. 8.6b,c plots source-drain current (I_{ds}) *versus* source-gate voltage (V_{gs}) on a linear and log scale, respectively, using a source-drain voltage (V_{ds}) of 0.1 V. Hysteresis is exhibited, as expected for ribbons on SiO_2 measured in air.[242,243] Moreover, noise is relatively high, as expected for single-ribbon devices, likely due to interactions of ribbons with species originating from the ambient environment. The black, red, and blue curves are measured from three representative ribbons with on/off conductance ratio (G_{on}/G_{off}) of 19, 110, and 570, respectively, and on-state conductance (G_{on}) of 18, 11, and 8.0 μS, respectively. The high G_{on}/G_{off} of 570 indicates a bandgap

>> k_BT at room temperature is achieved, and the ribbons can be semiconducting rather than semi-metallic. G_{on}/G_{off} can vary by orders of magnitude from ribbon to ribbon, which can be attributed to nanoribbon width polydispersity.[75] We have recently shown that polydispersity can be reduced by initiating nanoribbon growth on Ge(001)-0° from nanoscale seeds.[225] Therefore, polydispersity and the resulting device variability are not necessarily intrinsic limitations of nanoribbon synthesis on Ge via CVD. In future studies, it may be possible to adapt seeded ribbon synthesis on vicinal Ge(001) surfaces to synthesize aligned ribbons with reduced polydispersity. The nanoribbon width in FETs cannot be precisely determined via SEM due to charging from the SiO_2 substrate and screening from the electrodes. However, the ribbon width and bandgap can be estimated from its G_{on}/G_{off}, as shown previously.[75,244] From these relationships, a ribbon with G_{on}/G_{off} of 570 has an expected width of ~8 nm and bandgap of ~0.2 eV. Fig. 8.6d plots I_{ds} against V_{ds} for the ribbon in Fig. 8.6b,c (blue curve) with G_{on}/G_{off} of 570 and G_{on} of 8.0 μS at varying V_{gs}. The I_{ds} *versus* V_{ds} curves are nonlinear at low V_{ds}, indicating G_{on} is likely at least partially limited by a Schottky barrier at the nanoribbon/contact interface.[245]

We plot G_{on} against G_{on}/G_{off} for 18 nanoribbons grown on Ge(001)-9° with $G_{on}/G_{off} > 20$ in Fig. 8.6e (red stars). Also plotted are data for nanoribbons synthesized via CVD on Ge(001)-0° (black and grey circles)[72,75] as well as fabricated using subtractive top-down lithography (blue diamonds),[246–249] narrowing of wider ribbons via etching (green upward triangles),[250–252] polymerization/cyclodehydrogenation (orange rightward triangles),[215] sonochemical exfoliation (pink squares),[244,253,254] and unzipping nanotubes (purple downward triangles).[221,255] For a given G_{on}/G_{off}, nanoribbons grown on Ge(001)-9° via CVD have among the highest G_{on} of ribbons produced using any method. Similar charge transport has been measured for ribbons grown on Ge(001)-0°, indicating that charge transport is not compromised by growing on the miscut

Ge(001)-9° surface.

8.3 Conclusions

In summary, we show ~90% of the nanoribbons grown on Ge(001)-9° via CVD can be aligned within ±1.5° perpendicular to the miscut. The ribbons can have sub-10 nm widths, aspect ratios > 10 on average and as high as 25, and smooth armchair edges – enabled by conducting synthesis using relatively slow growth rate. The nanoribbons display excellent charge transport, simultaneously exhibiting high G_{on} and G_{on}/G_{off} in FETs. The crystal shape evolution with growth rate may indicate a strong interaction between the ribbon edges and the Ge surface is important for achieving anisotropic growth and ribbons with smooth armchair edges on all Ge(001)-like surfaces. Provided the packing density can be increased (*e.g.*, by seeding growth[225] or by increasing nucleation density via growth at lower temperature), large-area alignment of semiconducting nanoribbons on vicinal Ge(001) via CVD could be an important step towards realizing graphene-based semiconductor technologies.

8.4 Methods

Graphene synthesis via CVD: Ge(001) substrates with 0° nominal miscut (Wafer World, resistivity > 50 Ω-cm), 6° miscut (University Wafer, 0.01-0.05 Ω cm, Ga dopants), and 9° miscut (Wafer World, 0.4 Ω cm, Sb dopants) toward Ge[110] are loaded into a horizontal furnace with a quartz tube inner diameter of 34 mm. The system is evacuated to < 10^{-5} torr and then refilled to atmospheric pressure with a flow of Ar and H_2. After annealing the substrates at 910 °C, a flow of CH_4 is introduced to begin graphene synthesis. The furnace is slid away from the growth zone to terminate synthesis while maintaining the atmosphere used during growth. Specific growth conditions used throughout this work are provided in Table H.1. We previously found dopants in Ge wafers do not significantly alter growth on Ge(001).[72]

SEM characterization: After growth, samples are imaged with SEM (Zeiss LEO 1530) using an in-lens detector. Contrast reversal of graphene on Ge (see Fig. 8.2a-i) is attributed to amorphous carbon deposition upon exposure to the electron beam and oxidation of the Ge surface (Fig. H.7 and H.8). Amorphous carbon does not affect the measured island size nor shape.

STM characterization: STM images are acquired using a CreaTec STM at 4.5 K with a Nanonis control system and are processed using WSxM[256]. The system base pressure is 7×10^{-11} mBar. Pt/Ir tips are prepared via electrochemical etching in a $CaCl_2$ solution and subsequent field emission in-situ. Tip quality and stability is determined by constant height measurements on a clean Au(111) crystal. Samples are annealed overnight at 350 °C and 5×10^{-10} mBar.

AFM characterization: Surface morphology is characterized using atomic force microscopy (AFM) (Veeco MultiMode SPM) in tapping mode.

XRD characterization: The Ge miscut angle and miscut direction are determined with XRD. A low-angle x-ray specular reflection is used to level the sample to within ± 0.01°. The miscut angle is determined by measuring the maximum angle between (004) and the specular direction. The miscut azimuth is determined from the difference between the rotational angle, phi, where the (224) reflection is maximized to the phi where the miscut angle is maximized. Ge(001)-6° and Ge(001)-9° have miscut angles of 5.99 ± 0.05° and 8.75 ± 0.05°, respectively, and azimuthal deviation from Ge[110] of 4 ± 1° and 0.5 ± 1°, respectively.

LEEM and LEED characterization: The crystallinity of the graphene islands and their registration with Ge(001)-9° are characterized with LEEM and LEED (SPECS Fe-LEEM/PEEM P90). The substrates are annealed at 600 °C for 5 min under ultra-high vacuum (10^{-9} torr) before LEEM and LEED measurements. Incident electron energies of 25–30 eV are used. LEEM and LEED modes are aligned with a precision of ± 3°. To increase contrast of the graphene diffraction

spots, samples are tilted relative to the incident electron beam.

TEM and SAED characterization: The TEM and SAED experiments in Fig. 6.3c,d are conducted in a Tecnai T-12 Cryo TEM at 120 kV. After growth on Ge(001)-9°, the graphene crystals are transferred onto Si_3N_4 windows that are 5 nm in thickness (TEM Windows, product #SN100-A05Q33A), as described previously[225].

***Raman characterization*:** Raman spectroscopy in Fig. H.3 is conducted using a Thermo-Fisher Scientific DXRxi Raman Imaging Microscope with laser excitation wavelength of 532 nm and power of 10 mW.

DFT calculations: DFT calculations are performed using the PBE-D2[79,257] exchange correlation functional as implemented in the Vienna *Ab Initio* Simulation Package (VASP)[81]. k-point sampling is restricted to the Γ point. The Ge substrate is modeled as a slab with eight layers, with the bottom surface passivated by H, the bottom four Ge layers fixed in bulk positions, and the top four Ge layers relaxed. Structures of nanoribbons placed on the Ge surface are optimized, and phase diagrams are constructed by calculating the grand potential of the ribbons exposed to CH_4 and H_2 in the gas phase. A detailed description of the computations is in Section H.1 of Appendix H.

Charge transport measurements: Nanoribbons grown on Ge(001)-9° are transferred from Ge onto 15 nm of SiO_2 on Si using a dry transfer method with thermal release tape, as described previously. FETs are fabricated using electron-beam lithography to define the source and drain contact regions. Thermal evaporation is used to deposit Cr/Pd/Au (0.7/10/10 nm) contacts. The Si substrate is used as a back gate and 15 nm of SiO_2 is used as the gate dielectric. All devices are measured at room temperature in ambient laboratory conditions using a Keithley 2636A SourceMeter.

Chapter 9: Anisotropic Synthesis of Armchair Graphene Nanoribbon Arrays from Sub-5 nm Seeds at Variable Pitches on Germanium*

9.1 Introduction

Graphene nanoribbons are promising candidates for a variety of applications, including high-frequency communication devices, logic circuits, optoelectronics, photonics, and sensors.[1-10] Unlike graphene, which is a semimetal, graphene nanoribbons can be semiconducting with a bandgap greater than room-temperature thermal energy when they are narrower than 10 nm. Theoretical studies indicate that the bandgap of ribbons varies inversely with their width and find that an armchair edge orientation provides the largest bandgaps.[11]

The synthesis of sub-10 nm nanoribbons with smooth edges, controlled orientation, and controlled placement remains a challenge. Top-down techniques that lithographically pattern ribbons from monolayer graphene can address the issues of placement and orientation; however, these techniques yield nanoribbons with disordered edge structures which degrade electrical and thermal properties.[12-19] Furthermore, sub-10 nm resolution is also beyond the limit of conventional

---

* Adapted from **"Anisotropic Synthesis of Armchair Graphene Nanoribbon Arrays from Sub-5 nm Seeds at Variable Pitches on Germanium"**, A. J. Way, E. A. Murray, F. Göltl, V. Saraswat, R. M. Jacobberger, M. Mavrikakis, M. S. Arnold, *Journal of Physical Chemistry Letters* **10**, 4266 (2019).

Synthesis and characterization experiments were performed by A. J. Way, R. M. Jacobberger, and M. S. Arnold. A. J. Way served as the primary author for this work.

lithography. Alternate techniques such as the unzipping of graphite[20] and nanotubes[21,22] can result in narrow ribbons with smooth edges but do not provide control over placement, orientation, and edge chirality. A promising bottom-up method is polymerization followed by cyclodehydrogenation,[23-28] which results in smooth, armchair edges and sub-10 nm widths; however, it has not yet been possible to uniformly control the orientation and placement of these ribbons. Polymerization approaches also yield nanoribbons that are narrower than 1.5 nm, whereas wider nanoribbons may be needed for applications that demand more bandgap tunability.

Jacobberger et al. have recently demonstrated a bottom-up synthesis process in which graphene nanoribbons can be grown directly on Ge(001) by chemical vapor deposition (CVD) from CH_4. This technique yields nanoribbons aligned to Ge⟨110⟩, with smooth armchair edges, widths as narrow as 1.7 nm, and aspect ratios up to 70.[29,30] These ribbons possess excellent charge transport properties, as compared to other synthesized ribbons in the literature, demonstrating an on/off conduction modulation of 2×10^4 and an on-state conductance of 5 μS.[31] However, the synthesis of nanoribbons on bare Ge(001) yields nanoribbons that nucleate and grow in random locations and that begin growing at different times over the course of the synthesis, resulting in size polydispersity.

These issues have been partially addressed by using graphene seeds to act as initiation sites for ribbon growth. Previously, we have demonstrated that nanoscale seeds of graphene lithographically patterned on Ge(001) can initiate the synthesis of nanoribbons. When the armchair direction of the graphene seed is aligned with a particular Ge[110] direction, the resulting ribbon is aligned to the same Ge[110] direction, which enables the synthesis of unidirectionally aligned arrays of ribbons.[32] Furthermore, the seeded nanoribbons also begin growing at the same time,

thereby reducing size polydispersity, which occurs due to spontaneous (or secondary) nucleation. Therefore, this seeding technique is promising because it yields armchair nanoribbons with naturally faceted edges while enabling control over the nanoribbons' orientation and placement. However, for the seeded CVD synthesis of graphene nanoribbons to become reproducible and commercially viable, methods for creating graphene seeds that are sub-5 nm in diameter *and monodisperse* will be needed. Furthermore, a dense packing (*i.e.*, a small pitch) of ribbons is required for many technologically important applications, whereas the impact of dense packing on growth kinetics has not been explored.

Here, we advance the seed-initiated synthesis in two ways. To reduce the width of the obtained ribbons, we demonstrate the viability of initiating nanoribbon synthesis from sub-5 nm seeds. Furthermore, we also reduce the pitch between nanoribbons in periodic arrays from 500 nm to 50 nm and find that nanoribbon-crowding effects do not perturb growth kinetics. We furthermore use DFT calculations to estimate the order of magnitude of the diffusion coefficient (D), diffusion length (L_D), and lifetime (τ) of the rate-limiting hydrocarbon intermediate species on Ge(001). The experimental invariance of the kinetics and the DFT calculations indicate two possibilities: (1) the diffusion length of the rate-limiting hydrocarbon intermediate species is << 50 nm and/or (2) the nanoribbon growth kinetics are strongly attachment-limited.

9.2 Results and Discussion

As discussed above, the seeded CVD synthesis of graphene nanoribbons can only become reproducible and commercially viable if there are efficient methods for creating seeds that are sub-5 nm in diameter *and monodisperse*. While this goal is still elusive, the first step in our analysis focuses on generating sub-5 nm seeds with some polydispersity to demonstrate that growing

nanoribbons from seeds that are vanishing in diameter is viable. Subsequently, we focus on the spacing between the seeds and the impact of this spacing on growth kinetics. Finally, we perform DFT calculations to estimate diffusion properties of potential graphene growth species on the surface.

To create and approximately control the diameter of the graphene seeds, a two-step process is employed. The first half of this process closely relies on previous work in generating seeds for ribbon growth[32] and uses electron-beam lithography to fabricate seeds. This fabrication involves: (i) the polymer-assisted transfer of graphene crystals grown on Cu foil to Ge(001), (ii) the deposition of a thin film of electron-beam resist, (iii) electron-beam lithography to create 20–55 nm openings in the resist, (iv) the deposition of a 10 nm film of Ni to serve as a hardmask, followed by lift-off to yield 20–55 nm discs of Ni on graphene on Ge(001), (v) oxygen reactive ion etching to produce isolated graphene seeds on Ge(001) protected by the Ni hardmask, and (vi) the removal of the Ni in a dilute aqua regia etchant solution. At this stage, graphene seeds are 20–55 nm in diameter. Next, we focus on reducing their size. Previously, it was demonstrated that annealing graphene seeds in Ar and H_2 slowly reduces their diameter.[32] We therefore expose the seeds to an Ar and H_2 atmosphere and reduce their diameter to a desired size before initiating ribbon growth (Fig. 9.1a).

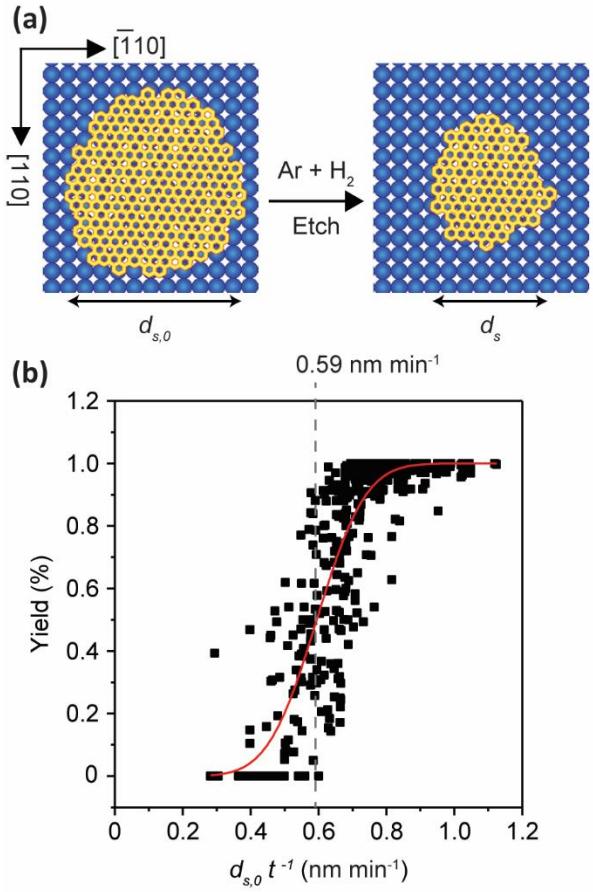

Figure 9.1: (a) Schematic of a lithographically patterned graphene seed before and after annealing in an Ar and H_2 environment. The seed diameter reduces from $d_{s,o}$ (patterned seed diameter) to d_s (seed diameter after etch). **(b)** Plot of yield (% of seeds resulting in ribbons) versus $d_{s,o}$ divided by t (anneal time). A normal cumulative distribution function (red line) is fit to the data and determines a diametric etch rate of 0.59 nm min^{-1}.

Obtaining a detailed understanding of the size of the seeds and the associated etching rate is difficult due to challenges in quantifying the size of nanostructures once their dimensions are reduced below 10 nm. We therefore rely on an alternative, indirect strategy to quantify etch rates. Seeds of various, known diameters are created via electron-beam lithography and then etched for a specific amount of time. Subsequently, nanoribbon synthesis is attempted from each seed and if a ribbon is formed, a seed is assumed to be present. The absence of a ribbon indicates that the entire seed has been etched away (*i.e.*, the diameter is reduced to 0 nm). The diametric etch rate is then calculated as the initial diameter of the seeds divided by the time needed to completely etch

the seeds. There may be a critical, non-zero seed size below which the growth of a nanoribbon is not possible. However, data, in the section below confirm that this critical size is very close to 0 nm.

Seeds are fabricated with initial diameters of 20–55 nm and then etched for 45–67.5 min at 910 °C in an environment of 33% H_2 in Ar. The fraction of etched seeds that yield nanoribbons against initial seed diameter, $d_{s,0}$, divided by etching (anneal) time, t, is plotted in Fig. 9.1b. We find that the nanoribbon yield is nearly 0%, when the initial seed diameter divided by etching time is small (and less than the etching rate) and conclude that the seeds in this scenario are destroyed by the etching. On the other hand, when the initial seed diameter divided by etching time is large (and greater than the etching rate), nanoribbons evolve from the seeds with a yield of nearly 100%, which implies that the seeds are still present. As shown in Fig. 9.1a, we fit a continuous distribution function to these data, which characterize thousands of seeds and ribbons, and identify an average diametric etch rate, R_s, of 0.59 ± 0.02 nm min^{-1}.

Next, we use this information to closely control the seed size and demonstrate that the growth of nanoribbons can be initiated from such seeds. Seeds that are initially 20–55 nm in diameter are defined by electron-beam lithography and then etched for times ranging from 45–67.5 min to produce seeds with expected diameters after etching, $d_s = d_{s,0} - R_s \cdot t$, ranging from 0 to 25 nm. Nanoribbons are then grown from these etched seeds at a CH_4 mole fraction, x_{CH4}, of 0.0066 for 6 hr. The measured length and width of the nanoribbons initiated from seeds of d_s are shown in Fig. 9.2a-b, respectively. Comparatively large error bars are found due to uncertainty in measuring the nanoribbon width *via* scanning electron microscopy (SEM) and because of variation inherent to our electron-beam lithography and Ni etch mask fabrication procedures that result in

seed-to-seed deviation in diameter. The average width, w, and length, l, of nanoribbons that form on a control sample during unseeded growth are 9.7 ± 4.1 nm and 218 ± 53 nm, respectively, indicating a growth rate R_l of l / 2t = 18.2 nm hr^{-1} along the nanoribbon length direction and a growth rate of $R_w = w$ / 2t = 0.81 nm hr^{-1} along the nanoribbon width direction (Fig. I.1) (factor of 2 arises since nanoribbons grow along both directions).

The length and width of nanoribbons initiated from seeds are expected to vary as d_s+2R_l·t and d_s+2R_w·t, respectively. These expected dependencies are plotted as solid lines in Fig. 9.2a-b, and experimental data in most cases lies within error bars. Fig. 9.2b shows that the narrowest seeded nanoribbons have widths of 10 nm, approximately equal to the widths of the unseeded nanoribbons. In this case, d_s+2R_w·t ≈ 2R_w·t, revealing that the narrowest nanoribbons in Fig. 9.2b have evolved from seeds with d_s ≈ 0. These data are promising and confirm that the anisotropic synthesis of graphene on Ge(001) can be initiated from sub-5 nm seeds that are potentially smaller than 1 nm in diameter. To seed the synthesis of nanoribbons of final w < 5 nm, it will be necessary to limit d_s+2R_w·t to less than 5 nm. These results show that achieving w < 5 nm will be viable because d_s can be reduced to << 5 nm, and R_w can be minimized while maintaining a large R_l by conducting growth at low x_{CH4} and high x_{H2}.[29,33]

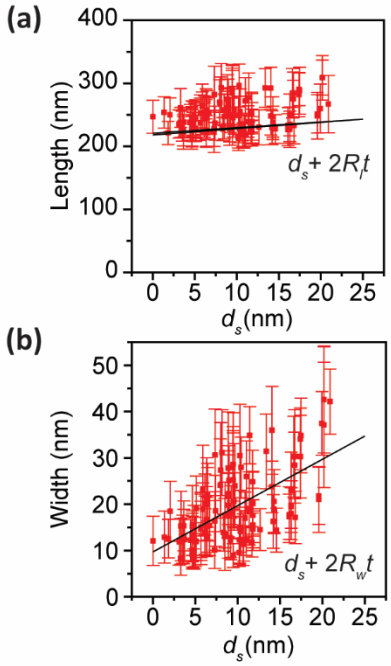

Figure 9.2: Plots of nanoribbon length **(a)** and width **(b)** versus etched seed diameter, d_s, following seed-initiated nanoribbon synthesis at a x_{CH4} of 0.0066 for t = 6 hr. Synthesis on a control sample without seeds yields ribbons of length = $2R_l \cdot t$ = 218 ± 53 nm and width = $2R_w \cdot t$ = 9.7 ± 4.1 nm. Solid black lines denote expected length and width of seeded nanoribbons, assuming that the dimensions increase as $d_s + 2R_l \cdot t$ and $d_s + 2R_w \cdot t$, respectively

Next, periodic arrays of nanoribbons are grown from seeds at different pitches. Arrays of nanoribbons will be needed for future electronic devices such as field-effect transistors. In this regard, one open question is: *Are the anisotropic growth kinetics of nanoribbons altered when they grow in arrays that are closely spaced due to crowding effects?* To answer this question, arrays with a pitch of 50, 100, 200, 300, and 400 nm are fabricated. Here, an initial seed diameter of 35 nm is used, and the seeds are etched for 52.5 min, resulting in an expected d_s of 4 nm. Nanoribbons are then grown from the seed arrays at x_{CH4} of 0.0066 for 6 hr. The length and width of the resulting nanoribbons are compared in Fig. 9.3 as a function of pitch. The median length of the nanoribbons does not change with pitch, varying only from 223 to 243 nm over the entire range of pitches (Fig. 9.3a). The median width is also largely independent of pitch (Fig. 9.3b), varying only from 10.5 to 13.9 nm. The nanoribbon width appears to slightly increase for the smallest 50 and 100 nm

pitches (Fig. 9.3b); however, this increase can be attributed to patterned seeds occasionally merging or losing uniformity, as discussed below, due to challenges with patterning and lift-off that become more prevalent as the spacing between seeds decreases.

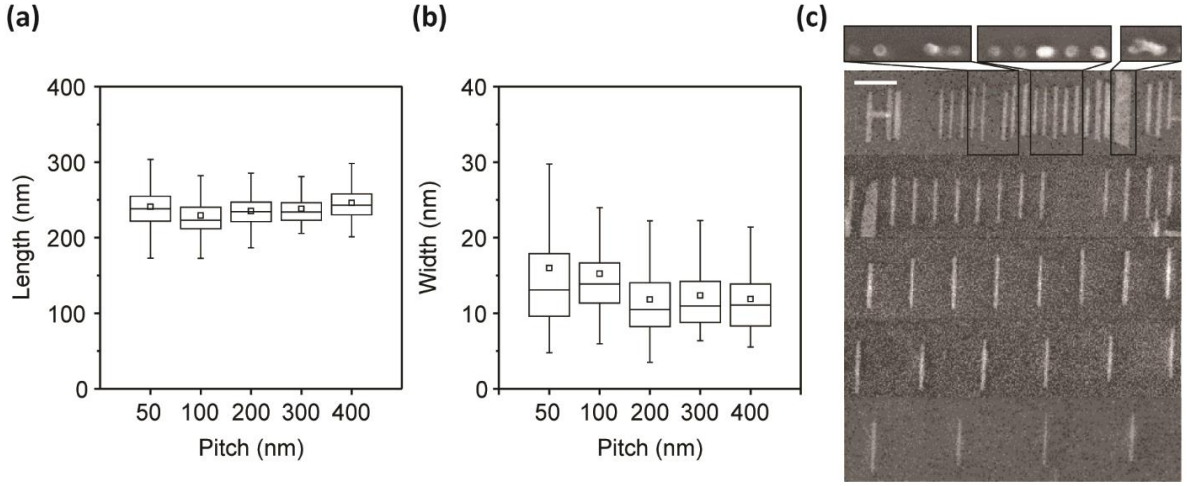

Figure 9.3: Plots of length **(a)** and width **(b)** of graphene nanoribbons synthesized in arrays with pitches of 50, 100, 200, 300, and 400 nm. The $d_{s,0}$ is 35 nm. All samples are annealed for 52.5 min before growth, resulting in an expected d_s of 4 nm. **(c)** Representative SEM images of a single row from arrays with pitches of 50, 100, 200, 300, and 400 nm (top to bottom). Scale bar is 200 nm. Inset is three different sequences of seeds that demonstrate a missing seed (left), a regular sequence of seeds (middle), and a merged seed (right), and resulting representative ribbon characteristics for a 50 nm pitch.

Fig. 9.3c shows representative SEM images of the nanoribbon arrays for all five pitches explored. There are no noticeable differences in the shape and size of the nanoribbons as a function of pitch – other than missing nanoribbons (from the 50 and 100 nm pitch arrays) and merged nanoribbons (in the 50 nm pitch array). These missing and merged nanoribbons can be attributed to imperfections in the seed definition process (rather than perturbation of nanoribbon growth kinetics). These imperfections are illustrated *via* SEM in the inset of Fig. 9.3c, which shows 50 nm pitch seed arrays prior to nanoribbon synthesis. Three different types of features are apparent: (i) a perfect sequence of seeds, (ii) an imperfect sequence of seeds with a missing seed, and (iii) a large, merged seed. These features dictate the configuration of nanoribbons that evolve from the

seeds. When a seed is not present at a spot in an array sequence, a ribbon will not grow at this spot. When all of the seeds are regular, a regular array of ribbons will grow. When seeds merge, nanoribbons evolve that are more than double the width of the others. Improved patterning and lift-off procedures will reduce or eliminate these issues, making smaller pitches viable. Another observation is that seeds occasionally rotate, yielding nanoribbons orthogonal to the intended Ge[110] direction (see for example the horizontal nanoribbon in the 50 nm pitch array in Fig. 9.3c). This rotation was not observed in our previous studies of nanoribbon synthesis from larger seeds, but might be correlated to the smaller seed sizes, the etching time, or surface impurities.

Previous work studying the kinetics of graphene synthesis have found growth to be attachment, diffusion, or dissociation-limited depending on the substrate and growth conditions.[34-38] The rate-limiting step of graphene nanoribbon growth on Ge(001) is not yet clear, but could impact tightly-pitched ribbon synthesis. The experimental data presented in this study indicate that the pitch of the graphene seed arrays has no effect on nanoribbon growth kinetics down to a pitch of 50 nm. Thus, there are no crowding effects that perturb the size or shape of the nanoribbons. The absence of crowding effects indicates one of two scenarios: (a) the diffusion length of the hydrocarbon intermediate(s) primarily driving nanoribbon growth is much less than 50 nm or (b) the synthesis is in a strongly attachment-limited regime. Distinguishing between the two scenarios based on experimental data alone is particularly complicated because the active growth species is unknown. Previously measured rate laws indicate that there are $x_{CH4}^{2.23 \pm 0.05}$ and $x_{H2}^{-4.0 \pm 0.2}$ dependencies for nanoribbon length growth kinetics on Ge(001), suggesting that C_2H_x carbon dimers act as the primary growth species on the Ge(001) surface.[29]

To obtain estimates for the mobility and lifetimes of all possible dimers, we rely on

theoretical modeling. We use DFT calculations using the PBE functional[39] as implemented in the Vienna *Ab Initio* Simulation Package (VASP)[40,41] and focus on a Ge(001) surface with a 2 × 1 reconstruction that forms dimer rows on the surface (see Fig. 9.4a). After we optimize the structures of the different adsorbates, we then use the nudged elastic band method[42] to calculate the diffusion barriers for the different species on the surface. Explicit values for diffusion parallel and perpendicular to the dimer rows are shown in Table I.1. We find that, in particular, CC and CHC show significant diffusion anisotropies and low diffusion barriers for along or perpendicular to Ge dimer rows for CC and CHC, respectively. We next calculate prefactors from vibrational entropies and use these values under the assumption of an Arrhenius behavior to calculate diffusion constants D for all considered C_2 species.[43] All numerical values are given in Table I.1.

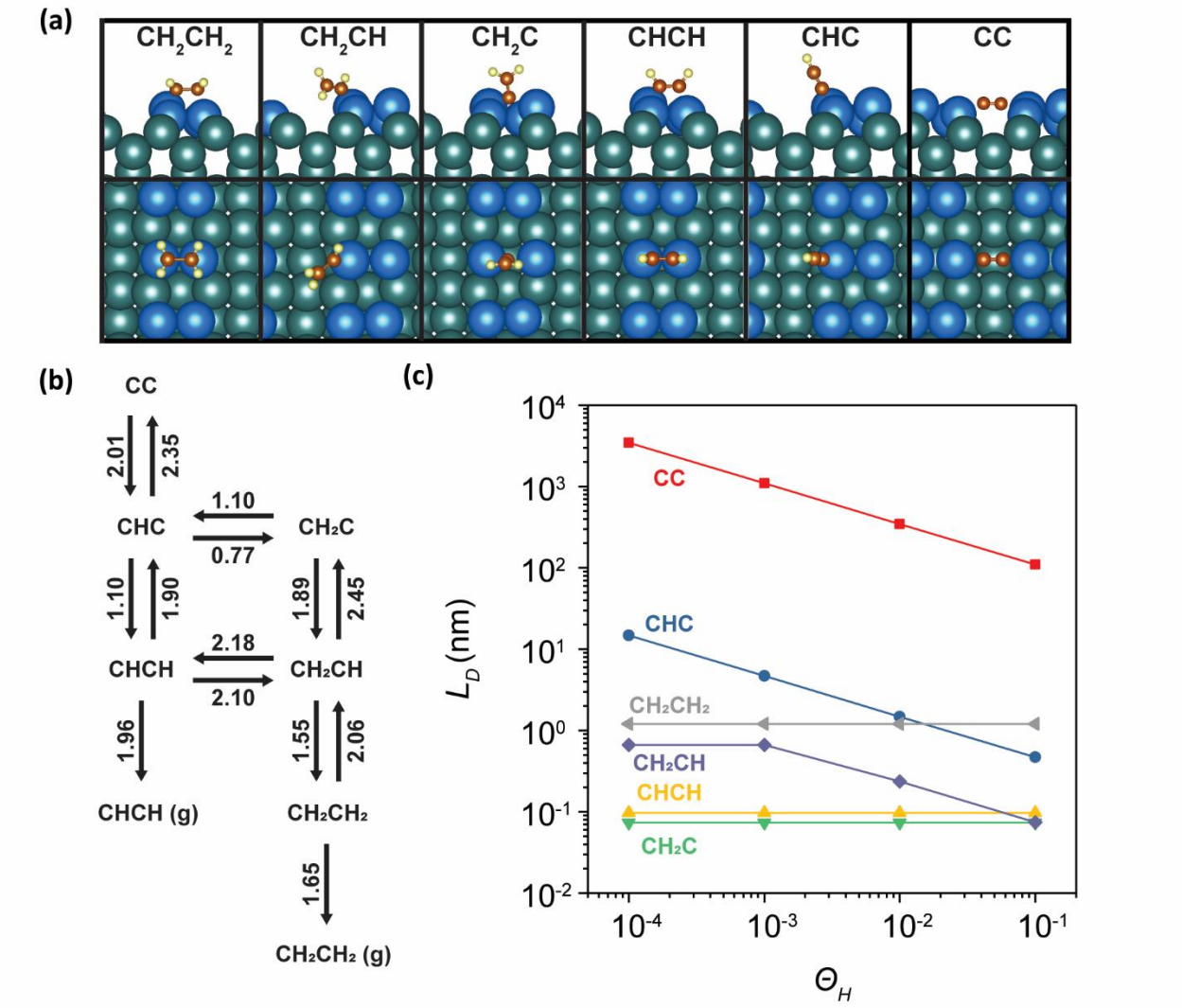

Figure 9.4: (a) Atomistic picture of the different C_2H_x species on the Ge(001) surface. C atoms are shown in brown, H atoms in yellow, and Ge atoms in green (bulk) or blue (under-coordinated dimers). **(b)** Reaction network for the interconversion and desorption of C_2H_x species. Values for the activation energies for forward and backward reactions are given in eV. **(c)** H-coverage, Θ_H, dependent values of the average diffusion length L_D for the different C_2H_x species.

The lifetimes of the different species will be closely connected to the reaction network describing the interconversion of the different species on the Ge(001) surface. To reduce the computational effort, we assume that dehydrogenation/hydrogenation and desorption reactions are fast compared to C-C bond breaking and forming reactions. We therefore focus on calculating the reaction network for the interconversion of C_2H_x species, where $0 \leq x \leq 4$, and desorption of CHCH

and CH_2CH_2. Similar to the diffusion calculations above, we rely on static DFT calculations and the nudged elastic band method to calculate activation barriers for the entire reaction network, and results are shown in Fig. 9.4b. This network implies that most species can undergo different reactions, and the diffusion of several species will need to be considered to calculate an average lifetime for each respective species on the Ge(001) surface. Accounting for all the possible reactions is complicated and will require the construction of an explicit kinetic Monte Carlo model, which goes beyond the scope of this work. Therefore, we assume that one surface species will be the dominant growth species. Consequently, we only calculate an upper bound for the characteristic lifetime, τ, of this dominant growth species as the lowest value of all the inverse reaction rates. Additionally, hydrogenation reactions will rely on the H coverage on the Ge(001) surface, which is not known. We therefore explore different H coverage values between 0.1 and 0.0001. The corresponding lifetimes of all intermediates are shown in Table I.2 and Fig. I.4.

Next, we combine the information for the diffusion barriers and lifetimes to estimate the average diffusion length, L_D, for each of the hydrocarbon intermediate species. L_D will depend on the diffusion constant, D, and the characteristic lifetime, τ, of each species. Additionally, we assume that L_D results from a random walk of the growth species, which leads to $L_D = \sqrt{D\tau}$. To focus the discussion, we only include the lowest diffusion barrier (*i.e.*, largest D) of each species and assume that only one species can contribute to ribbon growth. We plot the diffusion length values for the different species at different H coverages in Fig. 9.4c. We find that only one C_2H_x species has an L_D above the nanoribbon pitch, L_P, namely CC (3460 to 109 nm). The rest of the C_2H_x species have an L_D below L_P with CHC (15 to 0.5 nm) and CH_2CH_2 (1.2 nm) being within two orders of magnitude of L_P. All other potential growth species have L_D values at least two orders

of magnitude smaller than L_P.

To correlate the calculated L_D parameters to the observed width growth rate, R_w, and explicitly account for crowding effects, we develop a transport model. Two extreme cases are considered, in which (a) the nanoribbon growth kinetics are limited only by diffusion of hydrocarbon intermediates to ribbon edges (and not by attachment), and therefore, the concentration of growth species is the decisive factor, and (b) the nanoribbon growth kinetics are limited only by attachment of hydrocarbon intermediates to the ribbon edges (and not by diffusion). In scenario (a), R_w between long, parallel nanoribbons should decay as:

$$R_w = R_{w,\infty} \frac{1 - e^{-L_P/L_D}}{1 + e^{-L_P/L_D}} \tag{9.1}$$

where L_P is the nanoribbon pitch, L_D is the hydrocarbon intermediate diffusion length, and $R_{w,\infty}$ is the growth rate in the width direction without crowding effects (*i.e.*, L_P is large). A detailed derivation of this formula and schematic of the physical setup is given in Appendix I and Fig. I.2. This mathematical correlation indicates that R_w will begin to decrease due to crowding effects when L_P is reduced to several times L_D (for example decreasing by 20% when $L_P = 2.2L_D$). In contrast, in scenario (b), R_w depends only on the attachment barrier and does not vary with L_P.

Under the assumption that growth is purely diffusion-limited (*i.e.*, scenario (a) from above), it is now possible to use the DFT calculated L_D values and study their impact on the observed R_w. In particular, when using calculated L_D values in equation (1) (L_P = 50 nm), we find that if the growth species is CC (L_D = 109 nm, at minimum as seen in Fig. 9.4c), CHC (L_D = 15 nm, at maximum as seen in Fig. 9.4c) or CH_2CH_2 (L_D = 1.2 nm, as seen in Fig. 9.4c), the width growth rate should decline by ~78% (for CC), ~7% (for CHC), or ~0% (for CH_2CH_2). A decrease

is not observed in the experimental measurements (Fig. 9.3b). Thus, the growth kinetics are either strongly attachment-limited, or the growth is diffusion-limited with a growth species with an L_D significantly smaller than L_P (*i.e.*, essentially every growth species other than CC for L_p of 50 nm used in this study). Based on this work, it is not possible to distinguish between these two scenarios, and answering this question will require a rigorous study of the kinetics of precursor formation and graphene growth. Nonetheless, provided that the growth species is not CC or CHC, these results indicate that nanoribbons can be grown to pitches of less than 5 nm without significant perturbation of the growth kinetics, regardless of whether growth is attachment or diffusion limited. If growth is predominately limited by attachment, these results indicate that sub-5 nm pitches are possible regardless of the growth species. This study therefore provides a theoretical upper limit of nanoribbon pitch, assisting integration of nanoribbon arrays into semiconductor electronics.

9.3 Conclusions

We have investigated the possibility of growing graphene nanoribbons on Ge(001) from sub-5nm seeds. Sub-5 nm seeds of graphene are obtained from lithographically patterned seeds of graphene that are ≥ 20 nm in diameter via controlled etching. Subsequently, the viability of initiating nanoribbon synthesis from sub-5 nm seeds is investigated, and periodic arrays of narrow (w ≤ 10 nm) and long (l ≈ 200 nm) graphene nanoribbons on Ge(001) are synthesized using lithographically defined seeds to control alignment and placement. We find that even if the spacing between nanoribbons in the array is reduced to 50 nm, growth kinetics and shape evolution are unperturbed. In combination with density functional theory calculations, this result indicates that graphene ribbon growth is either correlated to a growth species with a diffusion length significantly

below 10 nm or is strongly attachment-limited. Through the results of future modeling, the limits of ribbon spacing can be further explored and exploited. Another challenge moving forward will be controlling the size monodispersity of the seeds before and after etching so that more monodisperse nanoribbons can be obtained. Despite these remaining challenges, this work clearly demonstrates that seed-initiated synthesis of tightly spaced graphene nanoribbons on Ge(001) is a promising route for creating arrays of armchair graphene nanoribbons, with possible applications in semiconductor electronics.

Chapter 10: Characterizing How Graphene Nanoribbons Interact with Ge(001) Through First-Principles Calculations and Monte Carlo Simulations

10.1 Introduction

For the past five decades, silicon has reigned as the dominant material in microelectronics because it is highly abundant and utilizes well-established processing routes. However, as microelectronics become smaller and more sophisticated, silicon-based technologies have begun to reach their fundamental physical limits, and there is a growing push towards utilizing alternative materials with high charge carrier mobility and the potential for further miniaturization. One such material that is currently under consideration is graphene, which exhibits excellent charge and thermal conduction.[62–65] However, extended graphene sheets are semi-metallic and contain no band gap, making them unsuitable for applications in semi-conductor logic. Reducing the width of a graphene sheet to form graphene nanoribbons (GNRs) leads to a band gap within the material,[66] allowing GNRs to be utilized in semiconductor logic, photonics, and sensing applications.[67–69] GNRs with armchair edges have been predicted to have the largest band gaps,[70,71] and a technologically-relevant band gap can be induced in GNRs when they have smooth, armchair edges and are restricted to 10 nm or less in width.[72,73]

A promising bottom-up approach for producing narrow GNRs with armchair edges was discovered by Jacobberger et al., who found that chemical vapor deposition (CVD) of methane and hydrogen on Ge(001) causes GNRs to grow on the Ge surface.[72] This technique produces high-aspect ratio GNRs with smooth armchair edges and widths below 5nm.[74] Furthermore, ribbons

produced using this method have more promising charge transport properties compared to others in the literature, with an on/off conductance ratio of up to 2×10^4 and an on-state conductance of 5 μS.[75] However, these GNRs: (i) grow in random locations on the Ge(001) surface, (ii) are polydisperse due to varying nucleation times during the growth process, and (iii) grow in both Ge⟨110⟩ directions, meaning that the obtained GNRs are rotated 90° from each other.[72,76] Furthermore, some of the graphene crystals that are produced are mis-aligned from the Ge⟨110⟩ directions by 15° and form undesirable, low-aspect ratio graphene crystals.[11,15] These properties limit the application of this method in semiconductor electronics applications, which require arrays of monodispersed, parallelly aligned, and equally spaced GNRs.

Way et al. suggested that these limitations can be overcome by seeding graphene to produce ordered arrays of GNRs at variable pitches (i.e., distances) on Ge(001).[258,259] They demonstrated that using seeds allows for control of (i) the locations of the GNRs, (ii) the orientations of the GNRs, and (iii) the length and width dispersity of the GNRs (because all of the nanoribbons start to grow at the same time). In further work, Way et al. studied the impact of seed size on GNR growth. They estimated that seeds larger than ~18 nm in diameter do not rotate, causing aligned seeds to grow GNRs and mis-aligned seeds to grow low-aspect ratio graphene crystals. Seeds smaller than 18 nm in diameter, on the other hand, can rotate and grow GNRs aligned with Ge⟨110⟩ when annealed at 910 °C.[260] These results indicate that using seeds is a crucial step towards making GNR synthesis on Ge(001) technologically viable, and fundamental insights into seed alignment could help further optimize the synthesis of GNR arrays with desirable properties. However, the driving forces that govern the alignment of seeds on the nano-scale on the Ge(001) surface are still poorly understood.

Because evaluating these nano-scale interactions between GNRs and Ge(001) can be nearly impossible at the growth conditions typically used to grow GNRs, density functional theory (DFT) can provide insights into growth phenomena that are otherwise inaccessible. In the past, Zhang et al. used DFT calculations to evaluate the preferential orientation of graphene crystals on the Cu(111) surface.[261] In their approach, they divided the interactions between graphene and the substrate into two components: (i) the orientation-dependent interactions between the graphene wall (i.e. the bulk of a graphene crystal) and the substrate and (ii) interactions between Cu-passivated graphene edges and the substrate. Using this approach, they found that below diameters of 10-19 nm, interactions between carbon atoms on graphene edges and Cu determine the orientation of graphene crystals, while interactions between the graphene wall and Cu dominate at larger crystal sizes. While the work from Zhang et al. focused on the main contributions to graphene seed orientation on Cu(111), similar insights into graphene crystal alignment on Ge(001) could provide crucial insights into driving forces behind graphene seed alignment on Ge(001) and would help to evaluate the size-dependent rotational barriers for graphene seeds.

Here, we use theoretical modeling to understand the dominant interactions between graphene and the Ge(001) surface. As a first step, we use DFT calculations to understand the preferential orientation of the graphene wall with respect to the Ge(001) surface. Subsequently, we combine DFT calculations with Monte Carlo simulations to analyze the binding of the graphene edge with the underlying substrate. In the end, we combine this information to estimate seed sizes where the graphene-Ge(001) interactions are dominated by interactions with the graphene wall or the graphene edge and give estimates for size-dependent rotational barriers of graphene seeds.

10.2 Methods

All DFT calculations are performed using the Vienna *Ab Initio* Simulation Package (VASP),[81,82] a plane-wave code that utilizes periodic boundary conditions and PAW psuedopotentials.[120] Exchange correlation interactions are modeled using the generalized gradient approximation (GGA) utilizing the Perdew, Burk, and Ernzerhof (PBE) functional,[79] and van der Waals forces are modeled with DFT-D2 dispersion corrections.[257] Electron wave functions are expanded using a plane-wave basis set and a kinetic energy cutoff of 400 eV. The surface of the Brillouin zone is sampled using a 4 x 4 x 1 Monkhorst-Pack k-point mesh.[122]

We perform calculations using a slab model that consists of a (4 x 4) supercell containing 8 Ge layers where the bottom 4 layers are fixed at the bulk Ge lattice constant and the bottom layer is terminated with hydrogen. The bulk lattice constant of Ge is set as 6.04 Å to eliminate strain along graphene in the armchair direction of the unit cell (graphene has a calculated bulk C-C bond length of 1.42 Å). This approach has been utilized in previous work[262] to prevent unphysical corrugation along the length of GNRs. We model the Ge(001) surface with a 2x1 dimer reconstruction, which is found experimentally under GNRs grown on Ge(001)[72] and is a thermodynamically favorable and common surface reconstruction[263] (see Fig. 10.1a)). The primitive unit cell for this surface is a 4.28 Å by 8.55 Å rectangle. Periodic images in the z direction are separated by at least 14 Å of vacuum. The energies of edge structures were calculated using the grand potential (Ω) of each ribbon structure. The grand potential (Ω) is defined as:

$$\Omega = (E_{slab+ribbon} - E_{slab} - N_H * \mu_H - N_C * \mu_C)/l \qquad (10.1)$$

where $E_{slab+ribbon}$ is the total energy of the Ge slab with adsorbed ribbon, E_{slab} is the total energy of the clean Ge slab, N_H is the total number of H atoms in the ribbon, μ_H is the chemical potential of an H atom, N_C is the total number of C atoms in the ribbon, and μ_C is the chemical potential of a

C atom, and l is the length of the ribbon within a unit cell. We relate the chemical potentials μ_H and μ_C to the chemical potentials of CH_4 and H_2 in the gas phase by assuming that the following reactions are at equilibrium: $H_2(g) \leftrightarrow 2H^*$ and $CH_4(g) \leftrightarrow C^* + 4H^*$ (* signifies an adsorbed species on the Ge surface). Therefore, we can relate μ_H and μ_C in the GNR to μ_{H_2} and μ_{CH_4} by $\mu_H = \frac{1}{2}\mu_{H_2}$ and $\mu_C = \mu_{CH_4} - 2\mu_{H_2}$, respectively. The chemical potential of species j, where j = CH_4 or H_2, is calculated as:

$$\mu_j = k_B * T * ln\left(\frac{P_j}{P_o}\right) + E_j + E_{ZPE} + H_j - H_{jo} - T * S_j \quad (10.2)$$

where k_B is the Boltzmann constant, T is the temperature, P_j is the partial pressure of species j, P_o is the reference pressure of 1 atm, E_j is the electronic energy of species j in the gas phase determined by DFT, E_{ZPE} is the zero point energy, H_j is the enthalpy of species j in the gas phase referenced at standard conditions, H_{jo} is the enthalpy at 0K as reported in the NIST JANAF tables referenced at standard conditions,[264] and S_j is the entropy of species j in the gas phase. In this work, we use data from NIST to calculate the thermochemical data of all species.[264]

10.3 Results and Discussion

10.3.1 Modeling the Graphene Wall

Constructing a model: As a first step, we focus on quantifying the interactions between the graphene wall (i.e. the bulk of a graphene sheet) and the Ge(001) surface. We are primarily interested how these interactions control the preferred orientation of the graphene lattice with respect to the Ge(001) surface. In our model, we use periodic boundary conditions for graphene and Ge. These periodic boundary conditions require matching unit cell sizes for graphene and the substrate, and only specific orientations of graphene satisfy this constraint while remaining

computationally accessible. Our aim is therefore to identify rectangular graphene unit cells that fit within multiples of the primitive Ge(001) unit cells. Representative images of the Ge(001) surface and the primitive Ge(001) surface unit cell are shown in Fig. 10.1a.

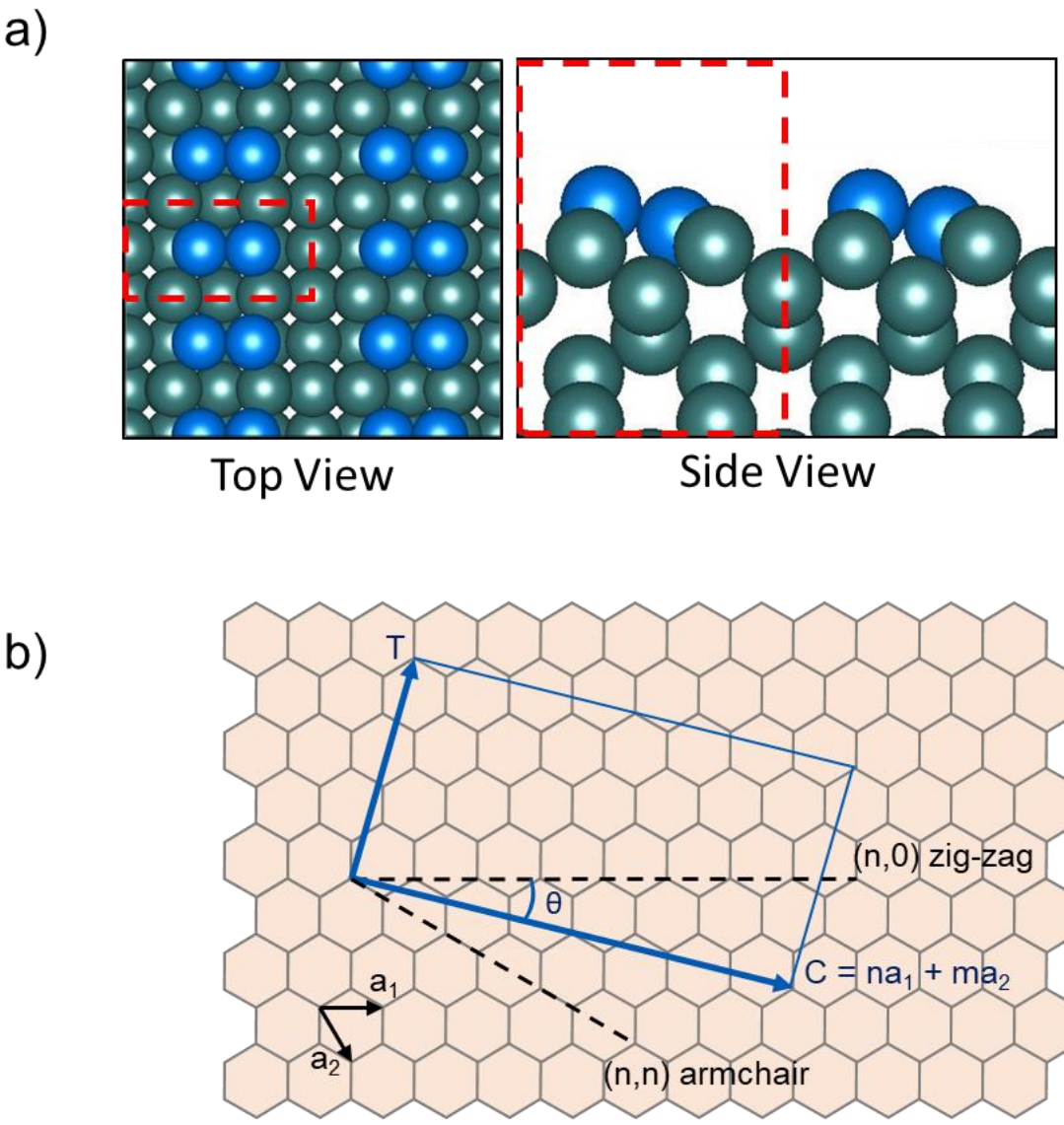

Figure 10.1: (a) Top and side views of Ge(001) surface with 2 ×1 buckled dimer surface reconstruction. The primitive Ge(001) unit cell is shown with a dashed red box. Ge dimer atoms are shown in blue and Ge bulk atoms are shown in green. **(b)** Schematic of graphene unit cell. In this schematic, a_1 and a_2 are the unit vectors for graphene, C is the chiral vector of the graphene sheet, and T is the translational vector of the graphene sheet. The chiral vector is defined by n and m, where the zig-zag direction is defined by the coordinates (n, m=0) and the armchair direction is defined by (n, m=n). The chiral angle θ indicates the angle between the chiral angle and the zig-zag edge.

We calculate the length, L, (equation 3) and width, W, (equation 4) of a rectangular graphene sheet as[265]:

$$L = |\bar{C}| = a\sqrt{n^2 + m^2 + nm} \tag{10.3}$$

and

$$W = |\bar{T}| = \frac{\sqrt{3}L}{d_R} \tag{10.4}$$

where a is the graphene lattice constant (calculated to be 2.49 Å), n and m are integer multipliers of the graphene lattice vectors that describe the orientation of the graphene sheet (see Fig. 10.1b), and d_R is the greatest common devisor of 2n+m and 2m+n. The angle between the zig-zag direction of the graphene sheet with respect to the Ge$[110]$ or Ge$[\bar{1}10]$ direction can then be expressed as[265]:

$$\theta = \tan^{-1}\left(\frac{\sqrt{3}}{2n+m}\right) \tag{10.5}$$

The hexagonal symmetry of graphene furthermore implies that all potential orientations can be described by graphene orientations with θ between 0˚and 30˚.

Using these relations, we then identify values of n and m where: (i) L and W are multiples of the length and width of the Ge(001) primitive unit cell, within a 5% error, (ii) the resulting graphene unit cell is small enough to be described with DFT (i.e., less than ~1500 atoms/unit cell for graphene and Ge(001) surface), and (iii) there is a range of rotation values for θ between 0 and 30˚with respect to the dimer rows on the surface. Based on these criteria, we select (n,m) = (1,0), (10,1), (11,2), and (3,1), which correspond to rotation angles of 0˚(Fig. 10.2a) & 30˚(Fig. 10.2b),

25˚ (Fig. 10.2c) & 5˚ (Fig. 10.2d), 8˚ (Fig. 10.2e) & 22˚ (Fig. 10.2f), and 16˚ (Fig. 10.2g) & 14˚ (Fig. 10.2h), respectively, between the armchair direction of graphene and the dimer rows on the Ge(001) surface. For the data point at 16˚, the converged structure contains a graphene sheet that is unphysically corrugated and has a positive binding energy; therefore, this structure was omitted in further analyses.

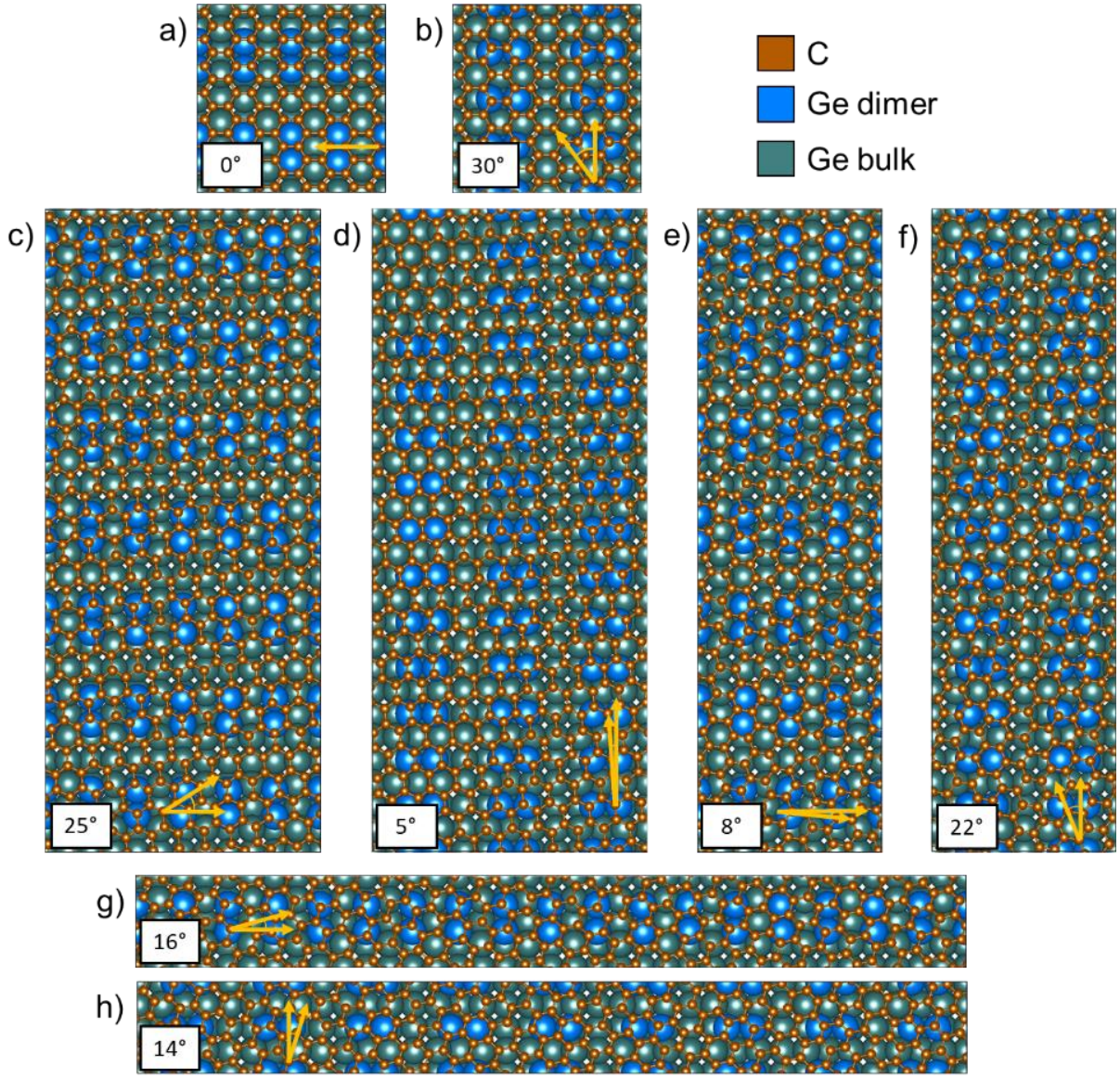

Figure 10.2: Unit cells for analyzing interactions between Ge(001) and graphene wall. The angle between the armchair direction of the graphene sheet and the dimer rows of the surface are **(a)** 0˚, **(b)** 30˚, **(c)** 25˚, **(d)** 5˚, **(e)** 8˚, **(f)** 22˚, **(g)** 16˚, and **(h)** 14˚. Yellow arrows in a) and b) indicate the angle between the armchair direction and the dimer rows. C atoms are shown in brown, Ge surface dimer atoms are shown in blue, and Ge bulk atoms are shown in green.

How the graphene wall interacts with Ge(001): To quantify the interaction strength between bulk graphene and the surface, we calculate the binding energy of the graphene sheet per wall C atom (BE/C), defined as:

$$BE/C = (E_{slab+graphene} - E_{slab} - E_{graphene})/N_C \quad (10.6)$$

where $E_{slab+graphene}$ is the total energy of the Ge slab with graphene adsorbed, E_{slab} is the total energy of the clean surface, $E_{graphene}$ is the total energy of isolated graphene, and N_C is the number of carbon atoms in the unit cell. Representative images of the graphene sheet adsorbed on the Ge(001) surface are shown in Fig. 10.3a (side view) and Fig. 10.3b (top view). The binding energies and average distances between the graphene sheet and the surface are shown in Fig. 10.3c.

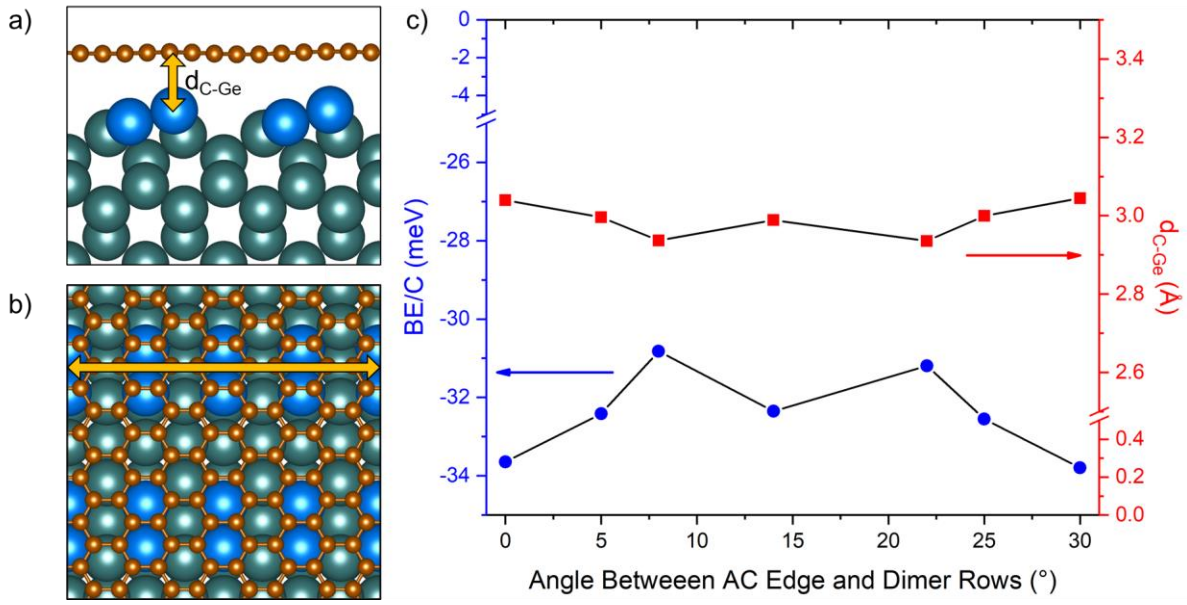

Figure 10.3: (a) Side view of Ge(001) with graphene layer adsorbed on top. The distance between graphene and the upper Ge atom in the buckled dimer is marked as d_{C-Ge}. **(b)** Top view of Ge(001) with a graphene layer adsorbed on top. The direction of the dimer rows is indicated with a yellow arrow. In this figure, the armchair direction of the graphene sheet is oriented 0˚ from the dimer rows. **(c)** Binding energy per wall C atom (BE/C, shown with blue circles) and distance between the surface and graphene (d_{C-Ge}, shown with red squares) as a function of the angle between the armchair (AC) direction of the graphene sheet and the dimer rows on the Ge(001) surface. C atoms are shown in brown, Ge surface dimer atoms are shown in blue, and Ge bulk atoms are shown in green.

In Fig. 10.3c, we see that the minimum energy states for the graphene wall interacting with the surface are when the armchair edge is rotated 0˚ or 30˚ from the dimer rows. These angles correspond to the armchair direction of graphene being aligned along the Ge⟨110⟩ directions of a Ge(001) surface, which is the same way GNRs grown on Ge(001) orient themselves. At these conditions, the distance between graphene and the closest Ge atom is 3.04 Å and graphene binds with an energy of -34 meV/C to the surface. Additionally, we find that there is a local energy minimum when the armchair direction is rotated 14˚from the dimer rows, which could lead to mis-aligned graphene if graphene seeds or crystals cannot overcome the barrier needed to rotate to a more favorable state. Indeed, experimental results show that for unseeded growth, a small portion of graphene crystals grown on Ge(001) are low aspect ratio, non-ribbon crystals where the AC direction of the crystals is rotated 15˚from the Ge⟨110⟩ directions.[72] We discuss the role of wall interactions in contributing to rotation barriers further in the Section 10.3.3.

10.3.2 Modeling the Graphene Edge

Constructing a model: The relative amount of H- or Ge-passivated edges on a graphene seed or GNR plays a critical role in how strongly graphene binds to Ge surfaces. In previous work, we demonstrated that on vicinal Ge(001) surfaces, GNR growth rates and orientations are controlled by whether graphene edges are largely passivated by H or Ge.[262] More specifically, we found that one long edge of each ribbon is largely passivated by Ge at a step edge of the vicinal Ge(001) surface, anchoring this edge to the surface and causing this edge to grow slowly. Conversely, the other three edges of the GNRs are passivated by a larger proportion of H and grow at faster rates than the edge anchored to the Ge step edge. Starting with this study as our inspiration, we create DFT models of the graphene edges with various edge structures containing H- and Ge-passivated sites along the graphene edge to model edge passivation on a Ge(001) terrace.

To model the graphene edge, we optimize the structures of fully H-passivated armchair and zig-zag nanoribbons that run both parallel and perpendicular to dimer rows on the Ge(001) surface (i.e., along the Ge⟨110⟩ directions of the Ge(001) surface). We note that the analyses in this paper focus on armchair nanoribbons because they are relevant experimentally, but we provide data for zig-zag ribbons and briefly comment on trends in our calculations for comparison. Unit cells for armchair ribbons are shown in Fig. 10.4, and the unit cells for zig-zag ribbons are shown in Fig. J.1. We select N = 13 armchair GNRs (where N is the number of C atoms along the zig-zag chain that spans the ribbon width) and N=16 zig-zag GNRs (where N is the number of C atoms along the armchair chain that spans the ribbon width) so that the ribbons are wide enough to sufficiently model both the edge and the wall of graphene. After we optimize each structure, we constrain the atoms on one side of the nanoribbon to represent the bulk of a graphene crystal so that the opposite edge of the ribbon is in an optimal position to interact with Ge(001) on the surface. This allows us to maximize the potential interactions between the GNR edges and Ge atoms on the surface.

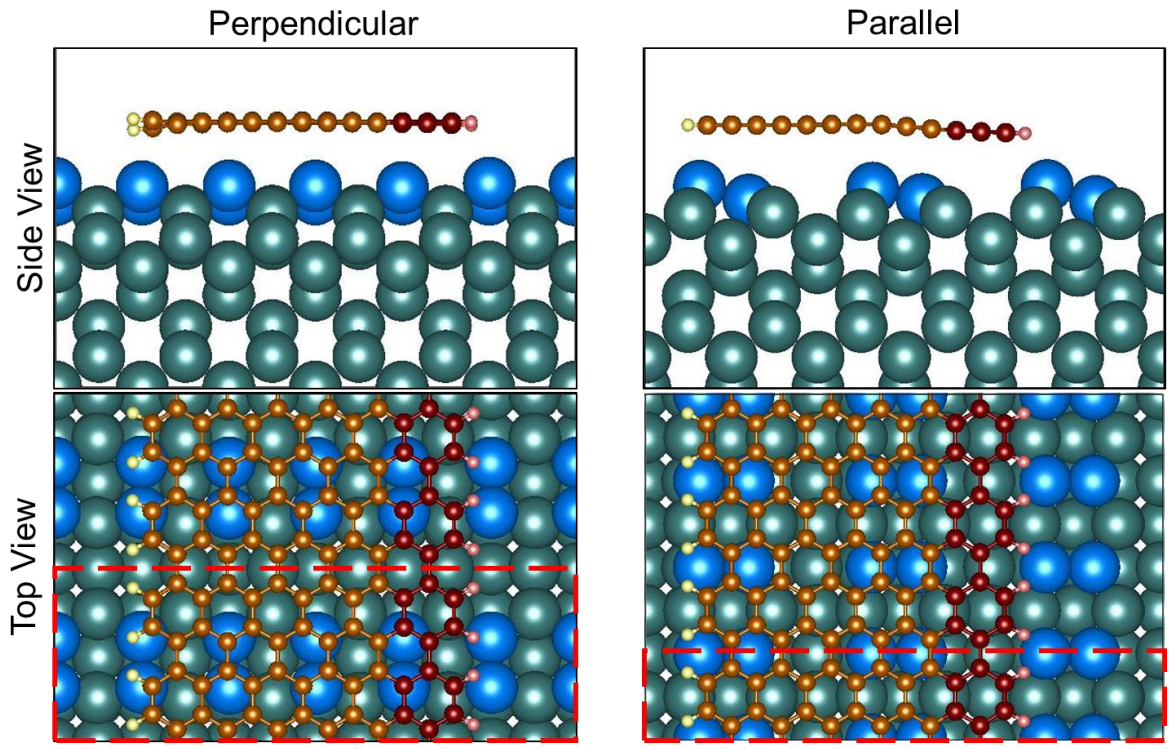

Figure 10.4: Top and side views of armchair GNRs on the Ge(001) surfaces. The nanoribbons are aligned perpendicular and parallel to buckled-dimer rows of Ge atoms on the surface. Red boxes indicate the smallest repeating unit of graphene along the edge. Relaxed C atoms are shown in brown, fixed C atoms are shown in dark red, relaxed H atoms are shown in yellow, fixed H atoms are shown in pink, Ge surface dimer atoms are shown in blue, and Ge bulk atoms are shown in green. Fixed portions of the GNRs are representative of the wall (bulk) of graphene.

By looking at the armchair structures in Fig. 10.4, we can see that the edge structures form periodic units consisting of either two (parallel alignment) or four (perpendicular alignment) edge C atoms, which are outlined with dashed red boxes. For zig-zag edges, these periodic edge units contain seven edge atoms for both alignments (Fig. J.1). These units serve as the basis for our edge model. In our initial optimization, all edge C atoms are passivated with H atoms. However, edge C atoms can also form bonds with the Ge. We therefore systematically remove H to allow the edge C atoms to bond to Ge and re-optimize the edge structure for every possible combination of H- and Ge-passivated edge C atoms. All possible combinations for armchair edges running parallel and perpendicular to the dimer rows are shown in Fig. 10.5, and the energies of all possible edge structures for armchair edges (Tables J.1 and J.2 for parallel and perpendicular edges, respectively)

and zigzag edges (Tables J.3 and J.4 for parallel and perpendicular edges, respectively) are tabulated in Appendix J, Section J.2.

Armchair edges aligned parallel to the dimer rows consist of repeating edge units containing two binding sites where H or Ge can bond at the edge. Therefore, there are three possible edge motifs that are possible for this unit: (i) These sites can both be bound to an H atom, (ii) one site can be bound to one H atom and the other to one Ge atom (swapping the binding sites is symmetrically equivalent in this case), or (iii) both sites can be bound to Ge atoms. For armchair edges aligned perpendicular to dimer rows, each edge unit contains four distinct binding sites due to the orientation of the edge relative to buckled Ge dimers on the surface; in total, there are sixteen distinct edge motifs for the perpendicular edge. Due to the differences in stoichiometry, we cannot directly compare the DFT energies of edge structures; however, we can compare the relative energies of isomeric perpendicular motifs (Fig. 10.5). Overall, we find that removing H from either of the two binding sites directly above the Ge dimer is energetically most favorable.

For zig-zag edges running both parallel and perpendicular to dimer rows, each graphene edge unit contains seven distinct binding sites, and edge units are made up of a full unit cell (Fig. J.1). In total, there are 128 different combinations of H- and Ge- passivated edge C atoms per unit cell for the perpendicular edge. All of the possible edge structures are tabulated in Table J.3 and J.4 for parallel and perpendicular zig-zag ribbons, respectively.

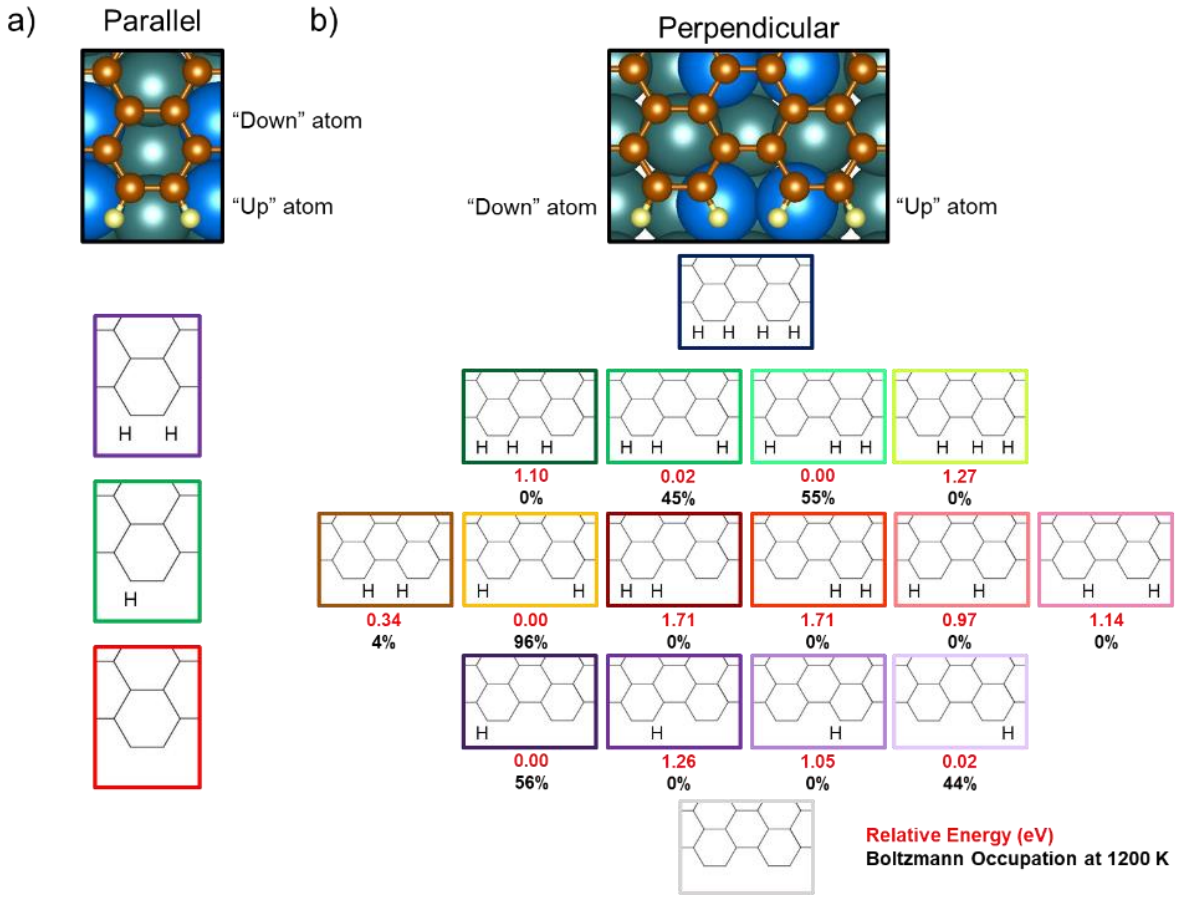

Figure 10.5: Possible edge unit structures for armchair edges running **(a)** parallel and **(b)** perpendicular to the buckled dimer rows on the Ge(001) surface. For perpendicular edges with a mixture of H- and Ge-passivated sites, we report the energies relative to the minimum energy isomer and the corresponding Boltzmann occupation at 1200 K, the temperature at which GNRs are typically grown.[11] C atoms are shown in brown, H atoms are shown in yellow, Ge surface dimer atoms are shown in blue, and Ge bulk atoms are shown in green. "Up" atom and "Down" atom indicate the relative position of atoms in the Ge buckled dimer.

Given that these edge units have varying ratios of H- to Ge-passivated sites (and that armchair and zig-zag edges have different numbers of C atoms per unit cell), we cannot directly compare all of the edge motifs to one another to determine the most energetically favorable edge structure. Depending on the temperature and partial pressure of growth precursors CH_4 and H_2, we expect different combinations of these graphene edge structures to be present on growing graphene crystals. Previous studies from Li at al. have shown that Monte Carlo simulations are a useful tool to model the structure of graphene edges that are grown using CVD of methane on Cu(111).[241]

Therefore, we use the DFT-calculated energies of these edge structures on Ge(001) as an input in a Monte Carlo algorithm to evaluate the energetics and structures of an extended graphene edge.

As a first step towards such a model, we represent the graphene edge as a vector, $\vec{N}$, with N components. The i-th unit has a value n_i, which can vary between one and the number of potential edge configurations of the specific edge. Next, we assign a total energy E^{tot} to the edge vector by calculating:

$$E^{tot} = \sum_{i=1}^{N} \left(E_{n_i} + 0.5E^{int}_{n_i,n_{i-1}} + 0.5E^{int}_{n_i,n_{i+1}} \right) \tag{10.7}$$

where E_{n_i} corresponds to the DFT energies calculated for each edge unit n_i, and $E^{int}_{n_i,n_{i-/+1}}$ is the interaction energy between edge segments n_i and $n_{i-/+1}$. For the first and last units of the edge, we assumed $n_{i-1} = n_N$ for n_1 and that $n_{i+1} = n_1$ for n_N so that the first and last edge units interact with each other. To calculate E_{n_i}, we set $E^{int}_{n_i,n_i} = 0$. In other words, we set the interaction energies for neighboring edge units of the same type to zero. This allows us to use our DFT models to calculate the energy of each edge unit:

$$E_{n_i} = \frac{E^{DFT}_{full}}{k} - \frac{w_{n_i}}{2}\mu_{H_2}(P,T) \tag{10.8}$$

where E^{DFT}_{full} is the DFT energy of the modeled unit cell containing k edge units of type n_i. The second term in equation (8) corrects the energy of the edge segment for the w_{n_i} H atoms adsorbed to the graphene edge with respect to $\mu^{H_2}(P,T)$, the pressure- and temperature-dependent chemical potential of H_2. Subsequently, we calculate:

$$E_{n_i,n_j}^{int} = (E_{full}^{DFT} - m_{n_i}E_{n_i} - m_{n_j}E_{n_j})/k \quad (10.9)$$

where E_{full}^{DFT} is the DFT energy of a unit cell containing m_{n_i} and m_{n_j} numbers of edge units n_i and n_j in the unit cell, and k is again the total number of edge segments in the modeled unit cell. We calculate E_{n_i,n_j}^{int} for all armchair edges running parallel and perpendicular to the Ge(001) dimer rows (numerical values given in Table J.5 and J.6 for parallel and perpendicular edges, respectively).

For zig-zag edges we omit the calculation of the E_{n_i,n_j}^{int} for two reasons. (i) The contribution of E_{n_i,n_j}^{int} to the total edge energy per C atom gets smaller as the edge unit size becomes longer. For the zig-zag edge, an edge segment consists of seven unique edge C atoms and is thus significantly larger than the edge segments of the armchair edges. This implies that the impact of the E_{n_i,n_j}^{int} will be significantly smaller for zig-zag edges than for armchair edges. (ii) When considering all possible H and Ge terminations, seven unique edge C atoms allow for 128 different edge units, which would require a total of 32,768 calculations to calculate all E_{n_i,n_j}^{int} values. Additionally, calculating these interactions requires unit cells that are twice as large as the ones used in this study. The significant computational cost for these of these calculations render them unfeasible.

To calculate the energy of the graphene edges at various conditions, we minimize the total energy of the graphene edge using a Monte Carlo model based on the vector $\vec{N}$ and E^{tot} (shown in Scheme 10.1). First, we initialized $\vec{N}$ with a random guess for the edge structure. In each subsequent trial move, we then changed one n_i and decided whether that trial move was accepted based on the Metropolis-Hastings algorithm. We allowed the system to equilibrate until the total

energy of the edge changed by less than 10^{-2} eV between trial moves and then collected energetic data for 10^8 successful trial moves. Each simulation contains 2000 edge C atoms that could be passivated by H or Ge, and we achieved convergence after at most 10^4 trial moves. We utilize this algorithm to simulate armchair and zig-zag edges aligned parallel and perpendicular to dimer rows as a function of the partial pressure of hydrogen in the gas phase.

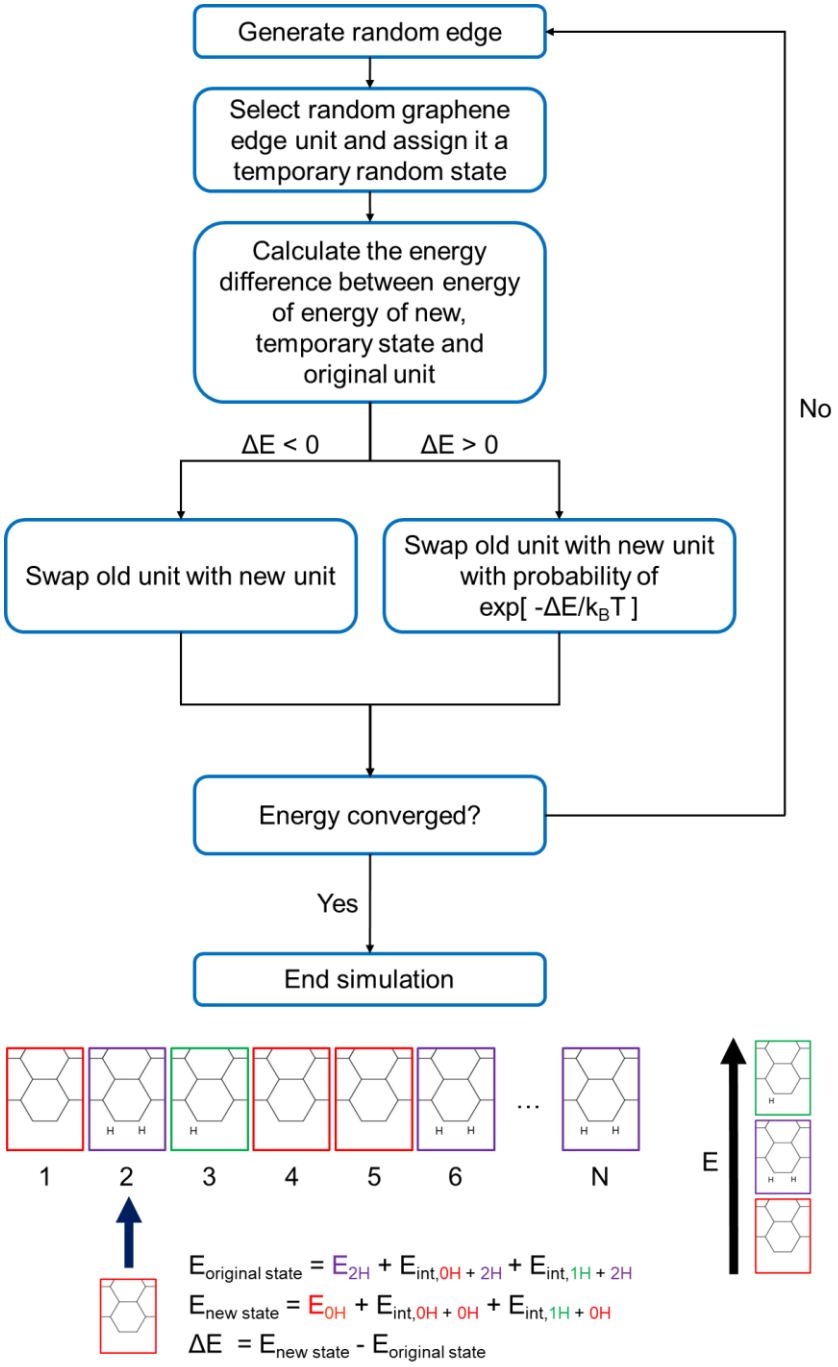

Scheme 10.1: Metropolis Monte Carlo algorithm used to model graphene edges as a function of the chemical potential of H. In the bottom portion of the figure, we show an example edge vector $\vec{N}$ and the relative energy of potential edge units. In the Metropolis algorithm, we randomly select an edge unit (i=2, in this example) and randomly select a new edge unit. We calculate the total energy of the original state and the new state, including interaction energies before calculating ΔE.

How Graphene Edges Interact with Ge(001): In this section, we used the results from our Monte Carlo algorithm to investigate the interactions between the edges of graphene and Ge(001)

by focusing on armchair edges that run parallel and perpendicular to dimer rows on the surface. We also briefly comment on zig-zag edges. As mentioned above, the edges of the ribbons are aligned near Ge atoms on the surface to gauge the maximum Ge passivation at each edge. To keep the discussion tractable, we will focus results for armchair edges in the main text. Results and figures for zig-zag edges are given in Appendix J, Section J.1 and only the main conclusions will be mentioned in the main text.

First, we analyze the hydrogen coverage (i.e. the percentage of an edge passivated by hydrogen) of the different edge structures as a function of H_2 gas pressure and temperature. The H coverage for armchair edges running perpendicular and parallel to the surface at different conditions is shown in Fig. 10.6a. Corresponding figures for zig-zag edges can be found in Fig. J.2a. We begin our analysis by discussing the results for armchair edges. At large hydrogen partial pressures, edges running both perpendicular and parallel to dimer rows have edges where the majority of sites are passivated by hydrogen. Parallel edges in particular are essentially passivated entirely by hydrogen at high hydrogen partial pressures. By reducing the hydrogen pressure, the hydrogen coverage decreases on both edges. For perpendicular edges, the hydrogen coverage asymptotically approaches 0.5, meaning that half of the edge sites are bound to H while half are bound to Ge. For every two edge binding sites, there is only one dangling Ge bond on the surface when edges run perpendicular to dimer rows. Thus, we would expect that the hydrogen coverage should never be less than 0.5 for perpendicular edges. For parallel edges, we find that lowering the partial pressure of hydrogen causes the edges to be entirely passivated by Ge. Unlike perpendicular edges, parallel edges are exposed to one dangling Ge bond per edge binding site. Thus, the hydrogen coverage can be reduced far more on parallel edges than perpendicular edges.

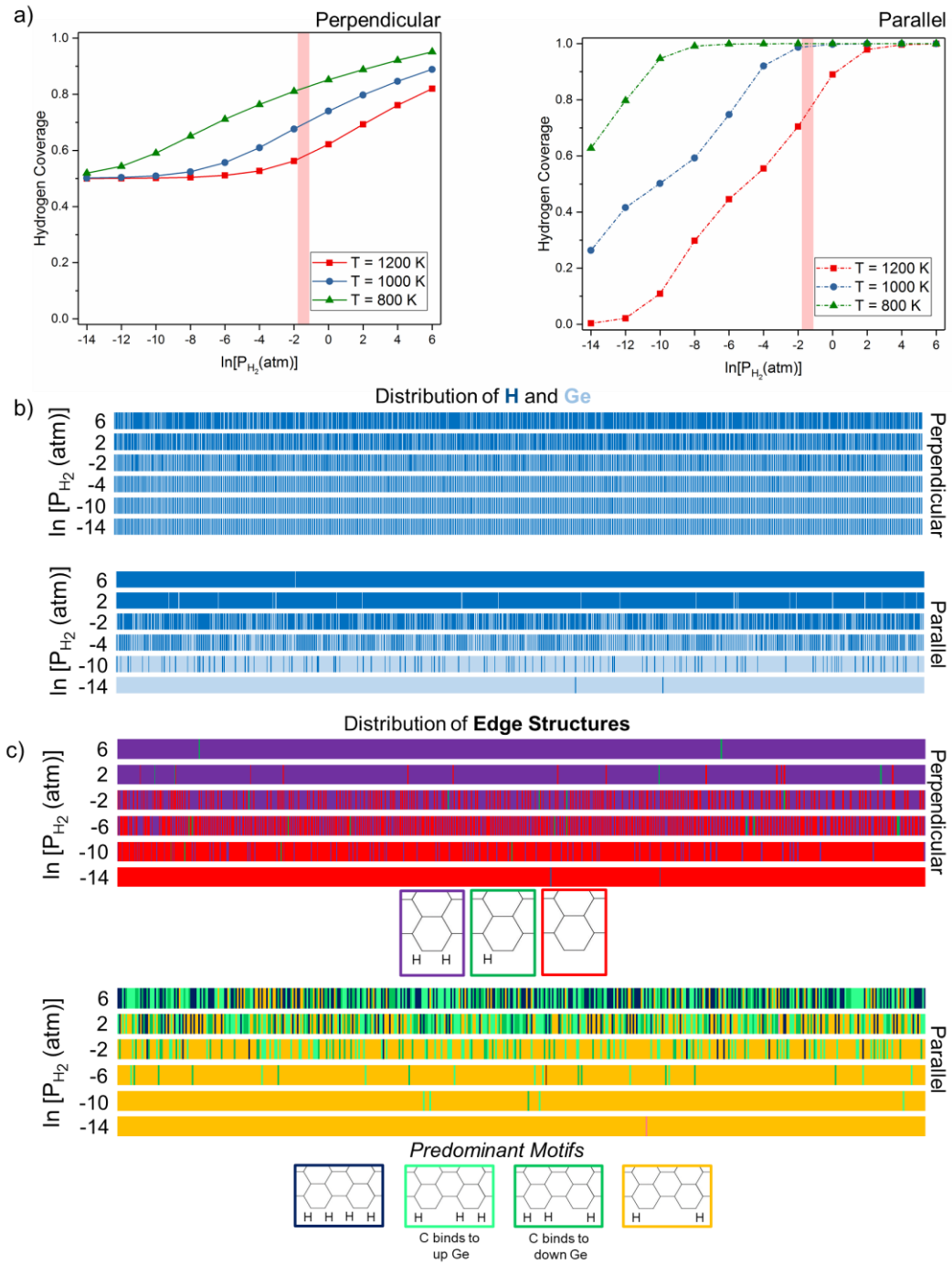

Figure 10.6: (a) Hydrogen coverage on perpendicular and parallel armchair edges as a function of gas-phase hydrogen pressure and temperature. The red bar indicates typical growth conditions for GNRs. **(b)** The distribution of H or Ge passivated sites of edge vector $\vec{N}$ for perpendicular and parallel armchair edges at T = 1200 K for several H_2 pressures. H passivated sites are in dark blue and Ge passivated sites are in light blue. **(c)** The distribution of edge unit structures of edge vector $\vec{N}$ for perpendicular and parallel armchair edges at T =1200 K for several H_2 pressures. Colors in **(c)** correspond to color code in Fig. 10.5, and most prevalent edge structures for perpendicular edges are shown as "predominant motifs".

Additionally, we analyze the effect of interaction energies on determining the coverage of H on perpendicular and parallel armchair edges. We show the coverage of H with and without interaction energies for armchair edges running perpendicular and parallel to Ge dimer rows in Fig. J.3. For perpendicular edges (which have edge units containing four edge C atoms), including interaction energies has little effect on the H coverage. However, removing interaction energies for parallel edges (which have edge units containing two edge C atoms) causes armchair edges to be fully passivated by H at lower P_{H_2} values. This is because there is an energetically favorable interaction energy between an edge unit passivated by two H atoms and an edge unit passivated by two Ge atoms. Because there are only three possible arrangements of H and Ge passivated sites, including this favorable interaction energy increases the odds that parallel edge sites are passivated by Ge. Additionally, these results show that interaction energies are more important for edge unit containing small numbers of edge C atoms and help validate our assumption that we do not need to include interaction energies for zig-zag edge units due to their large size.

We can also examine the role of temperature in determining the H coverage of edge sites. By increasing the temperature, a higher fraction of edge sites is passivated by Ge until the maximum asymptotic Ge passivation is reached. Furthermore, we find that at typical GNR growth conditions (P_{H_2} values indicated by a red bar and T ~1200 K), edges perpendicular to dimer rows are ~55% passivated by H, and edges parallel to dimer rows are about 75% passivated by H. We also find that zig-zag edges behave in a manner that is similar to that of armchair edges. Although the edge structures are different, both armchair and zig-zag edges interact with similar ratios of edge binding sites to dangling Ge bonds for parallel and perpendicular edges. Thus, the orientation of the graphene edge relative to surface Ge atoms plays a substantial role in determining the

passivation of the graphene edges.

As a next step in our analysis, we focused on the distribution of H-passivated sites along the edge structures. Fig. 10.6b shows the distribution of H- and Ge-passivated sites along a graphene edge for perpendicular and parallel armchair edges, respectively, at 1200 K and several H_2 partial pressures. The corresponding images for zig-zag edges are shown in Fig. J.2b. For all the cases we have studied, H is homogenously distributed along the edge, and the edges do not contain extended regions of varying H concentrations. Additionally, we examined the most common motifs of edge units that appeared in the Monte Carlo simulation along the graphene edges. Fig. 10.6c shows the distribution edge motif structures along the graphene edge for perpendicular and parallel armchair edges, respectively, at 1200 K at several H_2 partial pressures. For parallel edges, we found that edge units are either passivated with two H or with two Ge, but almost never with one of each. For perpendicular edges we find that H can only be removed from the central two C atoms in each unit (which are directly positioned above the Ge dimer).

These results indicate that two driving forces control the passivation of graphene edge structures: (i) graphene crystals avoid strain caused by bending at the edge, and (ii) graphene binds strongly to Ge. Based on observation (i), edge C atoms that are farther away from Ge atoms on the surface will have higher amounts of hydrogen coverage on their edges, because interacting with Ge will require a significant bending of the graphene bulk. At the same time, edge C atoms that are close to a surface Ge atom will have a lower H coverage, since C forms strong bonds with Ge and only a minor bend of graphene is required to allow for this bonding configuration. Depending on the temperature and partial pressure of H_2, this balance can shift. The results in Fig. 10.6a show that decreasing the amount of available hydrogen or increasing the temperature of the system

makes Ge passivated sites more accessible.

Beyond H coverages, the Monte Carlo algorithm also provides a total energy for armchair and zig-zag edges in specific orientations with respect to the surface. First, we determine how armchair and zig-zag edges prefer to orient themselves with the Ge(001) surface. Fig. J.4 shows the energy difference between being oriented parallel or perpendicular to the dimer rows for both edge structures. For armchair edges, the preferred orientation is parallel at low H_2 pressures, perpendicular at medium H_2 pressures, and parallel at high H_2 pressures. Increasing the temperature shifts the point at which perpendicular edges are preferred to higher H_2 pressures. At typical operating conditions (P_{H_2} values indicated by the red bar and T ~1200 K), armchair edges prefer to align themselves perpendicular to the dimer rows by ~0.06 eV/Å. Although this difference may appear small, it becomes large when considering that GNRs can be hundreds of nanometers long. Zig-zag edges always prefer to be oriented parallel to dimer rows at all conditions studied.

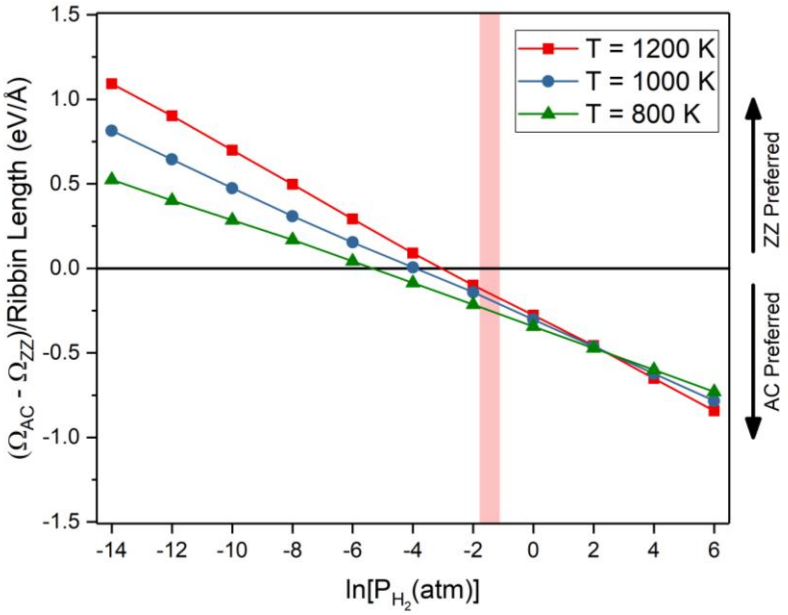

Figure 10.7: Difference in grand potential for armchair (AC) and zig-zag (ZZ) edges as a function of H_2 partial pressure at several temperatures. Typical GNR growth conditions are indicated with a red bar. Grand potentials are calculated using a CH_4 partial pressure of 6.7 x 10^{-3} atm, which is typical for GNR growth conditions.

Next, we compare the energy difference between the lowest energy armchair edges and zig-zag edges as a function of H_2 partial pressure and temperature as shown in Fig. 10.7. At low H_2 partial pressures, zig-zag edges are energetically more stable. As the partial pressure of H_2 increases, the relative energies linearly decrease until armchair edges become more favorable. This transition point between the two edge structures occurs at higher partial pressures of H_2 as temperature increases. Most importantly, we find that at typical GNR growth conditions, armchair edges are more energetically favorable by ~0.15 eV/Å. Again, this is a large difference considering the length of GNRs. These findings explain why GNRs grown on Ge(001) have armchair edges as opposed to zig-zag edges.

10.3.3 When Graphene Wall Interactions Dominate Graphene Edge Interactions

Finally, we combine the above information on bulk graphene interactions and graphene edge interactions to examine which forces control the orientation of graphene crystals.

Understanding the interplay of these forces is particularly important for understanding seeded GNR growth on Ge(001). In experiments that utilize graphene seeds, seeds are annealed in an array on a Ge(001) surface before GNRs are grown from these seeds using CVD of CH_4 and H_2. The orientation of the seeds is directly correlated to the orientation of the GNRs; therefore, controlling the orientation of small graphene islands is crucial for arriving at well-aligned GNRs.[259,260]

Zhang et al. describes a simple method for determining when interactions between the bulk of graphene and the surface or interactions between the edges of the graphene and the surface dominate the orientation of circular graphene seeds.[261] This method uses geometrical correlations to estimate the total binding energy between the graphene bulk and the surface as:

$$E_{GW,Tot} \sim E_{GW} \times N_C \tag{10.10}$$

where $E_{GW,Tot}$ is the total binding energy of the graphene wall with the surface, E_{GW} is the binding energy per carbon atom of the graphene wall, and N_C is the number of carbon atoms in the graphene wall of the graphene seed. Similarly, we can estimate the total binding energy of the edge of graphene with the surface as:

$$E_{GE,Tot} \sim E_{GE} \times N_E \sim E_{GE}\sqrt{6N_C} \tag{10.11}$$

where $E_{GE,Tot}$ is the total binding energy of the graphene edge with the surface, E_{GE} is the binding energy per carbon atom of the graphene edge, and N_E is the number of carbon atoms along the graphene edge. Assuming that the larger energy contribution between $E_{GW,Tot}$ and $E_{GE,Tot}$ will determine graphene orientation, we can then determine the critical graphene size, N_{crit}, above which bulk graphene interactions dominate graphene edge interactions:

$$N_{crit} = 6(E_{GE}/E_{GW})^2 \quad (10.12)$$

In the case of graphene seeds on Ge(001), we calculate E_{GB} as -0.03 eV, and we can estimate E_{GE} as ~-0.26 eV (the binding energy of the most probable edge motif per C edge site for an armchair edge at typical growth conditions minus graphene wall interactions). We find that N_{crit} is about 450 carbon atoms, which corresponds to a graphene seed diameter of ~4 nm. Therefore, we estimate that the orientation of graphene seeds above ~4 nm will be dominated by interactions between the wall of graphene rather than the edge of graphene.

Additionally, we can also estimate the maximum size for which we expect that mis-aligned graphene seeds can rotate. Experimentally, seeds less than ~18 nm in diameter are able to rotate after ~1 hour of annealing so that the armchair direction is aligned with a Ge$\langle 110 \rangle$ direction.[260] We can utilize the binding energy per graphene wall C (BE/C) of seeds that are greater than 4 nm in diameter to estimate the rotational barrier for a graphene seed. We note that the edges of graphene seeds likely form bonds with Ge, so this barrier serves as lower bound for the total rotation barrier. Using the BE/C plot shown in Fig. 10.3c, we estimate the barrier for rotating from the metastable position where the armchair direction is mis-aligned from the direction of the dimer rows by 14º to 0º or 30º. If the seed rotates so the armchair direction rotates from 14º to 0º relative to the dimer rows (i.e. aligned with Ge$[110]$), the barrier is the difference between the BE/C for an 8º mis-alignment and the BE/C for a 14º mis-alignment. Similarly, if the seed rotates so the armchair direction is aligned from 14º to 30º relative to the dimer rows (i.e. aligned with the Ge$[\bar{1}10]$ direction), the barrier is the difference between the BE/C for a 22º mis-alignment and the BE/C for a 14º mis-alignment. For our analysis, we will focus on the lower of the two barriers, which is 1.29 meV/C for rotating from BE/C from 14º to 30º (the reverse barrier for rotating from

30º to 14º is 1.44 meV/C). Using this barrier, we can evaluate how the total rotation barrier changes as size of the seed changes. Additionally, we can calculate the probability, P, of a graphene seed of a given diameter rotating within 1 hour from 14º to 30º as:

$$P = 1 - e^{-\lambda}; where\ \lambda = \frac{k_B T}{h}\ e^{-\frac{E_A(d)}{k_B T}} \tag{13}$$

where λ is the turnover frequency (in hr^{-1}), h is the Planck constant, and $E_A(d)$ is the total rotation barrier for a graphene seed as a function of seed diameter. The probability of seeds rotating within 1 hour and the rotation barrier as a function of seed diameter are shown in Fig. 10.8.

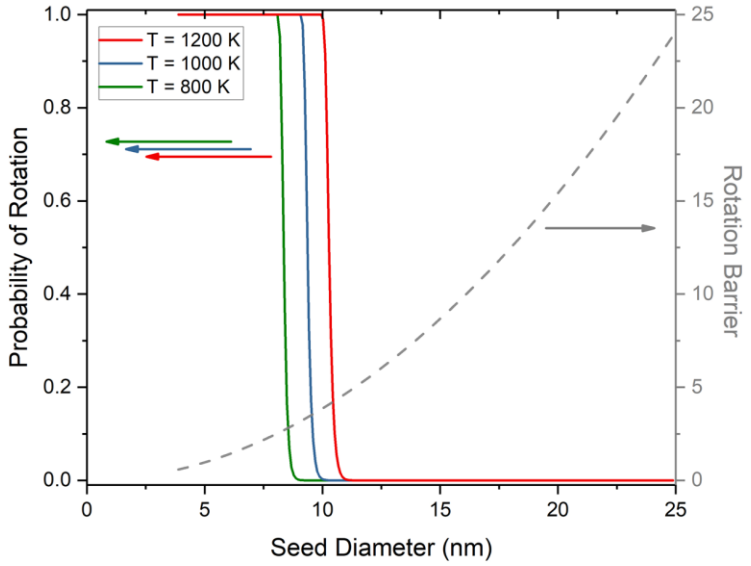

Figure 10.8: The probability of a graphene seed rotating so that the armchair direction is oriented 14º from dimer rows to 30º from dimer rows (left axis) at a range of temperatures. We also show the total rotational barrier from the graphene wall interacting with the Ge(001) surface (right axis).

Overall, we find that the total rotation barrier for a graphene seed rotating from a meta-stable position where the armchair edges are not aligned with the Ge$[\bar{1}10]$ direction to being aligned with Ge$[\bar{1}10]$ scales exponentially with the seed diameter. This leads to the probability of a misaligned seed rotating to decreasing rapidly for seeds around ~10 nm, which we calculate is the maximum size that a graphene seed can rotate at experimental conditions. We note that

experimental results also find a similar step function relating the probability of rotating to the seed diameter.[260] This result is of the same order of magnitude but lower than the estimated experimental value of ~18 nm for the maximum seed diameter for rotation. We note that this mismatch between experiments and theory can arise from in errors calculating van der Waals interactions in our DFT calculations or errors in estimating this maximum diameter from experiments. Regardless, we find a similar relationship between the probability of rotation and seed diameter seen in experiments.

10.4 Conclusions

In this contribution, we used a combination of DFT calculations and Monte Carlo simulations to evaluate the interactions between graphene and Ge(001). Our efforts were focused on two interactions, namely the interactions of the graphene wall and the graphene edges with the Ge(001) surface. We find that the armchair direction of the graphene bulk prefers to be aligned with the ⟨110⟩ directions of the Ge(001) surface. Additionally, we find a local energetic minimum where graphene is rotated by 14° with respect to its preferred orientation. We also studied the relative stability of various graphene edges on Ge(001) and found that they are predominantly passivated by hydrogen under growth conditions. Additionally, we found that armchair edges are energetically favorable when the armchair direction of graphene is oriented along the Ge⟨110⟩ directions. Finally, we used our model to determine the dominant bonding interactions between graphene and Ge(001) and found that for graphene seeds smaller than 4 nm, edge interactions control the orientation of graphene seeds. Above this diameter, bulk interactions determine the preferred orientation.

Our model helps explain several aspects of graphene growth on Ge(001) observed in

experimental measurements. We find that the orientation of GNRs on Ge(001) is mainly determined by the interactions between the graphene wall and the Ge substrate. This leads to a preferential alignment between GNRs and the high symmetry axes of the substrate, but can also result in mis-aligned, low-aspect crystals, which correspond to a local energy minimum in graphene bulk interaction with respect to the substrate. In the end, we use this model to estimate a lower bound for rotational barriers of graphene seeds and find qualitative agreement with experimental measurements. In the future, we hope that the insights gained here will aid in optimizing graphene seeds and seeded growth of GNR arrays on Ge(001).

Chapter 11: Conclusions and Future Directions

11.1 Conclusions

In this thesis, we presented several examples of how we can utilize first-principles calculations to evaluate and design catalytic materials. In particular, this work characterizes interfacial interactions between the liquid and solid phases of electrocatalytic systems and interfacial interactions between graphene and Ge(001). These insights serve as a basis for the development of materials descriptors that can be leveraged to design improved electrocatalytic and electronic materials.

Our work demonstrates that interfacial water plays a key role in determining the activity and selectivity of reactions on charged electrode surfaces. We showed that by only modeling adsorbates on unsolvated and uncharged surfaces, we could not capture experimental trends in reactivity for the oxygen reduction reaction (ORR). However, by utilizing a holistic model that captures the interactions between water, adsorbates (including spectator species), and charged electrode surfaces, we can accurately evaluate the reactivity of the overall interfacial system. On Au(100), the Au(100)-hex surface forms a high density of hydrogen bonds within interfacial water that leads to a particularly active ORR catalyst. Furthermore, we showed that Au(111), which has a similar hexagonal surface structure, cannot catalyze the ORR as effectively as Au(100)-hex because of differences in the electronic structure between the two surfaces. Our calculations also revealed that when we examine the ORR on Pt(111) at experimentally relevant hydroxyl coverages, water destabilizes ORR intermediates, facilitating the reaction at lower overpotentials.

Inspired by these results, we further analyzed the structure of interfacial water on Au(100) and Pt(111) electrode surfaces for both clean and hydroxyl covered surfaces.

In addition to screening for new reactivity descriptors, we also utilized well-developed reactivity descriptors to screen for improved catalysts for formic acid electrooxidation. Using high-throughput DFT calculations, we screened bimetallic Pt- and Pd-based alloys with improved activity and resistance to CO poisoning. Through this analysis, we determined that alloying Pt or Pd with Ir, Ru, or Re may result in far more active catalysts for this reaction.

Finally, we demonstrated how a combination of experiments and theory allow us to optimize graphene nanoribbon (GNR) growth on Ge(001). By using vicinal Ge(001) surfaces, we can achieve unidirectional GNR growth, a prerequisite for creating uniform arrays of GNRs. Our DFT calculations demonstrated that the interactions between one edge of each GNR and Ge anchor graphene to the surface, leading to unidirectional alignment and the anchored edge having a slower growth rate. Additionally, we examined seed-initiated GNR growth on Ge(001), which allowed us to control the position, orientation, and length/width dispersity of GNRs. Using a combination of a transport model and DFT calculations, we evaluated the transport properties of several potential graphene growth species. Furthermore, we used a combination of DFT and Monte Carlo calculations to examine the forces at the interface between graphene and Ge(001) that control the orientation of graphene crystals and the structure of GNR edges.

11.2 Future Directions

11.2.1 Microkinetic and Kinetic Modeling of ORR on Au(100), Au(111), and Pt(111)

In Chapters 3 and 4, we used *ab initio* molecular dynamics (AIMD) simulations to evaluate

the structures and energies of oxygen reduction reaction (ORR) intermediates on catalytic surfaces to examine the effect of an applied potential drop across a water layer on Au(100), Au(111), and Pt(111) electrode surfaces. These simulations assumed coverages of reaction intermediates and spectator species based on estimates from cyclic voltammetry (CV) measurements from experiments. To provide a link between our *ab initio* calculations and experiments, we then utilized the computational hydrogen electrode to calculate the onset potential ORR pathways in our calculations to compare with experiments. Our analysis assumed that if we calculated a similar onset potential as was seen experimentally, then we captured all relevant structural information about the water/electrode interface.

In future work, microkinetic modeling can provide a more extensive analysis of ORR kinetics on each of the catalyst surfaces we studied. In this model, we can derive rate expressions for each elementary step involved in the ORR. These rate expressions should be a function of the potential-dependent reaction energies calculated from AIMD simulations and the energy barriers for each elementary step. Thus, reaction barriers for each elementary step must first be calculated before constructing a model. In this work, we have not calculated reaction barriers because we were limited by the use of a DFT code that utilizes a conventional canonical-ensemble algorithm to model electronic structures. In periodic DFT calculations, modeling charge transfer reactions using a canonical ensemble can lead to artificial overcharging of the surface during the course of reaction that results in barriers that are far too large. DFT codes that utilize a grand canonical algorithm avoid this problem and should be used in these types of calculations.[266] After calculating all the necessary energetic information to calculate reaction rates, we can then define a set of ordinary differential equations that describe these rates.

By adjusting the applied potential and pH in a microkinetic model, we can then calculate the onset potential for the ORR as well as the current that we would generate at a given potential. This information can be directly compared with polarization sweeps in rotating disc electrode experiments. Furthermore, microkinetic models can provide us with updated coverages of ORR reaction intermediates. If the expected coverages under relevant conditions vary from the coverages modeled using AIMD simulations, we can then repeat our AIMD simulations with the microkinetic-model-predicted coverages. We can iteratively reformulate and update our AIMD models and the potential-dependent energies that we utilize in our microkinetic models until the coverages predicted with AIMD simulations and microkinetic models are consistent and the calculated potential sweeps match experiments. This process will provide us with the most accurate picture of the active site as well as additional information about reaction fluxes and rate-controlling steps in the ORR as a function of potential and coverage.

11.2.2 Evaluating Trends in the Role of Water in Electrochemistry on Transition Metal Surfaces

Over the past several decades, researchers have made tremendous efforts in extracting reactivity descriptors and designing new heterogeneous catalysts with optimized properties based on these reactivity descriptors. While these design principles have proven to also be useful for designing catalysts in liquid-phase reactions, these reactivity descriptors often neglect the role that solvent plays in catalysis. As we have shown in Chapters 3-6 of this work, the catalytic properties of an electrocatalytic system can be dictated not only by the interactions between the solid and reaction intermediates, but also by the interactions between the surface, solvent, and reaction intermediates. Therefore, rational catalyst design does not have to be limited to the properties of a

solid catalyst surface alone.

Given the large range of potential solvent systems that could be utilized in electrocatalysis, we must first understand how common solvents impact the reactivity of electrocatalytic systems. No solvent is more ubiquitous than water— even ‘dry’ solvents often contain some amount of water. Despite the prevalence of water in electrocatalytic systems, many researchers tend to apply simple energy corrections to account for stabilization effects from water or model unrealistic honeycomb bilayer structures to capture the effects of water. In this work, we show that the role of water can be complex and can strongly depend on the identity of the catalyst surface. Furthermore, water can both stabilize and destabilize adsorbates. To better characterize the role of water, we must first identify trends in how water impacts the structures and binding energies of common adsorbates on a range of catalyst surfaces. Using AIMD simulations, one can calculate the structure and energy of adsorbates to a catalyst surface with and without water for a range of transition metals and several facets often studied in catalysis literature. Additionally, these studies can also evaluate the role of OH*, O*, or other adsorbates that may be present on the catalyst surface during reaction conditions at a range of relevant coverages.

11.2.3 Determining the Role of Alkali Metal ions in Electrochemistry on Transition Metal Surfaces

In addition to solvents, alkali metal ions are always present in electrocatalytic systems and can play a role in altering the catalytic activity of an electrocatalytic solid/liquid interface. For example, experimental work has demonstrated that Li^+ ions in aqueous media form Li_2O_2, which the authors suggest play a role in activating water in the ORR in alkaline environments on Au(100).[36] Additionally, non-covalent interactions between partially solvated alkali metal ions,

such as Cs^+, K^+, Na^+, Li^+, and Ba^{2+} can also impact the kinetics of the ORR and hydrogen oxidation reaction (HOR).[95,126] Because the hydration energy and charge of these species vary, we expect that these species will form different solvated structures that interact with adsorbates on the surface. For example, these solvated clusters can bind to adsorbates on the surface to block reaction sites or alter the binding energy of adsorbates on the surface. Because of how ubiquitous these ions are in electrochemistry, AIMD models that address how the interplay of water, ions, metal surfaces, and adsorbates impact adsorbate structures and energies can provide valuable information that can be used to tailor electrochemical interfaces for improved activity and selectivity of electrocatalysts.

11.2.4 Constructing a Full Kinetic and Transport Model of GNR Growth from DFT-based Parameters

Finally, in Chapters 7-10, we utilized a combination of theory and experiments to evaluate and tailor the graphene nanoribbon (GNR) growth process on the Ge(001) surface. Throughout this work, we utilized DFT calculations to model interactions between the edge and wall of graphene with Ge(001). We also considered the interactions of graphene precursor species with the Ge(001) surface and calculated the barriers for interconverting between these species. While these insights provide key information about the driving forces for graphene growth on Ge(001), they cannot easily be utilized to determine how GNR growth will change under different growth conditions. In the past, our group has created an empirical kinetic Monte Carlo (kMC) model to describe the growth of GNRs on the Ge(001) surface.[267] By integrating our DFT-derived parameters into this type of kMC model, we can study how growth species evolve on the Ge(001) surface at various conditions to form GNRs. These insights can then be used to further optimize

the GNR growth process.

Appendix: A Comparing the Performance of Density Functionals in Describing the Adsorption of Atoms and Small Molecules on Ni(111)*

A.1 Introduction

A variety of reactions take place on the surface of heterogeneous catalysts to produce a plethora of desired chemical products. The preference of one chemical pathway in a reaction network over another, as well as the associated selectivity of the process, depends on the stability of various reaction intermediates and activation energy barriers for their interconversion. This information is therefore necessary to understand and predict catalyst performance.[268] However, because reactions in heterogeneous catalysis are complex, multi-step processes, obtaining energetic data for all reaction intermediates and activation energies from experimental measurements is often not practical or even possible.

The advent of first-principles modeling has offered a critical toolset for obtaining energetics at the atomic level related to reaction kinetics and thermochemistry. In particular, first-principles calculations based on density functional theory (DFT) can provide binding energies that describe the interaction strength between reaction intermediates and catalyst surfaces, as well as activation and reaction energies for surface-catalyzed elementary reaction steps. These energetics can then

---

*Adapted from **"Comparing the performance of density functionals in describing the adsorption of atoms and small molecules on Ni(111)"**, F. Göltl‡, E. A. Murray‡, S. A. Tacey, S. Rangarajan, and M. Mavrikakis (‡ equal contribution), *Surface Science* **700**, 121675 (2020).

be used to rationalize experimental observations,[269] predict catalytic properties of specific catalysts,[270,271] and design improved catalysts for specific applications.[18,272] However, the quality of these insights is intimately linked to the accuracy of the applied DFT methods.

The accuracy of DFT is critically dependent on the density functional implemented to calculate energetics. Density functionals are typically parameterized to minimize the error for a specific test set of either molecular gas-phase systems or simple surface adsorbates;[79,273–276] yet, their ability to describe more complex interactions present in heterogeneous catalysis is often not considered. For specific systems, significant discrepancies between DFT calculations and experimental data have been shown.[277–279] Consequently, a detailed understanding of the errors associated with these calculations is crucial for assessing the reliability of DFT for predicting catalytic properties of a given material.[280,281]

Due to their pervasiveness in catalysis, the interaction between various hydrocarbons and transition-metal surfaces has been studied extensively.[282–285] A large portion of this research has focused on methyl (CH_3),[286,287] as it is one of the simplest hydrocarbon fragments interacting with transition-metal surfaces. Importantly, to arrive at a quantitative understanding of how CH_3 binds on a Ni surface, Carey et al. studied the adsorption of methyl iodide on Ni(111) using single-crystal adsorption calorimetry.[288] In particular, they determined heats of adsorption for the molecular and dissociative adsorption of methyl iodide by performing measurements at different temperatures. They subsequently extracted the coverage-dependent heat of adsorption of CH_3 using thermochemical cycles and compared their results to electronic-structure calculations in the literature. Based on these comparisons, they concluded that '*DFT calculations routinely underestimate this bond strength [i.e., that between CH_3 and the Ni(111) surface]*'. [288] Although

this statement correctly described the differences between their experimental measurements and the DFT studies they used for comparison, the DFT studies they considered utilized a limited number of density functionals and did not consider the exact same coverages and surface adsorbates represented in the experiments. Nevertheless, the disagreement between theory and experiment raises the following question: Are there currently available density functionals that accurately describe the interactions of CH_3 and I with the Ni(111) surface?

Here, we seek to answer this question by studying the adsorption of CH_3I, CH_3, and I on Ni(111) at different surface coverages and by utilizing different density functionals. We perform a rigorous analysis of the performance of these functionals and compare adsorption energetics to those measured experimentally.[288] In addition, we calculate the adsorption energy of H on the Ni(111) surface and compare the performance of different functionals in predicting the dissociative adsorption energy for CH_4 on Ni(111), an important step in CH_4 steam reforming over nickel catalysts.[289]

A.2 Methods

A.2.1 Theoretical Setup

All calculations were carried out using the Vienna *Ab Initio* Simulation Package (VASP),[82,290] a plane-wave code that uses periodic boundary conditions and projector augmented-wave (PAW) pseudopotentials.[120,121] All calculations were spin-polarized, the energy cut-off was set to 420 eV, and the electronic structure was assumed to be converged for energy differences between electronic iterations smaller than 10^{-6} eV. To minimize errors due to the computational implementation, we chose the 'Accurate' setting in VASP for all calculations.

In this work, we compare the performance of different functionals. Specifically, we choose

the local-density approximation (LDA), as well as the generalized-gradient approximation (GGA) functionals PW91,[291] PBE,[79] and RPBE,[273]. Additionally, we combine GGA functionals with the D2 (PBE-D2, RPBE-D2),[257] D3 (PBE-D3, RPBE-D3),[119] TS (PBE-TS),[292] and dDsC (PBE-dDsC)[293] dispersion corrections to account for dispersion force fields. We also include functionals with a non-local description of correlation: vdW-DF,[294] vdW-DF2,[295] BEEF-vdW,[274] optB86b-vdW,[276] optB88-vdW, [296] and optPBE-vdW.[276]

Lattice parameters for Ni were optimized in the primitive fcc bulk unit cell using a 15x15x15 Monkhorst-Pack k-point grid[122] for each functional. The DFT-calculated values are given in Table B.2. All parameters lie within 3% of the experimentally measured value of 3.524 Å.[123] Specifically, LDA (3.428 Å), PBE-TS (3.426 Å), and PBE-dDsC (3.498 Å) show the smallest DFT-calculated lattice constants, while vdW-DF (3.569 Å) and vdW-DF2 (3.608 Å) show the largest DFT-calculated lattice constants.

To model Ni(111), we constructed four-layer slabs with the bottom two layers fixed in their bulk lattice position and the top two layers relaxed. We used 6x6x1 (2x3 surface unit cell), 4x4x1 ($\sqrt{7}\times\sqrt{7}$ surface unit cell), and 2x2x1 (5x5 surface unit cell) Monkhorst-Pack k-point grids.[122] Successive slabs in the *z* direction were separated by a vacuum layer of at least 14 Å, and dipole corrections were applied to correct for bias in the *z* direction.[189,297] Reference gas-phase energies were calculated by placing each gas-phase species in a 10x11x12 Å rectangular unit cell and performing calculations for a fixed spin state (i.e., CH_3I, CH_4, and I_2 were fixed in a singlet spin state, while H and CH_3 were fixed in a doublet spin state). Structures were optimized using the limited-memory Broyden-Fletcher-Goldfarb-Shanno algorithm[298] and were considered to be converged for forces smaller than 0.02 eV/Å. Vibrational frequencies required for finite-

temperature effects were calculated using the Hessian by numerically differentiating energies using a second-order finite difference approach. In these calculations, vibrational frequencies for the adsorbates were calculated while surface atoms remained fixed[299] and the individual bonds were stretched/compressed with a step size of 0.01 Å.

We seek to compare our DFT predictions to heats of adsorption reported by Carey et al. at 160 K.[288] If not explicitly stated otherwise, we report enthalpies of adsorption of molecule A at 160 K ($\Delta H(A, T = 160\ \mathrm{K})$) as:

$$\Delta H(A, T = 160\ \mathrm{K}) = H^{A+slab}(T = 160\ \mathrm{K}) - H^{slab}(T = 160\ \mathrm{K}) - H^{A(g)}(T = 160\ \mathrm{K}) \qquad \text{(A.1)}$$

Here, *H* refers to the enthalpy for the systems as marked by the corresponding superscript (*slab* for the clean surface, *A+slab* for species A adsorbed on the surface, and *A(g)* for gas-phase species A). *H* for a specific system is obtained by calculating DFT energies and subsequently applying zero-point energy corrections and finite-temperature corrections based on the harmonic approximation. To make more direct comparisons with the work by Carey et al.,[288] the enthalpy of adsorption for CH_3I was calculated with respect to gas-phase CH_3I, while the enthalpies of adsorption for CH_3 and I were calculated with respect to gas-phase CH_3 and ½ I_2, respectively.

To assess the accuracy of our computational setup, we evaluated the impact of the slab thickness and the impact of the cutoff force for geometry optimization on the adsorption of CH_3 in the √7×√7 surface unit cell. More specifically, we increased the number of layers included in our slab model from four to six (where the two bottom layers were always fixed) and we optimized structures up until forces smaller than 0.005 eV/Å. For both cases the enthalpy of adsorption of CH_3 on Ni(111) increased by less than 3 kJ/mol. Due to these small changes, we suggest that the

slab thickness and force criterion chosen for the entire study are suitable to model the adsorption processes of interest.

A.2.2 Adsorption Geometries

To understand and reproduce the experimental results for CH_3I interacting with Ni(111)[288] through DFT calculations, we focus on three different systems: adsorption of CH_3, adsorption of I, and molecular versus dissociative adsorption of CH_3I. To correctly capture coverage effects discovered through calorimetry experiments, we studied three different unit cells: a 2×3 Ni(111) surface for a coverage of 1/6 monolayer (ML), a √7×√7 Ni(111) surface for a coverage of 1/7 ML, and a 5×5 Ni(111) surface for a coverage of 1/25 ML. Following the definition from Carey et al.,[288] coverage is defined as the number of gas-phase molecules adsorbed per surface atom. For example, we consider the coverage of co-adsorbed CH_3 and I that forms from the dissociative adsorption of CH_3I from the gas phase in a √7×√7 unit cell to be 1/7 ML.

To identify stable and minimum energy adsorption structures, we focus on a series of different possible adsorption geometries for each adsorbate. For CH_3 and I, we examine all possible high-symmetry sites (fcc, hcp, top, and bridge) on Ni(111), including several high-symmetry rotational structures for CH_3 [300] (the exact configurations are shown in Fig. A.1A for CH_3 and Fig. A.1B for I). We calculate the relative stability of all possible adsorption structures on the √7×√7 unit cell but focus our calculations on the most stable adsorbed structure on the 2×3 and 5×5 unit cells. Additionally, we further examined the adsorption site preference of CH_3 and compared the relative stability of adsorption in the top and fcc sites between functionals.

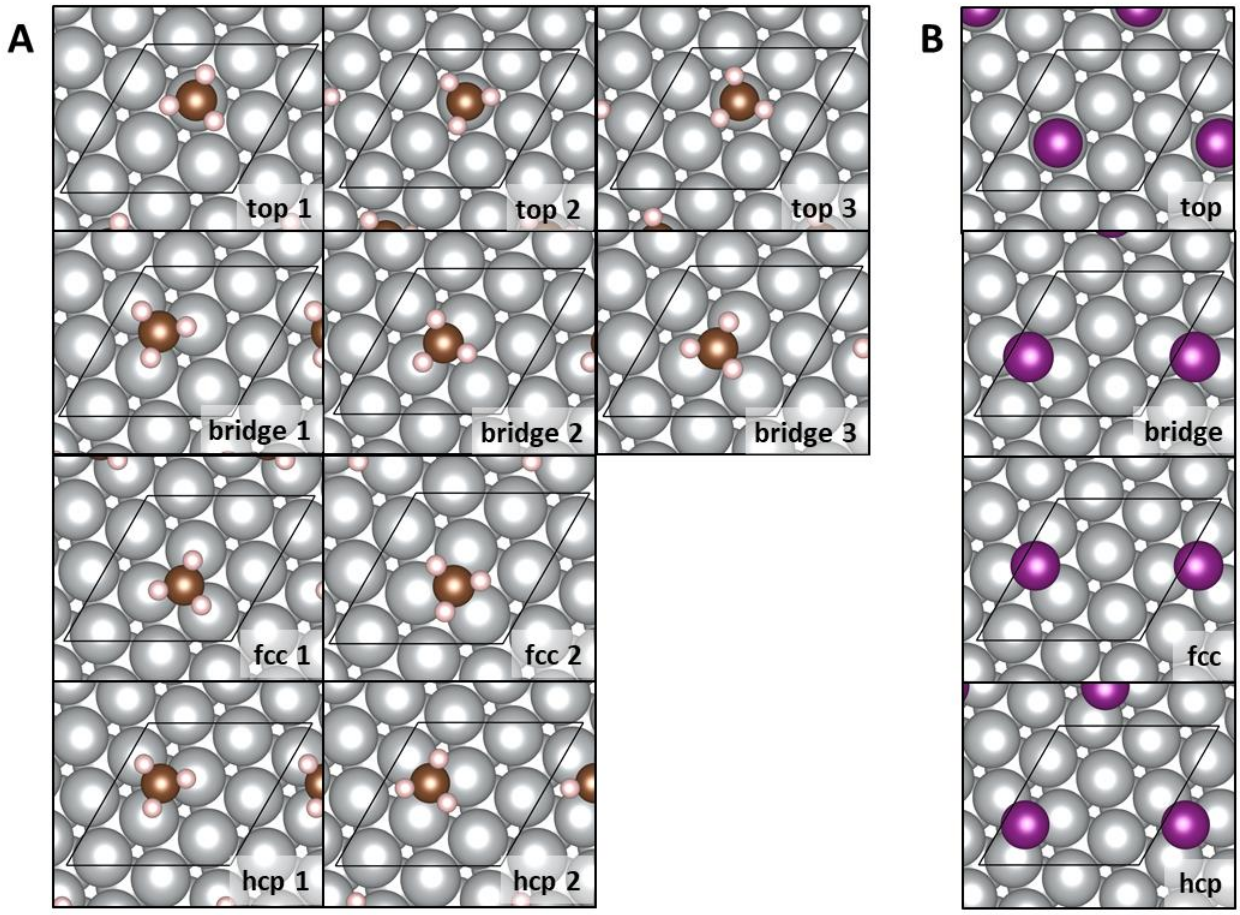

Figure A.1: Top view of stable adsorption structures for **(A)** CH_3 and **(B)** I on a √7×√7 Ni(111) surface. Ni atoms are shown in silver, C atoms in brown, H atoms in white, and I atoms in magenta. Black lines denote the surface unit cell.

We furthermore probe nine symmetrically different adsorption sites for the molecular adsorption of CH_3I on the √7×√7 unit cell. However, only three structures were predicted to be most stable using any functional. These structures are displayed in Fig. A.2A.

To describe the dissociative adsorption of CH_3I on Ni(111), we performed preliminary calculations at the PBE level for all unique co-adsorbed states of CH_3 and I. An fcc /hcp structure for CH_3/I co-adsorption is most stable for the 2×3 and √7×√7 unit cells (see Fig. A.2B) for all but one functional, which is discussed in more detail in Section B.2 of Appendix B. For these two unit

cells, CH_3 and I occupy third-nearest-neighbor hollow sites. For the 5×5 unit cell, however, both adsorbates are found in fcc sites with a significantly larger separation between CH_3 and I. Throughout the manuscript, we focus on these specific structures. To explore the adsorption site preference of co-adsorbed CH_3/I, we also modeled a top/hcp configuration for CH_3/I, which is displayed in Fig. B.1.

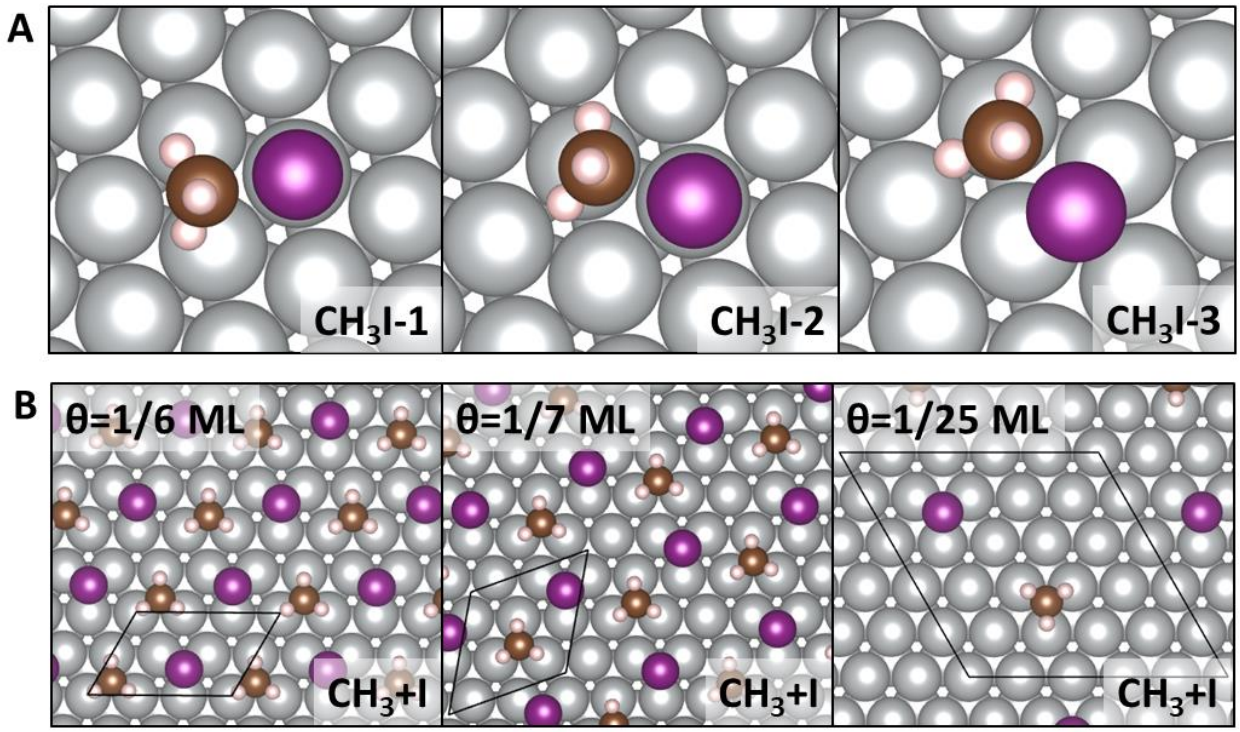

Figure A.2: (A) Preferred adsorption structures for the molecular adsorption of CH_3I at a coverage of 1/7 ML. **(B)** Preferred adsorption structures for the dissociative adsorption of CH_3I at a coverage (θ) of 1/6 ML (left), 1/7 ML (middle), and 1/25 ML (right). Structures shown were calculated using the PBE functional. Ni atoms are shown in silver, C atoms in brown, H atoms in white, and I atoms in magenta. In **(B)**, the unit cells for each coverage are marked by black lines.

A.3 Results and Discussion

We first present DFT data obtained from each functional and subsequently compare these values to experimental measurements. We start our discussion with the molecular adsorption of CH_3I, followed by the adsorption of CH_3 and I, and last discuss the dissociative adsorption of

CH_3I. Then, we present DFT results for the adsorption of H on Ni(111) and the dissociative adsorption of CH_4 on Ni(111). We report enthalpies of adsorption at 160K, but for comparison with data published in the literature, we also provide data calculated using the PBE functional without zero-point or finite-temperature corrections in Section B.1 of Appendix B. Further, a comprehensive discussion of the CH_3 adsorption site preference is given in Section B.2 of Appendix B.

A.3.1 Adsorption Energies from Different Functionals:

Molecular adsorption of CH_3I on Ni(111): The first step in our analysis was determining the enthalpy of adsorption for the molecular adsorption of CH_3I at 160 K. For each functional, we find several stable adsorption structures, all within 10 kJ/mol. However, the most stable structure varies depending on the functional. For some functionals, the I atom of CH_3I is located over a top position with the CH_3 group located above either a neighboring bridge site (CH_3I-1 in Fig. A.2A, observed for PBE-D2, RPBE-D2, and vdW-DF) or an adjacent top position (CH_3I-2 in Fig. A.2A, observed for vdW-DF2). For the remaining functionals, the minimum energy adsorption structure for CH_3I has the I atom located over an fcc site and the CH_3 group atop a neighboring Ni atom (CH_3I-3 in Fig. A.2A).

Several stable adsorption structures close lying in energy are typical for an adsorption process that is dominated by dispersion interactions, as these interactions are particularly difficult to describe in semi-local DFT calculations. These challenges are reflected by the large differences between the calculated enthalpies of adsorption at 160 K for CH_3I in a $\sqrt{7}\times\sqrt{7}$ unit cell across the studied functionals (see Fig. A.3, numerical values are given in Table B.3). Naturally, functionals that do not include dispersion interactions (e.g., RPBE (-17 kJ/mol), PBE (-48 kJ/mol), and PW91

(-51 kJ/mol)) lead to the weakest adsorption strengths. However, the calculated adsorption enthalpies for vdW-DF (-54 kJ/mol), vdW-DF2 (-48 kJ/mol), and BEEF-vdW (-56 kJ/mol) are comparable to functionals without dispersion corrections. PBE-TS (-140 kJ/mol), RPBE-D2 (-131 kJ/mol), and LDA (-130 kJ/mol), on the other hand, lead to the strongest adsorption strengths. Based on these results, the enthalpies of adsorption at 160 K vary dramatically depending on the selected functional, ranging from -17 kJ/mol for RPBE to -140 kJ/mol for PBE-TS (see Fig. A.3). Therefore, it is readily apparent that the choice of functional largely dictates the predicted adsorption behavior of CH_3I on Ni(111). The optB88-vdW functional best captures the experimentally measured energetics for CH_3I molecular adsorption on Ni(111). A more detailed discussion is forthcoming in Section A.3.2.

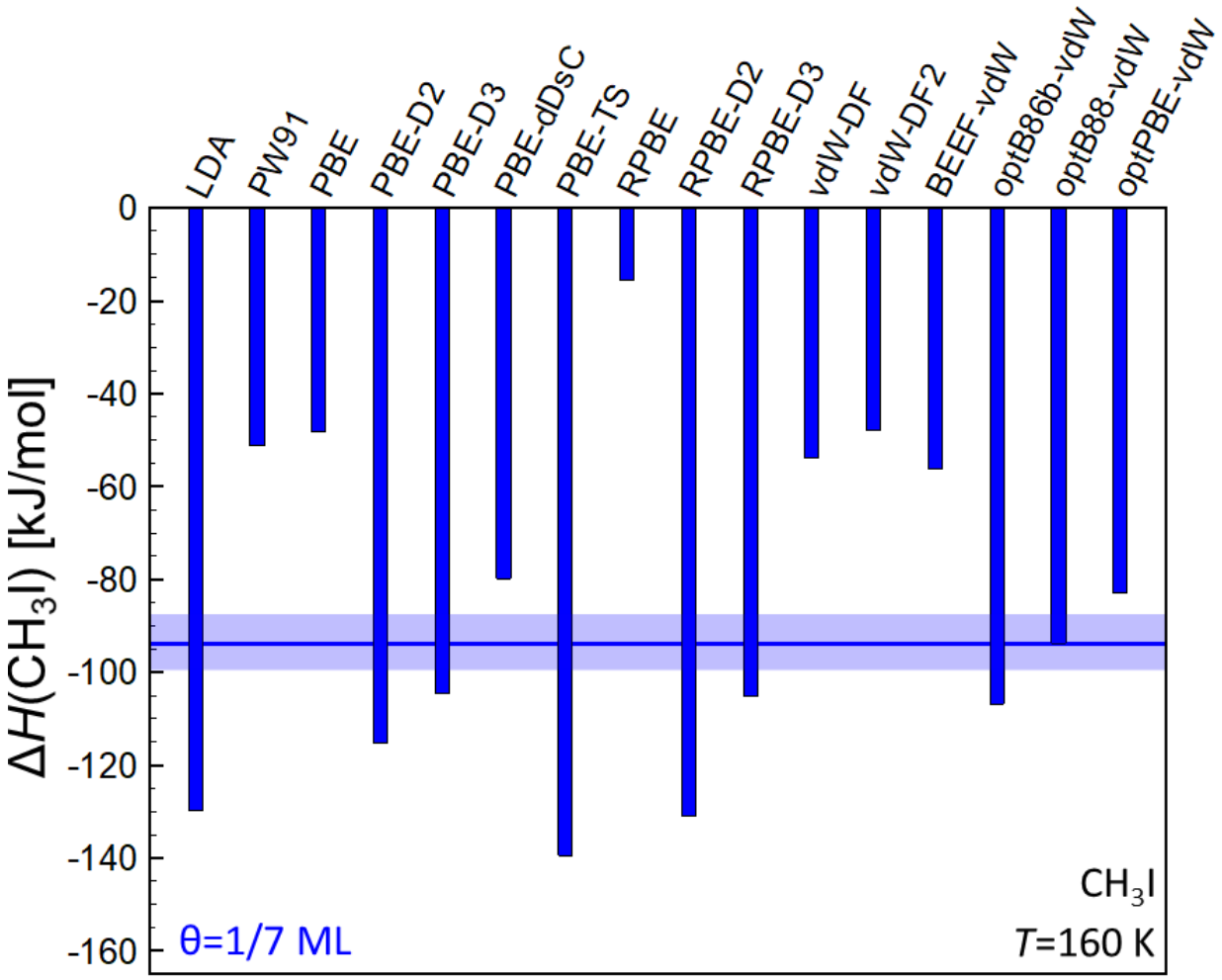

Figure A.3: Enthalpies of molecular adsorption for CH_3I ($\Delta H(CH_3I)$) on Ni(111) at 160 K calculated for different density functionals at a coverage (θ) of 1/7 ML. Vertical blue bars represent the calculated value for each functional. The horizontal blue bars correspond to the experimentally determined heat of adsorption for a coverage of 1/7 ML, where the solid line represents the measured value of -94 kJ/mol. The width of the blue shaded area represents the experimental error (±6 kJ/mol). Experimental data is from ref. 288.

Adsorption of CH_3 on Ni(111): Next, we studied the adsorption of CH_3 on Ni(111). All but one functional prefers CH_3 adsorption at an fcc site, which is in agreement with experimental measurements.[286,287] The only exception is for the vdW-DF2 functional, which predicts that CH_3 preferentially adsorbs at a top site. A more detailed discussion on CH_3 adsorption site preference is given in Section B.2 of Appendix B.

The calculated enthalpy of adsorption for CH_3 at 160 K for each functional is given in Fig.

A.4 (tabulated data in Table B.4) for coverages of 1/25 ML (green bars), 1/7 ML (blue bars), and 1/6 ML (orange bars). Again, the choice of functional leads to a large spread in the enthalpy of adsorption. For example, the LDA functional at a coverage of 1/7 ML results in the highest enthalpy of adsorption (-295 kJ/mol), while the lowest values arise from the RPBE (-143 kJ/mol) and vdW-DF2 (-142 kJ/mol) functionals, which are both less than half the magnitude of the LDA value. Additionally, lateral interactions slightly weaken the adsorption strength by 1–7 kJ/mol when moving from a 1/25 ML to a 1/7 ML coverage. Enthalpies of adsorption for coverages of 1/7 ML and 1/6 ML are similar to each other. The PBE-D2, PBE-D3, PBE-TS, RPBE-D2, RPBE-D3, and optB86b-vdW functionals best capture the experimentally measured energetics for CH_3 adsorption on Ni(111). A more detailed discussion is forthcoming in Section A.3.2.

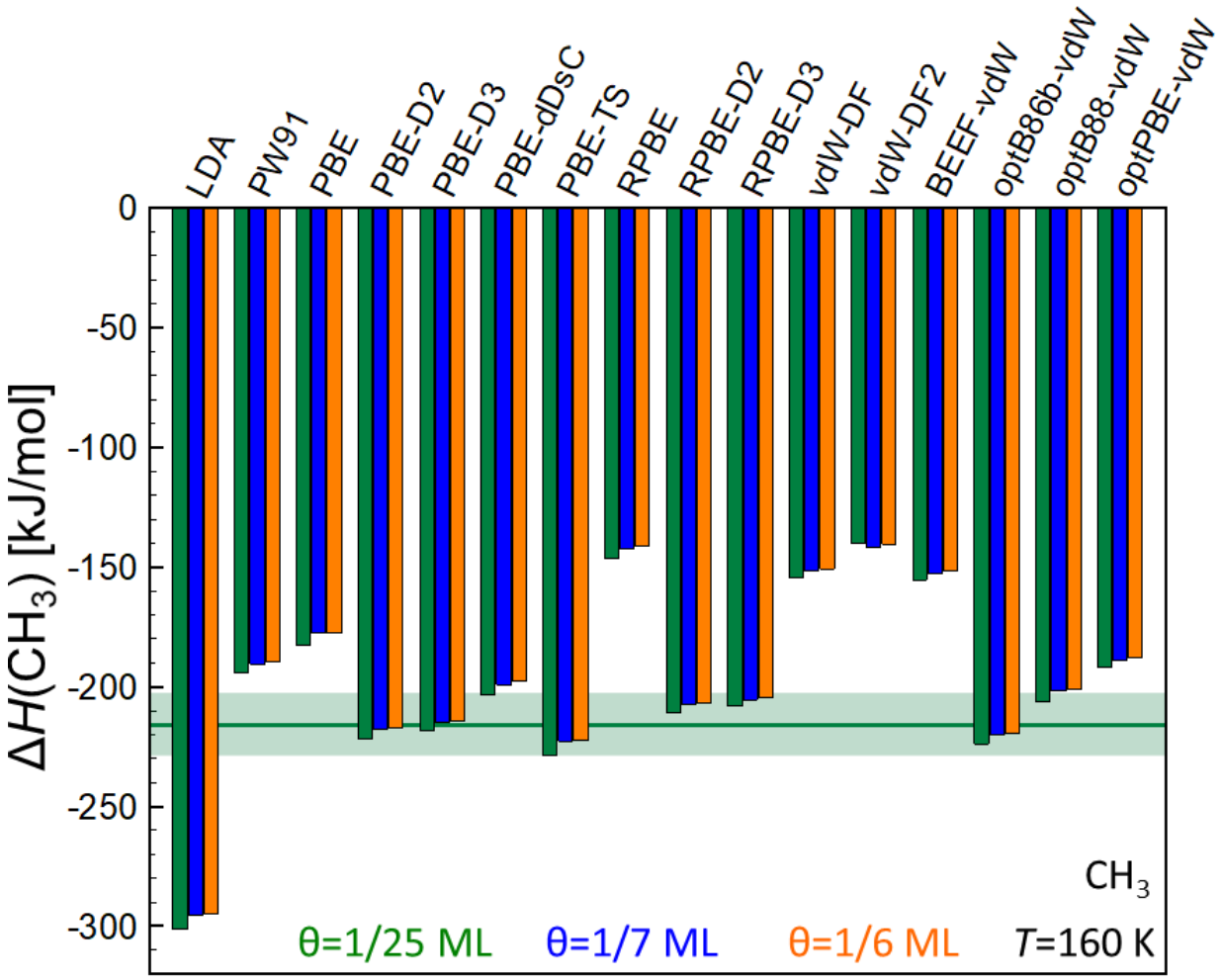

Figure A.4: Enthalpy of adsorption for CH_3 ($\Delta H(CH_3)$) on Ni(111) at 160 K calculated using different density functionals at a coverage (θ) of 1/25 ML (green bars), 1/7 ML (blue bars), and 1/6 ML (orange bars). The horizontal green bar corresponds to the experimentally determined heat of adsorption for a coverage of 1/25 ML where the solid line represents the measured value, and the width of the green shaded area represents the experimental error. The experimental data is from ref. 288.

Adsorption of I on Ni(111): For all functionals studied, atomic iodine always prefers to bind to an fcc site on Ni(111). The overall trends for how the functionals describe the enthalpy of adsorption for I on Ni(111) are similar to those for CH_3 on Ni(111); respective values are shown in Fig. A.5 (numerical values in Table B.5). While lateral interactions between adsorbed atomic iodine species are comparable (3–8 kJ/mol) to those between adsorbed CH_3 species (1–7 kJ/mol), it is interesting to note that the adsorption of atomic I is weakest at 1/7 ML coverage, rather than for a 1/6 ML coverage, opposite to what we found for CH_3 adsorption. Overall, the difference in

the calculated enthalpy of adsorption between functionals is smaller than that for CH_3. For example, the LDA, PBE-TS, RPBE-D2, and PBE-D2 functionals lead to heats of adsorption between -239 kJ/mol and -214 kJ/mol, whereas the vdW-DF2 and RPBE functionals lead to values between -157 kJ/mol and -147 kJ/mol. The PW91, PBE, BEEF-vdW, and optPBE-vdW functionals best capture the experimentally measured energetics for atomic I adsorption on Ni(111). A more detailed discussion is forthcoming in Section A.3.2.

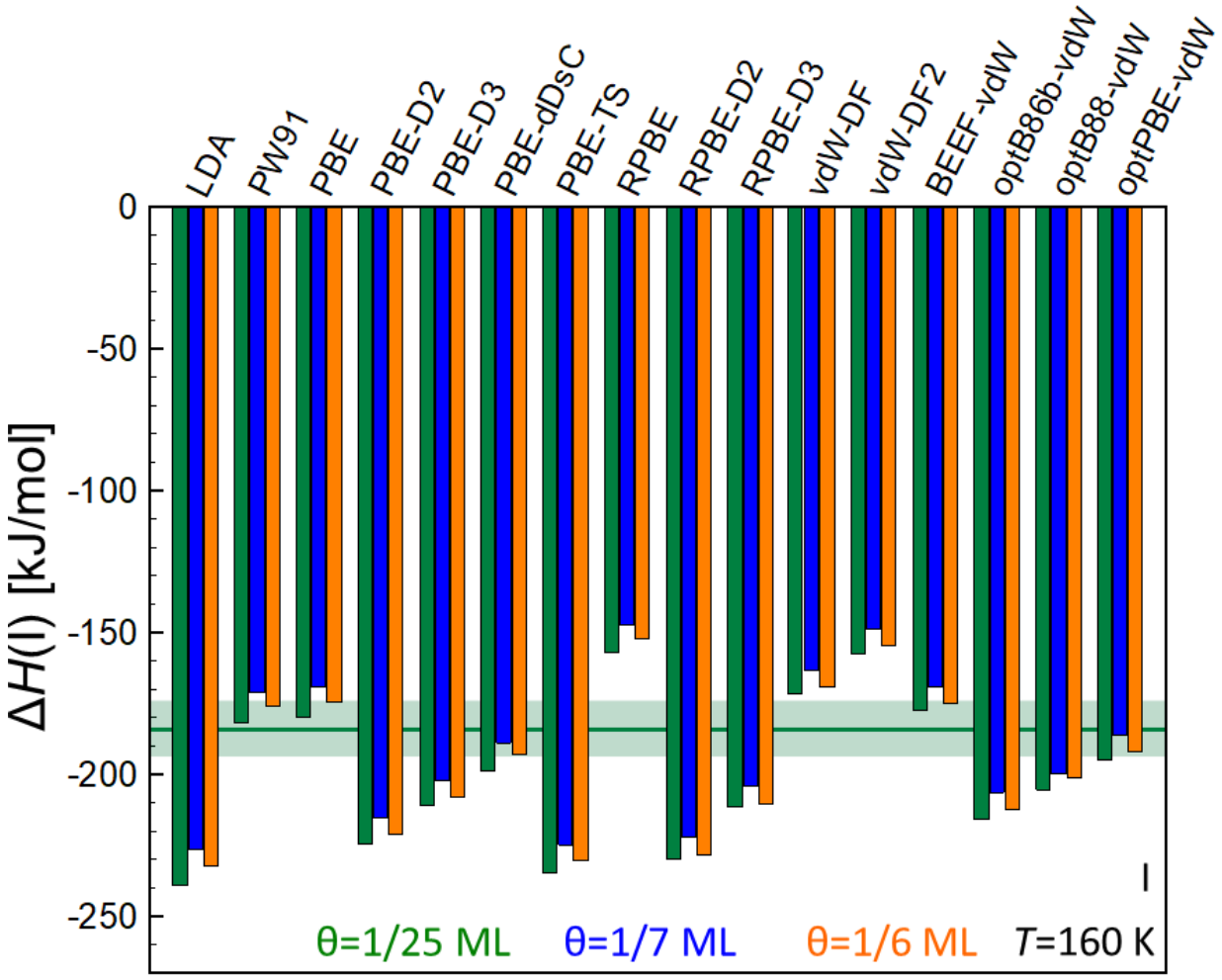

Figure A.5: Heat of adsorption for atomic I (ΔH(I)) on Ni(111) at 160 K calculated using different density functionals at a coverage (θ) of 1/25 ML (green bars), 1/7 ML (blue bars), and 1/6 ML (orange bars). The horizontal green bar corresponds to the experimentally determined heat of adsorption for a coverage of 1/25 ML, where the solid line represents the measured value, and the width of the green shaded area represents the experimental error. The experimental data is from ref. 288.

Dissociative adsorption of CH_3I on Ni(111): The dissociative adsorption of CH_3I on

Ni(111) produces CH_3 and I adsorbed on the surface. First, we compared the relative stability of co-adsorbed CH_3+I with CH_3 binding to an fcc or a top site and I binding to an hcp site at a surface coverage of 1/7 ML (a detailed discussion for adsorption site preference is given in Section B.2 of Appendix B). The preferred minimum energy co-adsorbed structure for all but one of the studied functionals has CH_3 bound to an fcc site and I bound to an hcp site (see Fig. A.2B). Only the vdW-DF2 functional leads to a preferred co-adsorption structure with CH_3 on a top site and I in an hcp site (see Fig. B.2).

The enthalpy change upon the dissociative adsorption of CH_3I from the gas phase on Ni(111) is displayed in Fig. A.6 (numerical values are given in Table B.6) for coverages of 1/25 ML (green bars), 1/7 ML (blue bars), and 1/6 ML (orange bars). For all functionals, we find significant differences between the calculated value at a coverage of 1/25 ML and those at coverages of 1/7 ML and 1/6 ML, with differences ranging from 7 kJ/mol to 32 kJ/mol. The heats of adsorption for coverages of 1/6 ML and 1/7 ML are similar. These values indicate that lateral interactions destabilize co-adsorbed CH_3 and I. The LDA functional predicts the largest dissociative adsorption enthalpy at 160 K, while the RPBE, vdW-DF, and vdW-DF2 functionals predict the smallest dissociative adsorption enthalpies. Interestingly, there is no single functional among those studied that would do well in all three reported experimental coverages. At 1/25 ML coverage (Fig. A.6, green bars), the PBE-D2, RPBE-D2, and optB86b-vdW functionals compare well with the experimental value, whereas at 1/7 ML coverage (Fig. A.6, blue bars) only the PBE-D2 and RPBE-D3 functionals agree with the experimental values. At 1/6 ML coverage (Fig. A.6, yellow bars), only the PBE-D3 and optB86b-vdW functionals agree well with experiments. A more

detailed discussion is forthcoming in Section B.3.2.

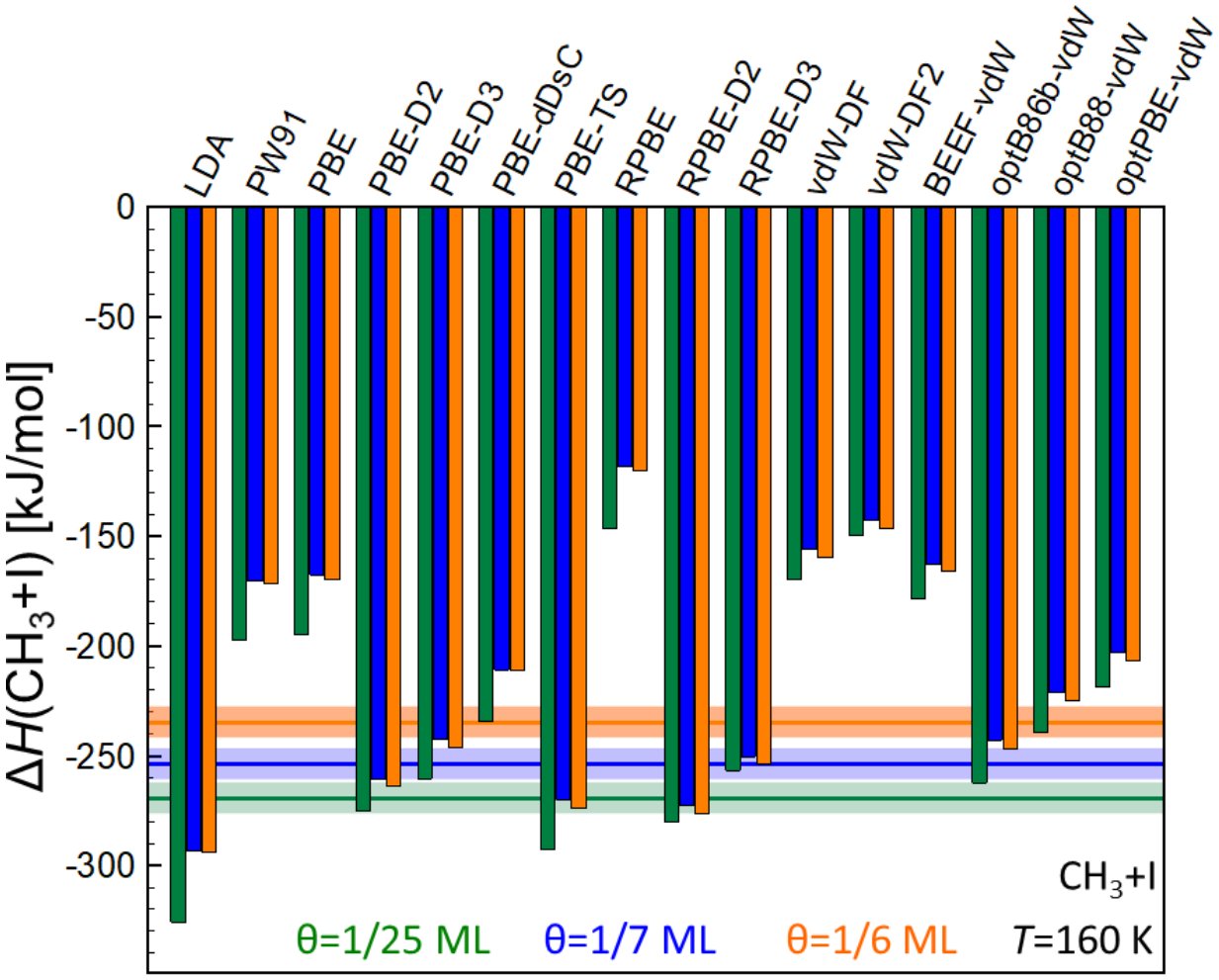

Figure A.6: Heat of adsorption for the dissociative adsorption of CH_3I ($\Delta H(CH_3 + I)$) on Ni(111) at 160 K calculated using different density functionals at a coverage (θ) of 1/25 ML (green bars), 1/7 ML (blue bars), and 1/6 ML(orange bars). Horizontal bars correspond to the experimentally determined heats of adsorption for a coverage of 1/25 ML (green), 1/7 ML (blue), and 1/6 ML (orange), where the solid lines represent the measured values and the width of each shaded area represents the experimental error for each coverage. The experimental data are from ref. 288.

A.3.2 Gas phase recombination energy for CH_3I

One possible source of error for each of the functionals is how they describe the gas-phase energetics. To address this effect, we report the reaction enthalpies for $CH_3I \rightarrow CH_3 + ½\ I_2$ at 0 K (see Table A.1). We find that optB86b-vdW (0 kJ/mol error relative to the experimental value of -163 kJ/mol) and PW91 (-1 kJ/mol relative to the experimental value) accurately describe the overall gas-phase reaction compared to experimental measurements performed at standard

conditions.[301] LDA produces the largest error (-36 kJ/mol relative to the experimental value). All other functionals underestimate the reaction energy, where optB88-vdW, optPBE-vdW, and the PBE-based functionals underestimate the reaction energy by ~10 kJ/mol or less, while the remaining functionals underestimate the reaction energy by ~20-30 kJ/mol. To avoid referencing energies of gas-phase radicals, we also report the reaction enthalpies for $CH_3I + ½ H_2 \rightarrow CH_4 + ½ I_2$ (see Table A.1). We find that all functionals describe the reaction energy within 5 kJ/mol of the experimental value at standard conditions.[301]

Table A.1: Gas phase reaction enthalpies (ΔH, in kJ/mol) for $CH_3I \rightarrow CH_3 + ½ I_2$ and $CH_3I + ½ H_2 \rightarrow CH_4 + ½ I_2$

Functional	**$CH_3I \rightarrow CH_3 + ½ I_2$ ΔH [kJ/mol]**	**$CH_3I + ½ H_2 \rightarrow CH_4 + ½ I_2$ ΔH [kJ/mol]**
LDA	-199	-65
PW91	-164	-62
PBE	-153	-63
PBE-D2	-156	-63
PBE-D3	-155	-68
PBE-dDsC	-152	-66
PBE-TS	-153	-66
RPBE	-142	-68
RPBE-D2	-146	-67
RPBE-D3	-148	-67
vdW-DF	-142	-68
vdW-DF2	-135	-65
optB86b-vdW	-140	-63
optB88-vdW	-163	-64
optPBE-vdW	-157	-68
BEEF-vdW	-154	-65
Experimental[301]	-163	-63

A.3.3 Comparison to Experimental Measurements

In this section, we compare our calculated results with experimental data from Carey et al.,

who performed calorimetric measurements on the adsorption of CH_3I on Ni(111).[288] These authors present the differential heat of adsorption as a function of coverage, $f(\theta)$. To obtain values that are comparable to the theoretical calculations, we calculate $H(\theta)$, the heat of adsorption at coverage θ, as:

$$H(\theta) = \frac{\int_0^{\theta} f(\theta) d\theta}{\theta} \tag{A.2}$$

Additionally, we rely on experimental data from Carey et al. and use error propagation[302] to assign an experimental error to their obtained measurements.[288]

We classify the density functionals used in our study into three groups: (i) a group that predicts enthalpies of adsorption within the experimental errors, (ii) a group of functionals that lead to errors smaller than the experimental errors ± 20 kJ/mol (a value typically used to describe DFT error[303]), and (iii) a group of functionals with errors larger than the experimental error ±20 kJ/mol.

Molecular adsorption of CH_3I on Ni(111): We start our analysis by considering the adsorption of CH_3I on Ni(111) (shown in Fig. A.3 and Table B.3). We compare theoretical values for the enthalpies of adsorption to the experimental heats of adsorption at a coverage of 1/7 ML and find that only optB88-vdW (+0 kJ/mol error) leads to values within the reported experimental error range of ±6 kJ/mol (see Fig. A.3). Several other functionals (PBE-D2 (-11 kJ/mol error), PBE-D3 (+11 kJ/mol error), PBE-dDsC (+14 kJ/mol error), RPBE-D2 (-19 kJ/mol error), optB86b-vdW (-13 kJ/mol error), and optPBE-vdW (+11 kJ/mol error)) lie within an additional error of ±20 kJ/mol.

Dissociative adsorption of CH_3I on Ni(111): Comparing the proficiency of different functionals in capturing the dissociative adsorption of CH_3I is more complicated (see Fig. A.6 and Table B.6). While calculating *H*(1/25 ML) (-270±8 kJ/mol) and *H*(1/7 ML) (-253±8 kJ/mol) is straightforward using the equations reported by Carey et al.,[288] it is more complex to do so for a coverage of 1/6 ML. Since the long-term sticking probabilities at this coverage are 0,[288] accurately measuring the differential heat of adsorption at this coverage is impossible. To arrive at an estimate of this value, we assume that CH_3I adsorption can be described with an Arrhenius expression where the lifetime of CH_3I adsorbed on the surface is 60 ms (below the time resolution of heat of adsorption measurements of 120 ms) and the vibrational prefactor is 10^{-14} s^{-1}.[304] These assumptions lead to a calculated differential heat of adsorption of -40 kJ/mol for CH_3I at 1/6 ML coverage at 160 K, in good agreement with the formation of multilayers reported for physisorption[288]. We assume a linear decrease in adsorption strength between coverages of 1/7 ML and 1/6 ML and find an integral heat of adsorption of -235±8 kJ/mol for the dissociative adsorption of CH_3I at 1/6 ML.

Comparing these values to our theoretical predictions shows that, for a coverage of 1/25 ML, only two functionals (PBE-D2 (-6 kJ/mol error) and optB86b-vdW (+7 kJ/mol error)) lead to an enthalpy of adsorption at 160 K within the experimental error bars of ±8 kJ/mol. Four more functionals lie within an additional error ±20 kJ/mol (PBE-D3 (+9 kJ/mol error), PBE-TS (-23 kJ/mol error), RPBE-D2 (+11 kJ/mol error), and RPBE-D3 (+13 kJ/mol error); see Fig. A.6, green bars).

For a coverage of 1/7 ML, PBE-D2 (-7 kJ/mol error) and RPBE-D3 (+4 kJ/mol error) are accurate within experimental error. Furthermore, the PBE-D3 (+11 kJ/mol error), PBE-TS (-16 kJ/mol error), RPBE-D2 (-19 kJ/mol error), and optB86b-vdW (+11 kJ/mol error) functionals are

accurate within an additional DFT error of ±20 kJ/mol.

For a coverage of 1/6 ML, no functional is accurate within experimental error, while six functionals lie within an additional error of ±20 kJ/mol (PBE-D3 (-11 kJ/mol error), PBE-dDsC (+24 kJ/mol error), RPBE-D3 (-19 kJ/mol error), optB88-vdW (-12 kJ/mol error), optB88-vdW (+10 kJ/mol error), and optPBE-vdW (+28 kJ/mol error)).

For all three coverages, several functionals (LDA (-30 kJ/mol to -59 kJ/mol), PW91 (-63 kJ/mol to +84 kJ/mol), PBE (+65 kJ/mol to +87 kJ/mol), RPBE (+115 kJ/mol to +136 kJ/mol), vdW-DF (+75 kJ/mol to +100 kJ/mol), vdW-DF2 (+89 kJ/mol to +120 kJ/mol), and BEEF-vdW (+69 kJ/mol to +92 kJ/mol)) show errors larger than the experimental error combined with the typically assumed DFT error range of ±20 kJ/mol.[303] Such large errors can lead to significant errors in the quantitative description of reaction thermodynamics or reaction kinetics. When using a microkinetic model, for example, large errors would vastly influence predicted outcomes, such as surface coverages, reaction rates, and selectivities. This observation is alarming, as some of these functionals are among the most used for studying surface-catalyzed reactions.

One potential explanation for the large errors in the DFT calculations is that the functionals do not properly capture dispersion interactions encountered during molecular adsorption. Yet, if subsequent reaction steps were described accurately by the applied functional, quantitative errors for molecular adsorption would be far less concerning. In this scenario, the bulk of a reaction network would be described accurately, and only adsorption energies would need to be corrected. To explore this possibility, we studied the dissociation enthalpy of CH_3I on the Ni(111) surface, i.e., the difference in enthalpy between molecularly and dissociatively adsorbed CH_3I at a coverage of 1/7 ML, and compared the results to experimental values. Numerical values (Table B.9) and a

graphical representation (Fig. B.3) are shown in Section B.5 of Appendix B. We find that only the LDA functional (-4 kJ/mol) quantitatively captures the dissociation enthalpy of adsorbed CH_3I to adsorbed CH_3 and I while all other functionals underestimate this quantity. Furthermore, the PBE-D2 (+14 kJ/mol), PBE-D3 (+21 kJ/mol), RPBE-D2 (+18 kJ/mol), RPBE-D3 (+14 kJ/mol) and optB86b-vdW (+23 kJ/mol) functionals are accurate within an additional ±20 kJ/mol on top of the experimental error. The largest errors are found for the vdW-DF2 (+64 kJ/mol), RPBE (+58 kJ/mol), vdW-DF (+58 kJ/mol) and BEEF-vdW (+53 kJ/mol) functionals. However, these error ranges are smaller than those for the dissociative adsorption from the gas phase (the largest error is +134 kJ/mol for the RPBE functional). This observation indicates that quantitative errors for dissociative adsorption of CH_3I from the gas phase on Ni(111) are only in part caused by challenges in describing the molecular adsorption of CH_3I to this surface.

Aside from these large quantitative errors, our model also fails to correctly predict the qualitative features of the experimental measurements. Carey et al. observed a modest increase in adsorption strength up to a coverage of 1/7 ML, followed by a steep decrease in the adsorption strength at higher coverages.[288] These authors attribute this observed behavior to a favorable 1/7 ML adsorption geometry. In the calculations presented here, the 1/7 ML adsorption structure is less stable than the 1/6 ML structure for all functionals except vdW-DF2. It is not obvious what phenomena lead to the differences between the experimentally observed and the theoretically calculated behaviors. A possible reason for explaining these inconsistencies is the following: While we studied all possible co-adsorption configurations of CH_3 and I on the $\sqrt{7}\times\sqrt{7}$ Ni(111) surface unit cell to determine the most stable configuration, the structure attained in experiments might have a longer-range periodicity than the one captured in this unit cell and yet have the same

total coverage of ~1/7 ML.

Adsorption of either CH_3 or I on Ni(111): While Carey et al. only measured the molecular and dissociative adsorption of CH_3I, they also combined thermochemical cycles with literature data to extrapolate their measurements to determine heats of adsorption for both CH_3 and atomic I on Ni(111).[288] Importantly, lateral interactions between co-adsorbed species can significantly influence the adsorption energetics, particularly at higher coverages. Therefore, their analysis focused on a coverage of 1/25 ML to reduce interaction effects. To better understand the ability of the studied functionals to describe the adsorption behavior of both CH_3 and I, we further compared the individual adsorption strengths for each species on Ni(111) at this coverage. Using this approach, we expect to identify which functionals correctly describe the adsorption behavior of these two adsorbed species on Ni(111).

For CH_3 adsorption on Ni(111) at a coverage of 1/25 ML, we see that several functionals (PBE-D2 (-6 kJ/mol), PBE-D3 (-2 kJ/mol), PBE-dDsC (+13 kJ/mol), PBE-TS (-12 kJ/mol), RPBE-D2 (+5 kJ/mol), RPBE-D3 (+8 kJ/mol), optB86b-vdW (-8 kJ/mol), and optB88-vdW (+10 kJ/mol); DFT error with respect to the experimental value in parentheses) predict enthalpies of adsorption within the experimental error of ±13 kJ/mol [288] (see Fig. A.4, green bars; tabulated data in Table B.4). Furthermore, two functionals predict values within an additional error of ±20 kJ/mol (PW91 (+22 kJ/mol error) and optPBE-vdW (+24 kJ/mol error).

For atomic I adsorption on Ni(111) at a 1/25 ML coverage (see Fig. A.5, green bars, Table B.5), a different set of functionals (PW91 (+2 kJ/mol error), PBE (+4 kJ/mol error), and BEEF-vdW (+7 kJ/mol error)) predict values within the experimental error of ±9 kJ/mol.[288] Other functionals (PBE-D3 (-27 kJ/mol), PBE-dDsC (-14 kJ/mol), RPBE (+27 kJ/mol), RPBE-D3 (-27

kJ/mol), vdW-DF (+13 kJ/mol), vdW-DF2 (+27 kJ/mol), optB88-vdW (-21 kJ/mol), and optPBE-vdW (-11 kJ/mol); DFT error with respect to experimental value in parentheses) predict values within an additional error of ±20 kJ/mol.

A.3.4 Dissociative Adsorption of CH_4 on Ni(111)

Because it is the rate-controlling step in, e.g., methane steam reforming on Ni catalysts under specific reaction conditions,[289] we hereby explore how each density functional affects the enthalpy change during the dissociative adsorption of CH_4 on Ni(111). To estimate the dissociative adsorption enthalpy of CH_4 at the infinite-separation limit for the products, we used our calculated data for CH_3 adsorption on the 5×5 surface (see Fig. A.4, green bars) and calculated the respective data for the adsorption enthalpy of H on Ni(111) at 160 K (see Fig. A.7A).

Adsorption of H on Ni(111): We calculated the heat of adsorption for H on Ni(111) at coverages of 1/25 ML, 1/7ML, and 1/6 ML (see Fig. A.7A and Table B.7). Importantly, the calculated heats of adsorption show a variation of less than 3 kJ/mol across the studied range of coverages, indicating that coverage effects for H adsorption are small for coverages of 1/6 ML or lower. We find that all functionals studied predict that H prefers to adsorb at an fcc site and that all functionals, except the LDA functional, lead to an enthalpy of adsorption of H on Ni(111) at 160 K of -275±18 kJ/mol. Only the LDA functional leads to a significantly increased enthalpy of adsorption (~-326 kJ/mol). Experimental measurements show a heat of adsorption of -47 kJ/mol for the dissociative adsorption of H_2 on Ni(111).[305] Accounting for the enthalpy of formation of H_2 in the gas phase (-216 kJ/mol),[306] this leads to an experimental value of -263 kJ/mol for the heat of adsorption of H on Ni(111) at 160 K. Three functionals (RPBE (+4 kJ/mol), vdW-DF2 (+0 kJ/mol), and BEEF-vdW (+0 kJ/mol)) show chemical accuracy with respect to the experimental

value (i.e., an error smaller than 4.2 kJ/mol). Furthermore, the remaining functionals, with the exception of LDA (+63 kJ/mol error), optB86b-vdW (+30 kJ/mol error), and optB88-vdW (+25 kJ/mol error), predict enthalpies of adsorption that lie within an additional error of ±20 kJ/mol on top of the experimental error, which is the typically accepted error of DFT.[303]

Dissociative adsorption of CH_4 on Ni(111): Next, we calculated the enthalpy for the dissociative adsorption of CH_4 as adsorbed CH_3 and atomic H on the (5×5) surface unit cell of Ni(111) at 160 K and at the infinite-separation limit ($\Delta H(CH_4, \infty, T = 160\ K)$):

$$\Delta H(CH_4, \infty, T = 160\ K) = H^{slab+CH_3}(T = 160\ K) + H^{slab+H}(T = 160\ K) - \quad \text{(A.3)}$$

$$-2H^{slab}(T = 160\ K) - H^{CH_4(g)}(T = 160\ K)$$

Here, *H* represents the enthalpy at 160 K for the system denoted by the superscript (*slab* for the clean metal slab, *slab+CH₃* for one CH_3 adsorbed on the slab, *slab+H* for one H atom adsorbed on the slab, and *CH₄(g)* for a gas-phase CH_4 molecule) after applying both zero-point vibrational energy and finite-temperature corrections. The results of this analysis are provided in Fig. A.7B, and numerical values are given in Table B.8. As expected from the data for CH_3 adsorption, we find a large range of enthalpy changes for the dissociative adsorption of CH_4, ranging from highly exothermic (LDA: -70 kJ/mol) to highly endothermic (vdW-DF2: +51 kJ/mol). Three functionals (PBE-D3 (-3 kJ/mol error), PBE-D2 (+4 kJ/mol error), and optB86b-vdW (+4 kJ/mol error)) accurately predict the experimental value of -43 kJ/mol reported by Carey et al..[288] The PBE-dDsC (+18 kJ/mol error), PBE-TS (-11 kJ/mol error), RPBE-D2 (+5 kJ/mol error), and RPBE-D3 (+5 kJ/mol error) functionals all lie within an additional error of ±20 kJ/mol on top of the experimental value. These trends strongly agree with those established for the adsorption of CH_3 alone on

Ni(111), suggesting that accurately capturing the adsorption properties of CH_3 on Ni(111) is critical to accurately describe the dissociative adsorption of CH_4 on Ni(111).

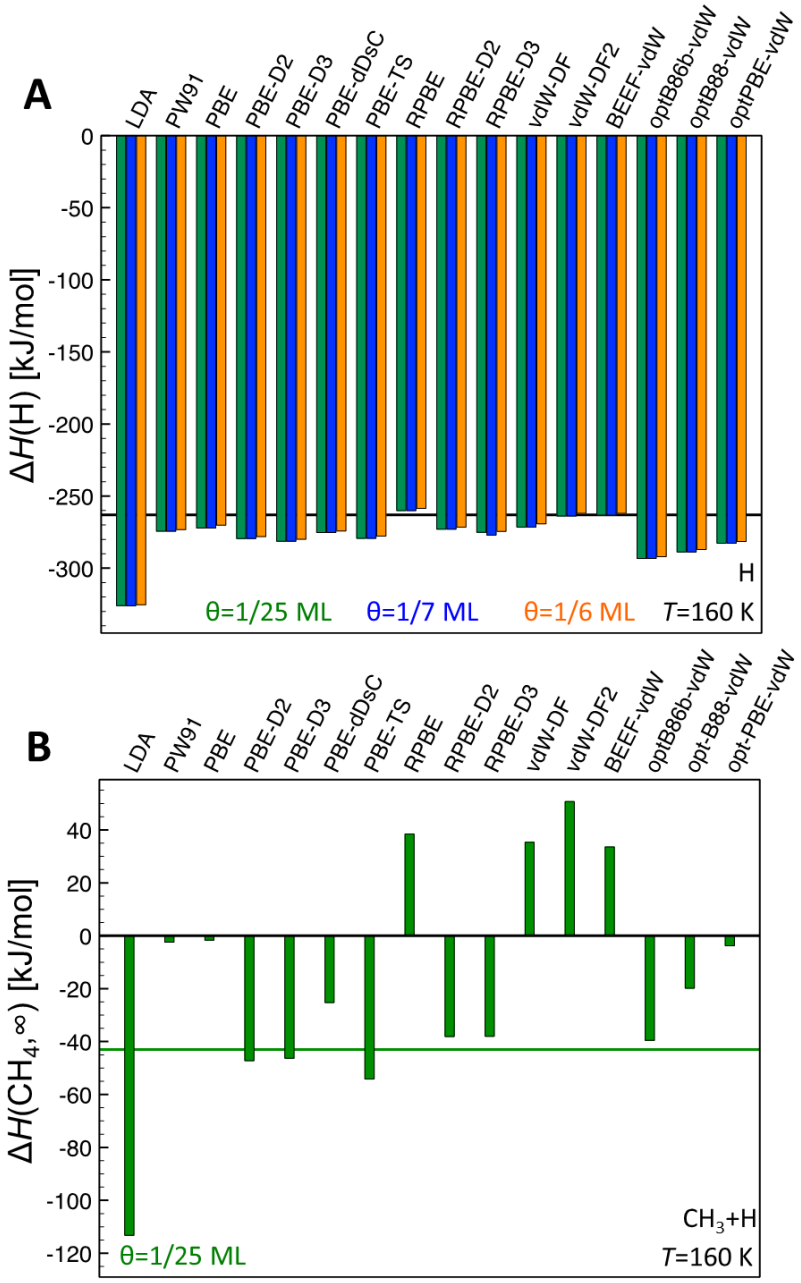

Figure A.7: (A) Enthalpy of adsorption for atomic H ($\Delta H(\mathrm{H})$) on Ni(111) at 160 K calculated using different density functionals at a coverage of 1/25 ML (green bars), 1/7 ML (blue bars), and 1/6 ML (orange bars). The experimental value (from references [305] and [306]) is a non-calorimetric based estimate and marked by a black horizontal line. **(B)** The enthalpy change for the dissociative adsorption of gas-phase CH_4 to adsorbed CH_3 and atomic H on Ni(111) at 160 K ($\Delta H(\mathrm{CH_4}, \infty)$) calculated using different density functionals at the infinite-separation limit between adsorbed CH_3 and atomic H. The experimental value of -43 kJ/mol was calculated at a coverage of 1/25 ML and is denoted by a green horizontal line. The data was obtained from reference [288].

3.4 Performance of the adaptively weighted SW method:

Comparisons between experimental work and DFT calculations have shown that different functionals perform very differently for various types of adsorption processes. In the past, large errors have been attributed to how dispersion forces are included in semi-local density functionals. While some of the functionals used in this work include dispersion forces, others are not able to capture them. To address this problem for adsorption on transition-metal surfaces, Hensley *et al.* developed the sigmoid-weighted (SW) method which relies on two different functionals.[307] In their approach, they combined adsorption energies of two different functionals using a weighting function that allowed them to switch between the two functionals. If the chosen weighting function is 0, the adsorption energy will correspond to the RPBE-calculated energy, which should accurately describe chemisorption. Conversely, if the weighting function is 1, the adsorption energy will correspond to the optB86b-vdW (SW-R86) or optB88-vdW (SW-R88) calculated energy, which should accurately describe physisorption. So far, the performance of this method has mainly been evaluated for the CE39 experimental test set,[308] but it has not been tested for a system such as the adsorption of CH_3I or CH_4 on a Ni(111) surface.

In most cases, the SW method will reproduce the values of the underlying functionals. These values have already been discussed in detail in the results section, and we will focus on the question of whether the SW method correctly switches between the functionals. More specifically, we evaluate the switching function for each studied adsorption process (see Table A.2) and see whether it correctly reproduces the adsorption energy with smaller errors with respect to the experiment values.

Indeed, we find that the SW-R86 and SW-R88 switching functionals correctly predict that

opt-B86b and opt-B88 are more suitable than RPBE for modeling the molecular or dissociative adsorption of CH_3I and the adsorption of CH_4. Furthermore, SW-R86 and SW-R88 also predict that RPBE is a more suitable functional for describing H adsorption. However, for the adsorption of I and CH_3, the SW method predicts that RPBE should be used, even though optB86b-vdW and optB88-vdW lead to significantly better agreement with experimental measurements. For both species, SW-R88 incorrectly predicts that RPBE describes CH_3 adsorption best, while SW-R86 prefers a mixture of RPBE and optB86-vdW that shows a larger error with respect to experiments than the optB86-vdW functional alone.

Table A.2: Values of the switching function in the SW method for the adsorption processes studied in this work. For a value of 1, enthalpies of adsorption for the SW method correspond to the optB86b-vdW values (SW-R86) or optB88-vdW values (SW-R88); For a value of 0, enthalpies of adsorption for the SW method correspond to RPBE values.

Adsorbate	**SW-R86**	**SW-R88**
CH_3I, molecular	1	1
CH_3I, dissociative	1	1
CH_3	0.34	0
I	0	0
H	0	0
CH_4	1	1

Overall, the SW method does not improve the description of enthalpies for the adsorption processes on Ni(111) studied here. This shortcoming is related in part to the functionals used in the SW method, which are not among the most accurate methods for describing the adsorption of the studied surface intermediates. Additionally, this method only selects the functional with the smaller error for four out of six adsorption processes studied here. These problems might be addressed by parameterizing the SW method for different functionals, e.g. by choosing functionals based on PBE and using the SW method to include or exclude dispersion corrections. However,

the performance of such a method will need to be thoroughly evaluated in the future.'

3.5 Mean absolute errors of functionals:

To evaluate the overall performance of each functional in describing the chemistries discussed in this paper, we evaluate the mean absolute error (MAE) for each functional (see Fig. A.8, numerical values given in Table B.10). Overall, RPBE-D3 (13 kJ/mol) and PBE-D3 (15 kJ/mol) have the smallest MAEs, but PBE-D2 (18 kJ/mol) and optB86b-vdW (18 kJ/mol) also have MAEs below 20 kJ/mol. These four functionals therefore fall within the ±20 kJ/mol often ascribed to DFT error. Another group of functionals have MAEs smaller than 30 kJ/mol (PBE-dDsC (22 kJ/mol), RPBE-D2 (22 kJ/mol), optB88-vdW (20 kJ/mol), optPBE-vdW (29 kJ/mol), and PBE-TS 27 (kJ/mol)). All other functionals show MAEs larger than 40 kJ/mol.

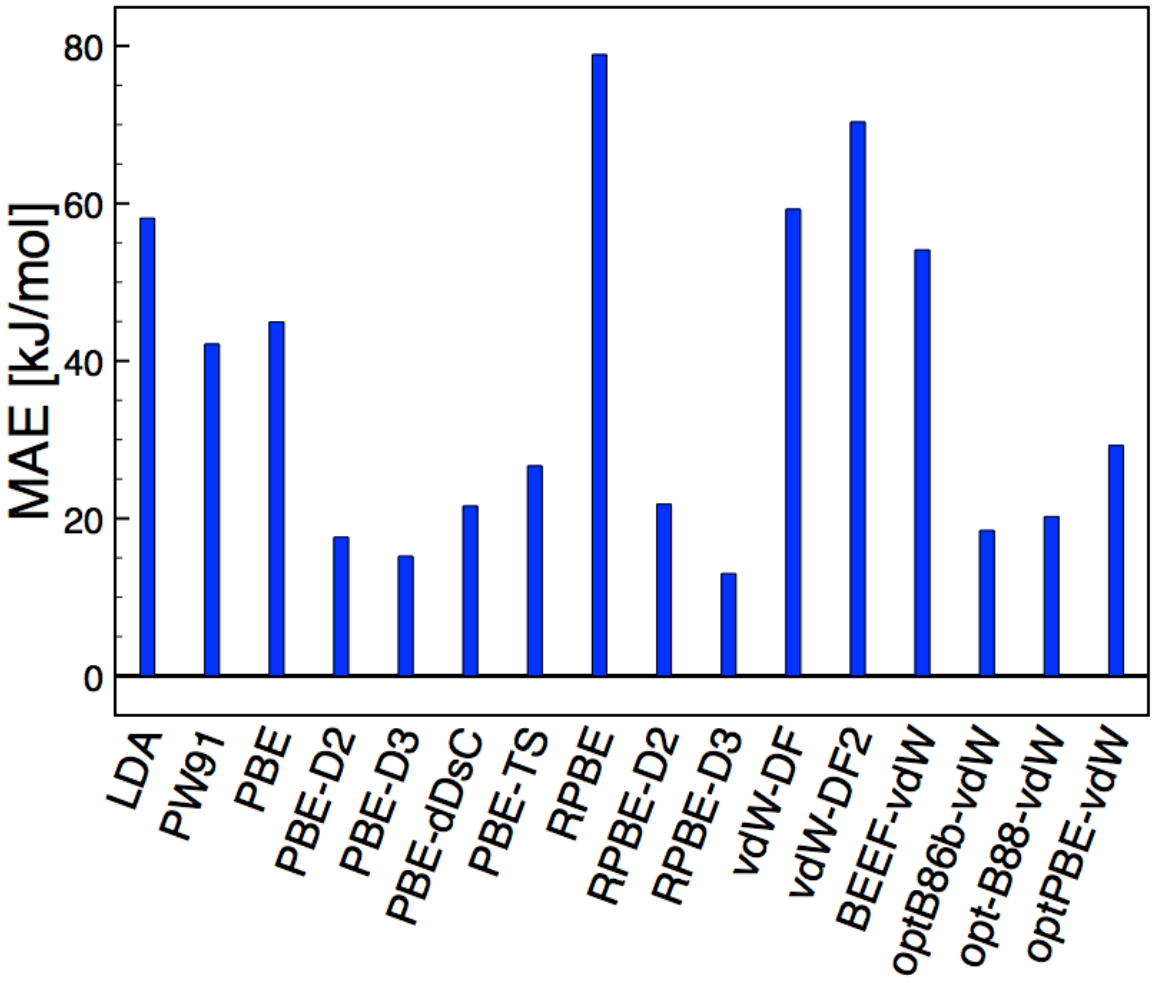

Figure A.8: Mean absolute error (MAE) in enthalpies of adsorption for the six adsorption processes studied in this work.

A.4 Conclusions

In this work, we determined the accuracy of currently available density functionals for describing the thermochemistry of: the molecular and dissociative adsorption of CH_3I, the adsorption of CH_3, I, and H, and the dissociative adsorption of CH_4 on Ni(111). We found that for each adsorption process at least one functional exists that quantitatively reproduces experimental measurements within experimental error. For the molecular adsorption of CH_3I, this is the optB88-vdW functional; for the dissociative adsorption of CH_3I, these are the PBE-D2 and optB86b-vdW functionals; for the adsorption of CH_3, these are the PBE-D2, PBE-D3, PBE-dDsC, RPBE-D2,

RPBE-D3, optB86b-vdW, and optB88-vdW functionals; for the adsorption of I, these are the PW91, PBE, and BEEF-vdW functionals; for the adsorption of H, these are the RPBE, vdW-DF2, and BEEF-vdW functionals; and for the dissociative adsorption of CH_4, these are the PBE-D2, PBE-D3, and optB86b-vdW functionals. However, not a single functional of those evaluated here can describe all adsorption processes accurately within the respective experimental error. Only when an additional error of ±20 kJ/mol is considered on top of the experimental error, the PBE-D3 and RPBE-D3 functionals are accurate for all adsorption processes studied, whereas the PBE-D2, PBE-dDsC, and RPBE-D2 functionals are accurate for five out of the six adsorption processes considered. Similar conclusions are reached when focusing on the mean absolute error (MAE) for each functional. PBE-D2, PBE-D3, RPBE-D3, and optB86b-vdW are the only functionals with MAEs below 20 kJ/mol. Another group of functionals have MAEs smaller than 30 kJ/mol (PBE-dDsC, RPBE-D2, optB88-vdW, optPBE-vdW, and PBE-TS). All other functionals have MAEs larger than 40 kJ/mol.

These results indicate that density functionals could exist for describing the thermochemistry of a specific adsorption process accurately. However, identifying a specific functional that accurately describes the thermochemistry of several elementary processes that could be relevant to a specific catalytic reaction might be a significant challenge. To select the most suitable functional for developing an accurate theoretical model, it is therefore important to critically evaluate the performance of various functionals for specific catalytic reactions. Accordingly, accurate single-crystal adsorption microcalorimetry experiments will continue to play an important role for benchmarking density functionals.

Appendix: B Supplementary Materials for 'Comparing the Performance of Density Functionals in Describing the Adsorption of Atoms and Small Molecules on Ni(111)'[†*]

B.1 PBE Calculations without Enthalpic Corrections

To compare with experimental data, calculated adsorption enthalpies at 160K are reported in the main manuscript. However, DFT literature typically reports adsorption energies directly obtained from static DFT calculations at 0 K.[286,287,300,309] These numbers are not directly comparable to data reported in the main text, even though such a comparison would be desirable. In this section, we report the structures and adsorption energies for CH_3 and I calculated at the PBE level without including zero-point energy or finite-temperature corrections. These results can be directly compared to computational data reported in the literature.

We first determine the preferred binding site and orientation of CH_3 on the $\sqrt{7}x\sqrt{7}$ surface unit cell. Following Che et al.,[300] we examined all possible high-symmetry sites (fcc, hcp, top, and bridge) on Ni(111) and several high-symmetry rotational structures for CH_3 (the exact configurations are shown in the main text, Fig. A.1A). All numerical values for the relative adsorption energies with respect to the most stable structures are given in Table B.1.

---

[*]Adapted from **"Comparing the performance of density functionals in describing the adsorption of atoms and small molecules on Ni(111)"**, F. Göltl[‡], E. A. Murray[‡], S. A. Tacey, S. Rangarajan, and M. Mavrikakis ([‡] equal contribution), *Surface Science* **700**, 121675 (2020).

Table B.1: Relative stability (ΔE) of CH_3 and I adsorbed at the high-symmetry sites of Ni(111) in a $\sqrt{7}\times\sqrt{7}$ surface unit cell. An entry of zero for ΔE corresponds to the most stable adsorption structure (using the PBE functional). Structures are shown in Figure A.1 of the main text. n.s. stands for not stable.

CH_3		**I**	
Site	ΔE [kJ/mol]	Site	ΔE [kJ/mol]
top.1	31.1	top	47.3
top.2	31.2	bridge	n.s.
top.3	31.3	fcc	0.0
bridge.1	19.9	hcp	2.8
bridge.2	n.s.		
bridge.3	17.7		
fcc.1	0.0		
fcc.2	38.2		
hcp.1	3.1		
hcp.2	38.9		

In agreement with the literature, the PBE functional predicts that the fcc and hcp sites are the most stable for adsorbed CH_3 and I.[286,287,300,309] with the fcc position being slightly favored over the hcp for both adsorbates. The most energetically favorable adsorption structure for CH_3 has its H atoms aligned with the top positions of the surrounding Ni atoms for both hollow sites, with an adsorption energy (without zero-point energy or finite-temperature corrections) of -183.8 kJ/mol in the fcc site and -180.7 kJ/mol in the hcp site. CH_3 adsorption to the bridge and top states of CH_3 is 20 kJ/mol and 31 kJ/mol less stable than to the fcc site, respectively. While these relative values agree well with the study by Che et al.,[300] who used the PW91 functional for their adsorption energy calculations, the adsorption energy of CH_3 is about 15 kJ/mol more positive than the reported values. These differences could be rooted in the differences in the computational setup, the choice of unit cell, or the pseudopotentials used.

We further calculate that I prefers to bind to fcc and hcp sites, with an adsorption energy of

-173.8 kJ/mol and -171.0 kJ/mol, respectively (see Fig. A.1B in the main manuscript and Table B.1). The reference state for calculating the CH_3 and I adsorption energies is gas-phase CH_3 and gas-phase I_2, respectively.

B.2 Adsorption Site Preference for Different Functionals

The ability of a functional to predict the correct adsorption site is critical in evaluating its performance. In this context, the CO adsorption puzzle,[277] i.e. the prediction of the correct adsorption sites of CO on metal surfaces, is one of the most famous shortcomings of semi-local GGA functionals. For the adsorption of CH_3 on Ni(111), the preference for the fcc site is well-established experimentally,[310] and we probe whether this property is well-reproduced by the different functionals used in this work. In the following, we investigate the adsorption site preference for CH_3 between top and fcc sites on Ni(111) at a coverage of 1/7 ML. These structures are shown Fig. A.1A of the main text. In this context, we calculate $\Delta E^{top\text{-}fcc}$, the energetic difference between CH_3 in the top and fcc positions, as:

$$\Delta E^{top-fcc} = E^{CH_3-top} - E^{CH_3-fcc} \quad \text{(B.1)}$$

where E^{CH_3-top} is the DFT-calculated energy of CH_3 in the top position and E^{CH_3-fcc} is the DFT-calculated energy for CH_3 in the fcc position.

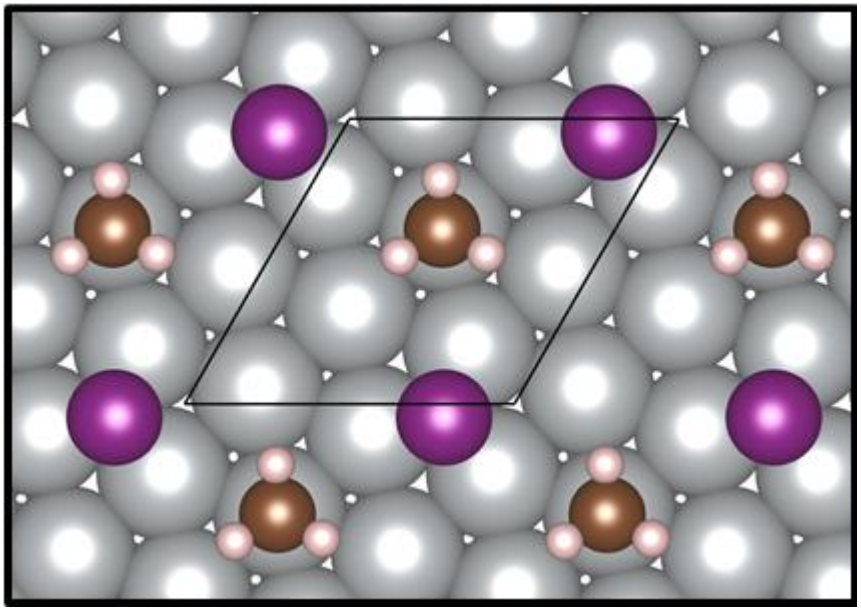

Figure B.1: Adsorption structure for the dissociative adsorption of CH_3I with CH_3 in the top position and I in the fcc position for a coverage of 1/7 ML. In the atomistic representation, Ni atoms are shown in silver, C atoms in brown, H atoms in white, and I atoms in magenta. The unit cell is shown by the black lines.

For CH_3 adsorption (red bars in Fig. B.2), we find significant variations in the preference for adsorption structures between functionals. Almost all functionals predict the experimentally verified adsorbed fcc position as most stable. Only the vdW-DF2 functional prefers the top site over the fcc site. Additionally, the numerical values for $\Delta E^{top\text{-}fcc}$ vary significantly. The LDA functional shows the largest preference for the fcc position (+67 kJ/mol for CH_3), while the vdW-DF2 functional prefers the top site over the fcc site by -4 kJ/mol for CH_3. In this context especially, the disagreement between the vdW-DF2 functional and experiments in terms of adsorption site preference is concerning and indicates that this functional might not be ideal to describe the studied adsorption process.

When comparing the relative stability of co-adsorbed CH_3 and I between an fcc/hcp structure (see Fig. 2B in the main text) and a top/fcc structure (see Fig. B.1), we find similar trends in adsorption site preference as with adsorption of CH_3 (see blue bars in Fig. B.2).

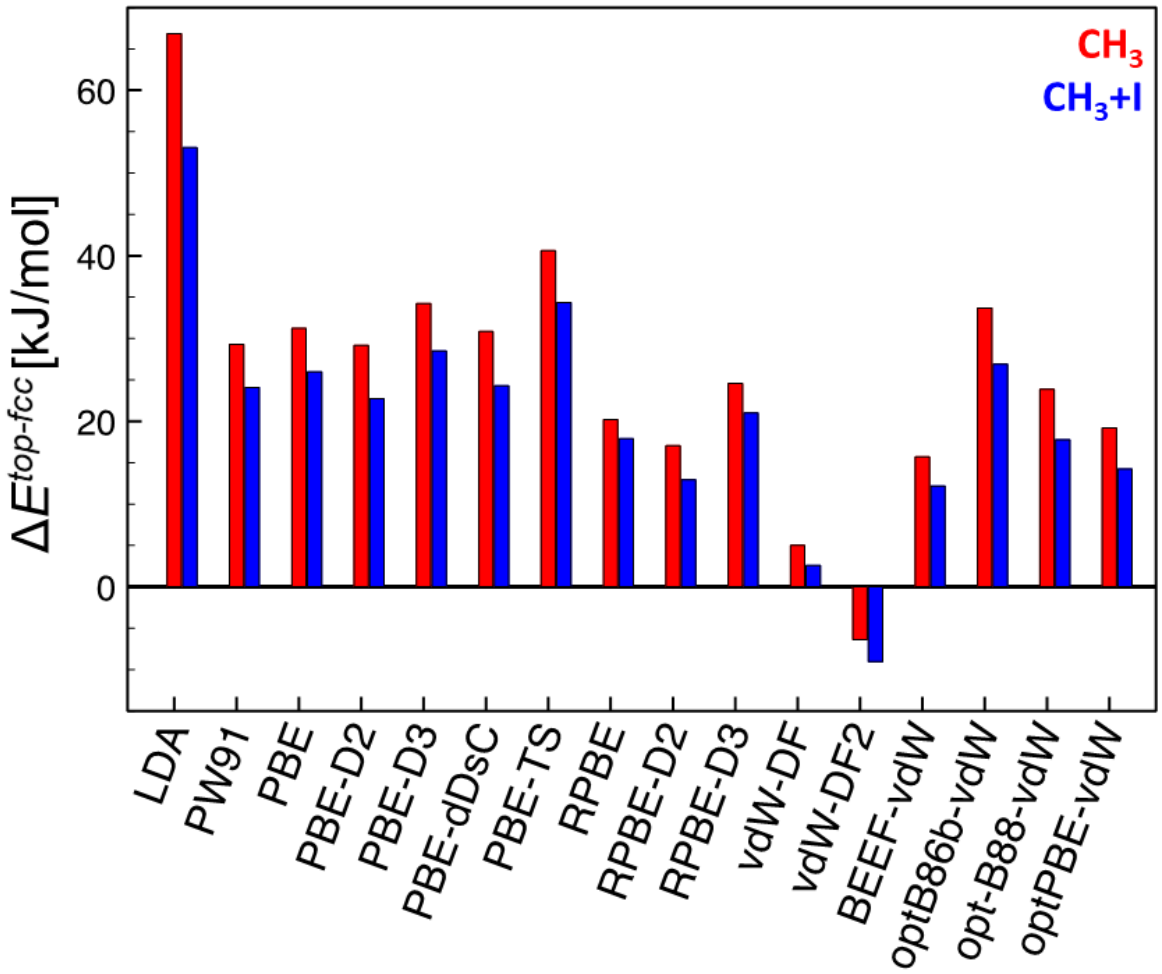

Figure B.2: Energetic differences $\Delta E^{top-fcc}$ between CH_3 bound to a top site and to an fcc site calculated using different density functionals for CH_3 adsorption (red bars) and the dissociative adsorption of CH_3I to adsorbed CH_3 and I (blue bars) at a surface coverage of 1/7 ML.

B.3 Lattice Constants for Ni

Table B.2: DFT-calculated minimum energy lattice constants (*a*) and error with respect to experimental values (Δa)[123] for bulk Ni using different density functionals.

Functional	***a* [Å]**	**Δa [%]**
LDA	3.428	-3
PW-91	3.523	0
PBE	3.520	0
PBE-D2	3.462	-2
PBE-D3	3.479	-1
PBE-dDsC	3.498	-3
PBE-TS	3.426	-3
RPBE	3.545	+1
RPBE-D2	3.444	-2
RPBE-D3	3.465	-2
vdW-DF	3.569	+1
vdW-DF2	3.608	+2
BEEF-vdW	3.539	+1
optB86b-vdW	3.484	-1
optB88-vdW	3.507	0
optPBE-vdW	3.526	0
Experimental[123]	**3.524**	

B.4 Numerical Values for Enthalpies of Adsorption

Table B.3: Enthalpy of molecular adsorption (ΔH) for CH_3I on Ni(111) at 160 K in a $\sqrt{7}\times\sqrt{7}$ surface unit cell. Energy reference state is CH_3I in the gas phase.

Functional	**ΔH[kJ/mol]**
LDA	-129.8
PW91	-51.2
PBE	-48.3
PBE-D2	-115.2
PBE-D3	-104.5
PBE-dDsC	-79.8
PBE-TS	-139.5
RPBE	-16.2
RPBE-D2	-131.0
RPBE-D3	-105.2
vdW-DF	-53.9
vdW-DF2	-47.9
BEEF-vdW	-56.3
optB86b-vdW	-106.8
optB88-vdW	-93.8
optPBE-vdW	-83.0
Experimental [288]	**-93.8±6**

Table B.4: Enthalpy of adsorption (ΔH) of CH_3 on Ni(111) at 160 K using different unit cells and different density functionals. The most stable site is listed for comparison. Energy reference state is CH_3 in the gas phase.

		ΔH [kJ/mol]		
Functional	**Site**	**2×3**	**√7×√7**	**5×5**
LDA	fcc	-295.0	-295.2	-301.3
PW91	fcc	-189.8	-190.5	-194.4
PBE	fcc	-177.6	-177.5	-182.9
PBE-D2	fcc	-217.1	-217.7	-221.7
PBE-D3	fcc	-214.1	-214.7	-218.4
PBE-dDsC	fcc	-197.9	-199.2	-203.3
PBE-TS	fcc	-222.6	-222.7	-228.4
RPBE	fcc	-141.4	-142.5	-146.4
RPBE-D2	fcc	-206.7	-207.6	-210.8
RPBE-D3	fcc	-204.5	-205.4	-208.2
vdW-DF	fcc	-150.8	-151.7	-154.5
vdW-DF2	top	-140.4	-141.8	-140.2
optB86b-vdW	fcc	-151.6	-152.7	-155.4
optB88-vdW	fcc	-219.4	-219.9	-223.9
optPBE-vdW	fcc	-201.1	-201.7	-206.1
BEEF-vdW	fcc	-188.0	-188.8	-192.1
Experimental [288]				**-216±13**

Table B.5: Enthalpy of adsorption (ΔH) for I on Ni(111) at 160 K using different unit cells and density functionals. The most stable site is fcc in all cases. Energy reference state is $\frac{1}{2}I_2$ in the gas phase.

		ΔH [kJ/mol]		
Functional	**Site**	**2×3**	**√7×√7**	**5×5**
LDA	fcc	-232.1	-226.4	-239.2
PW91	fcc	-176.0	-171.3	-181.9
PBE	fcc	-174.4	-169.3	-179.8
PBE-D2	fcc	-220.2	-214.1	-223.5
PBE-D3	fcc	-208.0	-202.3	-210.9
PBE-dDsC	fcc	-192.2	-187.9	-198.1
PBE-TS	fcc	-229.4	-223.8	-233.5
RPBE	fcc	-152.2	-147.1	-157.0
RPBE-D2	fcc	-228.2	-221.9	-229.7
RPBE-D3	fcc	-209.5	-203.1	-210.6
vdW-DF	fcc	-169.1	-163.1	-171.5
vdW-DF2	fcc	-154.7	-148.7	-157.4
BEEF-vdW	fcc	-174.9	-169.2	-177.5
optB86b-vdW	fcc	-212.2	-206.3	-215.9
optB88-vdW	fcc	-201.4	-199.7	-205.3
optPBE-vdW	fcc	-192.0	-186.1	-195.0
Experimental [288]				**-184±9**

Table B.6: Enthalpy of dissociative adsorption (ΔH) of CH_3I on Ni(111) at 160 K using different unit cells and a variety of density functionals. The most stable site is listed for comparison. Energy reference state is CH_3I in the gas phase.

		***ΔH* [kJ/mol]**		
Functional	**CH_3/I Site**	**2×3**	**√7×√7**	**5×5**
LDA	fcc/hcp	-294.0	-293.3	-325.8
PW91	fcc/hcp	-171.6	-170.4	-197.3
PBE	fcc/hcp	-169.7	-167.5	-194.5
PBE-D2	fcc/hcp	-264.0	-260.7	-275.3
PBE-D3	fcc/hcp	-246.3	-242.7	-260.5
PBE-dDsC	fcc/hcp	-211.2	-210.9	-234.3
PBE-TS	fcc/hcp	-274.0	-269.8	-292.6
RPBE	fcc/hcp	-120.3	-118.3	-146.4
RPBE-D2	fcc/hcp	-276.4	-272.7	-280.2
RPBE-D3	fcc/hcp	-253.9	-250.3	-256.8
vdW-DF	fcc/hcp	-159.9	-155.9	-170.0
vdW-DF2	top/hcp	-146.3	-142.5	-149.6
BEEF-vdW	fcc/hcp	-165.9	-162.5	-178.4
optB86b-vdW	fcc/hcp	-246.6	-242.9	-262.3
optB88-vdW	fcc/hcp	-224.8	-221.2	-239.4
optPBE-vdW	fcc/hcp	-206.9	-203.1	-218.7
Experimental [288]		**-234.9±8**	**-253.3±8**	**-269.9±8**

Table B.7: Enthalpy of adsorption (ΔH) of atomic H on Ni(111) at 160 K calculated in different surface unit cells using different density functionals. Energy reference state is gas-phase atomic H.

		ΔH [kJ/mol]		
Functional	**Site**	**2×3**	**√7×√7**	**5×5**
LDA	fcc	-325.3	-325.7	-326.1
PW91	fcc	-273.3	-274.1	-274.4
PBE	fcc	-270.2	-270.9	-272.1
PBE-D2	fcc	-278.1	-278.8	-279.4
PBE-D3	fcc	-280.0	-280.9	-281.4
PBE-dDsC	fcc	-274.2	-274.6	-275.3
PBE-TS	fcc	-277.7	-278.6	-279.3
RPBE	fcc	-258.6	-259.2	-260.0
RPBE-D2	fcc	-271.6	-272.5	-273.0
RPBE-D3	fcc	-274.5	-275.5	-275.2
vdW-DF	fcc	-269.2	-270.8	-271.5
vdW-DF2	fcc	-262.0	-262.6	-263.9
optB86b-vdW	fcc	-262.0	-263.2	-263.2
optB88-vdW	fcc	-292.0	-292.8	-293.3
optPBE-vdW	fcc	-287.0	-287.8	-288.8
BEEF-vdW	fcc	-281.5	-282.3	-282.7
Experimental [123,311]				**-263.0**

Table B.8: Enthalpy of adsorption (ΔH) for the dissociative adsorption of CH_4 on Ni(111) at 160 K on a 5×5 surface unit cell using different density functionals. Energy reference state is CH_4 in the gas phase.

Functional	**ΔH [kJ/mol]**
LDA	-113.2
PW91	-2.5
PBE	-1.7
PBE-D2	-47.2
PBE-D3	-46.3
PBE-dDsC	-25.3
PBE-TS	-54.1
RPBE	38.4
RPBE-D2	-38.1
RPBE-D3	-38.0
vdW-DF	36.3
vdW-DF2	50.7
optB86b-vdW	33.6
optB88-vdW	-39.6
optPBE-vdW	-19.8
BEEF-vdW	-3.8
Experimental [288]	-43.0

B.5 Enthalpy Change Upon the Dissociation of CH_3I to CH_3 and I on Ni(111)

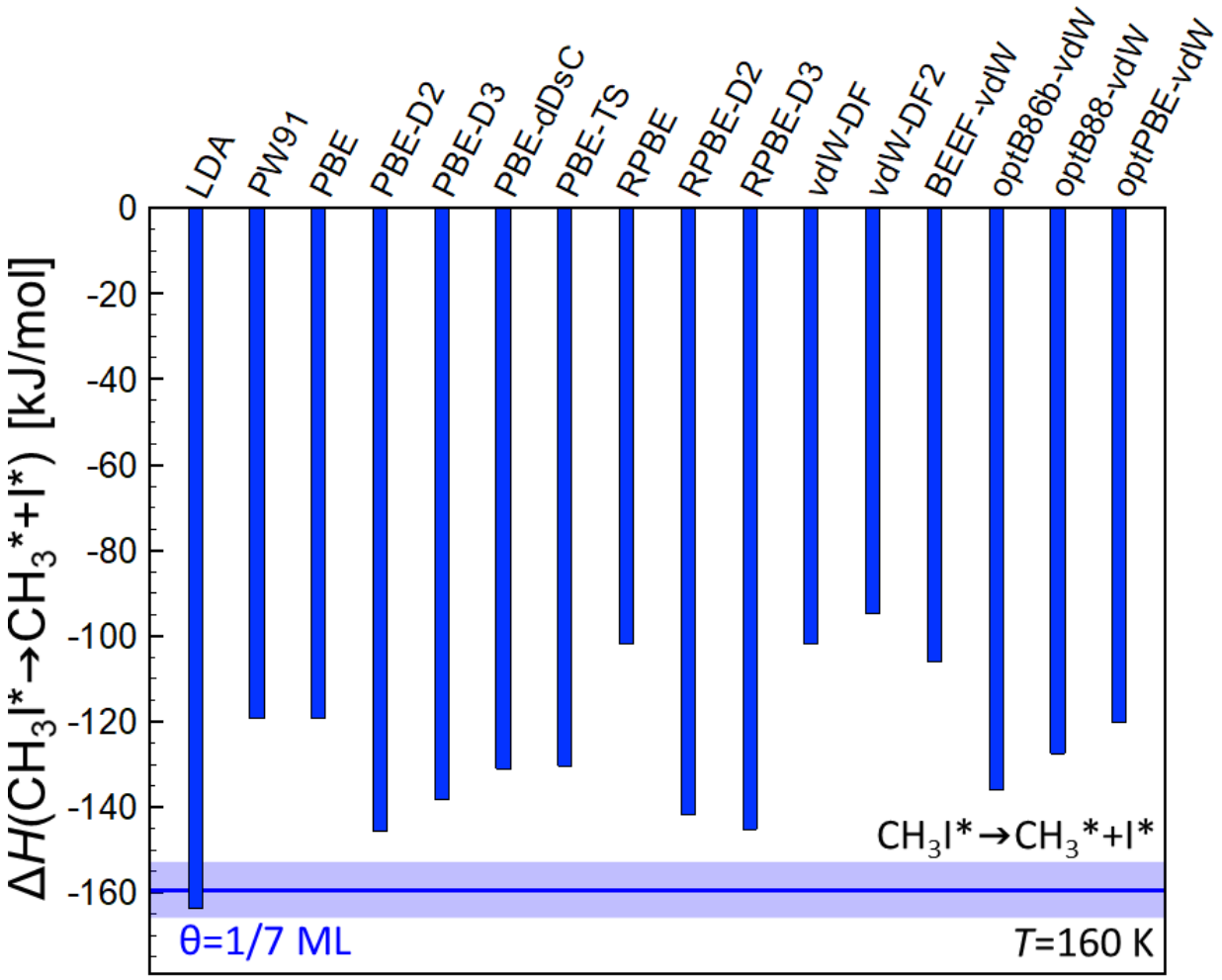

Figure B.3: Enthalpies of dissociation for adsorbed CH_3I to adsorbed CH_3 and I ($\Delta H(CH_3I^* \rightarrow CH_3^* + I^*)$) on Ni(111) at 160 K calculated for different density functionals at a coverage (θ) of 1/7 ML. Vertical blue bars represent the calculated value for each functional. The horizontal blue bars correspond to the experimentally determined heat of adsorption for a coverage of 1/7 ML. The solid line represents the measured value of -160 kJ/mol, while the width of the blue shaded area denotes the experimental error (±8 kJ/mol). Experimental data from ref. 288.

Table B.9: Enthalpy of dissociation (ΔH) for adsorbed CH_3I to adsorbed CH_3 and I on Ni(111) at 160 K in a $\sqrt{7}\times\sqrt{7}$ surface unit cell.

Functional	**ΔH[kJ/mol]**
LDA	-163.6
PW91	-119.2
PBE	-119.2
PBE-D2	-145.5
PBE-D3	-138.2
PBE-dDsC	-131.1
PBE-TS	-130.2
RPBE	-101.7
RPBE-D2	-141.7
RPBE-D3	-145.2
vdW-DF	-102.0
vdW-DF2	-94.7
BEEF-vdW	-106.2
optB86b-vdW	-136.1
optB88-vdW	-127.4
optPBE-vdW	-120.1
Experimental [288]	**-159.5±8**

Table B.10: Mean absolute errors (MAE, kJ/mol) of functionals with respect to experimental values for all adsorption processes studied in this work.

Functional	**MAE [kJ/mol]**
LDA	58
PW91	42
PBE	45
PBE-D2	18
PBE-D3	15
PBE-dDsC	22
PBE-TS	27
RPBE	79
RPBE-D2	22
RPBE-D3	13
vdW-DF	59
vdW-DF2	70
BEEF-vdW	54
optB86b-vdW	19
optB88-vdW	20
optPBE-vdW	29

Appendix: C Supplementary Materials for 'Interfacial Water Structures on Gold Electrodes Lead to Increased Oxygen Reduction Rates in Alkaline Media'

C.1 Supplementary Methods

C.1.1 Static DFT Calculations

For static DFT calculations, we relaxed each structure until the forces acting upon each atom were ≤ 0.01 eV/Å. We calculated the vibrational frequencies of species using a numerical differentiation of forces using a second-order finite difference approach as determined from diagonalizing the mass-weighted Hessian matrix. We fixed all Au atoms in the surface for vibrational frequency calculations.

We calculated the free energy of a species as:

$$G = E_{DFT} + ZPE - TS \tag{C.1}$$

where E_{DFT} is the total energy of a system from DFT, ZPE is the zero-point energy, and S is the vibrational entropy.

C.1.2 AIMD Simulations

Our molecular dynamics simulations utilized the standard Verlet algorithm to propagate the ionic trajectories with a 1 fs time step. We utilized the mass of deuterium for hydrogen to accelerate convergence. All simulations were performed in the NVT ensemble at 298 K, and the ionic temperature was controlled using a Nosé-Hoover thermostat.[129,130] To probe multiple adsorption sites, we initialized a series of simulations where each species was adsorbed in various positions on the Au(100) surface. Each trajectory was typically run for at least a 2 ps equilibrium

period and a production period of at least 10 ps. For systems with multiple binding sites, we used up to 200 ps of molecular dynamics data at a given potential consisting of many trajectories. We then calculated the average free energy of all trajectories for a given system as:

$$G(T) = \langle E \rangle + 1/\beta(\langle exp(\beta \Delta E) \rangle) \quad \text{(C.2)}$$

where β is $1/k_BT$, E is the potential energy and ΔE is the difference between the average potential energy and the energy in each step.

In our AIMD structural analysis, we defined a hydrogen bond with a cutoff of 3.5 Å for the O-O distance and an H-O-O angle less than 30°.[136]

C.1.3 Reference States

In static, unsolvated DFT calculations, we used gas-phase O_2, H_2O, and H_2O_2 for our reference states for species not bound to the Au(100) surface. The energy of each species was calculated in a 14×15×16 Å box. In our static, solvated DFT calculations, we reference gas-phase O_2 and solvated H_2O and H_2O_2 energies. The energy of each species was calculated in a 14 ×15×16 Å box with implicit solvent. In our solvated AIMD analysis, we reference gas-phase O_2 and solvated H_2O and H_2O_2 energies. To calculate the solvated energy of H_2O and H_2O_2, we ran AIMD simulations in a 14.23×14.23×14.23Å box containing 96 water molecules and 97 water molecules + H_2O_2, respectively.

C.2 Supplementary Figures

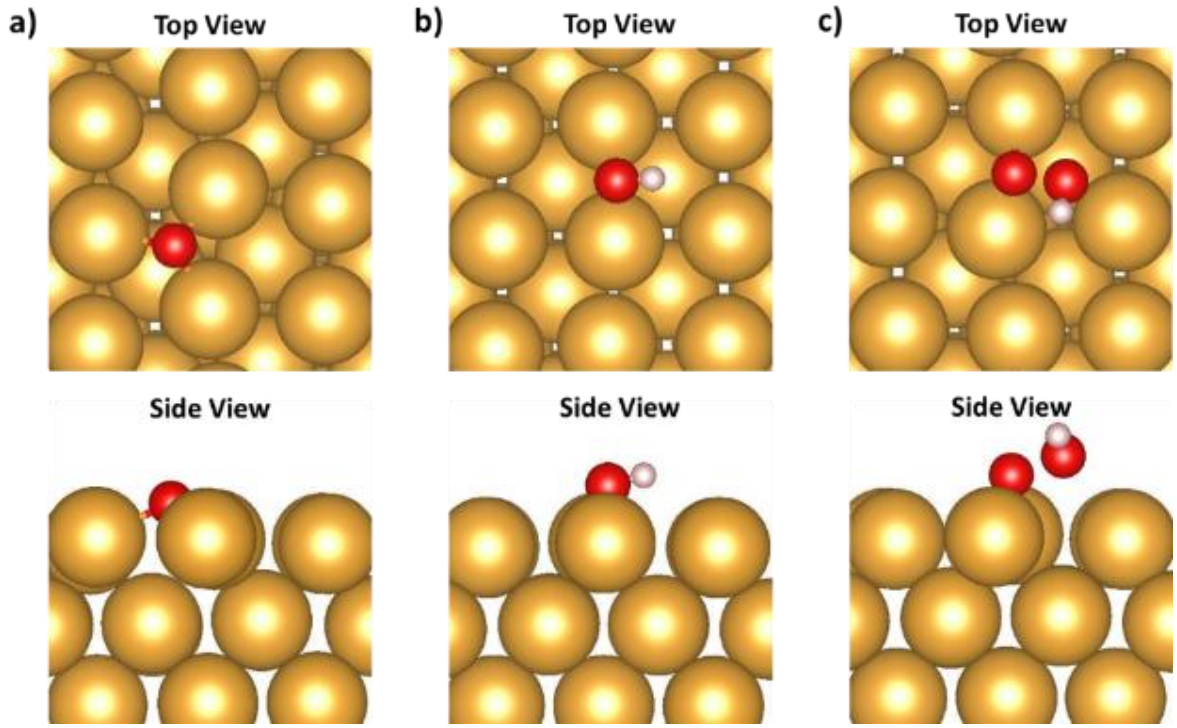

Figure C.1: Top (top image) and side image (bottom image) of most stable adsorption structures on Au(100)-(1×1) based on static DFT calculations including **(a)** O*, **(b)** OH*, and **(c)** OOH*. Au atoms are shown in gold, O is shown in red, and H is shown in white.

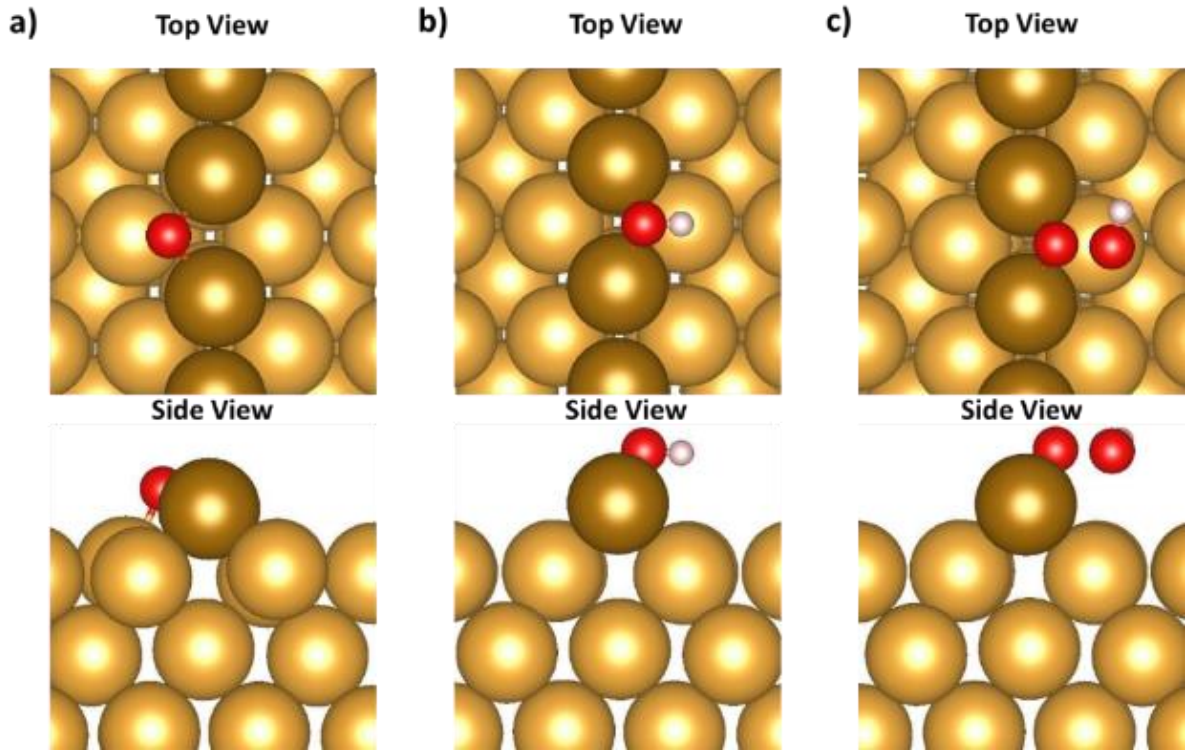

Figure C.2: Top (top image) and side image (bottom image) of most stable adsorption structures on Au(100)-AR based on static DFT calculations including **(a)** O*, **(b)** OH*, and **(c)** OOH*. Au atoms are shown in gold, Au additional row atoms (AR) are shown in brown, O is shown in red, and H is shown in white.

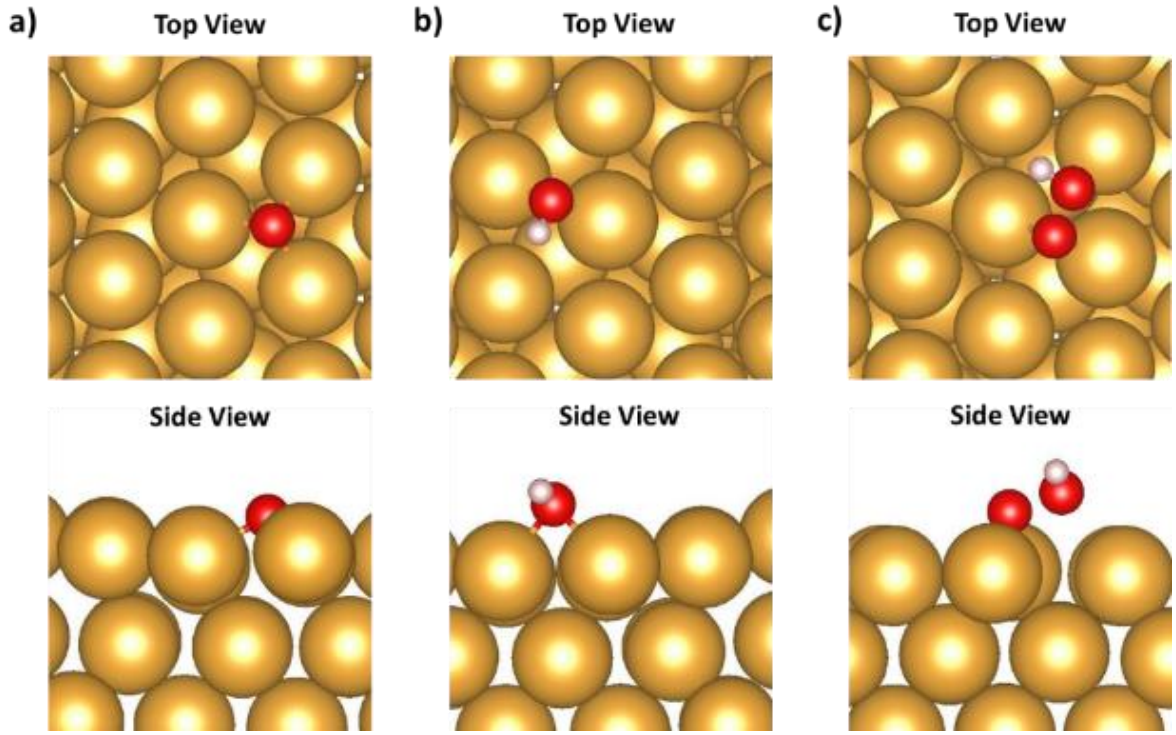

Figure C.3: Top (top image) and side image (bottom image) of most stable adsorption structures on Au(100)-hex based on static DFT calculations including **(a)** O*, **(b)** OH*, and **(c)** OOH*. Au atoms are shown in gold, O is shown in red, and H is shown in white.

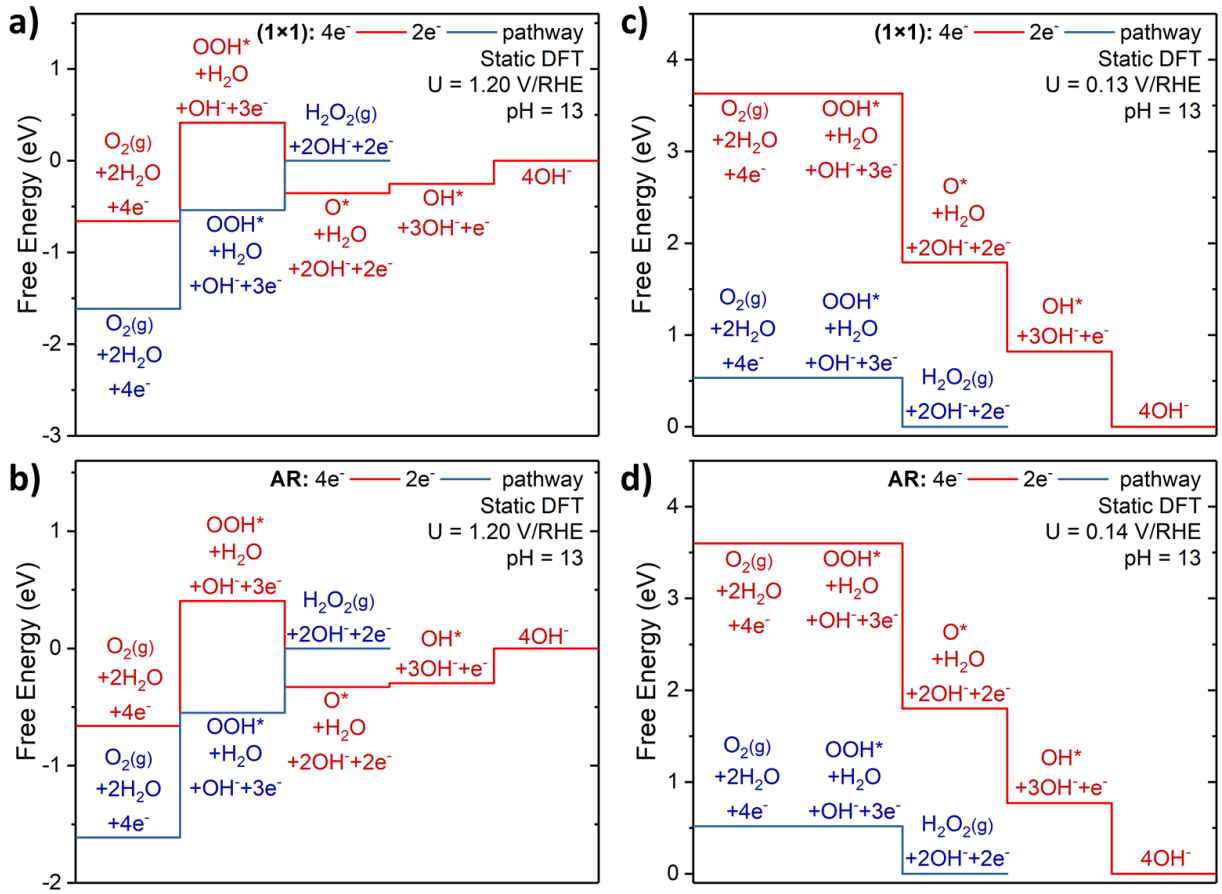

Figure C.4: Free energy diagram determined by static, unsolvated DFT calculations for the ORR at pH = 13 on **(a)** Au(100)-(1×1) at a potential of 1.20 V/RHE, **(b)** Au(100)-AR at a potential of 1.20 V/RHE, **(c)** Au(100)-(1×1) at a potential of 0.57 V/RHE (onset potential for $4e^-$ and $2e^-$ pathways), and **(d)** Au(100)-AR at a potential of 0.58 V/RHE (onset potential for $4e^-$ and $2e^-$ pathways).

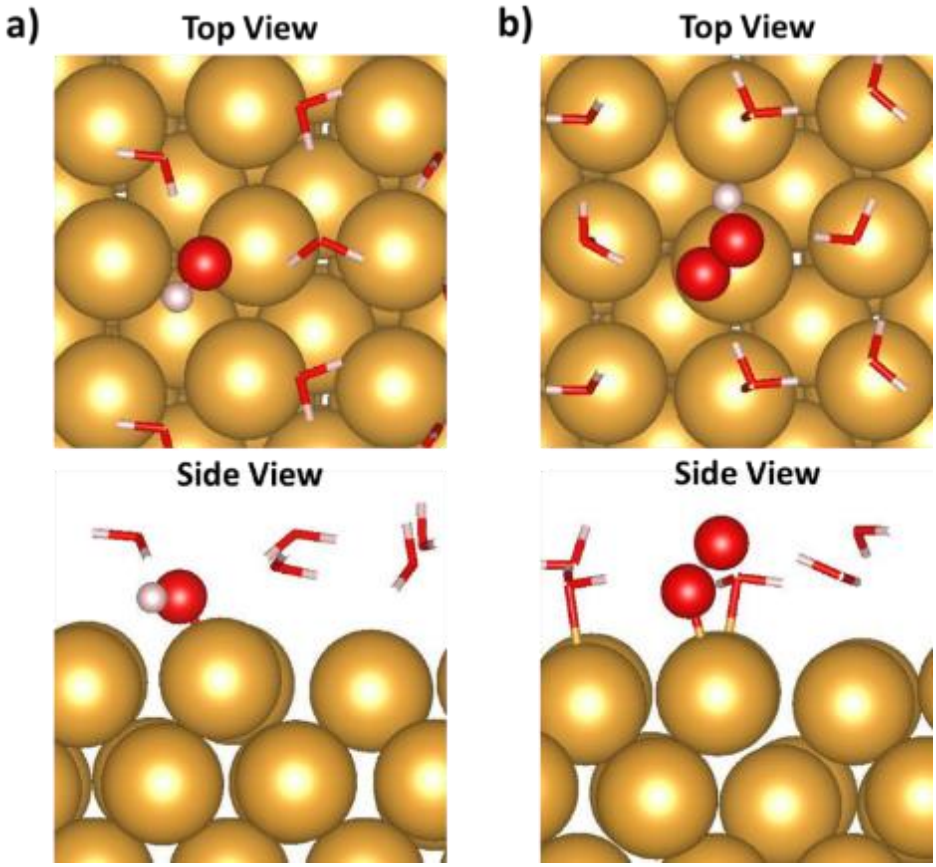

Figure C.5: Top (top image) and side image (bottom image) of representative stable adsorption structures on Au(100)-(1×1) at the pzc based on AIMD calculations including **(a)** OH* and **(b)** OOH*. Au atoms are shown in gold, O is shown in red, and H is shown in white. Interfacial water is shown as stick models for clarity.

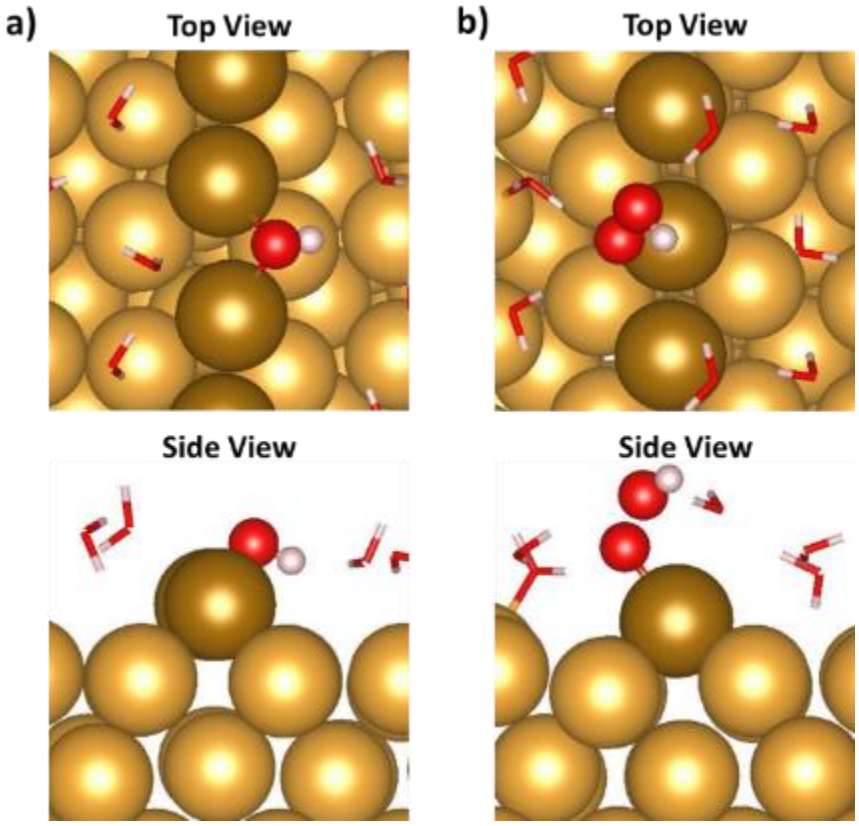

Figure C.6: Top (top image) and side image (bottom image) of representative stable adsorption structures on Au(100)-AR at the pzc based on AIMD calculations including **(a)** OH* and (**b)** OOH*. Au atoms are shown in gold, Au additional row atoms (AR) are shown in brown, O is shown in red, and H is shown in white. Interfacial water is shown as stick models for clarity.

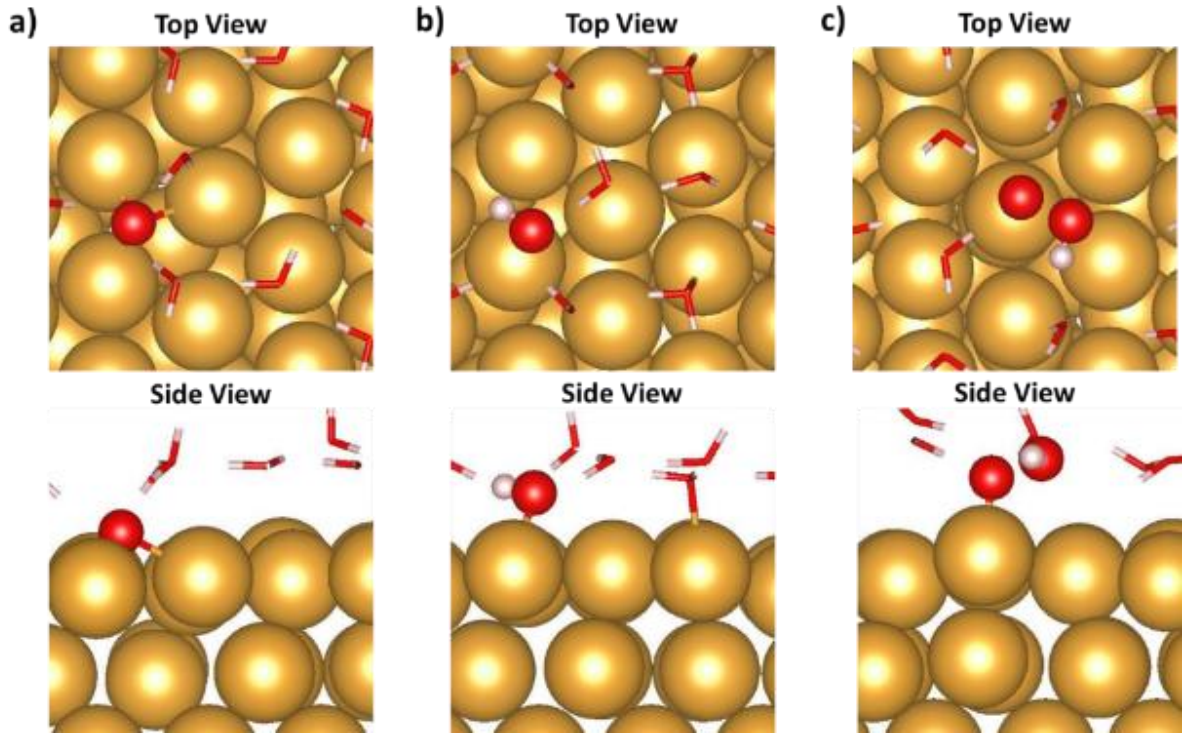

Figure C.7: Top (top image) and side image (bottom image) of representative stable adsorption structures on Au(100)-hex at the pzc based on AIMD calculations including **(a)** O*, **(b)** OH*, and **(c)** OOH*. Au atoms are shown in gold, O is shown in red, and H is shown in white. Interfacial water is shown as stick models for clarity.

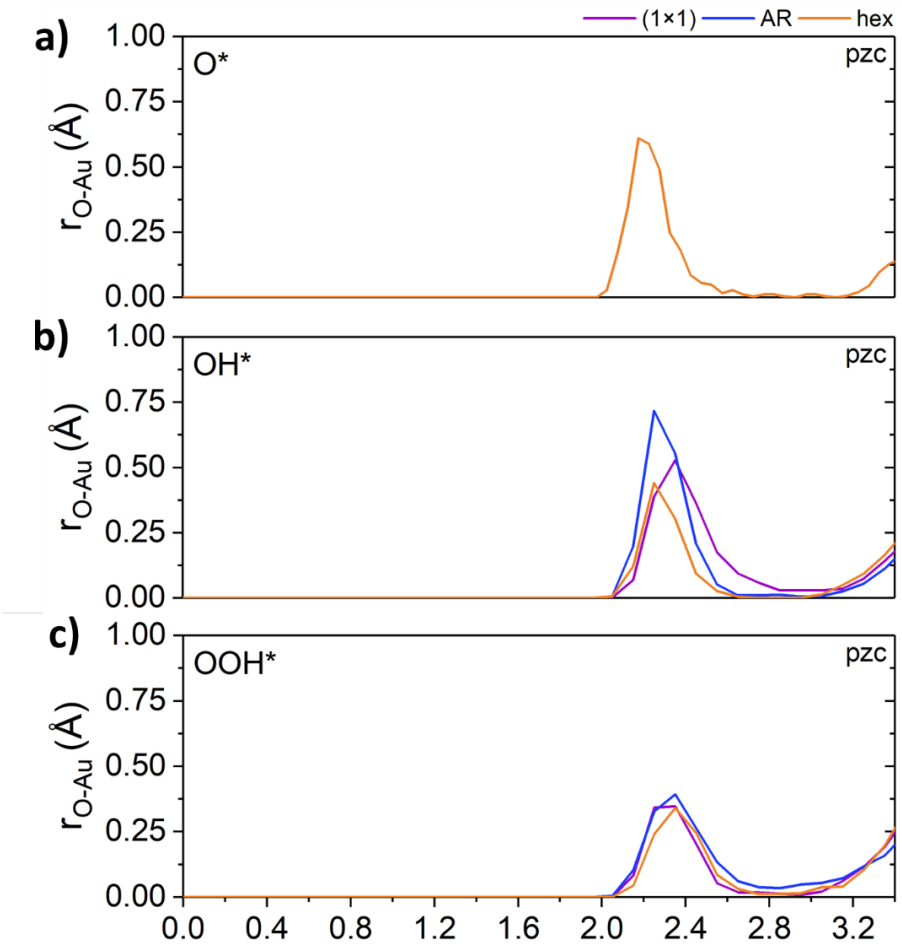

Figure C.8: Radial distribution function between bottom-most oxygen (closest to the surface) of adsorbate and Au for **(a)** O*, **(b)** OH*, and **(c)** OOH* at the pzc in the most energetically favorable AIMD simulations. Data for Au(100)-(1×1) is shown in purple, data for Au(100)-AR is shown in blue, and data for Au(100)-hex is shown in orange.

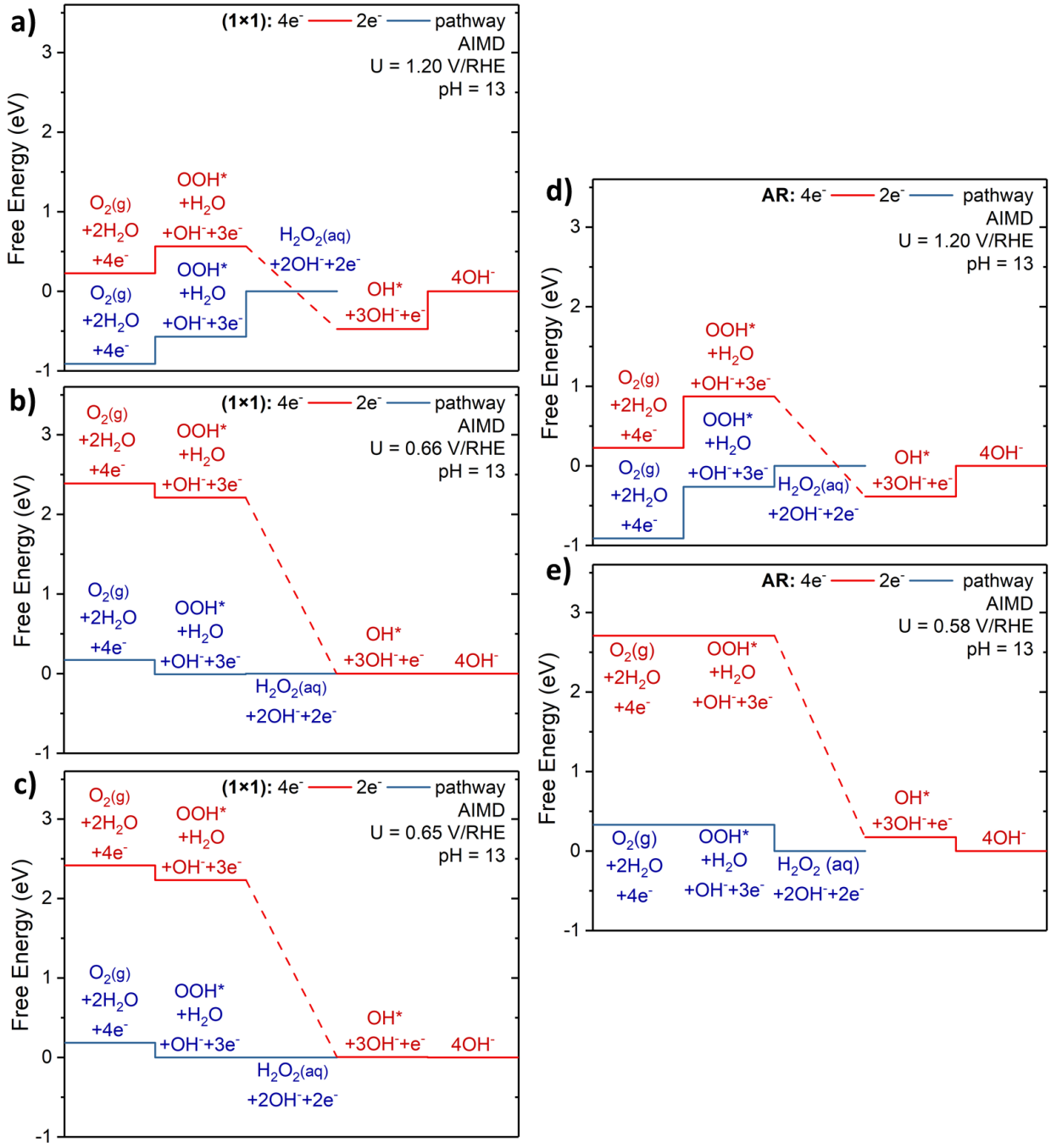

Figure C.9: Free energy diagram determined by solvated AIMD simulations for the ORR at pH = 13 on **(a)** Au(100)-(1×1) at a potential of 1.20 V/RHE, **(b)** Au(100)-(1×1) at a potential of 0.66 V/RHE (onset potential for $4e^-$ pathway), **(c)** Au(100)-(1×1) at a potential of 0.65 V/RHE (onset potential for $2e^-$ pathway), **(d)** Au(100)-AR at a potential of 1.20 V/RHE, and **(e)** Au(100)-AR at a potential of 0.58 V/RHE (onset potential for $4e^-$ and $2e^-$ pathways).

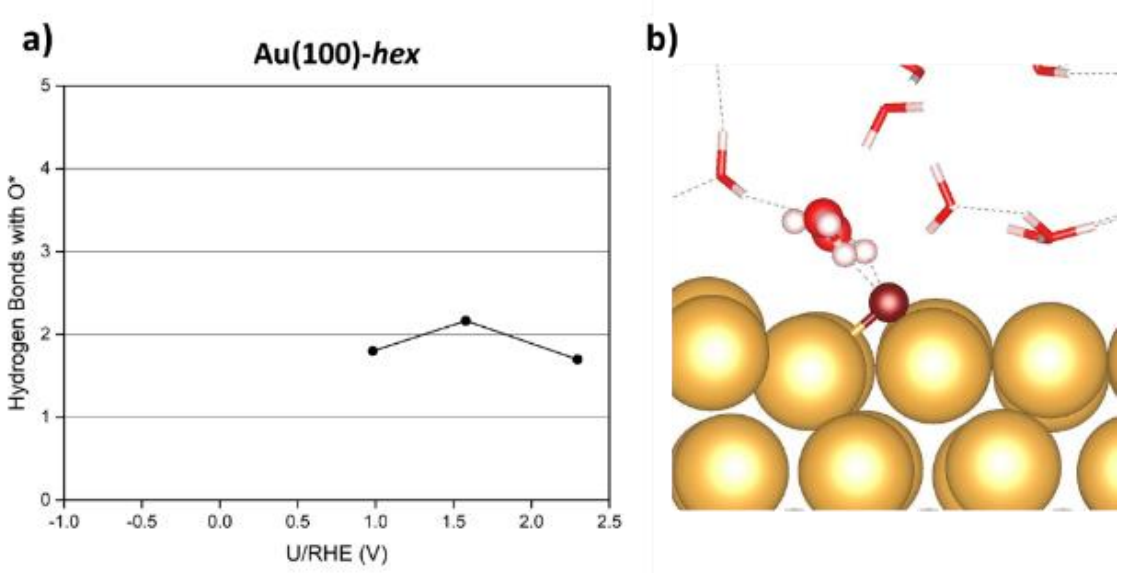

Figure C.10: Average number of hydrogen bonds formed between O* and water at all potentials studied on Au(100)-hex, the only Au(100) reconstruction where O* is stable. Lines in the figure are to guide the eye. **(b)** Snapshot of O* on Au(100)-hex from AIMD simulations with representative hydrogen bonding environments. Au atoms are shown in gold, oxygen is shown in red, and hydrogen is shown in white. Water not hydrogen bonded to adsorbate are shown as stick models for clarity.

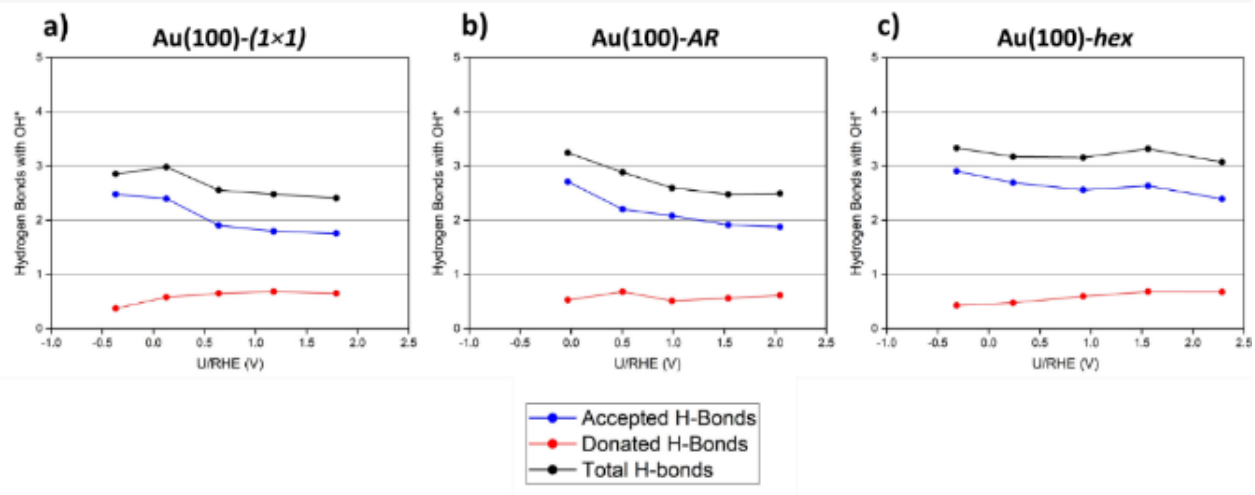

Figure C.11: Average number of hydrogen bonds formed between OH* and water at all potentials studied on **(a)** Au(100)-(1×1), **(b)** Au(100)-AR, and **(c)** Au(100)-hex. Accepted hydrogen bonds (blue) are bonds that are donated by water and accepted by OH*. Donated hydrogen bonds (red) are bonds that are donated by OH* and accepted by water. The total number of hydrogen bonds formed between OH* and water is shown in black.

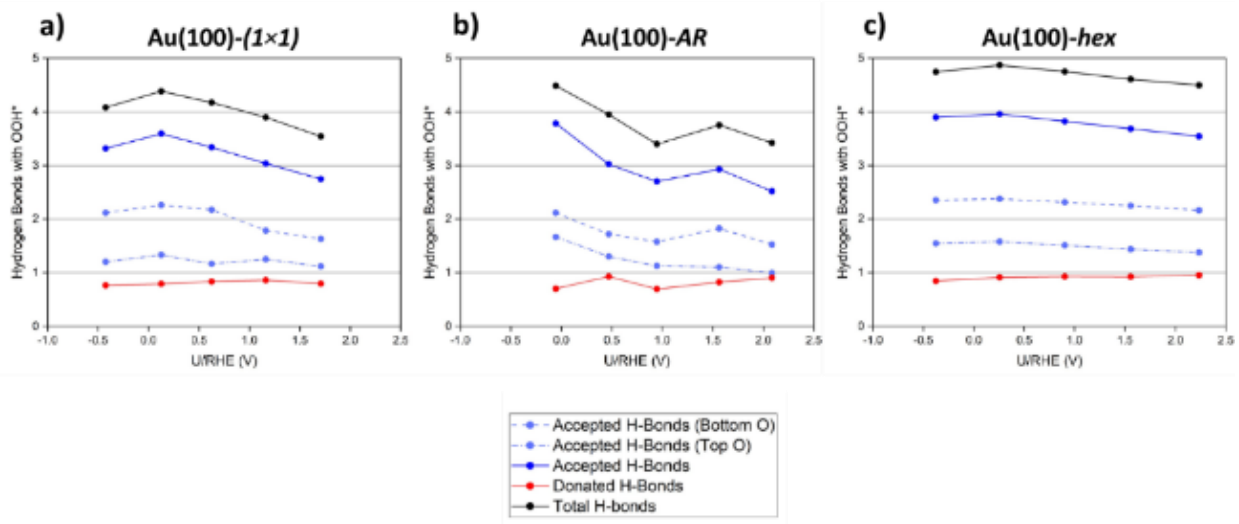

Figure C.12: Average number of hydrogen bonds formed between OOH* and water at all potentials studied on **(a)** Au(100)-(1×1), **(b)** Au(100)-AR, and **(c)** Au(100)-hex. Accepted hydrogen bonds (total; dark blue, sold line) are bonds that are donated by water and accepted by OOH* to either the bottom O atom (closest to the surface; dashed light blue lines) or the top O atom (farthest from the surface, dash-dotted light blue lines) of OOH*. Donated hydrogen bonds (red) are bonds that are donated by OOH* and accepted by water. The total number of hydrogen bonds formed between OOH* and water is shown in black.

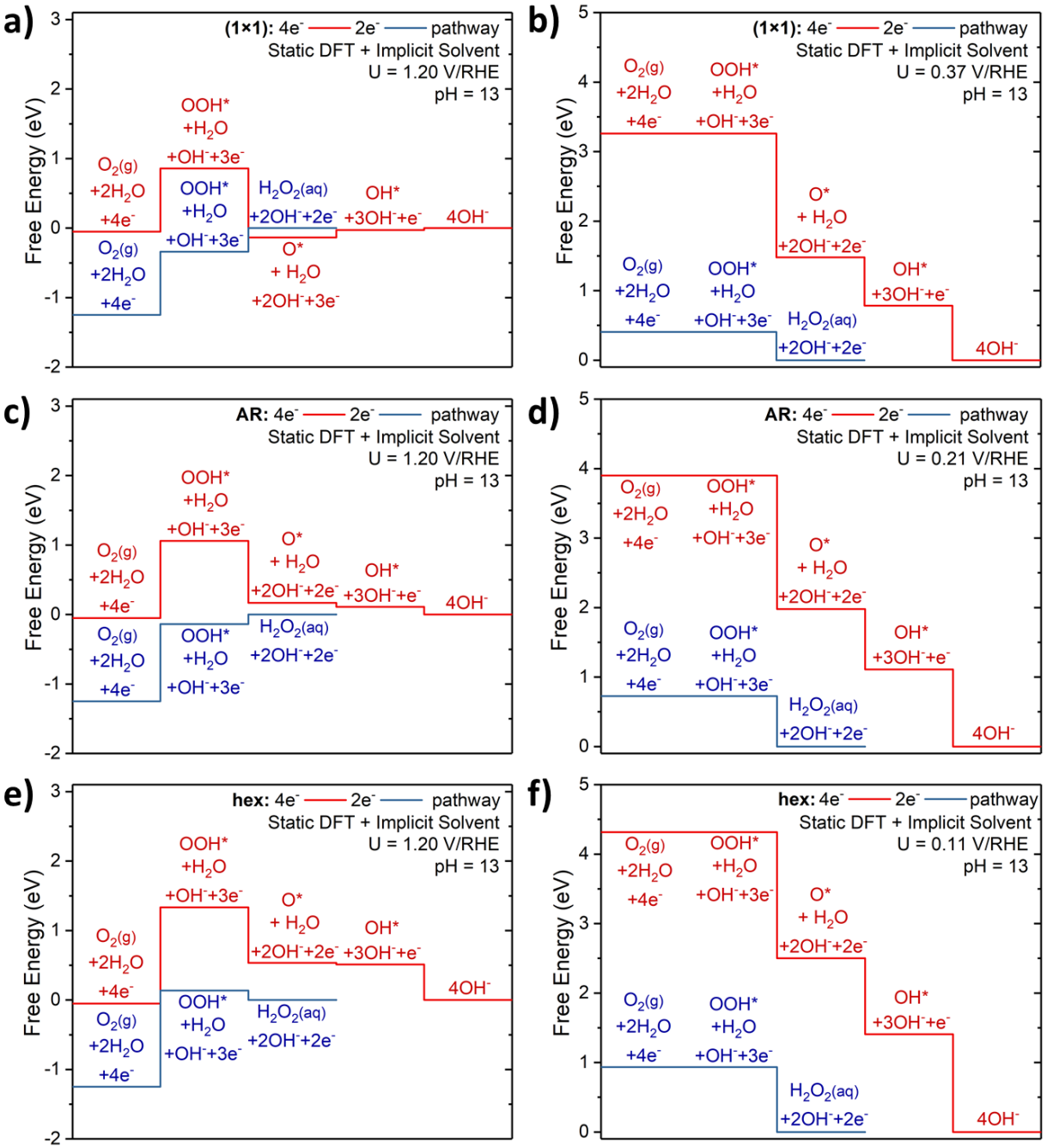

Figure C.13: Free energy diagram determined by static DFT calculations with implicit water for the ORR at pH = 13 on **(a)** Au(100)-(1×1) at a potential of 1.20 V/RHE, **(b)** Au(100)-(1×1) at a potential of 0.46 V/RHE (onset potential for $4e^-$ and $2e^-$ pathways), **(c)** Au(100)-AR at a potential of 1.20 V/RHE, **(d)** Au(100)-AR at a potential of 0.29 V/RHE (onset potential for $4e^-$ and $2e^-$ pathways), **(e)** Au(100)-hex at a potential of 1.20 V/RHE, and **(f)** Au(100)-hex at a potential of 0.13 V/RHE (onset potential for $4e^-$ and $2e^-$ pathways).

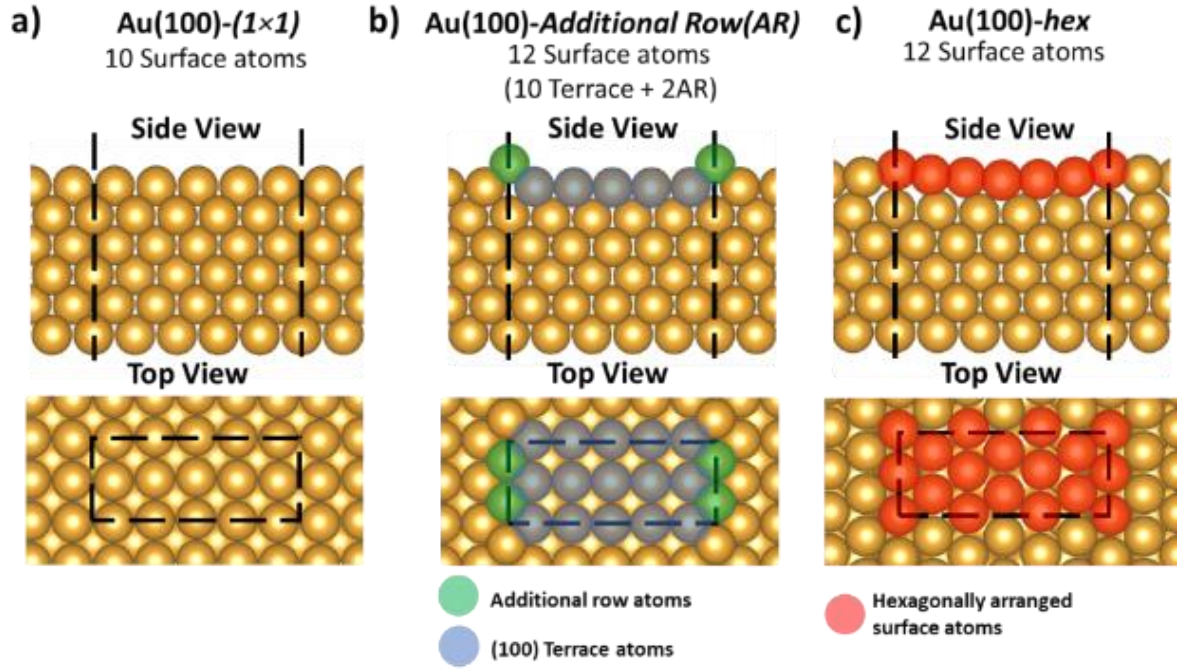

Figure C.14: Top (top image) and side views (bottom image) of Au(100) surface reconstructions including **(a)** Au(100)-(1×1) surface with no reconstruction, **(b)** Au(100)-hex surface with a hexagonal reconstruction on the top layer, and **(c)** an Au(100)-AR surface with an additional row of Au atoms on the top layer of the Au(100) surface. Au atoms are shown in gold. Unit cells are indicated with dashed black lines.

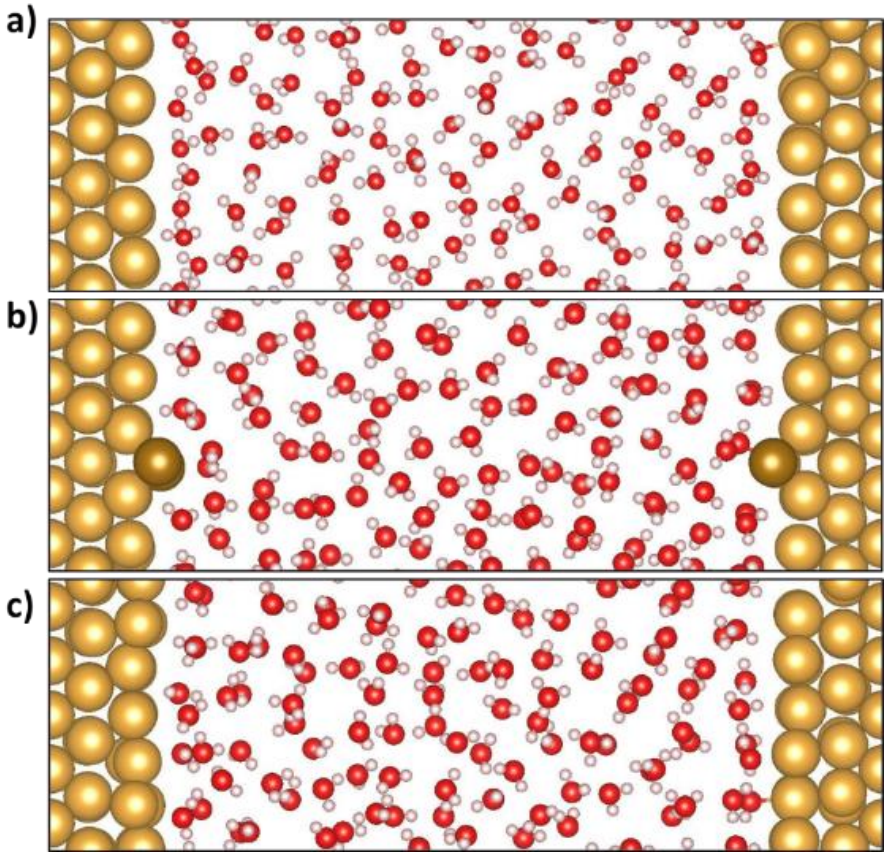

Figure C.15: Representative double-sided unit cell for Au(100) with interfacial water for **(a)** Au(100)-(1×1), **(b)** Au(100)-AR, and **(c)** Au(100)-hex surface reconstructions. Au atoms are shown in gold, Au additional row atoms (AR) are shown in brown, O is shown in red, and H is shown in white.

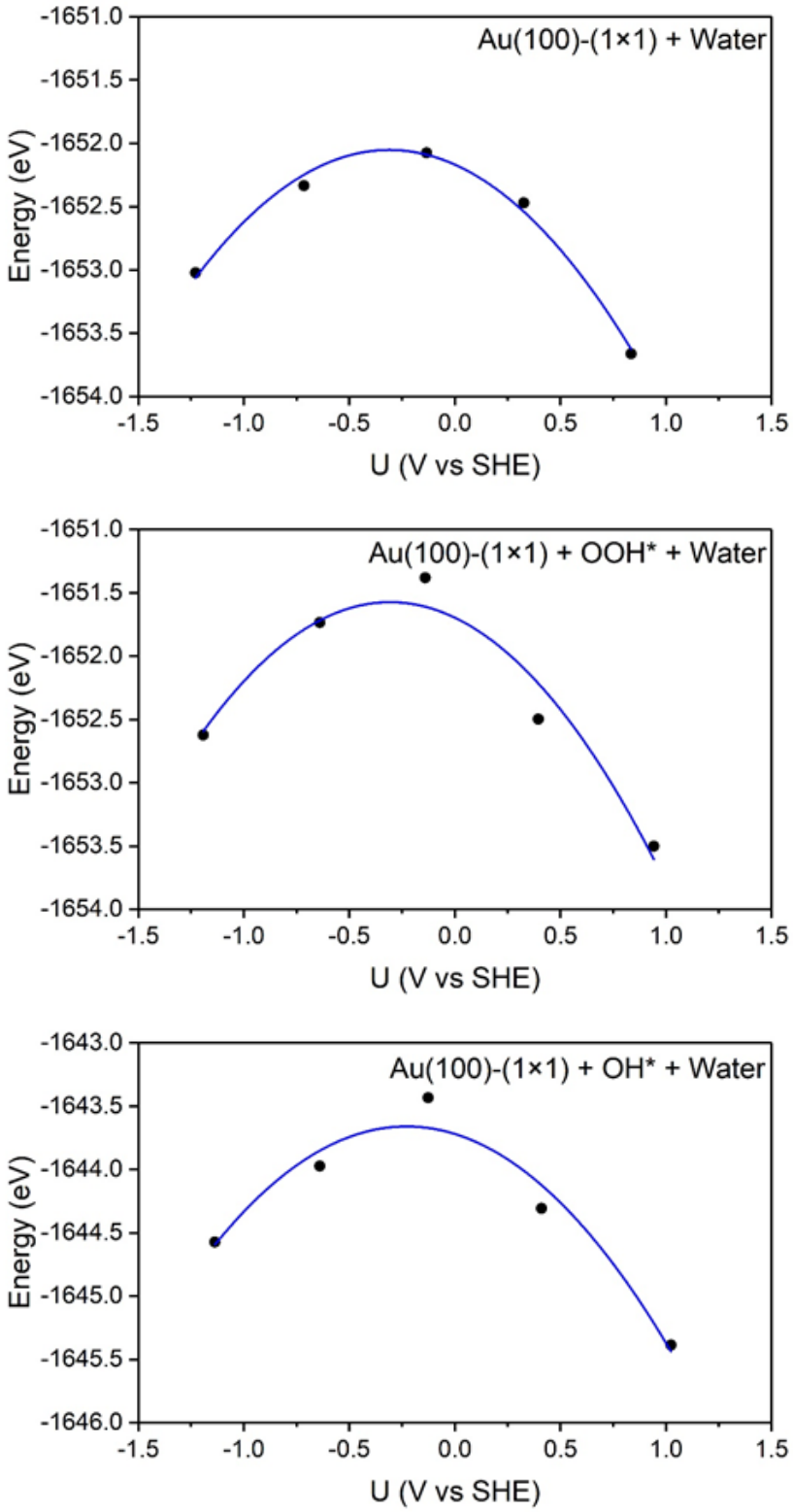

Figure C.16: Fitted total potential energies of Au(100)-(1×1) surface systems from AIMD simulations.

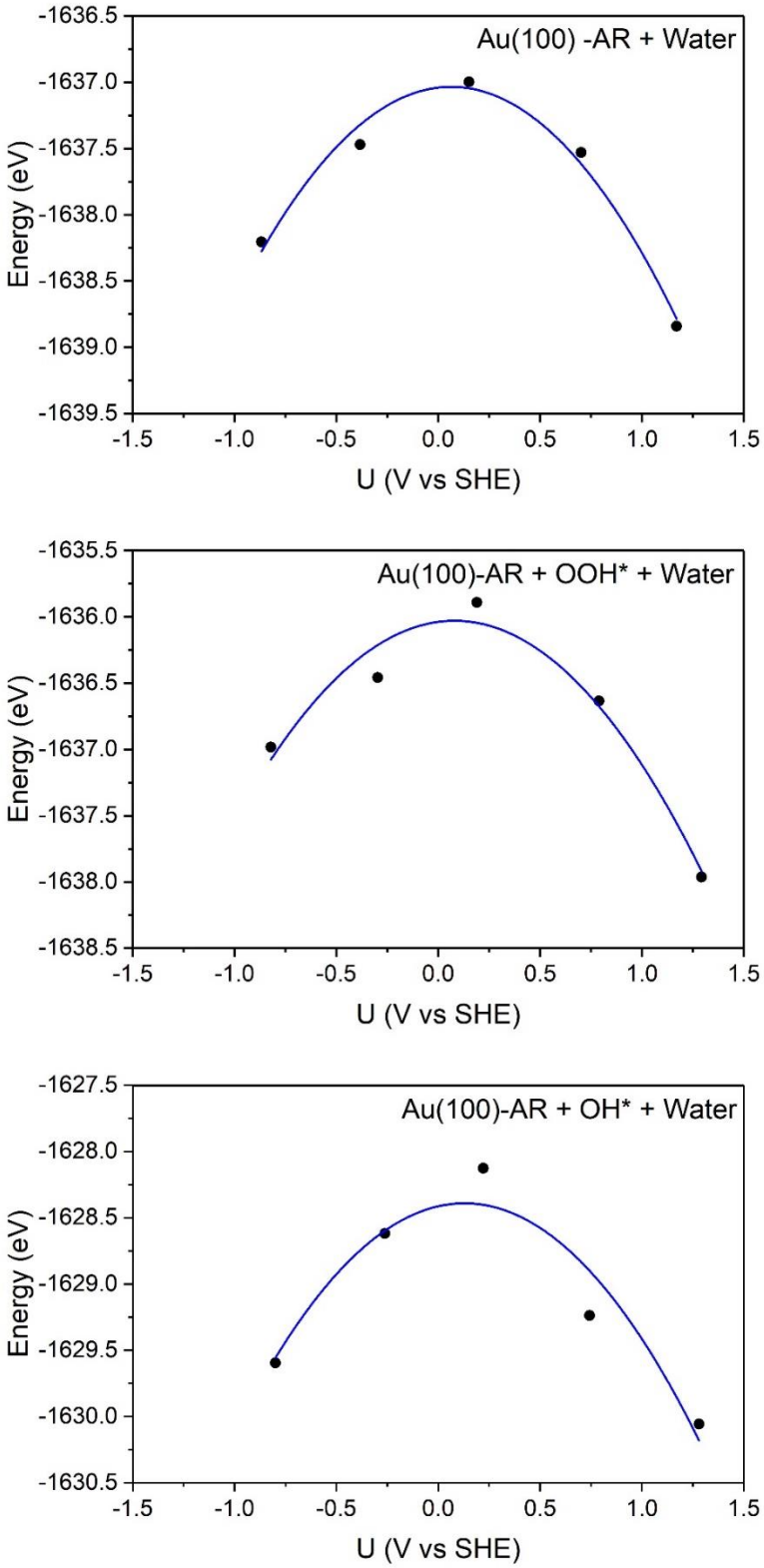

Figure C.17: Fitted total potential energies of Au(100)-AR surface systems from AIMD simulations.

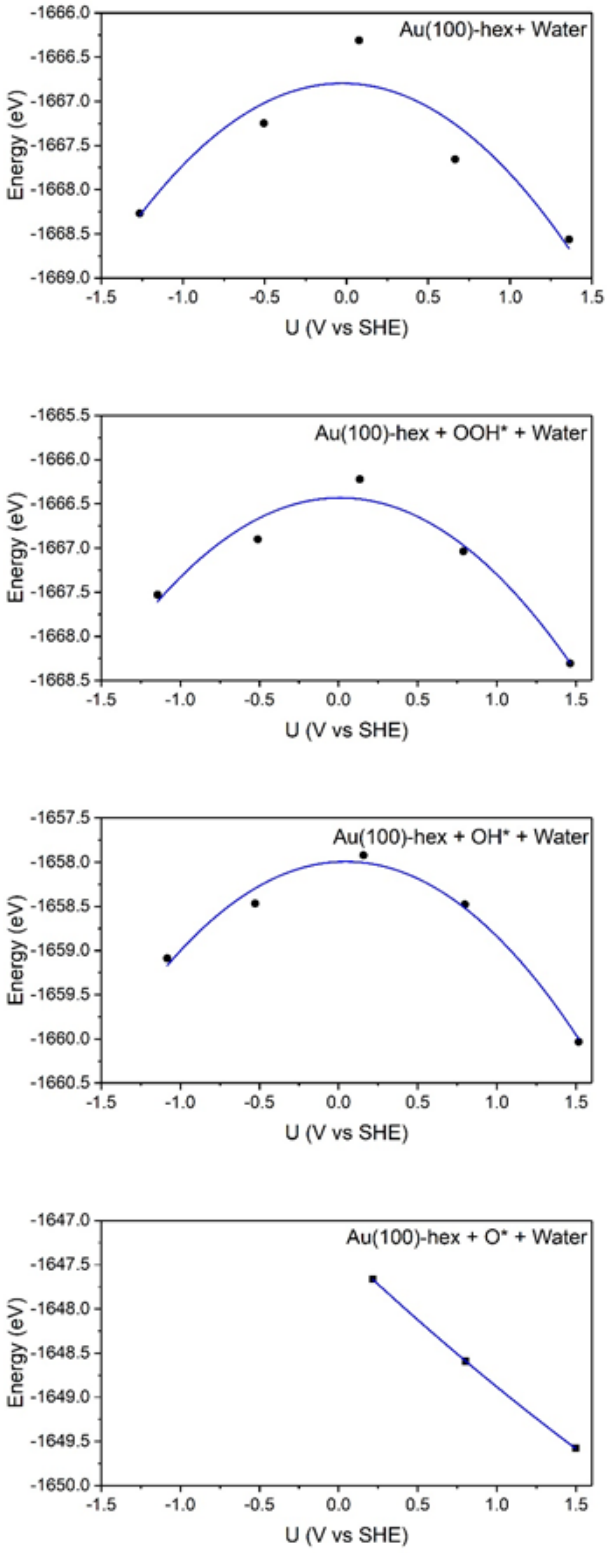

Figure C.18: Fitted total potential energies of Au(100)-hex surface systems from AIMD simulations.

C.3 Supplementary Tables

Table C.1: Fitted parameters for calculating the free energy of Au(100)-(1×1) systems from AIMD simulations

System	C (eV/V^2)	U_{pzc} (V vs SHE)	E_{pzc} (eV)	R^2
Water	2.40	-0.31	-1652.05	0.99
OOH*	2.60	-0.31	-1651.57	0.95
OH*	2.27	-0.23	-1643.66	0.95
O*	-	-	-	-

Table C.2: Fitted parameters for calculating the free energy of Au(100)-AR systems from AIMD simulations

System	C (eV/V^2)	U_{pzc} (V vs SHE)	E_{pzc} (eV)	R^2
Water	2.86	0.06	-1637.03	0.98
OOH*	2.47	0.09	-1636.04	0.96
OH*	2.75	0.13	-1628.37	0.93
O*	-	-	-	-

Table C.3: Fitted parameters for calculating the free energy of Au(100)-hex systems from AIMD simulations

System	C (eV/V^2)	U_{pzc} (V vs SHE)	E_{pzc} (eV)	R^2
Water	1.95	-0.02	-1666.80	0.85
OOH*	1.72	0.01	-1666.46	0.95
OH*	1.79	0.03	-1658.05	0.91
O*‡	-0.71	2.95	-1647.23	1.00

‡ Quadratic fit only contains 3 data points. Because of the poor fit, we took the C and U_{pzc} values from water for O* in Fig. 3.3d-f in the main text

Table C.4: Fitted parameters for calculating the free energy of Au(100)-(1×1) systems from VASPsol calculations

System	C (eV/V^2)	U_{pzc} (V vs SHE)	E_{pzc} (eV)	R^2
Water	1.21	0.14	-165.19	1.00
OOH*	1.58	0.16	-192.35	1.00
OH*	1.37	0.11	-184.68	1.00
O*	1.24	0.21	-175.38	1.00

Table C.5: Fitted parameters for calculating the free energy of Au(100)-AR systems from VASPsol simulations

System	C (eV/V^2)	U_{pzc} (V vs SHE)	E_{pzc} (eV)	R^2
Water	1.23	0.17	-179.69	1.00
OOH*	1.51	0.23	-206.92	1.00
OH*	1.31	0.12	-198.91	1.00
O*	1.31	0.39	-189.25	1.00

Table C.6: Fitted parameters for calculating the free energy of Au(100)-hex systems from VASPsol calculations

System	C (eV/V^2)	U_{pzc} (V vs SHE)	E_{pzc} (eV)	R^2
Water	1.08	0.10	-180.58	1.00
OOH*	1.50	0.31	-207.24	1.00
OH*	1.33	0.27	-198.98	1.00
O*	1.25	0.35	-189.40	1.00

Appendix: D Supplementary Materials for 'Determining the Role of Water in the Electric Double Layer on the Oxygen Reduction Reaction on Au(111) and Pt(111) in Alkaline Media'

D.1 Supplementary Figures

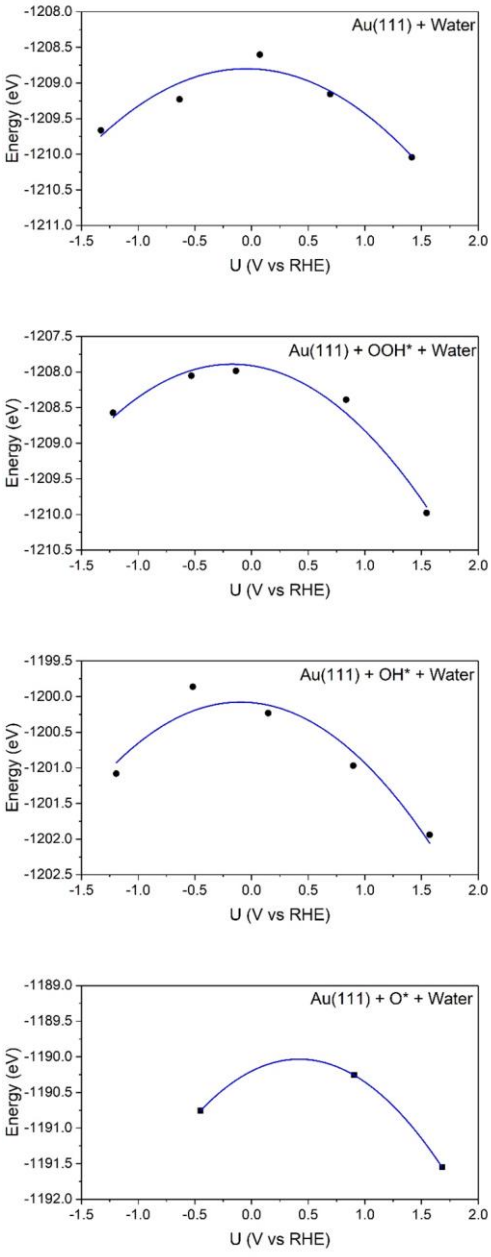

Figure D.1: Fitted total free energies of Au(111) surface systems from AIMD simulations.

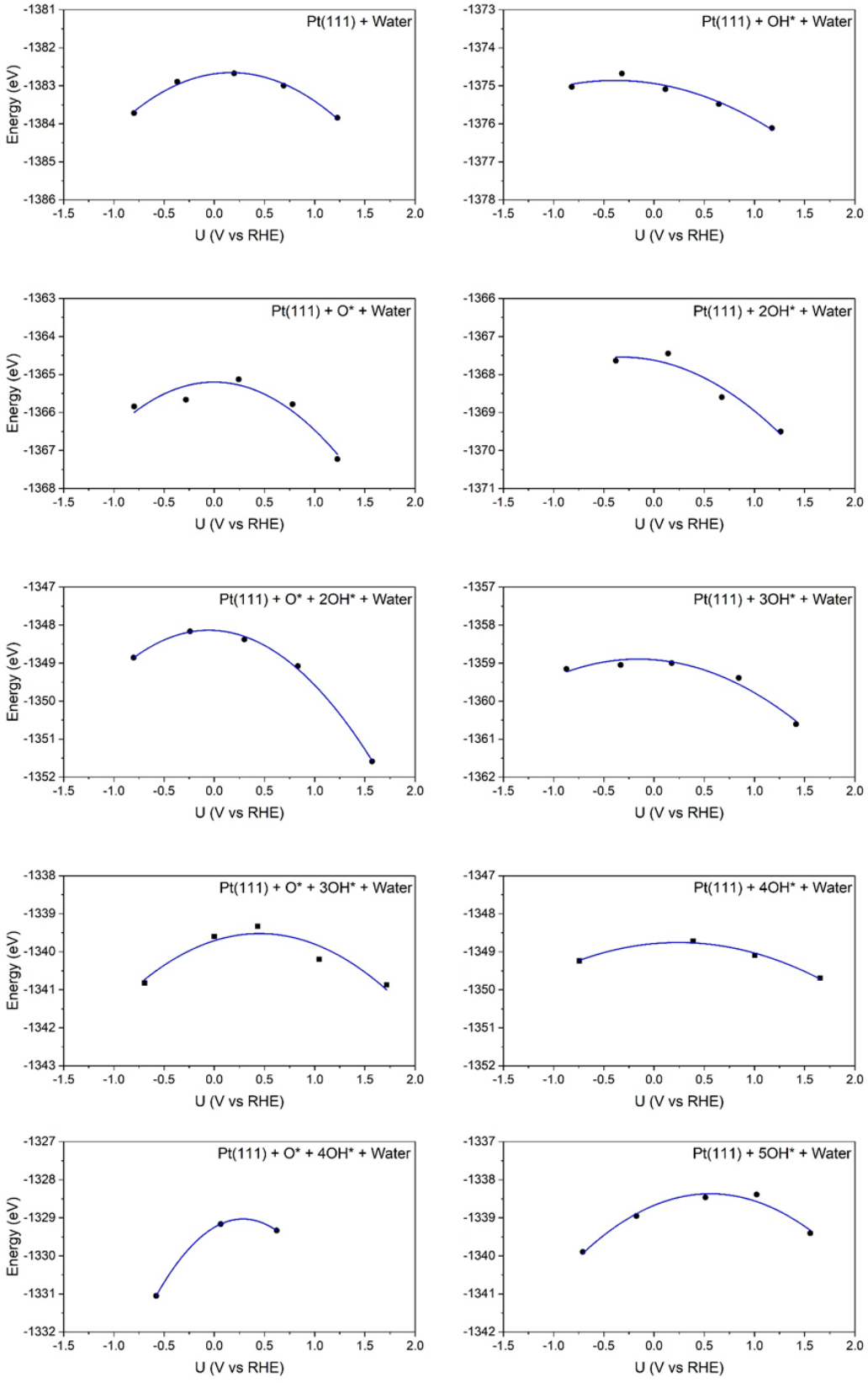

Figure D.2: Fitted total free energies of Pt(111) surface systems from AIMD simulations.

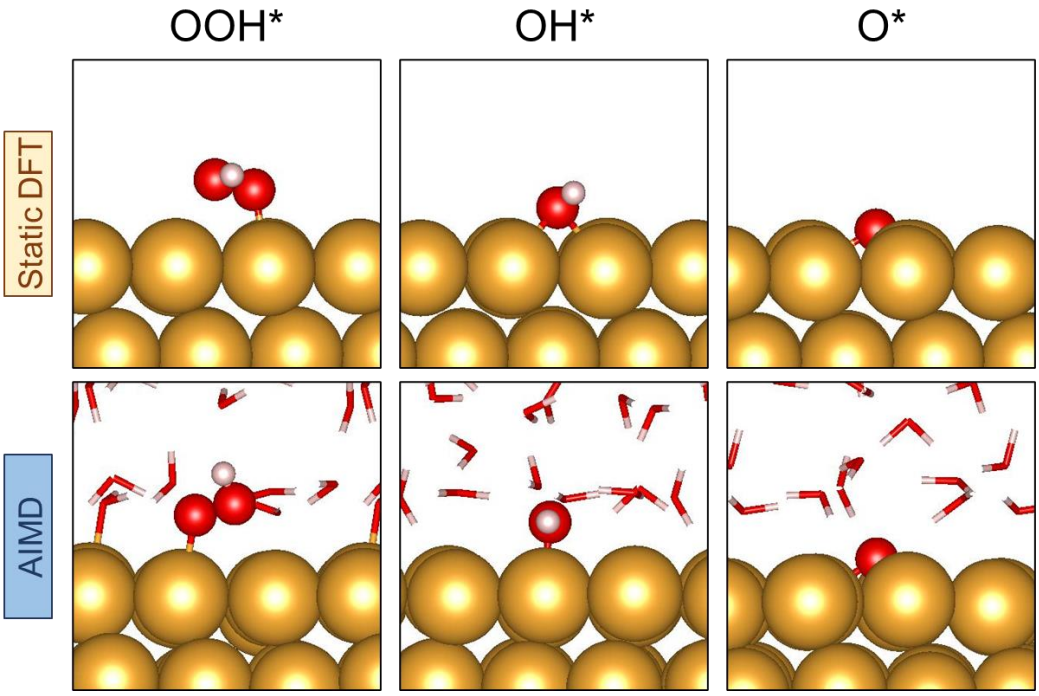

Figure D.3: Representative structures for adsorbates as seen from the side in static, unsolvated DFT and solvated AIMD simulations on Au(111). Au atoms are shown in gold, O atoms are shown in red, and H atoms are shown in white. Interfacial water molecules are shown as stick models for clarity.

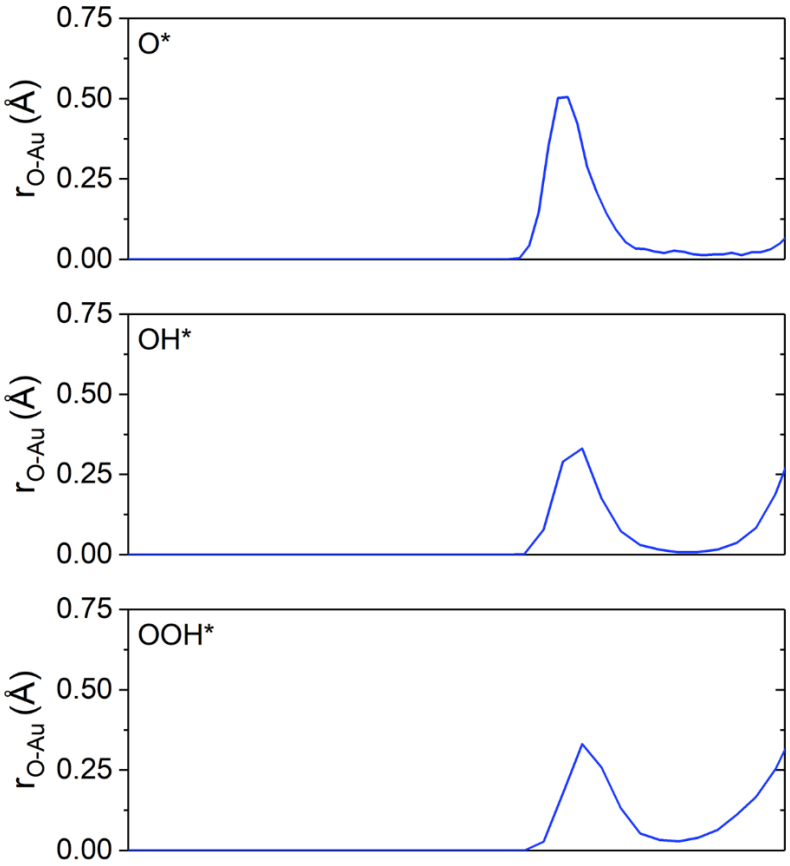

Figure D.4: Radial distribution functions between bottom-most oxygen (closest to the surface) of adsorbate and Au for O*, OH*, and OOH* from AIMD simulations.

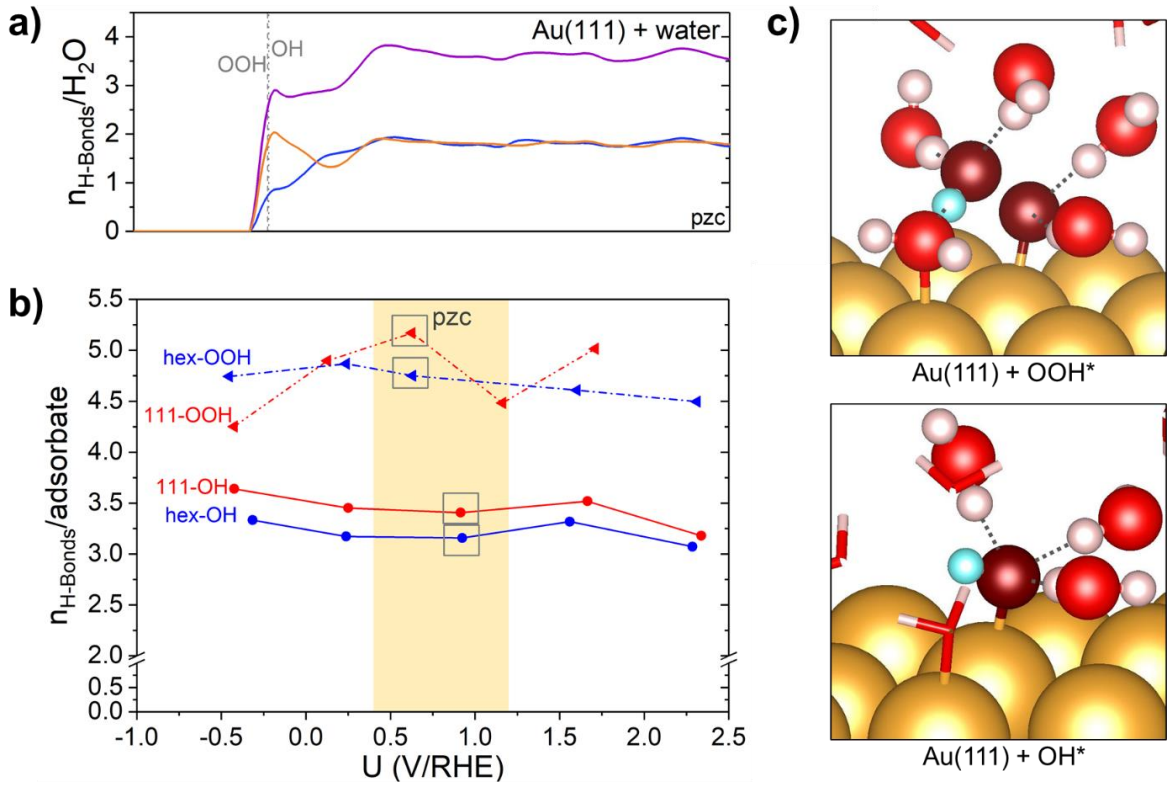

Figure D.5: (a) Average number of hydrogen bonds formed per water molecule ($n_{H\text{-}bonds}/H_2O$) along the surface normal direction (zero corresponds to Au atoms in the top layer of the slab) for solvated Au(111) surface without adsorbates at the pzc. The total $n_{H\text{-}bonds}/H_2O$ is shown purple, the accepted $n_{H\text{-}bonds}/H_2O$ is shown in blue, and the donated $n_{H\text{-}bonds}/H_2O$ is shown in orange. Grey dashed lines and dotted lines indicate the average position of the bottom-most oxygen in OH* and OOH*, respectively, in the most energetically favorable AIMD simulations for reference. **(b)** Average number of hydrogen bonds formed between OH* or OOH* and water ($n_{H\text{-}bonds}$/adsorbate) at all potentials studied. Yellow region corresponds to potential region typically considered for ORR. Lines in the figure are to guide the eye. **(c)** Snapshot of OOH* and OH*on Au(111) with representative hydrogen bonds (black dashed lines). Au atoms are shown in gold, oxygen atoms are shown in red, and hydrogen atoms are shown in white. Water not hydrogen-bonded to adsorbates in **(c)** are shown as stick models for clarity.

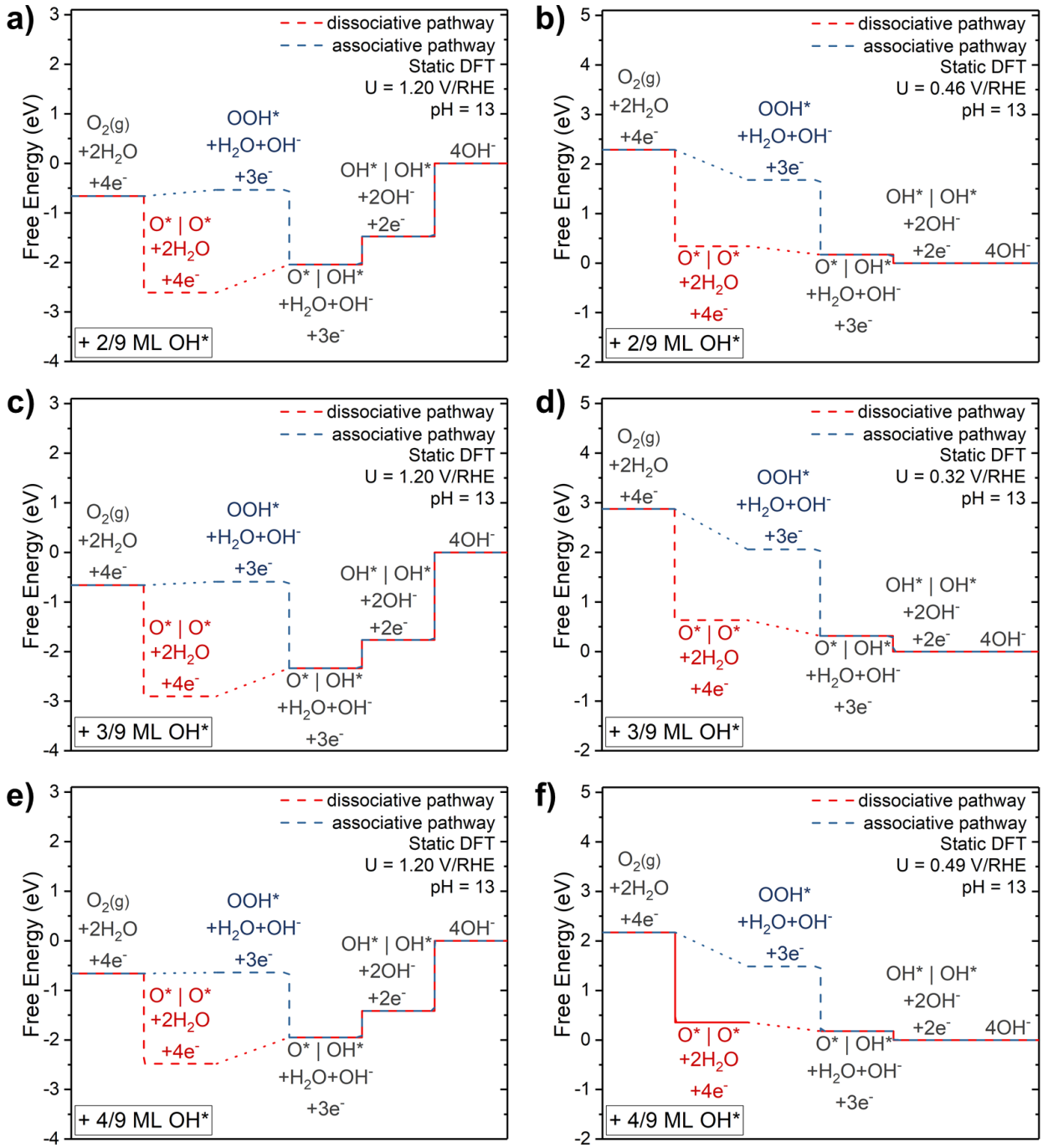

Figure D.6: Free energy diagrams for the ORR on Pt(111) from static, unsolvated DFT calculations in the presence of co-adsorbed OH* at pH=13, including: 2/9 ML OH* at **(a)** 1.20 V/RHE and **(b)** 0.46 V/RHE (the onset of the ORR); 3/9 ML OH* at **(c)** 1.20 V/RHE and **(d)** 0.32 V/RHE (the onset of the ORR); and 4/9 ML OH* at **(e)** 1.20 V/RHE and **(f)** 0.49 V/RHE (the onset of the ORR).

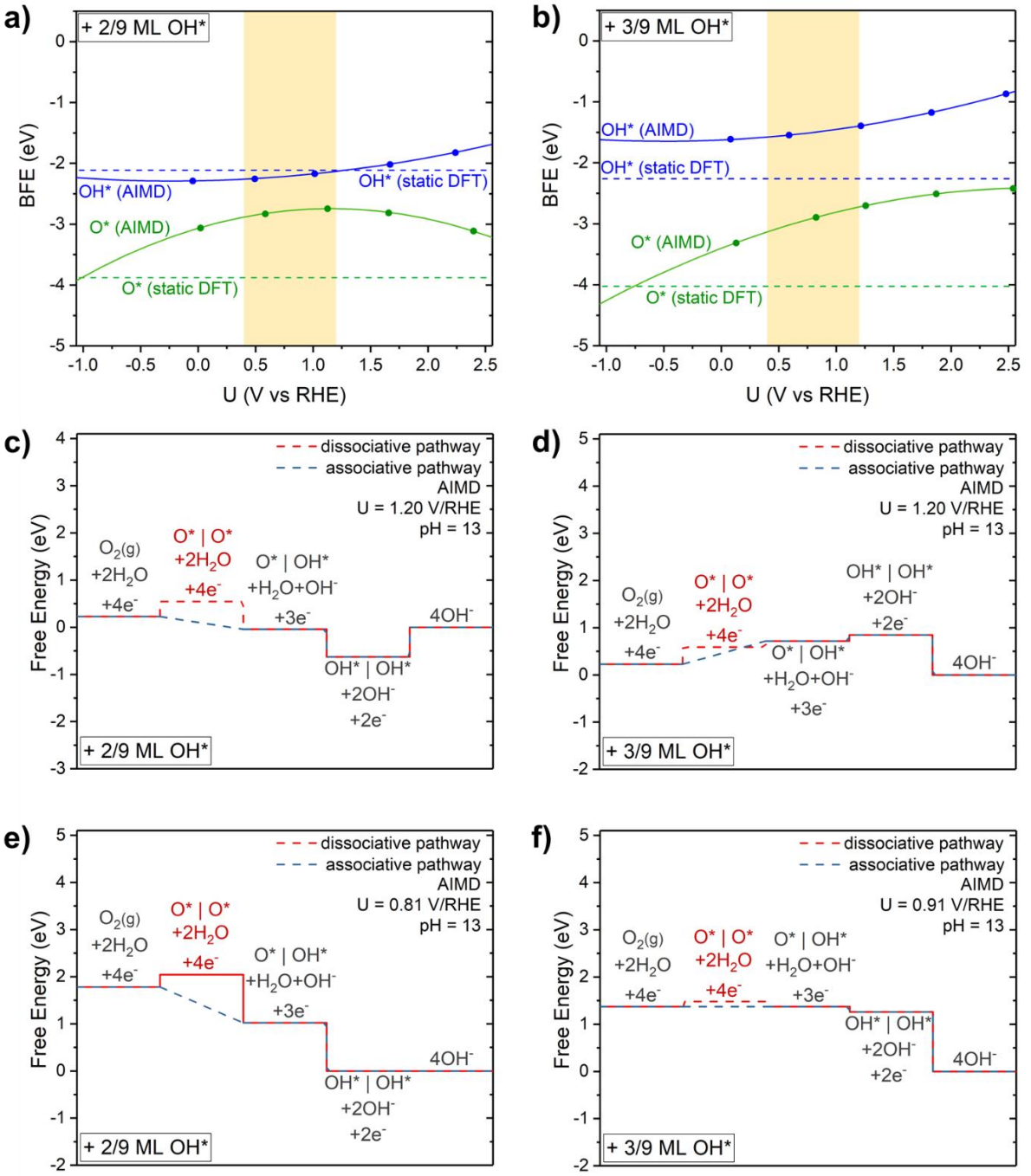

Figure D.7: Binding free energy (BFE) of OH and O relative to the gas phase energy of each respective species as a function of applied potential as calculated from static DFT and solvated AIMD simulations at pH = 13 in the presence of **(a)** 2/9 ML co-adsorbed OH* and **(b)** 3/9 ML co-adsorbed OH*. Free energy diagrams for the ORR on Pt(111) at 1.20 V/RHE and pH = 13 in the presence of **(c)** 2/9 ML co-adsorbed OH* and **(d)** 3/9 ML co-adsorbed OH* at 1.20 V/RHE. Free energy diagrams for the ORR on Pt(111) at 1.20 V/RHE and pH = 13 in the presence of **(e)** 2/9 ML co-adsorbed OH* and **(f)** 3/9 ML co-adsorbed OH* at the onset potentials for the ORR.

D.2 Supplementary Tables

Table D.1: Fitted parameters for calculating the free energy of Au(111) systems from AIMD simulations

System	C (eV/V^2)	U_{pzc} (V vs SHE)	E_{pzc} (eV)	R^2
Water	1.15	-0.05	-1208.80	0.91
1/9 ML OOH* + water	1.36	-0.17	-1207.89	0.98
1/9 ML OH* + water	1.42	-0.10	-1200.08	0.92
1/9 ML O* + water	1.91	0.42	-1190.03	1.00

Table D.2: Fitted parameters for calculating the free energy of Pt(111) systems from AIMD simulations

System	C (eV/V^2)	U_{pzc} (V vs SHE)	E_{pzc} (eV)	R^2
Water	2.17	0.17	-1382.65	0.99
1/9 ML OH* + water	1.06	-0.39	-1374.86	0.96
2/9 ML OH* + water	1.63	-0.32	-1367.54	0.94
3/9 ML OH* + water	1.32	-0.16	-1358.89	0.97
4/9 ML OH* + water	0.96	0.24	-1348.76	0.99
5/9 ML OH* + water	1.94	0.56	-1338.37	0.97
1/9 ML O* + water	2.52	0.00	-1365.20	0.91
1/9 ML O* + 2/9 ML OH* + water	2.60	-0.05	-1348.14	0.99
1/9 ML O* + 3/9 ML OH* + water	1.85	0.45	-1339.52	0.90
1/9 ML O* + 4/9 ML OH* + water	5.40	0.29	-1329.03	1.00

Appendix: E Supplementary Materials for 'Evaluating Interfacial Water Structures on Clean and Hydroxyl-covered Electrified Au(100) Surface Reconstructions with *Ab Initio* Molecular Dynamics Simulations'

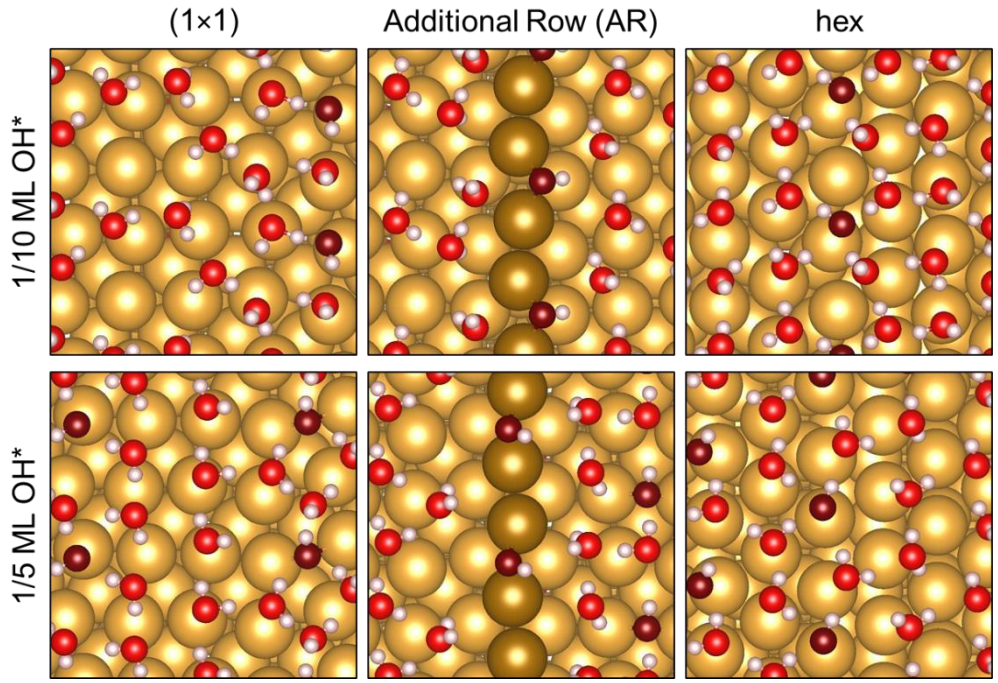

Figure E.1: Representative images of water and OH* on Au(100) surface reconstructions at the point of zero charge (pzc) for the most energetically stable configurations of OH* as determined from AIMD calculations (red: O in water, dark red: O in OH*, white: H, gold: Au, dark gold: additional row (AR) Au). Top views of Au(100) surfaces are 4 Å from the surface and include water in the high-density sub layer closest to the surface.

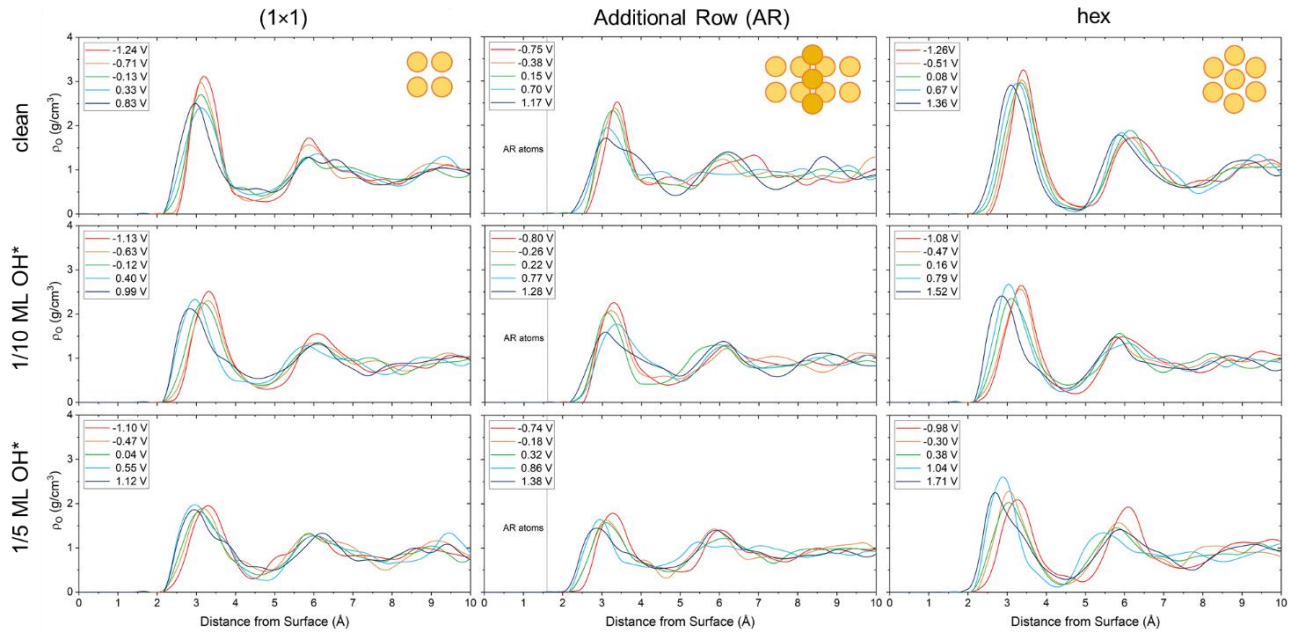

Figure E.2: Density of oxygen atoms (ρ_O) in water as a function of distance from the surface for Au(100)-(1×1), Au(100)-AR, and Au(100)-hex surfaces with and without OH* at a range of potentials. The zero coordinate corresponds to average position of Au atoms on the top surface layer of each model (excluding AR atoms on Au(100)-AR)). Position of AR atoms is denoted with a line.

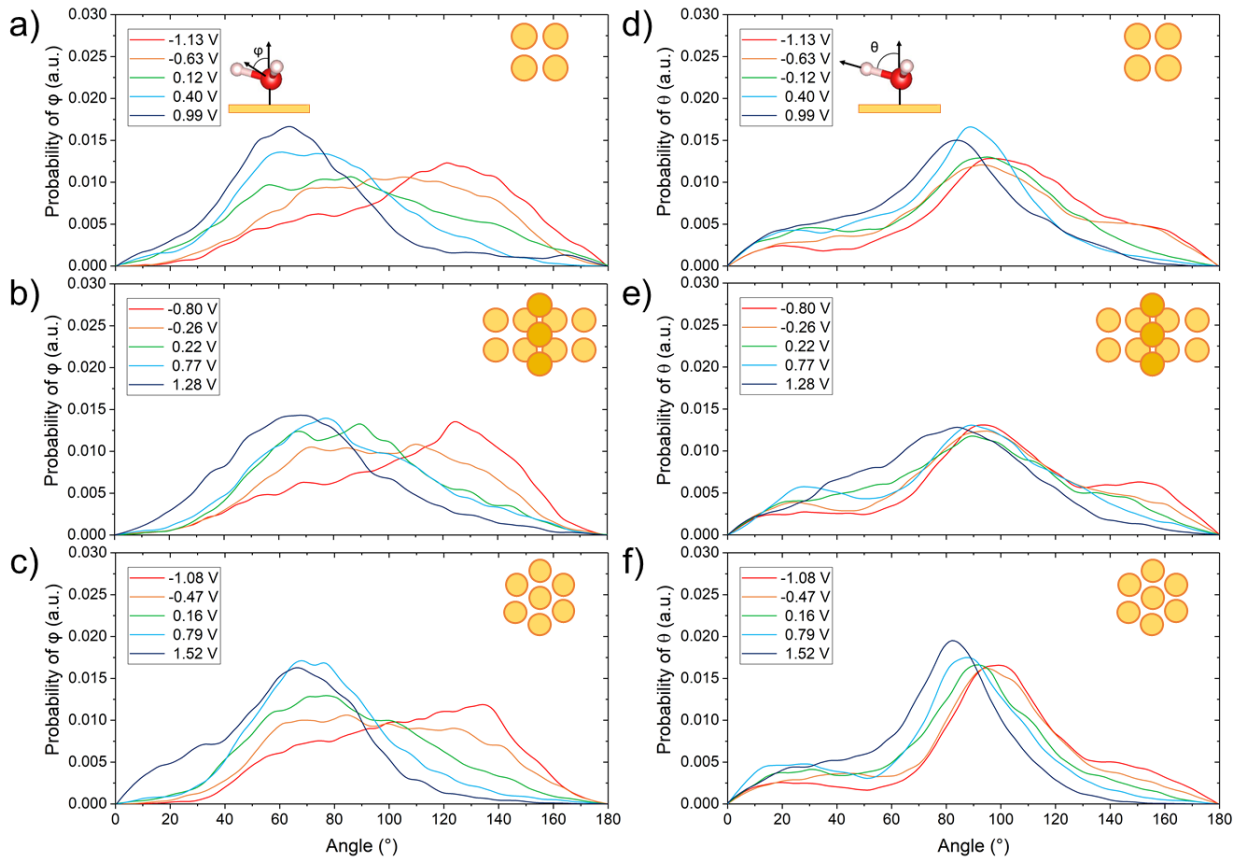

Figure E.3: Orientation of water on Au(100) surface reconstructions with 1/10 ML OH*. Distribution of the angle between the water bisector and the surface normal, φ, within 4 Å of the **(a)** Au(100)-(1×1), **(b)** Au(100)-AR, and **(c)** Au(100)-hex surfaces at a range of potentials. Distribution of the angle between the O-H bonds of water and the surface normal, θ, within 4 Å of the **(d)** Au(100)-(1×1), **(e)** Au(100)-AR, and **(f)** Au(100)-hex surfaces at a range of potentials. Inset of **(a)** illustrates φ, while the inset of **(d)** illustrates θ. All potentials are referenced with respect to the SHE.

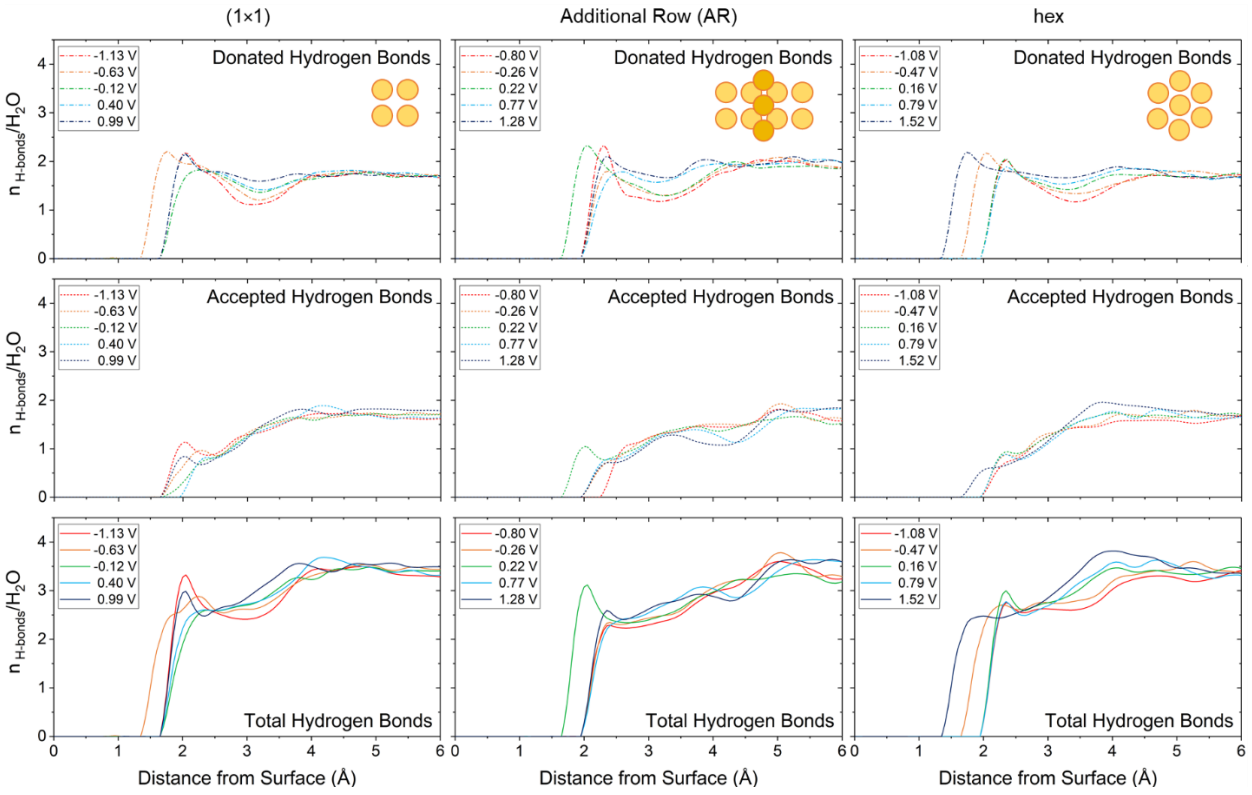

Figure E.4: Hydrogen bond density ($n_{H\text{-}bonds}/H_2O$) along the surface normal direction on Au(100) surface reconstructions covered with 1/10 ML OH* at a range of potentials. Donated hydrogen bonds include H-bonds donated to OH* or other water molecules, and accepted hydrogen bonds include H-bonds accepted by OH* or other water molecules. The zero coordinate corresponds to average position of Au atoms on the top surface layer of each model (excluding AR atoms on Au(100)-AR)). All potentials are referenced with respect to the SHE.

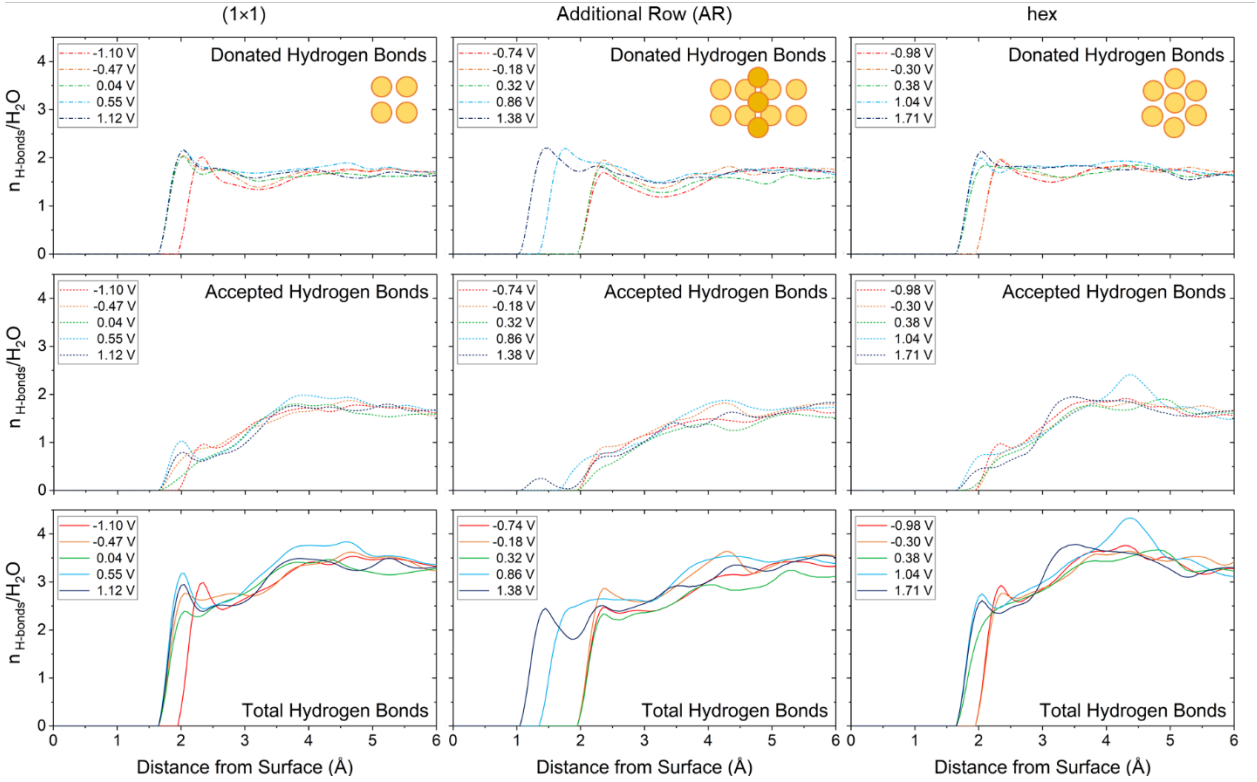

Figure E.5: Hydrogen bond density ($n_{H\text{-}bonds}/H_2O$) along the surface normal direction on Au(100) surface reconstructions covered with 2/10 ML OH* at a range of potentials. Donated hydrogen bonds include H-bonds donated to OH* or other water molecules, and accepted hydrogen bonds include H-bonds accepted by OH* or other water molecules. The zero coordinate corresponds to average position of Au atoms on the top surface layer of each model (excluding AR atoms on Au(100)-AR)). All potentials are referenced with respect to the SHE.

Appendix: F Supplementary Materials for 'Evaluating Interfacial Water Structures on Electrified Hydroxyl-covered Pt(111) through *Ab Initio* Molecular Dynamics Simulations'

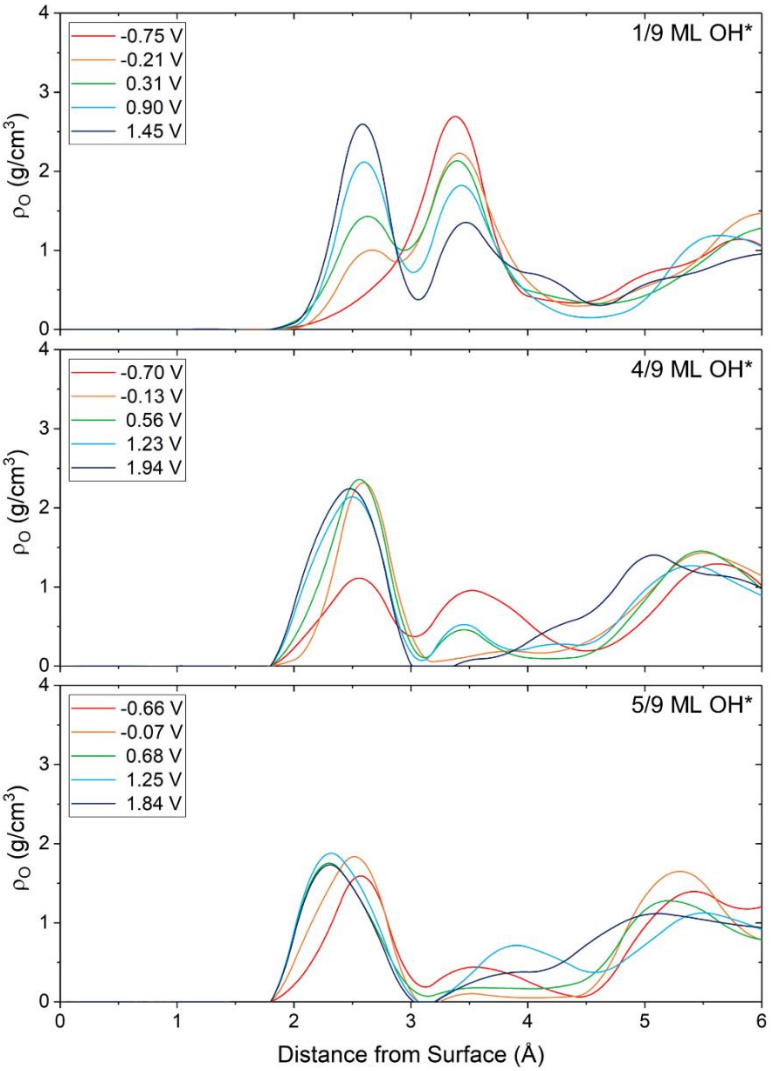

Figure F.1: Density of oxygen in water (ρ_O) along the surface normal direction on hydroxyl-covered, electrified Pt(111) surfaces, where zero distance corresponds to the center of the top layer of Pt. All potentials are referenced with respect to the SHE.

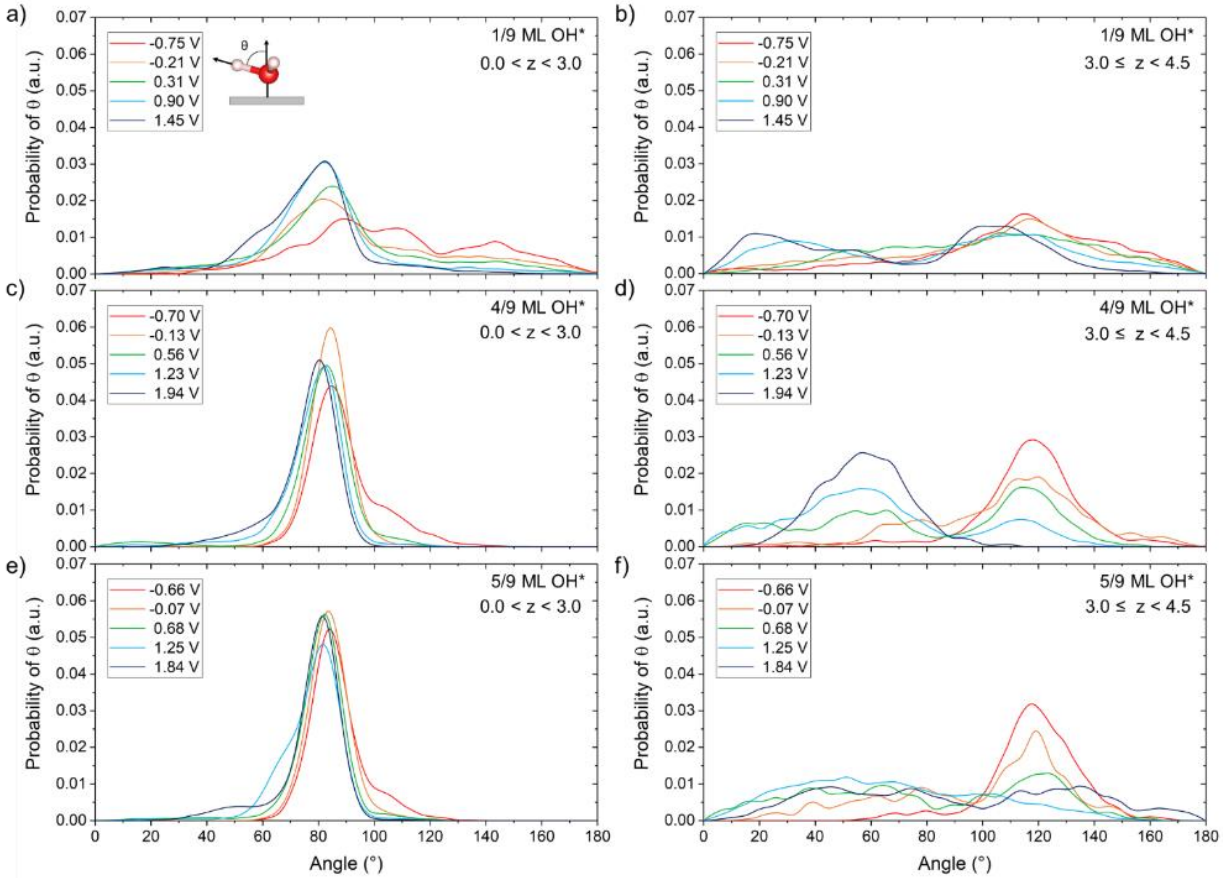

Figure F.2: Probability distribution of angle θ between the O-H bonds of water and the surface normal for interfacial water for the OH* coverages not present in Pourbaix diagram within 3.0 Å of the surface and within 3.0 and 4.5 Å of the surface. All potentials are referenced with respect to the SHE.

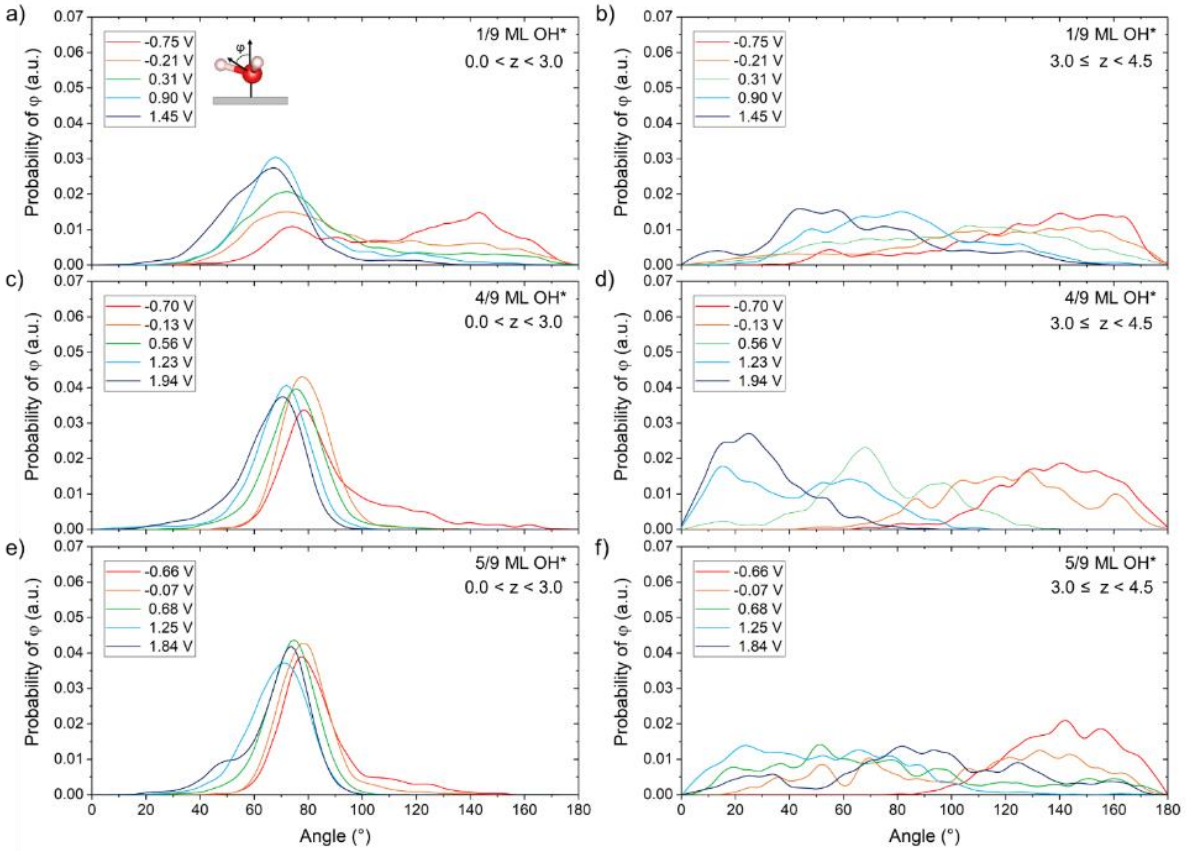

Figure F.3: Probability distribution of angle φ between the water bisector and the surface normal of interfacial water for the OH* coverages not present in Pourbaix diagram within 3.0 Å of the surface and within 3.0 and 4.5 Å of the surface. All potentials are referenced with respect to the SHE.

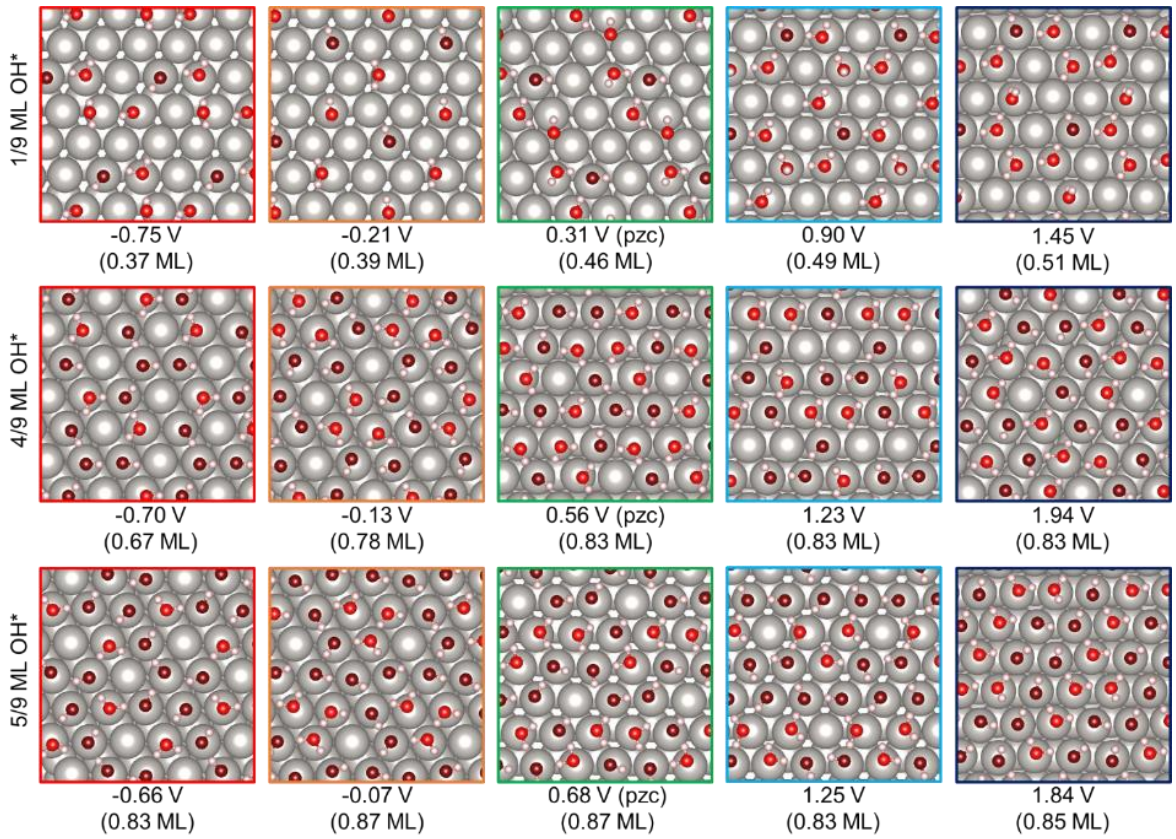

Figure F.4: Representative images of interfacial water within 3.1 Å of the surface from AIMD simulations. Coverages refer to the average total coverage of oxygenates (OH* + H_2O). Pt atoms are shown in gray, O atoms from water are shown in red, O atoms from OH* are shown in dark red, and H atoms are shown in white. All potentials are referenced with respect to the SHE.

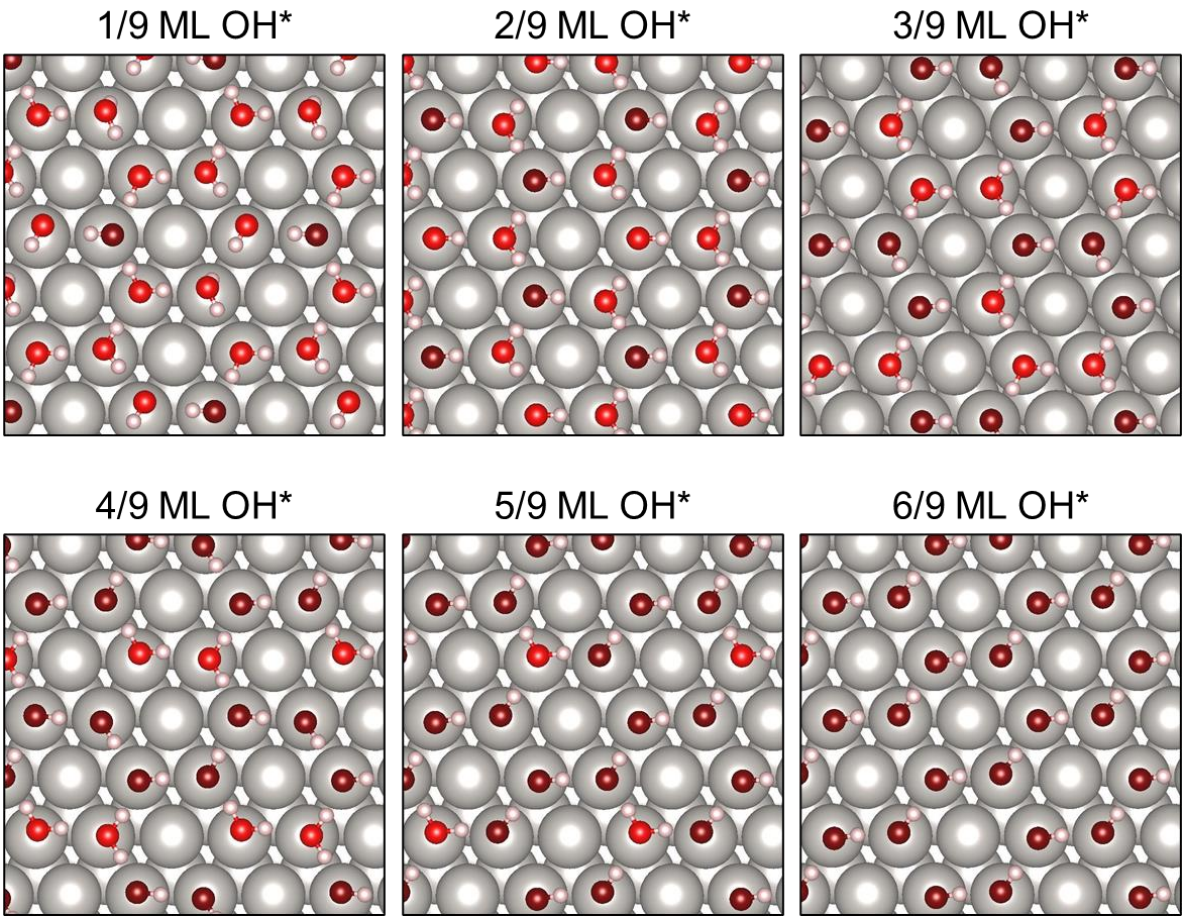

Figure F.5: Minimum energy structures of OH* adsorbates adsorbed on Pt(111) with a honeycomb water bilayer model. Pt atoms are shown in gray, O atoms from water are shown in red, O atoms from OH* are shown in dark red, and H atoms are shown in white.

Appendix: G Supplementary Materials for 'First-Principles Trends of Formic Acid Electro-oxidation on Transition Metals Alloyed with Platinum and Palladium'

G.1 Supplementary Tables

Table G.1: Lattice constants of transition metals and platinum or palladium alloyed with transition metals. Lattice constants for bulk alloys were calculated using a cubic unit cell with one overall lattice constant.

System	a_{DFT} (Å)	a_{Exp} (Å)[123]
Au	4.174	4.065
Ag	4.158	4.079
Cu	3.636	3.597
Ir	3.882	3.839
Pd	3.956	3.859
Pt	3.986	3.924
Rh	3.844	3.803
Ru	2.727 (c/a = 1.580)	2.706 (c/a = 1.582)
Re	2.778 (c/a = 1.615)	2.761 (c/a = 1.614)
Pt_3Au	4.030	-
Pt_3Ag	4.015	-
Pt_3Cu	3.911	-
Pt_3Ir	3.960	-
Pt_3Pd	3.975	-
Pt_3Rh	3.951	-
Pt_3Ru	3.944	-
Pt_3Re	3.960	-
Pd_3Au	4.011	-
Pd_3Ag	4.002	-
Pt_3Cu	3.890	-
Pd_3Ir	3.931	-
Pd_3Pd	3.961	-
Pd_3Rh	3.929	-
Pd_3Ru	3.918	-
Pd_3Re	3.940	-

Table G.2: Gibbs free energy (eV) of adsorbates relative to gas-phase CO_2, H_2, and H_2O bound to transition metals and platinum alloyed with transition metals at 298 K. The bulk-terminated alloys are bolded.

Surface	G(CO)	G(COOH)	G(OH)	G(HCOO)
Pt	-0.84	0.28	1.33	0.71
Pt_3Au-0_1	-0.81	0.35	1.42	0.85
Pt_3Au-0_2	-1.03	0.16	1.20	0.63
Pt_3Au-1_1	**-0.68**	**0.50**	**1.47**	**0.87**
Pt_3Au-1_2	-1.05	0.10	1.16	0.53
Pt_3Au-1_3	-1.04	0.11	1.15	0.50
Pt_3Au-2_1	-0.55	0.55	1.46	0.81
Pt_3Au-2_2	-0.93	0.16	1.18	0.47
Au	0.56	1.24	1.77	1.15
Pt_3Ag-0_1	-0.81	0.36	1.44	0.91
Pt_3Ag-0_2	-1.00	0.22	1.21	0.68
Pt_3Ag-1_1	**-0.70**	**0.47**	**1.31**	**0.79**
Pt_3Ag-1_2	-1.14	-0.01	1.00	0.43
Pt_3Ag-1_3	-1.12	0.00	0.99	0.39
Pt_3Ag-2_1	-0.76	0.35	1.20	0.53
Pt_3Ag-2_2	-1.17	-0.10	0.91	0.22
Ag	0.57	1.38	1.05	0.57
Pt_3Cu-0_1	-0.45	0.51	1.63	1.02
Pt_3Cu-0_2	-0.67	0.42	1.25	0.67
Pt_3Cu-1_1	**-0.52**	**0.54**	**1.37**	**0.82**
Pt_3Cu-1_2	-1.00	-0.02	0.98	0.44
Pt_3Cu-1_3	-1.01	0.06	0.95	0.46
Pt_3Cu-2_1	-0.87	0.17	1.05	0.41
Pt_3Cu-2_2	-1.27	-0.27	0.69	0.10
Cu	-0.02	0.88	0.58	0.24
Pt_3Ir-0_1	-0.38	0.58	1.57	0.93
Pt_3Ir-0_2	-0.69	0.33	1.25	0.60
Pt_3Ir-1_1	**-0.96**	**0.43**	**1.12**	**0.71**
Pt_3Ir-1_2	-1.32	0.12	0.80	0.38
Pt_3Ir-1_3	-1.31	0.09	0.80	0.34
Pt_3Ir-2_1	-1.13	0.09	1.08	0.38
Pt_3Ir-2_2	-1.42	-0.29	0.72	-0.01
Ir	-1.02	0.12	1.00	0.23
Pt_3Pd-0_1	-0.67	0.44	1.48	0.89
Pt_3Pd-0_2	-0.86	0.27	1.30	0.70
Pt_3Pd-1_1	**-0.71**	**0.42**	**1.36**	**0.81**
Pt_3Pd-1_2	-0.93	0.16	1.16	0.58
Pt_3Pd-1_3	-0.96	0.14	1.16	0.57
Pt_3Pd-2_1	-0.81	0.31	1.26	0.68
Pt_3Pd-2_2	-1.04	0.06	1.06	0.46
Surface	G(CO)	G(COOH)	G(OH)	G(HCOO)

Pd	-1.02	0.42	1.13	0.62
$Pt_3Rh\text{-}0_1$	-0.40	0.59	1.66	1.00
$Pt_3Rh\text{-}0_2$	-0.67	0.35	1.37	0.72
$Pt_3Rh\text{-}1_1$	**-0.69**	**0.37**	**1.34**	**0.72**
$Pt_3Rh\text{-}1_2$	-0.96	0.11	1.08	0.46
$Pt_3Rh\text{-}1_3$	-0.96	0.07	1.05	0.44
$Pt_3Rh\text{-}2_1$	-0.83	0.20	1.00	0.40
$Pt_3Rh\text{-}2_2$	-1.09	-0.06	0.72	0.11
Rh	-1.07	0.06	0.63	0.09
$Pt_3Ru\text{-}0_1$	-0.24	0.67	1.70	0.99
$Pt_3Ru\text{-}0_2$	-0.54	0.41	1.35	0.67
$Pt_3Ru\text{-}1_1$	**-0.86**	**0.31**	**0.98**	**0.57**
$Pt_3Ru\text{-}1_2$	-1.07	-0.04	0.63	0.20
$Pt_3Ru\text{-}1_3$	-1.02	-0.08	0.67	0.24
$Pt_3Ru\text{-}2_1$	-0.90	0.11	0.67	0.05
$Pt_3Ru\text{-}2_2$	-1.25	-0.19	0.36	-0.30
Ru	-0.95	-0.03	0.25	-0.34
$Pt_3Re\text{-}0_1$	-0.55	0.36	1.07	0.42
$Pt_3Re\text{-}0_2$	-0.44	0.47	1.29	0.61
$Pt_3Re\text{-}1_1$	**-1.51**	**-0.10**	**-0.24**	**-0.12**
$Pt_3Re\text{-}1_2$	-0.94	-0.16	-0.08	-0.19
$Pt_3Re\text{-}1_3$	-0.93	-0.16	0.02	-0.05
$Pt_3Re\text{-}2_1$	-1.41	-0.70	-0.62	-1.04
$Pt_3Re\text{-}2_2$	-1.16	-0.41	0.01	-0.85
Re	-0.96	0.10	-0.13	-0.47

Table G.3: Gibbs free energy (eV) of adsorbates relative to gas-phase CO_2, H_2, and H_2O bound to transition metals and palladium alloyed with transition metals at 298 K. The bulk-terminated alloys are bolded.

Surface	G(CO)	G(COOH)	G(OH)	G(HCOO)
Pd	-1.02	0.42	1.13	0.62
Pd_3Au-0_1	-0.99	0.49	1.19	0.69
Pd_3Au-0_2	-1.07	0.44	1.11	0.61
Pd_3Au-1_1	**-0.93**	**0.62**	**1.35**	**0.81**
Pd_3Au-1_2	-0.99	0.49	1.21	0.70
Pd_3Au-1_3	-1.08	0.42	1.12	0.58
Pd_3Au-2_1	-0.95	0.62	1.36	0.81
Pd_3Au-2_2	-0.56	0.71	1.39	0.83
Au	0.56	1.24	1.77	1.15
Pd_3Ag-0_1	-0.96	0.50	1.18	0.73
Pd_3Ag-0_2	-1.10	0.38	1.02	0.61
Pd_3Ag-1_1	**-0.87**	**0.57**	**1.18**	**0.68**
Pd_3Ag-1_2	-0.94	0.59	1.22	0.70
Pd_3Ag-1_3	-1.16	0.35	0.97	0.45
Pd_3Ag-2_1	-0.71	0.57	1.11	0.55
Pd_3Ag-2_2	-0.89	0.36	0.96	0.38
Ag	0.57	1.38	1.05	0.57
Pd_3Cu-0_1	-0.71	0.62	1.33	0.82
Pd_3Cu-0_2	-0.89	0.49	1.10	0.62
Pd_3Cu-1_1	**-0.73**	**0.63**	**1.14**	**0.68**
Pd_3Cu-1_2	-1.02	0.38	0.97	0.49
Pd_3Cu-1_3	-1.05	0.38	0.92	0.50
Pd_3Cu-2_1	-0.79	0.45	0.85	0.49
Pd_3Cu-2_2	-0.94	0.25	0.66	0.33
Cu	-0.02	0.88	0.58	0.24
Pd_3Ir-0_1	-0.66	0.59	1.12	0.63
Pd_3Ir-0_2	-0.81	0.41	0.95	0.43
Pd_3Ir-1_1	**-1.24**	**0.10**	**0.82**	**0.47**
Pd_3Ir-1_2	-1.48	-0.11	0.52	0.19
Pd_3Ir-1_3	-1.45	-0.07	0.55	0.19
Pd_3Ir-2_1	-1.40	-0.17	0.75	0.17
Pd_3Ir-2_2	-1.58	-0.49	0.48	-0.14
Ir	-1.02	0.12	1.00	0.23
Pd_3Pt-0_1	-0.85	0.51	1.16	0.66
Pd_3Pt-0_2	-1.03	0.35	1.01	0.50
Pd_3Pt-1_1	**-0.86**	**0.28**	**1.28**	**0.76**
Pd_3Pt-1_2	-1.05	0.04	1.00	0.53
Pd_3Pt-1_3	-1.04	0.01	0.98	0.50
Pd_3Pt-2_1	-0.88	0.28	1.33	0.79
Pd_3Pt-2_2	-1.04	0.15	1.15	0.60
Surface	G(CO)	G(COOH)	G(OH)	G(HCOO)

Pt	-0.84	0.28	1.33	0.71
$Pd_3Rh\text{-}0_1$	-0.73	0.60	1.20	0.71
$Pd_3Rh\text{-}0_2$	-0.87	0.44	1.05	0.55
$Pd_3Rh\text{-}1_1$	**-0.98**	**0.24**	**0.95**	**0.47**
$Pd_3Rh\text{-}1_2$	-1.17	0.08	0.76	0.28
$Pd_3Rh\text{-}1_3$	-1.15	0.10	0.76	0.28
$Pd_3Rh\text{-}2_1$	-1.17	-0.06	0.63	0.13
$Pd_3Rh\text{-}2_2$	-1.34	-0.29	0.44	-0.10
Rh	-1.07	0.06	0.63	0.09
$Pd_3Ru\text{-}0_1$	-0.58	0.68	1.17	0.70
$Pd_3Ru\text{-}0_2$	-0.76	0.54	1.02	0.50
$Pd_3Ru\text{-}1_1$	**-1.17**	**0.24**	**0.67**	**0.27**
$Pd_3Ru\text{-}1_2$	-1.18	0.16	0.36	0.00
$Pd_3Ru\text{-}1_3$	-1.15	0.16	0.43	0.06
$Pd_3Ru\text{-}2_1$	-1.18	-0.24	0.22	-0.28
$Pd_3Ru\text{-}2_2$	-1.36	-0.34	0.15	-0.43
Ru	-0.95	-0.03	0.25	-0.34
$Pd_3Re\text{-}0_1$	-0.70	0.45	0.78	0.28
$Pd_3Re\text{-}0_2$	-0.62	0.62	1.07	0.50
$Pd_3Re\text{-}1_1$	**-1.66**	**-0.20**	**-0.43**	**-0.35**
$Pd_3Re\text{-}1_2$	-1.07	0.10	-0.32	-0.40
$Pd_3Re\text{-}1_3$	-1.03	0.09	-0.16	-0.19
$Pd_3Re\text{-}2_1$	-1.69	-1.13	-0.87	-1.43
$Pd_3Re\text{-}2_2$	-1.26	-0.66	-0.30	-1.00
Re	-0.96	0.10	-0.13	-0.47

Table G.4: Onset potential of FA electro-oxidation pathways on transition metals and platinum alloyed with transition metals. The bulk-terminated alloys are bolded.

Surface	Direct Formic Oxidation Onset Potential (U_{RHE})	Direct Carboxyl Oxidation Onset Potential (U_{RHE})	Indirect Carboxyl Oxidation Onset Potential (U_{RHE})
Pt	0.45	0.02	1.12
$Pt_3Au\text{-}0_1$	0.60	0.09	1.16
$Pt_3Au\text{-}0_2$	0.37	-0.09	1.19
$Pt_3Au\text{-}1_1$	**0.62**	**0.25**	**1.19**
$Pt_3Au\text{-}1_2$	0.27	-0.10	1.16
$Pt_3Au\text{-}1_3$	0.24	-0.11	1.15
$Pt_3Au\text{-}2_1$	0.55	0.30	1.10
$Pt_3Au\text{-}2_2$	0.22	-0.10	1.09
Au	0.89	0.98	0.68
$Pt_3Ag\text{-}0_1$	0.65	0.10	1.16
$Pt_3Ag\text{-}0_2$	0.42	-0.04	1.21
$Pt_3Ag\text{-}1_1$	**0.53**	**0.21**	**1.17**
$Pt_3Ag\text{-}1_2$	0.18	0.01	1.00
$Pt_3Ag\text{-}1_3$	0.14	0.00	0.99
$Pt_3Ag\text{-}2_1$	0.27	0.09	1.11
$Pt_3Ag\text{-}2_2$	-0.04	0.10	0.91
Ag	0.31	1.12	0.81
$Pt_3Cu\text{-}0_1$	0.77	0.26	0.96
$Pt_3Cu\text{-}0_2$	0.42	0.16	1.09
$Pt_3Cu\text{-}1_1$	**0.57**	**0.29**	**1.06**
$Pt_3Cu\text{-}1_2$	0.19	0.02	0.98
$Pt_3Cu\text{-}1_3$	0.20	-0.06	0.95
$Pt_3Cu\text{-}2_1$	0.15	-0.09	1.04
$Pt_3Cu\text{-}2_2$	0.01	0.27	0.69
Cu	-0.02	0.62	0.58
$Pt_3Ir\text{-}0_1$	0.67	0.33	0.96
$Pt_3Ir\text{-}0_2$	0.35	0.07	1.02
$Pt_3Ir\text{-}1_1$	**0.46**	**0.17**	**1.12**
$Pt_3Ir\text{-}1_2$	0.12	-0.12	0.80
$Pt_3Ir\text{-}1_3$	0.08	-0.09	0.80
$Pt_3Ir\text{-}2_1$	0.12	-0.09	1.08
$Pt_3Ir\text{-}2_2$	-0.11	0.29	0.72
Ir	-0.02	-0.12	1.00
$Pt_3Pd\text{-}0_1$	0.63	0.18	1.11
$Pt_3Pd\text{-}0_2$	0.45	0.02	1.12
$Pt_3Pd\text{-}1_1$	**0.56**	**0.17**	**1.13**
$Pt_3Pd\text{-}1_2$	0.32	-0.09	1.09
$Pt_3Pd\text{-}1_3$	0.31	-0.12	1.10
$Pt_3Pd\text{-}2_1$	0.43	0.06	1.12

Surface	Direct Formic Oxidation Onset Potential (U_{RHE})	Direct Carboxyl Oxidation Onset Potential (U_{RHE})	Indirect Carboxyl Oxidation Onset Potential (U_{RHE})
$Pt_3Pd\text{-}2_2$	-0.11	-0.06	1.06
Pd	0.37	0.16	1.13
$Pt_3Rh\text{-}0_1$	0.75	0.33	0.99
$Pt_3Rh\text{-}0_2$	0.46	0.09	1.01
$Pt_3Rh\text{-}1_1$	**0.46**	**0.12**	**1.07**
$Pt_3Rh\text{-}1_2$	0.20	-0.11	1.07
$Pt_3Rh\text{-}1_3$	0.18	-0.07	1.04
$Pt_3Rh\text{-}2_1$	0.15	-0.06	1.00
$Pt_3Rh\text{-}2_2$	-0.11	0.06	0.72
Rh	-0.09	-0.06	0.63
$Pt_3Ru\text{-}0_1$	0.74	0.42	0.92
$Pt_3Ru\text{-}0_2$	0.42	0.16	0.95
$Pt_3Ru\text{-}1_1$	**0.32**	**0.05**	**0.98**
$Pt_3Ru\text{-}1_2$	-0.06	0.04	0.63
$Pt_3Ru\text{-}1_3$	-0.02	0.08	0.67
$Pt_3Ru\text{-}2_1$	-0.05	-0.11	0.67
$Pt_3Ru\text{-}2_2$	-0.11	0.19	0.89
Ru	0.34	0.03	0.70
$Pt_3Re\text{-}0_1$	0.17	0.10	0.90
$Pt_3Re\text{-}0_2$	0.36	0.22	0.91
$Pt_3Re\text{-}1_1$	**0.12**	**0.10**	**1.41**
$Pt_3Re\text{-}1_2$	0.19	0.16	0.78
$Pt_3Re\text{-}1_3$	0.05	0.16	0.77
$Pt_3Re\text{-}2_1$	1.04	0.70	0.71
$Pt_3Re\text{-}2_2$	0.85	0.41	0.75
Re	0.47	-0.10	1.05

Table G.5: Onset potential of FA electro-oxidation pathways on transition metals and palladium alloyed with transition metals. The bulk-terminated alloys are bolded.

Surface	Direct Formic Oxidation Onset Potential (U_{RHE})	Direct Carboxyl Oxidation Onset Potential (U_{RHE})	Indirect Carboxyl Oxidation Onset Potential (U_{RHE})
Pd	0.37	0.16	1.13
Pd_3Au-0_1	0.44	0.23	1.19
Pd_3Au-0_2	0.35	0.18	1.11
Pd_3Au-1_1	**0.55**	**0.36**	**1.35**
Pd_3Au-1_2	0.44	0.23	1.21
Pd_3Au-1_3	0.33	0.17	1.12
Pd_3Au-2_1	0.55	0.37	1.36
Pd_3Au-2_2	0.58	0.45	1.26
Au	0.89	0.98	0.68
Pd_3Ag-0_1	0.47	0.24	1.18
Pd_3Ag-0_2	0.35	0.13	1.02
Pd_3Ag-1_1	**0.43**	**0.32**	**1.18**
Pd_3Ag-1_2	0.45	0.33	1.22
Pd_3Ag-1_3	0.19	0.09	0.97
Pd_3Ag-2_1	0.29	0.32	1.11
Pd_3Ag-2_2	0.12	0.10	0.96
Ag	0.31	1.12	0.81
Pd_3Cu-0_1	0.57	0.37	1.33
Pd_3Cu-0_2	0.37	0.24	1.10
Pd_3Cu-1_1	**0.42**	**0.37**	**1.14**
Pd_3Cu-1_2	0.24	0.12	0.97
Pd_3Cu-1_3	0.25	0.12	0.92
Pd_3Cu-2_1	0.23	0.20	0.85
Pd_3Cu-2_2	0.14	0.00	0.66
Cu	-0.02	0.62	0.58
Pd_3Ir-0_1	0.38	0.34	1.12
Pd_3Ir-0_2	0.17	0.16	0.95
Pd_3Ir-1_1	**0.21**	**-0.10**	**0.82**
Pd_3Ir-1_2	-0.06	0.11	0.96
Pd_3Ir-1_3	-0.07	0.07	0.90
Pd_3Ir-2_1	-0.09	0.17	0.75
Pd_3Ir-2_2	0.14	0.49	1.10
Ir	-0.02	-0.12	1.00
Pd_3Pt-0_1	0.40	0.25	1.16
Pd_3Pt-0_2	0.24	0.10	1.01
Pd_3Pt-1_1	**0.50**	**0.02**	**1.14**
Pd_3Pt-1_2	0.27	-0.04	1.00
Pd_3Pt-1_3	0.24	-0.01	0.98
Pd_3Pt-2_1	0.53	0.02	1.16

Surface	Direct Formic Oxidation Onset Potential (U_{RHE})	Direct Carboxyl Oxidation Onset Potential (U_{RHE})	Indirect Carboxyl Oxidation Onset Potential (U_{RHE})
$Pd_3Pt\text{-}2_2$	0.35	-0.11	1.15
Pt	0.45	0.02	1.12
$Pd_3Rh\text{-}0_1$	0.45	0.35	1.20
$Pd_3Rh\text{-}0_2$	0.29	0.19	1.05
$Pd_3Rh\text{-}1_1$	**0.22**	**-0.02**	**0.95**
$Pd_3Rh\text{-}1_2$	0.02	-0.08	0.76
$Pd_3Rh\text{-}1_3$	0.02	-0.10	0.76
$Pd_3Rh\text{-}2_1$	-0.13	0.06	0.63
$Pd_3Rh\text{-}2_2$	0.10	0.29	0.91
Rh	-0.09	-0.06	0.63
$Pd_3Ru\text{-}0_1$	0.44	0.42	1.17
$Pd_3Ru\text{-}0_2$	0.24	0.28	1.02
$Pd_3Ru\text{-}1_1$	**0.01**	**-0.02**	**0.67**
$Pd_3Ru\text{-}1_2$	0.00	-0.09	0.83
$Pd_3Ru\text{-}1_3$	-0.06	-0.10	0.72
$Pd_3Ru\text{-}2_1$	0.28	0.24	0.94
$Pd_3Ru\text{-}2_2$	0.43	0.34	1.02
Ru	0.34	0.03	0.70
$Pd_3Re\text{-}0_1$	0.03	0.20	0.78
$Pd_3Re\text{-}0_2$	0.24	0.37	1.07
$Pd_3Re\text{-}1_1$	**0.35**	**0.20**	**1.47**
$Pd_3Re\text{-}1_2$	0.40	-0.10	1.17
$Pd_3Re\text{-}1_3$	0.19	-0.09	1.12
$Pd_3Re\text{-}2_1$	1.43	1.13	0.56
$Pd_3Re\text{-}2_2$	1.00	0.66	0.60
Re	0.47	-0.10	1.05

Table G.6: Gibbs free energy (eV) of steps in FA electro-oxidation pathways on transition metals and platinum alloyed with transition metals. The bulk-terminated alloys are bolded.

Surface	HCOOH(g) → HCOO* + 1/2H_2	HCOO* → CO2(g) + 1/2H_2	HCOOH(g) → COOH* + 1/2H_2	COOH* →CO2(g) + 1/2H_2	CO* + H2O(g) → COOH* + 1/2H_2	H2O(g) → OH* + 1/2H_2	CO* + OH* → CO2(g) + 1/2H_2
Pt	0.45	-0.71	0.02	-0.28	1.12	1.33	-0.49
Pt_3Au-0_1	0.60	-0.85	0.09	-0.35	1.16	1.42	-0.61
Pt_3Au-0_2	0.37	-0.63	-0.09	-0.16	1.19	1.20	-0.16
Pt_3Au-1_1	**0.62**	**-0.87**	**0.25**	**-0.50**	**1.19**	**1.47**	**-0.79**
Pt_3Au-1_2	0.27	-0.53	-0.16	-0.10	1.16	1.16	-0.10
Pt_3Au-1_3	0.24	-0.50	-0.15	-0.11	1.15	1.15	-0.11
Pt_3Au-2_1	0.55	-0.81	0.30	-0.55	1.10	1.46	-0.91
Pt_3Au-2_2	0.22	-0.47	-0.10	-0.16	1.09	1.18	-0.25
Au	0.89	-1.15	0.98	-1.24	0.68	1.77	-2.33
Pt_3Ag-0_1	0.65	-0.91	0.10	-0.36	1.16	1.44	-0.63
Pt_3Ag-0_2	0.42	-0.68	-0.04	-0.22	1.22	1.21	-0.21
Pt_3Ag-1_1	**0.53**	**-0.79**	**0.21**	**-0.47**	**1.17**	**1.31**	**-0.61**
Pt_3Ag-1_2	0.18	-0.43	-0.26	0.01	1.13	1.00	0.14
Pt_3Ag-1_3	0.14	-0.39	-0.25	0.00	1.12	0.99	0.12
Pt_3Ag-2_1	0.27	-0.53	0.09	-0.35	1.11	1.20	-0.44
Pt_3Ag-2_2	-0.04	-0.22	-0.36	0.10	1.07	0.91	0.26
Ag	0.31	-0.57	1.12	-1.38	0.81	1.05	-1.61
Pt_3Cu-0_1	0.77	-1.02	0.26	-0.51	0.96	1.63	-1.18
Pt_3Cu-0_2	0.42	-0.67	0.16	-0.42	1.09	1.25	-0.57
Pt_3Cu-1_1	**0.57**	**-0.82**	**0.29**	**-0.54**	**1.06**	**1.37**	**-0.85**
Pt_3Cu-1_2	0.19	-0.44	-0.27	0.02	0.98	0.98	0.02
Pt_3Cu-1_3	0.20	-0.46	-0.20	-0.06	1.07	0.95	0.06
Pt_3Cu-2_1	0.15	-0.41	-0.09	-0.17	1.04	1.05	-0.17
Pt_3Cu-2_2	0.01	-0.27	-0.53	0.27	0.99	0.69	0.58
Cu	-0.02	-0.24	0.62	-0.88	0.90	0.58	-0.56
Pt_3Ir-0_1	0.67	-0.93	0.33	-0.58	0.96	1.57	-1.19
Pt_3Ir-0_2	0.35	-0.60	0.07	-0.33	1.02	1.25	-0.56
Pt_3Ir-1_1	**0.46**	**-0.71**	**0.17**	**-0.43**	**1.39**	**1.12**	**-0.16**
Pt_3Ir-1_2	0.12	-0.38	-0.14	-0.12	1.43	0.80	0.52
Pt_3Ir-1_3	0.08	-0.34	-0.16	-0.09	1.40	0.80	0.50
Pt_3Ir-2_1	0.12	-0.38	-0.16	-0.09	1.23	1.08	0.05
Pt_3Ir-2_2	-0.11	-0.15	-0.55	0.29	1.12	0.72	0.69
Ir	-0.02	-0.23	-0.13	-0.12	1.14	1.00	0.01
Pt_3Pd-0_1	0.63	-0.89	0.18	-0.44	1.11	1.48	-0.80
Pt_3Pd-0_2	0.45	-0.70	0.01	-0.27	1.13	1.30	-0.44
Pt_3Pd-1_1	**0.56**	**-0.81**	**0.17**	**-0.42**	**1.13**	**1.36**	**-0.65**
Pt_3Pd-1_2	0.32	-0.58	-0.09	-0.16	1.09	1.16	-0.23

Surface	HCOOH(g) → HCOO* + 1/2H_2	HCOO* → CO2(g) + 1/2H_2	HCOOH(g) → COOH* + 1/2H_2	COOH* →CO2(g) + 1/2H_2	CO* + H2O(g) → COOH* + 1/2H_2	H2O(g) → OH* + 1/2H_2	CO* + OH* → CO2(g) + 1/2H_2
Pt_3Pd-1_3	0.31	-0.57	-0.12	-0.14	1.10	1.16	-0.20
Pt_3Pd-2_1	0.43	-0.68	0.06	-0.31	1.12	1.26	-0.46
Pt_3Pd-2_2	-0.11	-0.15	-0.20	-0.06	1.10	1.06	-0.02
Pd	0.37	-0.62	0.16	-0.42	1.44	1.13	-0.11
Pt_3Rh-0_1	0.75	-1.00	0.33	-0.59	0.99	1.66	-1.25
Pt_3Rh-0_2	0.46	-0.72	0.09	-0.35	1.01	1.37	-0.71
Pt_3Rh-1_1	**0.46**	**-0.72**	**0.12**	**-0.37**	**1.07**	**1.34**	**-0.64**
Pt_3Rh-1_2	0.20	-0.46	-0.15	-0.11	1.07	1.08	-0.12
Pt_3Rh-1_3	0.18	-0.44	-0.18	-0.07	1.04	1.05	-0.09
Pt_3Rh-2_1	0.15	-0.40	-0.06	-0.20	1.02	1.00	-0.17
Pt_3Rh-2_2	-0.15	-0.11	-0.31	0.06	1.03	0.72	0.36
Rh	-0.17	-0.09	-0.20	-0.06	1.13	0.63	0.44
Pt_3Ru-0_1	0.74	-0.99	0.42	-0.67	0.92	1.70	-1.45
Pt_3Ru-0_2	0.42	-0.67	0.16	-0.41	0.95	1.35	-0.81
Pt_3Ru-1_1	**0.32**	**-0.57**	**0.05**	**-0.31**	**1.17**	**0.98**	**-0.12**
Pt_3Ru-1_2	-0.06	-0.20	-0.30	0.04	1.03	0.63	0.44
Pt_3Ru-1_3	-0.02	-0.24	-0.33	0.08	0.94	0.67	0.35
Pt_3Ru-2_1	-0.21	-0.05	-0.14	-0.11	1.01	0.67	0.23
Pt_3Ru-2_2	-0.11	-0.15	-0.45	0.19	1.06	0.36	0.89
Ru	-0.59	0.34	-0.28	0.03	0.92	0.25	0.70
Pt_3Re-0_1	0.17	-0.42	0.10	-0.36	0.90	1.07	-0.53
Pt_3Re-0_2	0.36	-0.61	0.22	-0.47	0.91	1.29	-0.85
Pt_3Re-1_1	**-0.38**	**0.12**	**-0.35**	**0.10**	**1.41**	**-0.24**	**1.75**
Pt_3Re-1_2	-0.45	0.19	-0.42	0.16	0.78	-0.08	1.02
Pt_3Re-1_3	-0.30	0.05	-0.42	0.16	0.77	0.02	0.90
Pt_3Re-2_1	-1.29	1.04	-0.96	0.70	0.71	-0.62	2.04
Pt_3Re-2_2	-1.10	0.85	-0.66	0.41	0.75	0.01	1.15
Re	-0.73	0.47	-0.16	-0.10	1.05	-0.13	1.09

Table G.7: Gibbs free energy (eV) of steps in FA electro-oxidation pathways on transition metals and palladium alloyed with transition metals. The bulk-terminated alloys are bolded.

Surface	HCOOH(g) → HCOO* + 1/2H_2	HCOO* → CO2(g) + 1/2H_2	HCOOH(g) → COOH* + 1/2H_2	COOH* →CO2(g) + 1/2H_2	CO* + H2O(g) → COOH* + 1/2H_2	H2O(g) → OH* + 1/2H_2	CO* + OH* → CO2(g) + 1/2H_2
Pd	0.37	-0.62	0.16	-0.42	1.44	1.13	-0.11
Pd_3Au-0_1	0.44	-0.69	0.23	-0.49	1.47	1.19	-0.21
Pd_3Au-0_2	0.35	-0.61	0.18	-0.44	1.51	1.11	-0.04
Pd_3Au-1_1	**0.55**	**-0.81**	**0.36**	**-0.62**	**1.55**	**1.35**	**-0.42**
Pd_3Au-1_2	0.44	-0.70	0.23	-0.49	1.47	1.21	-0.22
Pd_3Au-1_3	0.33	-0.58	0.17	-0.42	1.50	1.12	-0.05
Pd_3Au-2_1	0.55	-0.81	0.37	-0.62	1.57	1.36	-0.41
Pd_3Au-2_2	0.58	-0.83	0.45	-0.71	1.26	1.39	-0.83
Au	0.89	-1.15	0.98	-1.24	0.68	1.77	-2.33
Pd_3Ag-0_1	0.47	-0.73	0.24	-0.50	1.45	1.18	-0.22
Pd_3Ag-0_2	0.35	-0.61	0.13	-0.38	1.48	1.02	0.08
Pd_3Ag-1_1	**0.43**	**-0.68**	**0.32**	**-0.57**	**1.45**	**1.18**	**-0.31**
Pd_3Ag-1_2	0.45	-0.70	0.33	-0.59	1.53	1.22	-0.28
Pd_3Ag-1_3	0.19	-0.45	0.09	-0.35	1.51	0.97	0.19
Pd_3Ag-2_1	0.29	-0.55	0.32	-0.57	1.28	1.11	-0.40
Pd_3Ag-2_2	0.12	-0.38	0.10	-0.36	1.25	0.96	-0.07
Ag	0.31	-0.57	1.12	-1.38	0.81	1.05	-1.61
Pd_3Cu-0_1	0.57	-0.82	0.37	-0.62	1.33	1.33	-0.61
Pd_3Cu-0_2	0.37	-0.62	0.24	-0.49	1.38	1.10	-0.21
Pd_3Cu-1_1	**0.42**	**-0.68**	**0.37**	**-0.63**	**1.35**	**1.14**	**-0.41**
Pd_3Cu-1_2	0.24	-0.49	0.12	-0.38	1.40	0.97	0.06
Pd_3Cu-1_3	0.25	-0.50	0.12	-0.38	1.43	0.92	0.13
Pd_3Cu-2_1	0.23	-0.49	0.20	-0.45	1.24	0.85	-0.06
Pd_3Cu-2_2	0.14	-0.40	0.00	-0.25	1.19	0.66	0.28
Cu	-0.02	-0.24	0.62	-0.88	0.90	0.58	-0.56
Pd_3Ir-0_1	0.38	-0.63	0.34	-0.59	1.25	1.12	-0.46
Pd_3Ir-0_2	0.17	-0.43	0.16	-0.41	1.22	0.95	-0.14
Pd_3Ir-1_1	**0.21**	**-0.47**	**-0.16**	**-0.10**	**1.33**	**0.82**	**0.42**
Pd_3Ir-1_2	-0.06	-0.19	-0.36	0.11	1.37	0.52	0.96
Pd_3Ir-1_3	-0.07	-0.19	-0.32	0.07	1.39	0.55	0.90
Pd_3Ir-2_1	-0.09	-0.17	-0.43	0.17	1.24	0.75	0.65
Pd_3Ir-2_2	-0.40	0.14	-0.74	0.49	1.10	0.48	1.10
Ir	-0.02	-0.23	-0.13	-0.12	1.14	1.00	0.01
Pd_3Pt-0_1	0.40	-0.66	0.25	-0.51	1.36	1.16	-0.31
Pd_3Pt-0_2	0.24	-0.50	0.10	-0.35	1.38	1.01	0.02
Pd_3Pt-1_1	**0.50**	**-0.76**	**0.02**	**-0.28**	**1.14**	**1.28**	**-0.42**
Pd_3Pt-1_2	0.27	-0.53	-0.21	-0.04	1.09	1.00	0.05

Surface	HCOOH(g) → HCOO* + 1/2H_2	HCOO* → CO2(g) + 1/2H_2	HCOOH(g) → COOH* + 1/2H_2	COOH* →CO2(g) + 1/2H_2	CO* + H2O(g) → COOH* + 1/2H_2	H2O(g) → OH* + 1/2H_2	CO* + OH* → CO2(g) + 1/2H_2
Pd_3Pt-1_3	0.24	-0.50	-0.24	-0.01	1.06	0.98	0.07
Pd_3Pt-2_1	0.53	-0.79	0.02	-0.28	1.16	1.33	-0.45
Pd_3Pt-2_2	0.35	-0.60	-0.11	-0.15	1.19	1.15	-0.11
Pt	0.45	-0.71	0.02	-0.28	1.12	1.33	-0.49
Pd_3Rh-0_1	0.45	-0.71	0.35	-0.60	1.34	1.20	-0.47
Pd_3Rh-0_2	0.29	-0.55	0.19	-0.44	1.32	1.05	-0.18
Pd_3Rh-1_1	**0.22**	**-0.47**	**-0.02**	**-0.24**	**1.21**	**0.95**	**0.02**
Pd_3Rh-1_2	0.02	-0.28	-0.18	-0.08	1.25	0.76	0.41
Pd_3Rh-1_3	0.02	-0.28	-0.16	-0.10	1.25	0.76	0.39
Pd_3Rh-2_1	-0.13	-0.13	-0.31	0.06	1.12	0.63	0.54
Pd_3Rh-2_2	-0.35	0.10	-0.54	0.29	1.06	0.44	0.91
Rh	-0.17	-0.09	-0.20	-0.06	1.13	0.63	0.44
Pd_3Ru-0_1	0.44	-0.70	0.42	-0.68	1.26	1.17	-0.60
Pd_3Ru-0_2	0.24	-0.50	0.28	-0.54	1.30	1.02	-0.26
Pd_3Ru-1_1	**0.01**	**-0.27**	**-0.02**	**-0.24**	**1.41**	**0.67**	**0.49**
Pd_3Ru-1_2	-0.26	0.00	-0.09	-0.16	1.35	0.36	0.83
Pd_3Ru-1_3	-0.19	-0.06	-0.10	-0.16	1.30	0.43	0.72
Pd_3Ru-2_1	-0.54	0.28	-0.50	0.24	0.94	0.22	0.96
Pd_3Ru-2_2	-0.68	0.43	-0.60	0.34	1.02	0.15	1.21
Ru	-0.59	0.34	-0.28	0.03	0.92	0.25	0.70
Pd_3Re-0_1	0.03	-0.28	0.20	-0.45	1.15	0.78	-0.08
Pd_3Re-0_2	0.24	-0.50	0.37	-0.62	1.24	1.07	-0.45
Pd_3Re-1_1	**-0.61**	**0.35**	**-0.46**	**0.20**	**1.47**	**-0.43**	**2.09**
Pd_3Re-1_2	-0.66	0.40	-0.15	-0.10	1.17	-0.32	1.39
Pd_3Re-1_3	-0.45	0.19	-0.17	-0.09	1.12	-0.16	1.19
Pd_3Re-2_1	-1.69	1.43	-1.38	1.13	0.56	-0.87	2.56
Pd_3Re-2_2	-1.25	1.00	-0.92	0.66	0.60	-0.30	1.57
Re	-0.73	0.47	-0.16	-0.10	1.05	-0.13	1.09

Table G.8: Relative energy (eV) of 2×2 unit cells with platinum alloyed with transition metals compared to the bulk-terminated alloy system (in bold).

Surface	clean	CO	COOH	OH	HCOO
$Pt_3Au\text{-}0_1$	0.38	0.25	0.23	0.34	0.36
$Pt_3Au\text{-}0_2$	0.64	0.29	0.30	0.37	0.39
$Pt_3Au\text{-}1_1$	**0.00**	**0.00**	**0.00**	**0.00**	**0.00**
$Pt_3Au\text{-}1_2$	0.32	-0.05	-0.09	0.00	-0.03
$Pt_3Au\text{-}1_3$	0.34	-0.01	-0.05	0.02	-0.03
$Pt_3Au\text{-}2_1$	-0.36	-0.23	-0.31	-0.38	-0.42
$Pt_3Au\text{-}2_2$	0.02	-0.23	-0.33	-0.28	-0.38
$Pt_3Ag\text{-}0_1$	0.22	0.11	0.10	0.35	0.34
$Pt_3Ag\text{-}0_2$	0.50	0.20	0.25	0.41	0.40
$Pt_3Ag\text{-}1_1$	**0.00**	**0.00**	**0.00**	**0.00**	**0.00**
$Pt_3Ag\text{-}1_2$	0.32	-0.11	-0.15	0.02	-0.03
$Pt_3Ag\text{-}1_3$	0.39	-0.03	-0.08	0.07	-0.01
$Pt_3Ag\text{-}2_1$	-0.23	-0.29	-0.35	-0.33	-0.49
$Pt_3Ag\text{-}2_2$	0.26	-0.21	-0.32	-0.14	-0.31
$Pt_3Cu\text{-}0_1$	-0.12	-0.05	-0.14	0.14	0.09
$Pt_3Cu\text{-}0_2$	0.39	0.24	0.27	0.27	0.24
$Pt_3Cu\text{-}1_1$	**0.00**	**0.00**	**0.00**	**0.00**	**0.00**
$Pt_3Cu\text{-}1_2$	0.51	0.03	-0.05	0.12	0.13
$Pt_3Cu\text{-}1_3$	0.73	0.23	0.25	0.31	0.36
$Pt_3Cu\text{-}2_1$	0.65	0.30	0.28	0.33	0.24
$Pt_3Cu\text{-}2_2$	1.11	0.36	0.30	0.43	0.39
$Pt_3Ir\text{-}0_1$	-0.56	0.02	-0.40	-0.11	-0.34
$Pt_3Ir\text{-}0_2$	-0.34	-0.07	-0.43	-0.20	-0.44
$Pt_3Ir\text{-}1_1$	**0.00**	**0.00**	**0.00**	**0.00**	**0.00**
$Pt_3Ir\text{-}1_2$	0.19	-0.17	-0.12	-0.13	-0.15
$Pt_3Ir\text{-}1_3$	0.09	-0.25	-0.24	-0.22	-0.28
$Pt_3Ir\text{-}2_1$	0.30	0.13	-0.03	0.27	-0.03
$Pt_3Ir\text{-}2_2$	0.60	0.14	-0.12	0.20	-0.12
$Pt_3Pd\text{-}0_1$	-0.03	0.01	-0.02	0.09	0.04
$Pt_3Pd\text{-}0_2$	0.17	0.02	0.02	0.11	0.06
$Pt_3Pd\text{-}1_1$	**0.00**	**0.00**	**0.00**	**0.00**	**0.00**
$Pt_3Pd\text{-}1_2$	0.22	0.00	-0.04	0.02	-0.01
$Pt_3Pd\text{-}1_3$	0.24	-0.01	-0.04	0.04	0.00
$Pt_3Pd\text{-}2_1$	0.08	-0.01	-0.03	-0.01	-0.04
$Pt_3Pd\text{-}2_2$	0.31	-0.02	-0.06	0.02	-0.04
$Pt_3Rh\text{-}0_1$	-0.38	-0.10	-0.17	-0.07	-0.10
$Pt_3Rh\text{-}0_2$	-0.12	-0.10	-0.15	-0.08	-0.12
$Pt_3Rh\text{-}1_1$	**0.00**	**0.00**	**0.00**	**0.00**	**0.00**
$Pt_3Rh\text{-}1_2$	0.25	-0.02	-0.02	-0.01	-0.01
$Pt_3Rh\text{-}1_3$	0.26	-0.02	-0.04	-0.03	-0.03
$Pt_3Rh\text{-}2_1$	0.45	0.32	0.27	0.12	0.14

Surface	clean	CO	COOH	OH	HCOO
$Pt_3Rh\text{-}2_2$	0.68	0.29	0.25	0.07	0.08
$Pt_3Ru\text{-}0_1$	-1.00	-0.38	-0.63	-0.29	-0.58
$Pt_3Ru\text{-}0_2$	-0.85	-0.53	-0.74	-0.48	-0.75
$Pt_3Ru\text{-}1_1$	**0.00**	**0.00**	**0.00**	**0.00**	**0.00**
$Pt_3Ru\text{-}1_2$	0.07	-0.14	-0.27	-0.28	-0.30
$Pt_3Ru\text{-}1_3$	-0.12	-0.28	-0.51	-0.43	-0.46
$Pt_3Ru\text{-}2_1$	0.58	0.55	0.38	0.27	0.06
$Pt_3Ru\text{-}2_2$	0.71	0.32	0.21	0.09	-0.16
$Pt_3Re\text{-}0_1$	-2.16	-1.20	-1.70	-0.84	-1.61
$Pt_3Re\text{-}0_2$	-2.81	-1.74	-2.24	-1.28	-2.08
$Pt_3Re\text{-}1_1$	**0.00**	**0.00**	**0.00**	**0.00**	**0.00**
$Pt_3Re\text{-}1_2$	-1.23	-0.66	-1.29	-1.06	-1.30
$Pt_3Re\text{-}1_3$	-1.64	-1.06	-1.70	-1.38	-1.56
$Pt_3Re\text{-}2_1$	0.02	0.11	-0.59	-0.37	-0.89
$Pt_3Re\text{-}2_2$	-0.76	-0.41	-1.07	-0.51	-1.48

Table G.9: Relative energy (eV) of 2×2 unit cells palladium alloyed with transition metals compared to the bulk-terminated alloy system (in bold).

Surface	clean	CO	COOH	OH	HCOO
$Pd_3Au\text{-}0_1$	0.40	0.35	0.27	0.24	0.28
$Pd_3Au\text{-}0_2$	0.21	0.07	0.02	-0.03	0.01
$Pd_3Au\text{-}1_1$	**0.00**	**0.00**	**0.00**	**0.00**	**0.00**
$Pd_3Au\text{-}1_2$	0.40	0.35	0.27	0.26	0.29
$Pd_3Au\text{-}1_3$	0.26	0.12	0.07	0.04	0.04
$Pd_3Au\text{-}2_1$	0.00	-0.02	0.00	0.01	0.00
$Pd_3Au\text{-}2_2$	-0.14	0.23	-0.05	-0.10	-0.11
$Pd_3Ag\text{-}0_1$	0.23	0.15	0.15	0.23	0.28
$Pd_3Ag\text{-}0_2$	0.38	0.16	0.19	0.22	0.31
$Pd_3Ag\text{-}1_1$	**0.00**	**0.00**	**0.00**	**0.00**	**0.00**
$Pd_3Ag\text{-}1_2$	-0.05	-0.11	-0.03	-0.01	-0.02
$Pd_3Ag\text{-}1_3$	0.18	-0.11	-0.04	-0.03	-0.05
$Pd_3Ag\text{-}2_1$	-0.18	-0.02	-0.19	-0.26	-0.31
$Pd_3Ag\text{-}2_2$	0.01	-0.01	-0.21	-0.21	-0.29
$Pd_3Cu\text{-}0_1$	-0.01	0.00	-0.02	0.18	0.13
$Pd_3Cu\text{-}0_2$	0.23	0.07	0.10	0.19	0.17
$Pd_3Cu\text{-}1_1$	**0.00**	**0.00**	**0.00**	**0.00**	**0.00**
$Pd_3Cu\text{-}1_2$	0.24	-0.06	-0.01	0.07	0.05
$Pd_3Cu\text{-}1_3$	0.32	0.00	0.08	0.11	0.15
$Pd_3Cu\text{-}2_1$	0.32	0.26	0.14	0.03	0.12
$Pd_3Cu\text{-}2_2$	0.50	0.28	0.12	0.02	0.14
$Pd_3Ir\text{-}0_1$	-0.78	-0.20	-0.28	-0.47	-0.61
$Pd_3Ir\text{-}0_2$	-0.69	-0.27	-0.38	-0.56	-0.73
$Pd_3Ir\text{-}1_1$	**0.00**	**0.00**	**0.00**	**0.00**	**0.00**
$Pd_3Ir\text{-}1_2$	-0.02	-0.26	-0.22	-0.32	-0.30
$Pd_3Ir\text{-}1_3$	-0.23	-0.45	-0.39	-0.50	-0.51
$Pd_3Ir\text{-}2_1$	0.13	-0.03	-0.13	0.07	-0.16
$Pd_3Ir\text{-}2_2$	0.39	0.04	-0.19	0.06	-0.22
$Pd_3Pt\text{-}0_1$	-0.01	-0.01	0.22	-0.13	-0.11
$Pd_3Pt\text{-}0_2$	0.13	-0.03	0.21	-0.14	-0.12
$Pd_3Pt\text{-}1_1$	**0.00**	**0.00**	**0.00**	**0.00**	**0.00**
$Pd_3Pt\text{-}1_2$	0.15	-0.04	-0.08	-0.13	-0.08
$Pd_3Pt\text{-}1_3$	0.16	-0.02	-0.11	-0.15	-0.10
$Pd_3Pt\text{-}2_1$	0.02	0.00	0.02	0.07	0.05
$Pd_3Pt\text{-}2_2$	0.18	0.01	0.05	0.05	0.03
$Pd_3Rh\text{-}0_1$	-0.45	-0.21	-0.08	-0.20	-0.22
$Pd_3Rh\text{-}0_2$	-0.35	-0.25	-0.14	-0.25	-0.28
$Pd_3Rh\text{-}1_1$	**0.00**	**0.00**	**0.00**	**0.00**	**0.00**
$Pd_3Rh\text{-}1_2$	0.09	-0.11	-0.07	-0.11	-0.11
$Pd_3Rh\text{-}1_3$	0.01	-0.17	-0.13	-0.18	-0.19
$Pd_3Rh\text{-}2_1$	0.27	0.07	-0.02	-0.05	-0.08

Surface	clean	CO	COOH	OH	HCOO
$Pd_3Rh\text{-}2_2$	0.44	0.07	-0.08	-0.07	-0.13
$Pd_3Ru\text{-}0_1$	-1.24	-0.65	-0.80	-0.74	-0.81
$Pd_3Ru\text{-}0_2$	-1.23	-0.83	-0.93	-0.88	-1.00
$Pd_3Ru\text{-}1_1$	**0.00**	**0.00**	**0.00**	**0.00**	**0.00**
$Pd_3Ru\text{-}1_2$	-0.29	-0.30	-0.36	-0.60	-0.56
$Pd_3Ru\text{-}1_3$	-0.57	-0.55	-0.65	-0.82	-0.78
$Pd_3Ru\text{-}2_1$	0.21	0.20	-0.27	-0.24	-0.34
$Pd_3Ru\text{-}2_2$	0.18	-0.01	-0.40	-0.33	-0.51
$Pd_3Re\text{-}0_1$	-2.82	-1.86	-2.17	-1.61	-2.19
$Pd_3Re\text{-}0_2$	-3.57	-2.53	-2.75	-2.07	-2.72
$Pd_3Re\text{-}1_1$	**0.00**	**0.00**	**0.00**	**0.00**	**0.00**
$Pd_3Re\text{-}1_2$	-1.86	-1.27	-1.56	-1.76	-1.91
$Pd_3Re\text{-}1_3$	-2.34	-1.71	-2.06	-2.07	-2.18
$Pd_3Re\text{-}2_1$	-0.61	-0.63	-1.53	-1.04	-1.68
$Pd_3Re\text{-}2_2$	-1.35	-0.95	-1.81	-1.22	-1.99

G.2 Scaling Relationships

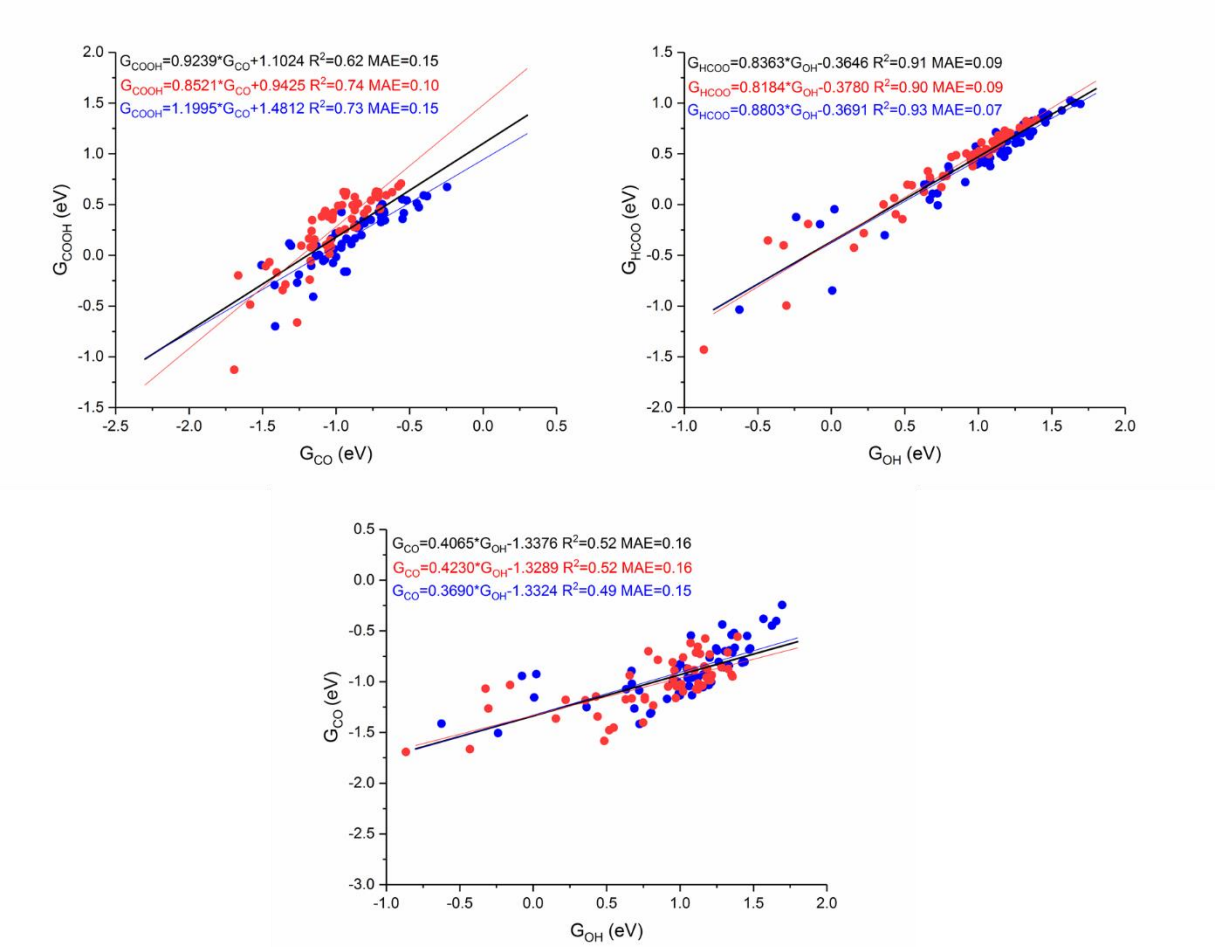

Figure G.1: Scaling relationships between G_{CO} & G_{COOH}, between G_{HCOO} & G_{OH}, and between G_{CO} & G_{OH}. These scaling relationships are formulated from the free energy of adsorbates on all reconstructions of all of the alloys studied in this work in addition to pure Pt and Pd. Data points and scaling relationships for just Pt and Pt alloys are shown in red, data points and scaling relationships for just Pd and Pd alloys are shown in blue, and the scaling relationships for the two systems combined are shown in black. The scaling relationships for the combined systems were used in generating the volcano plots shown in Figure 7.9 of the main text.

G.3 Top-down Images of Binding Structures of Adsorbates on Alloyed Surfaces

Text below each structure indicates the alloy(s) for which the structure is the most stable. Each structure is denoted as $P_3M\text{-}x_y$, where x is the number of solute atoms in the topmost layer per unit cell (x = 0, 1, or 2) and y differentiates between structures with the same x value. Note that while the top atom structures may appear similar, the hollow site structures vary between different models. Pt or Pd atoms are shown in grey, solute atoms (Au, Ag, Cu, Ir, Pd, Pt, Ir, Rh, Ru, and Re) are shown in blue, O atoms are shown in red, C atoms are shown in brown, and H atoms are shown in white.

$P_3M\text{-}0_1$: CO* Structures

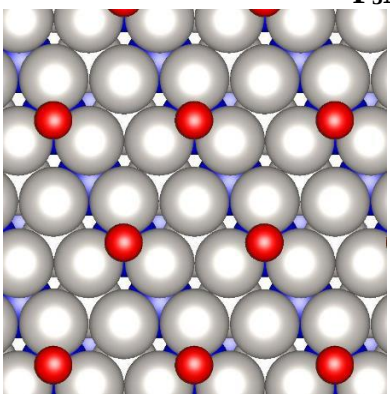

Pt_3Ag, Pt_3Au, Pt_3Cu, Pt_3Pd, Pd_3Ag

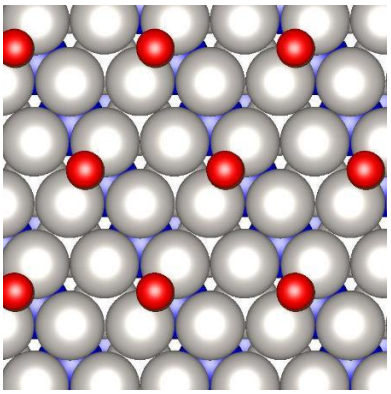

Pt_3Ir, Pt_3Rh

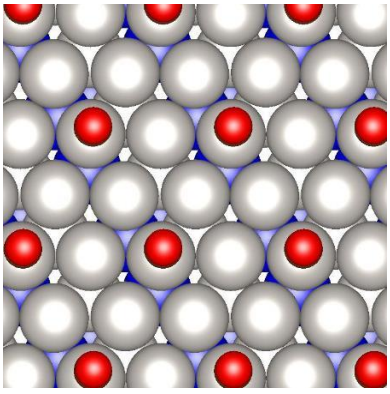

Pt_3Re

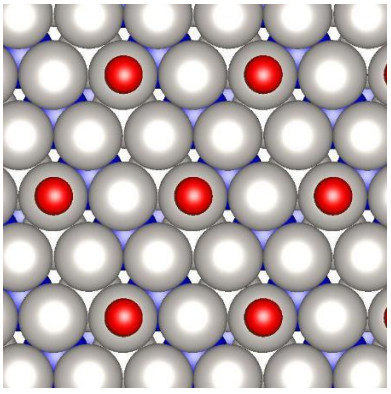

Pt_3Ru

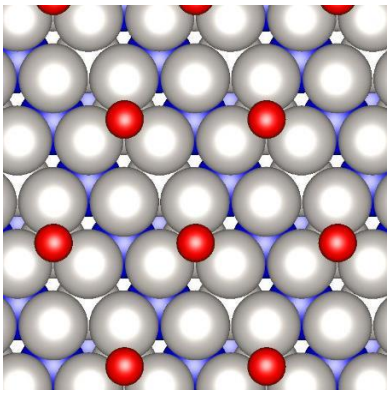

Pd_3Au

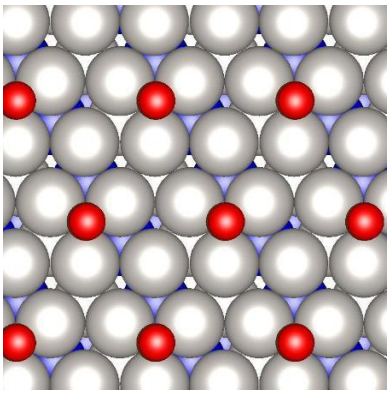

Pd_3Cu, Pd_3Ir, Pd_3Re, Pd_3Rh, Pd_3Ru

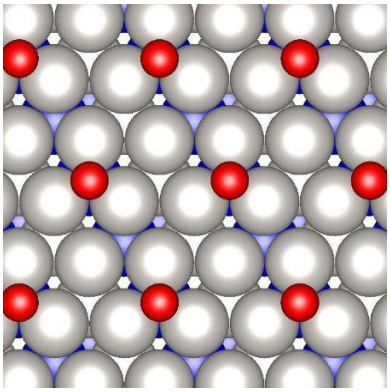

Pd_3Pt

$P_3M\text{-}0_1$: OH* Structures

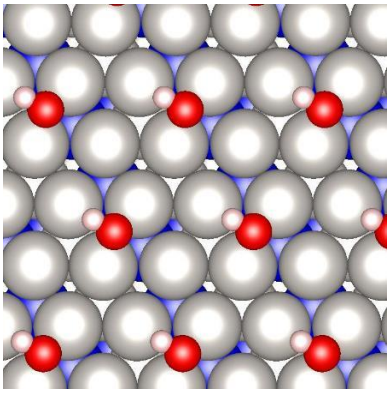

Pt_3Ag, Pt_3Au, Pt_3Pd

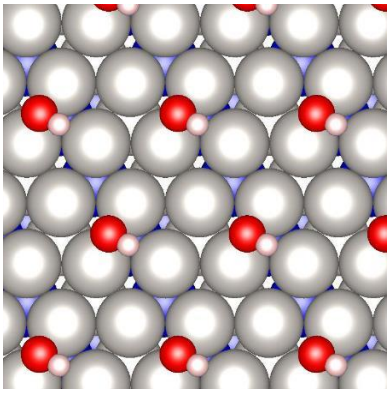

Pt_3Cu

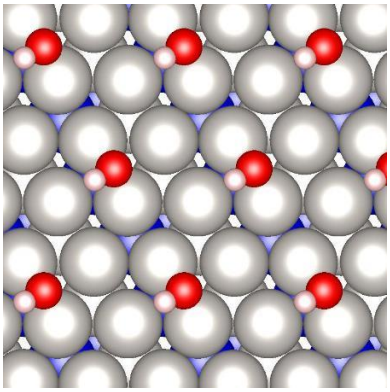

Pt_3Ir, Pd_3Pt, Pd_3Rh

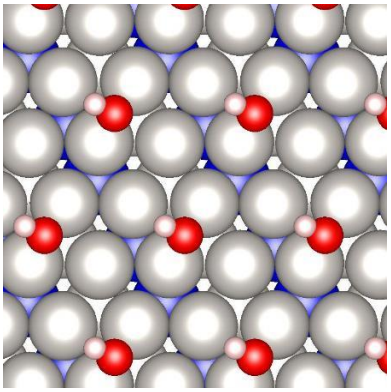

Pt_3Re

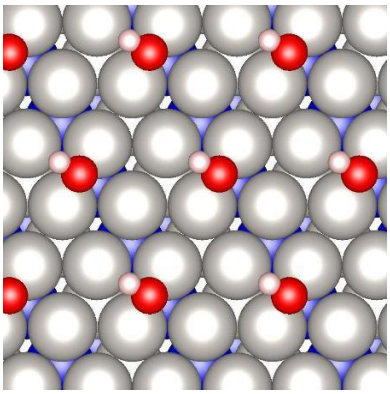

Pt_3Rh

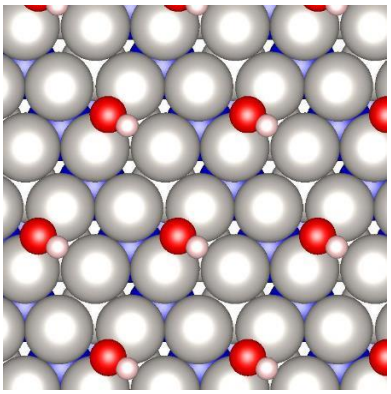

Pt_3Ru

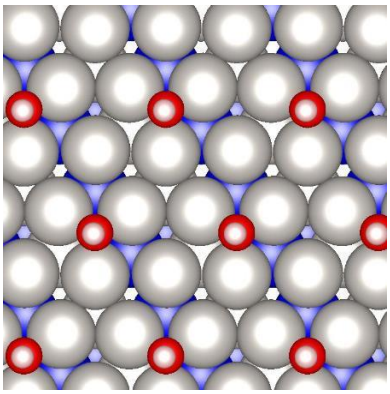

Pd_3Ag, Pd_3Au

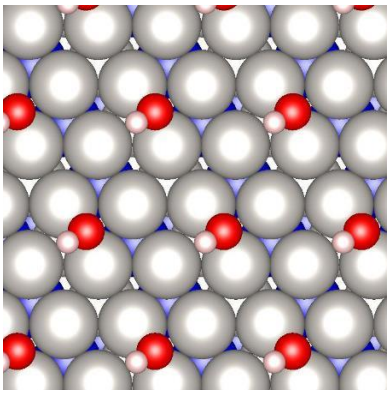

Pd_3Cu

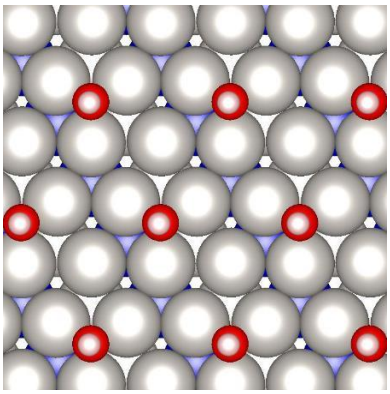

Pd_3Ir, Pd_3Re, Pd_3Ru

$P_3M\text{-}0_1$: COOH* Structures

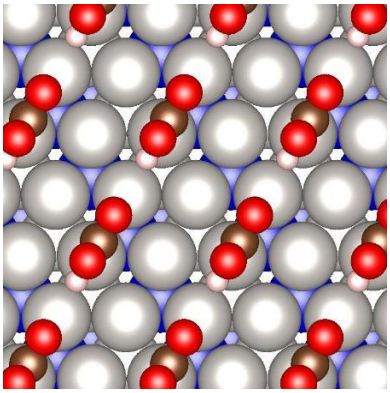

Pt_3Ag, Pt_3Au, Pt_3Cu, Pt_3Pd, Pd_3Ag, Pd_3Au, Pd_3Cu

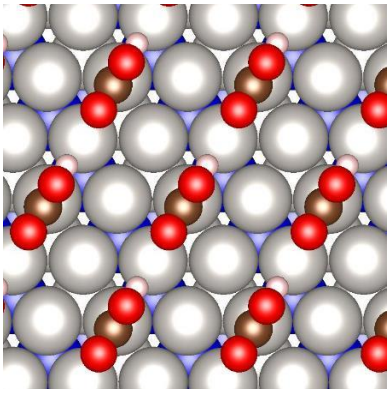

Pt_3Ir, Pt_3Re, Pt_3Rh, Pt_3Ru, Pd_3Ir,Pd_3Re, Pd_3Rh, Pd_3Ru

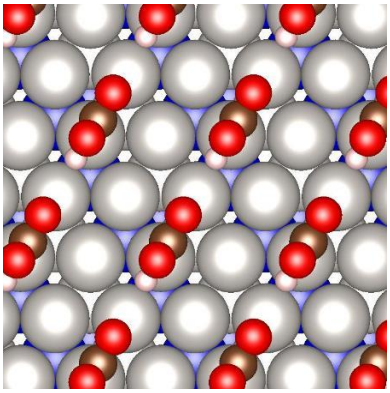

Pd_3Pt

$P_3M\text{-}0_1$: HCOO* Structures

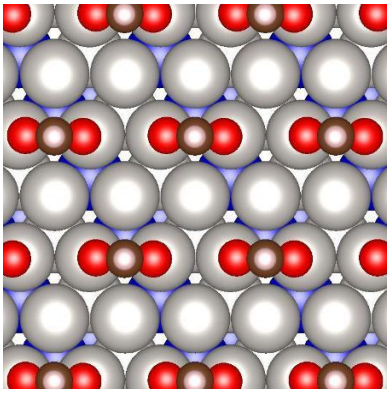

Pt_3Ag, Pt_3Au, Pt_3Pd, Pd_3Ag, Pd_3Au

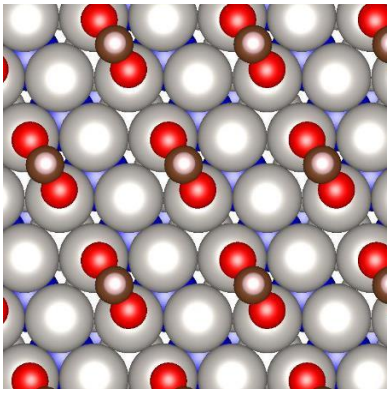

Pt_3Cu, Pd_3Cu

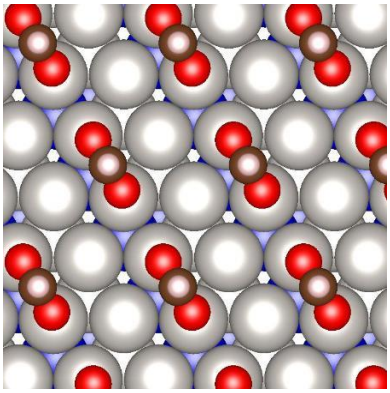

Pt_3Ir, Pd_3Ir

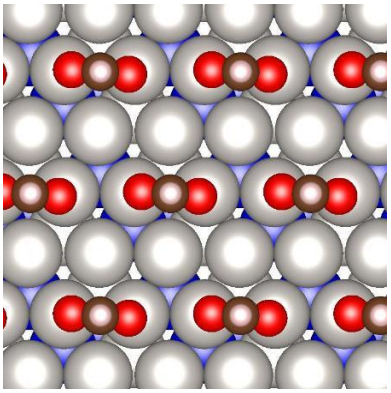

Pt_3Re, Pt_3Ru, Pd_3Pt, Pd_3Re, Pd_3Rh, Pd_3Ru

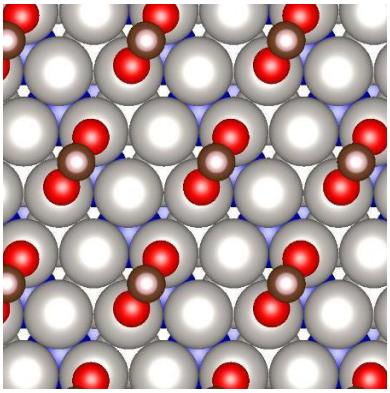

Pt_3Rh

$P_3M\text{-}0_2$: CO* Structures

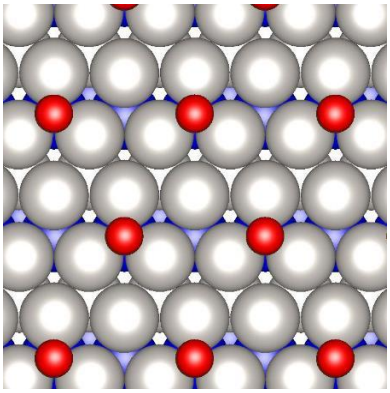

Pt_3Ag, Pt_3Au, Pt_3Cu, Pt_3Pd, Pd_3Ag

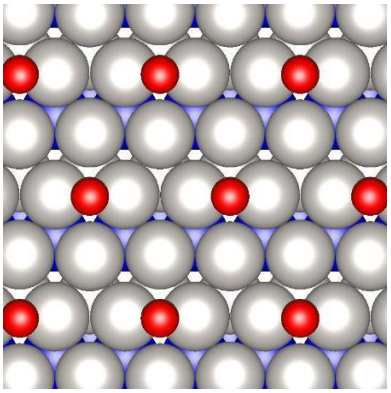

Pt_3Ir, Pt_3Rh, Pt_3Ru

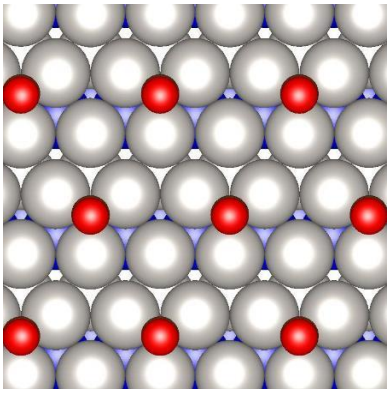

Pt_3Re, Pd_3Ir, Pd_3Re, Pd_3Ru

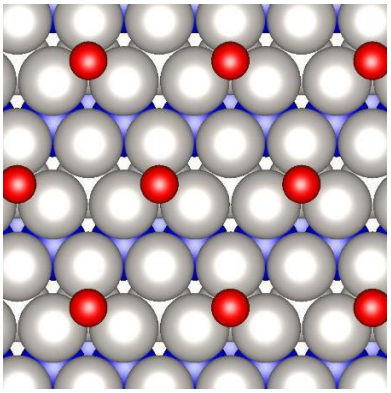

Pd_3Au

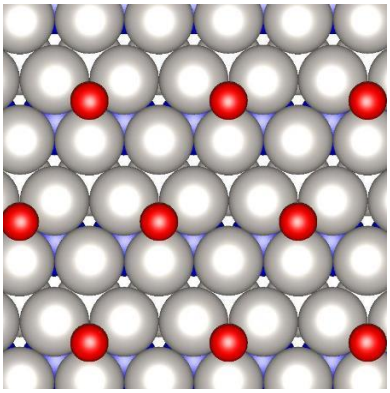

Pd_3Cu, Pd_3Rh

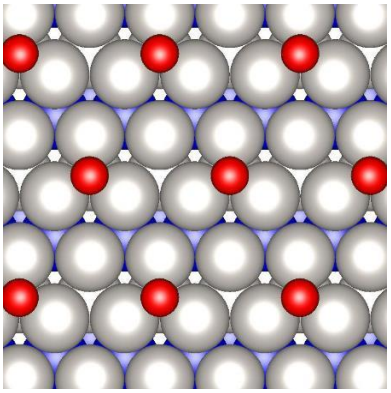

Pd_3Pt

$P_3M\text{-}0_2$: OH* Structures

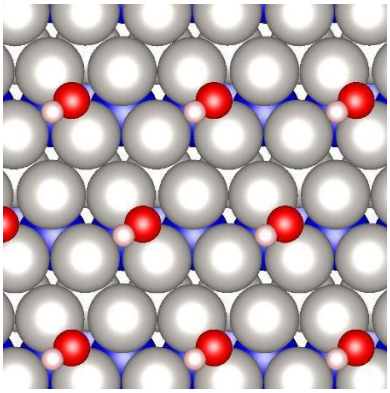

Pt_3Ag, Pt_3Au

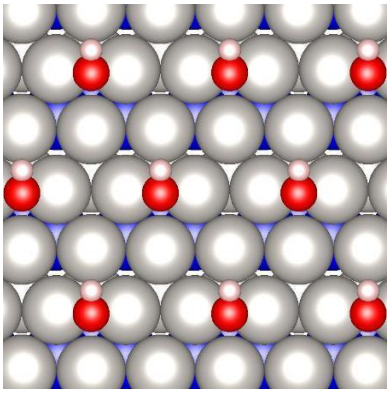

Pt_3Cu, Pd_3Cu

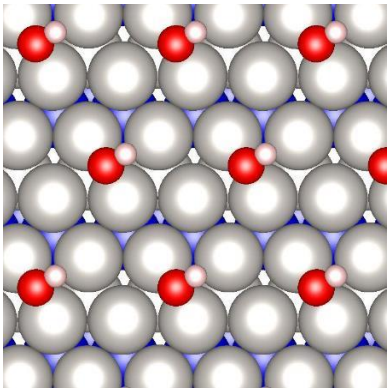

Pt_3Ir, Pt_3Re, Pt_3Ru, Pd_3Ir
Pd_3Re, Pd_3Rh, Pd_3Ru

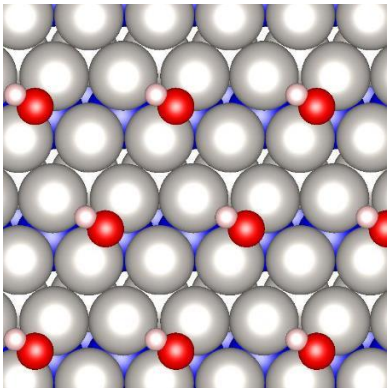

Pt_3Pd

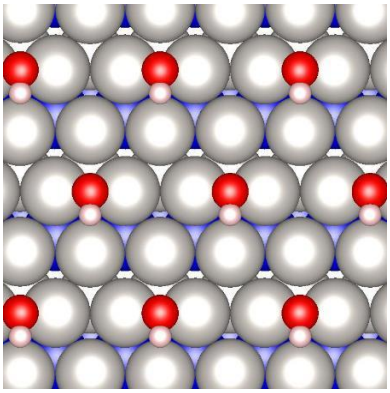

Pt_3Rh

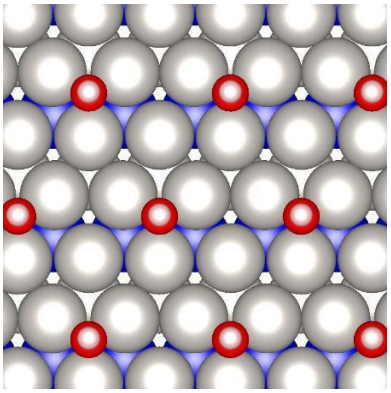

Pd_3Ag
Pd_3Au

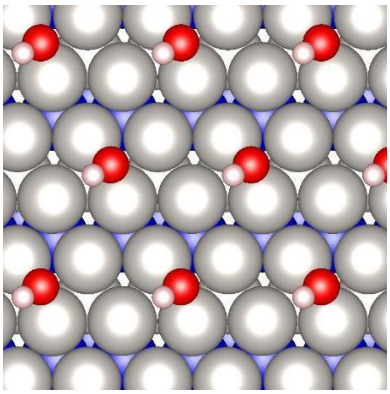

Pd_3Pt

P_3M-0_2: COOH* Structures

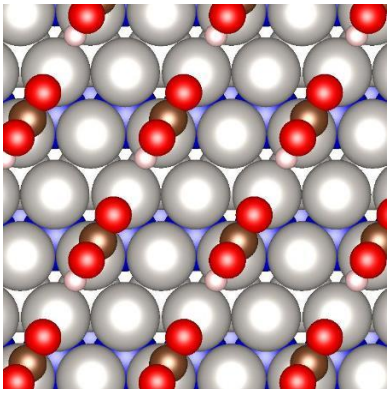

Pt_3Ag, Pt_3Au, Pt_3Pd,
Pd_3Ag, Pd_3Au

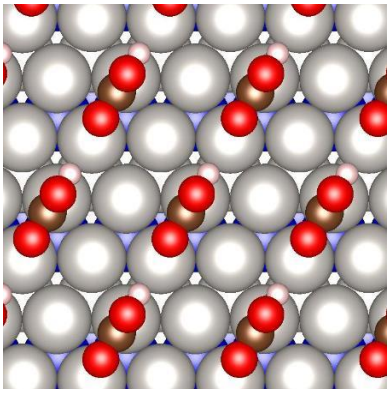

Pt_3Cu

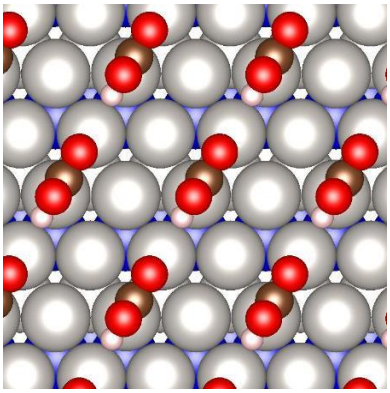

Pt_3Ir, Pt_3Re, Pt_3Rh, Pt_3Ru,
Pd_3Ir, Pd_3Re, Pd_3Rh, Pd_3Ru

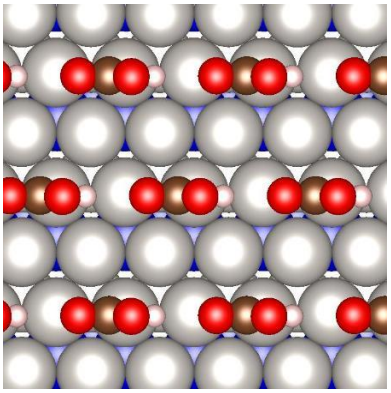

Pd_3Cu

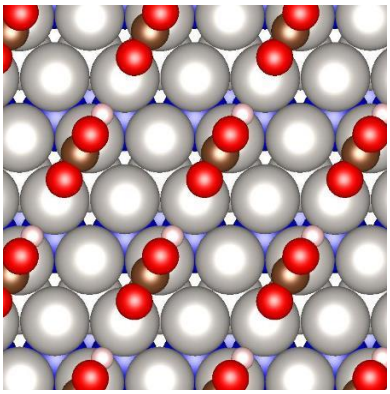

Pd_3Pt

P_3M-0_2: HCOO* Structures

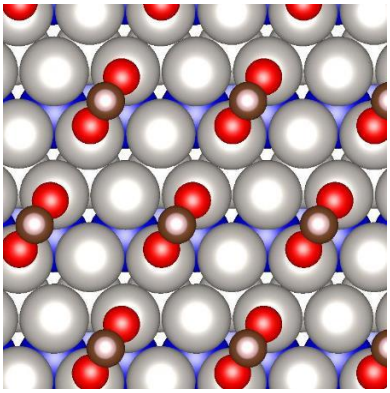

Pt_3Ag, Pt_3Au

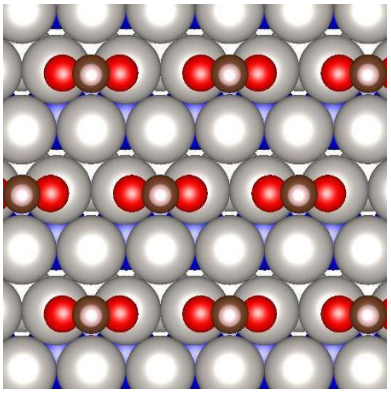

Pt_3Cu, Pd_3Cu

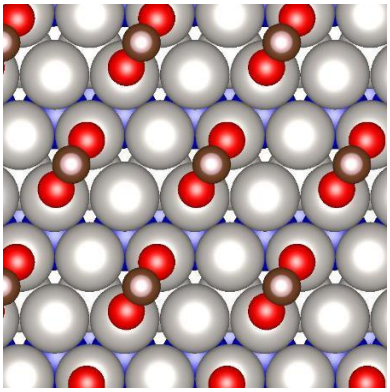

Pt_3Ir, Pt_3Re, Pt_3Ru, Pd_3Ir, Pd_3Pt, Pd_3Re, Pd_3Rh, Pd_3Ru

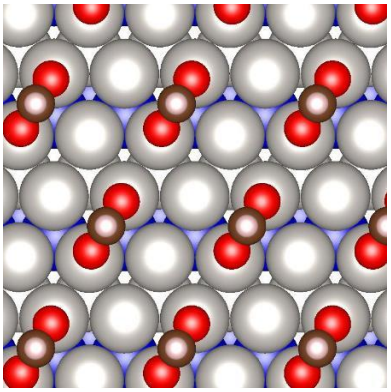

Pt_3Pd, Pd_3Ag, Pd_3Au

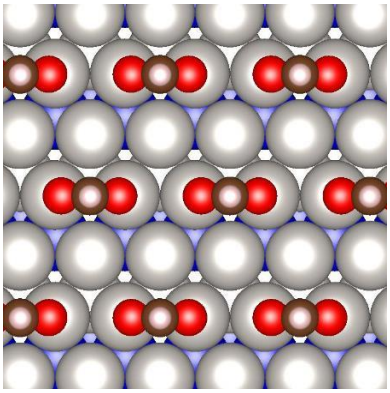

Pt_3Rh

$P_3M\text{-}1_1$: CO* Structures

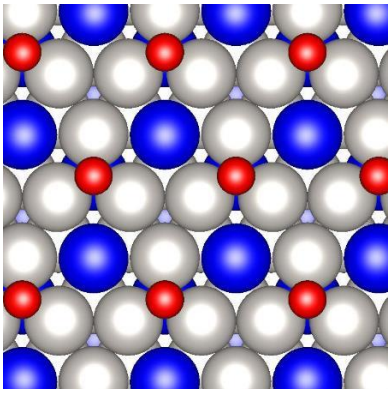

Pt_3Ag, Pt_3Cu, Pd_3Cu

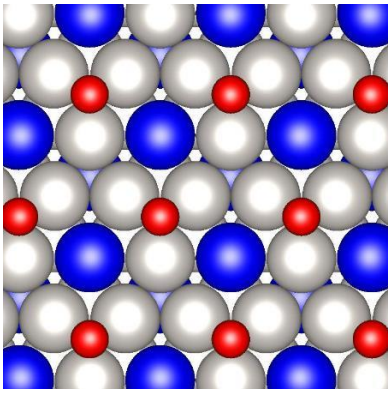

Pt_3Au, Pt_3Pd, Pd_3Ag, Pd_3Au

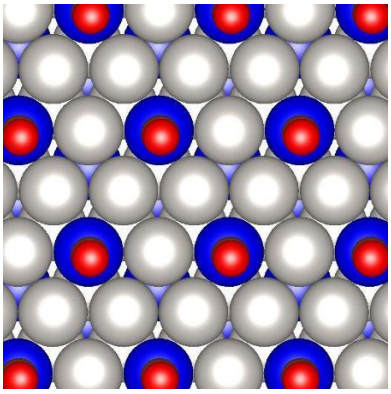

Pt_3Ir, Pt_3Re, Pt_3Rh, Pt_3Ru,
Pd_3Ir, Pd_3Re, Pd_3Rh, Pd_3Ru

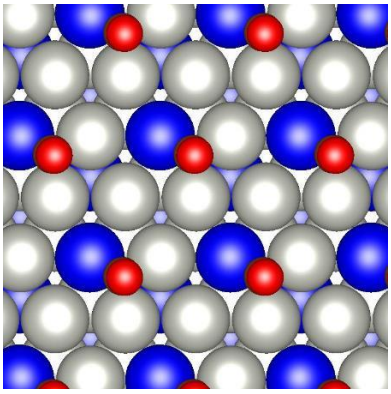

Pd_3Pt

$P_3M\text{-}1_1$: OH* Structures

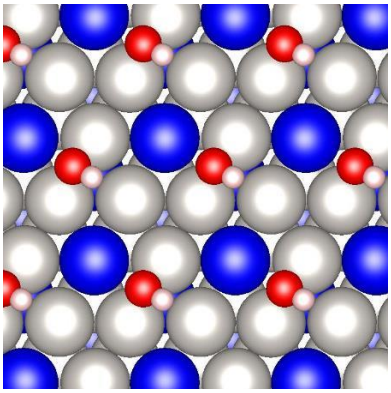

Pt_3Ag, Pt_3Au, Pt_3Cu, Pt_3Pd, Pd_3Ag

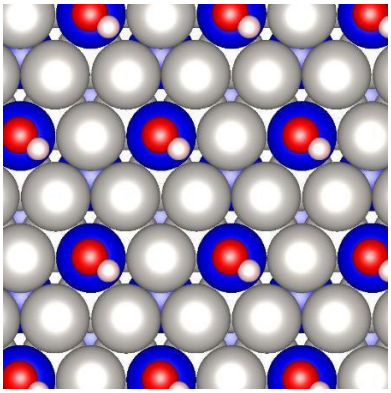

Pt_3Ir, Pt_3Re, Pt_3Ru, Pd_3Ir, Pd_3Re

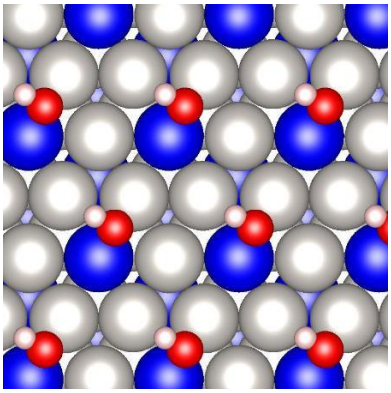

Pt_3Rh, Pd_3Pt,Pd_3Rh, Pd_3Ru

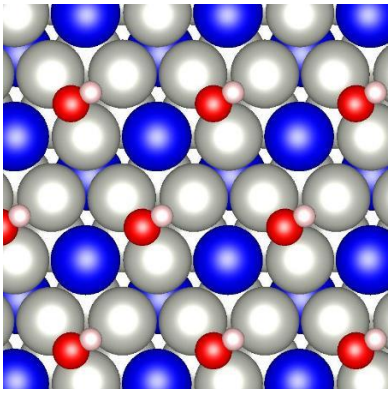

Pd_3Au

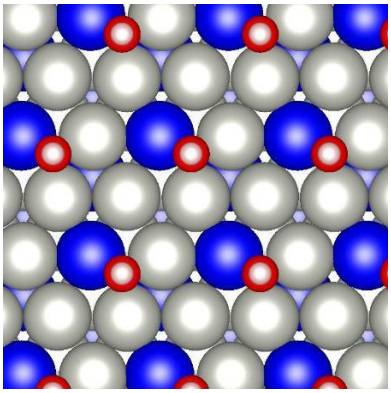

Pd_3Cu

$P_3M\text{-}1_1$: COOH* Structures

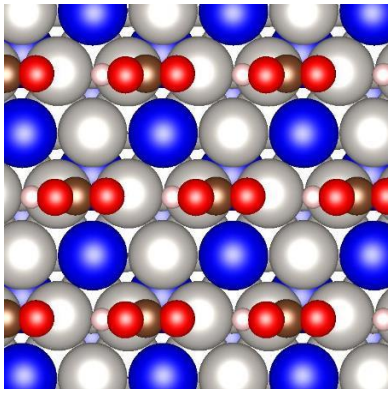

Pt_3Ag, Pt_3Au, Pt_3Cu, Pt_3Pd, Pd_3Ag, Pd_3Au, Pd_3Cu

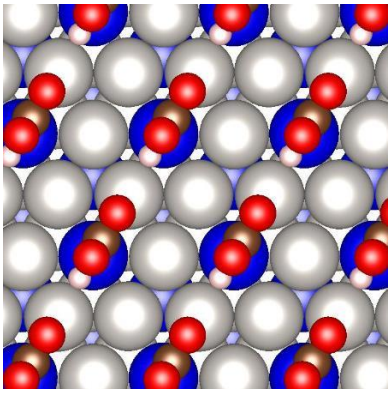

Pt_3Ir, Pd_3Ir, Pd_3Pt, Pd_3Re, Pd_3Rh, Pd_3Ru

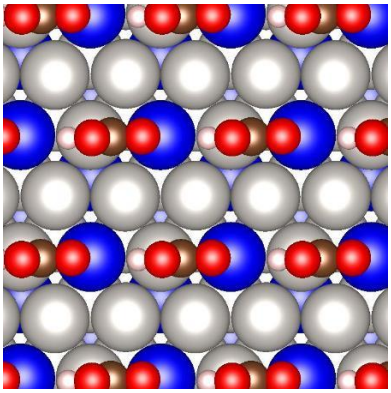

Pt_3Re, Pt_3Rh, Pt_3Ru

$P_3M\text{-}1_1$: HCOO* Structures

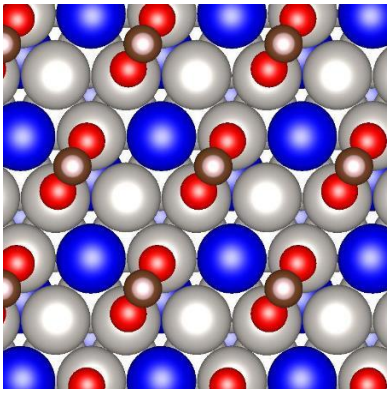

Pt_3Ag, Pt_3Au, Pt_3Cu,
Pt_3Pd, Pd_3Ag, Pd_3Au

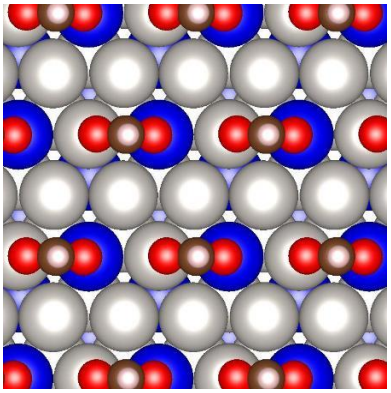

Pt_3Ir, Pt_3Re,Pt_3Rh, Pt_3Ru, Pd_3Cu,
Pd_3Ir, Pd_3Pt, Pd_3Re, Pd_3Rh, Pd_3Ru

$P_3M\text{-}1_2$: CO* Structures

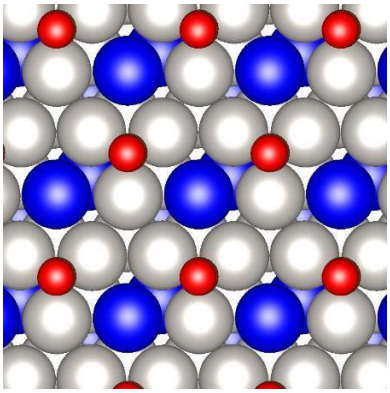

Pt_3Ag, Pt_3Au, Pt_3Cu,
Pd_3Ag, Pd_3Au, Pd_3Cu

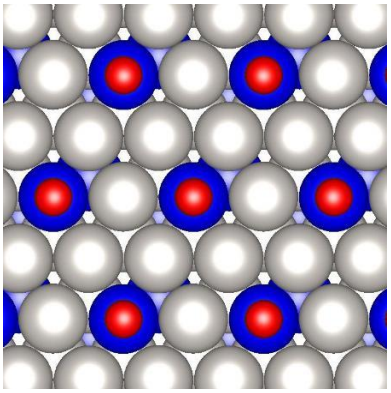

Pt_3Ir, Pt_3Re, Pt_3Rh,
Pt_3Ru, Pd_3Ir, Pd_3Rh

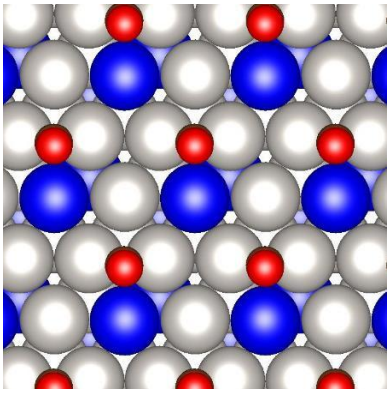

Pt_3Pd

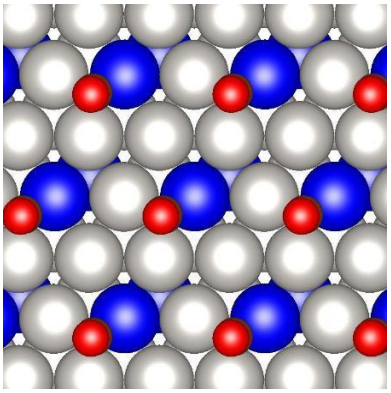

Pd_3Pt

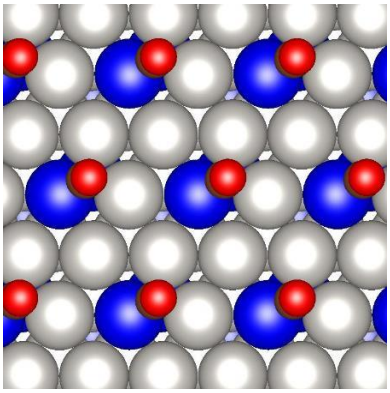

Pd_3Re, Pd_3Ru

$P_3M\text{-}1_2$: OH* Structures

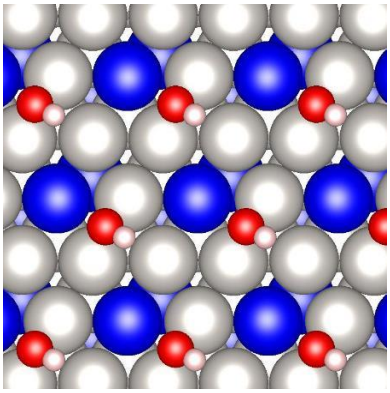

Pt_3Ag, Pt_3Cu, Pt_3Pd, Pd_3Ag, Pd_3Au

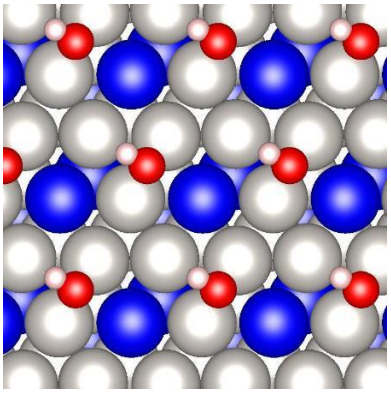

Pt_3Au

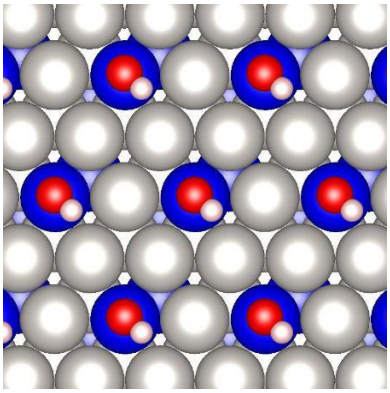

Pt_3Ir, Pt_3Ru, Pd_3Ir, Pd_3Ru

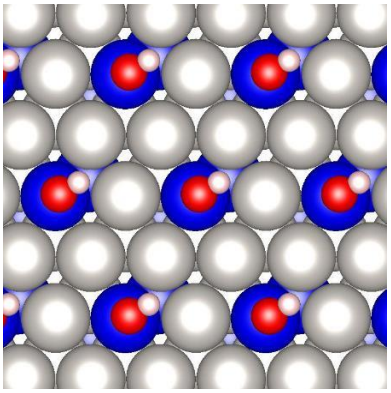

Pt_3Re, Pd_3Re

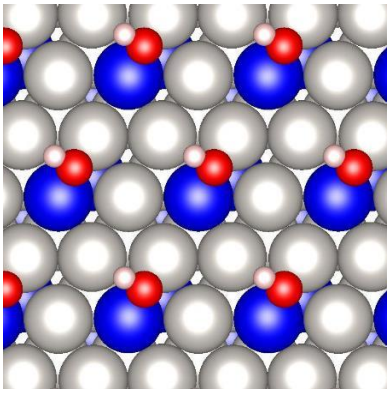

Pt_3Rh

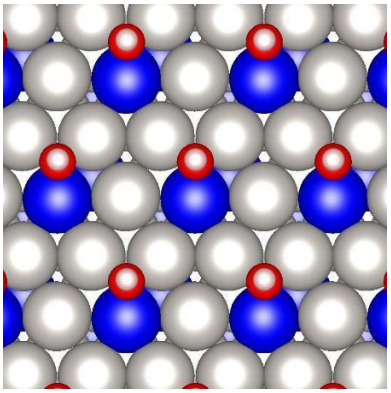

Pd_3Cu

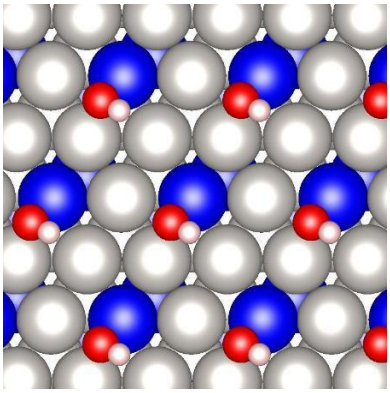

Pd_3Pt

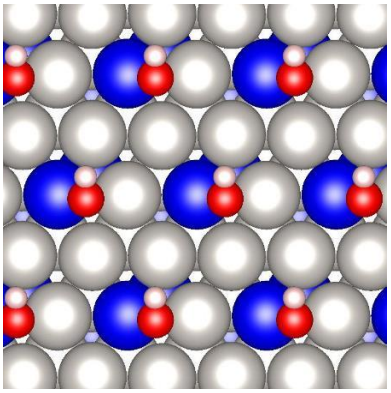

Pd_3Rh

$P_3M\text{-}1_2$: COOH* Structures

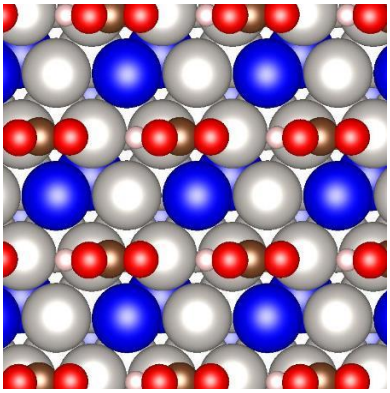

Pt_3Ag, Pt_3Au, Pt_3Cu, Pt_3Pd, Pd_3Ag, Pd_3Au, Pd_3Cu

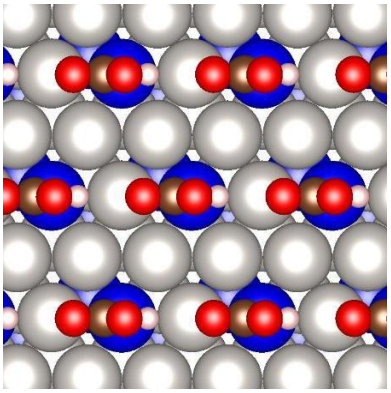

Pt_3Ir, Pd_3Ir, Pd_3Rh

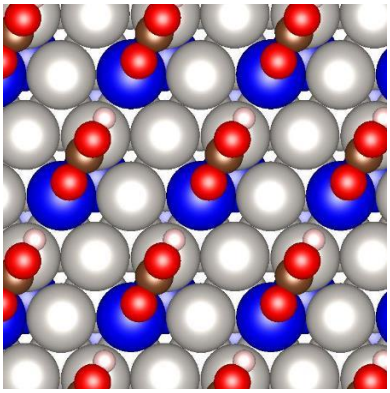

Pt_3Re, Pt_3Rh, Pt_3Ru, Pd_3Re, Pd_3Ru

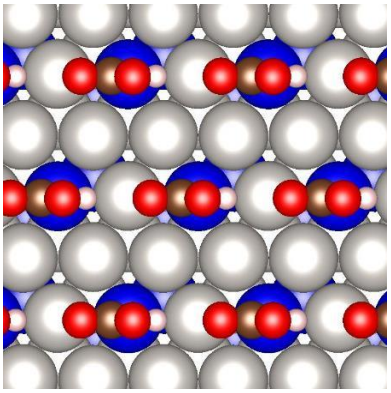

Pd_3Pt

$P_3M\text{-}1_2$: HCOO* Structures

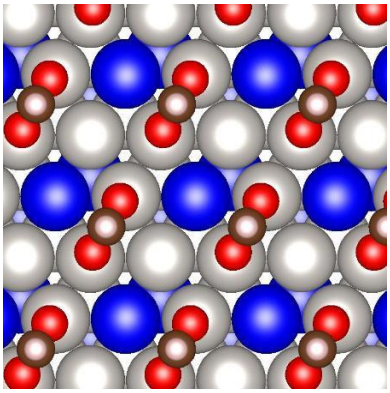

Pt_3Ag, Pt_3Au, Pt_3Cu, Pt_3Pd, Pd_3Ag

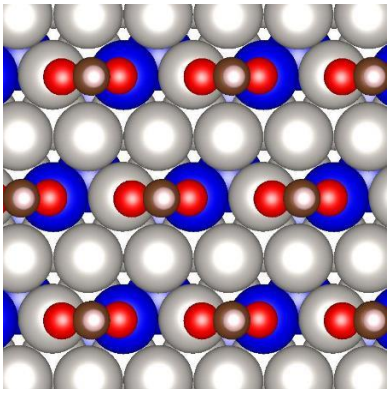

Pt_3Ir, Pd_3Pt, Pd_3Rh

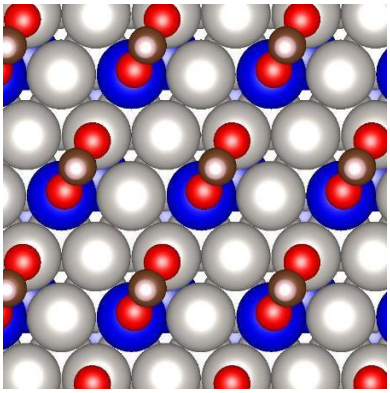

Pt_3Re, Pt_3Rh, Pt_3Ru, Pd_3Ir, Pd_3Re, Pd_3Ru

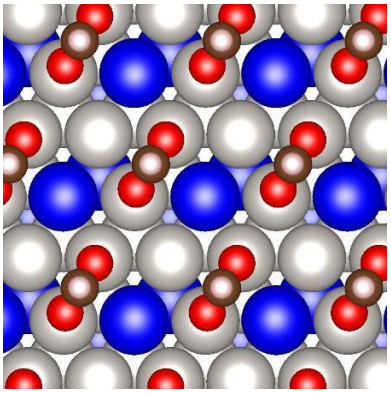

Pd_3Au

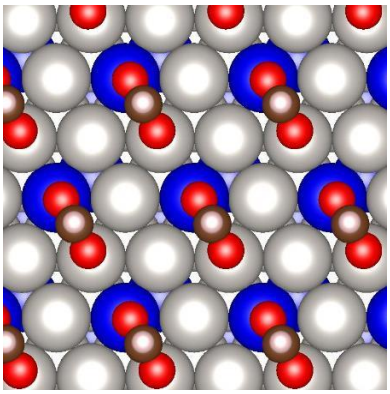

Pd_3Cu

$P_3M\text{-}1_3$: CO* Structures

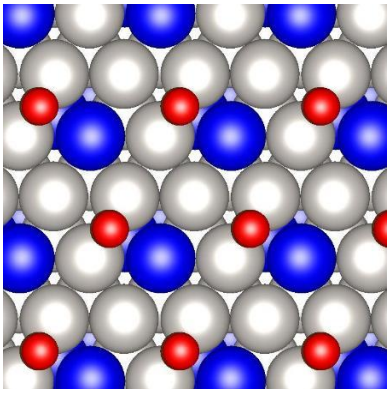

Pt_3Ag, Pt_3Cu, Pt_3Pd,
Pd_3Ag, Pd_3Au, Pd_3Cu

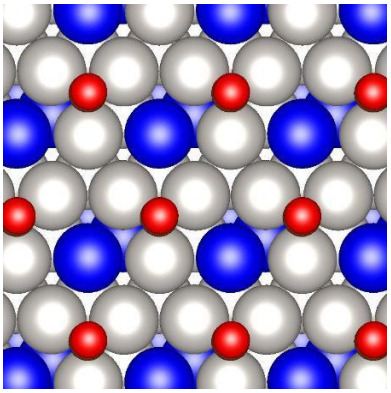

Pt_3Au

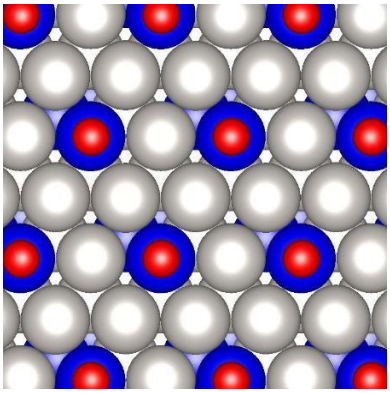

Pt_3Ir, Pt_3Re, Pt_3Rh, Pt_3Ru,
Pd_3Ir, Pd_3Re, Pd_3Rh

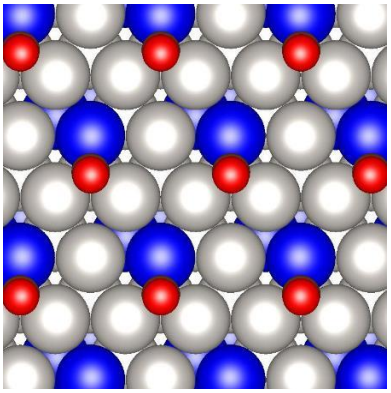

Pd_3Pt

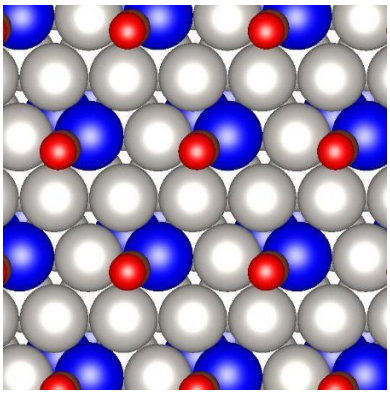

Pd_3Ru

$P_3M\text{-}1_3$: OH* Structures

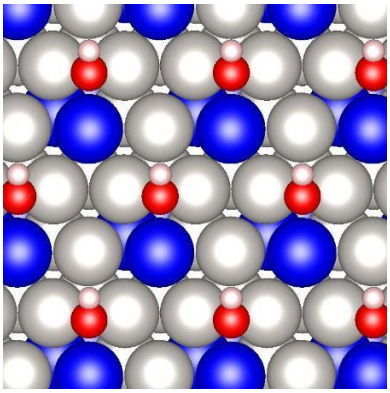

Pt_3Ag, Pt_3Cu

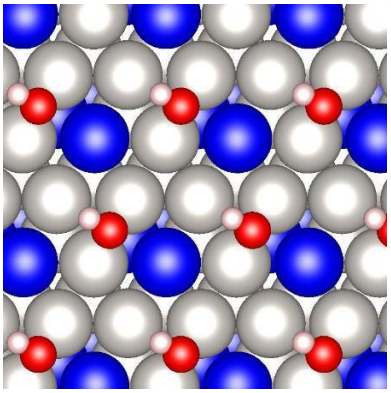

Pt_3Au

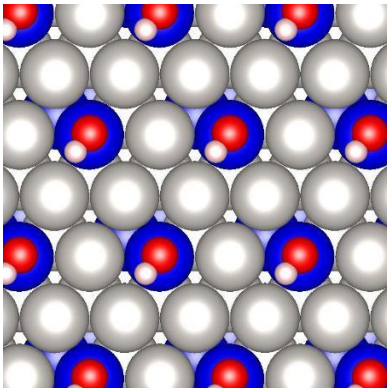

Pt_3Ir, Pd_3Ir

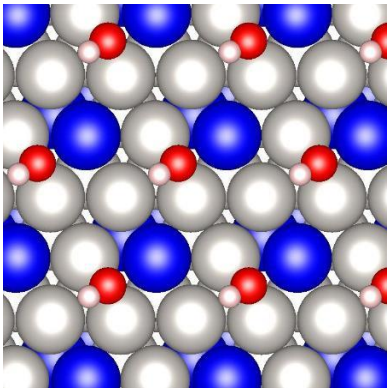

Pt_3Pd

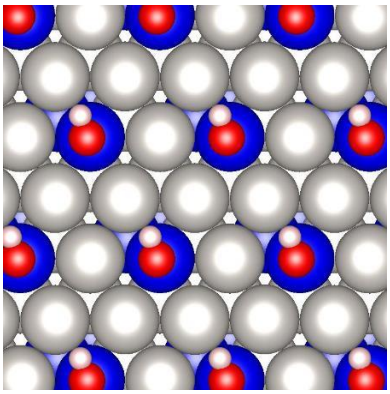

Pt_3Re, Pt_3Ru, Pt_3Re

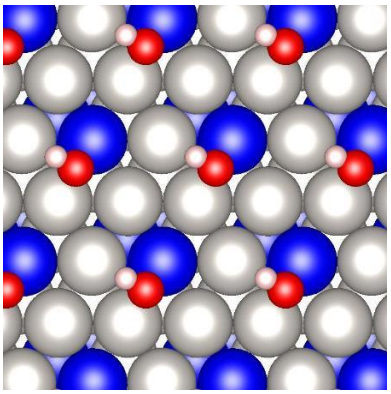

Pt_3Rh, Pd_3Ag, Pd_3Rh, Pd_3Ru

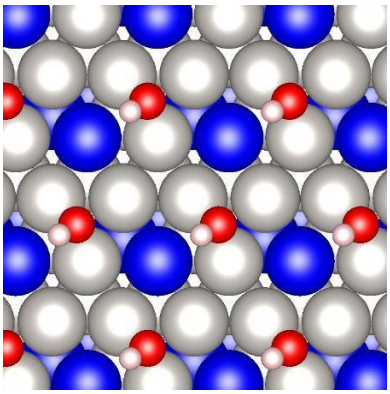

Pd_3Au

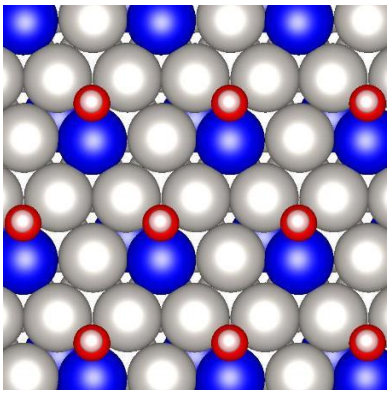

Pd_3Cu

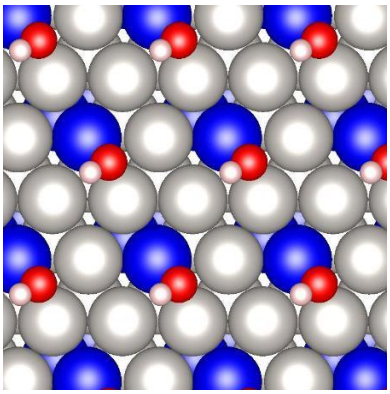

Pd_3Pt

$P_3M\text{-}1_3$: COOH* Structures

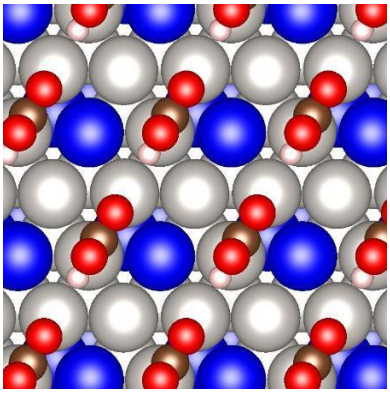

Pt_3Ag, Pt_3Au, Pt_3Cu,
Pd_3Ag, Pd_3Au, Pd_3Cu

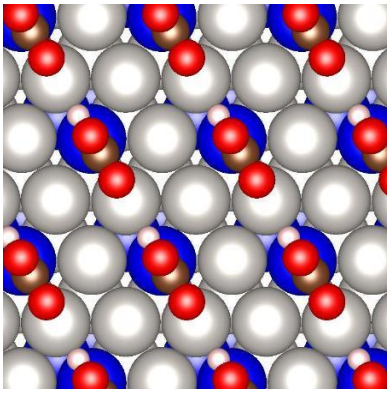

Pt_3Ir, Pd_3Ir, Pd_3Pt, Pd_3Rh

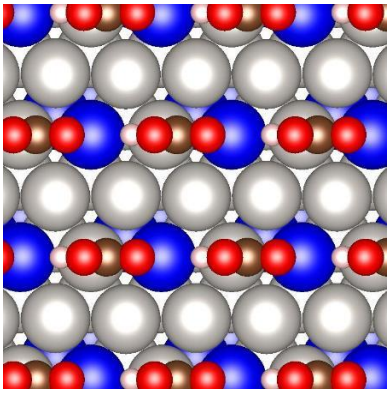

Pt_3Pd

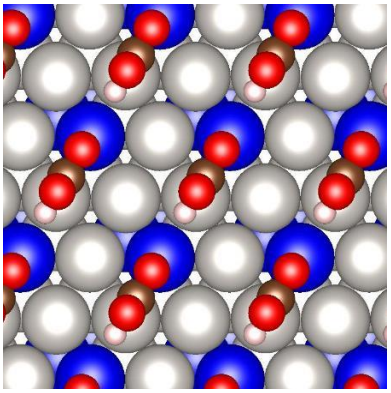

Pt_3Re, Pt_3Rh, Pt_3Ru, Pd_3Ru

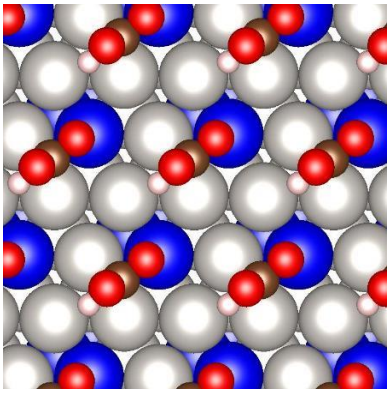

Pd_3Re

$P_3M\text{-}1_3$: HCOO* Structures

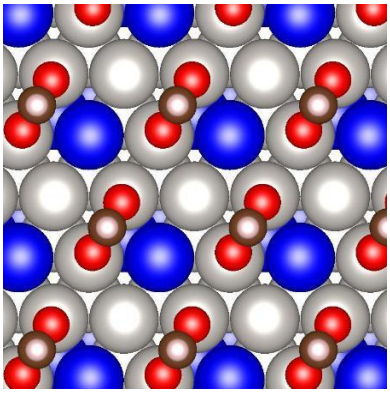

Pt_3Ag, Pt_3Au, Pt_3Pd,
Pd_3Ag, Pd_3Au, Pd_3Cu

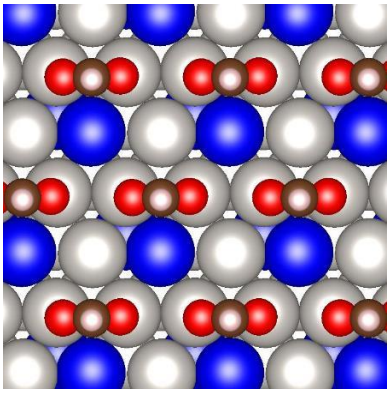

Pt_3Cu

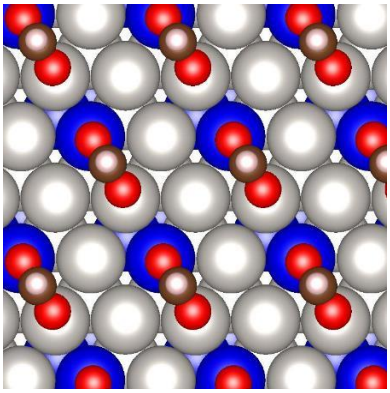

Pt_3Ir, Pd_3Ir, Pd_3Pt, Pd_3Rh

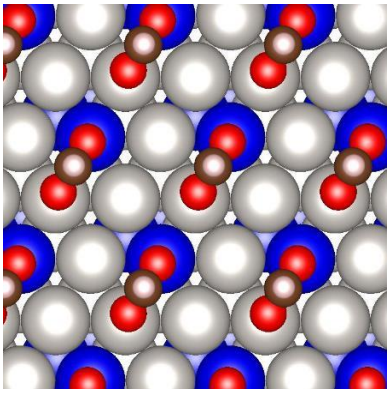

Pt_3Rh, Pt_3Ru

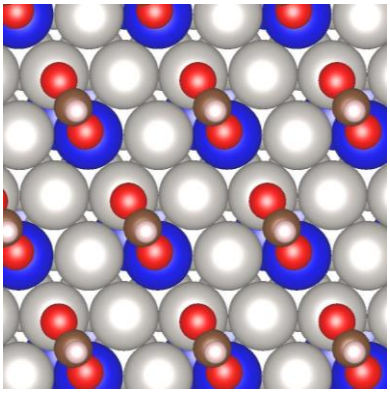

Pt_3Re, Pd_3Re, Pd_3Ru

$P_3M\text{-}2_1$: CO* Structures

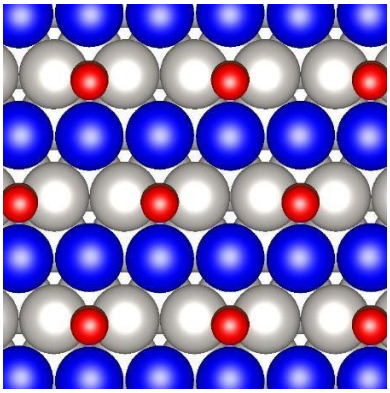

Pt_3Ag, Pt_3Au, Pt_3Cu, Pt_3Pd, Pd_3Ag, Pd_3Au, Pd_3Cu

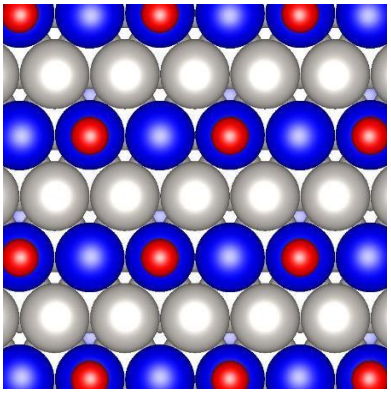

Pt_3Ir, Pt_3Rh, Pd_3Ir, Pd_3Ru

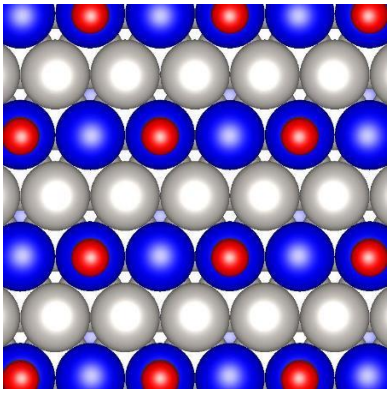

Pt_3Re, Pt_3Ru, Pd_3Re

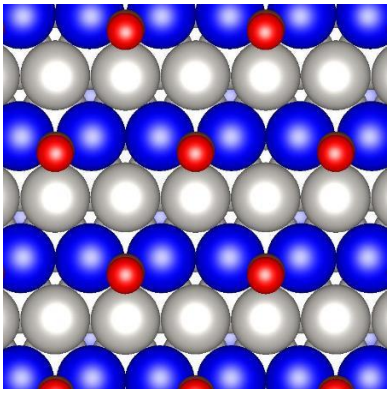

Pd_3Pt, Pd_3Rh

P_3M-2_1: OH* Structures

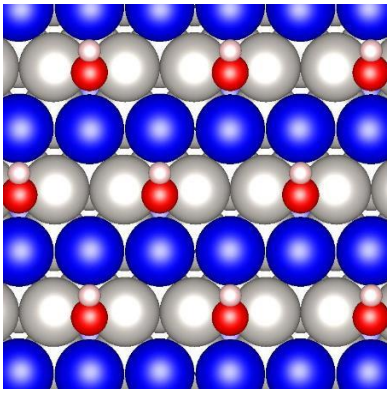

Pt_3Ag, Pt_3Au, Pt_3Cu, Pt_3Pd, Pd_3Ag

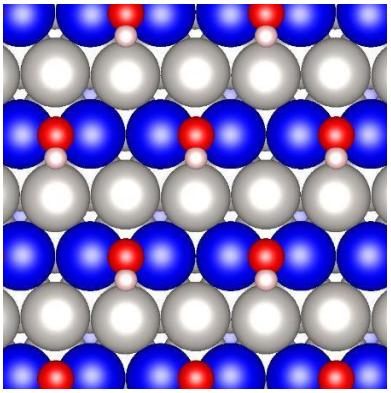

Pt_3Ir, Pt_3Rh

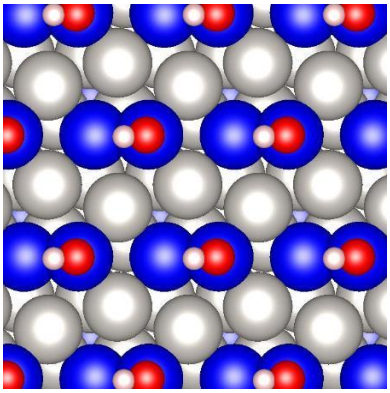

Pt_3Re, Pd_3Re

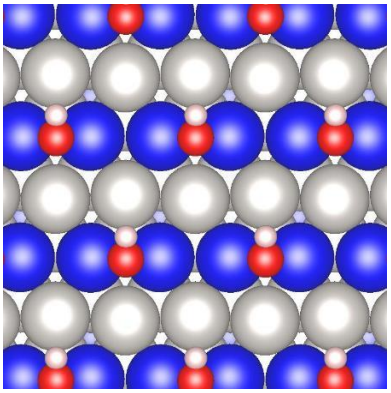

Pt_3Ru, Pd_3Ir, Pd_3Pt

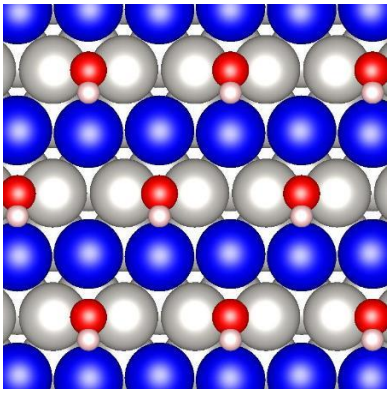

Pd_3Au

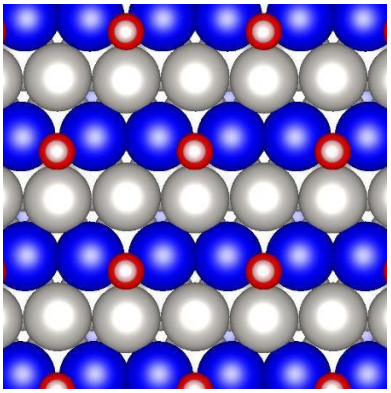

Pd_3Cu, Pd_3Ru

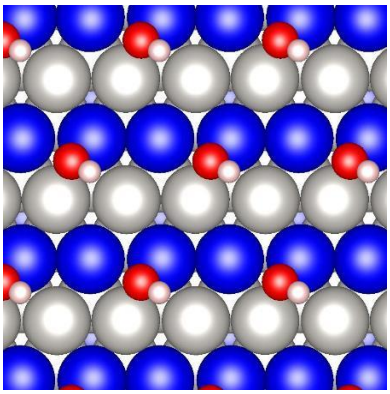

Pd_3Rh

$P_3M\text{-}2_1$: COOH* Structures

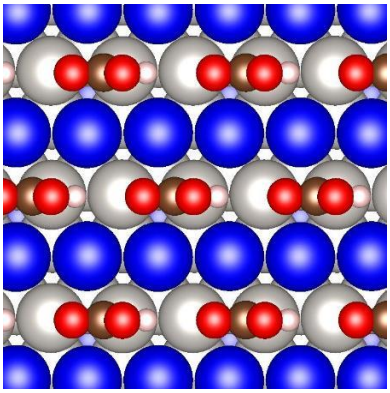

Pt_3Ag, Pt_3Au, Pt_3Cu,
Pd_3Ag, Pd_3Au, Pd_3Cu

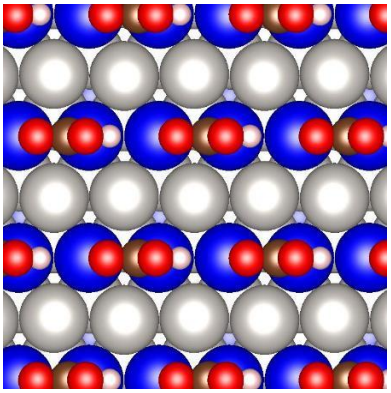

Pt_3Ir, Pt_3Ru, Pd_3Ir, Pd_3Rh

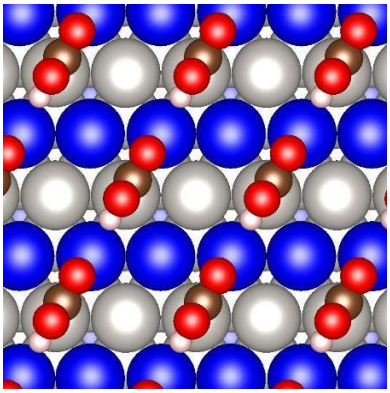

Pt_3Pd

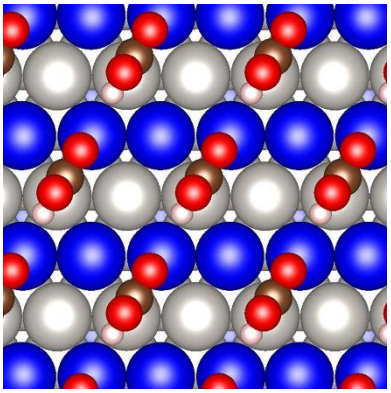

Pt_3Rh

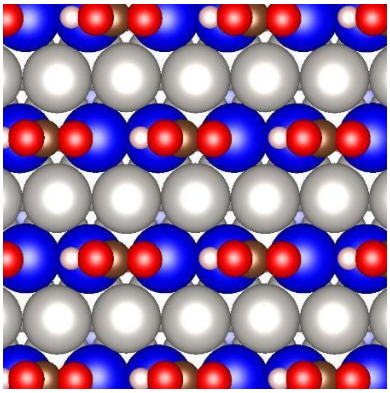

Pt_3Re, Pd_3Re, Pd_3Ru

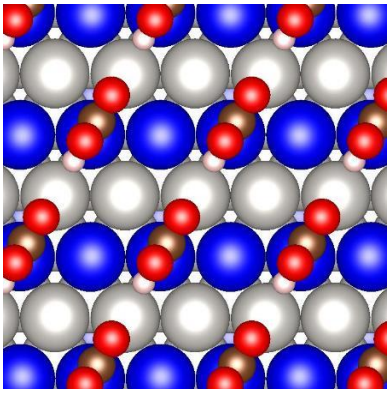

Pd_3Pt

$P_3M\text{-}2_1$: HCOO* Structures

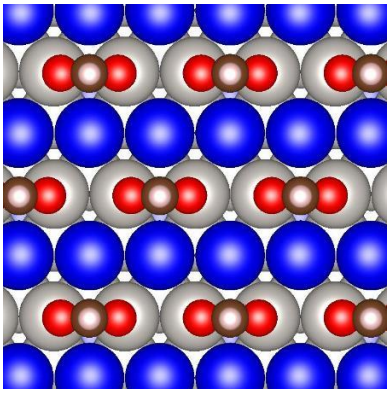

Pt_3Ag, Pt_3Au, Pt_3Cu, Pt_3Pd, Pd_3Ag, Pd_3Au, Pd_3Cu

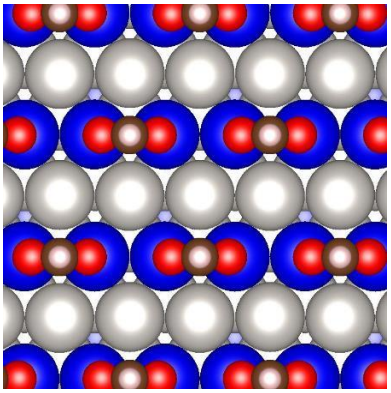

Pt_3Ir, Pt_3Re, Pt_3Rh, Pt_3Ru, Pd_3Ir, Pd_3Pt, Pd_3Re, Pd_3Rh, Pd_3Ru

$P_3M\text{-}2_2$: CO* Structures

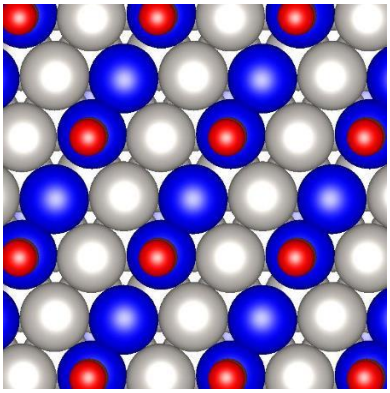

Pt_3Ag, Pt_3Au, Pd_3Ir, Pd_3Re, Pd_3Ru

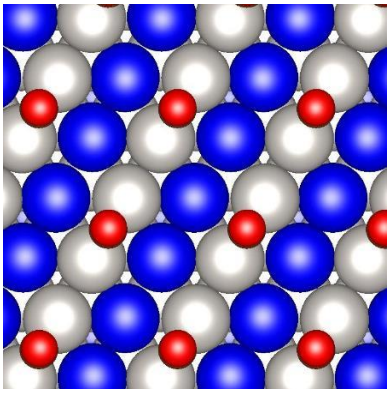

Pt_3Cu, Pt_3Pd, Pd_3Ag, Pd_3Au, Pd_3Cu

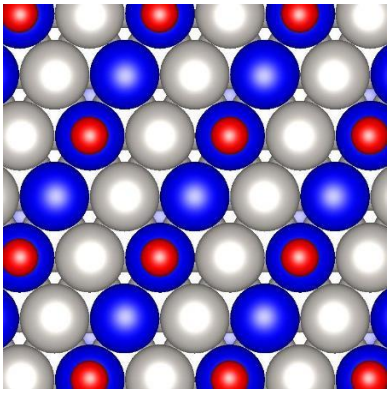

Pt_3Ir, Pt_3Re, Pt_3Rh, Pt_3Ru

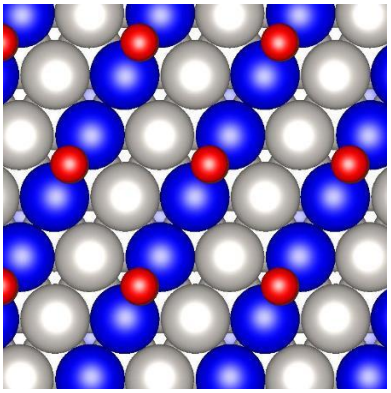

Pd_3Pt

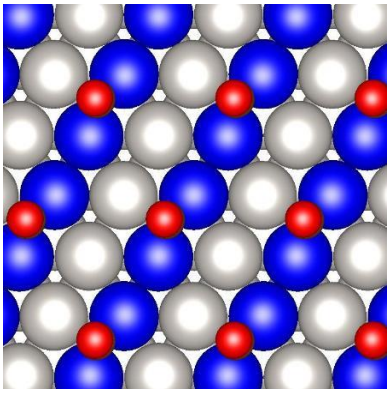

Pd_3Rh

$P_3M\text{-}2_2$: OH* Structures

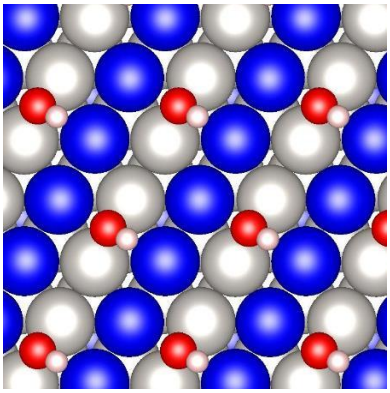

Pt_3Ag, Pt_3Au, Pt_3Pd, Pd_3Ag

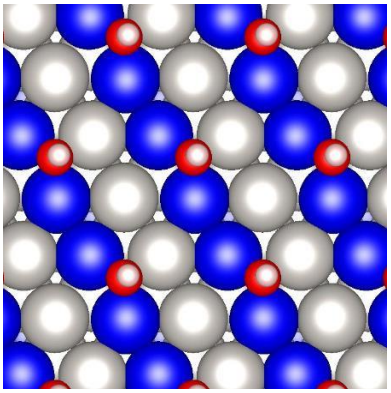

Pt_3Cu

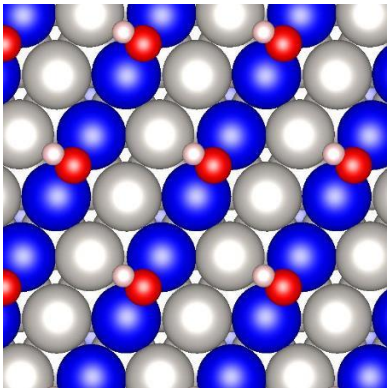

Pt_3Ir, Pt_3Rh, Pd_3Ir,
Pd_3Rh, Pd_3Ru

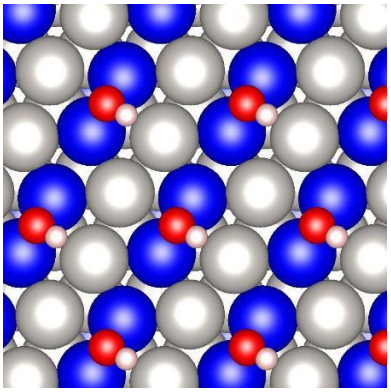

Pt_3Re

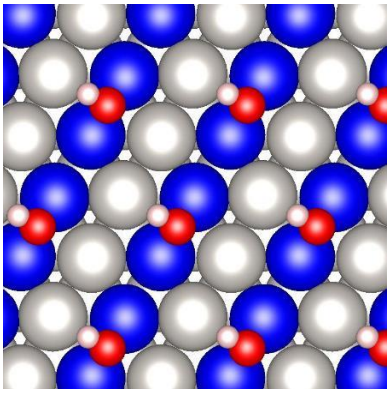

Pt_3Ru

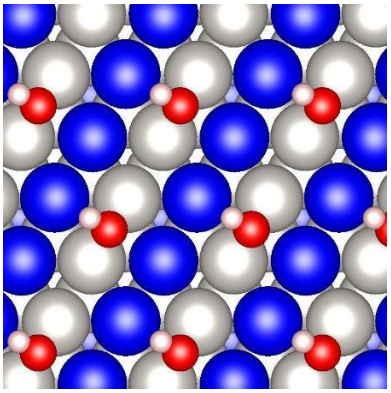

Pd_3Au

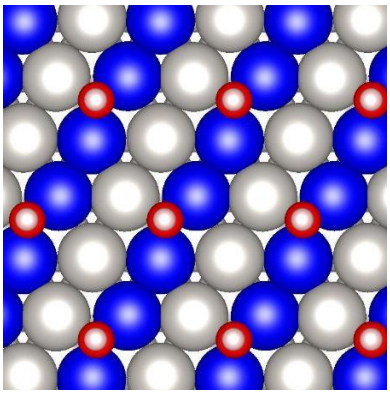

Pd_3Cu

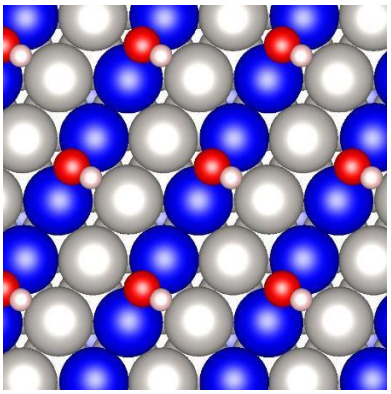

Pd_3Pt

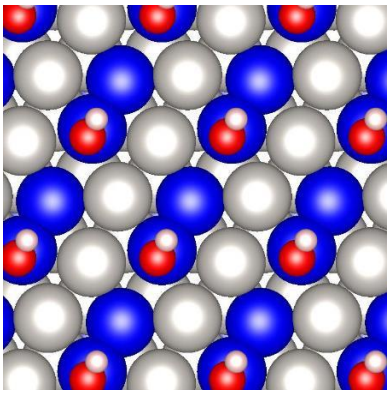

Pd_3Re

$P_3M\text{-}2_2$: COOH* Structures

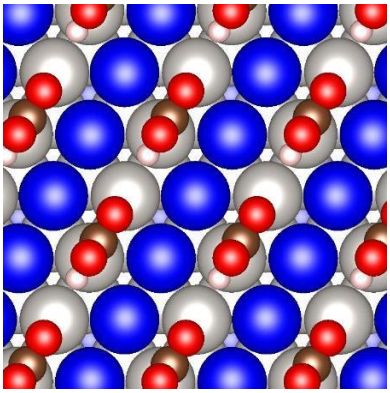

Pt_3Ag, Pt_3Au, Pt_3Cu,
Pd_3Ag, Pd_3Au, Pd_3Cu

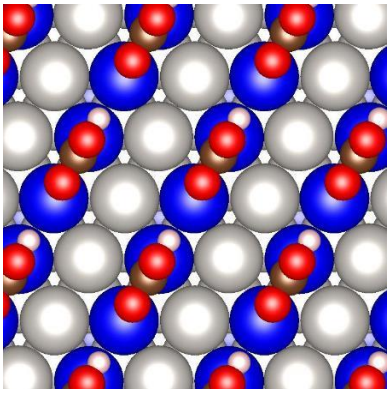

Pt_3Ir, Pt_3Rh, Pd_3Ir, Pd_3Rh

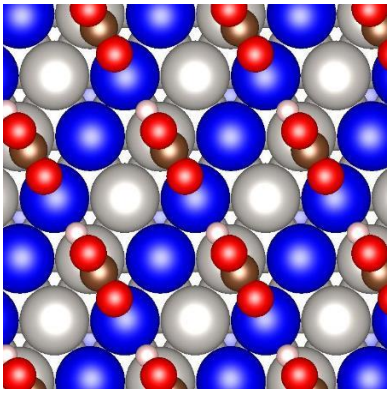

Pt_3Pd

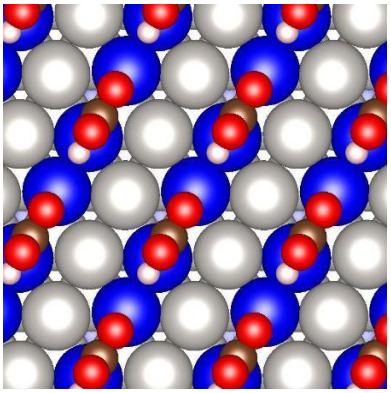

Pt_3Re, Pd_3Re, Pd_3Ru

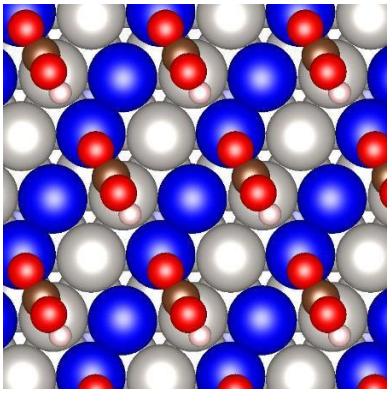

Pt_3Ru

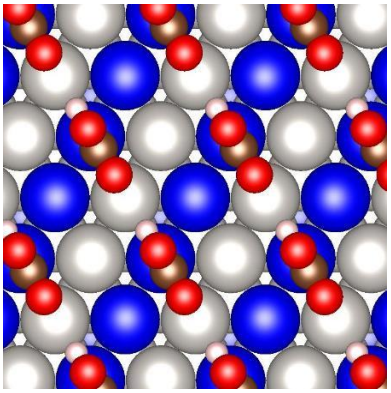

Pd_3Pt

$P_3M\text{-}2_2$: HCOO* Structures

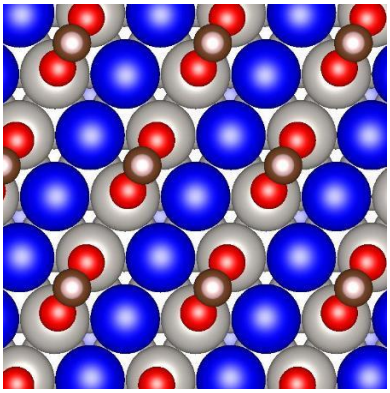

Pt_3Ag, Pt_3Cu, Pt_3Pd,
Pd_3Ag, Pd_3Au, Pd_3Cu

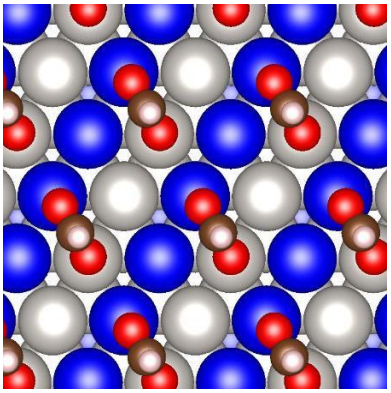

Pt_3Au

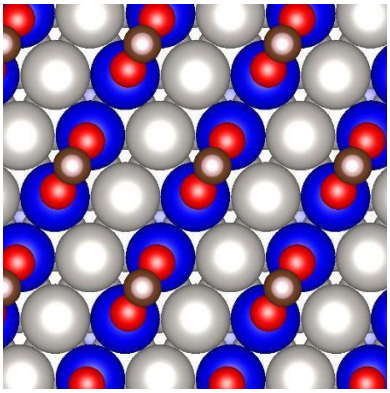

Pt_3Ir,Pt_3Re,Pt_3Rh,Pt_3Ru,Pd_3Ir,
Pd_3Pt, Pd_3Re, Pd_3Rh, Pd_3Ru

Appendix: H Supplementary Materials for 'Alignment of Semiconducting Graphene Nanoribbons on Vicinal Ge(001)'*

H.1 DFT calculations

DFT calculations are performed using a plane wave basis set and the projector augmented wave method (PAW)[120,121] as implemented in the Vienna *Ab Initio* Simulation Package (VASP).[81,82] Exchange-correlation interactions are treated using the generalized gradient approximation (GGA) in the parameterization of Perdew, Burke, and Ernzerhof (PBE).[79] Van der Waals forces are modeled with DFT-D2[257] dispersion corrections and gamma-point-only k-point settings are utilized.[122] The electron wave function is expanded in a plane-wave basis with truncated kinetic energy cutoff of 400 eV. Calculations are performed using two Ge lattice constants: (1) the calculated bulk lattice constant of 5.67 Å, referred to as "relaxed" in the main text, and (2) an expanded lattice constant of 6.04 Å, referred to as "strained" in the main text, to eliminate strain in the graphene lattice along the length of the ribbon, which has a calculated bulk C–C bond distance of 1.42 Å. Ge unit cells are modeled using a supercell with eight layers, in which the top four layers are allowed to relax and the bottom four layers are fixed at either of the lattice constants described above, and range from 16 × 24 $Å^2$ to 24 × 37 $Å^2$ to accommodate the surface miscut and minimize interactions of ribbons between periodic unit cells. Periodic images

*Adapted from **"Alignment of semiconducting graphene nanoribbons on vicinal Ge(001)"**, R. M. Jacobberger, E. A. Murray, M. Fortin-Deschênes, F. Göltl, W. A. Behn, Z. J. Krebs, P. L. Levesque, D. E. Savage, C. Smoot, M. G. Lagally, P. Desjardins, R. Martel, V. Brar, O. Moutanabbir, M. Mavrikakis, M. S. Arnold, *Nanoscale* **11**, 4864 (2019).

in the z-direction are separated by at least 14 Å of vacuum.

Phase diagrams for H coverage of Ge are constructed by calculating the grand potential (Ω) of a Ge(001)-0° surface ranging from 1/16th monolayer (ML) of H to 1 ML of H (where 1 ML of H is defined as one H atom per one surface Ge atom) exposed to varying pressures of H_2 (Fig. H.10a,b).[312,313] The grand potential (Ω) for each coverage is defined as $\Omega = E_{slab+H} - E_{slab} - N_H{*}\mu_H$, where E_{slab+H} is the total energy of the slab and the adsorbed H, E_{slab} is the total energy of the clean Ge slab, N_H is the total number of H atoms, and μ_H is the chemical potential of H. The chemical potential of H_2 in the gas phase is calculated by $\mu_{H2} = k_B{*}T{*}\ln(P_{H2}/P_o) + E_{H2} + H_{H2} - H_{H2O} - T{*}S_{H2}$, where k_B is the Boltzmann constant, T is temperature, P_{H2} is the partial pressure of H_2, P_o is the reference pressure of 1 atm, E_{H2} is the total energy of H_2 in the gas phase determined by DFT, H_{H2} is the enthalpy of H_2, H_{H2O} is found in the NIST JANAF tables for H_2,[10] and S_{H2} is the entropy of H_2 in the gas phase. We assume $H_2(g) \leftrightarrow 2H^*$ is at equilibrium where * signifies that H is adsorbed on the Ge surface. Thus, the chemical potential of H on Ge(001)-0° is described as $\mu_H = 1/2\mu_{H2}$.

At temperatures at which graphene is grown (~ 1183 K), 1/16th ML of H is the most stable coverage by at least ~80 kJ mol^{-1} at all P_{H2} (Fig. H.10c-f). Thus, all Ge surfaces are modeled without H passivation in subsequent calculations.

Phase diagrams for nanoribbons (Fig. 8.5e, Fig. H.11e and H.12) are constructed by calculating the grand potential (Ω) of N = 13 armchair graphene nanoribbons (where N is the number of C atoms along the zigzag chain that spans the ribbon width) that are ~ 1.5 nm wide on Ge(001)- 9º exposed to a gas phase with partial pressure of CH_4 (P_{CH4}) of 0.0067 atm and varying P_{H2}.[8, 9] The grand potential is defined as $\Omega = E_{slab+ribbon} - E_{slab} - N_C{*}\mu_C - N_H{*}\mu_H$, where $E_{slab+ribbon}$

is the total energy of the slab and the ribbon, E_{slab} is the total energy of the clean Ge slab, N_i is the total number of *i* atoms in a ribbon, and μ_i is the chemical potential of atom *i*.

The chemical potential of CH_4 and H_2 in the gas phase are calculated by $\mu_j = k_B*T*\ln(P_j/P_o) + E_j + H_j - H_{jo} - T*S_j$, where k_B is the Boltzmann constant, T is the temperature, P_j is the partial pressure of species *j*, P_o is the reference pressure of 1 atm, E_j is the total energy of species *j* in the gas phase determined by DFT, H_j is the enthalpy of species *j*, H_{jo} is found in the NIST JANAF tables for species *j*,[10] and S_j is the entropy of species *j* in the gas phase. We assume the following reactions are at equilibrium: $H_2(g) \leftrightarrow 2H^*$ and $CH_4(g) \leftrightarrow C^* + 4H^*$, where * signifies that a species is adsorbed on the Ge surface. Therefore, the chemical potential of H and C atoms on the Ge surface are described as $\mu_H = 1/2\mu_{H2}$ and $\mu_C = \mu_{CH4} - 4\mu_{H2}$, respectively.

The energy difference between ribbons with their downhill edge pinned and uphill edge pinned to Ge(001)-9º are calculated by comparing the total energy per edge C atom that forms a covalent bond with the Ge surface in each unit cell. Relative energies of graphene nanoribbons and Ge slabs are calculated by performing single-point calculations on the ribbon with the slab removed and on the slab with the ribbon removed, respectively.

H.2 Supplementary Data

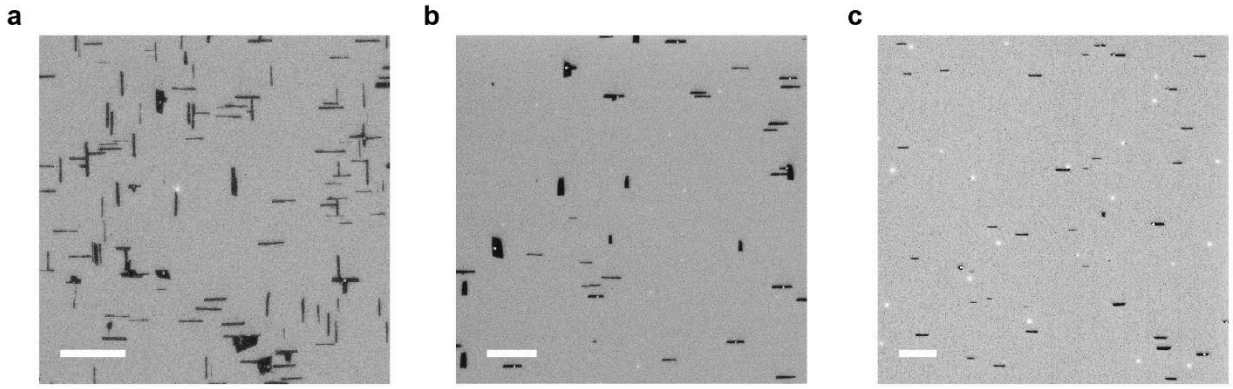

Figure H.1: SEM images of graphene grown on **(a)** Ge(001)-0°, **(b)** Ge(001)-6°, and **(c)** Ge(001)-9°.

Images of ribbons synthesized using this growth condition are used to characterize alignment, width, length, and aspect ratio in Fig. 8.1g-j, respectively. Particles are likely due to surface contaminants that are present on the as-purchased Ge wafers. Scale bars are 2 μm.

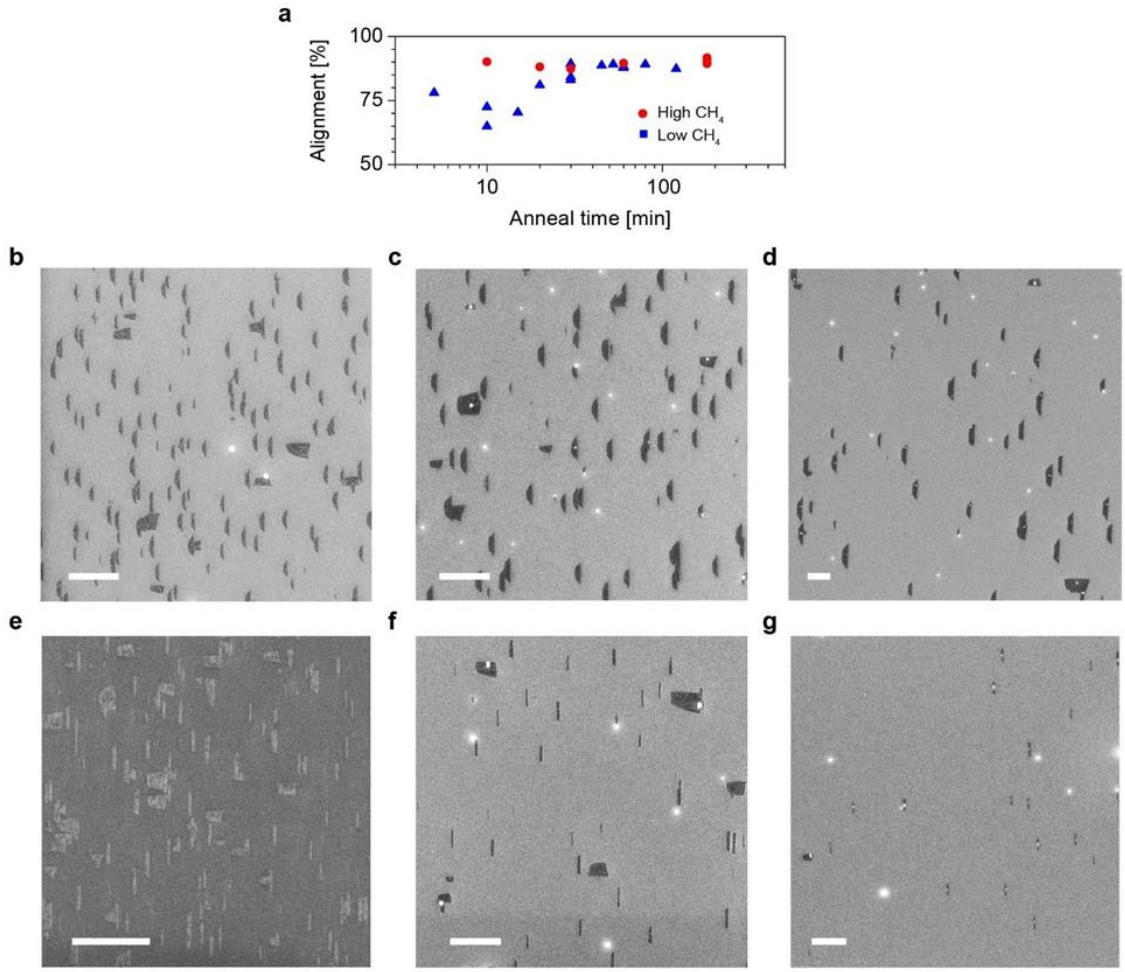

Figure H.2: Effect of pre-growth anneal time on ribbon alignment. (a) Plot of alignment versus anneal time for growth using 4.6 (red circles) and 2.8 (blue triangles) sccm of CH_4 on Ge(001)-9°. (b-g) SEM images of graphene crystals grown using 4.6 **(b-d)** and 2.8 **(e-g)** sccm of CH_4 and anneal time of **(a)** 10, **(b)** 20, **(c)** 60, **(d)** 10, **(e)** 30, and **(f)** 45 min. Scale bars are 500 nm in **(b,e)** and 1 μm in **(c,d,f,g)**. Pre-growth anneal time affects Ge surface topography,[72] which in turn determines the Ge sites available for graphene nucleation, and CH_4 concentration affects feedstock chemical potential, which in turn impacts the type of graphene crystals formed.[239] Characterization of the graphene nucleation sites is beyond the scope of this work. Nonetheless, it is clear that aligned ribbons preferentially nucleate when anneal time is long or CH_4 concentration is high.

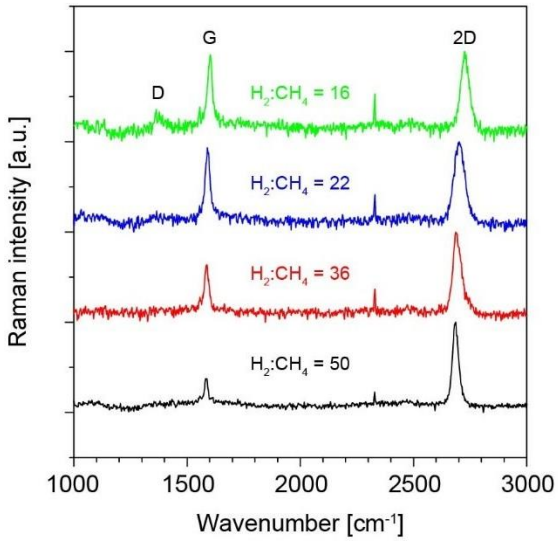

Figure H.3: Raman spectroscopy of single-layer graphene grown on Ge(001)-9° using the same H_2:CH_4 used in Fig. 8.2, H.4, and H.5 of 50 (black), 36 (red), 22 (blue), and 16 (green). Each spectrum is the average of at least 25 spectra obtained at different locations on the sample surface. Spectra are normalized to the intensity of the 2D band at ~2700 cm^{-1}.

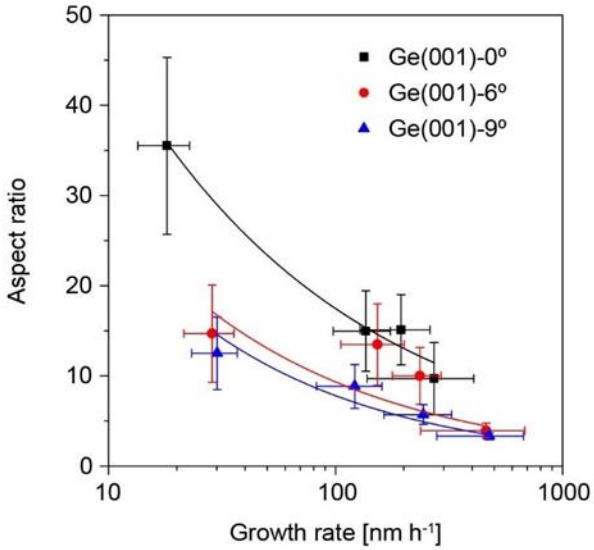

Figure H.4: Effect of growth rate on nanoribbon aspect ratio. Aspect ratio of graphene nanoribbons with lengths of 200–600 nm grown on Ge(001)-0° (black squares), Ge(001)-6° (red circles), and Ge(001)-9° (blue triangles) plotted against growth rate in the direction of the ribbon length. x and y error bars are one standard deviation. Trend lines are added to highlight the decreasing aspect ratio with increasing growth rate on each surface. We define growth rate in the length direction to be $l/(2t)$, where l is crystal length and t is growth time. This formula does not account for the incubation time required to form stable nuclei, during which graphene does not grow. However, we have found this incubation time is significantly less than the total growth time used in our experiments (see Fig. H.6), and therefore its effect on the calculated growth rate is relatively small (< 10%).[72]

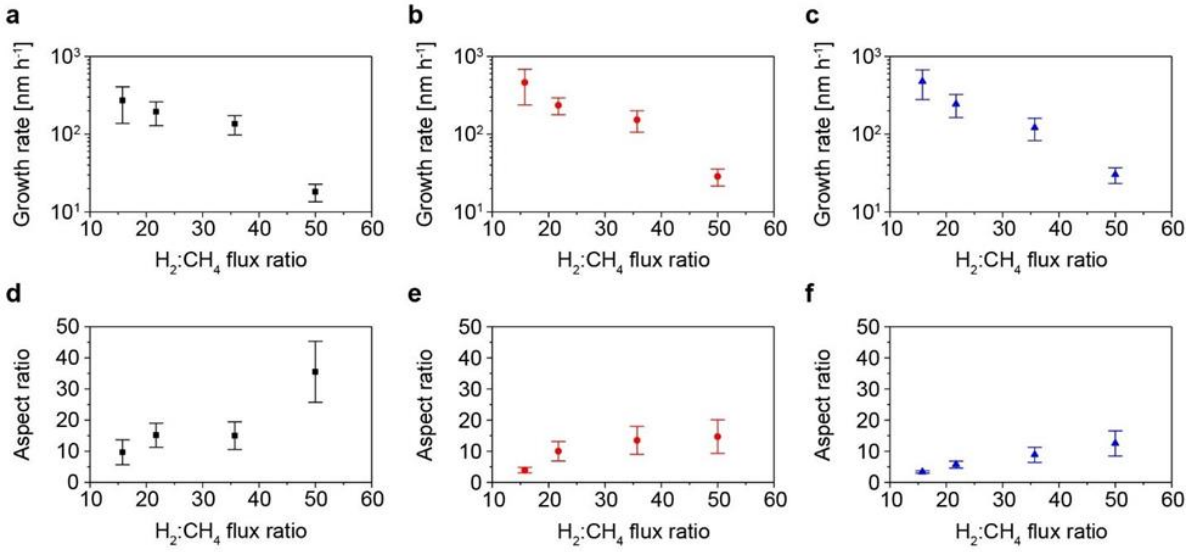

Figure H.5: Effect of H_2:CH_4 on growth rate and aspect ratio. **(a-f)** Plot of growth rate **(a-c)** and aspect ratio **(d-f)** versus H_2:CH_4 on Ge(001)-0° **(a,d)**, Ge(001)-6° **(b,e)**, and Ge(001)-9° **(c,f)**.

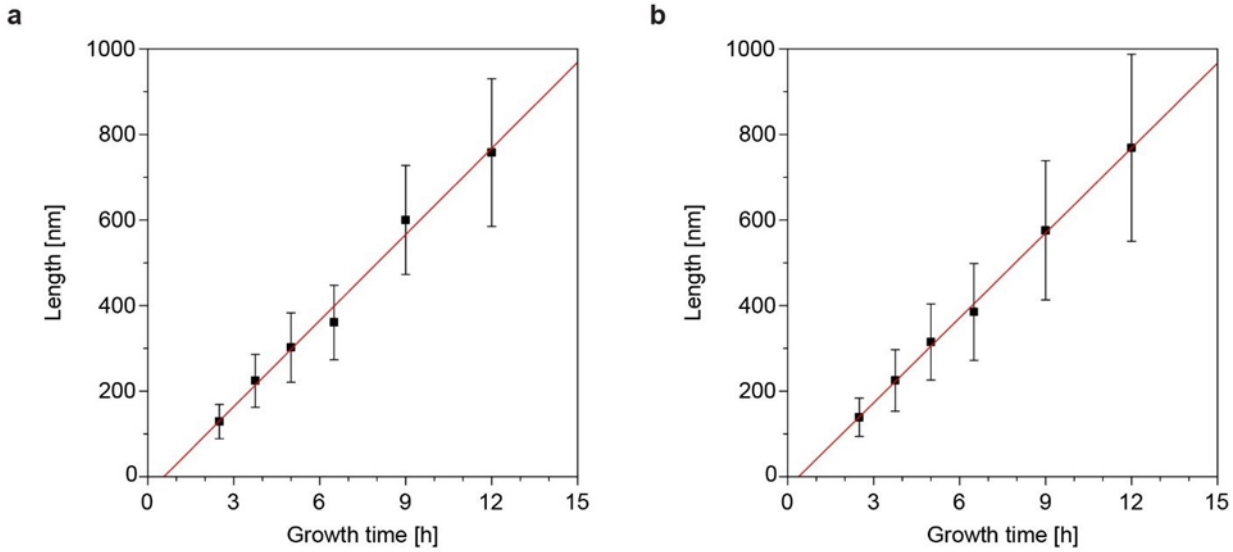

Figure H.6: Effect of growth time on ribbon length. **(a-b)** Plot of ribbon length versus growth time on **(a)** Ge(001)9° and **(b)** Ge(001)-6° for samples grown at 910 °C with a flow of 200 sccm of Ar, 100 sccm of H_2, and 2.0 sccm of CH_4. The extracted incubation time for nucleation is ~0.5 h on both surfaces. In comparison, the growth time used to determine growth rate in Fig. H.4 and H.5a-c is 6 h. The incubation time, therefore, may increase the calculated growth rate by < 10%.

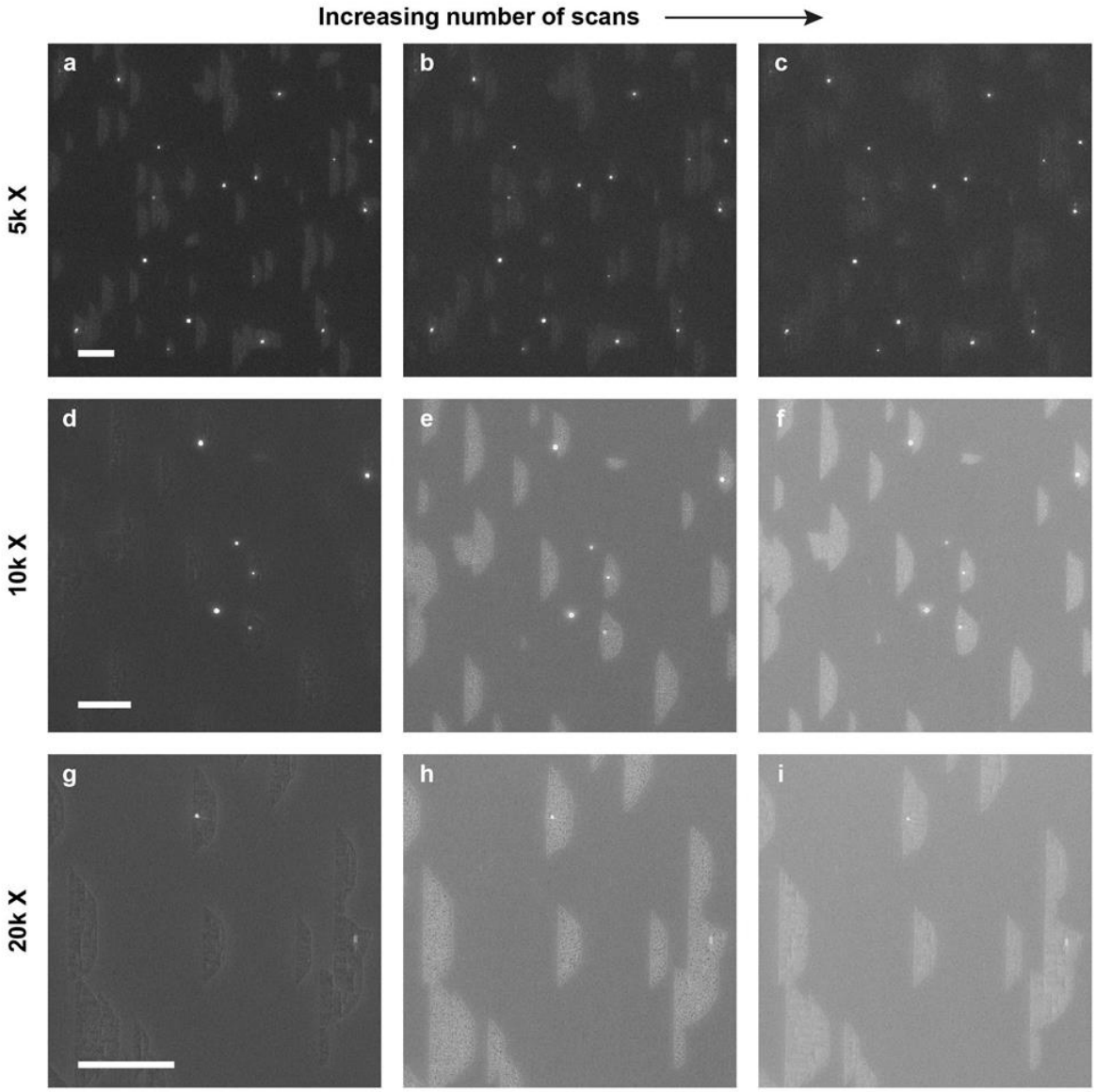

Figure H.7: Effect of magnification and number of scans on SEM contrast after exposure of the sample to air for 0 h. Representative SEM images of graphene on Ge(001)-9° at 5k (top), 10k (middle), and 20k (bottom) magnification factor with increasing number of scans (left to right). Number of scans in a-i is 1, 2, 3, 1, 5, 9, 1, 2, and 3, respectively. All images are obtained using the same brightness and contrast. Scale bars are 1 μm. At each magnification factor, graphene appears lighter than Ge after 1 scan. As the number of scans increases, graphene still appears lighter than Ge, but the contrast is enhanced.

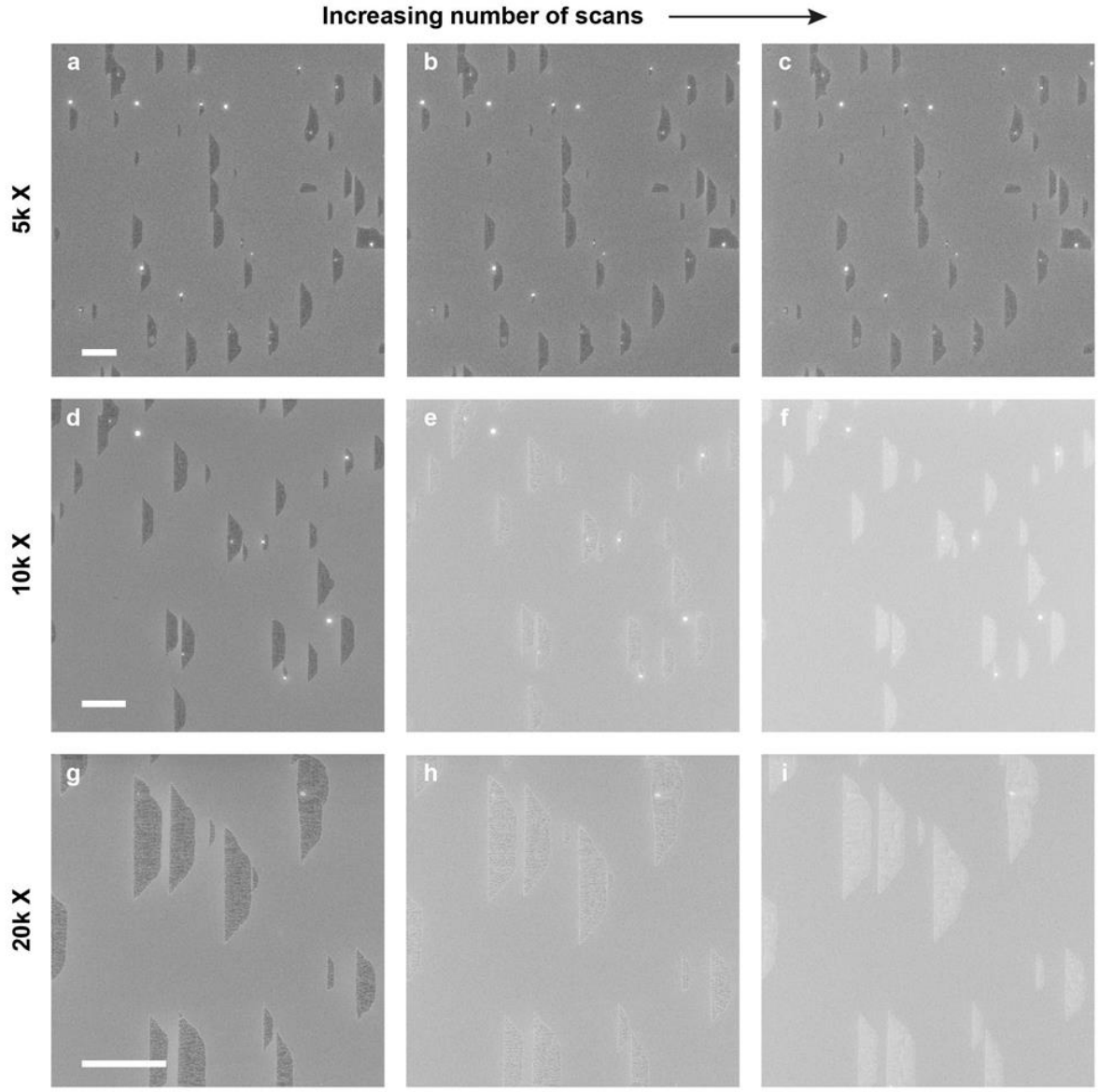

Figure H.8: Effect of magnification and number of scans on SEM contrast after exposure of the sample to air for 32 h. Representative SEM images of graphene on Ge(001)-9° at 5k (top), 10k (middle), and 20k (bottom) magnification with increasing number of scans (left to right). Number of scans in **(a-i)** is 1, 4, 6, 1, 5, 9, 1, 2, and 3, respectively. All images are obtained using the same brightness and contrast. Scale bars are 1 μm. At each magnification factor, graphene appears darker than Ge after 1 scan. Conversely, graphene appears lighter than Ge after 1 scan on samples that are exposed to air for 0 h (Fig. H.7a,d,g) instead of 32 h (Fig. H.8a,d,g), indicating that increasing the air exposure time can cause contrast reversal. Contrast reversal upon exposure to air is likely due to oxidation of the Ge surface. As the number of scans increases in Fig. H.8, contrast reverses and graphene appears lighter than Ge, which is likely due to deposition of amorphous carbon upon sample exposure to the electron beam.

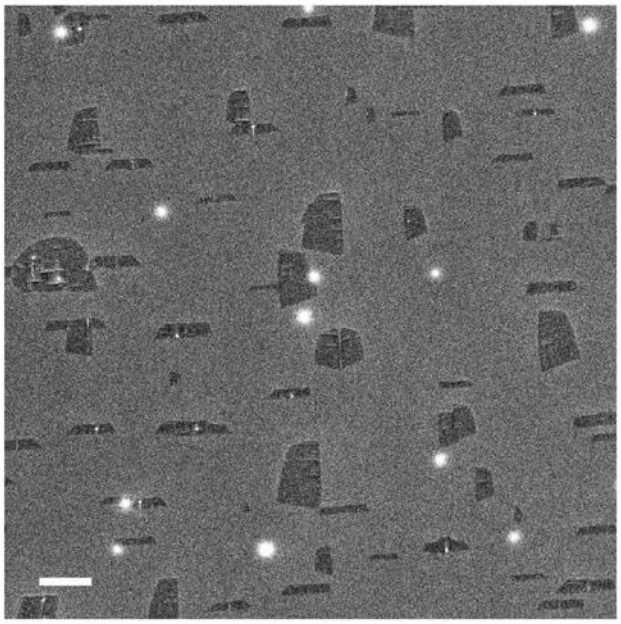

Figure H.9: SEM image of graphene crystals on Ge(001)-9° used for LEEM and LEED studies in Fig. 8.3a,b. Scale bar is 1 μm.

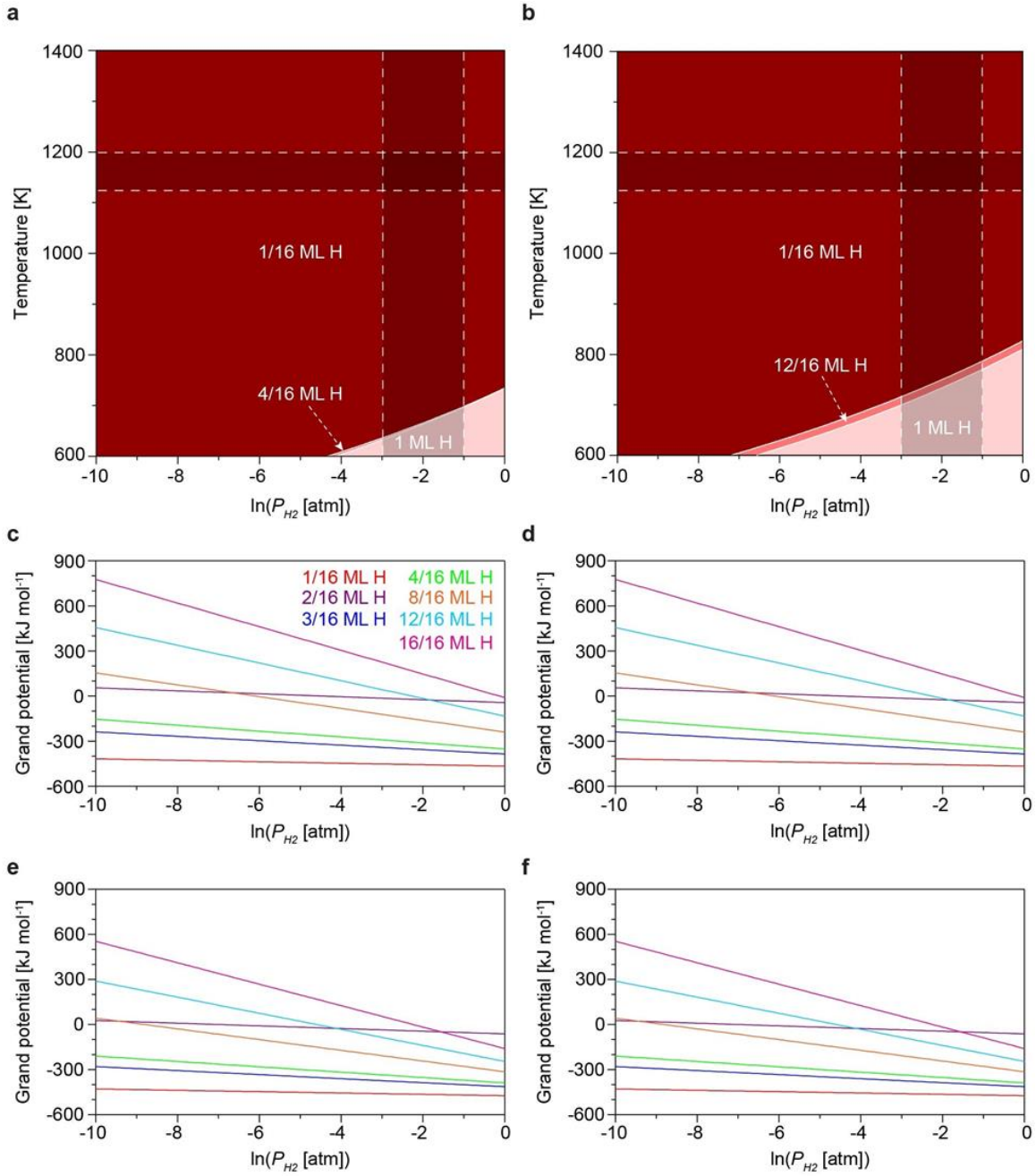

Figure H.10: DFT calculations of H coverage on Ge(001)-0°. **(a,b)** Thermodynamic phase diagram plotted against temperature and P_{H_2}using the **(a)** strained and **(b)** relaxed Ge lattice. Regions of stability are shown for Ge surfaces with 1/16th, 4/16th, and 1 ML of H **(a)** and 1/16th, 12/16th, and 1 ML of H **(b)**. Shaded regions indicate a range of temperatures and P_{H_2} at which ribbons have been grown.[72] **(c-f)** Cutouts of the phase diagrams in **(a,b)**, plotting grand potential for 1/16th (red), 2/16th (purple), 3/16th (blue), 4/16th (green), 8/16th (orange), 12/16th (cyan), and 1 ML (magenta) of H versus P_{H_2} at 1183 K **(c,d)** and 1073 K **(e,f)** using the strained **(c,e)** and relaxed **(d,f)** Ge lattice.

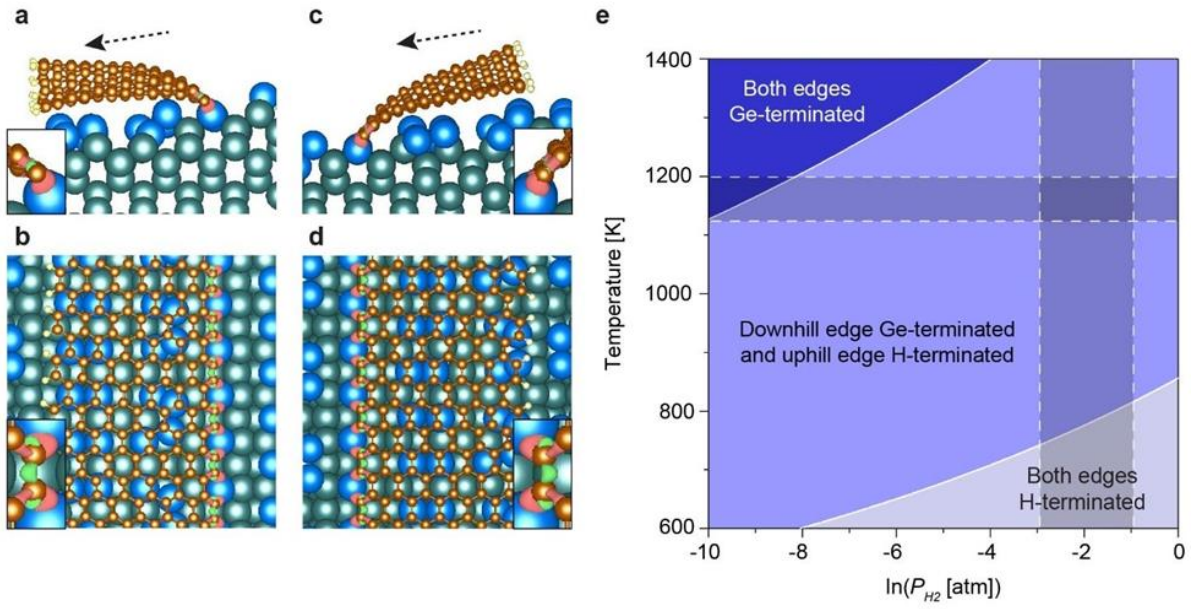

Figure H.11: DFT calculations of graphene nanoribbons on Ge(001)-9°. **(a-d)** Side view **(a,c)** and top view **(b,d)** of the minimum-energy structure in which the uphill (downhill) edge is not (is) terminated by H **(a,b)** and vice versa **(c,d)**. Charge density isosurfaces (insets) show regions of increased (red) and decreased (green) electron density upon ribbon adsorption onto Ge(001)-9º. Green, blue, orange, and white atoms are Ge (saturated, bulk), Ge (unsaturated, surface), C, and H, respectively, and dashed arrows point downhill. **(e)** Thermodynamic phase diagram plotted against temperature and P_{H_2}. Regions of stability are shown for ribbons with both edges pinned, only the downhill edge pinned, and both edges unpinned. $P_{\mathrm{CH_4}}$ is 0.0067 atm. Shaded regions indicate a range of temperatures and P_{H_2} at which ribbons have been grown.[72] Results in a-e are calculated using the relaxed Ge lattice. Results for strained Ge are shown in Fig. 8.5.

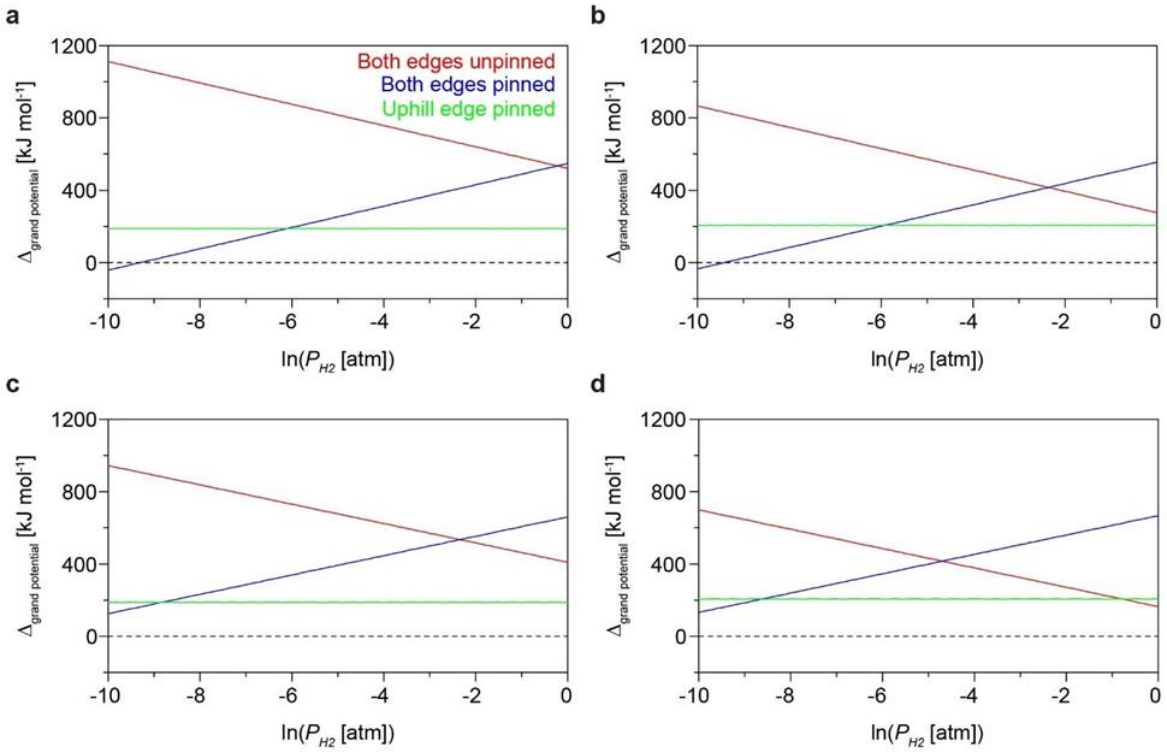

Figure H.12: DFT grand potential of nanoribbons on Ge(001)-9°. Cutouts of the phase diagrams in Fig. 8.5e and Fig. H.11e, plotting the difference in grand potential between a ribbon with its downhill edge pinned and a ribbon with both edges unpinned (red), both edges pinned (blue), and only the uphill edge pinned (green) versus P_{H_2} at 1183 K **(a,b)** and 1073 K **(c,d)** using the strained **(a,c)** and relaxed **(b,d)** Ge lattice.

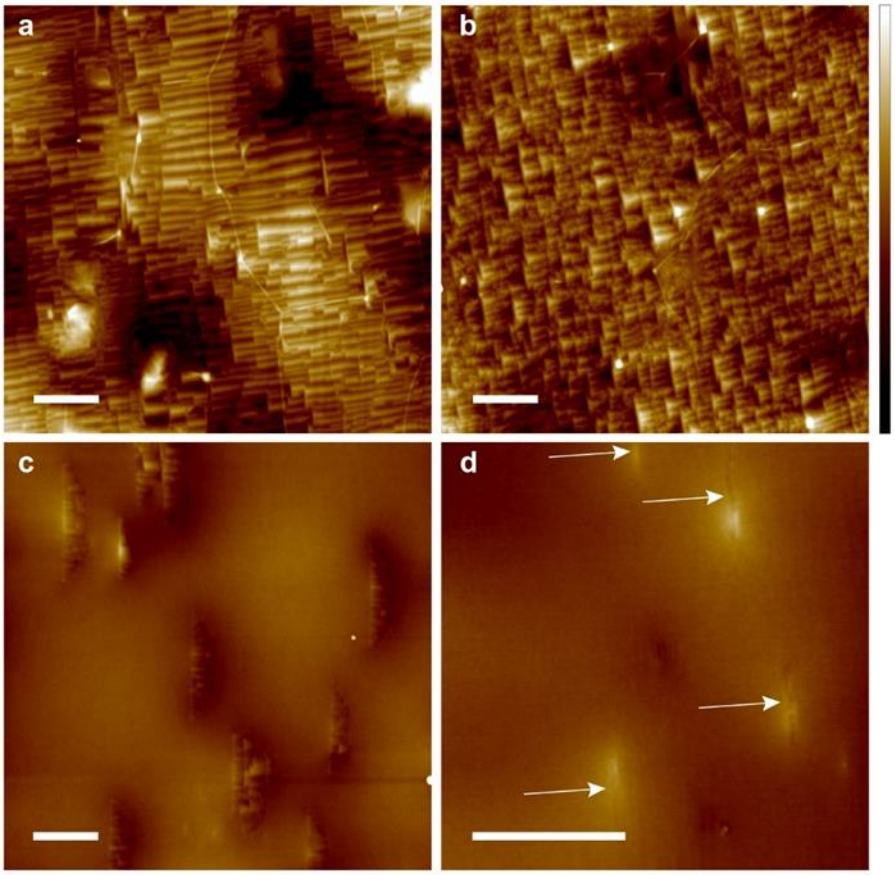

Figure H.13: AFM of graphene on Ge(001)-6° and Ge(001)-9°. **(a-d)** AFM images of continuous graphene films **(a,b)** and isolated graphene islands **(c,d)** grown on **(a)** Ge(001)-6° and **(b-d)** Ge(001)-9° in which the Ge surface below graphene is nanofaceted. The faceting of Ge is selective and only occurs below graphene, as shown in Fig. H.13c. Furthermore, the facet angle is relatively shallow below narrow ribbons (Fig. H.13d and Fig. 8.4c,d) and only becomes steeper as the ribbons grow wider (Fig. H.13c) and eventually merge to form a continuous graphene film (Fig. H.13b). Scale bars are 500 nm. Height scale is 20 nm. Arrows in d highlight the position of graphene ribbons.

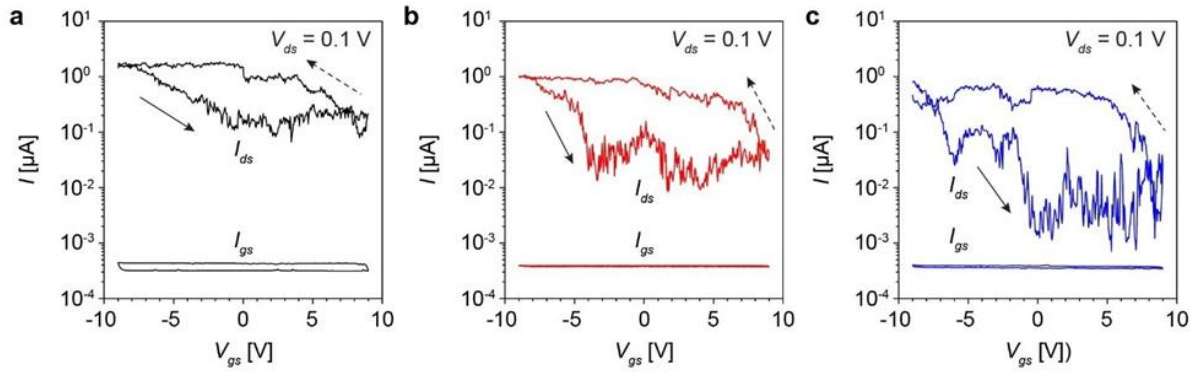

Figure H.14: Charge transport of nanoribbons grown on Ge(001)-9°. **(a-c)** Plot of I_{ds} (top curve) and I_{gs} (bottom curve) *versus* V_{gs} for three nanoribbons at V_{ds} of 0.1 V, corresponding to the I_{ds} *versus* V_{gs} curves with the same color in Fig. 8.6b,c.

Table H.1: Summary of growth conditions. Conditions used in this work, including temperature (*T*), anneal time (t_{anneal}), growth time (t_{growth}), Ar flux (*Ar*), H_2 flux (H_2), and CH_4 flux (CH_4). For each synthesis, the same temperature, Ar flux, and H_2 flux are used for the anneal and growth steps.

Fig.	*T* [°C]	t_{anneal} [min]	t_{growth} [h]	*Ar* [sccm]	H_2 [sccm]	CH_4 [sccm]
1d,e,f	910	30	1.5	200	100	4.6
1g,h,i,j	910	60	2	200	100	2.8
2a	910	45	9	200	100	2.0
2b,e,h	910	30	1.5	200	100	4.6
2c,f,i	910	30	0.42	210	90	5.7
2d,g	910	15	6	200	100	2.0
3a,b	910	10	2	200	100	2.8
3c,d	910	30	1.5	200	100	4.6
4b	910	10	2.5	200	100	2.0
4c,d	910	0	0.67	200	100	1.7
6	910	~5	2	200	100	2.0
S1	910	60	2	200	100	2.8
S2b	910	10	0.33	200	100	4.6
S2c	910	20	0.67	200	100	4.6
S2d	910	60	1.5	200	100	4.6
S2e	910	10	0.75	200	100	2.8
S2f	910	30	2	200	100	2.8
S2g	910	45	2	200	100	2.8
S3	910	60	40	200	100	2.0
S3	910	60	18	200	100	2.8
S3	910	60	9	200	100	4.6
S3	910	60	2	210	90	5.7
S7	910	45	1.5	200	100	4.6
S8	910	45	1.5	200	100	4.6
S9	910	10	2	200	100	2.8
S13c	910	30	1.5	200	100	4.6
S13d	910	15	6	200	100	2.0
S14	910	~5	2	200	100	2.0

Appendix: I Supplementary Materials for 'Anisotropic Synthesis of Armchair Graphene Nanoribbon Arrays from Sub-5 nm Seeds at Variable Pitches on Germanium'[3*]

I.1 Experimental methods

***Preparation of the Ge(001) substrates*:** Ge(001) (Wafer World, resistivity > 40 Ω-cm) is coated with a 130 nm thick film of poly(methyl methacrylate) (PMMA). The wafers are then diced into 1.0 × 0.75 cm^2 rectangles along the Ge⟨110⟩ directions (precision of ± 1.5°) with a MicroAutomation 1006 dicing saw. Each sample is then soaked in acetone at 110 °C for 30 min to remove PMMA from the surface before rinsing with isopropyl alcohol (IPA). Finally, the substrates are annealed for 2 hr, in a horizontal quartz tube furnace, at 910 °C in a flow of 200 sccm of Ar (99.999% purity) and 100 sccm of H_2 (99.999% purity).

***Synthesis of graphene with sub-monolayer coverage on Cu foil via CVD*:** Cu foil (Alfa Aesar, 25 μm thick, 2.5 × 2.5 cm^2, 99.8% purity) is etched in nitric acid for 30s to remove surface contaminants. The CVD growth of graphene is performed as described previously.[72] The Cu foil is placed into a horizontal quartz tube furnace. The tube is filled with a mixture of 95% Ar and 5% H_2, with a total flow rate of 340 sccm at atmospheric pressure. The substrate is annealed at 1030 °C for 30 min before initiating graphene growth by introducing a mixture of 95% Ar and 5% CH_4 with a total flow rate of 0.275 sccm. Growth proceeds for 2.5 hr. Finally, the sample is removed

---

[*]Adapted from **"Anisotropic Synthesis of Armchair Graphene Nanoribbon Arrays from Sub-5 nm Seeds at Variable Pitches on Germanium"**, A. J. Way, E. A. Murray, F. Göltl, V. Saraswat, R. M. Jacobberger, M. Mavrikakis, M. S. Arnold, *Journal of Physical Chemistry Letters* **10**, 4266 (2019).

from the furnace and rapidly cooled to terminate synthesis. Growth time is tailored so that ~50% of the Cu foil surface is covered with hexagonally shaped crystals of graphene. These hexagons possess a diameter of approximately 20 μm and have zigzag edges.[314]

***Transfer of graphene onto Ge(001)*:** After partial monolayer growth on Cu foil, the hexagonally shaped domains of graphene are transferred onto Ge(001) through a wet transfer technique. The graphene/Cu foil substrate is spin-coated with PMMA to form a 300 nm thick film. Acetone is used to remove any PMMA on the back side of the Cu foil. The PMMA/graphene/Cu foil stack is placed in a solution of 3:1 deionized water to APS (ammonium persulfate, Transene Cu Etchant APS-100) and ultrasonicated to remove any graphene on the backside of the Cu foil. The stack is placed in the solution for ~12 hr for the Cu foil to fully etch. The PMMA/graphene membrane is removed from the etching solution and placed in three H_2O baths before being transferred onto Ge(001). The PMMA/graphene/Ge(001) is spin-dried for 4 min at 4000 rpm before being baked on a hot plate (in an N_2 environment with < 1 ppm of H_2O and < 1 ppm of O_2) at 150 °C for 10 min. Finally, the sample is submerged in acetone at 110 °C for 20 min to remove PMMA before rinsing in IPA. Scanning electron microscopy (SEM, Zeiss LEO 1530) is used to confirm the transfer of hexagonal crystals of graphene onto the Ge(001) wafers.

***Fabrication of the array of graphene seeds*:** The hexagonal crystals of graphene are patterned into arrays of circular seeds on Ge(001). Ni etch masks with diameters of 20–55 nm are fabricated by depositing PMMA electron-beam resist, performing electron-beam lithography, developing the pattern, depositing 10 nm of Ni into the exposed pattern, and conducting lift-off to remove residual material. The exposed graphene (not under the Ni etch mask) is removed by exposure to an O_2 plasma (50 W, 10 mTorr, 10 sccm of O_2) for 15 s (Unaxis 790 Reactive Ion

Etcher). The Ni etch mask is etched in dilute aqua regia (3:1:2 by volume of 37% HCl: 70% HNO_3:H_2O) for 3 min, resulting in arrays of circular graphene seeds on Ge(001). The samples are characterized throughout the process by SEM to confirm the Ni etch mask diameter and the angle between the armchair edge of the graphene hexagon with respect to the Ge[110] direction (measured in ImageJ).

Graphene nanoribbon growth via CVD: The arrays of graphene seeds on Ge(001) are loaded into a horizontal quartz tube furnace. The system is evacuated to ~10^{-6} torr. Next, the system is filled to atmospheric pressure with a mixture of 200 sccm of Ar and 100 sccm of H_2. The substrate is annealed at 910 °C for 45–67.5 min to remove surface contamination and etch the graphene seeds. After the anneal step, graphene nanoribbon growth is initiated by introducing a flow of 2.0 sccm of CH_4 (99.99% purity). The furnace is then slid away from the substrates, and the samples are rapidly cooled to terminate growth. Growth proceeds for 6 hr (unless otherwise stated). The ribbon arrays are then characterized using SEM, and the ribbon dimensions are measured using ImageJ. The armchair orientation of the graphene lattice with respect to Ge⟨110⟩ is random and differs for each hexagonally shaped crystal of graphene that is transferred from Cu to Ge. High-aspect ratio nanoribbons evolve from seeds only when an armchair orientation and the closest Ge[110] direction are aligned.[315] Analysis is therefore limited only to seeds aligned within 5° of the Ge[110] direction in which high aspect ratio ribbons evolve. Analysis in Fig. 9.2 is moreover limited to seed arrays in which the nanoribbon yield is > 50% to avoid analysis of over-etched arrays in which d_s is poorly defined.

I.2 Control growth of graphene nanoribbons without seeds

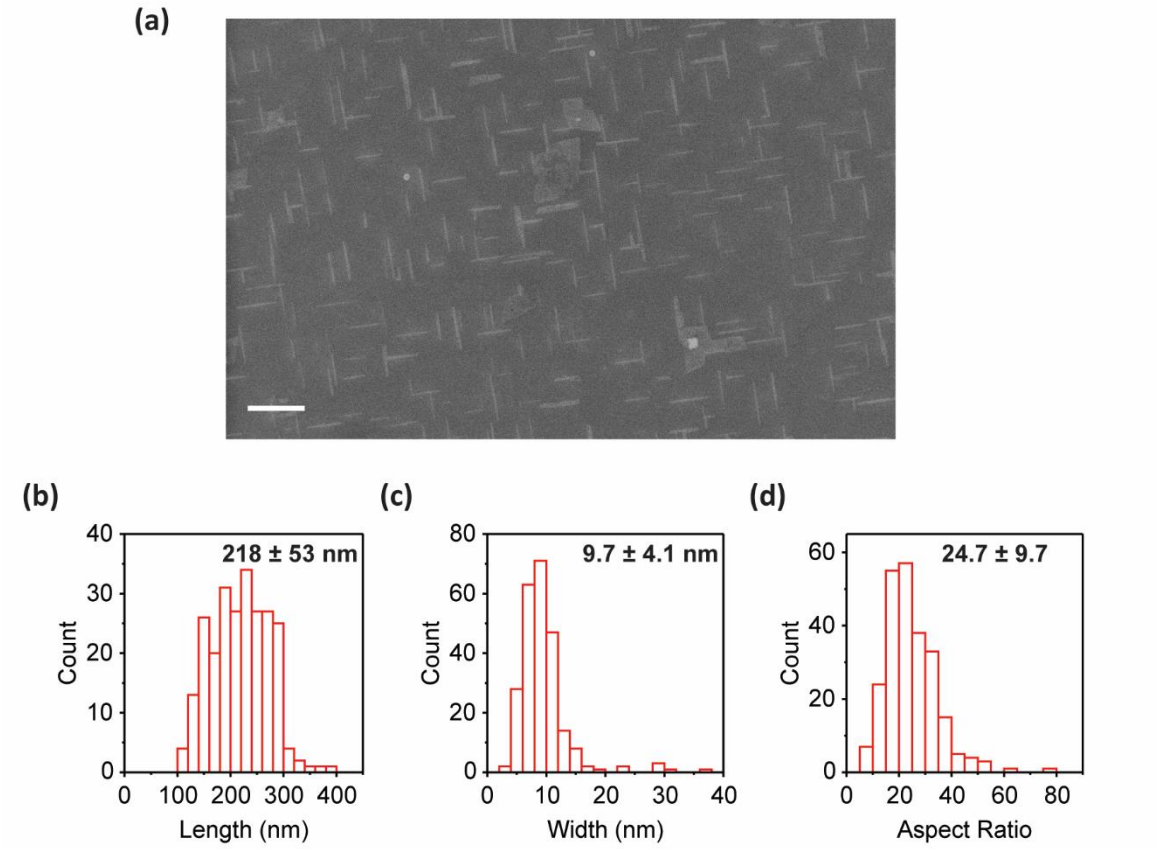

Figure I.1: (a) SEM image of graphene nanoribbons grown without seeds under 200 sccm of Ar, 100 sccm of H_2, and 2.0 sccm of CH_4, with a 20 min pre-growth anneal and 6 hr growth time. **(b-d)** Histograms of ribbon lengths, widths, and aspect ratios with averages stated. Scale bar is 400 nm.

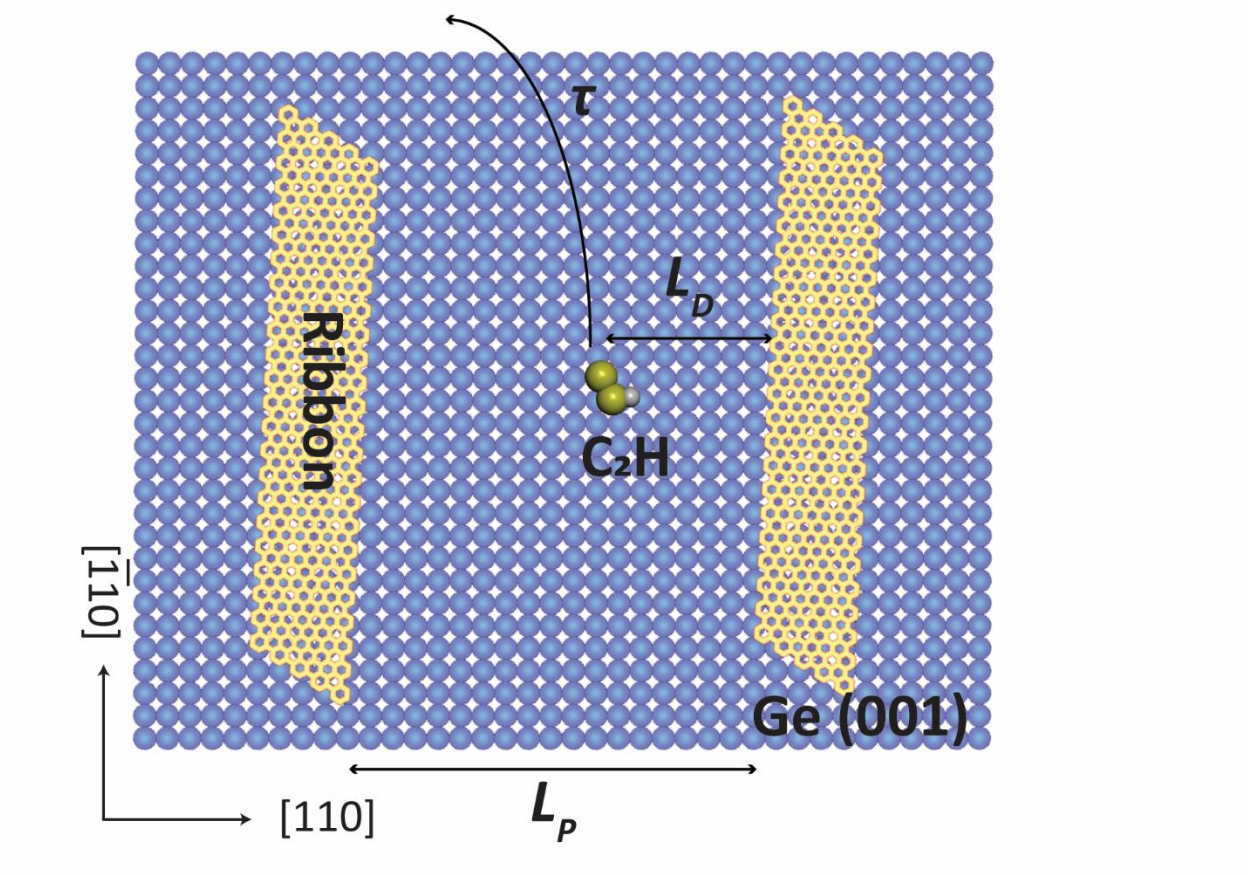

Figure I.2: Schematic of two graphene nanoribbons on Ge(001) with a pitch of L_P. The C_2H represents a potential growth species on the surface that has the capability of traveling a diffusion length, L_D, with an effective surface lifetime of τ until desorption from the surface.

I.3 Discussion of diffusion equation

One of the main goals of this work is to estimate the influence of nanoribbon pitch on growth kinetics. To derive an analytical expression for the reduction of growth kinetics with crowding effects, we choose a model system where parallel nanoribbons are aligned in the *y* direction. To represent this system, we choose periodic boundary conditions in the *x* direction, with a box width of L_P and the ribbon placed at $L_P/2$. Furthermore, we assume that the width of the graphene ribbons is negligible compared to the pitch and can be approximated as 0. A schematic of the system is shown in Fig. I.2. For this system, we need to solve the steady-state one-dimensional diffusion equation:

$$D\frac{\partial^2 C}{\partial x^2} + k[CH4] - \frac{C}{\tau} = 0 \tag{I.1}$$

where D is the diffusion constant of the growth species, k is the conversion rate of methane to the growth species, $[CH4]$ is the concentration of methane, and τ is the lifetime of the growth species on the surface. Equation (I.1) can be solved for concentration with an ansatz in the form of:

$$C(x) = Ae^{\frac{x}{L_D}} + Be^{-\frac{x}{L_D}} + k\tau\,[CH4];\ \sqrt{D\tau} = L_D \tag{I.2}$$

where L_D is the hydrocarbon intermediate diffusion length. Using equation (I.2) and the following boundary conditions:

$$\frac{dC}{dx}(x = 0) = 0 \tag{I.3}$$

$$\frac{dC}{dx}\left(x = \frac{L_P}{2}\right) = -\frac{h}{D}\left(C\left(\frac{L_P}{2}\right) - C_0\right) = \frac{-R_w}{D} \tag{I.4}$$

where L_P is the nanoribbon pitch, h is the rate at which the concentration of growth species at the edge of a ribbon converts into graphene, C_0 is the equilibrium concentration, and R_w is the growth rate in the width direction. We assume that the concentration gradient halfway between two ribbons (*i.e.*, at $x = 0$) is zero due to symmetry (I.3) and the reduction in concentration at a ribbon edge corresponds to the growth rate of the ribbon (I.4). We are able to solve for the concentration as:

$$C(x) = \frac{C_o - k\tau[CH_4]\left(e^{\frac{x}{L_D}} + e^{-\frac{x}{L_D}}\right)}{\left[\left(1 + \frac{D}{L_D h}\right)e^{\frac{L_P}{2L_D}} + \left(1 - \frac{D}{L_D h}\right)e^{-\frac{L_P}{2L_D}}\right]} + k\tau[CH_4] \tag{I.5}$$

The derivative of this expression with respect to x is the growth rate along the width direction, R_w, as a function of pitch, L_P, where:

$$R_w(L_P) = \frac{\frac{D}{L_D} C_0 S \left(1 - e^{-\frac{L_P}{L_D}}\right)}{\left(1 + \frac{D}{L_D h}\right) + \left(1 - \frac{D}{L_D h}\right) e^{-\frac{L_P}{L_D}}} \tag{I.6}$$

where S is a supersaturation term defined as:

$$S = -\frac{C_o - k\tau[CH_4]}{C_o} \tag{I.7}$$

By taking the limit of R_w (6) when L_P approaches infinity, we get the following expression:

$$R_w(\infty) = \frac{\frac{D}{L_D} C_0 S}{\left(1 + \frac{D}{L_D h}\right)} \tag{I.8}$$

Using equation (I.8), we can simplify equation (I.6) to the following:

$$R_w(L) = R_{w,\infty} \cdot \frac{\left(1 - e^{-\frac{L_P}{L_D}}\right)}{1 + \left(\frac{1 - \frac{D}{L_D h}}{1 + \frac{D}{L_D h}}\right) e^{-\frac{L_P}{L_D}}} \tag{I.9}$$

where the term to the right of $R_{w,\infty}$ is the reduction coefficient. Taking the limits of the reduction term in equation (I.9) for when nanoribbon growth kinetics are limited by diffusion of hydrocarbon intermediates (*i.e.*, h is large) (I.10) and when nanoribbon growth depends only on the attachment barrier (*i.e.*, D is large) (I.11) gives limits of the reduction term.

$$\text{Diffusion-limited reduction} = \frac{1-e^{-\frac{L_P}{L_D}}}{1+e^{-\frac{L_P}{L_D}}} \tag{I.10}$$

$$\text{Attachment-limited reduction} = \frac{1-e^{-\frac{L_P}{L_D}}}{1-e^{-\frac{L_P}{L_D}}} = 1 \tag{I.11}$$

I.4 Computational modeling details

All density functional theory (DFT) calculations reported in this work are performed using the Vienna *Ab Initio* Simulation Package (VASP),[4,5] a plane wave code using periodic boundary conditions and PAW pseudopotentials.[6,7] Exchange correlation interactions are modeled using the generalized gradient approximation (GGA) utilizing the Perdew, Burk, and Ernzerhof (PBE) parameterization[8]. van der Waals forces are modeled with DFT-D2 dispersion corrections.[257] The electron wave functions are expanded with a plane-wave basis and a kinetic energy cutoff of 400 eV. The surface of the Brillouin zone is sampled using a 4 × 4 × 1 Monkhorst-Pack k-point mesh.[122]

All calculations are performed on a slab model with an optimized bulk Ge lattice constant of 5.67 Å (see Fig. I.3), which compares well to the experimental value of 5.66 Å.[123] The Ge(001) unit cell is modeled with a (4×4) supercell containing 8 Ge layers, where the top 4 layers are relaxed and the bottom 4 layers are fixed at the bulk lattice constant and terminated with hydrogen. A dipole correction to the electrostatic potential is included in the *z* direction[124]. Periodic images in the *z* direction are separated by ~14 Å of vacuum.

Pre-factors are calculated as:

$$A = \frac{k_B T}{h} \exp\left(\frac{\Delta S^{\ddagger}}{k_B}\right) \tag{I.12}$$

where k_B is the Boltzmann constant, T is the temperature of the growth, h is Planck's constant and $\Delta S^{\ddagger}$ is the difference in entropy between the transition state and initial state. Entropy contributions

from translation, vibration, and rotation of surface adsorbates are calculated by assuming each species behaves as a quantum harmonic oscillator. The vibrational frequencies from these oscillations are calculated with a numerical differentiation of forces using a second-order finite difference approach, determined from the diagonalization of a mass-weighted Hessian matrix.

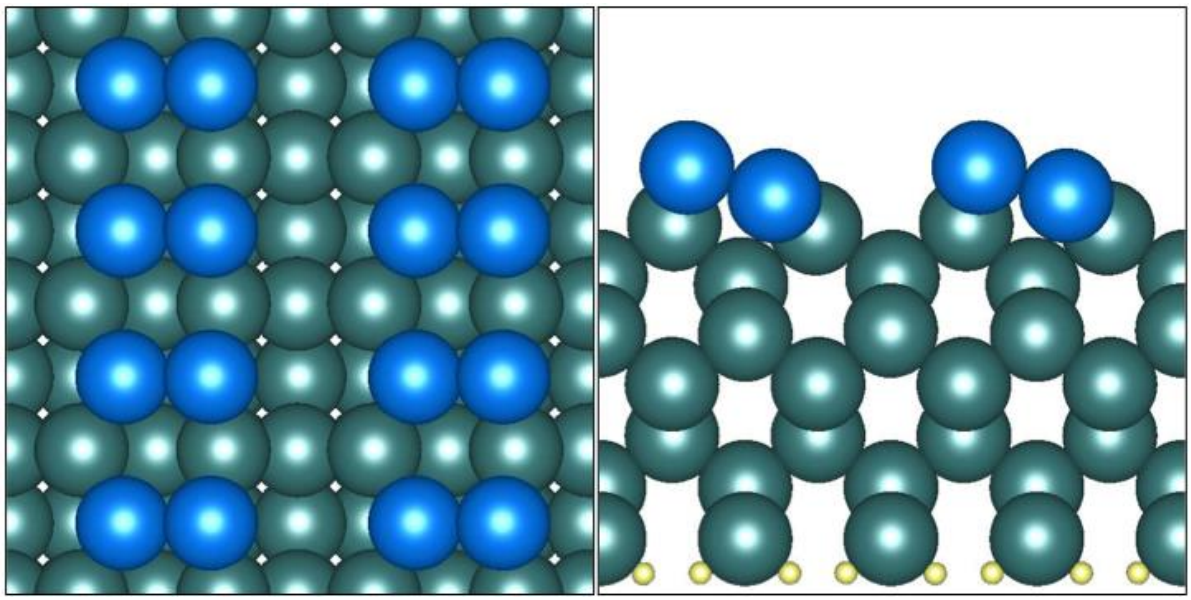

Figure I.3: Representation of the Ge slab model used in the DFT calculations. The surface shows a 2x1 dimer reconstruction. The bottom of the slab is terminated by H atoms. Ge atoms are represented in green (bulk) and blue (under-coordinated dimers). H atoms are shown in yellow.

Table I.1: Pre-factors (A_D), diffusion barriers (E_D) and diffusion coefficients (D) parallel and perpendicular to the dimer rows on the Ge(001) surface.

	$A_D^{\parallel}$ [s^{-1}]	$E_D^{\parallel}$ [eV]	$D^{\parallel}$ [Å^2 s^{-1}]	$A_D^{\perp}$ [s^{-1}]	$E_D^{\perp}$ [eV]	$D^{\perp}$[Å^2 s^{-1}]
CH_2CH_2	2.46×10^{13}	1.38	1.58×10^{8}	5.81×10^{12}	1.13	4.17×10^{8}
CH_2CH	2.98×10^{11}	1.68	1.05×10^{5}	3.94×10^{12}	1.81	3.94×10^{5}
CH_2C	2.46×10^{13}	1.57	2.51×10^{7}	2.46×10^{13}	1.54	3.36×10^{7}
CHCH	2.46×10^{13}	2.16	8.35×10^{4}	2.46×10^{13}	2.09	1.64×10^{5}
CHC	5.02×10^{11}	1.49	1.11×10^{6}	7.24×10^{12}	0.95	2.96×10^{9}
CC	2.46×10^{13}	0.97	8.31×10^{9}	2.46×10^{13}	2.03	2.94×10^{5}

Table I.2: Pre-factors (A) and activation energies (E_a) for forward (f) and backward (b) reactions in the reaction network shown in Fig. 9.4b in the main text.

	A_a^f [s^{-1}]	E_a^f [eV]	A_a^b [s^{-1}]	E_a^b [eV]
CH_2CH_2→CH_2CH + H	8.72×10^{11}	2.06	6.13×10^{12}	1.55
CH_2CH→CH_2C + H	2.18×10^{12}	2.45	2.46×10^{13}	1.89
CH_2CH→CHCH + H	3.39×10^{12}	2.18	2.46×10^{13}	2.1
CH_2C→CHC + H	2.60×10^{12}	1.1	2.31×10^{12}	0.77
CHCH→CHC + H	1.65×10^{13}	1.9	1.57×10^{13}	1.1
CHC→CC + H	2.55×10^{11}	2.35	1.92×10^{13}	2.01
CHCH→CHCH (g)	2.46×10^{13}	1.96	-	-
CH_2CH_2→CH_2CH_2 (g)	2.46×10^{13}	1.65	-	-

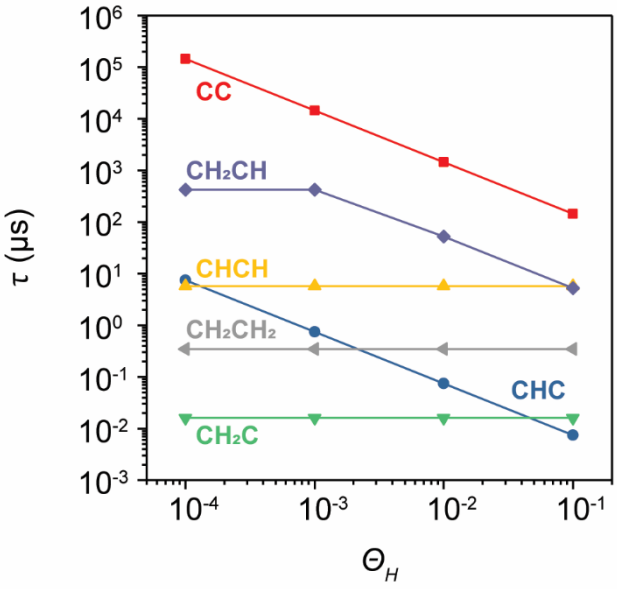

Figure I.4: H-coverage- (Θ_H) dependent upper bounds for the lifetimes, τ, of the different C_2H_x species. Values for τ were calculated as described in the main text. The red line corresponds to CC, the blue line to CHC, the yellow line to CHCH, the green line to CH_2C, the purple line to CH_2CH, and the grey line to CH_2CH_2, respectively.

Appendix: J Supplementary Materials for 'Characterizing How Graphene Nanoribbons Interact with Ge(001) Through First-Principles Calculations and Monte Carlo Simulations'

J.1 Zig-Zag Edges

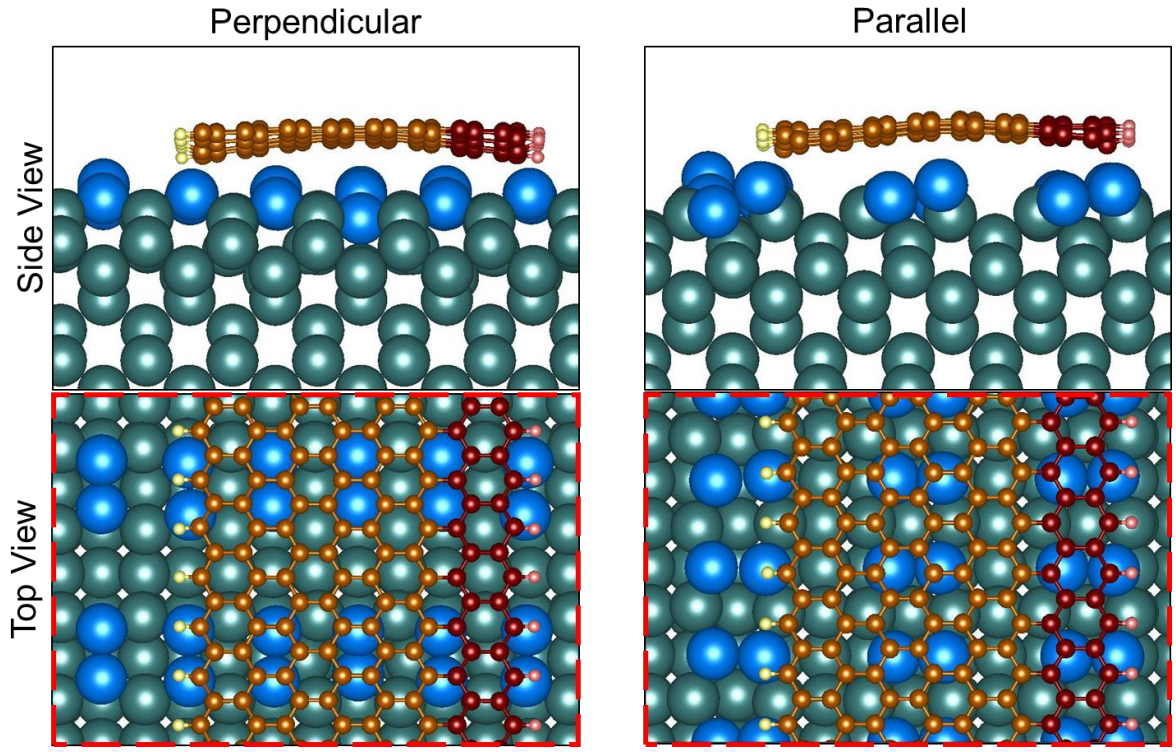

Figure J.1: Top and side views of zig-zag graphene nanoribbons on the Ge(001) surfaces. The nanoribbons are aligned perpendicular and parallel to buckled-dimer rows of Ge atoms on the surface. Red boxes indicate the smallest repeating unit of graphene along the edge. Relaxed C atoms are shown in brown, fixed C atoms are shown in dark red, relaxed H atoms are shown in yellow, fixed H atoms are shown in pink, Ge surface dimer atoms are shown in blue, and Ge bulk atoms are shown in green. Fixed portions of the GNRs are representative of the bulk of graphene.

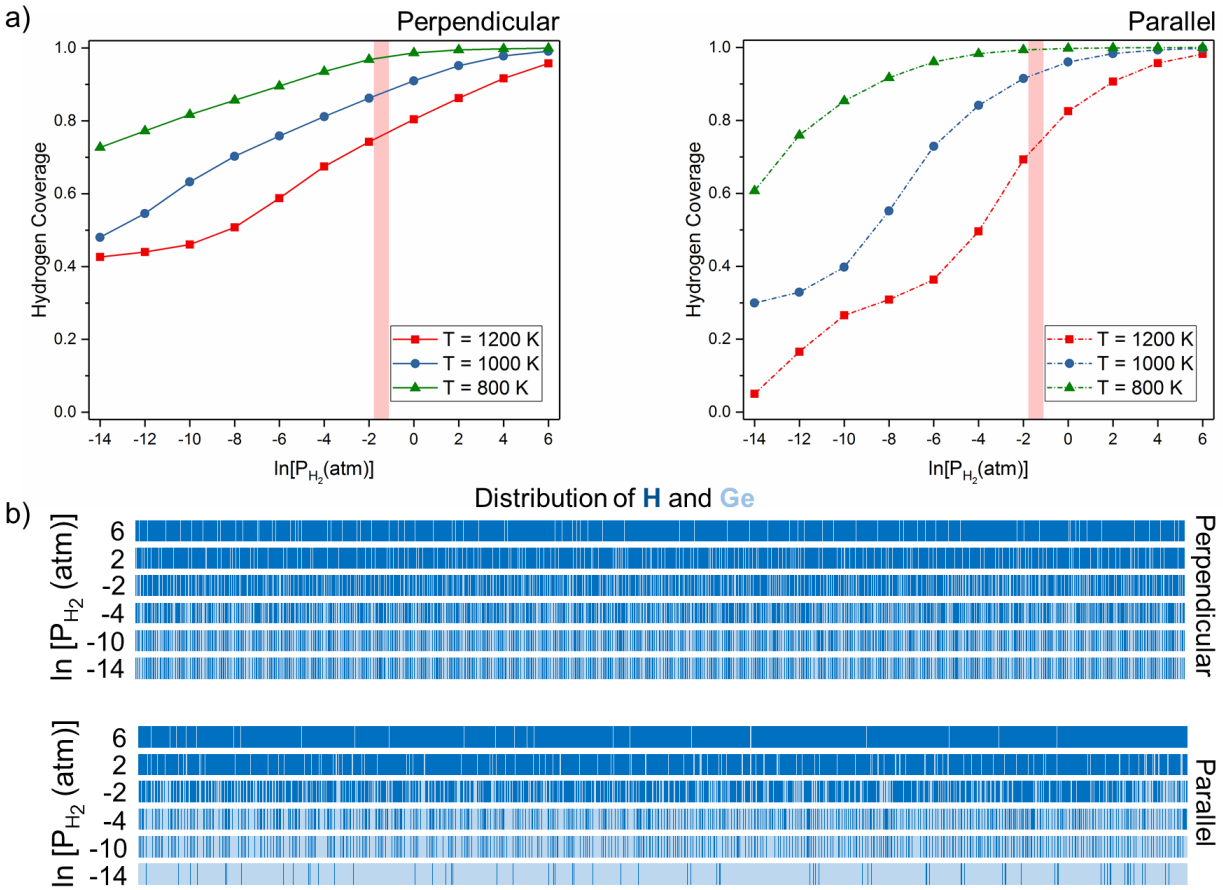

Figure J.2: (a) Hydrogen coverage on perpendicular and parallel zig-zig edges as a function of gas-phase hydrogen pressure and temperature. The red bar indicates typical growth conditions for GNRs. **(b)** The distribution of H or Ge passivated sites of edge vector $\vec{N}$ for perpendicular and parallel armchair edges at T = 1200 K for several H_2 pressures. H passivated sites are in dark blue and Ge passivated sites are in light blue.

J.2 Energies of Edge Structures

Table J.1: Relative energy of edge structures for armchair edges running parallel to Ge dimer rows on Ge(001). All energies reported relative to the energy of an edge unit with no hydrogen. Representative structure for unit cell is shown in Fig. 10.4c. The edge structure indicates the position of H on edge of the graphene unit cell, where H indicates an adsorbed hydrogen and x indicates an unsaturated site starting from the top-most edge site shown in Fig. 10.4c.

Structure Code	# of H/Unit Cell	Structure	Relative Energy (eV)
A	2	H H	-9.05
B	1	H x	-4.34
C	0	x x	0.00

Table J.2: Relative energy of edge structures for armchair edges running perpendicular to Ge dimer rows on Ge(001). All energies reported relative to the energy of an edge unit with no hydrogen. Representative structure for unit cell is shown in Fig. 10.4d. The edge structure indicates the position of H on edge of the graphene unit cell, where H indicates an adsorbed hydrogen and x indicates an unsaturated site starting from the top-most edge site shown in Fig. 10.4d**.**

Structure Code	# of H/Unit Cell	Structure	Relative Energy (eV)
A	4	H H H H	-19.78
B1	3	H H H x	-14.76
B2	3	H H x H	-15.84
B3	3	H x H H	-15.86
B4	3	x H H H	-14.59
C1	2	x H H x	-11.35
C2	2	H x x H	-11.68
D1	2	H H x x	-9.97
D2	2	x x H H	-9.97
E1	2	H x H x	-10.71
E2	2	x H x H	-10.54
F1	1	H x x x	-5.79
F2	1	x H x x	-4.53
F3	1	x x H x	-4.73
F4	1	x x x H	-5.76
G	0	x x x x	0.00

Table J.3: Relative energy of edge structures for zig-zag edges running parallel to Ge dimer rows on Ge(001). All energies reported relative to the energy of an edge unit with no hydrogen. Representative structure for unit cell is shown in Fig. J.1c. The edge structure indicates the position of H on edge of the graphene unit cell, where H indicates an adsorbed hydrogen and x indicates an unsaturated site starting from the top-most edge site shown in Fig. J.1c.

Structure Code	# of H/Unit Cell	Structure	Relative Energy (eV)
A	7	H H H H H H H	-31.68
B1	6	H H H H H H x	-27.37
B2	6	H H H H H x H	-27.33
B3	6	H H H H x H H	-26.94
B4	6	H H H x H H H	-27.20
B5	6	H H x H H H H	-25.94
B6	6	H x H H H H H	-27.45
B7	6	x H H H H H H	-26.83
C1	5	H H H H H x x	-23.10
C2	5	H H H H x x H	-21.78
C3	5	H H H x x H H	-22.71
C4	5	H H x x H H H	-21.93
C5	5	H x x H H H H	-22.13
C6	5	x x H H H H H	-22.63
C7	5	x H H H H H x	-21.70
D1	5	H H H H x H x	-22.42
D2	5	H H H x H x H	-22.96
D3	5	H H x H x H H	-21.52
D4	5	H x H x H H H	-23.01
D5	5	x H x H H H H	-21.34
D6	5	H x H H H H x	-23.00
D7	5	x H H H H x H	-22.41
E1	5	H H H x H H x	-22.93
E2	5	H H x H H x H	-21.63
E3	5	H x H H x H H	-22.55
E4	5	x H H x H H H	-22.56
E5	5	H H x H H H x	-21.55
E6	5	H x H H H x H	-22.89
E7	5	x H H H x H H	-21.45
F1	4	H H H H x x x	-17.62
F2	4	H H H x x x H	-17.64
F3	4	H H x x x H H	-17.77
F4	4	H x x x H H H	-18.25
F5	4	x x x H H H H	-17.67
F6	4	x x H H H H x	-17.29
F7	4	x H H H H x x	-17.38
G1	4	H H H x H x x	-18.72
G2	4	H H x H x x H	-16.28
G3	4	H x H x x H H	-18.29
G4	4	x H x x H H H	-17.62
G5	4	H x x H H H x	-17.75
G6	4	x x H H H x H	-18.20
G7	4	x H H H x H x	-16.68
G8	4	H H H x x H x	-17.62
G9	4	H H x x H x H	-18.29
G10	4	H x x H x H H	-16.28
G11	4	x x H x H H H	-18.72
G12	4	x H x H H H x	-16.68
G13	4	H x H H H x x	-18.20

Structure Code	# of H/Unit Cell	Structure	Relative Energy (eV)
G14	4	x H H H x x H	-17.75
H1	4	H H x H H x x	-17.32
H2	4	H x H H x x H	-17.35
H3	4	x H H x x H H	-17.20
H4	4	H H x x H H x	-17.98
H5	4	H x x H H x H	-18.00
H6	4	x x H H x H H	-17.16
H7	4	x H H x H H x	-17.27
I1	4	H H x H x H x	-16.92
I2	4	H x H x H x H	-18.47
I3	4	x H x H x H H	-16.22
I4	4	H x H x H H x	-18.52
I5	4	x H x H H x H	-17.14
I6	4	H x H H x H x	-18.14
I7	4	x H H x H x H	-18.15
J1	3	H H H x x x x	-13.49
J2	3	H H x x x x H	-12.56
J3	3	H x x x x H H	-13.96
J4	3	x x x x H H H	-13.71
J5	3	x x x H H H x	-12.35
J6	3	x x H H H x x	-13.16
J7	3	x H H H x x x	-12.04
K1	3	H H x H x x x	-12.23
K2	3	H x H x x x H	-13.18
K3	3	x H x x x H H	-12.35
K4	3	H x x x H H x	-13.70
K5	3	x x x H H x H	-13.32
K6	3	x x H H x H x	-12.24
K7	3	x H H x H x x	-13.11
K8	3	H H x x x H x	-12.35
K9	3	H x x x H x H	-13.18
K10	3	x x x H x H H	-12.23
K11	3	x x H x H H x	-13.11
K12	3	x H x H H x x	-12.24
K13	3	H x H H x x x	-13.32
K14	3	x H H x x x H	-13.70
L1	3	H H x x H x x	-13.60
L2	3	H x x H x x H	-12.63
L3	3	x x H x x H H	-12.82
L4	3	x H x x H H x	-12.13
L5	3	H x x H H x x	-13.47
L6	3	x x H H x x H	-12.40
L7	3	x H H x x H x	-12.47
M1	3	H x H x H x x	-14.31
M2	3	x H x H x x H	-11.51
M3	3	H x H x x H x	-13.84
M4	3	x H x x H x H	-13.28
M5	3	H x x H x H x	-13.22
M6	3	x x H x H x H	-13.84
M7	3	x H x H x H x	-11.29
N1	2	H H x x x x x	-8.55
N2	2	H x x x x x H	-8.64
N3	2	x x x x x H H	-8.29
N4	2	x x x x H H x	-8.66
N5	2	x x x H H x x	-8.20
N6	2	x x H H x x x	-7.51

Structure Code	# of H/Unit Cell	Structure	Relative Energy (eV)
N7	2	x H H x x x x	-8.76
O1	2	H x H x x x x	-9.13
O2	2	x H x x x x H	-7.64
O3	2	H x x x x H x	-9.26
O4	2	x x x x H x H	-9.29
O5	2	x x x H x H x	-7.36
O6	2	x x H x H x x	-8.79
O7	2	x H x H x x x	-6.92
P1	2	H x x x H x x	-9.80
P2	2	x x x H x x H	-7.54
P3	2	x x H x x H x	-7.93
P4	2	x H x x H x x	-8.61
P5	2	H x x H x x x	-8.61
P6	2	x x H x x x H	-7.94
P7	2	x H x x x H x	-7.52
Q1	1	H x x x x x x	-4.47
Q2	1	x H x x x x x	-4.24
Q3	1	x x H x x x x	-4.57
Q4	1	x x x H x x x	-2.60
Q5	1	x x x x H x x	-4.68
Q6	1	x x x x x H x	-3.37
Q7	1	x x x x x x H	-3.63
R	0	x x x x x x x	0.00

Table J.4: Relative energy of edge structures for zig-zag edges running perpendicular to Ge dimer rows on Ge(001). All energies reported relative to the energy of an edge unit with no hydrogen. Representative structure for unit cell is shown in Fig. J.1d. The edge structure indicates the position of H on edge of the graphene unit cell, where H indicates an adsorbed hydrogen and x indicates an unsaturated site starting from the top-most edge site shown in Fig. J.1d.

Structure Code	# of H/Unit Cell	Structure	Relative Energy (eV)
A	7	H H H H H H H	-33.67
B1	6	H H H H H H x	-27.38
B2	6	H H H H H x H	-29.46
B3	6	H H H H x H H	-29.58
B4	6	H H H x H H H	-27.54
B5	6	H H x H H H H	-29.30
B6	6	H x H H H H H	-29.20
B7	6	x H H H H H H	-28.54
C1	5	H H H H H x x	-23.45
C2	5	H H H H x x H	-25.00
C3	5	H H H x x H H	-23.41
C4	5	H H x x H H H	-23.72
C5	5	H x x H H H H	-24.86
C6	5	x x H H H H H	-23.61
C7	5	x H H H H H x	-23.12
D1	5	H H H H x H x	-23.23
D2	5	H H H x H x H	-23.27
D3	5	H H x H x H H	-25.24
D4	5	H x H x H H H	-23.54
D5	5	x H x H H H H	-23.88
D6	5	H x H H H H x	-23.82
D7	5	x H H H H x H	-24.56
E1	5	H H H x H H x	-21.19
E2	5	H H x H H x H	-25.15
E3	5	H x H H x H H	-25.16
E4	5	x H H x H H H	-22.43
E5	5	H H x H H H x	-23.75
E6	5	H x H H H x H	-25.06
E7	5	x H H H x H H	-24.52
F1	4	H H H H x x x	-18.81
F2	4	H H H x x x H	-18.86
F3	4	H H x x x H H	-19.12
F4	4	H x x x H H H	-19.27
F5	4	x x x H H H H	-19.08
F6	4	x x H H H H x	-18.41
F7	4	x H H H H x x	-18.81
G1	4	H H H x H x x	-17.92
G2	4	H H x H x x H	-20.70
G3	4	H x H x x H H	-19.31
G4	4	x H x x H H H	-16.99
G5	4	H x x H H H x	-20.14
G6	4	x x H H H x H	-19.27
G7	4	x H H H x H x	-18.42
G8	4	H H H x x H x	-16.99
G9	4	H H x x H x H	-19.31
G10	4	H x x H x H H	-20.70
G11	4	x x H x H H H	-17.92
G12	4	x H x H H H x	-18.42
G13	4	H x H H H x x	-19.27

Structure Code	# of H/Unit Cell	Structure	Relative Energy (eV)
G14	4	x H H H x x H	-20.14
H1	4	H H x H H x x	-19.23
H2	4	H x H H x x H	-20.62
H3	4	x H H x x H H	-18.34
H4	4	H H x x H H x	-17.39
H5	4	H x x H H x H	-20.63
H6	4	x x H H x H H	-19.57
H7	4	x H H x H H x	-16.90
I1	4	H H x H x H x	-18.89
I2	4	H x H x H x H	-18.92
I3	4	x H x H x H H	-19.86
I4	4	H x H x H H x	-17.63
I5	4	x H x H H x H	-19.90
I6	4	H x H H x H x	-19.31
I7	4	x H H x H x H	-18.36
J1	3	H H H x x x x	-12.67
J2	3	H H x x x x H	-14.61
J3	3	H x x x x H H	-14.65
J4	3	x x x x H H H	-13.53
J5	3	x x x H H H x	-13.83
J6	3	x x H H H x x	-13.87
J7	3	x H H H x x x	-14.12
K1	3	H H x H x x x	-15.00
K2	3	H x H x x x H	-14.54
K3	3	x H x x x H H	-12.69
K4	3	H x x x H H x	-13.97
K5	3	x x x H H x H	-14.69
K6	3	x x H H x H x	-14.09
K7	3	x H H x H x x	-12.09
K8	3	H H x x x H x	-12.69
K9	3	H x x x H x H	-14.54
K10	3	x x x H x H H	-15.00
K11	3	x x H x H H x	-12.09
K12	3	x H x H H x x	-14.09
K13	3	H x H H x x x	-14.69
K14	3	x H H x x x H	-13.97
L1	3	H H x x H x x	-14.63
L2	3	H x x H x x H	-16.14
L3	3	x x H x x H H	-13.35
L4	3	x H x x H H x	-13.48
L5	3	H x x H H x x	-14.82
L6	3	x x H H x x H	-15.15
L7	3	x H H x x H x	-14.03
M1	3	H x H x H x x	-14.50
M2	3	x H x H x x H	-15.41
M3	3	H x H x x H x	-14.67
M4	3	x H x x H x H	-13.70
M5	3	H x x H x H x	-14.84
M6	3	x x H x H x H	-13.34
M7	3	x H x H x H x	-14.06
N1	2	H H x x x x x	-8.41
N2	2	H x x x x x H	-10.14
N3	2	x x x x x H H	-10.13
N4	2	x x x x H H x	-8.91
N5	2	x x x H H x x	-9.37
N6	2	x x H H x x x	-9.34

Structure Code	# of H/Unit Cell	Structure	Relative Energy (eV)
N7	2	x H H x x x x	-7.89
O1	2	H x H x x x x	-8.40
O2	2	x H x x x x H	-9.30
O3	2	H x x x x H x	-10.31
O4	2	x x x x H x H	-10.12
O5	2	x x x H x H x	-9.36
O6	2	x x H x H x x	-9.13
O7	2	x H x H x x x	-9.42
P1	2	H x x x H x x	-10.28
P2	2	x x x H x x H	-10.57
P3	2	x x H x x H x	-9.27
P4	2	x H x x H x x	-9.46
P5	2	H x x H x x x	-10.22
P6	2	x x H x x x H	-8.99
P7	2	x H x x x H x	-9.48
Q1	1	H x x x x x x	-3.97
Q2	1	x H x x x x x	-3.23
Q3	1	x x H x x x x	-4.79
Q4	1	x x x H x x x	-4.80
Q5	1	x x x x H x x	-4.38
Q6	1	x x x x x H x	-4.40
Q7	1	x x x x x x H	-5.77
R	0	x x x x x x x	0.00

J.3 Interaction Energies for AC Edges

Table J.5: Interaction energies between armchair edge units running parallel to Ge dimer rows on Ge(001). Structure codes are provided in Table J.1.

Interaction Energies (eV)			
	A	B	C
A	0.00	0.00	-0.16
B	0.00	0.00	0.02
C	-0.16	0.02	0.00

Table J.6: Interaction energies between armchair edge units running perpendicular to Ge dimer rows on Ge(001). Structure codes are provided in Table J.2.

Interaction Energies (eV)																
	A	B1	B2	B3	B4	C1	C2	D1	D2	E1	E2	F1	F2	F3	F4	G
A	0.00	-0.07	-0.04	-0.05	-0.12	0.39	-0.15	-0.05	-0.04	-0.06	-0.07	-0.13	-0.10	-0.07	-0.12	-0.03
B1	-0.07	0.00	-0.23	0.05	-0.75	-0.18	-0.11	-0.03	-0.72	-0.01	-0.58	-0.08	-1.20	-0.70	-0.78	-0.68
B2	-0.04	-0.23	0.00	0.05	0.00	0.51	0.00	-0.10	0.04	0.05	0.00	0.02	-0.06	0.02	0.00	-0.35
B3	-0.05	0.05	0.05	0.00	-0.05	1.05	-0.01	-0.05	-0.04	0.01	0.00	-0.02	-0.06	-0.04	0.01	-0.35
B4	-0.12	-0.75	0.00	-0.05	0.00	-0.23	-0.09	-0.11	-0.04	0.03	-0.03	-0.08	-0.97	0.03	-0.06	0.03
C1	0.39	-0.18	0.51	1.05	-0.23	0.00	1.02	-0.29	-0.14	0.12	0.13	-0.26	-0.59	-0.54	-0.11	-0.78
C2	-0.15	-0.11	0.00	-0.01	-0.09	1.02	0.00	-0.13	-0.03	0.00	-0.04	-0.01	-0.07	-0.02	-0.01	-0.39
D1	-0.05	-0.03	-0.10	-0.05	-0.11	-0.29	-0.13	0.00	0.00	-0.09	-0.11	-0.12	-0.14	-0.03	-0.04	0.03
D2	-0.04	-0.72	0.04	-0.04	-0.04	-0.14	-0.03	0.00	0.00	0.01	0.00	-0.05	-0.07	-0.02	0.00	0.00
E1	-0.06	-0.01	0.05	0.01	0.03	0.12	0.00	-0.09	0.01	0.00	0.07	-0.01	0.02	-0.01	0.01	-0.35
E2	-0.07	-0.58	0.00	0.00	-0.03	0.13	-0.04	-0.11	0.00	0.07	0.00	0.00	-0.01	0.04	-0.04	-0.37
F1	-0.13	-0.08	0.02	-0.02	-0.08	-0.26	-0.01	-0.12	-0.05	-0.01	0.00	0.00	-0.03	-0.07	-0.08	-0.02
F2	-0.10	-0.06	-0.06	-0.06	-0.97	-0.59	-0.07	-0.14	-0.07	0.02	-0.01	-0.03	0.00	-0.03	-0.11	-0.33
F3	-0.07	0.02	0.02	-0.04	0.03	-0.54	-0.02	-0.03	-0.02	-0.01	0.04	-0.07	-0.03	0.00	0.00	-0.86
F4	-0.12	0.00	0.00	0.01	-0.06	-0.11	-0.01	-0.04	0.00	0.01	-0.04	-0.08	-0.11	0.00	0.00	-0.01
G	-0.03	-0.35	-0.35	-0.35	0.03	-0.78	-0.39	0.03	0.00	-0.35	-0.37	-0.02	-0.33	-0.86	-0.01	0.00

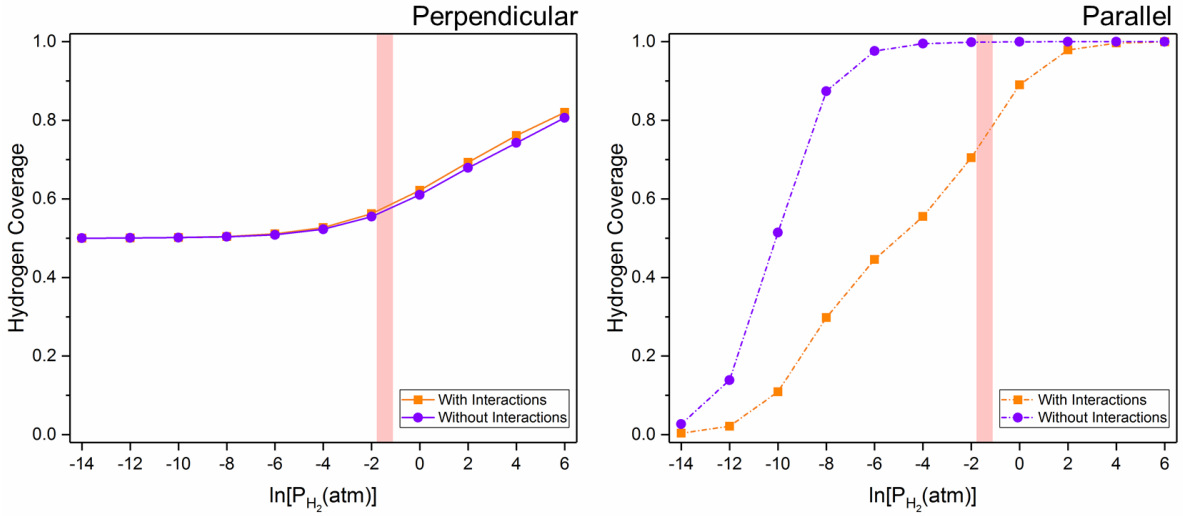

Figure S3: Dependence of hydrogen coverage on interaction energies for perpendicular and parallel armchair edges. Typical GNR growth conditions are indicated with a red bar. Simulations were performed at 1200 K.

J.4 Orientation Preference for AC and ZZ Edges

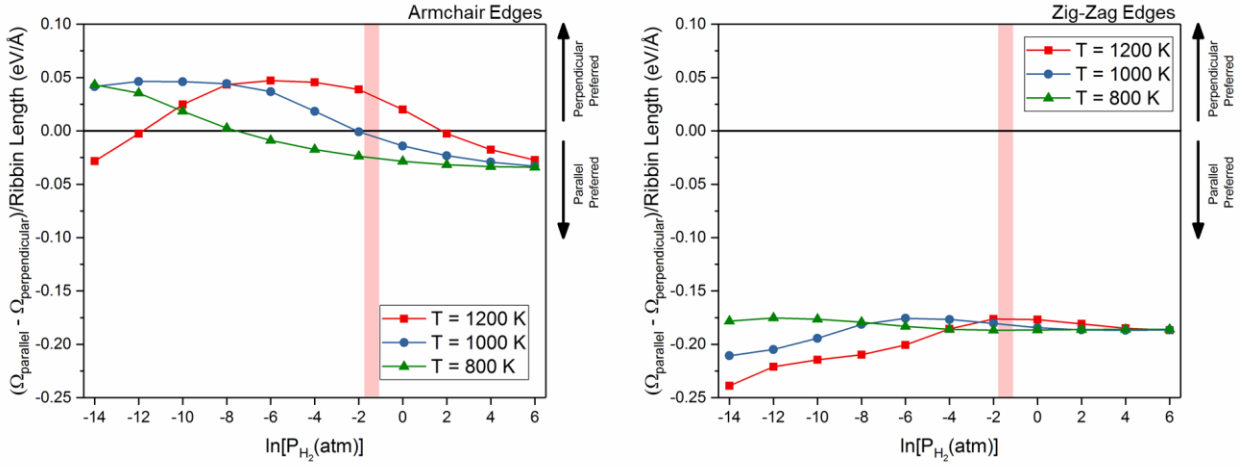

Figure SJ.3: Difference in grand potential for parallel and perpendicular edge alignment with dimer rows as a function of H_2 partial pressure at several temperatures for armchair edges and zig-zag edges. Typical GNR growth conditions are indicated with a red bar. Grand potentials are calculated using a CH_4 partial pressure of 6.7×10^{-3} atm, which is typical for GNR growth conditions.

Bibliography

1. Bligaard, T. *et al.* The Brønsted–Evans–Polanyi relation and the volcano curve in heterogeneous catalysis. *J. Catal.* **224**, 206–217 (2004).

2. Logadottir, A. *et al.* The Brønsted-Evans-Polanyi relation and the volcano plot for ammonia synthesis over transition metal catalysts. *J. Catal.* **197**, 229–231 (2001).

3. Nørskov, J. K. *et al.* The nature of the active site in heterogeneous metal catalysis. *Chem. Soc. Rev.* **37**, 2163–2171 (2008).

4. Mehmood, F., Rankin, R. B., Greeley, J. & Curtiss, L. A. Trends in methanol decomposition on transition metal alloy clusters from scaling and Bronsted-Evans-Polanyi relationships. *Phys. Chem. Chem. Phys.* **14**, 8644–8652 (2012).

5. Ferrin, P. *et al.* Modeling ethanol decomposition on transition metals: A combined application of scaling and brønsted-evans-polanyi relations. *J. Am. Chem. Soc.* **131**, 5809–5815 (2009).

6. Viswanathan, V., Hansen, H. A., Rossmeisl, J. & Nørskov, J. K. Universality in oxygen reduction electrocatalysis on metal surfaces. *ACS Catal.* **2**, 1654–1660 (2012).

7. Wang, S. *et al.* Universal Brønsted-Evans-Polanyi relations for C-C, C-O, C-N, N-O, N-N, and O-O dissociation reactions. *Catal. Letters* **141**, 370–373 (2011).

8. Wang, S. *et al.* Universal transition state scaling relations for (de)hydrogenation over transition metals. *Phys. Chem. Chem. Phys.* **13**, 20760–20765 (2011).

9. Studt, F. *et al.* Identification of non-precious metal alloy catalysts for selective hydrogenation of acetylene. *Science* **320**, 1320–1322 (2008).

10. Jones, G., Bligaard, T., Abild-Pedersen, F. & Nørskov, J. K. Using scaling relations to understand trends in the catalytic activity of transition metals. *J. Phys. Condens. Matter* **20**, 064239 (2008).

11. Abild-Pedersen, F. *et al.* Scaling properties of adsorption energies for hydrogen-containing molecules on transition-metal surfaces. *Phys. Rev. Lett.* **99**, 016105 (2007).

12. Greeley, J. & Nørskov, J. K. Combinatorial density functional theory-based screening of surface alloys for the oxygen reduction reaction. *J. Phys. Chem. C* **113**, 4932–4939 (2009).

13. Zhang, J. *et al.* Mixed-metal Pt monolayer electrocatalysts for enhanced oxygen reduction kinetics. *J. Am. Chem. Soc.* **127**, 12480–12481 (2005).

14. Zhang, J., Vukmirovic, M. B., Xu, Y., Mavrikakis, M. & Adzic, R. R. Controlling the

catalytic activity of platinum-monolayer electrocatalysts for oxygen reduction with different substrates. *Angew. Chemie - Int. Ed.* **44**, 2132–2135 (2005).

15. Greeley, J. *et al.* Alloys of platinum and early transition metals as oxygen reduction electrocatalysts. *Nat. Chem.* **1**, 552–556 (2009).

16. Stamenkovic, V. *et al.* Changing the Activity of Electrocatalysts for Oxygen Reduction by Tuning the Surface Electronic Structure. *Angew. Chemie Int. Ed.* **45**, 2897–2901 (2006).

17. Nørskov, J. K. *et al.* Origin of the Overpotential for Oxygen Reduction at a Fuel-Cell Cathode. *J. Phys. Chem. B* **108**, 17886–17892 (2004).

18. Greeley, J., Jaramillo, T. F., Bonde, J., Chorkendorff, I. B. & Nørskov, J. K. Computational high-throughput screening of electrocatalytic materials for hydrogen evolution. *Nat. Mater.* **5**, 909–13 (2006).

19. Greeley, J., Nørskov, J. K., Kibler, L. A., El-Aziz, A. M. & Kolb, D. M. Hydrogen evolution over bimetallic systems: Understanding the trends. *ChemPhysChem* **7**, 1032–1035 (2006).

20. Skúlason, E. *et al.* Modeling the Electrochemical Hydrogen Oxidation and Evolution Reactions on the Basis of Density Functional Theory Calculations. *J. Phys. Chem. C* **114**, 18182–18197 (2010).

21. Grabow, L. C., Gokhale, A. A., Evans, S. T., Dumesic, J. A. & Mavrikakis, M. Mechanism of the water gas shift reaction on Pt: First principles, experiments, and microkinetic modeling. *J. Phys. Chem. C* **112**, 4608–4617 (2008).

22. Gokhale, A. A., Dumesic, J. A. & Mavrikakis, M. On the mechanism of low-temperature water gas shift reaction on copper. *J. Am. Chem. Soc.* **130**, 1402–1414 (2008).

23. Madon, R. J. *et al.* Microkinetic analysis and mechanism of the water gas shift reaction over copper catalysts. *J. Catal.* **281**, 1–11 (2011).

24. Honkala, K. *et al.* Ammonia synthesis from first-principles calculations. *Science* **307**, 555–558 (2005).

25. Hellman, A. *et al.* Predicting catalysis: Understanding ammonia synthesis from first-principles calculations. *J. Phys. Chem. B* **110**, 17719–17735 (2006).

26. Grabow, L. C. & Mavrikakis, M. Mechanism of Methanol Synthesis on Cu through CO2 and CO Hydrogenation. *ACS Catal.* **1**, 365–384 (2011).

27. Studt, F. *et al.* CO hydrogenation to methanol on Cu-Ni catalysts: Theory and experiment. *J. Catal.* **293**, 51–60 (2012).

28. Studt, F., Abild-Pedersen, F., Varley, J. B. & Nørskov, J. K. CO and CO2 hydrogenation to methanol calculated using the BEEF-vdW functional. *Catal. Letters* **143**, 71–73 (2013).

29. Medford, A. J. *et al.* Activity and selectivity trends in synthesis gas conversion to higher alcohols. *Top. Catal.* **57**, 135–142 (2014).

30. Cheng, J. *et al.* Chain growth mechanism in fischer-tropsch synthesis: A DFT study of C-C coupling over Ru, Fe, Rh, and Re surfaces. *J. Phys. Chem. C* **112**, 6082–6086 (2008).

31. Ojeda, M. *et al.* CO Activation Pathways and the Mechanism of Fischer-Tropsch Synthesis. *J. Catal.* **272**, 287–297 (2010).

32. Desai, M. & Camobreco, V. *Inventory of U.S. Greenhouse Gas Emissions and Sinks: 1990-2018*. (2020).

33. Spendelow, J. S. & Papageorgopoulos, D. C. Progress in PEMFC MEA component R&D at the DOE fuel cell technologies program. *Fuel Cells* **11**, 775–786 (2011).

34. Mulder, G., Coenen, P., Martens, A. & Spaepen, J. Market-ready Stationary 6 kW Generator with Alkaline Fuel Cells. *ECS Trans.* **12**, 743–753 (2019).

35. Wang, Y. *et al.* Synergistic Mn-Co catalyst outperforms Pt on high-rate oxygen reduction for alkaline polymer electrolyte fuel cells. *Nat. Commun.* **10**, 1–8 (2019).

36. Staszak-Jirkovský, J. *et al.* Water as a Promoter and Catalyst for Dioxygen Electrochemistry in Aqueous and Organic Media. *ACS Catal.* **5**, 6600–6607 (2015).

37. Ledezma-Yanez, I. *et al.* Interfacial water reorganization as a pH-dependent descriptor of the hydrogen evolution rate on platinum electrodes. *Nat. Energy* **2**, 17031 (2017).

38. Ferrin, P. & Mavrikakis, M. Structure Sensitivity of Methanol Electrooxidation on Transition Metals. *J. Am. Chem. Soc.* **131**, 14381–14389 (2009).

39. Rossmeisl, J. *et al.* Bifunctional anode catalysts for direct methanol fuel cells. *Energy Environ. Sci.* **5**, 8335 (2012).

40. Ferrin, P., Nilekar, A. U., Greeley, J., Mavrikakis, M. & Rossmeisl, J. Reactivity descriptors for direct methanol fuel cell anode catalysts. *Surf. Sci.* **602**, 3424–3431 (2008).

41. Guillén-Villafuerte, O. *et al.* Carbon monoxide and methanol oxidations on Pt/X@MoO3/C (X = Mo2C, MoO2, Mo0) electrodes at different temperatures. *J. Power Sources* **231**, 163–172 (2013).

42. Koenigsmann, C. & Wong, S. S. One-dimensional noble metal electrocatalysts: A promising structural paradigm for direct methanol fuel cells. *Energy Environ. Sci.* **4**, 1161–1176 (2011).

43. Krewer, U., Vidakovic-Koch, T. & Rihko-Struckmann, L. Electrochemical Oxidation of Carbon-Containing Fuels and Their Dynamics in Low-Temperature Fuel Cells. *ChemPhysChem* **12**, 2518–2544 (2011).

44. Wasmus, S. & Küver, A. Methanol oxidation and direct methanol fuel cells: A selective review. *Journal of Electroanalytical Chemistry* **461**, 14–31 (1999).

45. Song, S. & Tsiakaras, P. Recent progress in direct ethanol proton exchange membrane fuel cells (DE-PEMFCs). *Appl. Catal. B Environ.* **63**, 187–193 (2006).

46. Antolini, E. Catalysts for direct ethanol fuel cells. *Journal of Power Sources* **170**, 1–12 (2007).

47. Lamy, C., Rousseau, S., Belgsir, E. M., Coutanceau, C. & Léger, J. M. Recent progress in the direct ethanol fuel cell: Development of new platinum-tin electrocatalysts. in *Electrochimica Acta* **49**, 3901–3908 (Pergamon, 2004).

48. Rousseau, S., Coutanceau, C., Lamy, C. & Léger, J. M. Direct ethanol fuel cell (DEFC): Electrical performances and reaction products distribution under operating conditions with different platinum-based anodes. *J. Power Sources* **158**, 18–24 (2006).

49. Zhou, W. J. *et al.* Pt-based anode catalysts for direct ethanol fuel cells. in *Solid State Ionics* **175**, 797–803 (Elsevier, 2004).

50. Herron, J. A., Ferrin, P. & Mavrikakis, M. First-Principles Mechanistic Analysis of Dimethyl Ether Electro-Oxidation on Monometallic Single-Crystal Surfaces. *J. Phys. Chem. C* **118**, 24199–24211 (2014).

51. Herron, J. A., Ferrin, P. & Mavrikakis, M. On the Structure Sensitivity of Dimethyl Ether Electro-oxidation on Eight FCC Metals: A First-Principles Study. *Top. Catal.* **58**, 1159–1173 (2015).

52. Roling, L. T., Herron, J. A., Budiman, W., Ferrin, P. & Mavrikakis, M. Dimethyl ether electro-oxidation on platinum surfaces. *Nano Energy* **29**, 428–438 (2016).

53. Zhang, Z., Wang, Y. & Wang, X. Nanoporous bimetallic Pt–Au alloy nanocomposites with superior catalytic activity towards electro-oxidation of methanol and formic acid. *Nanoscale* **3**, 1663 (2011).

54. Zhang, S. *et al.* Graphene Decorated with PtAu Alloy Nanoparticles: Facile Synthesis and Promising Application for Formic Acid Oxidation. *Chem. Mater.* **23**, 1079–1081 (2011).

55. Chandrani Roychowdhury, Futoshi Matsumoto, Paul F. Mutolo, Héctor D. Abruña, A. & DiSalvo, F. J. Synthesis, Characterization, and Electrocatalytic Activity of PtBi Nanoparticles Prepared by the Polyol Process. *Chem. Mater.* **17**, 5871–5876 (2005).

56. Roychowdhury, C. *et al.* Synthesis, Characterization, and Electrocatalytic Activity of PtBi and PtPb Nanoparticles Prepared by Borohydride Reduction in Methanol. *Chem. Mater.* **18**, 3365–3372 (2006).

57. Maiyalagan, T., Wang, X. & Manthiram, A. Highly active Pd and Pd–Au nanoparticles

supported on functionalized graphene nanoplatelets for enhanced formic acid oxidation. *RSC Adv.* **4**, 4028–4033 (2014).

58. Hu, S. *et al.* Carbon supported Pd-based bimetallic and trimetallic catalyst for formic acid electrochemical oxidation. *Appl. Catal. B Environ.* **180**, 758–765 (2016).

59. Du, C., Chen, M., Wang, W. & Yin, G. Nanoporous PdNi Alloy Nanowires As Highly Active Catalysts for the Electro-Oxidation of Formic Acid. *ACS Appl. Mater. Interfaces* **3**, 105–109 (2011).

60. Stamenkovic, V. R. *et al.* Trends in electrocatalysis on extended and nanoscale Pt-bimetallic alloy surfaces. *Nat. Mater.* **6**, 241–247 (2007).

61. Liu, Z., Zhang, X. & Tay, S. W. Nanostructured PdRu/C catalysts for formic acid oxidation. *J. Solid State Electrochem.* **16**, 545–550 (2012).

62. Castro Neto, A. H., Guinea, F., Peres, N. M. R., Novoselov, K. S. & Geim, A. K. The electronic properties of graphene. *Rev. Mod. Phys.* **81**, 109–162 (2009).

63. Novoselov, K. S. *et al.* Electric Field Effect in Atomically Thin Carbon Films. *Science* **306**, (2004).

64. Geim, A. K. & Novoselov, K. S. The rise of graphene. *Nat. Mater.* **6**, 183–191 (2007).

65. Novoselov, K. S. *et al.* Two-dimensional gas of massless Dirac fermions in graphene. *Nature* **438**, 197–200 (2005).

66. Fang, T., Konar, A., Xing, H. & Jena, D. Mobility in semiconducting graphene nanoribbons: Phonon, impurity, and edge roughness scattering. *Phys. Rev. B* **78**, 205403 (2008).

67. Yan, Q. *et al.* Intrinsic current-voltage characteristics of graphene nanoribbon transistors and effect of edge doping. *Nano Lett.* **7**, 1469– 1473 (2007).

68. Liang, G., Neophytou, N., Nikonov, D. E. & Lundstrom, M. S. Performance projections for ballistic graphene nanoribbon field-effect transistors. *IEEE Trans. Electron Devices* **54**, 677–682 (2007).

69. Ouyang, Y., Yoon, Y., Fodor, J. K. & Guo, J. Comparison of performance limits for carbon nanoribbon and carbon nanotube transistors. *Appl. Phys. Lett.* **89**, 203107 (2006).

70. Yang, L., Park, C.-H., Son, Y.-W., Cohen, M. L. & Louie, S. G. Quasiparticle Energies and Band Gaps in Graphene Nanoribbons. *Phys. Rev. Lett.* **99**, 186801 (2007).

71. Son, Y.-W., Cohen, M. L. & Louie, S. G. Energy Gaps in Graphene Nanoribbons. *Phys. Rev. Lett.* **97**, 216803 (2006).

72. Jacobberger, R. M. *et al.* Direct oriented growth of armchair graphene nanoribbons on

germanium. *Nat. Commun.* **6**, 8006 (2015).

73. Chen, L., Hernandez, Y., Feng, X. & Müllen, K. From Nanographene and Graphene Nanoribbons to Graphene Sheets: Chemical Synthesis. *Angew. Chemie Int. Ed.* **51**, 7640–7654 (2012).

74. Kiraly, B. *et al.* Sub-5 nm, globally aligned graphene nanoribbons on Ge(001). *Appl. Phys. Lett.* **108**, 213101 (2016).

75. Jacobberger, R. M. & Arnold, M. S. High-Performance Charge Transport in Semiconducting Armchair Graphene Nanoribbons Grown Directly on Germanium. *ACS Nano* **11**, 8924–8929 (2017).

76. Kiraly, B. *et al.* Electronic and Mechanical Properties of Graphene-Germanium Interfaces Grown by Chemical Vapor Deposition. *Nano Lett.* **15**, 7414–20 (2015).

77. White, J. A., Bird, D. M., Payne, M. C. & Stich, I. Surface corrugation in the dissociative adsorption of H2 on Cu(100). *Phys. Rev. Lett.* **73**, 1404–1407 (1994).

78. Perdew, J. P. & Wang, Y. Accurate and simple analytic representation of the electron-gas correlation energy. *Phys. Rev. B* **45**, 13244–13249 (1992).

79. Perdew, J. P., Burke, K. & Ernzerhof, M. Generalized Gradient Approximation Made Simple. *Phys. Rev. Lett.* **77**, 3865–3868 (1996).

80. Hammer, B., Hansen, L. B. & Nørskov, J. K. Improved adsorption energetics within density-functional theory using revised Perdew-Burke-Ernzerhof functionals. *Phys. Rev. B* **59**, 7413–7421 (1999).

81. Kresse, G. & Furthmüller, J. Efficient iterative schemes for ab initio total-energy calculations using a plane-wave basis set. *Phys. Rev. B* **54**, 11169–11186 (1996).

82. Kresse, G. & Furthmüller, J. Efficiency of ab-initio total energy calculations for metals and semiconductors using a plane-wave basis set. *Comput. Mater. Sci.* **6**, 15–50 (1996).

83. Gokhale, A. A., Kandoi, S., Greeley, J. P., Mavrikakis, M. & Dumesic, J. A. Molecular-level descriptions of surface chemistry in kinetic models using density functional theory. *Chem. Eng. Sci.* **59**, 4679–4691 (2004).

84. Henkelman, G., Uberuaga, B. P. & Jónsson, H. A climbing image nudged elastic band method for finding saddle points and minimum energy paths. *J. Chem. Phys.* **113**, 9901–9904 (2000).

85. Filhol, J.-S. & Neurock, M. Elucidation of the Electrochemical Activation of Water over Pd by First Principles. *Angew. Chemie Int. Ed.* **45**, 402–406 (2006).

86. Taylor, C. D., Wasileski, S. A., Filhol, J.-S. & Neurock, M. First principles reaction

modeling of the electrochemical interface: Consideration and calculation of a tunable surface potential from atomic and electronic structure. *Phys. Rev. B* **73**, 165402 (2006).

87. Trasatti, S. Structure of the metal/electrolyte solution interface: new data for theory. *Electrochim. Acta* **36**, 1659–1667 (1991).

88. Li, C.-Y. *et al.* In situ probing electrified interfacial water structures at atomically flat surfaces. *Nat. Mater.* **18**, 697–701 (2019).

89. Carrasco, J., Hodgson, A. & Michaelides, A. A molecular perspective of water at metal interfaces. *Nat. Mater.* **11**, 667–674 (2012).

90. Velasco-Velez, J. J. *et al.* The structure of interfacial water on gold electrodes studied by x-ray absorption spectroscopy. *Science* **346**, 831–834 (2014).

91. Scatena, L. F., Brown, M. G. & Richmond, G. L. Water at hydrophobic surfaces: Weak hydrogen bonding and strong orientation effects. *Science* **292**, 908–912 (2001).

92. Guo, J. *et al.* Real-space imaging of interfacial water with submolecular resolution. *Nat. Mater.* **13**, 184–189 (2014).

93. Dubouis, N. *et al.* Tuning water reduction through controlled nanoconfinement within an organic liquid matrix. *Nat. Catal.* **3**, 656–663 (2020).

94. Tong, Y., Lapointe, F., Thämer, M., Wolf, M. & Campen, R. K. Hydrophobic Water Probed Experimentally at the Gold Electrode/Aqueous Interface. *Angew. Chemie Int. Ed.* **56**, 4211–4214 (2017).

95. Strmcnik, D. *et al.* The role of non-covalent interactions in electrocatalytic fuel-cell reactions on platinum. *Nat. Chem.* **1**, 466–472 (2009).

96. Casalongue, H. S. *et al.* Direct observation of the oxygenated species during oxygen reduction on a platinum fuel cell cathode. *Nat. Commun.* **4**, 2817 (2013).

97. Herron, J. A., Morikawa, Y. & Mavrikakis, M. Ab initio molecular dynamics of solvation effects on reactivity at electrified interfaces. *Proc. Natl. Acad. Sci.* **113**, E4937-45 (2016).

98. Wang, X. *et al.* Palladium–platinum core-shell icosahedra with substantially enhanced activity and durability towards oxygen reduction. *Nat. Commun.* **6**, 7594 (2015).

99. Wang, D. *et al.* Spontaneous incorporation of gold in palladium-based ternary nanoparticles makes durable electrocatalysts for oxygen reduction reaction. *Nat. Commun.* **7**, 11941-1–9 (2016).

100. Yang, Y. *et al.* Combinatorial Studies of Palladium-Based Oxygen Reduction Electrocatalysts for Alkaline Fuel Cells. *J. Am. Chem. Soc.* **142**, 3980–3988 (2020).

101. Wang, D. *et al.* Structurally ordered intermetallic platinum-cobalt core-shell nanoparticles with enhanced activity and stability as oxygen reduction electrocatalysts. *Nat. Mater.* **12**, 81–87 (2013).

102. Lopes, P. P. *et al.* Eliminating dissolution of platinum-based electrocatalysts at the atomic scale. *Nat. Mater.* **19**, 1207–1214 (2020).

103. Zhang, L. *et al.* Platinum-based nanocages with subnanometer-thick walls and well-defined, controllable facets. *Science* **349**, 412–6 (2015).

104. Zhu, J. *et al.* Facet-controlled Pt–Ir nanocrystals with substantially enhanced activity and durability towards oxygen reduction. *Mater. Today* **35**, 69–77 (2020).

105. Hammer, B. & Norskov, J. K. Why gold is the noblest of all the metals. *Nature* **376**, 238–240 (1995).

106. Markovic, N. M., Tidswell, I. M. & Ross, P. N. Oxygen and hydrogen peroxide reduction on the gold(100) surface in alkaline electrolyte: the roles of surface structure and hydroxide adsorption. *Langmuir* **10**, 1–4 (1994).

107. Stamenkovic, V. R., Strmcnik, D., Lopes, P. P. & Markovic, N. M. Energy and fuels from electrochemical interfaces. *Nat. Mater.* **16**, 57–69 (2017).

108. Duan, Z. & Henkelman, G. Theoretical Resolution of the Exceptional Oxygen Reduction Activity of Au(100) in Alkaline Media. *ACS Catal.* **9**, 5567−5573 (2019).

109. Kelly, S. R., Kirk, C., Chan, K. & Nørskov, J. K. Electric Field Effects in Oxygen Reduction Kinetics: Rationalizing pH Dependence at the Pt(111), Au(111), and Au(100) Electrodes. *J. Phys. Chem. C* **124**, 14581–14591 (2020).

110. Edens, G. J., Gao, X., Weaver, M. J., Markovic, N. M. & Ross, P. N. Influence of adsorbed hydroxyl and carbon monoxide on potential-induced reconstruction of Au(100) as examined by scanning tunneling microscopy. *Surf. Sci.* **302**, L275–L282 (1994).

111. Gao, X., Hamelin, A. & Weaver, M. J. Potential-dependent reconstruction at ordered Au(100)-aqueous interfaces as probed by atomic-resolution scanning tunneling microscopy. *Phys. Rev. Lett.* **67**, 618–621 (1991).

112. Blizanac, B. B., Lucas, C. A., Gallagher, M. E., Ross, P. N. & Marković, N. M. Surface Structures and Phase Transitions at the Au(100)−Br Interface: pH and CO Effects. *J. Phys. Chem. B* **108**, 5304–5313 (2004).

113. Feng, Y. J., Bohnen, K. P. & Chan, C. T. First-principles studies of Au(100)-hex reconstruction in an electrochemical environment. *Phys. Rev. B* **72**, 125401 (2005).

114. Mavrikakis, M., Hammer, B. & Nørskov, J. K. Effect of strain on the reactivity of metal surfaces. *Phys. Rev. Lett.* **81**, 2819–2822 (1998).

115. Chung, D. Y. *et al.* Dynamic stability of active sites in hydr(oxy)oxides for the oxygen evolution reaction. *Nat. Energy* **5**, 222–230 (2020).

116. Yang, F. *et al.* Bismuthene for highly efficient carbon dioxide electroreduction reaction. *Nat. Commun.* **11**, 1088 (2020).

117. Xu, H., Cheng, D., Cao, D. & Zeng, X. C. A universal principle for a rational design of single-atom electrocatalysts. *Nat. Catal.* **1**, 339–348 (2018).

118. Liu, Y. *et al.* Self-optimizing, highly surface-active layered metal dichalcogenide catalysts for hydrogen evolution. *Nat. Energy* **2**, 17127 (2017).

119. Grimme, S., Antony, J., Ehrlich, S. & Krieg, H. A consistent and accurate *ab initio* parametrization of density functional dispersion correction (DFT-D) for the 94 elements H-Pu. *J. Chem. Phys.* **132**, 154104 (2010).

120. Blöchl, P. E. Projector augmented-wave method. *Phys. Rev. B* **50**, 17953–17979 (1994).

121. Kresse, G. & Joubert, D. From ultrasoft pseudopotentials to the projector augmented-wave method. *Phys. Rev. B* **59**, 1758–1775 (1999).

122. Monkhorst, H. J. & Pack, J. D. Special points for Brillouin-zone integrations. *Phys. Rev. B* **13**, 5188–5192 (1976).

123. Lide, D. R. *CRC Handbook of Chemistry and Physics*. (CRC Press, 2006).

124. Bengtsson, L. Dipole correction for surface supercell calculations. *Phys. Rev. B* **59**, 12301–12304 (1999).

125. Mathew, K. *et al.* Implicit solvation model for density-functional study of nanocrystal surfaces and reaction pathways. *J. Chem. Phys.* **140**, 084106 (2013).

126. Strmcnik, D. *et al.* Effects of Li+, K+, and Ba2+ cations on the ORR at model and high surface area Pt and Au surfaces in alkaline solutions. *J. Phys. Chem. Lett.* **2**, 2733–2736 (2011).

127. Adić, R. R., Marković, N. M. & Vešović, V. B. Structural effects in electrocatalysis: Oxygen reduction on the Au (100) single crystal electrode. *J. Electroanal. Chem. Interfacial Electrochem.* **165**, 105–120 (1984).

128. Marković, N. M., Adić, R. R. & Vešović, V. B. Structural effects in electrocatalysis: Oxygen reduction on the gold single crystal electrodes with (110) and (111) orientations. *J. Electroanal. Chem.* **165**, 121–133 (1984).

129. Nosé, S. A unified formulation of the constant temperature molecular dynamics methods. *J. Chem. Phys.* **81**, 511–519 (1984).

130. Hoover, W. G. Canonical dynamics: Equilibrium phase-space distributions. *Phys. Rev. A* **31**, 1695–1697 (1985).

131. Marković, N. M., Schmidt, T. J., Stamenković, V. & Ross, P. N. Oxygen Reduction Reaction on Pt and Pt Bimetallic Surfaces: A Selective Review. *Fuel Cells* **1**, 105–116 (2001).

132. Schmidt, T. J., Stamenkovic, V., Ross, P. N. & Markovic, N. M. Temperature dependent surface electrochemistry on Pt single crystals in alkaline electrolyte: Part 3. The oxygen reduction reaction. *Phys. Chem. Chem. Phys.* **5**, 400–406 (2003).

133. Toney, M. F. *et al.* Voltage-dependent ordering of water molecules at an electrode–electrolyte interface. *Nature* **368**, 444–446 (1994).

134. Mei, D., He, Z. Da, Zheng, Y. L., Jiang, D. C. & Chen, Y. X. Mechanistic and kinetic implications on the ORR on a Au(100) electrode: PH, temperature and H-D kinetic isotope effects. *Phys. Chem. Chem. Phys.* **16**, 13762–13773 (2014).

135. Le, J., Cuesta, A. & Cheng, J. The structure of metal-water interface at the potential of zero charge from density functional theory-based molecular dynamics. *J. Electroanal. Chem.* **819**, 87–94 (2018).

136. Luzar, A. & Chandler, D. Hydrogen-bond kinetics in liquid water. *Nature* **379**, 55–57 (1996).

137. Thiel, P. A., Hoffmann, F. M. & Weinberg, W. H. Monolayer and multilayer adsorption of water on Ru(001). *J. Chem. Phys.* **75**, 5556–5572 (1981).

138. Doering, D. L. & Madey, T. E. The adsorption of water on clean and oxygen-dosed Ru(011). *Surf. Sci.* **123**, 305–337 (1982).

139. Mitsui, T., Rose, M. K., Fomin, E., Ogletree, D. F. & Salmeron, M. Water diffusion and clustering on Pd(111). *Science* **297**, 1850–1852 (2002).

140. Morgenstern, K. & Nieminen, J. Intermolecular bond length of ice on Ag(111). *Phys. Rev. Lett.* **88**, 066102 (2002).

141. Morgenstern, K. & Rieder, K. H. Formation of the cyclic ice hexamer via excitation of vibrational molecular modes by the scanning tunneling microscope. *J. Chem. Phys.* **116**, 5746 (2002).

142. Schnur, S. & Groß, A. Properties of metal-water interfaces studied from first principles. *New J. Phys.* **11**, 125003 (2009).

143. Tonigold, K. & Groß, A. Dispersive interactions in water bilayers at metallic surfaces: A comparison of the PBE and RPBE functional including semiempirical dispersion corrections. *J. Comput. Chem.* **33**, 695–701 (2012).

144. Hodgson, A. & Haq, S. Water adsorption and the wetting of metal surfaces. *Surf. Sci. Rep.* **64**, 381–451 (2009).

145. Carrasco, J., Hodgson, A. & Michaelides, A. A molecular perspective of water at metal interfaces. *Nat. Mater.* **11**, 667–674 (2012).

146. Tripkovic, V., Björketun, M. E., Skúlason, E. & Rossmeisl, J. Standard hydrogen electrode and potential of zero charge in density functional calculations. *Phys. Rev. B* **84**, 115452 (2011).

147. Held, G. & Menzel, D. The structure of the p($\sqrt{3} \times \sqrt{3}$)R30° bilayer of D2O on Ru(001). *Surf. Sci.* **316**, 92–102 (1994).

148. Feibelman, P. J. Partial dissociation of water on Ru(0001). *Science* **295**, 99–102 (2002).

149. Ogasawara, H. *et al.* Structure and Bonding of Water on Pt(111). *Phys. Rev. Lett.* **89**, 276102 (2002).

150. Nie, S., Feibelman, P. J., Bartelt, N. C. & Thürmer, K. Pentagons and heptagons in the first water layer on Pt(111). *Phys. Rev. Lett.* **105**, 026102 (2010).

151. Feibelman, P. J., Bartelt, N. C., Nie, S. & Thürmer, K. Interpretation of high-resolution images of the best-bound wetting layers on Pt(111). *J. Chem. Phys.* **133**, 154703 (2010).

152. Habib, M. A. & Bockris, J. M. Potential-Dependent Water Orientation: An in Situ Spectroscopic Study. *Langmuir* **2**, 388–392 (1986).

153. Bewick, A. & Kunimatsu, K. Infra red spectroscopy of the electrode-electrolyte interphase. *Surf. Sci.* **101**, 131–138 (1980).

154. Bewick, A. & Russell, J. W. Structural investigation by infra-red spectroscopy of adsorbed hydrogen on platinum. *J. Electroanal. Chem. Interfacial Electrochem.* **132**, 329–344 (1982).

155. Nihonyanagi, S. *et al.* Potential-dependent structure of the interfacial water on the gold electrode. *Surf. Sci.* **573**, 11–16 (2004).

156. Schultz, Z. D., Shaw, S. K. & Gewirth, A. A. Potential dependent organization of water at the electrified metal-liquid interface. *J. Am. Chem. Soc.* **127**, 15916–15922 (2005).

157. Zheng, W. & Tadjeddine, A. Adsorption processes and structure of water molecules on Pt(110) electrodes in perchloric solutions. *J. Chem. Phys.* **119**, 13096 (2003).

158. Baldelli, S., Mailhot, G., Ross, P. N. & Somorjai, G. A. Potential-dependent vibrational spectroscopy of solvent molecules at the Pt(111) electrode in a water/acetonitrile mixture studied by sum frequency generation. *J. Am. Chem. Soc.* **123**, 7697–7702 (2001).

159. Ataka, K. I., Yotsuyanagi, T. & Osawa, M. Potential-dependent reorientation of water molecules at an electrode/electrolyte interface studied by surface-enhanced infrared absorption spectroscopy. *J. Phys. Chem.* **100**, 10664–10672 (1996).

160. Osawa, M., Tsushima, M., Mogami, H., Samjeské, G. & Yamakata, A. Structure of water at the electrified platinum-water interface: A study by surface-enhanced infrared absorption spectroscopy. *J. Phys. Chem. C* **112**, 4248–4256 (2008).

161. Lucas, C. A., Thompson, P., Gründer, Y. & Markovic, N. M. The structure of the electrochemical double layer: Ag(111) in alkaline electrolyte. *Electrochem. Commun.* **13**, 1205–1208 (2011).

162. Gründer, Y. *et al.* Structure and electrocompression of chloride adlayers on Cu(111). *Surf. Sci.* **605**, 1732–1737 (2011).

163. Escudero-Escribano, M. *et al.* Cyanide-modified Pt(1 1 1): Structure, stability and hydrogen adsorption. *Electrochim. Acta* **82**, 524–533 (2012).

164. Escudero-Escribano, M., Wildi, C., Mwanda, J. A. & Cuesta, A. Metallization of cyanide-modified Pt(111) electrodes with copper. *J. Solid State Electrochem.* **20**, 1087–1094 (2016).

165. Sakong, S., Forster-Tonigold, K. & Groß, A. The structure of water at a Pt(111) electrode and the potential of zero charge studied from first principles. *J. Chem. Phys.* **144**, 194701 (2016).

166. Sakong, S. & Groß, A. Water structures on a Pt(111) electrode from ab initio molecular dynamic simulations for a variety of electrochemical conditions. *Phys. Chem. Chem. Phys.* **22**, 10431–10437 (2020).

167. Hansen, H. A., Rossmeisl, J. & Nørskov, J. K. Surface Pourbaix diagrams and oxygen reduction activity of Pt, Ag and Ni(111) surfaces studied by DFT. *Phys. Chem. Chem. Phys.* **10**, 3722–3730 (2008).

168. Zheng, J., Sheng, W., Zhuang, Z., Xu, B. & Yan, Y. Universal dependence of hydrogen oxidation and evolution reaction activity of platinum-group metals on pH and hydrogen binding energy. *Sci. Adv.* **2**, e1501602 (2016).

169. Shevchuk, R., Agmon, N. & Rao, F. Network analysis of proton transfer in liquid water. *J. Chem. Phys.* **140**, 244502 (2014).

170. Stamenkovic, V. R. *et al.* Improved oxygen reduction activity on Pt3Ni(111) via increased surface site availability. *Science* **315**, 493–497 (2007).

171. Rees, N. V. & Compton, R. G. Sustainable energy: a review of formic acid electrochemical fuel cells. *J. Solid State Electrochem.* **15**, 2095–2100 (2011).

172. Kunze, J. & Stimming, U. Electrochemical Versus Heat-Engine Energy Technology: A

Tribute to Wilhelm Ostwald's Visionary Statements. *Angew. Chemie Int. Ed.* **48**, 9230–9237 (2009).

173. Herron, J. A., Ferrin, P. & Mavrikakis, M. Electrocatalytic Oxidation of Ammonia on Transition-Metal Surfaces: A First-Principles Study. *J. Phys. Chem. C* **119**, 14692–14701 (2015).

174. Elnabawy, A. O., Herron, J. A., Scaranto, J. & Mavrikakis, M. Structure Sensitivity of Formic Acid Electrooxidation on Transition Metal Surfaces: A First-Principles Study. *J. Electrochem. Soc.* **165**, J3109–J3121 (2018).

175. Demirci, U. B. Direct liquid-feed fuel cells: Thermodynamic and environmental concerns. *J. Power Sources* **169**, 239–246 (2007).

176. Demirci, U. B. Theoretical means for searching bimetallic alloys as anode electrocatalysts for direct liquid-feed fuel cells. *J. Power Sources* **173**, 11–18 (2007).

177. Moret, S., Dyson, P. J. & Laurenczy, G. Direct synthesis of formic acid from carbon dioxide by hydrogenation in acidic media. *Nat. Commun.* **5**, 4017 (2014).

178. Bozell, J. J. & Petersen, G. R. Technology development for the production of biobased products from biorefinery carbohydrates—the US Department of Energy's "Top 10" revisited. *Green Chem.* **12**, 539 (2010).

179. Xia, X. *et al.* Facile Synthesis of Palladium Right Bipyramids and Their Use as Seeds for Overgrowth and as Catalysts for Formic Acid Oxidation. *J. Am. Chem. Soc.* **135**, 15706–15709 (2013).

180. Singh, S. *et al.* Formic acid decomposition on Au catalysts: DFT, microkinetic modeling, and reaction kinetics experiments. *AIChE J.* **60**, 1303–1319 (2014).

181. Herron, J. A., Scaranto, J., Ferrin, P., Li, S. & Mavrikakis, M. Trends in Formic Acid Decomposition on Model Transition Metal Surfaces: A Density Functional Theory study. *ACS Catal.* **4**, 4434–4445 (2014).

182. Choi, S.-I. *et al.* A Comprehensive Study of Formic Acid Oxidation on Palladium Nanocrystals with Different Types of Facets and Twin Defects. *ChemCatChem* **7**, 2077–2084 (2015).

183. Li, S., Scaranto, J. & Mavrikakis, M. On the Structure Sensitivity of Formic Acid Decomposition on Cu Catalysts. *Top. Catal.* **59**, 1580–1588 (2016).

184. Schimmenti, R., Cortese, R., Duca, D. & Mavrikakis, M. Boron Nitride-supported Sub-nanometer Pd6 Clusters for Formic Acid Decomposition: A DFT Study. *ChemCatChem* **9**, 1610–1620 (2017).

185. Rhee, Y.-W., Ha, S. Y. & Masel, R. I. Crossover of formic acid through Nafion®

membranes. *J. Power Sources* **117**, 35–38 (2003).

186. Braden, D. J., Henao, C. A., Heltzel, J., Maravelias, C. C. & Dumesic, J. A. Production of liquid hydrocarbon fuels by catalytic conversion of biomass-derived levulinic acid. *Green Chem.* **13**, 1755 (2011).

187. Jiang, K., Zhang, H.-X., Zou, S. & Cai, W.-B. Electrocatalysis of formic acid on palladium and platinum surfaces: from fundamental mechanisms to fuel cell applications. *Phys. Chem. Chem. Phys.* **16**, 20360–20376 (2014).

188. Chen, W. & Chen, S. Iridium-platinum alloy nanoparticles: Composition-dependent electrocatalytic activity for formic acid oxidation. *J. Mater. Chem.* **25**, 9169–9178 (2011).

189. Neugebauer, J. & Scheffler, M. Adsorbate-substrate and adsorbate-adsorbate interactions of Na and K adlayers on Al(111). *Phys. Rev. B* **46**, 16067–16080 (1992).

190. Liang, Z. *et al.* Platinum and Palladium Monolayer Electrocatalysts for Formic Acid Oxidation. *Top. Catal.* **63**, 742–749 (2020).

191. Zhang, R., Liu, H., Wang, B. & Ling, L. Insights into the Preference of CO_2 Formation from HCOOH Decomposition on Pd Surface: A Theoretical Study. *J. Phys. Chem. C* **116**, 22266–22280 (2012).

192. Nørskov, J. K. *et al.* Universality in Heterogeneous Catalysis. *J. Catal.* **209**, 275–278 (2002).

193. Mortensen, J. J. *et al.* Bayesian error estimation in density-functional theory. *Phys. Rev. Lett.* **95**, 216401 (2005).

194. Roth, C., Benker, N., Theissmann, R., Nichols, R. J. & Schiffrin, D. J. Bifunctional Electrocatalysis in Pt−Ru Nanoparticle Systems. *Langmuir* **24**, 2191–2199 (2008).

195. Bao, J. *et al.* Composition-Dependent Electrocatalytic Activity of Palladium–Iridium Binary Alloy Nanoparticles Supported on the Multiwalled Carbon Nanotubes for the Electro-Oxidation of Formic Acid. *ACS Appl. Mater. Interfaces* **7**, 15223–15229 (2015).

196. Wu, D., Kusada, K. & Kitagawa, H. Recent progress in the structure control of Pd–Ru bimetallic nanomaterials. *Sci. Technol. Adv. Mater.* **17**, 583–596 (2016).

197. de Souza, J. P. I., Queiroz, S. L., Bergamaski, K., Gonzalez, E. R. & Nart, F. C. Electro-Oxidation of Ethanol on Pt, Rh, and PtRh Electrodes. A Study Using DEMS and in-Situ FTIR Techniques. *J. Phys. Chem. B* **106**, 9825–9830 (2002).

198. Ruban, A. V., Skriver, H. L. & Nørskov, J. K. Surface segregation energies in transition-metal alloys. *Phys. Rev. B* **59**, 15990–16000 (1999).

199. Hu, S. *et al.* Improving the electrochemical oxidation of formic acid by tuning the electronic

properties of Pd-based bimetallic nanoparticles. *Appl. Catal. B Environ.* **254**, 685–692 (2019).

200. Van Spronsen, M. A. *et al.* Dynamics of Surface Alloys: Rearrangement of Pd/Ag(111) Induced by CO and O2. *J. Phys. Chem. C* **123**, 8312–8323 (2019).

201. Ma, X. Y. *et al.* Electrocatalytic oxidation of ethanol and ethylene glycol on cubic, octahedral and rhombic dodecahedral palladium nanocrystals. *Chem. Commun.* **54**, 2562–2565 (2018).

202. Yu, J., Liu, G., Sumant, A. V., Goyal, V. & Balandin, A. A. Graphene-on-diamond devices with increased current-carrying capacity: Carbon sp 2-on-sp 3 technology. *Nano Lett.* **12**, 1603–1608 (2012).

203. Bae, M.-H. *et al.* Ballistic to diffusive crossover of heat flow in graphene ribbons. *Nat. Commun.* **4**, 1734 (2013).

204. Zhang, Q., Lu, Y., Xing, H. G., Koester, S. J. & Koswatta, S. O. Scalability of atomic-thin-body (ATB) transistors based on graphene nanoribbons. *IEEE Electron Device Lett.* **31**, 531–533 (2010).

205. Guo, J., Goasguen, S., Lundstrom, M. & Datta, S. Metal-insulator-semiconductor electrostatics of carbon nanotubes. *Appl. Phys. Lett.* **81**, 1486–1488 (2002).

206. Léonard, F. Crosstalk between nanotube devices: Contact and channel effects. *Nanotechnology* **17**, 2381–2385 (2006).

207. Linden, S. *et al.* Electronic structure of spatially aligned graphene nanoribbons on Au(788). *Phys. Rev. Lett.* **108**, (2012).

208. Ruffieux, P. *et al.* Electronic structure of atomically precise graphene nanoribbons. *ACS Nano* **6**, 6930–6935 (2012).

209. Talirz, L. *et al.* On-Surface Synthesis and Characterization of 9-Atom Wide Armchair Graphene Nanoribbons. *ACS Nano* **11**, 1380–1388 (2017).

210. Senkovskiy, B. V. *et al.* Making Graphene Nanoribbons Photoluminescent. *Nano Lett.* **17**, 4029–4037 (2017).

211. Passi, V. *et al.* Field-Effect Transistors Based on Networks of Highly Aligned, Chemically Synthesized N = 7 Armchair Graphene Nanoribbons. *ACS Appl. Mater. Interfaces* **10**, 9900–9903 (2018).

212. Denk, R. *et al.* Exciton-dominated optical response of ultra-narrow graphene nanoribbons. *Nat. Commun.* **5**, (2014).

213. Bennett, P. B. *et al.* Bottom-up graphene nanoribbon field-effect transistors. *Appl. Phys.*

Lett. **103**, (2013).

214. Ohtomo, M., Sekine, Y., Hibino, H. & Yamamoto, H. Graphene nanoribbon field-effect transistors fabricated by etchant-free transfer from Au(788). *Appl. Phys. Lett.* **112**, (2018).

215. Llinas, J. P. *et al.* Short-channel field-effect transistors with 9-atom and 13-atom wide graphene nanoribbons. *Nat. Commun.* **8**, (2017).

216. Han, M. Y., Özyilmaz, B., Zhang, Y. & Kim, P. Energy band-gap engineering of graphene nanoribbons. *Phys. Rev. Lett.* **98**, (2007).

217. Chen, Z., Lin, Y. M., Rooks, M. J. & Avouris, P. Graphene nano-ribbon electronics. *Phys. E Low-Dimensional Syst. Nanostructures* **40**, 228–232 (2007).

218. Sprinkle, M. *et al.* Scalable templated growth of graphene nanoribbons on SiC. *Nat. Nanotechnol.* **5**, 727–731 (2010).

219. Kato, T. & Hatakeyama, R. Site- and alignment-controlled growth of graphene nanoribbons from nickel nanobars. *Nat. Nanotechnol.* **7**, 651–656 (2012).

220. Solís-Fernández, P., Yoshida, K., Ogawa, Y., Tsuji, M. & Ago, H. Dense arrays of highly aligned graphene nanoribbons produced by substrate-controlled metal-assisted etching of graphene. *Adv. Mater.* **25**, 6562–6568 (2013).

221. Jiao, L., Zhang, L., Ding, L., Liu, J. & Dai, H. Aligned graphene nanoribbons and crossbars from unzipped carbon nanotubes. *Nano Res.* **3**, 387–394 (2010).

222. Joo, Y., Brady, G. J., Arnold, M. S. & Gopalan, P. Dose-controlled, floating evaporative self-Assembly and alignment of semiconducting carbon nanotubes from organic solvents. *Langmuir* **30**, 3460–3466 (2014).

223. Jinkins, K. R., Chan, J., Jacobberger, R. M., Berson, A. & Arnold, M. S. Substrate-Wide Confined Shear Alignment of Carbon Nanotubes for Thin Film Transistors. *Adv. Electron. Mater.* **5**, 1800593 (2019).

224. Kiraly, B. *et al.* Sub-5 nm, globally aligned graphene nanoribbons on Ge(001). *Appl. Phys. Lett.* **108**, (2016).

225. Way, A. J., Jacobberger, R. M. & Arnold, M. S. Seed-Initiated Anisotropic Growth of Unidirectional Armchair Graphene Nanoribbon Arrays on Germanium. *Nano Lett.* **18**, 898–906 (2018).

226. Lee, J. H. *et al.* Wafer-scale growth of single-crystal monolayer graphene on reusable hydrogen-terminated germanium. *Science* **344**, 286–289 (2014).

227. Dai, J. *et al.* How Graphene Islands Are Unidirectionally Aligned on the Ge(110) Surface. *Nano Lett.* **16**, 3160–3165 (2016).

228. Vlassiouk, I. *et al.* Role of Hydrogen in Chemical Vapor Deposition Growth of Large Single-Crystal Graphene. *ACS Nano* **5**, 6069–6076 (2011).

229. Jacobberger, R. M. & Arnold, M. S. Graphene Growth Dynamics on Epitaxial Copper Thin Films. *Chem. Mater.* **25**, 871–877 (2013).

230. Ma, T. *et al.* Edge-controlled growth and kinetics of single-crystal graphene domains by chemical vapor deposition. *Proc. Natl. Acad. Sci.* **110**, 20386–20391 (2013).

231. Tao, L. *et al.* Synthesis of high quality monolayer graphene at reduced temperature on hydrogen-enriched evaporated copper (111) films. *ACS Nano* **6**, 2319–2325 (2012).

232. Jacobberger, R. M. *et al.* Tailoring the growth rate and surface facet for synthesis of high-quality continuous graphene films from CH4 at 750 °c via chemical vapor deposition. *J. Phys. Chem. C* **119**, 11516–11523 (2015).

233. Li, X. *et al.* Graphene films with large domain size by a two-step chemical vapor deposition process. *Nano Lett.* **10**, 4328–4334 (2010).

234. Tegenkamp, C., Wollschläger, J., Pfnür, H., Meyer zu Heringdorf, F. J. & Horn-von Hoegen, M. Step and kink correlations on vicinal Ge(100) surfaces investigated by electron diffraction. *Phys. Rev. B* **65**, 1–8 (2002).

235. Sutter, P. W., Flege, J.-I. & Sutter, E. A. Epitaxial graphene on ruthenium. *Nat. Mater.* **7**, 406–411 (2008).

236. Chen, L. *et al.* Step-Edge-Guided Nucleation and Growth of Aligned WSe2 on Sapphire via a Layer-over-Layer Growth Mode. *ACS Nano* **9**, 8368–8375 (2015).

237. McElhinny, K. M., Jacobberger, R. M., Zaug, A. J., Arnold, M. S. & Evans, P. G. Graphene-induced Ge (001) surface faceting. *Surf. Sci.* **647**, 90–95 (2016).

238. Kiraly, B. *et al.* Electronic and Mechanical Properties of Graphene-Germanium Interfaces Grown by Chemical Vapor Deposition. *Nano Lett.* **15**, 7414–7420 (2015).

239. Artyukhov, V. I., Liu, Y. & Yakobson, B. I. Equilibrium at the edge and atomistic mechanisms of graphene growth. *Proc. Natl. Acad. Sci.* **109**, 15136–15140 (2012).

240. Patera, L. L. *et al.* Real-time imaging of adatom-promoted graphene growth on nickel. *Science* **359**, 1243–1246 (2018).

241. Li, P., Li, Z. & Yang, J. Dominant Kinetic Pathways of Graphene Growth in Chemical Vapor Deposition: The Role of Hydrogen. *J. Phys. Chem. C* **121**, 25949–25955 (2017).

242. Lee, J. S. *et al.* Origin of gate hysteresis in carbon nanotube field-effect transistors. *J. Phys. Chem. C* **111**, 12504–12507 (2007).

243. Kim, W. *et al.* Hysteresis caused by water molecules in carbon nanotube field-effect transistors. *Nano Lett.* **3**, 193–198 (2003).

244. Li, X., Wang, X., Zhang, L., Lee, S. & Dai, H. Chemically derived, ultrasmooth graphene nanoribbon semiconductors. *Science* **319**, 1229–1232 (2008).

245. Hazeghi, A., Krishnamohan, T. & Wong, H. S. P. Schottky-barrier carbon nanotube field-effect transistor modeling. *IEEE Trans. Electron Devices* **54**, 439–445 (2007).

246. Bai, J., Duan, X. & Huang, Y. Rational fabrication of graphene nanoribbons using a nanowire etch mask. *Nano Lett.* **9**, 2083–2087 (2009).

247. Liao, L. *et al.* Top-gated graphene nanoribbon transistors with ultrathin high- κ dielectrics. *Nano Lett.* **10**, 1917–1921 (2010).

248. Ponomarenko, L. A. *et al.* Chaotic dirac billiard in graphene quantum dots. *Science* **320**, 356–358 (2008).

249. Pan, Z., Liu, N., Fu, L. & Liu, Z. Wrinkle engineering: A new approach to massive graphene nanoribbon arrays. *J. Am. Chem. Soc.* **133**, 17578–17581 (2011).

250. Yang, R. *et al.* An anisotropic etching effect in the graphene basal plane. *Adv. Mater.* **22**, 4014–4019 (2010).

251. Wang, X. & Dai, H. Etching and narrowing of graphene from the edges. *Nat. Chem.* **2**, 661–665 (2010).

252. Xie, L., Jiao, L. & Dai, H. Selective etching of graphene edges by hydrogen plasma. *J. Am. Chem. Soc.* **132**, 14751–14753 (2010).

253. Wang, X. *et al.* Room-temperature all-semiconducting sub-10-nm graphene nanoribbon field-effect transistors. *Phys. Rev. Lett.* **100**, (2008).

254. Wang, X. *et al.* N-doping of graphene through electrothermal reactions with ammonia. *Science* **324**, 768–771 (2009).

255. Jiao, L., Zhang, L., Wang, X., Diankov, G. & Dai, H. Narrow graphene nanoribbons from carbon nanotubes. *Nature* **458**, 877–880 (2009).

256. Horcas, I. *et al.* WSXM: A software for scanning probe microscopy and a tool for nanotechnology. *Rev. Sci. Instrum.* **78**, (2007).

257. Grimme, S. Semiempirical GGA-type density functional constructed with a long-range dispersion correction. *J. Comput. Chem.* **27**, 1787–1799 (2006).

258. Way, A. J. *et al.* Anisotropic Synthesis of Armchair Graphene Nanoribbon Arrays from Sub-5 nm Seeds at Variable Pitches on Germanium. *J. Phys. Chem. Lett.* **10**, 4266–4272

(2019).

259. Way, A. J., Jacobberger, R. M. & Arnold, M. S. Seed-Initiated Anisotropic Growth of Unidirectional Armchair Graphene Nanoribbon Arrays on Germanium. *Nano Lett.* **18**, 898–906 (2018).

260. Way, A. J., Saraswat, V., Jacobberger, R. M. & Arnold, M. S. Rotational self-alignment of graphene seeds for nanoribbon synthesis on Ge(001) via chemical vapor deposition. *APL Mater.* **8**, 091104 (2020).

261. Zhang, X., Xu, Z., Hui, L., Xin, J. & Ding, F. How the Orientation of Graphene Is Determined during Chemical Vapor Deposition Growth. *J. Phys. Chem. Lett.* **3**, 2822–2827 (2012).

262. Jacobberger, R. M. *et al.* Alignment of semiconducting graphene nanoribbons on vicinal Ge(001). *Nanoscale* **11**, 4864–4875 (2019).

263. Vroonhoven, E. van, Zandvliet, H. J. W. & Poelsema, B. A quantitative evaluation of the dimer concentration during the (2×1)-(1×1) phase transition on Ge(001). *Surf. Sci.* **574**, L23–L28 (2005).

264. M.W. Chase Jr. *NIST-JANAF Themochemical Tables, Fourth Edition*. *J. Phys. Chem. Ref. Data* (1998).

265. Saito, R., Dresselhaus, G. & Dresselhaus, M. S. *Physical Properties of Carbon Nanotubes*. *Physical Properties of Carbon Nanotubes* (1998). doi:10.1142/p080

266. Sundararaman, R., Goddard, W. A. & Arias, T. A. Grand canonical electronic density-functional theory: Algorithms and applications to electrochemistry. *J. Chem. Phys.* **146**, 114104 (2017).

267. Göltl, F. *et al.* Exploring driving forces for length growth in graphene nanoribbons during chemical vapor deposition of hydrocarbons on Ge(0 0 1) via kinetic Monte Carlo simulations. *Appl. Surf. Sci.* **527**, (2020).

268. Dumesic, J. A., Rudd, D. F., Aparicio, L. M., Rekoske, J. E. & Trevino, A. A. *The Microkinetics of Heterogeneous Catalysis*. (American Chemical Society, 1993).

269. Grabow, L. C. & Mavrikakis, M. Mechanism of Methanol Synthesis on Cu through CO 2 and CO Hydrogenation. *ACS Catal.* **1**, 365–384 (2011).

270. Kropp, T. & Mavrikakis, M. Transition Metal Atoms Embedded in Graphene : How Nitrogen. *ACS Catal.* **9**, 6864–6868 (2019).

271. Xu, L., Stangland, E. E. & Mavrikakis, M. Ethylene versus ethane : A DFT-based selectivity descriptor for efficient catalyst screening. *J. Catal.* **362**, 18–24 (2018).

272. Greeley, J. & Mavrikakis, M. Alloy catalysts designed from first principles. *Nat. Mater.* **3**, 810–815 (2004).

273. Hammer, B., Hansen, L. & Nørskov, J. Improved adsorption energetics within density-functional theory using revised Perdew-Burke-Ernzerhof functionals. *Phys. Rev. B* **59**, 7413–7421 (1999).

274. Wellendorff, J. *et al.* Density functionals for surface science: Exchange-correlation model development with Bayesian error estimation. *Phys. Rev. B* **85**, 32–34 (2012).

275. Perdew, J. P., Ruzsinszky, A., Csonka, G. I., Constantin, L. A. & Sun, J. Workhorse semilocal density functional for condensed matter physics and quantum chemistry. *Phys. Rev. Lett.* **103**, 10–13 (2009).

276. Klimes, J., Bowler, D. & Michaelides, A. Chemical accuracy for the van der Waals density functional. *J. Phys. Condens. Matter* **22**, 022201 (2010).

277. Schimka, L. *et al.* Accurate surface and adsorption energies from many-body perturbation theory. *Nat. Mater.* **9**, 741–744 (2010).

278. Cheng, J., Libisch, F. & Carter, E. A. Dissociative Adsorption of O2 on Al(111): The Role of Orientational Degrees of Freedom. *J. Phys. Chem. Lett.* **6**, 1661–1665 (2015).

279. Göltl, F., Houriez, C., Guitou, M., Chambaud, G. & Sautet, P. Importance of a Nonlocal Description of Electron–Electron Interactions in Modeling the Dissociative Adsorption of H 2 on Cu(100). *J. Phys. Chem. C* **118**, 5374–5382 (2014).

280. Medford, A. J. *et al.* Assessing the reliability of calculated catalytic ammonia synthesis rates. *Science* **345**, 197–200 (2014).

281. Sutton, J. E., Guo, W., Katsoulakis, M. A. & Vlachos, D. G. Effects of correlated parameters and uncertainty in electronic-structure-based chemical kinetic modelling. *Nat. Chem.* **8**, 331–337 (2016).

282. Zaera, F. The Surface Chemistry of Hydrocarbons on Transition Metal Surfaces: A Critical Review. *Isr. J. Chem.* **38**, 293–311 (1998).

283. Zaera, F. Surface chemistry of hydrocarbon fragments on transition metals: Towards understanding catalytic processes. *Catal. Letters* **91**, 1–10 (2003).

284. Zaera, F. An Organometallic Guide to the Chemistry of Hydrocarbon Moieties on Transition Metal Surfaces. *Chem. Rev.* **95**, 2651–2693 (1995).

285. Gautier, S., Steinmann, S. N., Michel, C., Fleurat-lessard, P. & Sautet, P. Molecular adsorption at Pt(111). How accurate are DFT functionals? *Phys. Chem. Chem. Phys.* **17**, 28921–28930 (2015).

286. Michaelides, A. & Hu, P. Methyl chemisorption on Ni (111) and C-H-M multicentre bonding: a density functional theory study. *Surf. Sci.* **437**, 362–376 (1999).

287. Yang, Q. Y., Maynard, K. J., Johnson, A. D. & Ceyer, S. T. The structure and chemistry of CH3and CH radicals adsorbed on Ni(111). *J. Chem. Phys.* **102**, 7734–7749 (1995).

288. Carey, S. J., Zhao, W., Frehner, A., Campbell, C. T. & Jackson, B. Energetics of Adsorbed Methyl and Methyl Iodide on Ni(111) by Calorimetry: Comparison to Pt(111) and Implications for Catalysis. *ACS Catal.* **7**, 1286–1294 (2017).

289. Blaylock, D. W., Ogura, T., Green, W. H. & Beran, G. J. O. Computational Investigation of Thermochemistry and Kinetics of Steam Methane Reforming on Ni(111) under Realistic Conditions. *J. Phys. Chem. C* **113**, 4898–4908 (2009).

290. Kresse, G. & Hafner, J. Ab initio molecular dynamics for open-shell transition metals. *Phys. Rev. B* **48**, 13115–13118 (1993).

291. Perdew, J. P. *et al.* Atoms, molecules, solids, and surfaces: Applications of the generalized gradient approximation for exchange and correlation. *Phys. Rev. B* **46**, 6671–6687 (1992).

292. Tkatchenko, A. & Scheffler, M. Accurate molecular van der Waals interactions from ground-state electron density and free-atom reference data. *Phys. Rev. Lett.* **102**, 073005 (2009).

293. Steinmann, S. N. & Corminboeuf, C. A generalized-gradient approximation exchange hole model for dispersion coefficients. *J. Chem. Phys.* **134**, (2011).

294. Dion, M., Rydberg, H., Schröder, E., Langreth, D. C. & Lundqvist, B. I. Van der Waals density functional for general geometries. *Phys. Rev. Lett.* **92**, 246401–1 (2004).

295. Lee, K., Murray, É. D., Kong, L., Lundqvist, B. I. & Langreth, D. C. Higher-accuracy van der Waals density functional. *Phys. Rev. B* **82**, 3–6 (2010).

296. Klimeš, J. & Michaelides, A. Perspective: Advances and challenges in treating van der Waals dispersion forces in density functional theory. *J. Chem. Phys.* **137**, (2012).

297. Makov, G. & Payne, M. Periodic boundary conditions in ab initio calculations. *Phys. Rev. B* **51**, 4014–4022 (1995).

298. Sheppard, D., Terrell, R. & Henkelman, G. Optimization methods for finding minimum energy paths. *J. Chem. Phys.* **128**, 1–10 (2008).

299. Chen, B. W. J. & Mavrikakis, M. How coverage influences thermodynamic and kinetic isotope effects for H2/D2 dissociative adsorption on transition metals. *Catal. Sci. Technol.* **10**, 671–689 (2020).

300. Che, F., Zhang, R., Hensley, A. J., Ha, S. & McEwen, J.-S. Density functional theory studies

of methyl dissociation on a Ni(111) surface in the presence of an external electric field. *Phys. Chem. Chem. Phys.* **16**, 2399–2410 (2014).

301. *NIST Chemistry WebBook, NIST Standard Reference Database Number 69*. (National Institute of Standards and Technology, Gaithersburg MD, 20899).

302. Ku, H. H. Notes on the use of propagation of error formulas. *J. Res. Natl. Bur. Stand. Sect. C Eng. Instrum.* **70C**, 263 (1966).

303. Norskov, J. K., Abild-pedersen, F., Studt, F. & Bligaard, T. Density functional theory in surface chemistry and catalysis. *Proc. Natl. Acad. Sci.* **108**, 937–943 (2011).

304. Campbell, C. T. private communication.

305. Christmann, K., Behm, R. J., Ertl, G., Van Hove, M. A. & Weinberg, W. H. Chemisorption geometry of hydrogen on Ni(111): Order and disorder. *J. Chem. Phys.* **70**, 4168–4184 (1979).

306. Ruscic, B. *et al.* Introduction to Active Thermochemical Tables : Several " Key " Enthalpies of Formation. *J. Phys. Che* **108**, 9979–9997 (2004).

307. Hensley, A. J. R. *et al.* DFT-Based Method for More Accurate Adsorption Energies: An Adaptive Sum of Energies from RPBE and vdW Density Functionals. *J. Phys. Chem. C* **121**, 4937–4945 (2017).

308. Wellendorff, J. *et al.* A benchmark database for adsorption bond energies to transition metal surfaces and comparison to selected DFT functionals. *Surf. Sci.* **640**, 36–44 (2015).

309. Bai, Y., Kirvassilis, D., Xu, L. & Mavrikakis, M. Atomic and molecular adsorption on Ni(111). *Surf. Sci.* **accepted f**, (2018).

310. Lee, M. B., Yang, Q. Y. & Ceyer, S. T. Dynamics of the activated dissociative chemisorption of CH4and implication for the pressure gap in catalysis: A molecular beam-high resolution electron energy loss study. *J. Chem. Phys.* **87**, 2724–2741 (1987).

311. Behm, R. J., Christmann, K., Ertl, G., Van Hove, M. A. & Weinberg, W. H. Chemisorption geometry of hydrogen on a Ni(111) surface. *Surf. Sci.* **89**, 403 (1979).

312. Reuter, K. & Scheffler, M. Composition, structure, and stability of RuO2(110) as a function of oxygen pressure. *Phys. Rev. B* **65**, 1–11 (2002).

313. Greeley, J., Nørskov, J. K. & Mavrikakis, M. Electronic Structure and Catalysis on Metal Surfaces. *Annu. Rev. Phys. Chem.* **53**, 319–348 (2002).

314. Yu, Q. *et al.* Control and characterization of individual grains and grain boundaries in graphene grown by chemical vapour deposition. *Nat. Mater.* **10**, 443–449 (2011).

315. Way, A. J., Jacobberger, R. M. & Arnold, M. S. Seed-Initiated Anisotropic Growth of Unidirectional Armchair Graphene Nanoribbon Arrays on Germanium. *Nano Lett.* **18**, 898–906 (2018).